

AD-A210 215

FILE 102

4

OFFICE OF NAVAL RESEARCH
Contract N00014-87-K-0514

Technical Report
June, 1989

PARTICLE EMISSION AND CHARGING EFFECTS
INDUCED BY FRACTURE

J. Thomas Dickinson

DTIC
ELECTE
JUN 26 1989
S DCS D

Washington
State University

DEPARTMENT OF PHYSICS

DISTRIBUTION STATEMENT A

Approved for public release
Distribution Unlimited

89

6

26

029

4

OFFICE OF NAVAL RESEARCH
Contract N00014-87-K-0514

Technical Report
June, 1989

PARTICLE EMISSION AND CHARGING EFFECTS
INDUCED BY FRACTURE

J. Thomas Dickinson

Department of Physics
Washington State University
Pullman, WA 99164-2814

Reproduction in whole or in part is permitted for any purpose of the United States Government.

Approved for public release; distribution unlimited.

DTIC
ELECTE
JUN 26 1989
S D

SECURITY CLASSIFICATION OF THIS PAGE

REPORT DOCUMENTATION PAGE

Form Approved
OMB No. 0704-0188

1a. REPORT SECURITY CLASSIFICATION UNCLASSIFIED			1b. RESTRICTIVE MARKINGS		
2a. SECURITY CLASSIFICATION AUTHORITY			3. DISTRIBUTION / AVAILABILITY OF REPORT APPROVED FOR PUBLIC RELEASE DISTRIBUTION UNLIMITED		
2b. DECLASSIFICATION / DOWNGRADING SCHEDULE					
4. PERFORMING ORGANIZATION REPORT NUMBER(S) FRACTO89			5. MONITORING ORGANIZATION REPORT NUMBER(S)		
6a. NAME OF PERFORMING ORGANIZATION FRACTURE LABORATORY DEPARTMENT OF PHYSICS		6b. OFFICE SYMBOL (if applicable)	7a. NAME OF MONITORING ORGANIZATION OFFICE OF NAVAL RESEARCH PROPULSION AND ENERGETICS PROGRAM		
6c. ADDRESS (City, State, and ZIP Code) WASHINGTON STATE UNIVERSITY PULLMAN, WA 99164-2814			7b. ADDRESS (City, State, and ZIP Code) 800 NORTH QUINCY STREET ARLINGTON, VA 22217		
8a. NAME OF FUNDING / SPONSORING ORGANIZATION		8b. OFFICE SYMBOL (if applicable)	9. PROCUREMENT INSTRUMENT IDENTIFICATION NUMBER CONTRACT N00014-87-K-0514		
8c. ADDRESS (City, State, and ZIP Code)			10. SOURCE OF FUNDING NUMBERS		
			PROGRAM ELEMENT NO.	PROJECT NO.	TASK NO.
					WORK UNIT ACCESSION NO.
11. TITLE (Include Security Classification) PARTICLE EMISSION AND CHARGING EFFECTS INDUCED BY FRACTURE					
12. PERSONAL AUTHOR(S) J. THOMAS DICKINSON					
13a. TYPE OF REPORT		13b. TIME COVERED FROM 6/1/87 TO 6/30/89		14. DATE OF REPORT (Year, Month, Day) JUNE 15, 1989	
15. PAGE COUNT XXX					
16. SUPPLEMENTARY NOTATION					
17. COSATI CODES			18. SUBJECT TERMS (Continue on reverse if necessary and identify by block number)		
FIELD	GROUP	SUB-GROUP	CRACK PROPAGATION; FRACTURE; PARTICLE EMISSION; FRACTO-EMISSION; ENERGETIC MATERIALS; RDX; RADIATION DAMAGE; ESD; ELECTRICAL BREAKDOWN; MICROCRACKING; LASER ABLATION; SURFACE CHARGE; FRACTOGRAPHY; CRYSTAL DEFECTS; SCANNING TUNNELING MICROSCOPY; ATOMIC FORCE MICROSCOPY. ()		
19. ABSTRACT (Continue on reverse if necessary and identify by block number) A series of studies involving the physical consequences of deformation and fracture of materials are presented. These measurements include fracto-emission (FE) experiments on model rocket propellant, two studies on properties of ejecta (macroscopic particles) from materials including explosive crystals, fracture induced electrical breakdown, the detection of free charge carriers accompanying fracture in single crystal Si, FE studies on polymers, adhesives, single crystal and amorphous inorganics, studies of fracture surfaces using scanning tunneling microscopy and atomic force microscopy, and two studies on the interaction of intense uv laser radiation with materials. In an appendix, we present a review article on fracto-emission from interfacial failure.					
20. DISTRIBUTION / AVAILABILITY OF ABSTRACT <input type="checkbox"/> UNCLASSIFIED/UNLIMITED <input type="checkbox"/> SAME AS RPT <input type="checkbox"/> DTIC USERS			21. ABSTRACT SECURITY CLASSIFICATION UNCLASSIFIED		
22a. NAME OF RESPONSIBLE INDIVIDUAL R. S. MILLER			22b. TELEPHONE (Include Area Code) 202 696-4404		22c. OFFICE SYMBOL

TABLE OF CONTENTS

I.	Technical Summary	1
II.	Introduction	1
III.	Electron and Photon Emission from the Fracture of Metal-Elastomer Interfaces	5
IV.	Production and Properties of Ejecta Released by Fracture of Materials	39
V.	Electrical Charge Measurements on Ejecta from Impact Loading of Explosive Crystals	70
VI.	Fracto-Emission Induced Electrical Breakdown in Vacuum	87
VII.	Production of Free Charge Carriers During Fracture of Single Crystal Silicon	107
VIII.	Photon Emission as a Probe of Chaotic Processes Accompanying Fracture	117
IX.	Properties of the Photon Emission Accompanying the Peeling of a Pressure Sensitive Adhesive	144
X.	Autographs from Peeling Fiber Reinforced Pressure Sensitive Adhesives: Correlation with Failure Mechanisms	165
XI.	The Role of Damage in Post-Emission of Electrons from Cleavage Surfaces of Single Crystal LiF	184
XII.	Anisotropy Effects on Fracto-Emission from MgF ₂ Single Crystals	203
XIII.	Fracto-Emission from Fused Silica and Sodium Silicate Glasses	217
XIV.	Positive Ion Emission from the Fracture of Fused Silica	239
XV.	Fracto-Emission from High Density Polyethylene: Consequences of Abrasion	255
XVI.	The Interaction of Excimer Laser Ultraviolet Radiation with KAPTON-H under Mechanical Stress	270
XVII.	The Interaction of UV Excimer Laser Light with Sodium Trisilicate	284
XVIII.	Additional Work	316
APPENDIX I.	Fracto-Emission from Interfacial Failure	326
APPENDIX II.	Recent Presentations and Publications	340

I. TECHNICAL SUMMARY

When a crack propagates through a material, a number of elementary processes can occur which lead to departures from equilibrium. These processes involve breaking chemical and physical bonds, the motion of atoms, molecules, electrons, and ionic species in the vicinity of the crack tip, and production of localized heating due to plastic deformation. The consequences of such microscopic processes can result in surface and near surface defects being created, non-equilibrium surface stoichiometry and charge distributions (involving electrons, holes, point defects and radicals, as well as elementary (and transient) excitations such as excitons, excited states of color centers, and various vibrational excitations. We have shown that a number of emissions can result from these circumstances; we call such emission *fracto-emission*, which includes the emission of particles such as electrons, \pm ions, and neutral species, and photons before, during, and following the propagation of a crack in a stressed material. The major goals addressed in our emission work are: (1) characterization of *fracto-emission*, (2) improving our understanding of the emission mechanisms in terms of microscopic processes accompanying fracture (idealized systems), and (3) applications of *fracto-emission* to understand the energetics of crack growth and its influence on the physical and chemical state of the fracture and the near fracture surface. The characterization studies include identification of specific emitted species, energy distribution measurements, studies of the fractal features of emission from brittle materials, and determination of the spatial distribution of the emission (through imaging). Mechanism studies include fundamental studies of temperature dependences of the emission, modification of excitations via optical stimulation, experiments on well defined interfacial failure, and time resolved spectroscopy of the photon emission. The application studies include experiments on model inorganic crystalline materials and propellents, energetic crystalline materials, and elastomers/polymers of interest to the Navy.

A new emphasis in our work is to connect the *fracto-emission* work with the microscopic features of the newly created fracture surface. We are employing the scanning tunneling microscope (STM) in conjunction with other microscopies to correlate *fracto-emission* properties to determine the topographical nature of the fracture surface over a wide range of sizes. Such information should aid in the development of atomic-scale models of deformation and fracture in brittle materials. Of particular interest is the use of topography to examine the consequences of cracks moving into regions of high densities of dislocations. Furthermore, we are developing an atomic force microscope (AFM) to allow such studies to be done routinely on insulating materials.

We are also studying the interaction of radiation with materials under mechanical stress to explore possible synergisms in damage mechanisms due to they way mechanical and radiative energy couples. Recently, we have also been studying the emission products of UV laser irradiation on including a glassy inorganic material and RDX single crystals. The latter is of particular interest in terms of the decomposition paths and resulting plasma interactions the products can undergo. A somewhat esoteric application of this work is the potential use of lasers for micromachining explosive crystals into intricate shapes with submicron resolution.

II. INTRODUCTION

Model Rocket Propellant Studies: We have completed a collaborative study with Heidi Stacer, Air Force Aerospace Laboratories, involving the *fracto-emission* from binders filled with small aluminum particles (Section III). Of particular interest were correlations of electron, photon, and radiowave emissions with the composition of the filled binders *during* fracture. The failure modes were also determined using the SEM. We were able to observe profound effects on the *fracto-emission* due to the presence of a metallic filler. This work has been submitted to J. Rubber Chem. and Technol.

Properties of Ejecta Produced by Fracture of Materials: We have examined ejecta (particles in the size range 0.1 to 500 μm) which are released by fracture of a variety of materials (Section IV). The ejecta from most non-metallic materials are electrically charged and frequently have high velocities. The amount of ejecta produced depends on the material and the conditions of fracture. For unfilled glassy polymers, the ejecta are produced in regions of fast-hackled fracture. Detailed measurements have been made on the ejecta mass and size distributions from the fracture of composites. From these measurements the total particle surface area can be estimated and are found to be comparable to or greater than the cross-sectional area of the fractured samples. Thus, the ejecta should be a consideration in the analysis of surface energy and other parameters from fractographic analysis.

Properties of Ejecta From Impact Loading of Explosive Crystals: We discuss in Section V a series of measurements on the size distributions, approximate velocities, and electric charge contained on the ejecta produced by impact loading of small single crystals of PETN, RDX, and HMX, all tested below ignition. The PETN shows a relatively high degree of charge; RDX and HMX show very little charge. The PETN is known to be piezoelectric, which may explain why its ejecta exhibits charge. We confirmed the detection of radiowave emission (due to discharges occurring during crushing) on the PETN alone, again suggesting that charge separation was occurring. The importance of charge separation and electronic excitations in the fracture of energetic materials relates to potential detonation mechanisms relevant to solid rocket propellants. This work will appear in J. Mat. Sci.

Fracto-Emission Induced Electrical Breakdown in Vacuum: In Section VI we examine the consequences of fracturing materials between two planar electrodes across which we apply a voltage between 100 V and 5.5 kV. We show that the emission of charged particles during and following fracture can induce electrical breakdown. These studies have relevancy to certain ESD problems where fracture occurs (including during application of high E fields and during high energy discharges). This work has been submitted to the IEEE Transactions on Electrical Insulation.

Creation of Free Charge Carriers with Fracture: We present a study on the changes in conductivity in single crystal silicon due to a propagating crack in Section VII. We observed rapid increases in conductivity due to the production of free charge carriers during crack growth. The band gap of Si is 1.1 eV, which appears to be bridged via electronic excitations induced by the bond breaking at the crack tip. This is the first measurement of this kind and offers insight into the types of mechanically induced excitations that can occur in crystalline materials during fracture. These results appeared in Physical Review Letters 59, 2795 (1987). Currently, we are preparing samples to repeat these experiments on single crystal Ge which has a bandgap of 0.67 eV and therefore may result in more intense free carrier production.

Evidence of Chaos in the Photon Emission (phE) from Fracture: In Section VIII we examine the fluctuations in the photons (acquired at 10 ns intervals) accompanying fracture of an epoxy and single crystal MgO and found that these signals show *chaotic* as opposed to stochastic, random behavior. The evidence for deterministic chaos comes from analysis of the autocorrelation function, the Fourier transform, a correlation integral (Grassberger and Procaccia), and the fractal box dimension. We have also proven the existence of a positive Lyapunov exponent and the presence of a low dimensional attractor. The fracture surfaces of this epoxy are shown to be fractal with *equivalent* fractal dimension. Thus, the dynamic process of creating a fracture surface results in topographical features which are simultaneously reflected in the intensity variations of the photons emitted. We were not able to determine the fractal dimension of the MgO (should be quite low) but did find that the photon emission was chaotic. The relation of such parameters as fracture toughness and other measures of dissipation to these photon emission correlation parameters may prove very useful for the application of phE measurements to the characterization of materials. It should be emphasized that recent work by Mecholsky and Passoja (e.g., J. Am. Cer. Soc. 72, 60 (1989)) have shown a strong correlation of fractal dimension of the fracture surfaces with the corresponding fracture toughness, thus providing us with strong motivation to make links to fracto-emission properties. This article will appear in J. Mat. Research.

Spectra of Light Emitted During Peeling of an Adhesive Tape: In Section IX we study the visible light emitted from the region near the detachment zone during the peeling of pressure sensitive adhesives. This photon emission due to adhesive failure is a unique form of *triboluminescence*. We investigate the properties of this light from the peeling of a filament tape with a natural rubber-resin adhesive from its backing at various peel speeds. We show conclusively that small electrostatic discharges are the major source of the radiation. Total intensity vs time measurements show that the light consists of very intense bursts with typical duration of 50 ns which frequently induce additional discharges for times as long as 50-100 μ s. Time resolved spectra of these emission show them to be dominated by the line spectrum of molecular nitrogen for both the initial bursts and those that follow in the next 0.1-100 μ s. Thus, the "after-emission" is not due to phosphorescence of the polymer(s), but due to these additional electrostatic discharges. This work appeared J. Adhesion, 25, 63 (1988).

Autographs of Photon Emission from Adhesive Failure in a Composite Tape: A study utilizing a very unique method for producing contact prints (autographs) of the photon emission produced

during extremely slow peeling of a composite tape from Polaroid photographic film is presented in Section X. We continue to see direct evidence of small electrostatic discharges which occur in this type of fracture involving interfacial failure. The failure mechanism of this particular tape involves fracture of the reinforcing glass filaments which results in fluctuations in the microscopic detachment rate. This produces modulations in the photon emission corresponding to several orders of magnitude. These results will appear in J. Adhesion.

Damage and Electron Emission in the Cleavage of Single Crystal LiF: In the production of cleavage surfaces of LiF single crystals, we have discovered that the region of the crystal interacting strongly with the metal cleavage blade is the region of essentially all of the emission for this mode of loading. This work is presented in Section XI. Using scanning techniques, microscopy, and varying loading conditions, we conclude that the damaged region where the cleavage blade and crystal come into contact is extraordinarily "hot" in terms of electron emission. Macroscopic particles (ejecta) from the damaged region which frequently cling to the fracture surface are also shown to be highly emissive. In contrast, the "untouched" cleave surface emits little, if any long lasting, intense emission. We propose that the high intensity emission originates from defects created during the production of higher index plane fracture surfaces. This article appeared in J. Appl. Phys. **65**, 1923 (1989).

Fracto-Emission from MgF_2 : Studies of the electron emission produced from the fracture of single crystal MgF_2 were completed in a collaboration with K. C. Yoo (Westinghouse R & D) and R. G. Rosemeier (Brimrose Corporation). This work is described in Section XII. Here we were interested in the role of anisotropic effects due to the crystal structure of MgF_2 . We were able to observe considerable changes in the electron intensity with variation of the dominant orientations of the fracture surfaces. The separation of surfaces with {110} orientation produced typically a factor of 6-10 higher emission intensity than surfaces with {101} orientation. From elastic constant anisotropies, the production of {110} surfaces should require more fracture energy. In addition, we consider the possibility of higher defect densities on the {110} surfaces due to differences in local geometry and instantaneous rates of energy release in the region of the crack tip. This work will appear in Appl. Phys. Lett.

Fracto-Emission from Fused Silica and Sodium Silicate Glasses: Fracto-emission is the emission of photons and particles due to the fracture of materials. This work is described in Section XIII. We present characteristic intensity vs time measurements of photon emission (pHE), electron emission (EE), positive ion emission (PIE), and neutral emission (NE) due to the fracture of fused silica and sodium trisilicate glass. We show, for example, that the trisilicate is a copious emitter of atomic Na and both atomic and molecular oxygen. The pHE, EE, and PIE from the two glasses share a number of properties. This work appeared in J. Vac. Sci. A. **6**, 1084 (1988).

Ion Masses Emitted from Fracture of Fused Silica: Utilizing time-of-flight techniques as well as mass spectroscopy we have succeeded in determining the masses of the positive ions emitted during the fracture of fused silica (SiO_2). This work is presented in Section XIV. The major positive particles emitted (in order of decreasing intensities) are: SiO^+ , Si_2O^+ , Si^+ , and O^+ . We have proposed a sequence of bond breaking events which could lead to such species being liberated. Such species show unambiguously that non-equilibrium processes accompany bond breaking due to fracture. More importantly, in terms of composite fracture, we are obtaining unique signatures for distinguishing the various failure modes. In this case, silica or silica glass fiber fracture would yield Si containing species, whereas organic matrices free of Si would not. To appear in J. Vac. Sci. Tech.

Electron Emission from Abrasion of Polymers: In Section XV we examine previously claimed detection of electrons during deformation of high density polyethylene (prior to failure) and present evidence that this so-called mechano-emission is due to abrasion. Fracture induced excitations, probably involving free-radicals, are the likely cause of this emission; i.e., bond breaking is the initial stimulus. We have shown that electron emission is extremely sensitive to minute amounts of damage created by friction between metal or glass surfaces and high density PE. This work will be submitted to J. Mat. Sci.

Interaction of Excimer Laser Ultraviolet Radiation with KAPTON-H under Mechanical Stress: We examine the response of highly stressed polyimide films to excimer laser radiation (20 ns pulses @ 248 nm wavelength) in vacuum. This work is described in Section XVI. We present changes in

surface topology due to surface/near damage, crack initiation, and eventually crack growth over a wide range of applied stress. We show that the morphology of the stressed material has a significant influence on the resulting damage and suggest that the regions of highest damage are those experiencing the highest local stress. Initial results are also presented on the effect of mechanical stress on yields of the photoablation products ejected from the polymer surface. This work appeared J. Vac. Sci. Tech. A 6, 941 (1988).

Excimer Laser Induced Damage in Sodium Trisilicate Glass: Preliminary to studies of the combined influence of exposure of a glassy material to both mechanical stress and radiation, we have studied the influence of UV Excimer radiation on $\text{Na}_2\text{O} \cdot 3\text{SiO}_2$ glass (see Section XVII). This work was carried out in collaboration with Larry Pederson, Battelle Pacific Northwest Laboratories. We have characterized the damage to the surfaces of this material as well as determination of the type of particles and their velocities due to the pulsed laser bombardment. This includes measurements of the charged particle emission (photoelectrons, \pm ions, and neutral emission -- both ground state and excited) as a function of photon flux. We observe significant removal of matter from the glass (ablation), evidence for laser induced absorption at 248 nm (thus a threshold in exposure for damage to occur), and an electrostatic acceleration of positively charged particles interacting with laser heated electrons (inverse bremsstrahlung) resulting in ~ 30 eV Na atoms in high lying Rydberg states. These studies have very important implications regarding the energy transfer mechanisms of laser light to such surfaces and for describing the details of the ablation process. Careful characterization of these products can be extremely important for the applications of laser ablation to deposition. This work will appear in J. Vac. Sci. A.

Additional Work: In Section XVIII, we present ongoing work that is in preliminary stages. This includes a new set of experiments on the neutral molecule emission from the fracture of polymers. We have measured the kinetic energy of these gases and found them to correspond to temperatures on the order of 450 K. In addition, we present recent new measurements involving Scanning Tunneling Microscope images of fracture surfaces of insulating materials and similar results using a Atomic Force Microscope in a compressive mode.

Fracto-Emission from Interfacial Failure. In Appendix I, a review paper on the emission of particles and photons during and after adhesive failure is given. Recent work on the detection of photons from *embedded interfacial failure* (where the light is produced inside the specimen), and the photons and electrons from the detachment of metal films from treated silicon surfaces are discussed. This paper will appear in the Materials Research Society Proceedings of Symposium J, 1989.

Appendix II presents lists of participants, collaborators and visiting researchers, talks, and publications.



Accession For	
NTIS - CRA&I	<input checked="" type="checkbox"/>
DTIC - TAB	<input type="checkbox"/>
Unpublished	<input type="checkbox"/>
Justification	
By	
Distribution	
Availability Codes	
Dist	Availability for Special
A-1	

III. ELECTRON AND PHOTON EMISSION FROM THE FRACTURE OF METAL-ELASTOMER INTERFACES

J. T. DICKINSON, L. C. JENSEN

DEPARTMENT OF PHYSICS, WASHINGTON STATE UNIVERSITY, PULLMAN, WA 99164-2814, USA

AND

H. STACER

AIR FORCE ASTRONAUTICS LABORATORY, EDWARDS AIR FORCE BASE, CA, USA

SUMMARY

We examine the emission of electrons, photons, and long wavelength electromagnetic radiation accompanying failure of interfaces between two elastomers and aluminum. Interfacial failure on a macroscopic scale is examined for an uncrosslinked polybutadiene as well as a urethane-linked polybutadiene and metal surfaces. We also investigate the fracture of unfilled and metal particle filled urethane-linked polybutadiene. Experimental evidence is given in support of a previously presented model involving fracture induced microdischarges during crack propagation. The effects of variations in strain rate, crack velocity, and matrix crosslinking on the electron emission during the tensile fracture of the metal filled elastomer are also discussed.

INTRODUCTION

During and after fracture of materials one can measure the emission of photons (often called triboluminescence) (1,2) and particles including: electrons, negative and positive ions, and neutral species in both ground and excited states. This emission can often serve as a sensitive probe of crack growth, providing useful information concerning molecular and microscopic events accompanying crack growth and concerning the details of failure modes in a variety of materials. This emission is also of interest in terms of its relation to the electrostatic consequences of bond breaking (e.g., noise generated in sensitive circuits under stress, grinding of materials in confined spaces, mechanical and interfacial effects associated with explosives and solid propellants), the detection of fracture inside the earth's crust, and the transport of atoms and gases in geological systems. For a lengthy list of fracto-emission (FE) references, see Ref. 3.

Past studies of FE (3) have included work on the fracture of oxide coatings on metals, inorganic crystals and glasses, adhesive failure (including composites), organic crystals, neat polymers, and electrical phenomena/breakdown accompanying fracture. A number of investigations have focused on the emission of charged particles and photons from the fracture of materials in vacuum. The origin of electron and photon emission from cohesive fracture is best explained in terms of bond breaking phenomena where non-adiabatic processes occur involving fundamental excitations (e.g., exciton creation and decay), or the creation and recombination of point-like defects and charge carriers (e.g. charge trapping at defects followed by recombination with mobile charge carriers). These processes are initiated by bond breaking resulting in the creation of localized departures from equilibrium. For polymeric systems, the likely analogous participants are free radicals, ionic states (e.g., holes), and electrons all generated by bond

scissions during crack growth. The decay of these excitations can provide the energy necessary for particle or photon emission.

We have proposed a simple model for systems involving *charge separation* during fracture. These systems include piezoelectric materials and a wide variety of composite materials in which fracture involves interfacial failure (e.g., elastomers filled with particles or fibers). The basic features of this model as they relate to the fracture of materials in vacuum are the following:

- (a) During crack propagation, charge separation occurs on the freshly created fracture surfaces.
- (b) Neutral species are emitted into the crack tip region during crack propagation, producing a region of elevated pressure (in the atmosphere, air immediately fills the crack).
- (c) A microdischarge thus occurs during fracture yielding charged particles (generally electrons and positive ions) as well as photons and long wavelength electromagnetic radiation (RE for radiowave emission).
- (d) Static charge on the fracture surfaces leads to acceleration of the emitted electrons, modifying their energy distributions. A large portion of these electrons is pulled back to the surface resulting in a self-bombardment process. This results in the emission of positive and negative ions and excited neutrals via electron stimulated desorption (ESD) (4).
- (e) The bombardment of the fracture surfaces by the discharge products during fracture creates a variety of electronic excitations which can subsequently decay to yield after-emission. Thermally stimulated relaxation involving mobile charge carriers releasing energy at appropriate recombination centers describes very well the emission following fracture.

Different types of pHE have been observed. pHE can occur *prior* to fracture in a number of systems. In some cases, this light is due to microfracture events that precede failure (e.g., dewetting of particles). In single crystal inorganics there is evidence that moving dislocations can generate defects which recombine to yield light. Following fracture, some materials "glow" with characteristic decaying signals, much like phosphorescence. In addition, when charge separation is intense, light from microdischarges is quite evident. Typically, microdischarge events yield sharp spectral lines characteristic of the gases present in the crack tip.

We have previously performed a number of FE studies on elastomers, characterizing the FE from unfilled polybutadiene and styrene-polybutadiene (both crosslinked with dicumyl peroxide) (5,6) and examining the dependence of emission intensities on cross-link density (7). Because of the substantially greater emission intensities from filled elastomers (e.g., filled with small glass beads), we have examined FE from these materials in much greater detail, including the physics of the emission processes and crack speed dependence (8-14). Related to these studies are several works on emission accompanying the peeling of pressure sensitive tapes, many of which utilize elastomeric adhesives (15-20).

There is interest in the fracture properties of particulate filled elastomers and probing the various phenomena which occur before and during failure. Metal filled polymers are important because of their electrical properties and are also an important component of a number of solid fuel rocket propellents.

In this paper we explore the electron and photon emission accompanying the deformation and tensile fracture of urethane-linked polybutadiene, unfilled and filled with small aluminum particles. We will show that significant increases in emission intensity during fracture are observed in the filled vs unfilled material. We present experimental evidence in support of the model described above concerning strong electrostatic effects. We also examine the consequences of variations in strain rate, crack velocity, and elastomer crosslinking on the electron emission. We basically show that fracto-emission is a sensitive indicator of the fracture process and that the

emission is most sensitive to the charge state of the surfaces after fracture both in the peeling of polymers from metal surfaces and in the fracture of particulate filled elastomers.

EXPERIMENTAL

To examine the FE during adhesive and cohesive failure of a macroscopic metal-polymer system, samples were prepared from Diene 35NFA (Firestone Tire and Rubber Co.) and aluminum. Diene 35NFA is a mixture of *cis*- and *trans*-polybutadiene with approximately 1800 monomer units per chain. The 35NFA was dissolved in benzene, cast onto an aluminum foil substrate, and allowed to dry at room temperature to form a thin uniform film approximately 1 mm thick. Strips 20 mm wide by 150 mm long were cut from the sample sheet. A small crack was started by hand at the interface between the metal and the polymer and the resulting edges were secured in stainless steel clamps in a vacuum system so that separation of the clamps resulted in a "T-peel." Other samples were formed in a "butt joint" geometry by pressing one end of a rectangular block of freshly cut 35NFA against an aluminum block (cleaned in solvent) in compressive clamps to form a 10 mm x 5 mm contact surface. A pressure of 5 MPa was applied to the clamps for up to 30 minutes. The surfaces then were pulled apart and the resulting emissions recorded. Both sets of experiments were performed in vacuums of less than 10^{-7} torr to facilitate charged particle detection. All aluminum surfaces described in this paper have been exposed to air and thus have the usual ~ 50 Å native oxide film coating the outside surface.

FE from adhesive and cohesive failure was also studied using metal-filled and unfilled elastomers loaded in tension. The elastomer specimens were made from urethane-linked polybutadiene (ULPBR) by mixing hydroxyl-terminated polybutadiene with 23 to 26 monomer units per chain crosslinked with IPDI (isophorone diisocyanate, 5.6% and 9.27% by weight) and TPB (0.24% by weight) to produce NCO/OH ratios of 1.02 and 1.35. The filled samples contained small aluminum particles of average diameter 10 μm , 30 μm and 60 μm added to the ULPBR in concentrations of 8.5%, 17% and 25.5% by weight for each average particle diameter and both NCO/OH ratios. Notched and unnotched samples, typically 5 x 2 x 12 mm³, were broken in tension in a vacuum system at 10^{-7} torr. The notched samples contained a 1 mm notch in the 5 mm width.

Figure 1 illustrates a typical experimental arrangement. Electron emission (EE) was detected with an appropriately biased channel electron multiplier (CEM), Galileo Electro-Optics model 4821, which produced fast (10-20 ns) pulses with approximately 90% absolute detection efficiency. The gain of this CEM was typically 10^6 - 10^8 electrons per incident particle. The background noise counts ranged from one to ten counts per second. The pulses were amplified with fast current and voltage amplifiers and discriminated for pulse counting on a multichannel scaler. Photon emission (phE) was detected with a Thorn EMI model 9924QB photomultiplier tube (PMT) with a quartz window and a bialkali photosensitive surface. Normally, the PMT was used in the pulse counting mode. The PMT was mounted directly inside the vacuum system and could not be cooled; thus, the background count rate was relatively high, typically 1000 counts/s. The two detectors were normally positioned on opposite sides of the sample, approximately 1 cm from the region of crack growth. Both during and after fracture the newly created surfaces were well separated, providing favorable detection geometry for both charged particles and photons. The load during elongation and fracture was measured with a Sensotec Model 51 load cell, also mounted inside the vacuum system. Elongation (clamp displacement) was measured with a displacement-to-voltage transducer attached to the pulling mechanism outside the vacuum system. Long wavelength electromagnetic radiation (radio emission: RE) emitted during fracture was detected with a 20,000 turn solenoid of #30 magnet wire placed 2 mm from the sample. The coil output was connected to a differential amplifier (80 db common mode rejection) containing both high and low pass filters. This arrangement detects the near-field electromagnetic radiation due to the proximity of the coil to the source. The intensity of these oscillating fields is so weak that we would not be able to detect them at distances of several wavelengths where one sees only the propagating field. Placing an insulating glass plate between the sample and the coil did little to

reduce the intensity or timing of the RE bursts. Thus, the detected signals were due to electromagnetic radiation and not to charged particles reaching the antenna. Emission signals, applied force, and elongation were recorded on a Lecroy 3500 Data Acquisition System at rates varying from 1 μ s to 1 s.

Some fracture events were recorded on video tape with a Sony video camera and viewed in a freeze frame mode, allowing crack propagation to be measured at 17 ms intervals. After fracture, selected samples were gold coated and the fracture surfaces examined in a scanning electron microscope (SEM).

RESULTS AND DISCUSSION

UNCROSSLINKED POLYBUTADIENE DETACHED FROM ALUMINUM

We first present the results of the T-peel experiments involving the separation of uncrosslinked 35NFA material from an aluminum substrate. EE from the peel of a 35NFA sample from an aluminum substrate at a rate of 2.5 mm/s is shown in Fig. 2a. The resulting EE is very small with very little after-emission following detachment. Visual examination of the fracture surfaces revealed that a thin layer of polymer remained on the metal substrate and that tearing had occurred within the elastomer; i.e., the locus of fracture was in the polymer itself, rather than at the interface. This weak emission is typical of cohesive failure of an uncrosslinked polymer. In Fig. 2b we show the EE accompanying the fracture (tearing) of a 35NFA sample strained in tension at a rate of 2.5 mm/s. Elongation of an uncrosslinked polymer can lead to failure with minimal bond breaking, resulting in weak EE during the peel. The small number of bond scission-induced excitations yields miniscule after-emission as well.

To illustrate the difference in emission between adhesive and cohesive failure in a polymer-metal system, peel tests of samples with weaker adhesive bonds were performed. Suitably weak adhesion is displayed by 35NFA-aluminum samples formed by simply pressing the untreated polymer against the metal surface to create a butt joint. For contact times of less than an hour, no evidence of residual polymer on the metal or damage (tearing) of the polymer following failure is observed. Thus, the failure mode can be characterized as interfacial. The resulting EE is quite intense and persists for hundreds of seconds, as shown in Fig. 3. Clearly, the emissions produced by adhesive and cohesive failure of these specimens are quite distinct.

These and other studies (8,13,18) show that the EE intensities from adhesive failure during macroscopic peeling depends on the length of time the surfaces have been in contact, the rate of detachment, the applied pressure (how hard the surfaces are pushed together—this is most likely a contact area effect (21-23)), and the type of metal used. The longer the contact between the polymer and the metal surface the larger the emission during the peeling process. Several minutes of contact are required to produce a strong emission signal. The increase in EE with contact time levels off after about 30 minutes. This is consistent with contact charging at the metal-rubber interface. When the metal and the polymer are brought together, charge can flow from one material to the other to align the "Fermi levels" of the two materials in the region of contact. This flow of charge is slow because of the poor charge mobility in the rubber. In addition, any oxide layer on the metal also impedes the flow of charge across the interface. Upon separation, if the charge cannot flow back across the boundary, the polymer is left with a charged surface (22). As the rate of separation is increased the emission also increases because rapid surface separation hinders the reneutralization of the charged surfaces. Thus, the electric field across the crack is stronger and leads to more intense microdischarges during fracture. The type of metal to which the polymer is attached effects the amount of emission detected in that the position of the Fermi energy varies from metal to metal, thus requiring differing amounts of charge to flow across the interface to establish equilibrium. The nature of the oxide layer also strongly depends on the metal substrate and can influence the reneutralization process.

By artificially introducing free charge onto the surface of the polymer prior to contact with the Al surface, it might be possible to alter the amplitude of the electric field in the crack during separation. Suitable free charge can be provided by a commercial device called a *Zerostat 3*

(manufactured by Discwasher, Columbia, MO) designed to discharge vinyl phonograph records. This device utilizes piezoelectric transducers and field emission from a sharp metal point to produce free charges of both signs. The polymer surface was allowed to sit for approximately 1 minute after charging prior to contact with the metal surface. During this time a portion of the free charge diffuses into the sample. The joint was then formed and held for ~ 20 min. Although the magnitude of the free charge taken up by the polymer was not measured, we found that its presence indeed modified the EE intensity. Fig. 4 shows the EE from a 35NFA-Al sample peeled at a rate of ~2.5 mm/s, where in (a) the sprayed charge was positive and in (b) the sprayed charge was negative. We see that relative to the uncharged surface (Fig. 3), EE intensity increased for the positive charge and decreased for the negative charge.

Contact charging also occurs at sample clamps, which in our case are made of stainless steel. If the sample slips from beneath the clamp during loading, the resulting separation of charge is effectively in a direction parallel to the tensile direction. Fig. 5a shows the resulting EE from a sample of 35NFA that had been clamped ~20 min (time required to pump down the vacuum system) and subsequently slipped out of the clamp during rapid loading (strain rate ~600 %/s). Clearly, the EE activity is very high. As the material is pulled and detaches from the clamp, the detachment zone is highly charged and thus displays all the EE processes discussed above. The "tail" in the EE persists long after the end of the slipping event and consists of an unusual series of EE bursts separated by longer and longer periods of time, similar to a "relaxation oscillator". The baseline of the emission gradually decreases to zero and the bursts rise and fall rapidly. Fig. 5b shows a region of these bursts on a linear intensity scale. We have joined the data points with straight lines to better illustrate the shape of these bursts. The origin of this rather bizarre effect is likely related to interaction of high surface charge densities (perhaps of both signs) with the electric polarization of the rubber, obviously in a very non-linear fashion. We have planned additional experiments to explore this effect and to investigate any connection to the tribology of metal-rubber interfaces.

DETACHMENT OF URETHANE-LINKED POLYBUTADIENE FROM METAL SUBSTRATES

Adhesive failure of elastomer-metal interfaces can also be achieved using the urethane-linked polybutadiene; visual observation of the metal surface shows little residual polymer after separation. The macroscopic peeling of ULPBR from stainless steel (Fig. 6a) and aluminum (Fig. 6b) also results in intense, long lasting EE similar to the adhesive failure of the uncrosslinked 35NFA-aluminum samples. Both tests were carried out at peel rates of ~2.5 mm/s. T-peel and butt joint failure tests involving ULPBR yielded very similar emissions; the failure was interfacial in all cases.

FRACTURE OF UNFILLED AND ALUMINUM FILLED ULPBR

Considering the EE (and pH_E) during deformation and fracture of unfilled and aluminum particle filled ULPBR, one might expect considerable differences between these materials on the basis of the differences in their mechanical and electrical properties. Indeed, the possibility of interfacial failure in the filled material suggests that it will yield the especially intense, long lasting EE associated with interfacial failure above. EE and pH_E from the failure of notched samples of both filled and unfilled ULPBR are compared in Fig. 7. These samples were strained in tension at a rate of 0.6 %/s. The elongation at failure of the filled material was 64%, while that of the unfilled material was 75%. The filled material provided much more intense emissions (~ 10³ times higher) than the unfilled material, consistent with the intense emissions associated with the interfacial failure of other material systems (9-20). Note that the EE during the fracture of the filled ULPBR (Fig. 7a) shows considerably more structure (fluctuations) than the EE from the fracture of the unfilled material (Fig. 7c). EE from the filled material shows numerous spikes and associated "tails" superimposed on an increasing background, rapidly reaching a maximum at final separation. After separation, the EE decreases with a non-exponential decay; on all time scales the semilog plot of EE vs time has curvature. This is suggestive of a near-second order rate equation which we

have explored in detail for two systems: 1. polybutadiene filled with glass beads (9), and 2. single crystal MgO (24). In both of these materials the after-emission was well described by rate equations involving activated charge transport, a recombination reaction, and a competing retrapping process. With high retrapping probabilities, these equations result in second order-like decay, similar to that observed here.

The pH_E from the fracture of the filled ULPBR (Fig. 7b) is quite intense during fracture, but *immediately* drops to the background level of $\sim 10^3$ counts/s for the uncooled PMT. We tried very hard to find a decay curve in the pH_E which would match the EE decay, but were unsuccessful. This is contrary to what was observed in the glass filled PBR and MgO. Parallel decay of EE and pH_E is actually expected on the basis of our understanding of the recombination process, which typically involves both non-radiative (EE) de-excitation *and* radiative (pH_E) de-excitation.(9,24) We have not completely abandoned the "missing photons" and will make further attempts to increase our pH_E detection sensitivity. If they are missing, there may be a selective quenching mechanism which allows EE but forbids pH_E. In systems with strong electron traps (e.g., sulfur cured polybutadiene) the after-emission of both EE and pH_E is strongly suppressed, presumably due to the trapping of normally mobile charge carriers before recombination can occur.

pH_E from the unfilled ULPBR (Fig. 7d) is barely above the PMT background during fracture, showing only a single point in coincidence with the maximum of the EE.

The relationship between EE and the applied load for the unfilled ULPBR during very slow loading (0.5%/s) can be seen in Fig. 8. In this experiment, a series of magnifying lenses allowed direct observation of fibril formation and microfracture in the region of the crack tip. (We called this our "Graduate Student Microfracture Detector" (GSMD)). EE was measured simultaneously. The arrow near the rise in the EE indicates the first observation of fibril failure during the loading process. The onset of significant EE corresponds well with the onset of tearing within the crack tip. An important conclusion can be made from this simple correlation in light of the fact that a crosslinked polymer cannot fail without bond scissions: the EE is clearly associated with bond breaking.

Figure 8b shows markers generated by the GSMD for each detected microfracture event observed in the crack tip during loading of the sample to failure. The observed microfracture activity correlates very well with EE intensity during crack growth. Few fluctuations (spikes) are seen in the EE during failure of the unfilled ULPBR. The EE variations that do occur in Fig. 8a correspond to variations in the frequency of microfracture events which become equivalent to variations in crack velocity as fracture proceeds (i.e., in the high frequency limit).

The corresponding EE, load, and observed microfracture activity for an Al-filled ULPBR is shown in Fig. 9. The EE begins to rise prior to any observed microfracture. The EE is so intense that it is a better "Microfracture Detector" than the GSMD. Note again that EE during fracture of the filled material shows a large number of fluctuations (spikes) which are most likely due to variations in the rate of new surface formation (i.e., instantaneous rate of crack growth).

Although the locus of failure may be very complicated on the atomic level, scanning electron microscopy can provide a gross indication of the cohesive or adhesive nature of the fracture event. Figure 10 shows two views of an aluminum filled ULPBR fracture surface at different magnifications. Extensive adhesive failure is observed, with essentially all of the visible metal particles clearly detached from the polymer matrix. The individual aluminum particles have very little polymer matrix clinging to them and are either lying loose on the fracture surface or sitting in a void with the matrix totally detached from the particle. Thus, the intense EE appears to be associated with relatively poor particle-elastomer bonding.

An interesting comparison can be made between the EE from unnotched vs notched aluminum filled ULPBR samples under the same strain rate and loading conditions (~ 0.6 %/s). In Fig. 11a, we show the resulting EE for the unnotched sample. The onset of the rise in stress during loading and the duration of crack growth are marked with arrows. The EE displays pre-emission, an initial rise in EE prior to visible crack formation and growth. This pre-emission can be attributed to surface delamination or dewetting between the elastomer and filler particles on the surface of the sample. (Dewetting internal to the sample does not yield detectable EE, as any

emitted particles cannot escape to the detector). The pre-emission is followed by a decrease in EE intensity, which remains relatively weak until the onset of crack growth. Catastrophic failure follows quickly. Over 95% of the emission from the unnotched samples occurs in the few seconds of macroscopic crack growth. The strain energy prior to fracture of the unnotched sample (Fig. 11a) is much larger than for the notched specimens (Fig. 11b) due to both greater elongation and larger peak force. Thus, once crack growth initiates, the acceleration and resulting crack velocity are much higher for the unnotched samples. Also, note the lack of strong fluctuations in the EE from the unnotched sample compared to the large number of spikes from the notched samples of Figs. 9a and 11b. Recall that these fluctuations occur *during* fracture. Once crack growth initiates in the unnotched specimens, crack growth accelerates so rapidly that on the time scales shown here we do not observe such fluctuations. Since EE data can be readily acquired at rates as high as 100 MHz, we should be able to resolve the corresponding EE fluctuations from the filled elastomer if they are significant.

CORRELATION OF EE INTENSITY WITH CRACK VELOCITY (FILLED MATERIAL)

EE from the fracture of aluminum filled ULPBR is a very sensitive indicator of the crack formation and growth. Correlations between macroscopic crack motion down and EE intensities may be made with a video camera, using methods similar to those described in Ref. 5. From the video images (taken at 17 ms time intervals), increments in crack position can be measured as a function of time (i.e., the profile of the crack on the side towards the camera) and converted to crack velocity, V_c , vs time. Obviously, this provides only a gross measurement of the actual instantaneous rate of bond breaking at the crack tip. Because the fluctuations in EE were so rapid relative to our crack position measurements, we chose to smooth the EE data by a moving average technique. In Fig. 12 we show this average EE intensity as a function of crack velocity. As the crack progresses through the sample the EE first increases linearly. This corresponds to the linear increase in fracture surface area with crack velocity. Thus, in this region, EE intensity per unit area is independent of V_c . However at higher crack velocities the relationship between EE and V_c is highly non-linear. At these velocities, EE intensity per unit area is a strong function of V_c . These results are very similar to EE intensity vs crack speed results from other filled elastomers reported elsewhere (9).

Several factors could be involved in the emission increase at higher crack velocities. Since negligible intensity is expected from cohesive failure of the polymer relative to interfacial fracture, we expect that the details of the separation of the metal and polymer surfaces play an important role. As shown schematically in Fig. 13, raising V_c raises the velocity with which the two surfaces separate, V_\perp . As in the interfacial peel tests, increasing V_c results in increased charge densities on the fracture surfaces as a result of the decreased time available for reneutralization by current flow across the polymer-metal interface. Increased surface charge results in more intense discharge activity and thus more intense FE.

STRAIN RATE DEPENDENCE

The effect of strain rate on EE intensity from aluminum filled ULPBR is similar to the effect of crack velocity. Figures 14 and 15 show the EE and pH_E at two strain rates, 0.5% and 30%, respectively. Figures 14b and 15b show the EE data on slightly faster time scales. The average total EE counts at these two strain rates are 200 k and 1 M, respectively. Attempts to measure EE at higher strain rates resulted in detector saturation, but all indications suggest that further intensity increases followed. For the filled material, this increase with strain rate is again due to an increase in the interfacial separation velocity, which increases the net charge remaining on the fracture surfaces. Note that the kinetics of the EE after-emission decays are identical at these two strain rates. Once the system is excited by fracture, the relaxation is "determined."

EE intensities from unfilled ULPBR also increase with strain rate, but for entirely different reasons. EE data for three different strain rates is shown in Fig. 16. The peak intensities for each of these experiments appear below:

Strain Rate (%/s)	Peak Intensity
0.5	1 k
30	3 k
100	6 k

The increase in EE with strain rate is basically linear. Figure 16 shows only a 35 second time interval near fracture, so that only a small portion of the loading interval is shown in the case of low strain rates. For instance, the total time from the initial application of the load to failure at 0.5 %/s (Fig. 16c) is approximately 180 s. Note that on the time scale shown, the duration of fracture at 100 %/s (Fig. 16a) no more than a single channel. We recall that in the unfilled material, the emission mechanism is initiated by bond breaking. For a crosslinked elastomer at slow tear speeds the total number of broken bonds should be constant. However, we expect the number of broken bonds to increase at faster strain rates and crack speeds due to entanglement-induced bond breaking, which is known to be strain rate dependent. Thus the EE intensities, although relatively small for unfilled polymers, may provide useful information about the extent of bond breaking.

TIME DEPENDENCE OF EE AND PHE DURING FRACTURE (FILLED MATERIAL)

Because of the high intensities of both pH_E and EE during the fracture of metal filled ULPBR, intensity vs time data may be acquired on a wide range of time scales. In Fig. 17 we show detected emissions acquired at 100 μ s/channel for the filled material (25.5% by weight, average diameter 10 μ m). Both signals display a number of fluctuations, which are correlated to some extent. The intensity and frequency of these fluctuations increase as the crack propagates more rapidly. Video tapes of the fracture event indicate that the emission spikes are not necessarily associated with large macroscopic motions of the crack tip but occur randomly throughout crack propagation. We suspect that microscopic activity within the crack tip is being modulated in time and therefore producing these spikes. Interestingly, the EE shows a much larger RMS level of modulation than the pH_E. We plan to perform careful time correlations of both these signals to test for stochastic vs non-stochastic behavior and to determine the degree of cross correlation. We have recently shown that pH_E fluctuations from fracture of epoxy are *chaotic* in nature and may be related to the fractal geometry of the fracture surface (25). Clearly, the relationship between micromechanical events at the crack tip and FE signals should be clarified so that the FE signals can be used to monitor these events during dynamic crack growth. As mentioned previously, we have time resolution "to burn."

CORRELATION OF EE WITH RE (FILLED MATERIAL)

Another FE component that is indicative of the microdischarge during fracture is long wavelength electromagnetic radiation (i.e., radiowaves: RE). Figure 18 displays typical RE and EE during the fracture of filled ULPBR. A large proportion of the EE spikes correspond to RE spikes, as can be seen by the vertical lines joining the two curves. Further evidence of this correlation is provided by coincidence measurements of these signals. The coincidence data of Fig. 19 was acquired by using the RE bursts to trigger the operation of a multichannel scaler that then counts the accompanying EE. The sampling interval in Fig. 19 is 10 μ s. Each time an RE burst triggers the multichannel scaler, the EE signal is added to the previously scaled bursts. The RE electronics are slow relative to the EE electrons, preventing the detection of the most intense portion of the EE peak. Nevertheless, we see a distribution which builds up, clearly in synchronization with the RE bursts. This distribution, shown on a log scale, indicates that EE bursts of ~ 20 μ s duration are followed by a long (hundreds of μ s) decay. In work characterizing the pH_E accompanying the peeling of adhesive tapes (17-19) we have seen similar behavior associated with the mini-"lightning bolts" generated by peeling.

EE INTENSITY vs FILLER CONCENTRATION

The locus of fracture in the particle filled material is such that increases in particle concentration at a particular size range results in increases in the total area of surface detachment. Fig. 20 shows a plot of the total EE counts/mm² of sample cross-section vs the filler concentration (by weight). The EE is nearly proportional to the aluminum particle concentration and presumably is roughly proportional to the total area of interfacial failure produced by fracture.

VARYING THE CROSSLINK DENSITY OF THE ELASTOMER (FILLED MATERIAL)

The crosslink density of the matrix can influence microscopic aspects of fracture in the filled material. In the ULPBR, the crosslink density can be varied by changing the amount of isophorone diisocyanate (IPDI) added to the hydroxyl terminated polybutadiene. The oxygen of the hydroxyl group bonds to the carbon atom of one of the NCO groups on the IPDI, linking the monomer units through the IPDI groups. The NCO/OH ratio is thus a measure of the crosslink density in the resultant material. The larger the NCO/OH ratio, the higher the crosslink density. EE from the fracture of aluminum filled ULPBR with two NCO/OH ratios are shown in Fig. 21. The material with the higher ratio exhibited a higher stress and shorter elongation at failure. The EE from the higher NCO/OH material is considerably more intense than that from the lower ratio NCO/OH material, the average total EE being 285 k and 210 k, respectively. We believe that the higher crosslink density matrix is associated with higher strain energy densities at failure, and thus higher crack speeds and higher rates of interface separation as the metal and polymer surfaces snapping apart. This in turn encourages higher surface charge densities and more discharge activity. Note that the kinetics of the after-emission decay are nearly identical (parallel on a log scale), suggesting that the crosslink density has little effect on the recombination process.

CONCLUSION

We have shown that EE during the separation of a polymer-metal interface associated with adhesive failure is typically orders of magnitude more intense than that associated with cohesive failure and is also affected by the amount and type of charge on the resulting surfaces. This charge may be the result of contact charging at the interface or may be deliberately introduced by spraying one of the surfaces with free charge.

The observed FE (EE, pH_E, and RE) from the polymer-metal system is consistent with a previously proposed mechanism of charge separation and subsequent microdischarge during crack propagation. The amount, type, and time dependence (fluctuations) of the emission during fracture and the duration of the after-emission depend on factors known to affect details of the fracture process. EE during the tensile fracture of aluminum filled ULPBR is particularly sensitive to the crack formation and propagation process. In the metal filled material, factors associated with larger areas of detachment and higher charge densities (e.g., increased particle concentration, strain rate, and crack velocity) produce large increases in the detected emissions. In unfilled materials, factors that increase the number of broken bonds (e.g., increased strain rate and crosslink density (7)) tend to increase the emission.

Much work remains to be done on the correlation of microscopic aspects of the fracture and emission. High resolution time-resolved microscopy of the crack-tip during FE measurements will be helpful. We are also exploring improved imaging of the emission during crack growth. Confirmation of pH_E due to microdischarges may be achieved by spectral measurements on the emitted light, similar to our work with adhesive tape (14). Further pH_E measurements on the filled material must be made with a cooled photomultiplier tube to reduce the background. Faster time scale measurements will better determine the nature of fluctuations during fracture and the kinetics of the after-emission decay. Finally, we hope to examine in detail the influence of variations in the locus of failure on the FE using macroscopic surfaces with controlled adhesion. We predict a steady increase in EE and other FE components as the locus of failure approaches the interface.

ACKNOWLEDGMENTS

This work was supported by the Office of Naval Research Contract No. N00014-87-K-0514, the National Sciences Foundation DMR-8601281, the McDonnell Douglas Independent Research Program, and the Washington Technology Center. We wish to thank Steve Behler for his assistance in the laboratory for part of these experiments and Steve Langford and Wen-Liang Chang for their help in preparing this manuscript.

REFERENCES

1. J. I. Zink, Naturwissenschaften, **68**, 507 (1981).
2. A. J. Walton, Adv. Phys. **26**, 887 (1977).
3. J. T. Dickinson, "Fracto-Emission from Adhesive Failure", to appear in *Advances in Adhesion*, edited by L. H. Lee, (Plenum Press, New York).
4. M. L. Knotek, in AIP Conference Proc. No. 94, 772 (1982).
5. J. T. Dickinson and L. C. Jensen, J. Polym. Sci.: Polym. Phys. Ed. **23**, 873 (1985).
6. J. T. Dickinson, L. C. Jensen, and A. Jahan-Latibari, Rubber Chem. and Technol. **56**, 927 (1984).
7. J. T. Dickinson, L. C. Jensen, and A. Jahan-Latibari, J. Mater. Sci. **19**, 1510 (1984).
8. J. T. Dickinson, M. K. Park, E. E. Donaldson, and L. C. Jensen, J. Vac. Sci. Technol. **20**, 436 (1982).
9. J. T. Dickinson and L. C. Jensen, J. Polym. Sci.: Polym. Phys. Ed. **20**, 1925 (1982).
10. J. T. Dickinson, L. C. Jensen, and M. K. Park, Appl. Phys. Lett. **41**, 443 (1982).
11. J. T. Dickinson, L. C. Jensen, and M. K. Park, J. Mater. Sci. **17**, 3173 (1982).
12. J. T. Dickinson, L. C. Jensen, and M. K. Park, Appl. Phys. Lett. **41**, 827 (1982).
13. J. T. Dickinson, L. C. Jensen, and A. Jahan-Latibari, J. Vac. Sci. Technol. **A2**, 1112 (1984).
14. J. T. Dickinson, L. C. Jensen, M. H. Miles, and R. Yee, J. Appl. Phys. **62**, 2965 (1987).
15. J. T. Dickinson, X. A. Shen, and L. C. Jensen, Proceedings of the 30th National SAMPE Symposium, 1985.
16. J. T. Dickinson, M. J. Dresser, and L. C. Jensen, in Desorption Induced by Electronic Transitions (DIET II), edited by W. Brenig and D. Menzel, (Springer-Verlag, Berlin, 1985).
17. E. E. Donaldson, J. T. Dickinson, and X. A. Shen, J. Adhesion **19**, 267 (1986).
18. J. T. Dickinson and E. E. Donaldson, J. Adhesion **24**, 199 (1987).

19. Ma Zhenyi, Fan Jiawen, and J. T. Dickinson, J. Adhesion **25**, 63 (1988).
20. E. E. Donaldson and J. T. Dickinson, to appear in J. Adhesion.
21. T.J. Fabish, C.B. Duke, M.L. Hair and H.M. Saltsburg, J. Appl. Phys. **51**, 1247, (1980).
22. F.R. Ruckdeschel and L.P. Hunter, J. Appl. Phys. **46**, 4416 (1975).
23. W.R. Harper, Contact and Frictional Electrification, (Clarendon, Oxford, 1967), pp. 32-36, 60-70.
24. S. C. Langford and J. T. Dickinson, L. C. Jensen, J. Appl. Phys. **62**, 1437 (1987).
25. S. C. Langford, Ma Zhenyi, and J. T. Dickinson, J. Mater. Res., in press.

FIGURE CAPTIONS

- Fig. 1. Diagram of a typical experimental arrangement.
- Fig. 2. EE from (a) T-peel of 35NFA from aluminum foil and (b) tensile fracture of 35NFA. Arrows in (a) mark the duration of the peel. Arrow in (b) marks the time of fracture.
- Fig. 3. EE during and after failure of a butt joint formed by pressing 35NFA against an aluminum plate. Failure occurred at the interface.
- Fig. 4. EE accompanying failure of butt joints formed by pressing 35NFA against aluminum plates after treating the 35NFA surface with (a) positive charge and (b) negative charge provided by a *Zerostar 3*.
- Fig. 5. EE accompanying the loading of a 35NFA sample which has slipped in its clamps. The EE during the bracketed portion of the time scale in (a) is shown on an linear intensity scale in (b) to show EE bursts during the emission decay. The arrows in (a) indicate the duration of the slip event.
- Fig. 6. EE from the peel of ULPBR from (a) stainless steel and (b) aluminum. The peel geometry is shown in the inset of (a). Arrows indicate the duration of the peel events.
- Fig. 7. a) EE and b) pH_E accompanying the loading and failure of c) Al-filled and d) unfilled ULPBR. The filler concentration was 25.5% by wt.; 10 μm avg. Al particle size.
- Fig. 8. (a) EE, (b) incidence of fibril tear events, and (c) load force during and after loading unfilled ULPBR in tension. Arrows in each diagram indicate the onset of strain and the time of sample failure.
- Fig. 9. (a) EE, (b) incidence of fibril tear events, and (c) load force during and after loading Al-filled ULPBR (17.7% Al by wt.; 10 μm avg. Al particle size) in tension. Arrows in each diagram indicate the onset of strain and the time of sample failure.
- Fig. 10. SEM micrographs of the fracture surface of an Al-filled ULPBR (25.5% by wt.; 30 μm avg. Al particle size). Distance scales are indicated by the bars below each micrograph.
- Fig. 11. EE during the loading and fracture of (a) unnotched and (b) notched Al-filled ULPBR (25.5% by wt.; 60 μm avg. Al particle size). Arrows in each diagram indicate the onset of strain and the duration of macroscopic crack growth.
- Fig. 12. EE as a function of crack velocity during the fracture of Al-filled ULPBR (8.5% by wt.; 60 μm avg. Al particle size).
- Fig. 13. Schematic diagram of the notch geometry for a filled elastomer sample, showing the influence of crack speed on the surface charge resulting from interfacial failure between the filler particles and elastomer matrix.
- Fig. 14. EE and pH_E from an Al-filled ULPBR (8.5% by wt.; 10 μm avg Al particle size). Al particle size loaded at a rate of 0.5 %/s: (a) EE during loading and the first ~200 s after failure; (b) EE and (c) pH_E during the early stages of loading.

- Fig. 15. EE and pH_E from an Al-filled ULPBR (8.5% by wt.; 10 μ m avg Al particle size) loaded at a rate of 30 %/s: (a) EE during loading and the first ~300 s after failure; (b) EE and (c) pH_E during loading shown on a time scale comparable to that of Figs. 14b and c. Note that the EE detector was saturated during the period of most intense emission.
- Fig. 16. EE from unfilled ULPBR (8.5% by wt.; 10 μ m avg Al particle size) loaded at a rate of (a) 100 %/s, (b) 30 %/s, and (c) 0.5 %/s.
- Fig. 17. Simultaneous measurements of a) pH_E and b) EE on expanded time scale during fracture of Al filled ULPBR (25.5% by wt.; 10 μ m Al particle size).
- Fig. 18. Simultaneous measurements of (a) EE and (b) RE during the loading of Al-filled ULPBR (8.5% by wt.; 60 μ m avg Al particle size). Vertical lines show correspondence between RE bursts and periods of intense EE.
- Fig. 19. Correlation of EE with RE bursts during the fracture of Al-filled ULPBR (8.5% by wt.; 60 μ m avg Al particle size). Time $t=0$ corresponds to the arrival of an RE burst. EE data corresponding to several RE bursts have been summed at 10 μ s intervals.
- Fig. 20. Average total EE per mm² of sample cross-section from the fracture of Al-filled ULPBR (10 μ m Al particle size) as a function of Al particle concentration.
- Fig. 21. EE following fracture of two Al-filled ULPBR (25.5% by wt.; 30 μ m Al particle size) samples with different crosslink densities: NCO/OH = 1.35 and NCO/OH = 1.02.

TYPICAL EXPERIMENTAL ARRANGEMENT

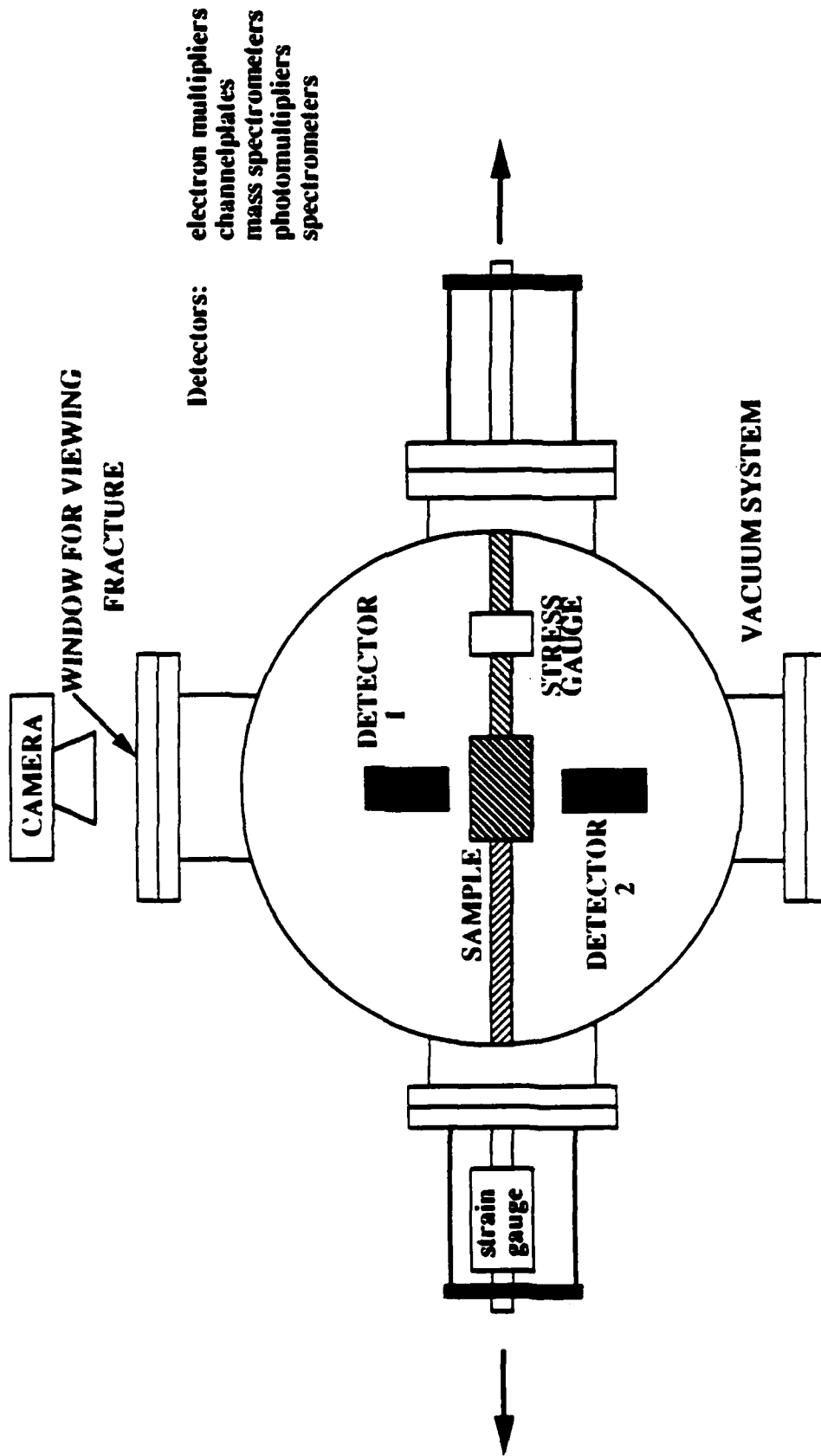


Fig. 1

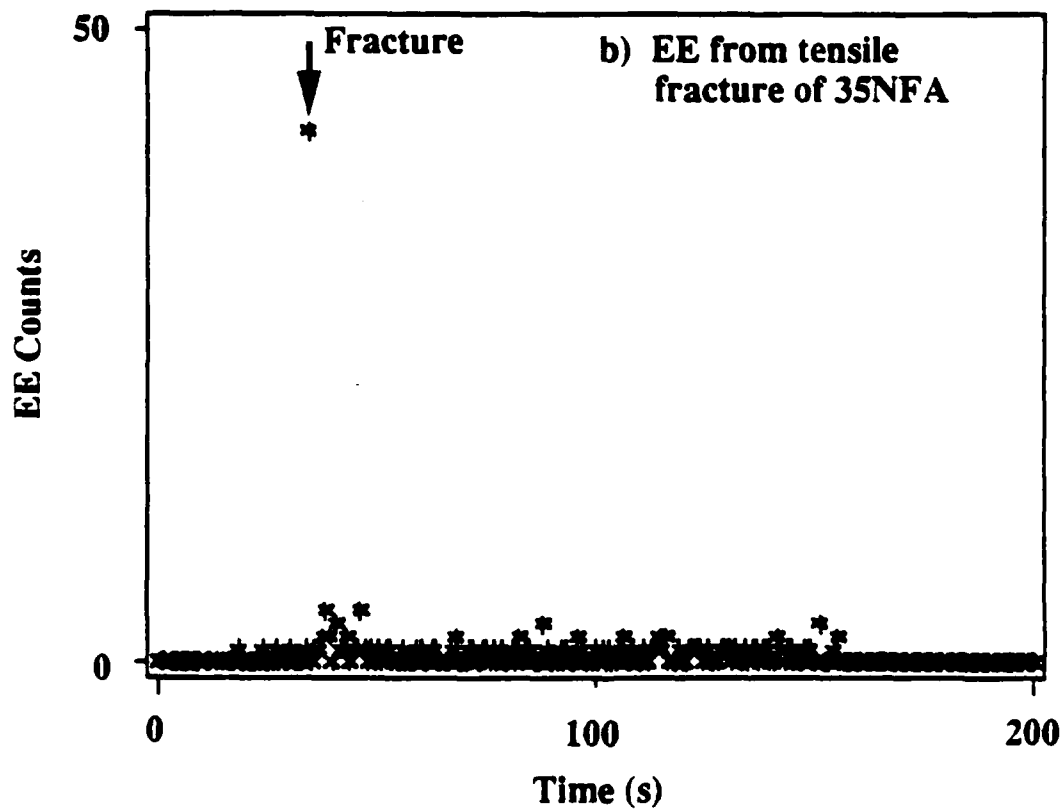
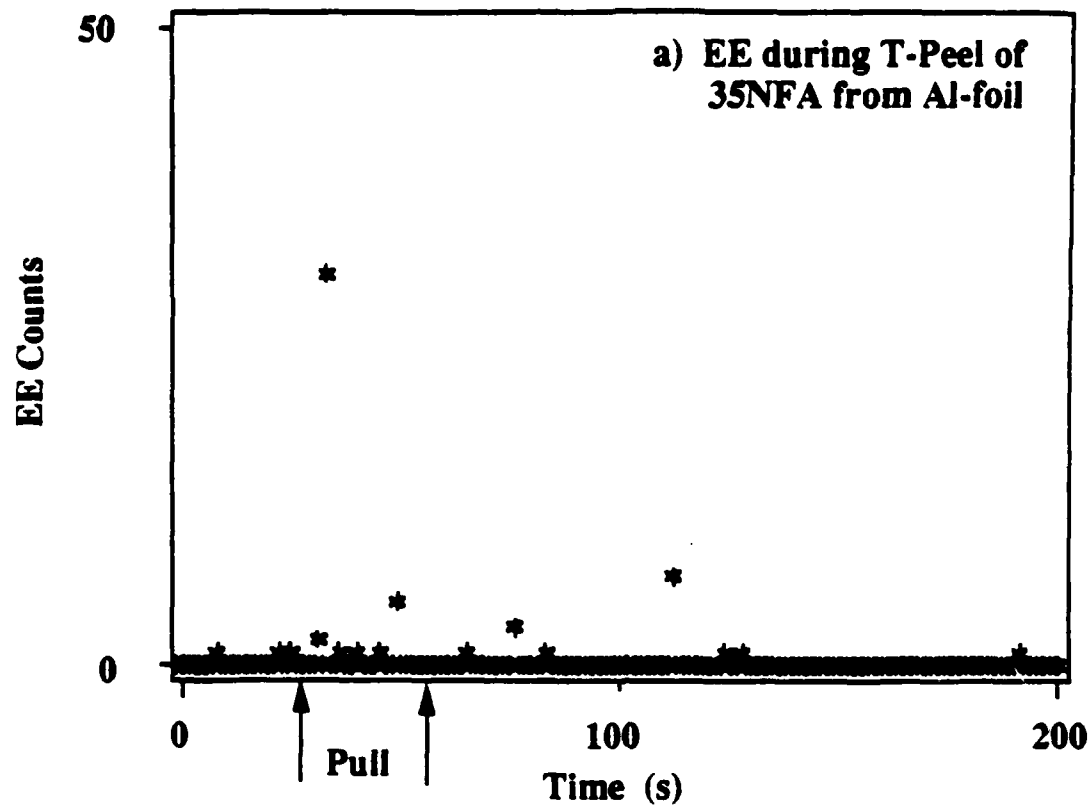


Fig. 2

EE During the Separation of 35NFA From an Aluminum Surface

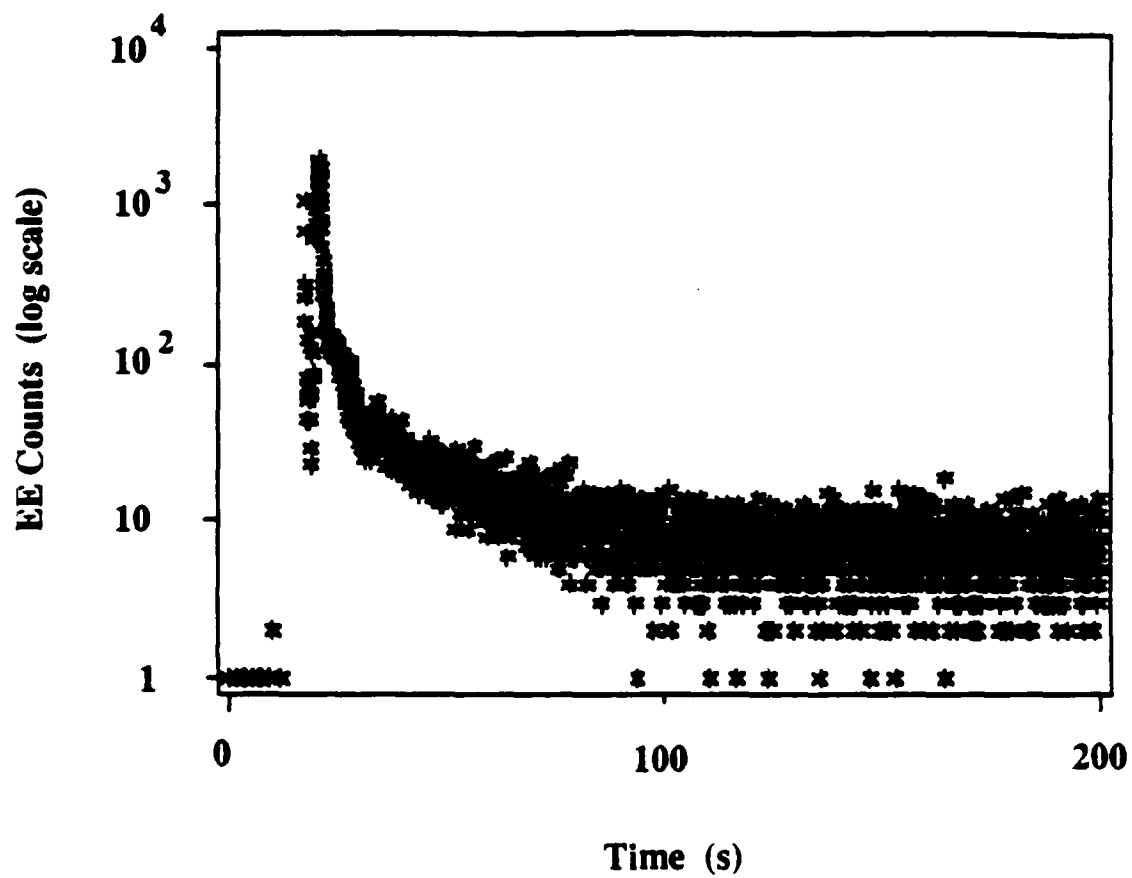


Fig. 3

EE During the Separation of Charged 35NFA from an Aluminum Surface

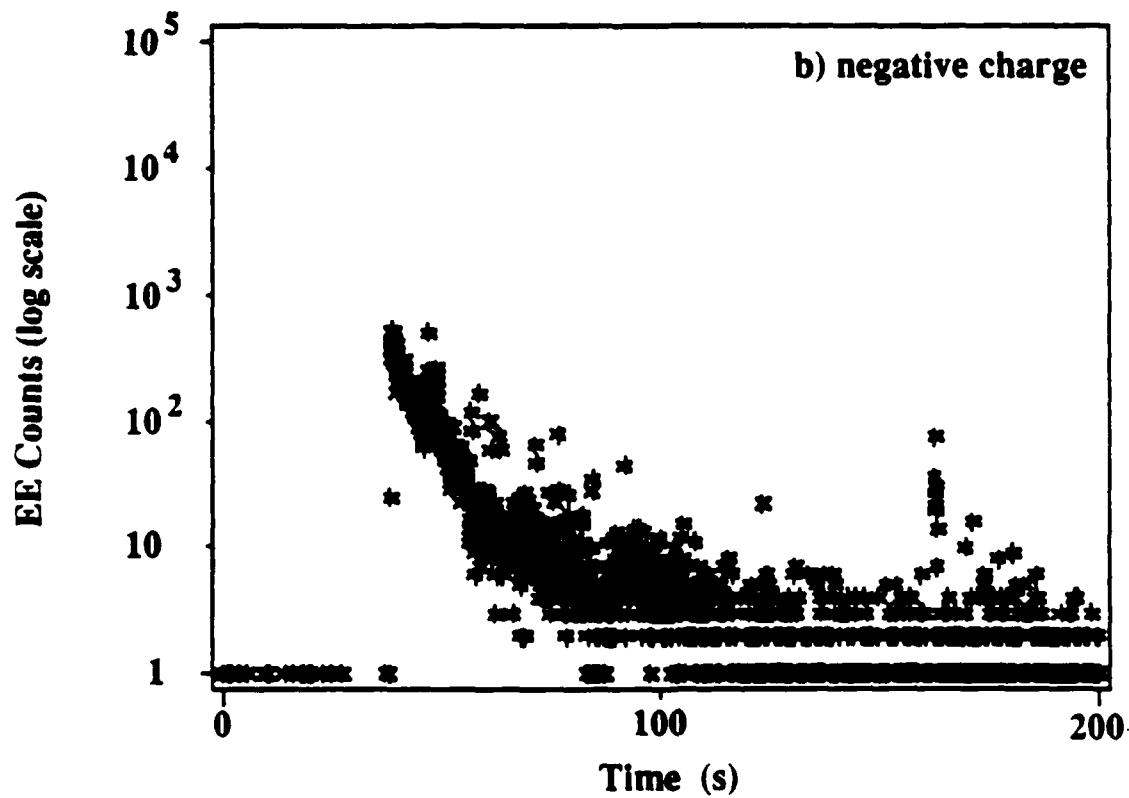
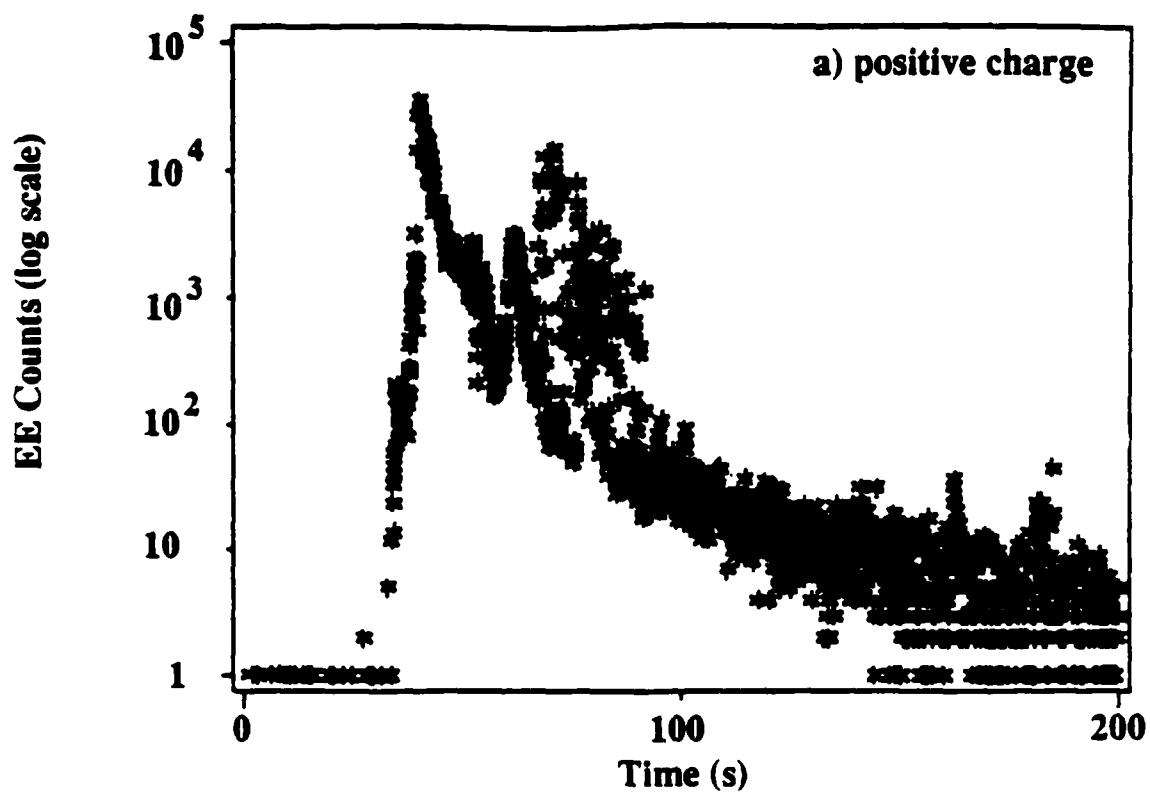


Fig. 4

EE from Uncrosslinked Polybutadiene Slipping in Clamps

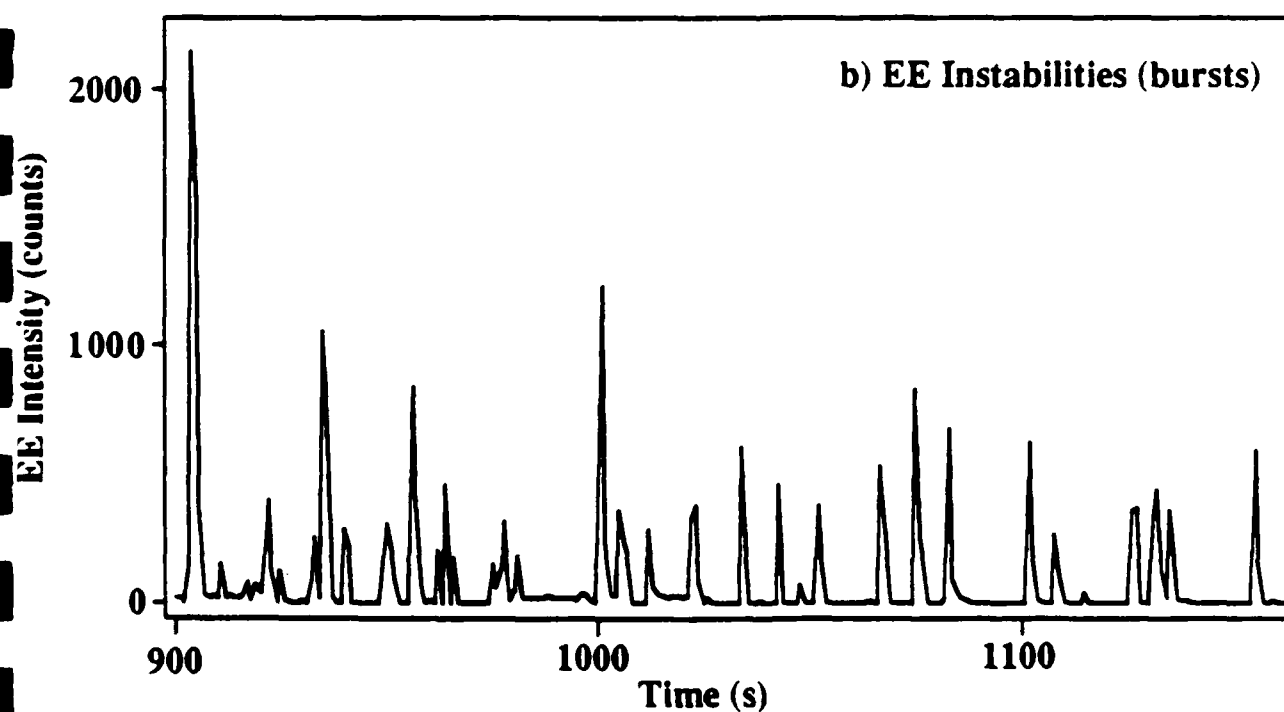
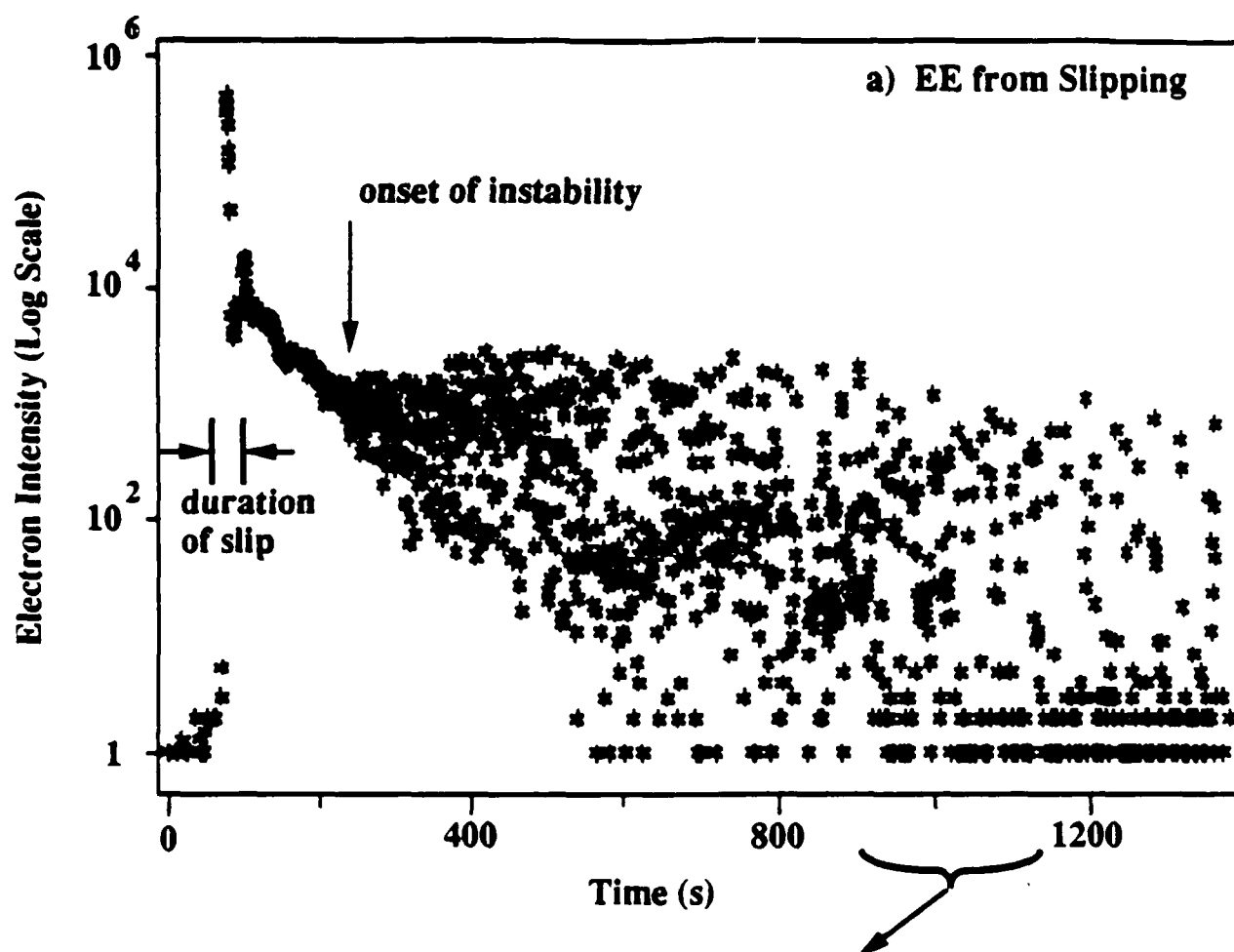


Fig. 5

ELECTRON EMISSION FROM
URETHANE LINKED POLYBUTADIENE
peeled from metals

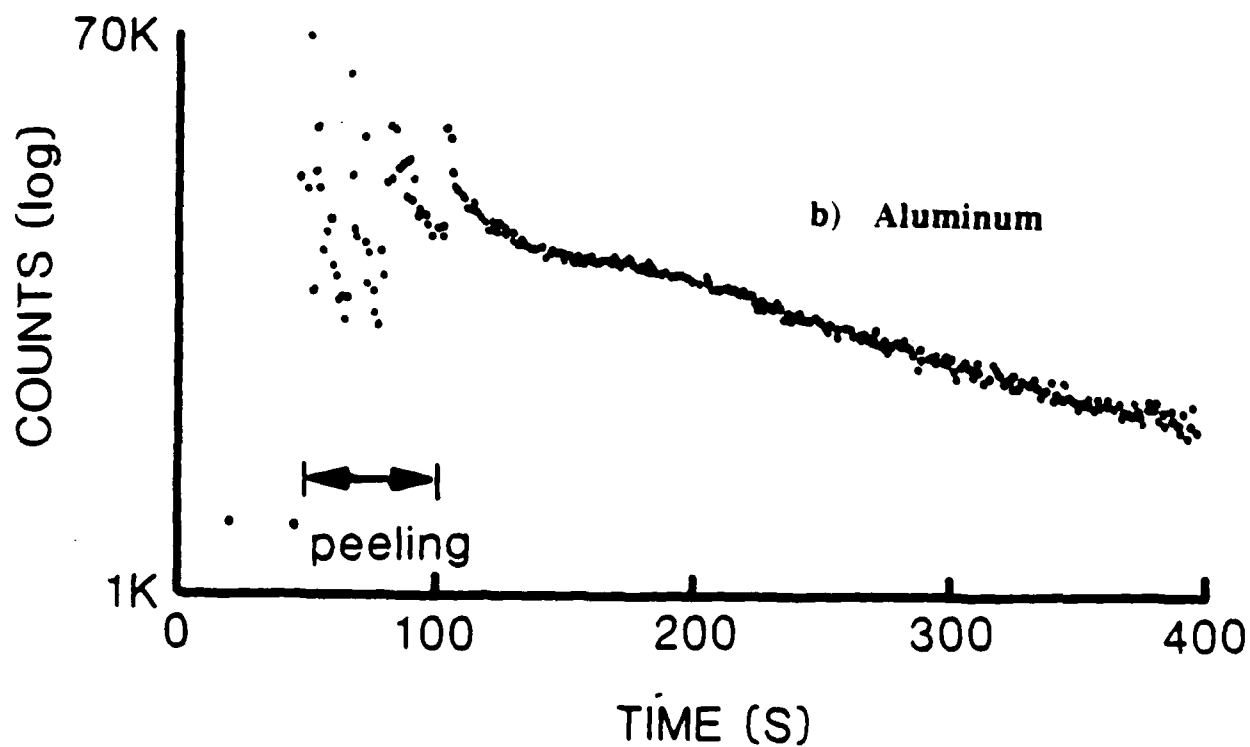
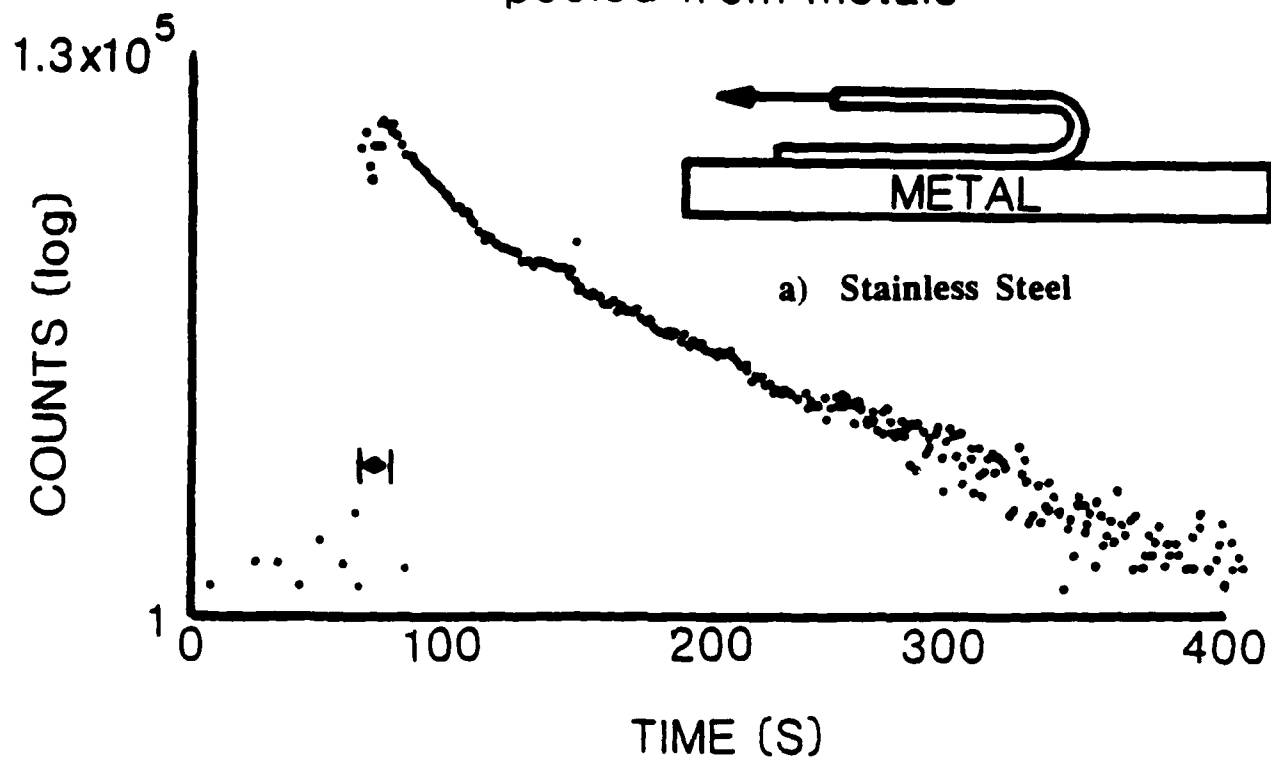


Fig. 6

URETHANE LINKED POLYBUTADIENE

FILLED WITH
10 μm DIAMETER ALUMINIUM PARTICLES
25.5 % BY WEIGHT

UNFILLED

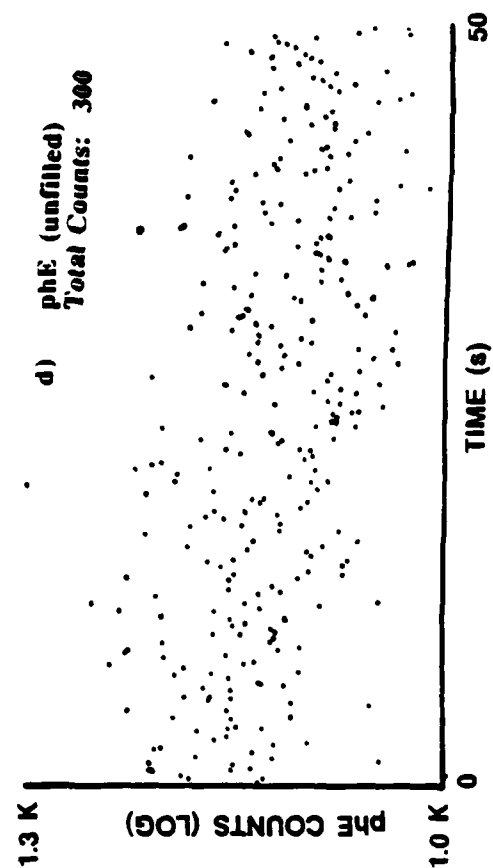
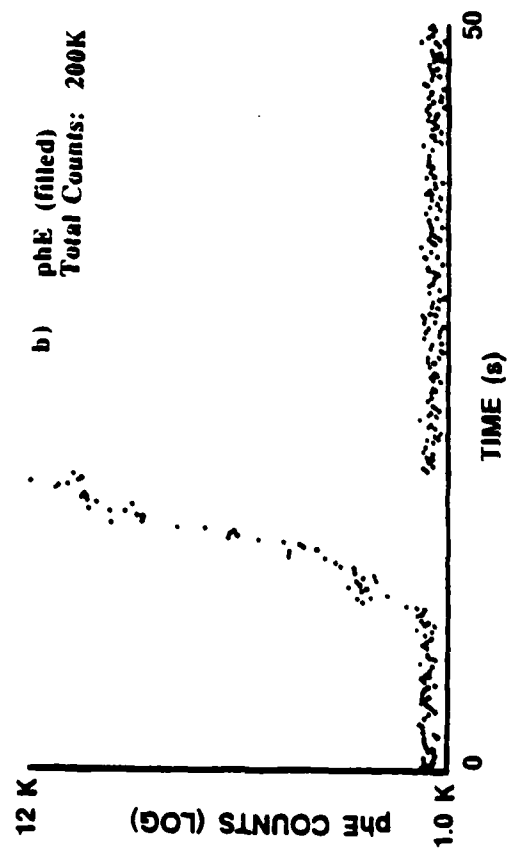
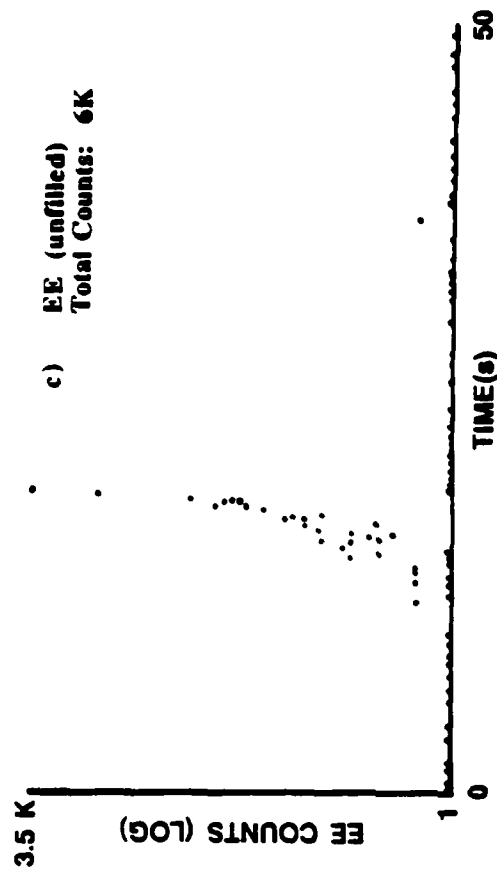
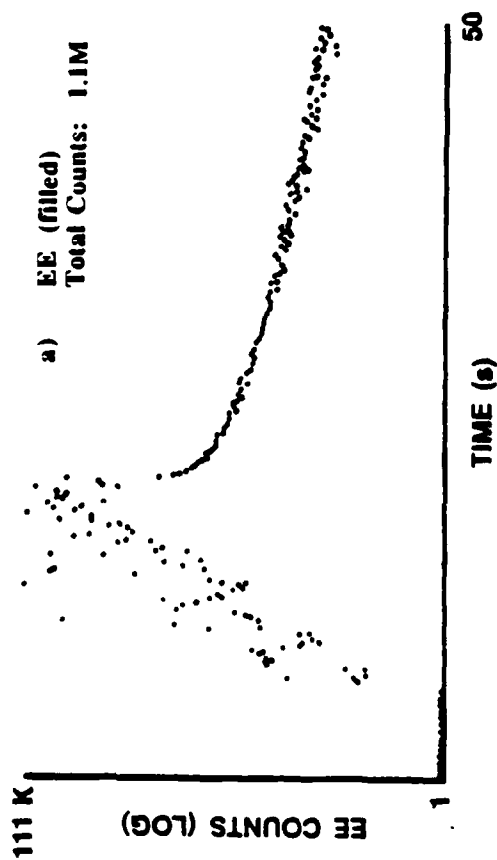


Fig. 7

Electron Emission from Unfilled ULPBR

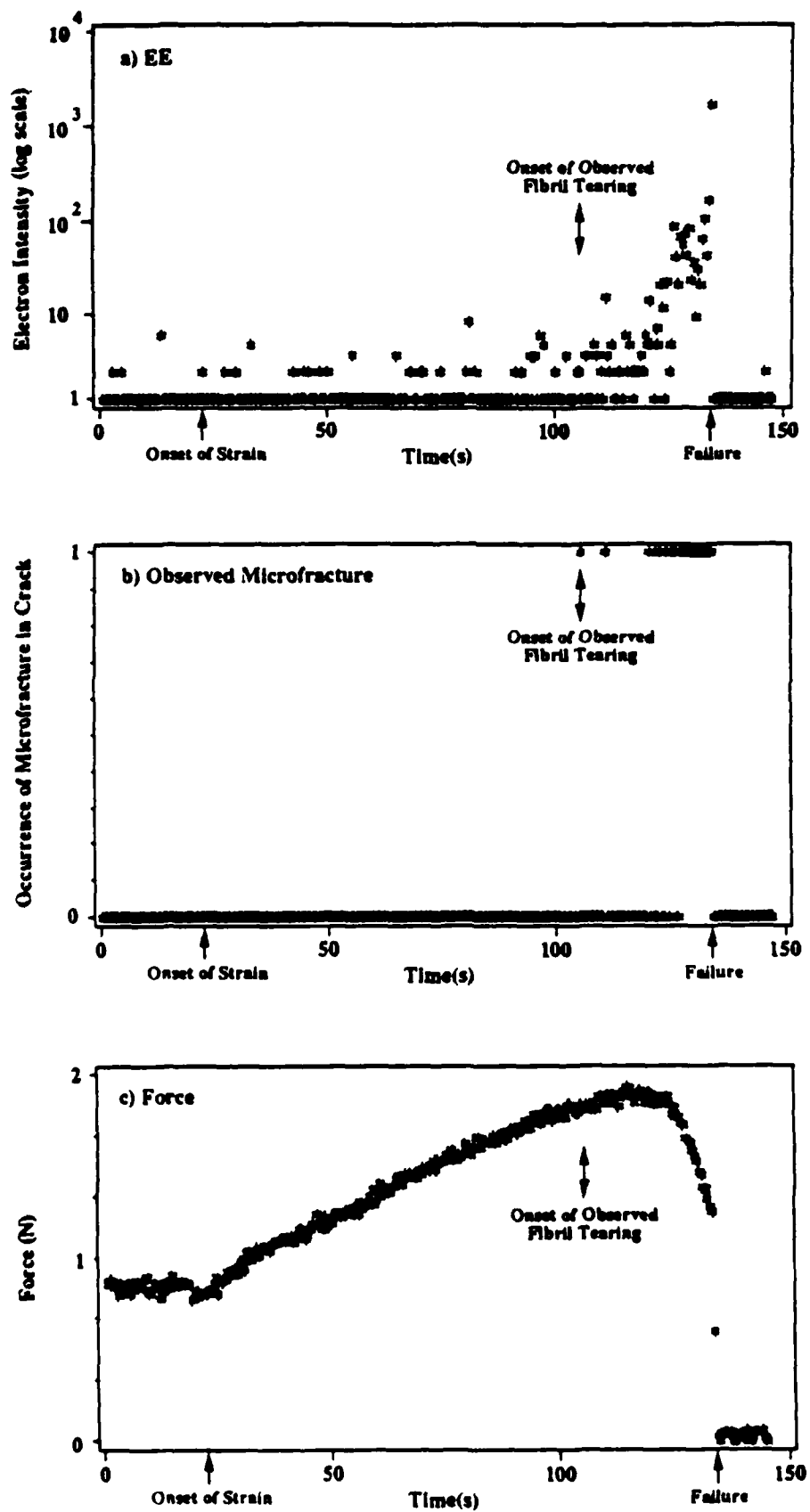


Fig. 8

Electron Emission from Al-filled ULPBR

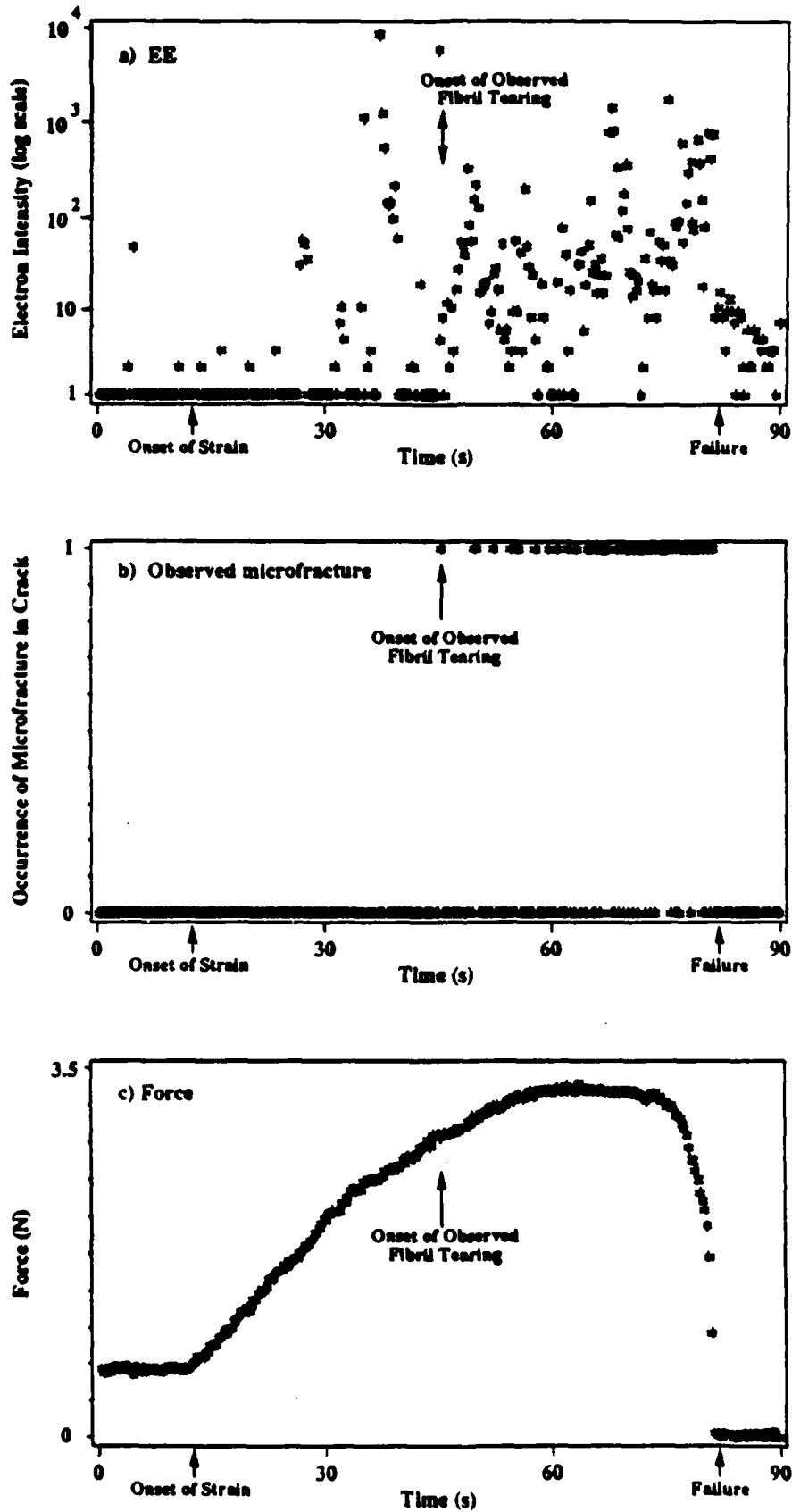
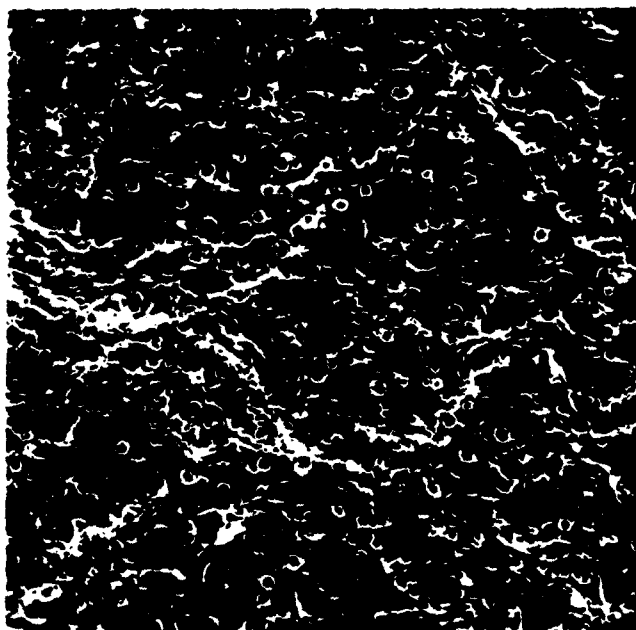


Fig. 9

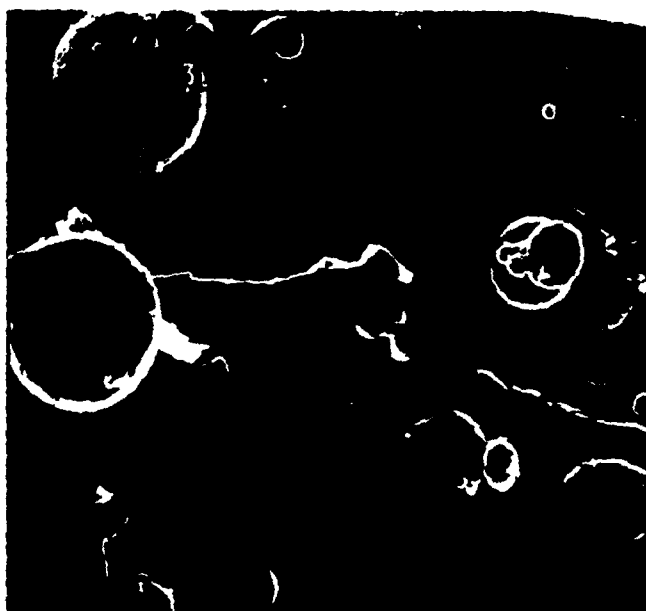
Urethane Linked Polybutadiene

FILLED WITH
30 μm DIAMETER ALUMINIUM PARTICLES
25.5 % BY WEIGHT



a)

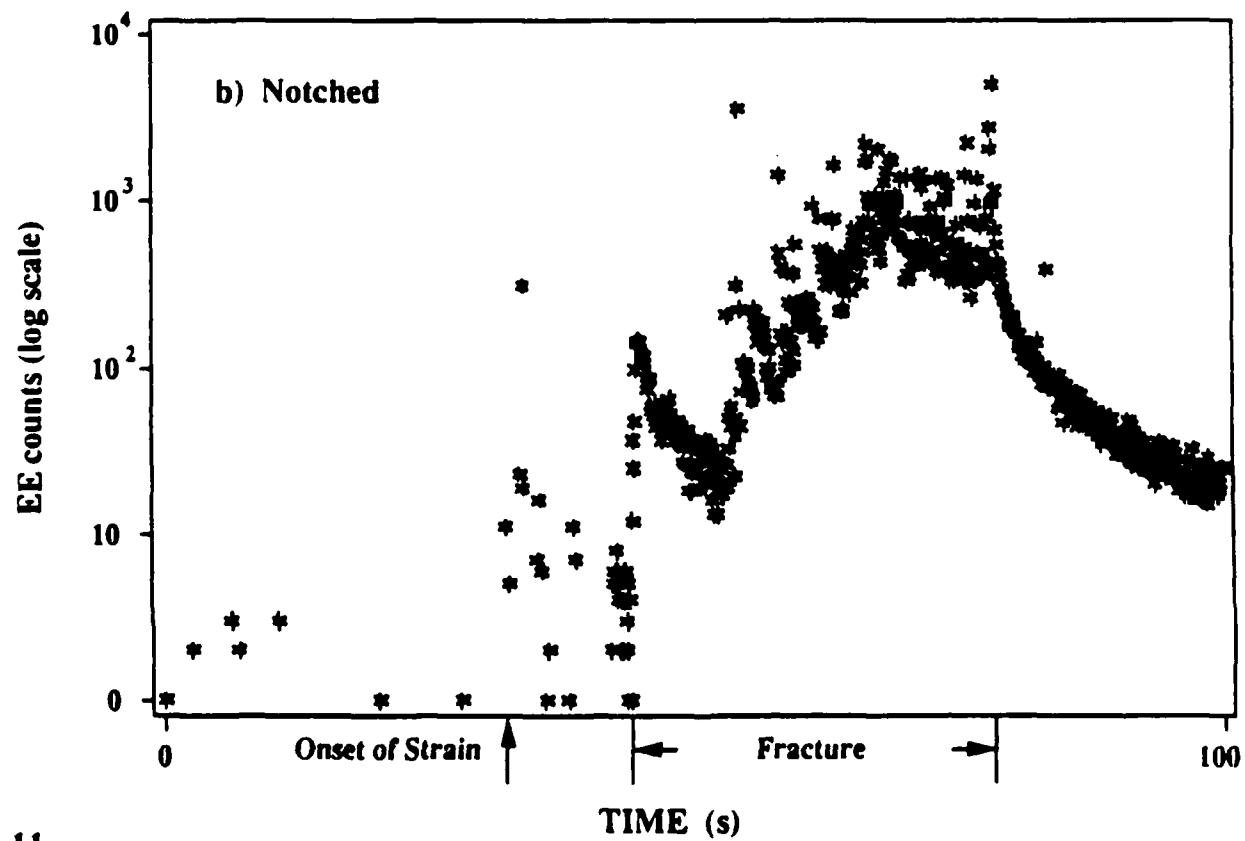
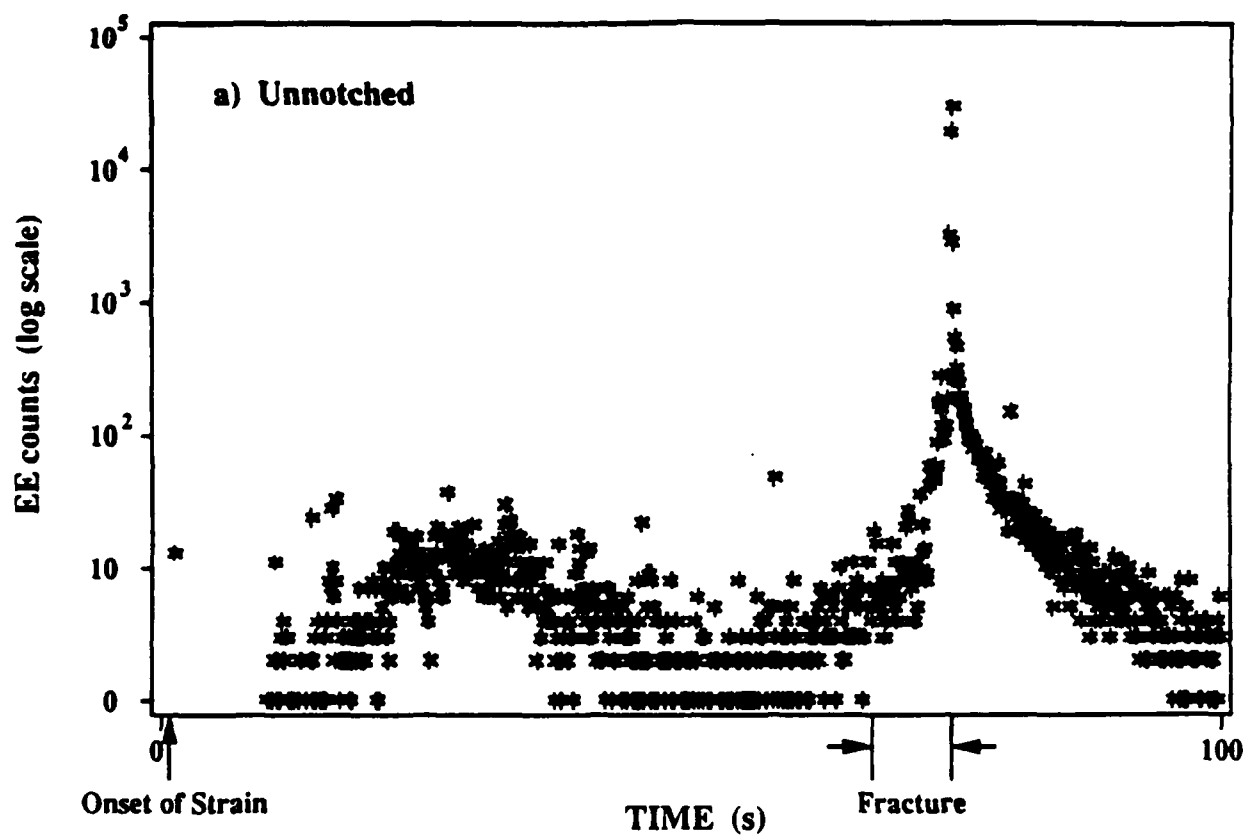
100 μm



b)

10 μm

EE During the Fracture of Notched and Unnotched Filled ULPBR



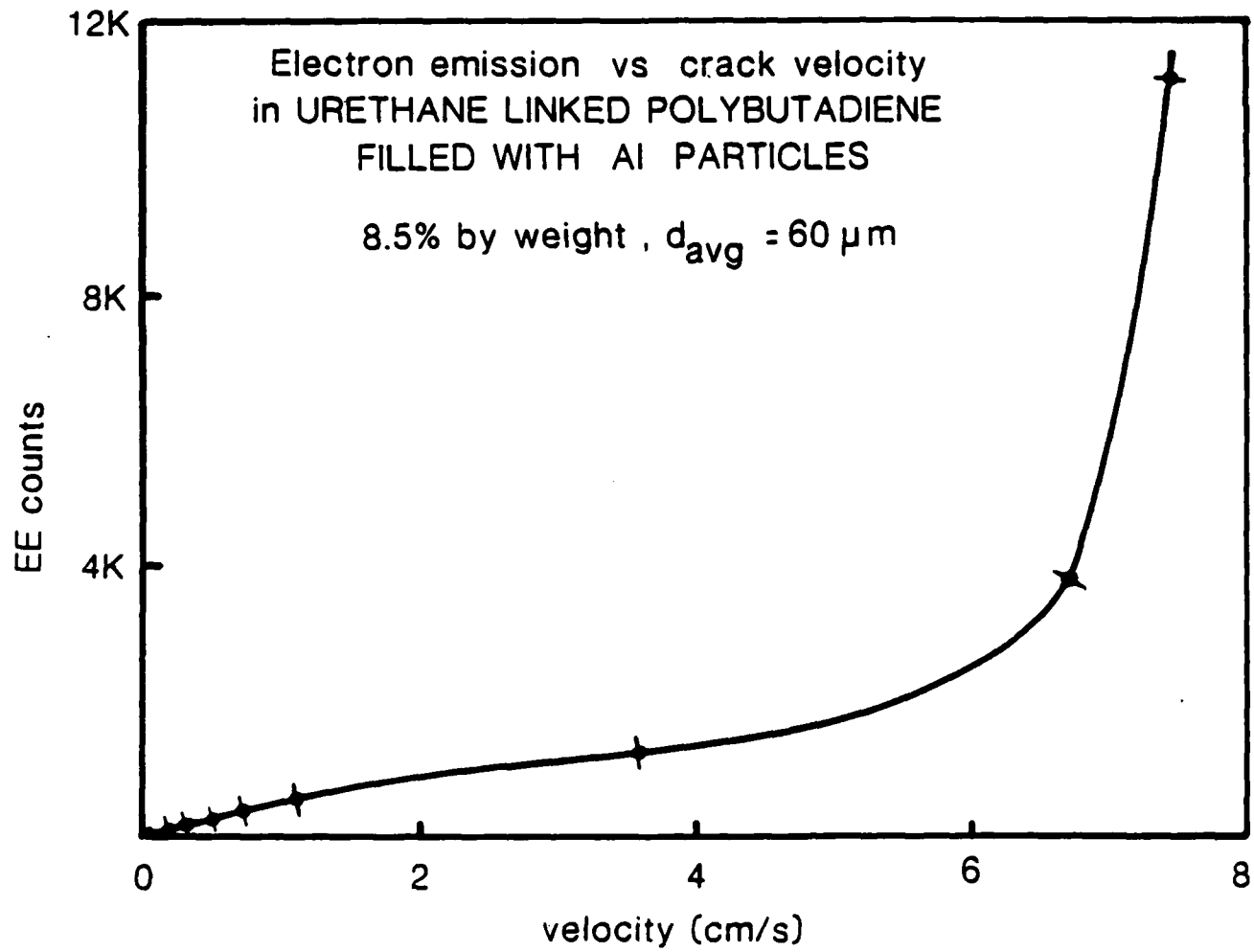
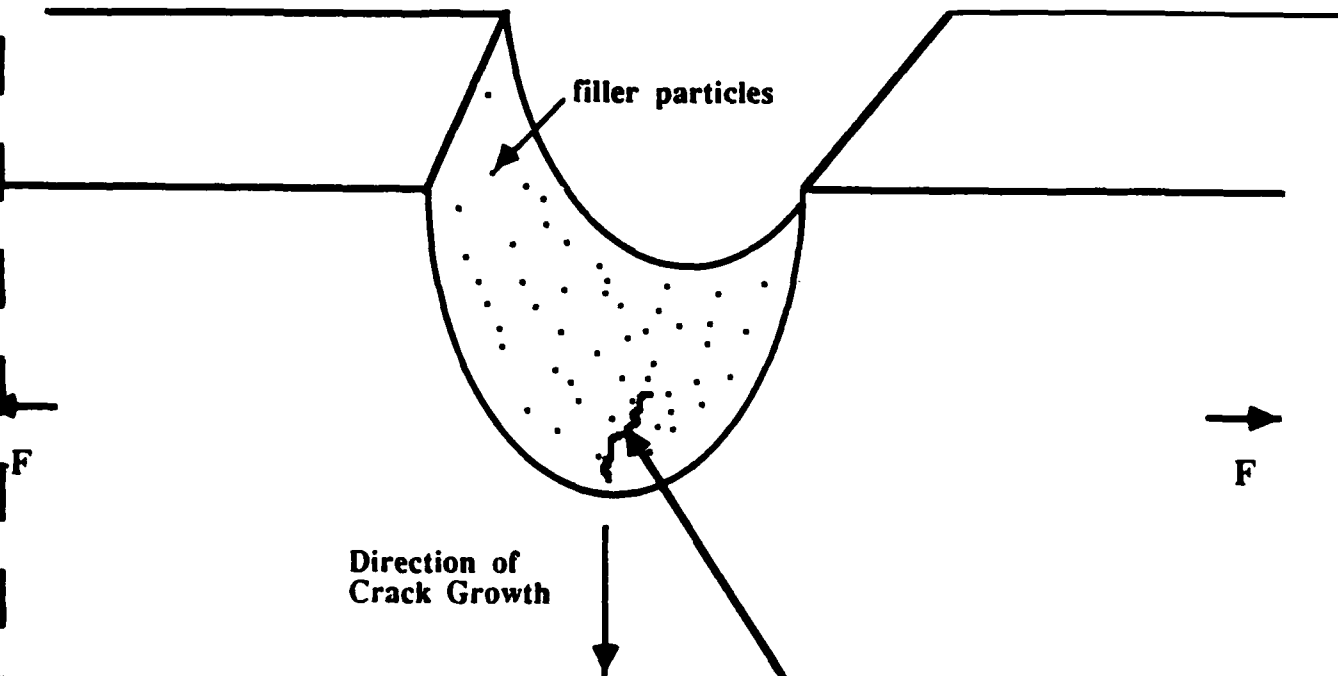


Fig. 12

Stressed Notch in Filled Elastomer

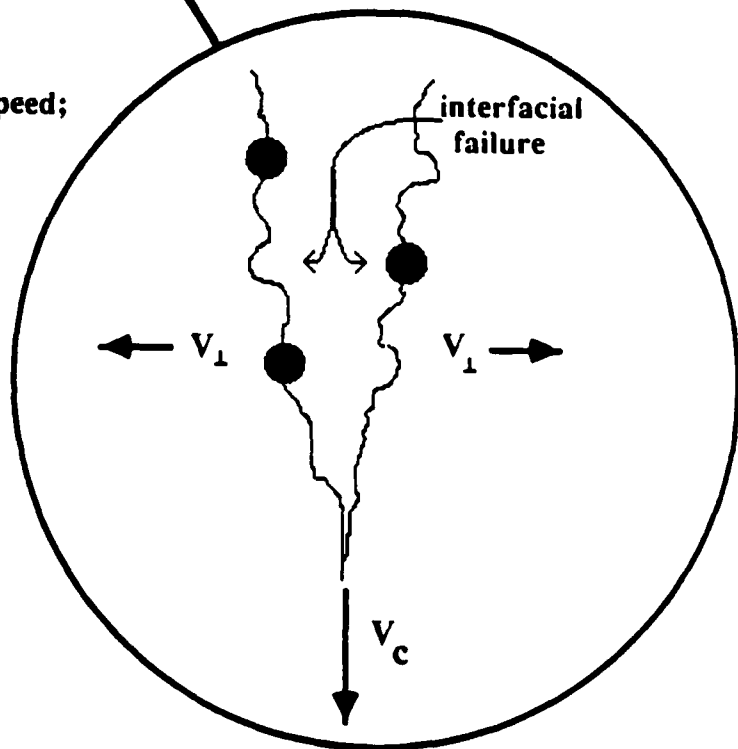


Separation Speed depends on Crack Speed;

LARGE V_{\perp}

Inhibits Charge Reneutralization via
Leakage Currents Across Crack;

Thus, Larger σ_{\pm} ; Larger \vec{E} field.



EE AND phE FROM PARTICULATE FILLED
URETHANE LINKED POLYBUTADIENE

STRAIN RATE 0.5%/S

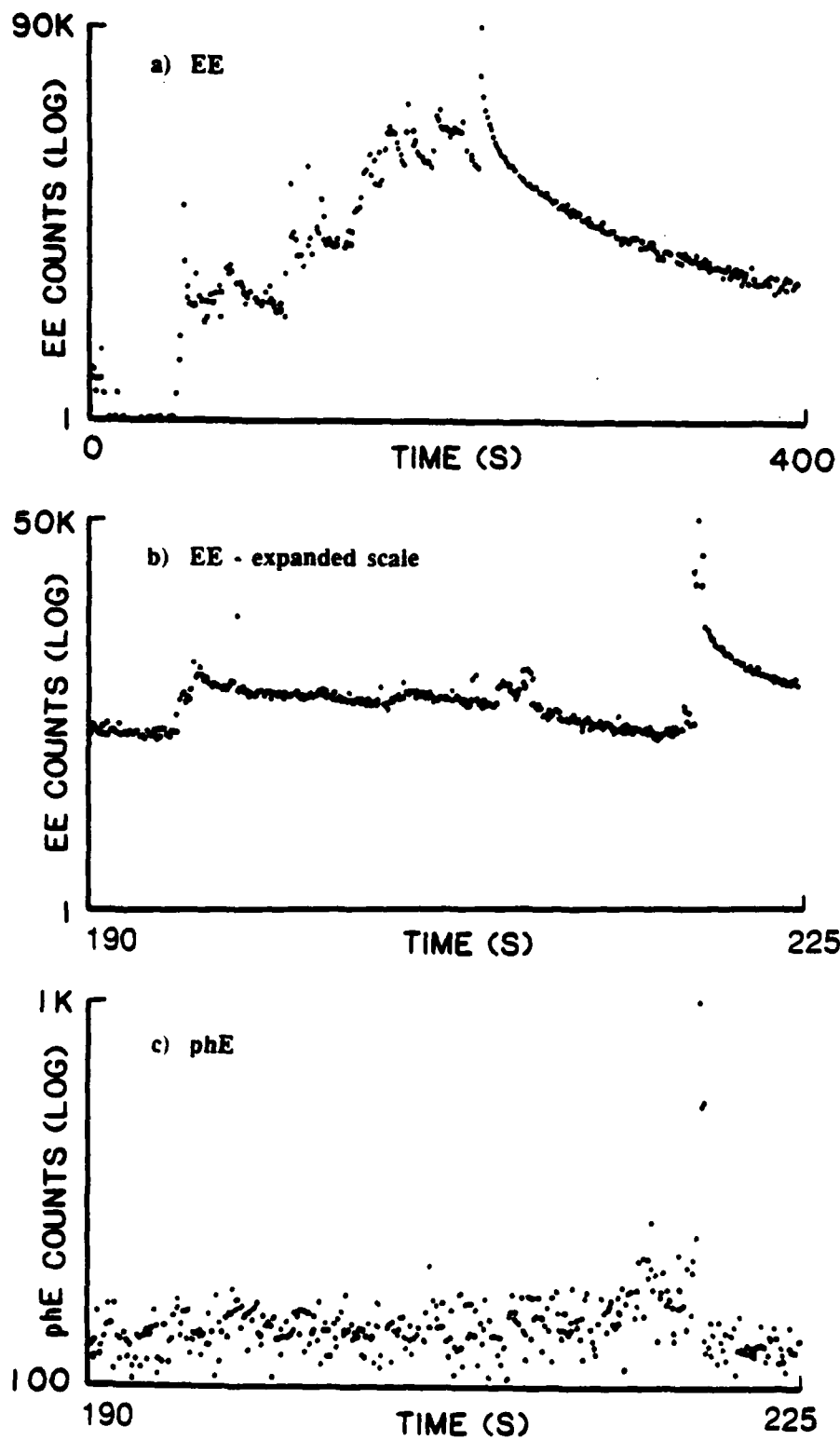


Fig. 14

EE AND phE FROM PARTICULATE FILLED
URETHANE LINKED POLYBUTADIENE

STRAIN RATE 30%/S

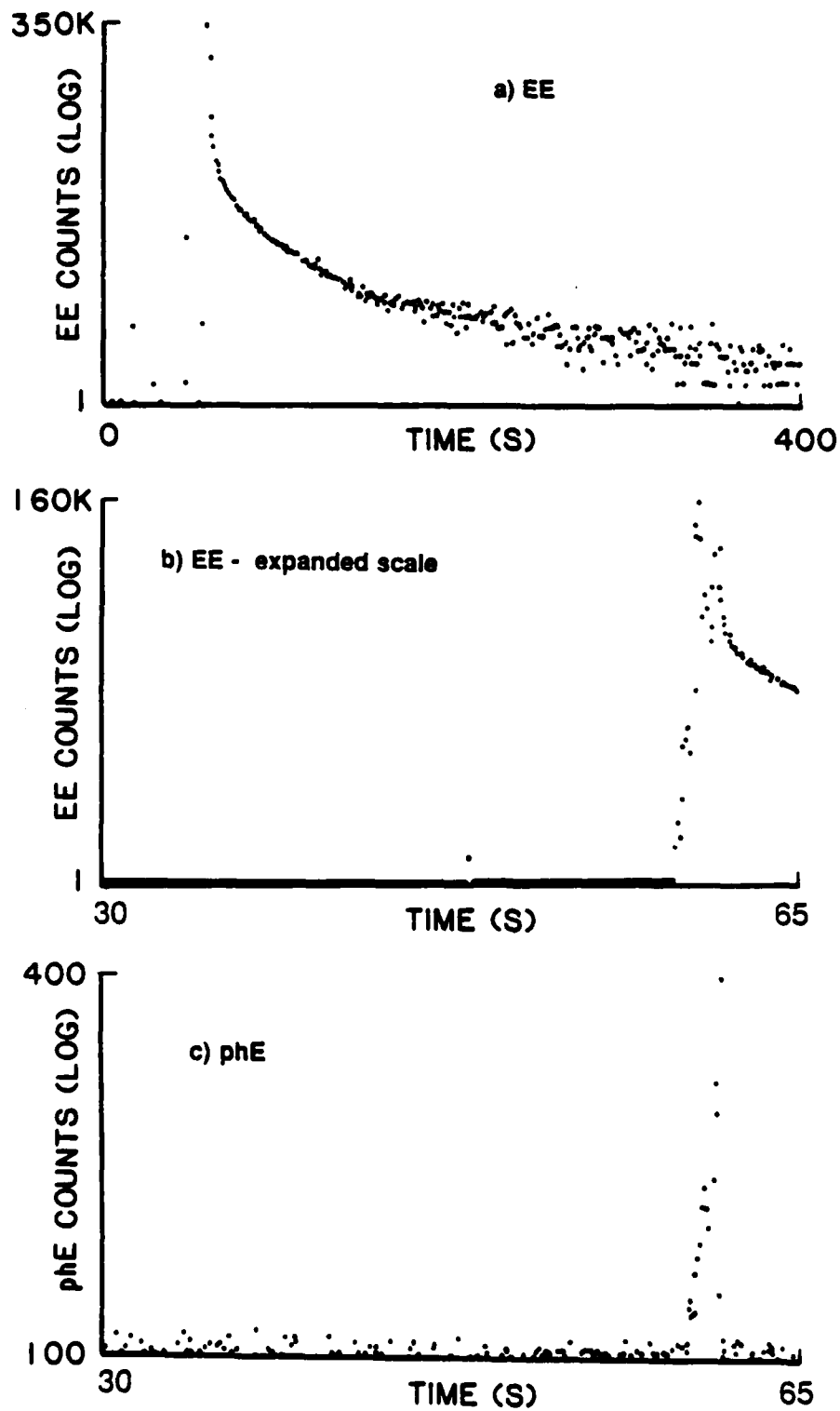


Fig. 15

EE FROM UNFILLED URETHANE LINKED POLYBUTADIENE

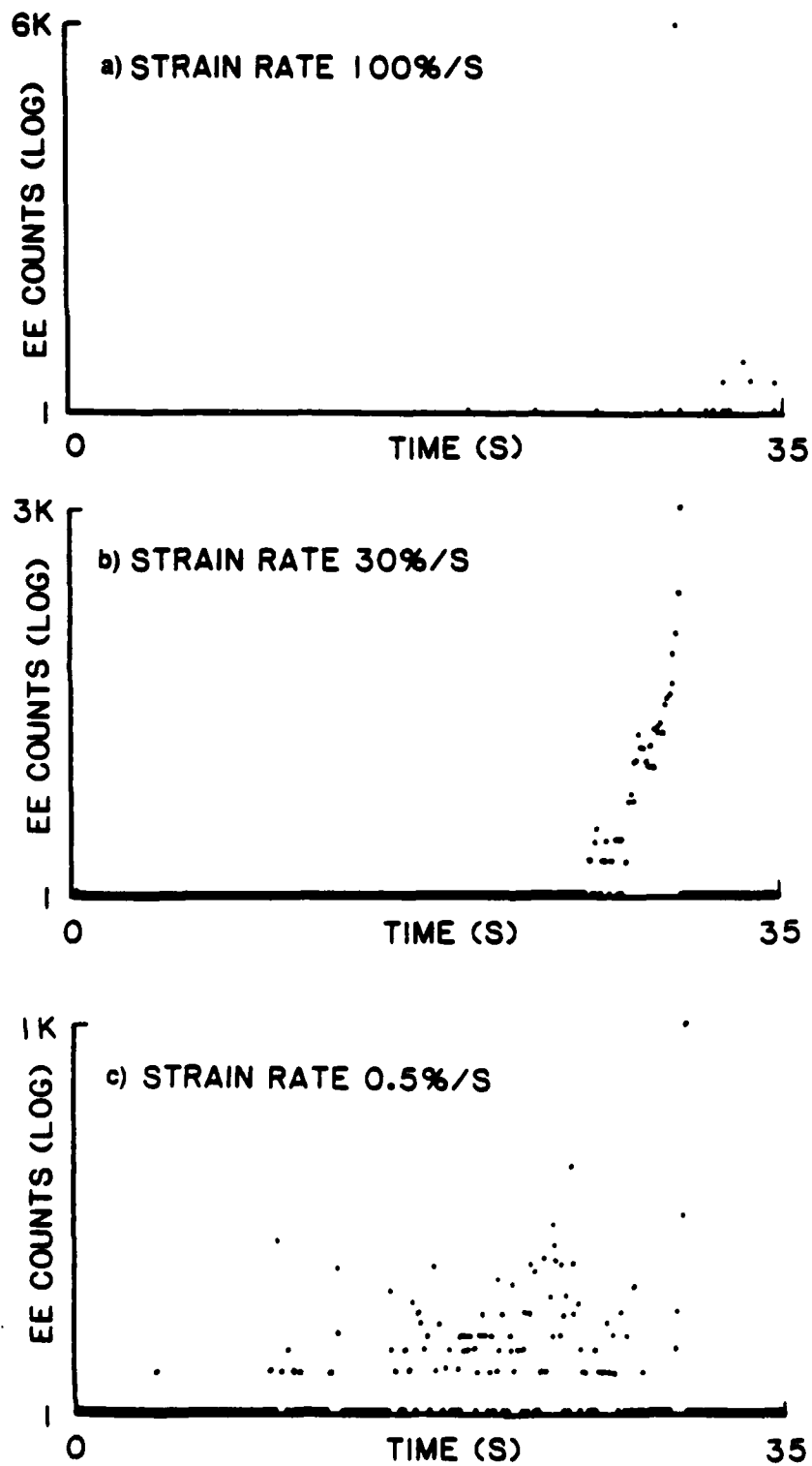


Fig. 16

ELECTRON AND PHOTON EMISSION FROM URETHANE LINKED
POLYBUTADIENE FILLED WITH Al PARTICLES

25.5% by weight, $d_{avg} = 10 \mu m$

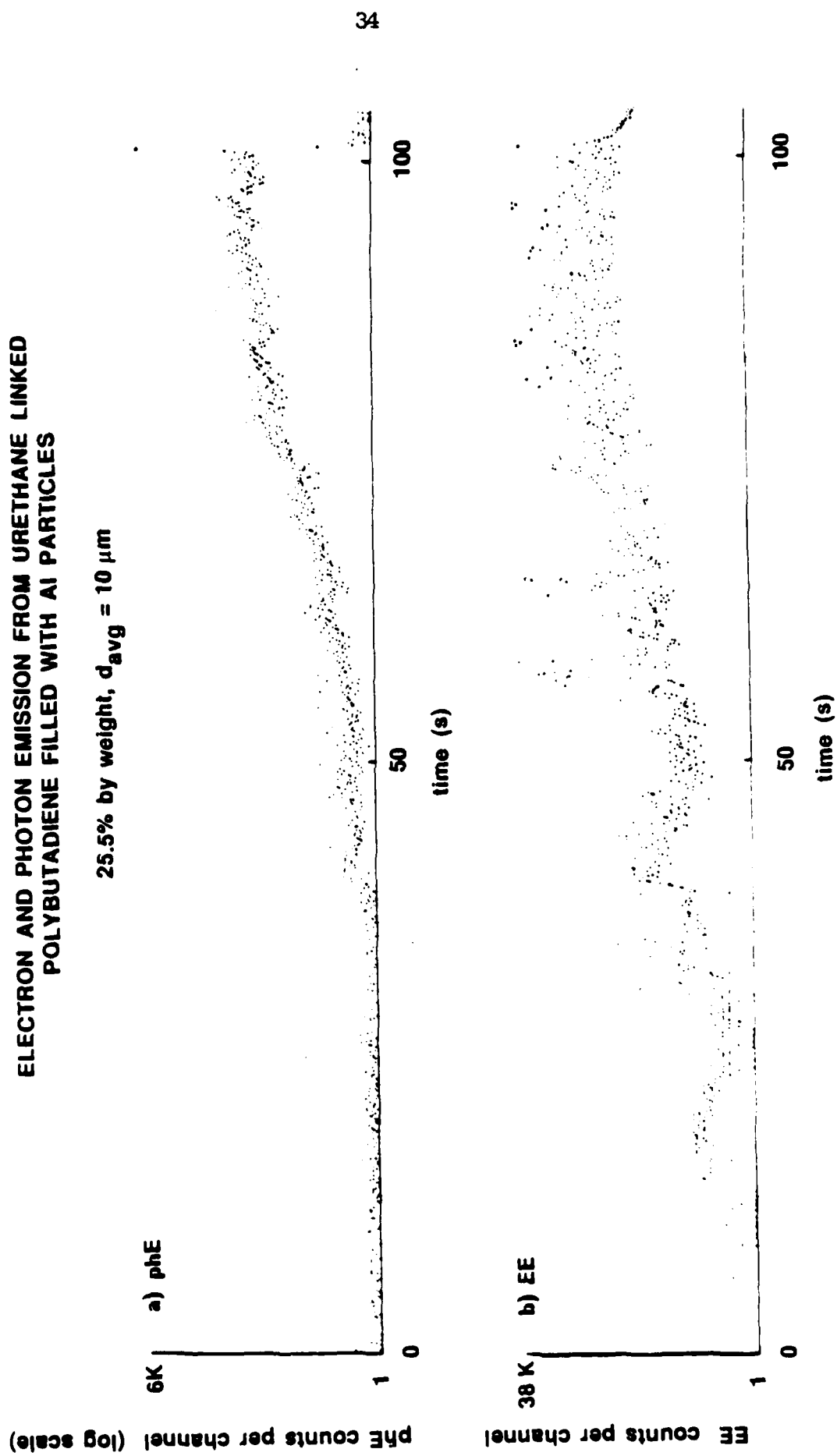


Fig. 17

SIMULTANEOUS EE AND RE DURING FRACTURE OF Al FILLED ULPBR

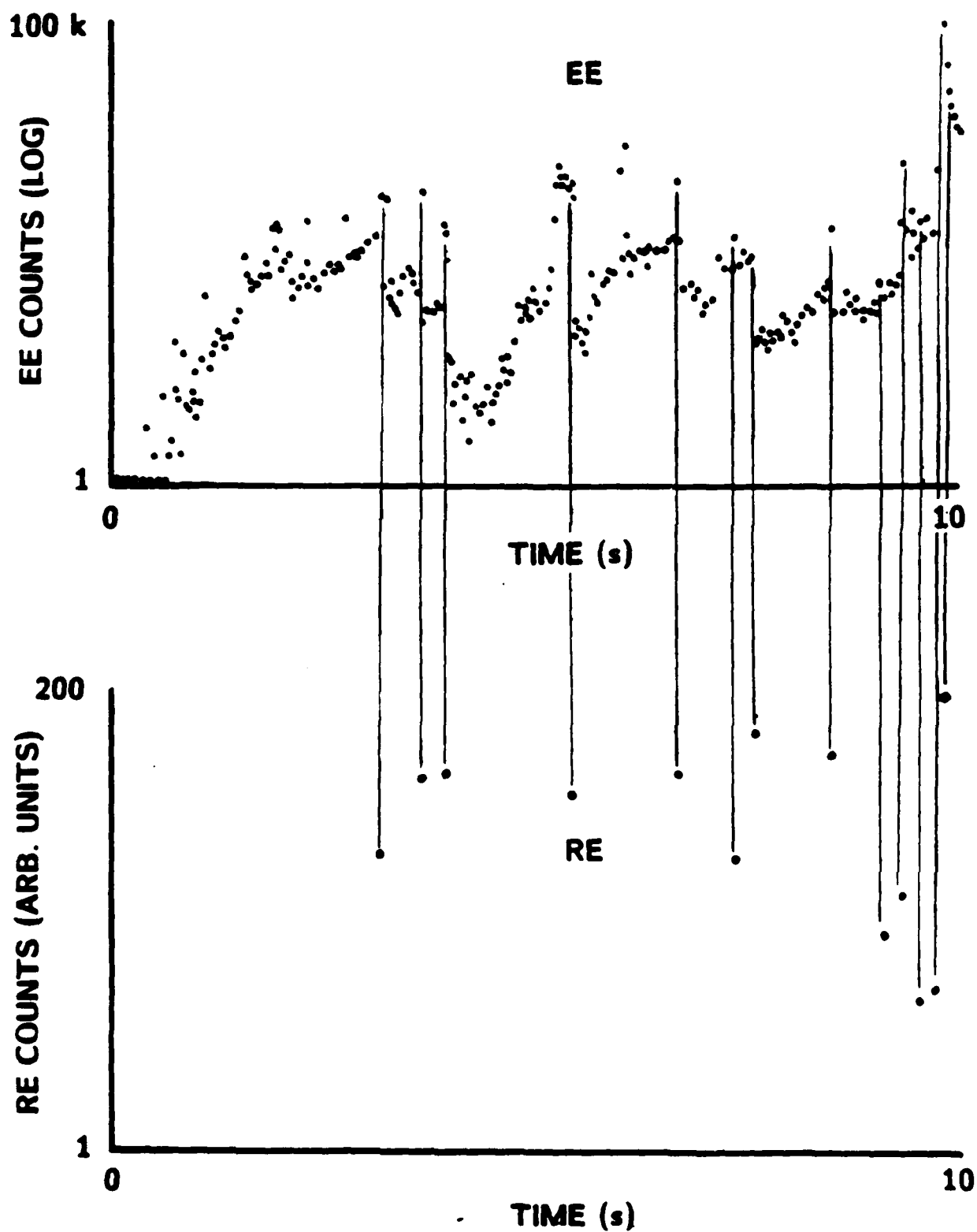
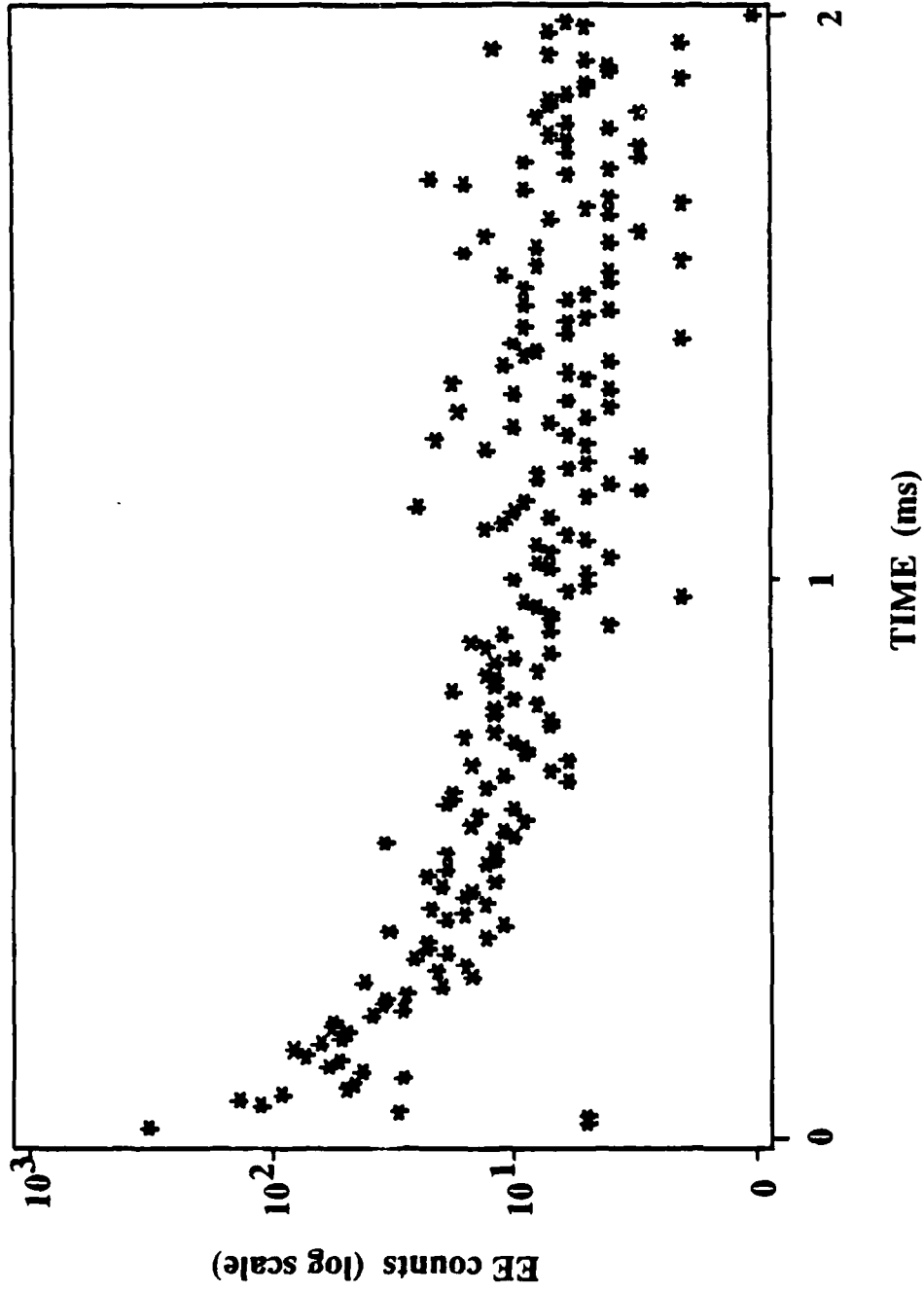


Fig. 18.

Time Correlation of EE with RE During Fracture of Filled ULPBR



86-136
ulpbr EE triggered with RE

Fig. 19

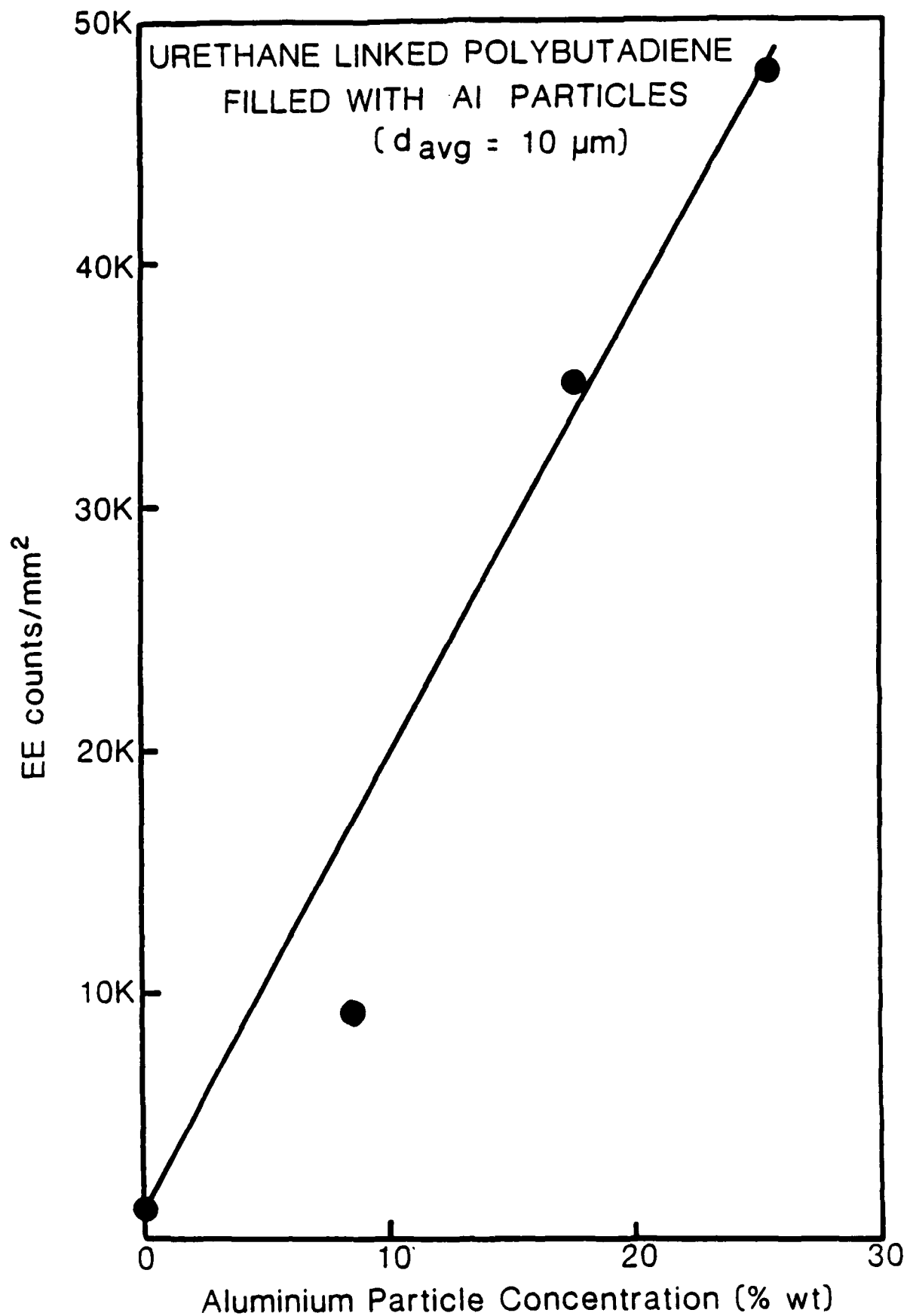


Fig. 20

ELECTRON EMISSION FROM
URETHANE LINKED POLYBUTADIENE
FILLED WITH Al PARTICLES

25.5% by weight, $d_{avg} = 30 \mu m$

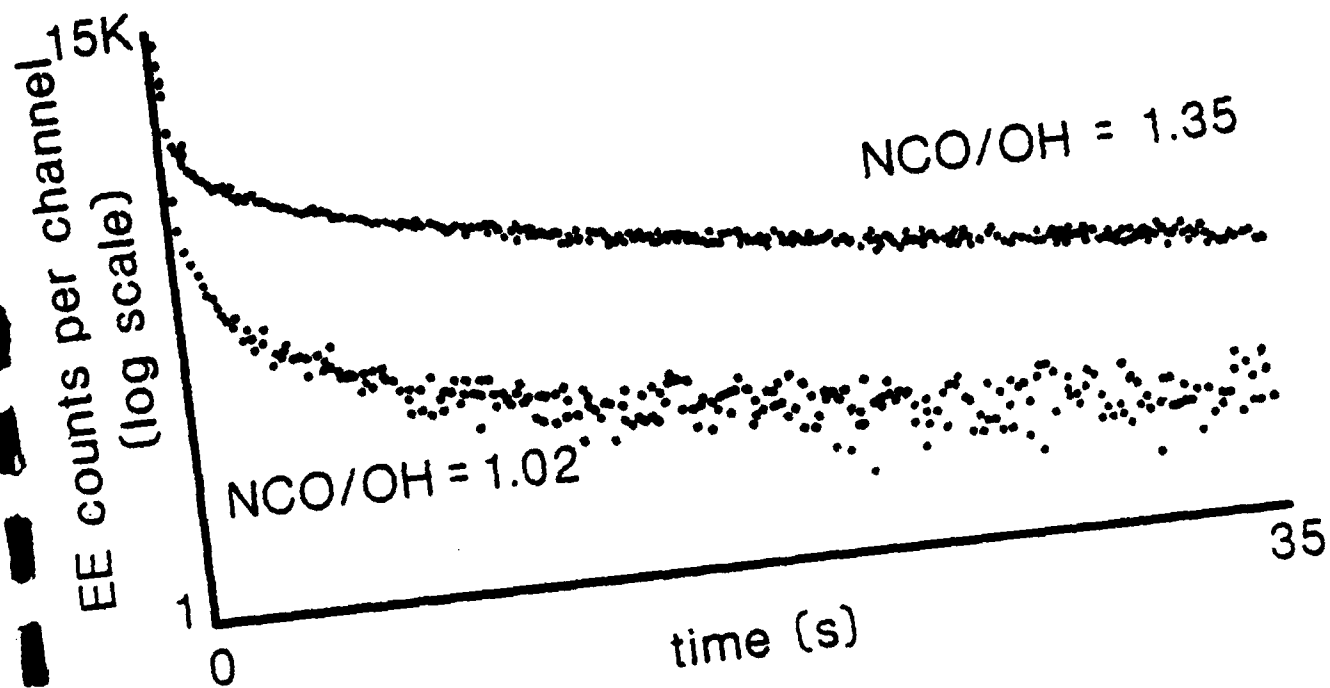


Fig. 21

IV. PRODUCTION AND PROPERTIES OF EJECTA RELEASED BY FRACTURE OF MATERIALS

E. E. Donaldson, J. T. Dickinson, and S. K. Bhattacharya

**Department of Physics
Washington State University
Pullman, WA 99164-2814**

ABSTRACT

We have examined ejecta (particles in the size range 0.1 to 500 μm) which are released by fracture of a variety of materials. The ejecta from most non-metallic materials are electrically charged and frequently have high velocities. The amount of ejecta produced depends on the material and the conditions of fracture. For unfilled, glassy polymers the ejecta are produced in regions of fast-hackled fracture. Detailed measurements have been made on the ejecta mass and size distributions from the fracture of composites. From these measurements the total particle surface areas can be estimated and are found to be comparable to or greater than the cross-sectional area of the fractured samples. Thus, the ejecta should be a consideration in the analysis of surface energy and other parameters from fractographical analysis.

Keywords: Fracture, Ejecta, Fluff, Fragmentation, Polymers, Composites, Epoxy, PEEK, Graphite.

I. INTRODUCTION

The fracture of a range of materials in several fracture geometries causes the ejection of visible particles. For example, in previous studies of fracto-emission¹, we noted that the front surfaces of our particle detectors (electron multipliers) accumulated tiny particles which clearly originated from the fracture zone. We decided to study the nature and origin of macroscopic particles arising from fracture, in particular those lying in size range from 0.1 to 500 μm . We refer to these particles as *ejecta* following the precedent of Asay who applied this name to the particles ejected by shock waves.²

Ejecta from the fracture of materials have been studied previously. Sharpe and Logioco photographed ejecta arising from the failure of lap shear specimens made of polycarbonate bonded with an acrylic adhesive.³ They pointed out that such ejecta could be of importance in any consideration of the fractography of the system; i.e., missing components of the original fracture surface.

In shock loaded materials, Asay² measured the mass and velocities of the ejecta produced when the shock wave emerges from the back side of a sample. In the case of porous tungsten samples the ejecta, having a mass of many milligrams, were shown to have significant momentum. Grady and Benson fragmented aluminum and copper rings by loading them electromagnetically⁴ so that they expanded radially, thereby failing in tension. These authors observed fragments in the size range from 0.1 to 1.0 g and found that the highest strain rates produced the smallest fragments.

In an unusual study involving considerably larger fragments, Kabo, Goldsmith, and Sackman⁵ examined the impact of several kinds of massive projectiles on rocks. These investigators used photography to determine that the rock fragments produced by impact had velocities which ranged up to 350 m/sec. In one series of experiments 20 and 40 mm cannons were mounted on a U.S. Army M-47 tank and fired at the nearly vertical shale walls of an open pit mine. Some fragments were collected near the point of impact on polyethylene sheets spread

on the floor of the mine. Other unanalyzed fragments were found within a radius of 100 m from the target.

Furthermore, there is considerable concern that ejecta may result in the formation of a belt of particles in orbit around the earth⁶. A large portion of this ejecta is produced from the breakup of earth satellites, explosions in space, and collisions between existing fragments and space vehicles. Satellites can be navigated to avoid the largest fragments, but smaller particles cannot be detected, and thus constitute a potential hazard to astronauts and space vehicles. As such particles continue to accumulate, an impassable belt may build up and render defense and scientific space systems inoperable in a few decades.

In addition to the above, ejecta from catastrophic fracture may have other implications and, in some cases, cause injury. An example, eye injuries can result from the ejection of tiny chips of glass due to fracture of glass corrective lenses. In large accidents, the optical absorption from high volumes of ejecta could be a danger in certain circumstances. Also, the sudden release of large quantities of conducting fibers (e.g., graphite) due to an airplane crash, etc. near high voltage transformers has been considered a possible hazard. In failure analysis, in the assessment of accidents, explosions, and criminal acts (where some form of fracture has occurred), examination of ejecta may provide additional clues as to the cause and/or sequence of events.

In the studies of fracture induced-ejecta presented here, we concentrate on the small fragments, arbitrarily choosing those with mass < 0.1 mg. The larger fragments, few in number, are commonly known to fracture scientists and are clearly attributable to crack bifurcation. Here we describe the results of a survey designed to reveal what types of materials release microscopic ejecta due to fracture. This survey showed that ejecta are produced by the fracture of many materials in several fracture modes and/or specimen geometries. Subsequently, we examine in more detail some of the properties of ejecta from graphite-epoxy composites, including measurements of the total quantity of material released, the size distributions of the ejecta, the general morphology of the particles, the presence of electrical charge on the ejecta,

and their kinetic energies. Finally, we also examine the ejecta from PMMA and unfilled epoxy in relation to features characterizing crack growth in these materials.

II. EXPERIMENTS AND RESULTS

A. Survey of Fracture Induced Ejecta

In order to determine the prevalence of ejecta, we began by fracturing a variety of pure and composite materials in several sample geometries. In many tests, a catcher of aluminum foil (called our "ejecta collecta") was placed under and around the fracture zone. For eye safety, plastic goggles were worn during the tests (called our "ejecta protecta"). After fracture, the larger fragments ($>1\text{mm}$ dimensions) were removed from the catcher and the remaining ("correcta") ejecta were weighed in a Cahn microbalance. The masses given in Table I have been normalized by division by the original cross-sectional areas of the unfractured samples. In Table I, "visible" indicates that the collector showed ejecta visible to the naked eye under oblique lighting. The blank spaces in Table I indicate that no experiment was done for that particular material and geometry. Our general observations as a result of this survey are as follows:

- 1) A wide range of materials produce detectable or measurable ejecta when fractured in several different geometries.
- 2) The only exceptions to this general result are adhesives and elastomers with $T_g < T_{\text{room}}$. For example, unfilled and particulate filled elastomers yield almost no ejecta when fractured in tension at relatively low strain rates and at room temperature. Similarly, the peeling of simple adhesives produced no measurable ejecta at room temperature. To date, we have not investigated these materials at low temperatures (below T_g) or at very high strain rates; these conditions would be more likely to produce ejecta.

- 3) When nonisotropic materials were fractured in the "strong" direction they produced more ejecta than when they were broken in the "weak" direction. For example, for uniaxial graphite fiber-epoxy composites (Table I), the ejecta yield is at least twice as great when tension is *along* the fibers (0° orientation) vs normal to the fibers (90° orientation).
- 4) When graphite-epoxy composites were fractured in three point bending geometry the ends split due to delamination. We found that the split ends of these samples which were far from the region of maximum tension but experiencing significant shear forces, were strong emitters of ejecta.
- 5) Unnotched samples (therefore, storing higher strain energy when stressed) produced more than ten times the mass of ejecta as compared to notched samples. This point is explored in more detail in Section E.

B. Properties of Ejecta from Graphite Fiber-Epoxy Composites

A more detailed analysis was made of the ejecta from the fracture of uniaxial graphite fiber-epoxy composites which were relatively strong ejecta emitters. The specimens were made from Union Carbide Thornel 300 graphite fibers and NARMCO 5208 epoxy resin. Three point bending experiments were done using 16-ply material having a sample cross-section of 2.4 x 6 mm. Tension experiments used 2-ply samples of the same material with a cross-section of 0.35 x 6 mm with the fibers aligned either along the tension direction (0° orientation) or perpendicular to this direction (90° orientation). The thinner material was used for the tensile experiments due to limitations on our straining device.

Figures 1 and 2 show SEM photographs of the end and side views of this composite. Fig. 1 is a polished and etched cross section of the specimen which reveals the distribution of the fibers in the matrix. Fig. 2 is a side view of the fibers on a fracture surface of a 0° specimen loaded to failure in a three point flexure. For size reference note that the graphite fibers are approximately 7 μm in diameter. Fig. 2 shows that after fracture, the graphite fibers and the

columns of epoxy matrix are covered with epoxy scales which sometimes exhibit evidence of plastic flow, shown enlarged in Fig. 3. These photographs suggest that the dominant composite failure mode is cohesive fracture through both matrix and fibers, although failure along the fiber-epoxy interface does occur to some extent.

Figures 4-6 are micrographs of the ejecta produced when the composite failed in three point flexure. The optical micrograph in Fig. 4 is a general view of ejecta and shows single graphite fibers, multiple fiber bundles, and smaller particles. It can be seen that some of the fibers appear clean and that others have scales or chips of the matrix attached. Fig. 5 is a low magnification SEM micrograph of typical ejecta, again revealing a range of ejecta morphology. Fig. 6 shows a typical aggregation or clump of fibers and flakes of epoxy which presumably formed after ejection due to agglomeration of individual ejecta particles.

The ejecta morphology exhibited in these micrographs is consistent with the fracture surface shown in Fig. 2; that is, the micrographs show pieces of epoxy adhering to the graphite fibers and also very finely divided epoxy particles. Again, these observations are consistent with failure that is largely via disruptive cohesive fracture of the epoxy and graphite fibers.

1. **Total Mass of Ejecta.** To determine the total mass of the ejecta, we placed an aluminum foil catcher under the sample and weighed the ejecta in a microbalance. Our findings were:

- (a) For 90° orientation (fibers perpendicular to tensile axis) we collected, on the average, 0.5 $\mu\text{g}/\text{mm}^2$ of sample cross-section. This is the "weak" direction of reinforcement.
- (b) For 0° orientation (fibers parallel to tensile axis) we collected, on the average, 2 $\mu\text{g}/\text{mm}^2$ of sample cross-section. This is the "strong" direction of reinforcement and yields significantly greater quantities of ejecta.

2. **Size and Morphology of Ejecta.** Because the ejecta exhibit a diversity of composition, shapes, and sizes, a single size distribution which would represent all of these

particles could not be obtained. We resolved the problem by counting all of the fiber-containing particles as single fibers. Separately we counted the other particles, which consisted mostly of epoxy, as matrix ejecta.

Under this simplifying classification we were able to measure the lengths of the graphite fibers and fiber bundles in an optical microscope because the graphite fibers are easy to identify by their black appearance. The length distributions of these graphite fibers and fiber bundles arising from four different fracture geometries are shown in Fig. 7. In determining all of these size distributions we used a geometric progression of particle size ranges. The points plotted in each case show the percentage frequency distribution⁷ vs particle size.

Because the ejecta composed of matrix material were very small and because they tended to form clusters or to cling to fibers, we produced SEM photographs which allowed the size of individual particles to be measured. Even though the matrix ejecta are very irregular in shape, an effective diameter was calculated for each particle by taking the average of its length and width. Fig. 8 shows this effective diameter distribution for matrix ejecta resulting from four different fracture geometries.

The size distributions of the matrix particles in Fig. 8 are quite similar for three point flexure and tensile fracture. This is probably due to the fact that in three point bending, front layers of the composite fail in tension in a manner similar to tensile specimens at the same local stress levels. Compression loading of the back side of the sample would play a small role in producing ejecta. In contrast, the fiber ejecta show size distributions dependent on fracture geometry (Fig. 7). Note that for the fracture of the 2-ply material in tension the fiber ejecta are much shorter than for other geometries.

Examination of Fig. 1 shows that the average width of the matrix filled channels between fibers is 10 to 20 μm . However, the mean matrix ejecta size (from Fig. 8) is only 1 μm . We know that the fibers in this composite are well bonded to the matrix because we find scales of epoxy attached to the graphite fibers following fracture. In composites with well

bonded fibers, failure is initiated by fiber fracture. Apparently when these fibers fail they cause a very disruptive fracture of the matrix leading to the release of small matrix ejecta.

3. **Surface Area of Ejecta.** Having obtained the total mass and size distribution of the ejecta, we can estimate the total particle surface area for two extreme cases where we assume that all of the ejecta are matrix particles or that all of the ejecta are fiber particles. Let us examine the case of "all matrix" particles and choose the size distribution from three point bending and 0° orientation of fibers (Fig. 8). Assuming that the particles are spheres, the calculated specific surface area of the ejecta is $8.2 \times 10^5 \text{ mm}^2/\text{g}$. Table I shows an average of 15 μg of ejecta from the fracture of such a sample with a cross-section of 7.35 mm^2 . This quantity of ejecta would therefore have a surface area of at least 12 mm^2 , which is comparable to the sample's cross-section.

A different result is calculated in the "all fiber" assumption. Because the specific surface area of ejecta in the form of fibers (assumed to be smooth cylinders) is about $5 \times 10^4 \text{ mm}^2/\text{g}$, the same mass of ejecta would have an area of only 0.1 mm^2 if composed solely of fibers.

The assumptions made in the calculated surface areas for ejecta from graphite fiber-epoxy should in most cases lead to underestimates. As evidence, we first note that the SEM photographs show that the ejecta are not cylindrical and spherical in shape but are extremely rough and irregular and therefore have surface areas considerably larger than we calculate. Second, the total ejecta mass measurements are low because some of the high energy ejecta components escape collection. Finally, as we later describe, the trapping of ejecta in and around the crack occurs; i.e., considerably more ejecta are created than released. All of these effects conspire to guarantee that the calculated areas are much lower than the actual areas.

C. Size Distributions of Ejecta From Fracture of Filled and Unfilled PEEK

For a comparison with the results reported under Section B, we measured the total mass and the size distribution of ejecta arising from the tensile fracture of polyether ether ketone (PEEK). This material was originally formed by injection molding PEEK either unfilled or filled 30% by weight with short carbon fibers averaging 80 μm in length. Dog bone shaped samples were tested in tension.

Fig. 9 is a plot of the size distribution of ejecta from the PEEK composite. Matrix ejecta from filled or unfilled PEEK have a mean diameter of 10 μm which is about an order of magnitude larger than the diameter of epoxy matrix ejecta (Fig. 8). This can be attributed to the greater fracture toughness of PEEK in comparison to epoxy. We note that the mean length of the fiber ejecta from the PEEK composite was approximately 60 μm which is very close to the mean length of the original fibers. Thus, the release of essentially unbroken fibers upon fracture is due to the fact that these fibers are shorter than the critical length associated with this particular PEEK/fiber interface.

Further evidence of a fairly weak interface was seen in SEM photographs (not included) which show extensive fiber pullout during fracture of the PEEK composite. Thus, the weaker interface and tougher matrix make the fracture of carbon fiber-PEEK composite differ greatly from the failure of the epoxy composite.

D. Studies of Electrical Charges on Ejecta

As we have noted earlier, we frequently found the fine ejecta particles clumped together in the form of large aggregates (e.g., see Fig. 6) suggesting that perhaps electrostatic forces were present. (A dramatic example of the aggregation of ejecta particles was experienced by those of us in Eastern Washington on May 18, 1980, a few hours after the eruption of Mt. St. Helens. The ash created during the rhyolitic explosion which began falling in Pullman, Washington

approximately 6 hours after the eruption was highly aggregated, probably due to electrostatic attraction of the charged particles.⁸⁾

We examined the electric charge on fracture-induced ejecta in two different ways. In the first experiments we fractured composite specimens in tension between parallel vertical plates at potentials ± 2 kV, respectively. The plates each had an area of 15 cm^2 and they were separated by 2.4 cm creating a nearly uniform field to minimize polarization forces due to field gradients. Most of the ejecta experienced significant deflection and were collected on the plates. We sought but did not find any segregation of particular types of particles by charge sign; i.e., fiber fragments were not separated from the matrix fragments on oppositely charged plates. This indicates that the ejecta composed primarily of matrix material or primarily of fiber material carry charge of either sign. Such a mixture of charge would encourage the aggregation or the clumping observed.

We also used three point flexure to launch ejecta toward metal collector plates connected to an electrometer thereby measuring the total net charges on the ejecta. We found that individual ejecta or ejecta showers usually carried net charges of approximately 10^{-14} C and that net integrated charge on ejecta produced by the complete fracture of a sample several mm^2 in cross-section was in the range of 10^{-13} to 10^{-12} C . It should be emphasized that the detection of charges of both *signs* implies that the quantity of charge of each *sign* is likely to be considerably larger than the *net* value and that larger individual ejecta also carry patches of charge of both signs.

We might expect that the ejecta should be charged for a number of materials. When fracture occurs in piezoelectric materials, those containing a high density of charged point defects, and specimens involving interfaces between dissimilar materials, we find that the newly created surfaces contain patches of \pm charge. This charge separation is particularly intense in the interfacial failure case, e.g. graphite and epoxy. Electrostatic discharges which occur during fracture frequently redistribute the charges in a variety of sign/density patches. Thus the ejecta can carry substantial charges of either sign. It is likely that electrostatic forces due to these

charge patches play a role in the subsequent behavior and trajectories of the ejecta as well, although the kinetic energies of the ejecta come predominantly from the release of mechanical energy.

E. Velocity of Ejecta

When uniaxial graphite fiber-epoxy composites are deformed in three point flexure (with the fibers aligned along the tensile direction), the rapid failure of the outer plies is accompanied by an easily detectable acoustic emission (AE) burst. Thus an AE transducer can be used to detect the time these failure events occur to within a few microseconds. The charged ejecta which are released at fracture can be made to pass through two parallel grids where they induce detectable electrical signals in the form of pulses. We used the AE signal to start a time measurement and the electrical pulses to signal the arrival of ejecta at the grids. The signal from the first grid told us that the ejecta are released in a short time ($t < 1$ ms) after the fracture event and the signals from the first and the second grids told us that at least some ejecta travel at 50 m/s in air. Calculations based on Stokes'⁹ law show that small spherical particles with diameters less than 5 μ m would travel horizontally less than 1 cm in still air even if launched at initial speeds of 100 m/sec. Lower speeds or irregular shapes would result in a smaller range. Thus, the charged ejecta whose velocity were measured, must necessarily have been the larger fragments.

In spite of this air drag, one particularly strong epoxy sample produced ejecta with sufficient kinetic energy to make 50 visible indentations in the aluminum foil (0.015 mm thick) which we used as a catcher, demonstrating that these fragments can have considerable momentum.

F. Correlation of Ejecta with Fracture Surface Roughness in Glassy Polymers

In glassy materials, the nature of the fracture surfaces created is governed by the crack velocity. Slow crack growth produces smooth mirror-like surfaces; intermediate speed produces "mist" or lightly rippled surfaces; fast fracture produces very rough or "hackled" surfaces which result from crack bifurcation and branching.¹⁰⁻¹⁵ When we examined the ejecta from PMMA and neat epoxy [Epon 828/Z Hardener] under a stereo microscope we identified particles in the shape of flakes and fibrils and saw other finely divided unresolved material. The hackled fracture surfaces of PMMA and epoxy displayed potential ejecta having a similar appearance in a wide range of sizes, shapes, and strengths of attachment to the surface. A typical fast fracture surface for an unfilled epoxy showing these surface features is seen in Fig. 10. We found that some of the particles were very loosely attached and could be dislodged by a blow to the back of the sample. These loose particles are ejecta which were trapped in the crack and remain bound to the surfaces. More tightly attached particles could be lifted off with adhesive tape. Even after tape had been peeled from the fracture surfaces they continued to hold flakes and fibrils which were firmly attached by one end.

A related observation was made on tensile fracture specimens of center notched samples of PMMA. Following the fracture, we microscopically examined the smooth faces of the sample adjacent to a fresh crack (i.e., in the region of the dashed lines in Fig. 11). Electrostatic charges on the ejecta and/or the surfaces caused the ejecta to be attracted to and captured by these surfaces. These finely divided ejecta were always concentrated near the rough or hackled fracture region, whereas very few ejecta were found near the mirror surfaces.

The above observations indicate a clear positive correlation between ejecta and hackled fracture. To provide further evidence of this association we weighed the ejecta produced by fracture initiated under different conditions. For example, unnotched tensile samples of epoxy were made with a smoothly tapered central section so that they would have little stress

concentration and high elastic energy. Such samples were of high strength and they fractured by rapid crack growth producing very rough, hackled fracture surfaces. Notched samples were prepared with cuts made by broad and narrow saw blades. These notches caused higher stress concentration with failure at less elongation. This resulted in slower crack growth and smooth fracture surfaces. We cleaned the samples before fracture to remove chips or dust caused by shaping them. Because manipulation of the samples produced surface charge, we electrically neutralized them by brief exposure to the plasma above a propane flame just before they were tested, thereby reducing electrostatic retrapping of the ejecta.

The fracture of unnotched samples always produced rough hackled surfaces and more than $30 \mu\text{g}/\text{mm}^2$ of ejecta (after the very large fragments were removed). In contrast, fracture of the samples with narrow saw notches produced smooth surfaces with much less total ejecta mass. The weakest samples with narrowest saw notches produced only $0.5 \mu\text{g}/\text{mm}^2$ of ejecta, all of which were very small particles. Samples with wider saw notches produced an intermediate quantity of ejecta, averaging $1.3 \mu\text{g}/\text{mm}^2$ of surface area. Thus, for glassy polymers such as PMMA, conditions encouraging fast crack propagation clearly encourage ejecta production. In viscoelastic materials, this would correspond to more brittle-like behavior. Therefore, we anticipate that low temperature fracture and/or high strain rate loading of polymers, including elastomers, would enhance the production of ejecta.

G. Mechanisms for Fracture Induced Ejecta

During rapid crack growth in glassy polymers, microcracks and voids form ahead of the crack tip. As the crack tip advances, the crack may branch or bifurcate along these microcracks.¹¹⁻¹⁵ Similarly, in inorganic materials such as glass, ceramics, and even single crystal brittle materials, such bifurcation can occur.¹⁶ The multiple cracks may grow around large or small regions of the sample frequently arresting a small distance from the dominant crack. Thus free, lightly bound, and securely attached flakes or projecting structures are

produced on the fracture surfaces. In polymers, material between microcracks may still remain under tension and be drawn plastically to produce fibrils which are frequently observed in the region of hackled fracture. In general, the fracture of brittle materials can produce a variety of particle-like protuberances in a number of shapes and sizes with varying degrees of attachment to the surfaces ranging from completely free to firmly bound. Similarly, in composites, the inhomogeneities cause crack paths to have extremes of crack bifurcation and branching, again creating numerous "near fragments" attached to the surface.

When a material is fractured there is a sudden release of strain energy. This sends mechanical release waves toward the gripped ends of the sample where they reflect back to the fracture zone. Fragments on the fracture surfaces which are partially detached by crack bifurcation can be ejected with momentum imparted by the wave.

Choosing PMMA as a model material and a sample size of a few mm in length, the wave would return to the fracture surfaces in 1 to 10 μ s. We can write the characteristic equation for small amplitude acoustic waves in the form:¹⁷

$$\Delta u = \frac{\Delta p}{\rho c}$$

where Δu is the particle velocity and Δp the pressure increase produced when the material fails. We set Δp equal to the tensile stress of PMMA (~ 60 MPa). For the density we take 1.2×10^3 kg/m³, and for the speed of sound, $c = 2500$ m/s. The calculated particle velocity, Δu , is then 20 m/s. When the reflected wave returns to the fracture surface, the free surface velocity is twice this value, i.e., 40 m/s. Assuming perfect coupling between the surface and partially attached fragments, the resulting ejecta could have final velocities of this magnitude. Focusing of the mechanical waves could produce even higher ejecta velocities, for example at edges, corners, and other anisotropic features. This calculated velocity is consistent with the velocities of larger ejecta which we report above.

Only some of these released particles actually escape with these higher velocities. Others undergo wall collisions inside the crack and are trapped at the walls by electrostatic or van der Waals forces, and are frequently observed under the microscope. One would expect that electrostatic attraction and/or repulsion caused by patches of charge would also play a role in altering the trajectories of ejecta.

III. CONCLUSIONS

Fracture-induced ejecta are produced when a variety of materials are broken in several modes of fracture. In a preliminary survey we have identified only a few materials such as elastomers and simple adhesives which do not produce observable fracture-induced ejecta at room temperature. Within a class of materials, the strongest samples yield the greater mass of ejecta. A geometry or a material which stores greater amounts of strain energy before failure will produce the greater mass of ejecta, emphasizing the importance of ejecta in the failure of strong and/or tough materials. Reinforced materials such as the graphite epoxy composite are copious sources of ejecta due to the high strain energies stored in the fibers.

The surface area of fracture-induced ejecta may be greater than the cross-sectional area of the fractured sample and thus ejecta should be considered in any description of fracture for most materials. High strength materials yield the most finely divided ejecta with high surface areas.

The ejecta from the nonmetallic materials and composites were found to be highly charged. One interesting question arises concerning the role such ejecta might play in inducing electrical breakdown if a fracture event occurred near high voltage gaps.

The relatively prompt release of the ejecta and the observed velocities are consistent with a mechanism involving the reflection of the release wave created during fracture. The reflected wave imparts to the free surface a particle velocity which can couple mechanically to

semi-attached fragments and thereby release them. Corners and edges are likely points of higher amplitude waves and therefore higher particle velocities.

When pure polymers fracture in tension the ejecta arise primarily from the regions corresponding to hackled surfaces. These surfaces contain numerous "chunks" which are more likely to be released. In a viscoelastic material, these hackled regions correspond to more brittle-like, higher velocity fracture. We anticipate that low temperature fracture and/or high strain rate loading would enhance the production of ejecta. It should be emphasized that the degree of crack bifurcation and branching is expected to increase with the total strain energy released during fracture. Likewise, the amplitude of the reflected waves would increase with the strain energy stored in the specimen. Therefore, one would expect a strong correlation between strain energy and quantity of ejecta released. Furthermore, any fractographic analysis of surface energy must take into account the fact that a large portion of the surface area carried away by the ejecta is created at the time of fracture and should therefore be included.

In summary, this study of fracture-induced ejecta has demonstrated their widespread occurrence and has provided initial information about ejecta morphology, size distributions, electrical charge, and velocity.

ACKNOWLEDGMENTS

We wish to thank G. R. Fowles and Les Jensen, Washington State University, for helpful discussions and assistance in this work. We also thank Howard Nelson, NASA-Ames Research Center for supplying the graphite-epoxy samples and Clarence Wolf, McDonnell Douglas Corporation for supplying the PEEK samples. This work was supported by the McDonnell Douglas Independent Development Fund and the Washington Technology Center.

REFERENCES

1. J. T. Dickinson, L. C. Jensen, and A. Jahan-Latibari, *J. Vac. Sci. Technol.* A2, 1112 (1984); J. T. Dickinson, A. Jahan-Latibari, and L. C. Jensen, in *Molecular Characterization of Composite Interfaces* edited by N. G. Kumar and H. Ishida (Plenum, New York, 1985) pg. 111.
2. J. R. Asay, *J. Appl. Phys.* 49, 6173 (1978). J. R. Asay, L. P. Mix, and F. C. Perry, *Appl. Phys. Lett.* 29, 284 (1976).
3. L. H. Sharpe and J. W. Logioco, unpublished work.
4. D. E. Grady and D. A. Benson, *Exptl. Mech.* 13, 393 (1983).
5. M. Kabo, W. Goldsmith, and J. L. Sackman, *Rock Mechanics* 9, 213 (1977).
6. Comment by E. Marshall, *Science* 230, 424 (1985).
7. T. Allen *Particle Size Measurement* (Chapman and Hall, London 1975) 2nd ed., Chapt. 4
8. R. K. Sorem, *J. Volcan. Geotherm. Res.* 13, 63 (1982).
9. E. H. Kennard, *Kinetic Theory of Gases* (McGraw-Hill, New York 1938) p. 309.
10. H. H. Kausch, *Polymer Fracture* (Springer-Verlag, Berlin 1978) pp. 300-306.
11. K. Ravi-Chandar and W. G. Knauss, *Internat. J. Fract.* 26, 65 (1984).
12. W. G. Knauss and K. Ravi-Chandar, *Internat. J. Fract.* 27, 127 (1985).
13. R. J. Morgan, J. E. O'Neal, and D. B. Miller, *J. Mater. Sci.* 14, 109 (1979).
14. A. B. J. Clark and G. R. Irwin, *Exptl. Mech.* 6, 321 (1966).
15. C. J. Phillips in *Fracture: An Advanced Treatise* edited by H. Liebowitz (Academic Press, New York, 1972) Chap 1, sec IX.
16. B. R. Lawn and T. R. Wilshaw, *Fracture of Brittle Solids* (Cambridge University Press, Cambridge, 1975) pp 100-105.
17. R. Courant and K. O. Friedrichs, *Supersonic Flow and Shockwaves* (Interscience Publishers NY 1948) p. 82.

FIGURE CAPTIONS

- Fig. 1. SEM photograph of graphite fiber-epoxy composite 16-ply. End view of fibers cut, polished, and lightly etched to free the fibers. The fibers are about 7 μm in diameter. Width of interstitial epoxy-filled channels 0 to 20 μm . Striations are visible on sides of some fibers.
- Fig. 2. SEM photograph of fracture surface of graphite fiber-epoxy composite formed by three point bending. Lengthwise striation of graphite fibers shown along with scales of adhering epoxy.
- Fig. 3. SEM photograph of surface like Fig. 2 at higher magnification showing scales of epoxy and evidence of plastic flow.
- Fig. 4. Optical micrograph of ejecta from three point bending 0° orientation fracture of graphite fiber-epoxy composite. Fiber lengths only were measured from such fields. Epoxy can be seen adhering to fibers. About 240x.
- Fig. 5. SEM photograph of ejecta from fracture as in Fig. 4 showing single graphite fibers, graphite fiber bundles and clusters of small ejecta.
- Fig. 6. SEM photograph of ejecta from fracture as in Fig. 4. Surfaces of fibers show clinging epoxy particles as small as 0.01 μm as well as scales of adhering epoxy. Presumably electrostatic forces form such clusters.
- Fig. 7. Size distributions (lengths) of fiber-containing ejecta from various fracture geometries for graphite fiber-epoxy composite obtained from optical microscopy.
- Fig. 8. Size distributions of matrix ejecta from fracture of graphite fiber-epoxy composite obtained from the SEM.
- Fig. 9. Size distributions of ejecta produced by tensile fracture of neat PEEK (curve A) and carbon fiber-PEEK composite (curve C-F for fibers and curve C-M for matrix ejecta).
- Fig. 10. SEM photograph of fast tensile fracture surface of unfilled epoxy showing flakes and fibrils.
- Fig. 11. Sketch of PMMA tensile fracture sample showing region where ejecta were examined microscopically

TABLE I. Observed Ejecta and Yields

	Yields $\mu\text{g}/\text{mm}^2$	
	Tensile Fracture	3 Point Flex
GLASSY MATERIALS		
Soda-Lime Glass Slide	0.80	1.0
PMMA	0.04	0.17
PS	0.11	0.09
Epoxy (EPON 828 Strong Samples)	30.0	0.63
Fused Silica		visible
Glass Fibers	visible	visible
Graphite Fibers	visible	visible
Epoxy (CEIBA GEIGY MY720 Cured with DDS)	visible	
PEEK	0.05	
COMPOSITE AND FILLED MATERIALS		
PS + Random Glass Fibers	2.15	0.13
Epoxy + Uniaxial Graphite Fibers (Thornel 300 in NARMCO 5208)		
Tension at 0° wrt Fibers		2.0
Tension at 90° wrt Fibers		0.5
Epoxy + Uniaxial Graphite Fibers (Fiberite 934)		
Tension at 0° wrt Fibers	visible	3.4
Tension at 90° wrt Fibers		1.8
Epoxy + Alumina Powder		
(EPON 828 filled with Alumina 1:1 by vol.)	2.5	0.13
PEEK + Carbon Fibers (80 μm length fibers, 30% by weight)	0.25	

TABLE I. (cont.)

CRYSTALLINE MATERIALS

Silicon (100) Fract to (110)	3.6
Fract 45° to (110)	5.4
Quartz	visible
Alumina	11.0
Sapphire	visible
MgO	visible
PZT	visible
LiF	visible
BN	1.0

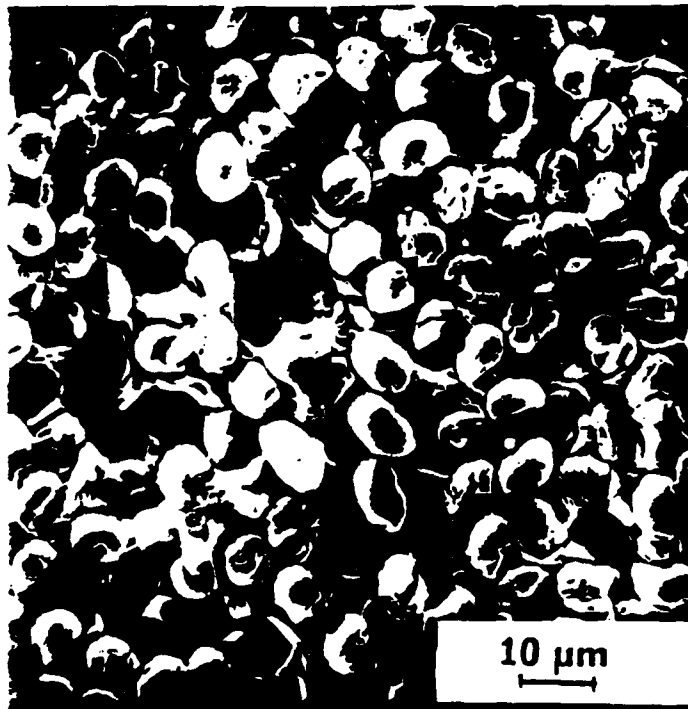


Fig. 1

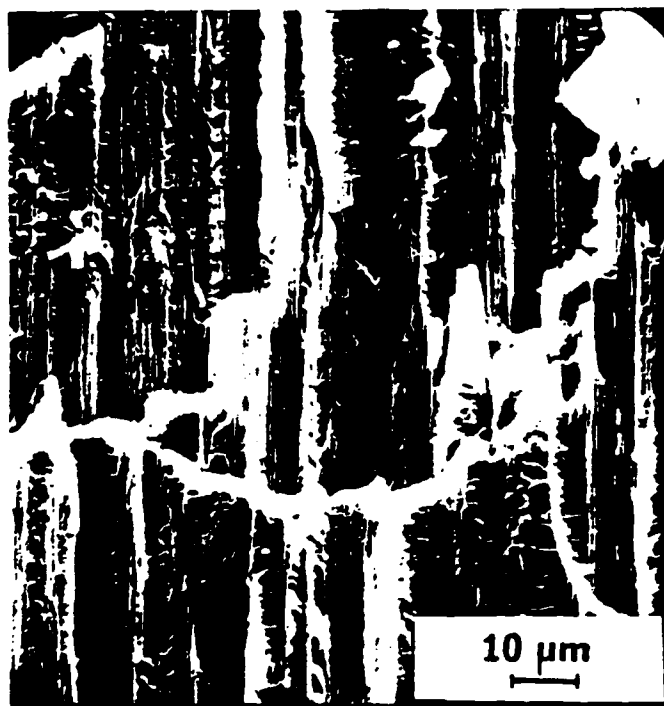


Fig. 2



Fig. 3



Fig. 4

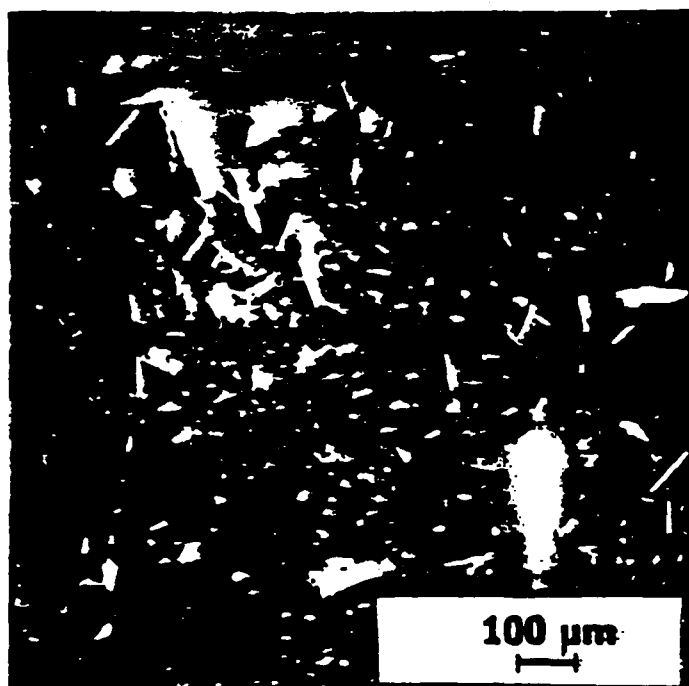


Fig. 5



Fig. 6

16 PLY CARBON FIBER - EPOXY COMPOSITE

FIBER SIZE ANALYSIS (OPTICAL MICROSCOPE)

GEOMETRY	MEAN SIZE	SYMBOL
TENSION 0° (2PLY)	50 μm	○
TENSION 90°	160	●
3 PT. BEND 0°	300	△
3 PT. BEND 90°	90	▲

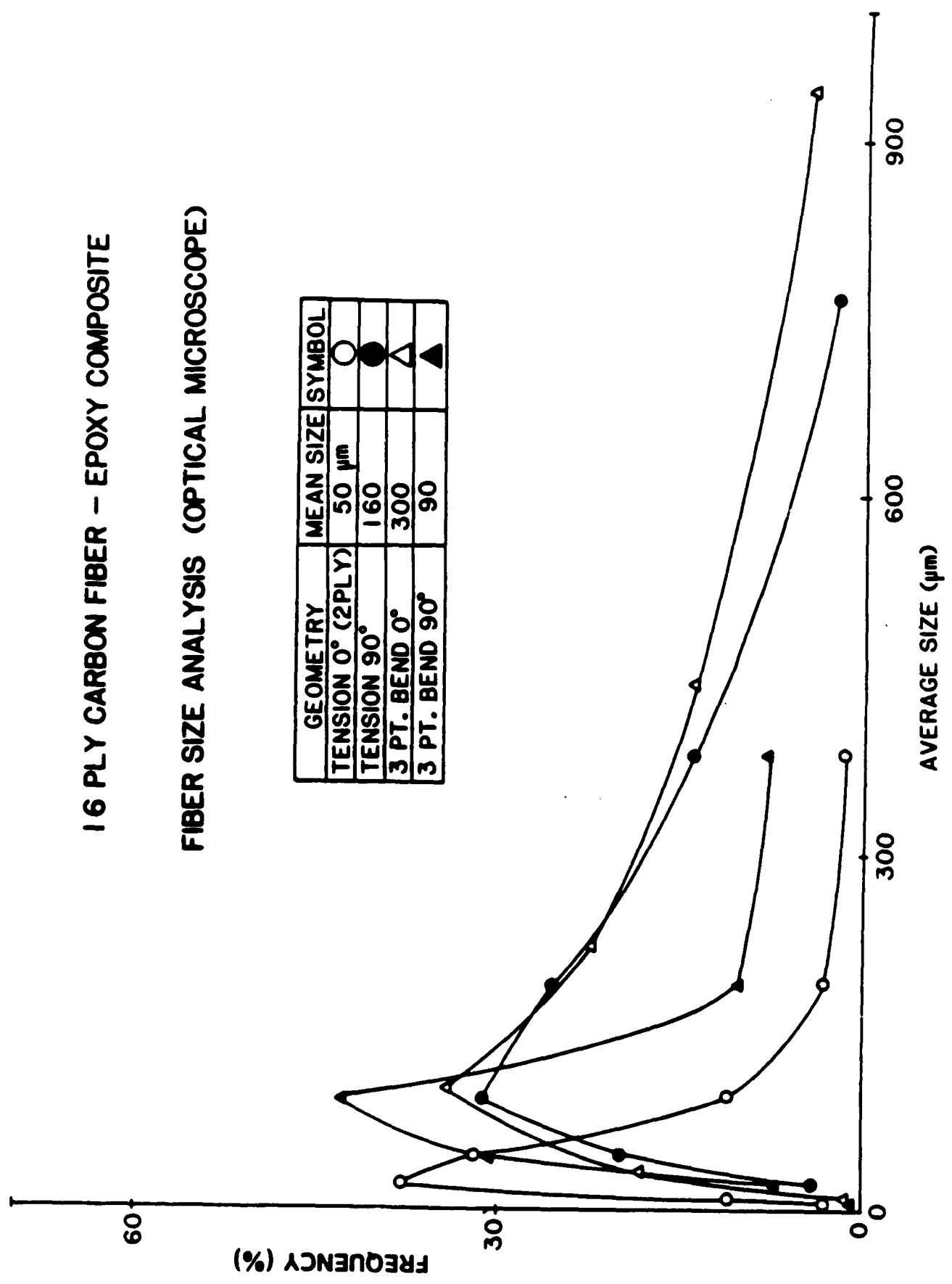


Fig. 7

16 PLY CARBON FIBER - EPOXY COMPOSITE

MATRIX SIZE ANALYSIS (SEM)

GEOMETRY	MEAN SIZE	SYMBOL
TENSION 0° (2PLY)	1.0 μm	○
TENSION 90°	1.5	●
3 PT. BEND 0°	1.0	△
3 PT. BEND 90°	2.0	▲

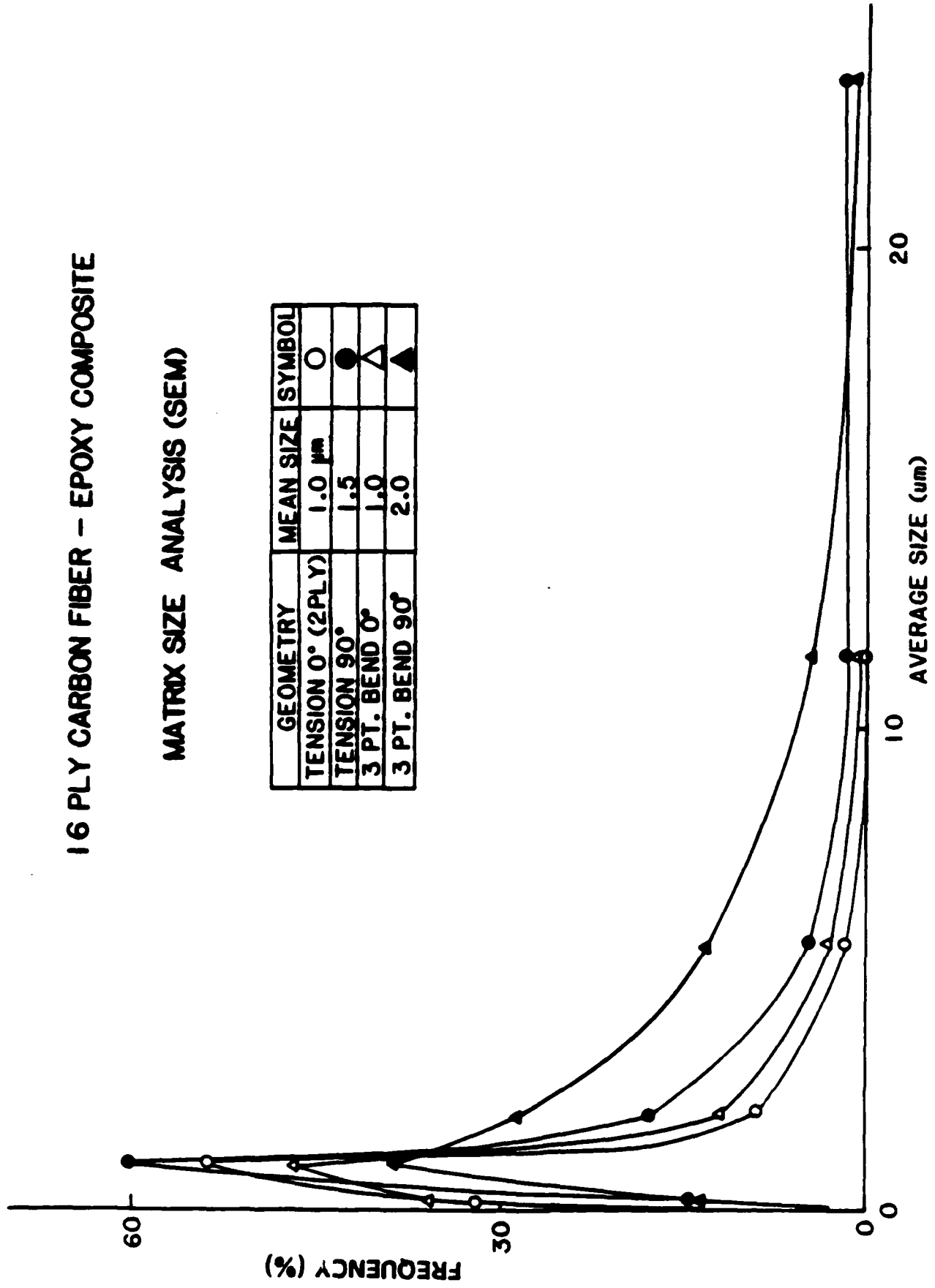


Fig. 8

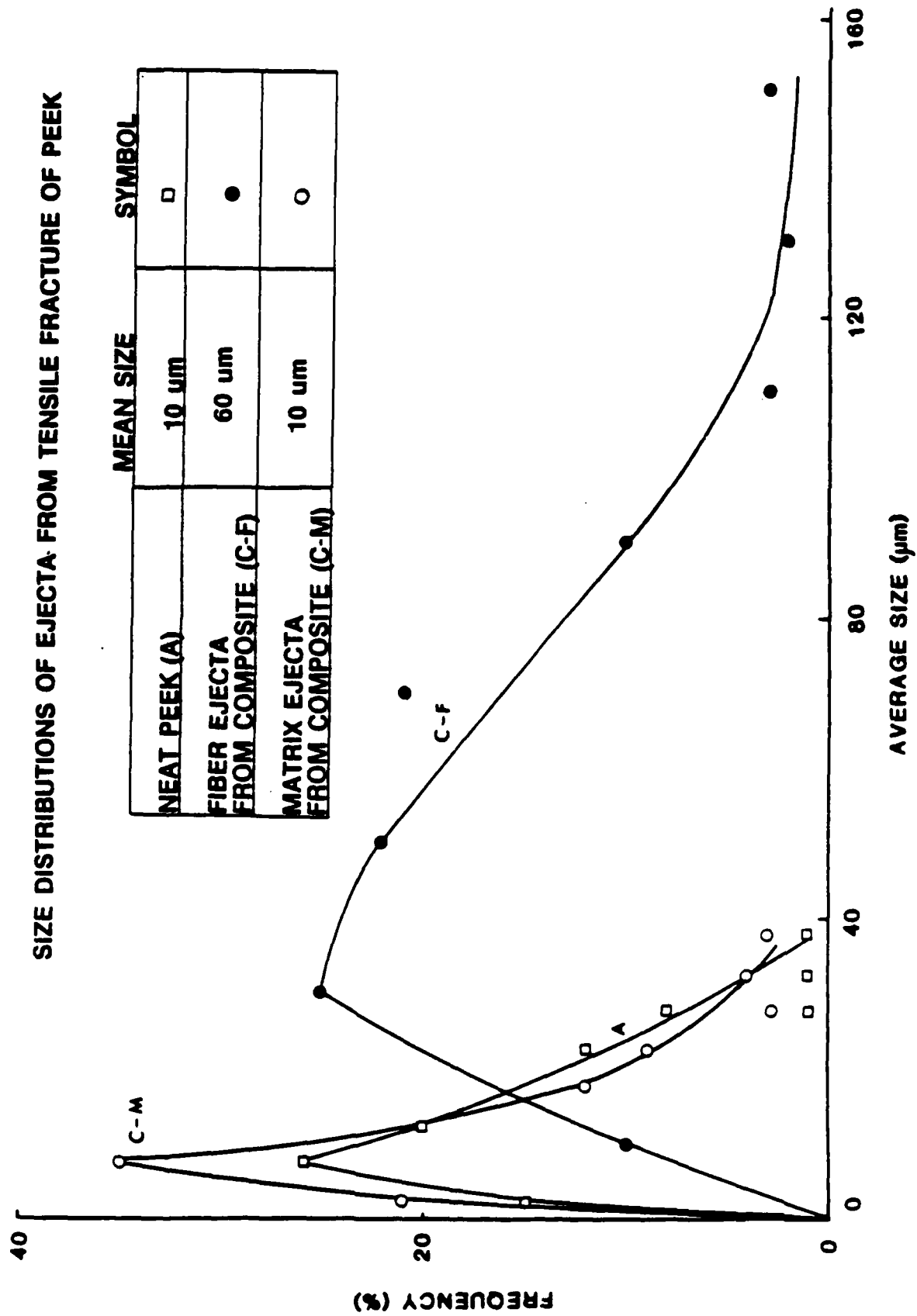


Fig. 9

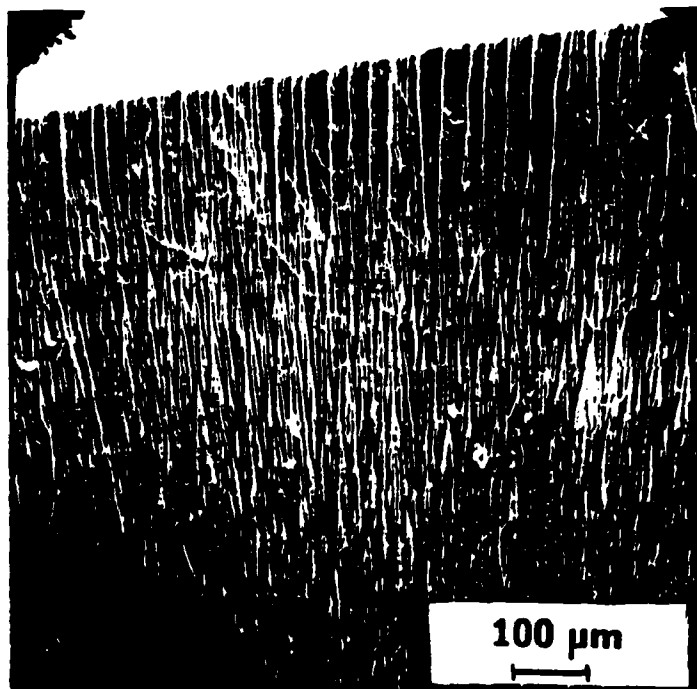


Fig. 10

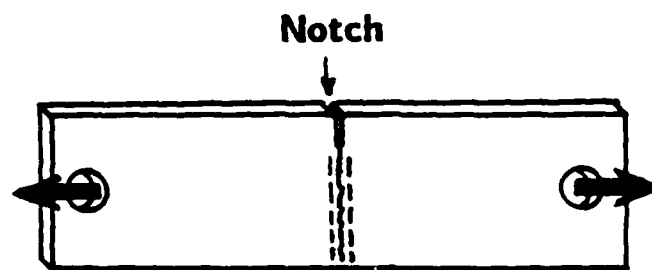


Fig. 11

V. Electrical Charge Measurements on Ejecta from Impact Loading of Explosive Crystals

E. E. Donaldson, M. H. Miles, and J. T. Dickinson
Department of Physics
Washington State University
Pullman, WA 99164-2814

ABSTRACT

We present measurements of the properties of the small, macroscopic particles (ejecta) that are released from the impact loading of single crystals of pentaerythritol tetranitrate (PETN). Total mass of the ejecta, total electrical charge on the ejecta, and approximate size distributions are presented. A few measurements were also performed on crystals of cyclotrimethylenetrinitramine (RDX) and cyclotetramethylene tetranitramine (HMX).

KEYWORDS: Ejecta, Impact Loading, Fracture, Explosives, PETN, RDX, HMX

INTRODUCTION

In a previous paper¹ we reported on the production and properties of small macroscopic particles (ejecta) in the size range of 0.1 - 500 μm released from the fracture of solid materials. The materials studied included: pure crystalline inorganic compounds, polymers, and polymer matrix composites. Briefly, we observed that when materials were fractured in tension or in 3 point flexure loading:

1. The fracture of most solid materials produced ejecta.
2. In many cases the surface area of ejecta was appreciable and, in some cases, was greater than the cross-sectional area of the sample.
3. Ejecta tended to carry electrical charge. Individual ejecta particles were found to be charged either + or -.
4. Ejecta were released with velocities as high as 50 m/s.

In this paper, we report the investigation of ejecta arising from the impact loading of crystalline PETN, RDX, and HMX. The choice of impact loading was made principally because of the small sample dimensions (typically, millimeter size crystals) and possible relevance to impact loading tests of explosive sensitivity.^{2,3} Earlier studies of PETN in our laboratory had demonstrated that impact crushing produced high levels of fracto emission⁴ (defined as the emission of electrons, ions, neutral atoms and molecules, and photons due to deformation and fracture). Furthermore, long wavelength radiation (radiowave emission-RE) was detected during crushing and was attributed to small electrostatic discharges due to charge separation occurring across fracture surfaces. Our

major goal in this study is to examine the possible electrical charge on the fragments produced by fracture. In addition, we measured the total yield and size distributions of the macroscopic particles created during impact loading which is used to estimate an *average* charge density on the ejecta surface.

EXPERIMENTS

A sketch of the impact device used in these studies is shown in Fig. 1. The crystals were crushed between planar hardened steel surfaces, each 12 mm in diameter. The striker was driven by a hammer blow to its top end providing an impulse of ~ 1 Kg m/sec. The time profile of the applied force was measured using a force transducer built into the anvil. When the hammer hit the striker, the force on the sample increased for approximately 100-200 μ s then fell rapidly as the crystal collapsed. The maximum applied force was typically 5000 N.

The tests were conducted by placing a single crystal or several crystals of mm dimensions at the center of the anvil and driving the striker down to impact them with a single blow. Under these experimental conditions, a single impact always crushed the crystals and produced ejecta without any evidence of ignition.

Subsequent impacts delivered to the sample after it had already been crushed usually caused ignition. The location of this ignition was usually near the edges of the crushing surfaces and produced ejecta in an obvious directional jet. Ignition always produced an accompanying plasma of highly charged species which we could not avoid collecting. To prevent this somewhat uncontrolled charge emission, we limited our measurements to single impact, purposefully avoiding ignition.

The mass of ejecta and their electrical charge was measured by catching the ejecta in a spun aluminum collector 28 mm in diameter positioned as shown in Fig. 1. An electrically grounded metal screen was placed in front of the collector to shield it from any

electrical activity in the fracture zone and also to prevent fragments larger than 1.5 mm from reaching the collector. Although the screen stopped some of the ejecta, it transmitted 60% of the smallest fragments. If the ejecta were to travel out in an axially symmetric distribution, then by geometry the screened collector should catch approximately 10% of all the ejecta released. In practice, the ejecta had a nonsymmetric randomly oriented distribution, even when ignition was avoided. However, by repeating experiments we were able to obtain average characteristics of the ejecta.

For charge measurements, the aluminum collector was connected by a short coaxial cable to a coulombmeter. As charged ejecta were captured by the collector, an equal charge would flow to the coulombmeter. After the total collected charge was determined, the ejecta were transferred to a small piece of thin aluminum foil for weighing with a Cahn Model No. 21 Automatic Electrobalance. Most of the results reported here are on PETN because of availability of sample material. A few measurements were also performed on crystals of RDX and HMX.

RESULTS AND DISCUSSION

Total Mass. In the case of PETN, the total mass of ejecta collected from impact was on the average 1.3% of the mass of the original PETN crystal samples. The samples were pulverized, with the greater part of each sample remaining attached to the metal impacting surfaces. As might be expected, the ejecta produced by impact formed a larger fraction of the total mass than the ejecta from materials examined in tensile or flexure loading¹. The large amount of ejecta was collected because the entire sample was pulverized, the efficient transfer of horizontal momentum to vertical momentum through compressive shear deformation, and because of channeling by the impacting surfaces in a planar distribution. Similar effects were obtained for RDX and HMX crystals.

Trajectories. We found that a large fraction of the ejecta reached the far end of our ejecta collecta, that is, they were able to travel at least 6 cm from the crushing region. Measurements described later indicate that the most probable ejecta size is about 5 μm . Calculations based on Stoke's law⁵ show that 5 μm spherical particles would travel horizontally less than 1 cm in still air even if they were launched with an initial speed of 100 m/sec. Lower initial speeds or irregularly shaped particles would result in a smaller range. Thus, we must conclude that a hydrodynamic effect is dominant, e.g., the burst of air created by rapid motion of the impacting surfaces carries entrained ejecta. This would imply that until turbulence set in, the particles would move at approximately the speed of

Electrical Charge. The PETN ejecta always carried a net *negative* charge. A comparison was made of the total mass of the collected PETN ejecta vs the total charge carried by the ejecta for repeated experiments on specimens of similar size. Figure 2 shows the resulting data and a least squares fit indicating that the total mass and total charge are positively correlated. We emphasize that these are total charge measurements and that the ejecta most likely contains charged patches of both signs, potentially involving considerably larger quantities of charge of each sign.

In contrast, the ejecta from crushing crystals of RDX displayed a much smaller charge per unit mass (1/20 of that for PETN) and the charge measured was positive or negative. The charging of HMX ejecta was similar to that of RDX, namely the total charges/mass were an order of magnitude smaller than for PETN and were of either sign.

Because the ejecta were insulating particles, they lost little of their surface charge to the collector. Using this fact, we could test the conclusion that the majority of the charge we measured was indeed carried by the ejecta with the following procedure: after the charge of a sample of ejecta had been measured and recorded, the collector was electrically grounded. The ground on the collector was then removed and the ejecta were spilled out of the collector. The new value of charge registered during the removal of the ejecta was of opposite sign and nearly equal in magnitude to the charge originally collected. This result

would not have occurred if a significant portion of the initial measured charge had been carried by electrons or ions emitted from the fracture zone, thus providing convincing evidence that the charge we measured was indeed carried by the ejecta particles.

Accompanying Long Wave Length Electromagnetic Signals. In order to determine if electrostatic phenomena were accompanying the fracture event itself, we placed a flat coil having a diameter of 2 cm and inductance of ~ 10 mH around the crushing region. Because the coil was sensitive to magnetic signals from the motion of steel components, we replaced the steel crusher with a brass-bronze impact device. The output of the coil was fed to a wide-band differential amplifier with a $1\text{ M}\Omega$ input impedance, the output of which was digitized. When a rapid change in B field occurred, i.e., due to an electrostatic discharge, a ring-down burst of emf at a frequency of 200 Khz was produced. Since our coil was so close to the impact region, it was sensitive only to near-field components of the electromagnetic field. Tests of signals from actual discharges, the peeling of adhesive tapes,⁶ and the crushing of single crystal quartz and sucrose (known to produce microdischarges in air) showed strong, rapidly rising signals, whereas rapid deformation

We found that crushing PETN regularly produced large, reproducible RE signals in the coil. The observed electrical signal rose early during the crushing, and frequently consisted of several discrete bursts which are most likely due to individual failure events in the crystal(s). Figure 3 shows a typical ringing signal (digitized at $20\text{ }\mu\text{s}$ per division) due to impact crushing of a single crystal of PETN. The onset of crushing is shown by the arrow. In contrast, crushing RDX did not produce convincing RE signals; thus, we see no evidence of electrostatic discharges during fracture of RDX. This observation is consistent with much lower charge densities on the RDX ejecta in comparison with the PETN ejecta.

Micrographs of Ejecta. Morphology and size distribution of ejecta were examined by using optical microscope photographs of the collected particles. The photographs, shown in Figs. 4 and 5, represent ejecta caught on microscope slides placed near the impact crushing of PETN and RDX. The PETN ejecta (Fig. 4) differ from the

RDX ejecta (Fig. 5) in several characteristics. They are more finely divided than RDX ejecta and they always exhibited considerably more clustering. This clustering of PETN ejecta could well be due to the presence of high densities of electrical charge on the fracture surfaces which cause electrostatic attraction and agglomeration.

Size Distributions. In order to determine a size distribution of the PETN ejecta, we collected several samplings of the ejecta on microscope slides. Using an optical microscope at 120x, we counted the number of particles in each size range, employing a geometrically increasing series of sizes.⁷ The resulting approximate size distribution is shown in Fig. 6. It shows that most of the collected ejecta are quite small ($< 5 \mu\text{m}$) and, thus, that the surface area of ejecta will be large, consistent with the findings in our previous fracture-induced ejecta study.

Average Charge Density. We can combine this particle size distribution with the mass and charge measurements to obtain a value for the average surface charge density on the PETN ejecta. We first assume that the net charge is uniformly distributed over the surface of the particles and that the ejecta are spheres (contrary to what is seen in Fig. 4). This yields a specific surface for these particles of $2.4 \times 10^5 \text{ mm}^2/\text{g}$. The ejecta mass collected, typically 430 μg , and the net charge collected, $2.5 \times 10^{-10} \text{ C}$, results in an average surface charge density of $2.4 \times 10^{-10} \text{ C/cm}^2$. The limiting E field imposed by the occurrence of corona discharge in air⁸ is approximately $2 \times 10^6 \text{ V/m}$ which will be reached at a surface density of $1.8 \times 10^{-9} \text{ C/cm}^2$ for uniformly charged spherical particles. An interesting but unanswered question is how does the surface charge vary with the size of the PETN ejecta?

We emphasize that these measurements involve only the *net* charge on a large number of particles. The sum of $\pm Q$, i.e., the actual charge on the ejecta, could be much greater than the net charge we measure.

There are two possible mechanisms for producing charge on the ejecta by impact loading. First, the crystals undergo a great deal of shear deformation and fracture during

crushing. Second, the fragments undergo frictional rubbing by the metal surfaces of the striker and the anvil, both during crushing and subsequently as the ejecta escape. Both of these mechanisms could be contributing to the production of surface charge on the ejecta.

We and others have observed evidence of charge separation accompanying fracture of a number of materials.⁹⁻¹² Fracture induced charge separation is particularly intense in piezo-electric crystals such as SiO_2 and BaTiO_3 . PETN has a non-centrosymmetric crystal structure and is known to be piezoelectric whereas RDX and β -HMX (the room temperature form) are centric and, therefore, non-piezoelectric.¹¹ This would suggest that ejecta from PETN should carry a greater charge, as is observed, due to charge separation assisted by stress-induced polarization.

Frictional and contact electrification are especially effective in producing charge separation when dissimilar materials, e.g. molecular crystals and metal surfaces, are involved. Thus, we might expect that the crystal fragments would also be charged by rubbing as they glanced off of the surfaces during ejection. We cannot rule out this charging mechanism. However, we point out first the striking *difference* in magnitude of charge on the ejecta from PETN compared with the other two types of explosive crystals, and second, the accompanying RE signals from impact of PETN vs the lack of RE from RDX. This strongly suggests that the charging of the PETN ejecta is due to deformation and fracture rather than the rubbing that follows.

CONCLUSIONS

In summary, we have shown that:

1. Impact crushing of PETN, RDX, and β -HMX produce large quantities of ejecta.

2. Small ejecta particles had a range in air of at least 6 cm. This would require substantial kinetic energy; however, under the conditions of this experiment the air surrounding the ejecta was put in motion by the compression of the impact device, thereby entraining the ejecta.
3. The ejecta carry electrical charge. Their net charge density for PETN approaches the corona limit for surface charge in air. Local charge densities on the ejecta could be greater.
4. The PETN crystals under impact created more finely divided ejecta which was more highly charged than that from RDX and β -HMX crystals. This was demonstrated by measurements of the total charge carried on ejecta, by measurement of the electrical signal produced during crushing and by the subsequent aggregation of the ejecta.
5. We suspect that the charging observed in the case of PETN arises from crushing (fracture) of the crystal rather than collisions with the metal surfaces during ejection.

ACKNOWLEDGEMENT

We wish to thank Dr. Howard Cady and Dr. Jerry Dick, Los Alamos National Laboratory, for providing us with the single crystals used in this experiment and Dr. Richard Gilardi, Naval Research Laboratory, for helpful discussions. This work was supported by the Office of Naval Research under Contract N00014-87-K-0514, Dr. R. S. Miller, Program Manager.

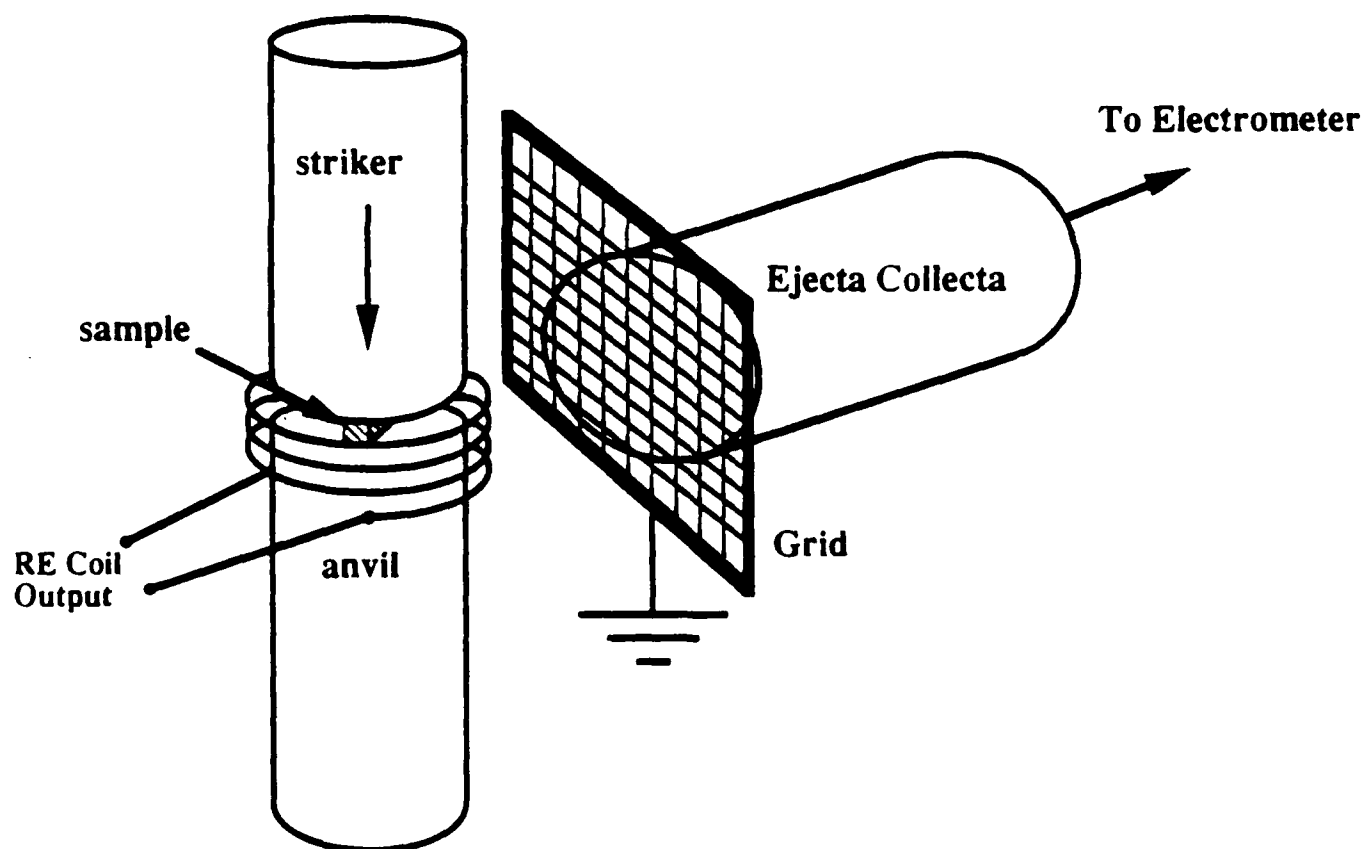
REFERENCES

1. E. E. Donaldson, J. T. Dickinson, and S. K. Battacharya, "Production and Properties of Ejecta from the Fracture of Materials", *J. Adhesion* **25**, 281 (1988).
2. L. Avrami and R. Hutchison in *Energetic Materials Volume 2* edited by H. D. Fair and R. F. Walker (Plenum Press, New York 1977) Chapter 4.
3. C.S. Coffey and V.R. DeVost, "Evaluation of Equipment Used to Impact Test Small-Scale Explosive and Propellant Samples", (Naval Surface Weapons Center, Silver Springs, Maryland 1982) NSWC TR 81-215.
4. M. H. Miles, J. T. Dickinson, and L. C. Jensen, *J. Appl. Phys.* **57**, 50, 48 (1985).
5. E. H. Kennard, *Kinetic Theory of Gases*, (McGraw-Hill, New York, 1983) p. 309.
6. E. E. Donaldson, X. A. Shen, and J. T. Dickinson, *J. Adhesion*, **19**, 267 (1986).
7. T Allen, Particle Size Measurement (Chapman and Hall, London 1975) Second edition, Chapter 4.
8. W. R. Harper, Contact and Frictional Electrification (Oxford, London, 1967).
9. J.T. Dickinson and L.C. Jensen, *Proceedings of SPIE-The International Society for Optical Engineering* **743**, 68 (1987), and references, therein.
10. J.T. Dickinson, L.C. Jensen, and A. Jahan-Latibari, *J. Vac. Sci. Technol. A* **2**, 1112 (1984).
11. S.G. Boev and A.N. Galanov, *Sov. Phys. Solid State* **22** 1792 (1980).
12. J. Wollbrandt, V. Bruckner, and E. Linke, *Phys. Stat. Sol. (A)* **77** 545 (1983).
13. Private Communication, H. Cady, Los Alamos National Laboratories.
14. Private Communication, R. Gilardi, Naval Research Laboratories.

FIGURE CAPTIONS

- Fig. 1. Sketch of the experimental configuration.
- Fig. 2. Graph of the electrostatic charge (negative) carried by the ejecta vs mass of ejecta collected for PETN.
- Fig. 3. Electrical signal induced in a pick-up coil from crushing PETN.
- Fig. 4. Optical micrograph of PETN ejecta deposited on a microscope slide.
- Fig. 5. Optical micrograph of ejecta from RDX.
- Fig. 6. Approximate size distribution of PETN ejecta.

Experimental Configuration



TOTAL CHARGE vs TOTAL MASS
FOR PETN EJECTA

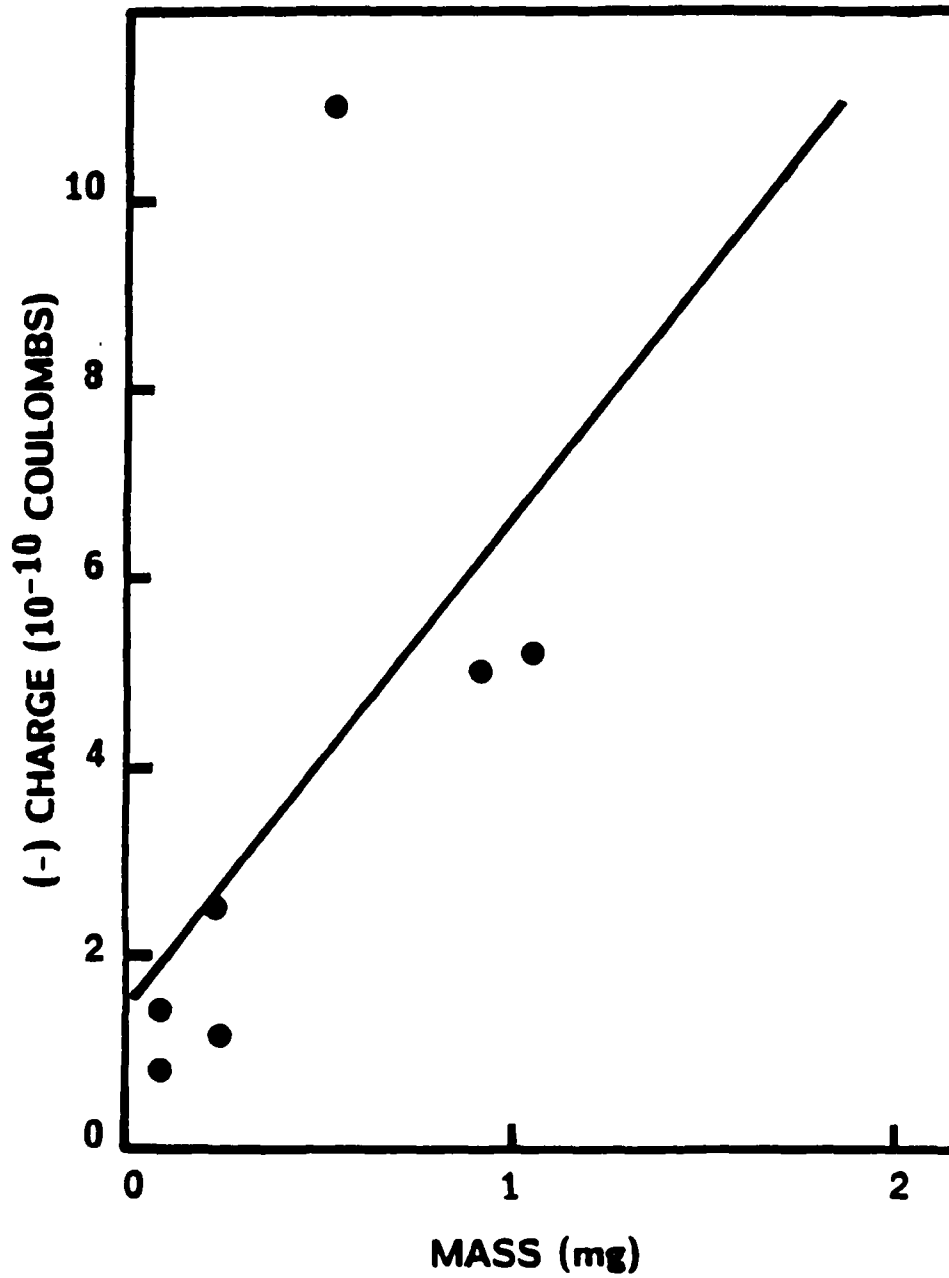


FIG 2

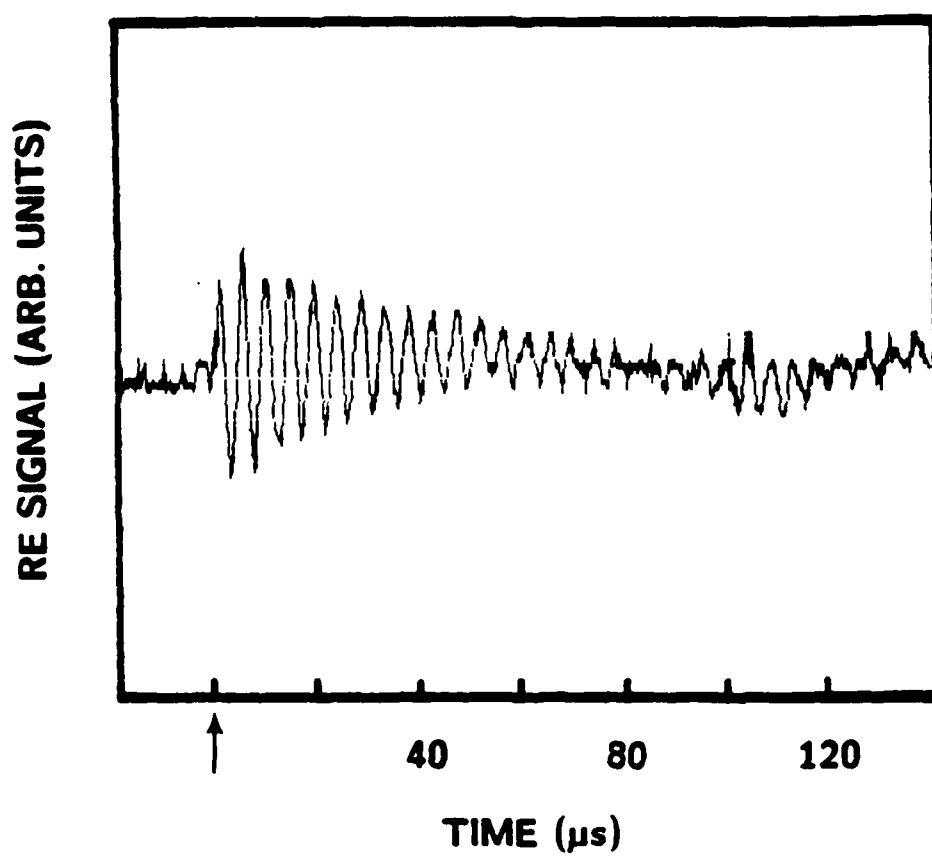


FIG 3

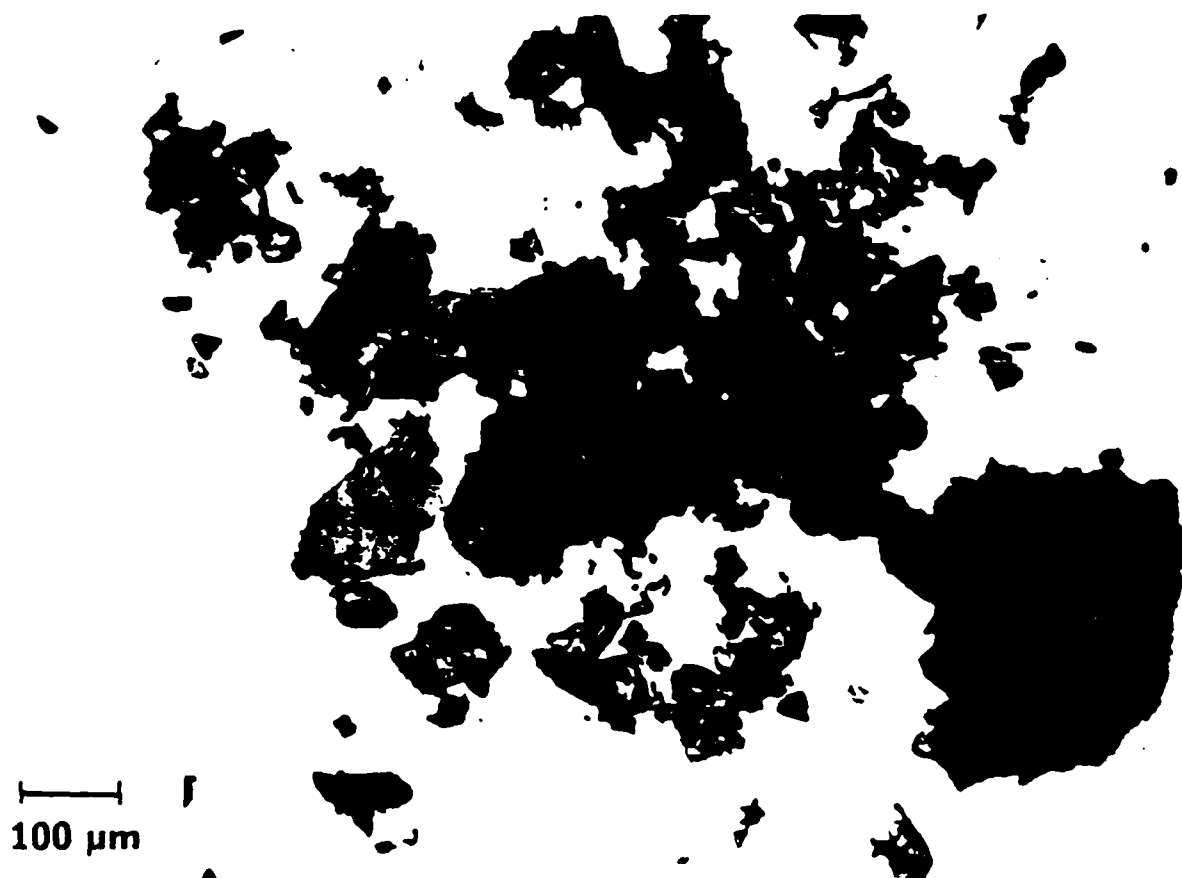
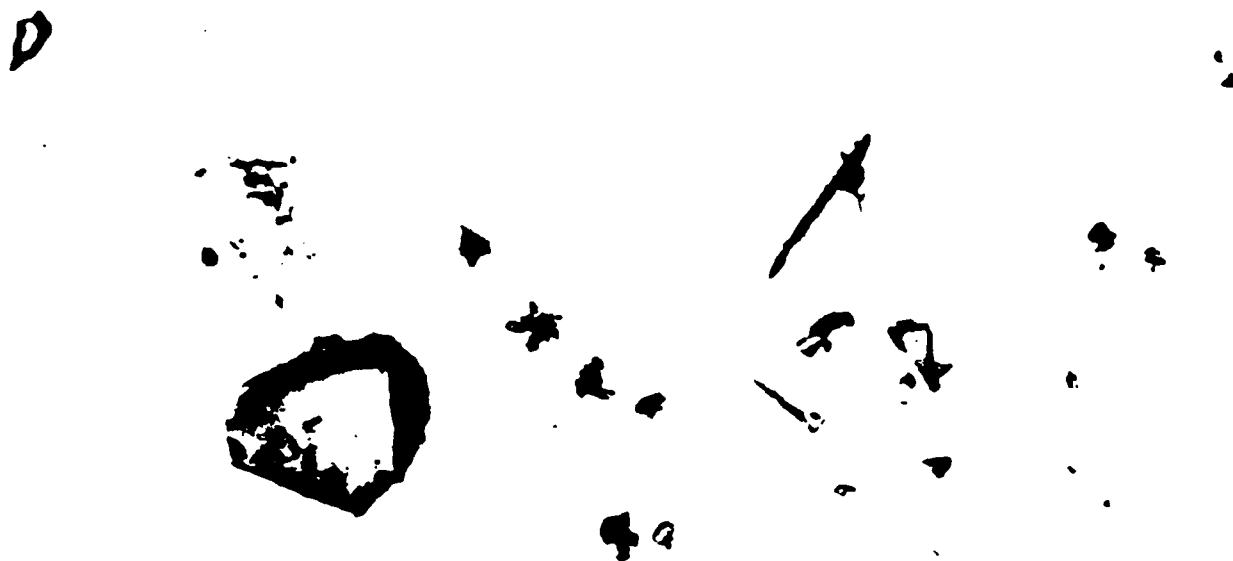


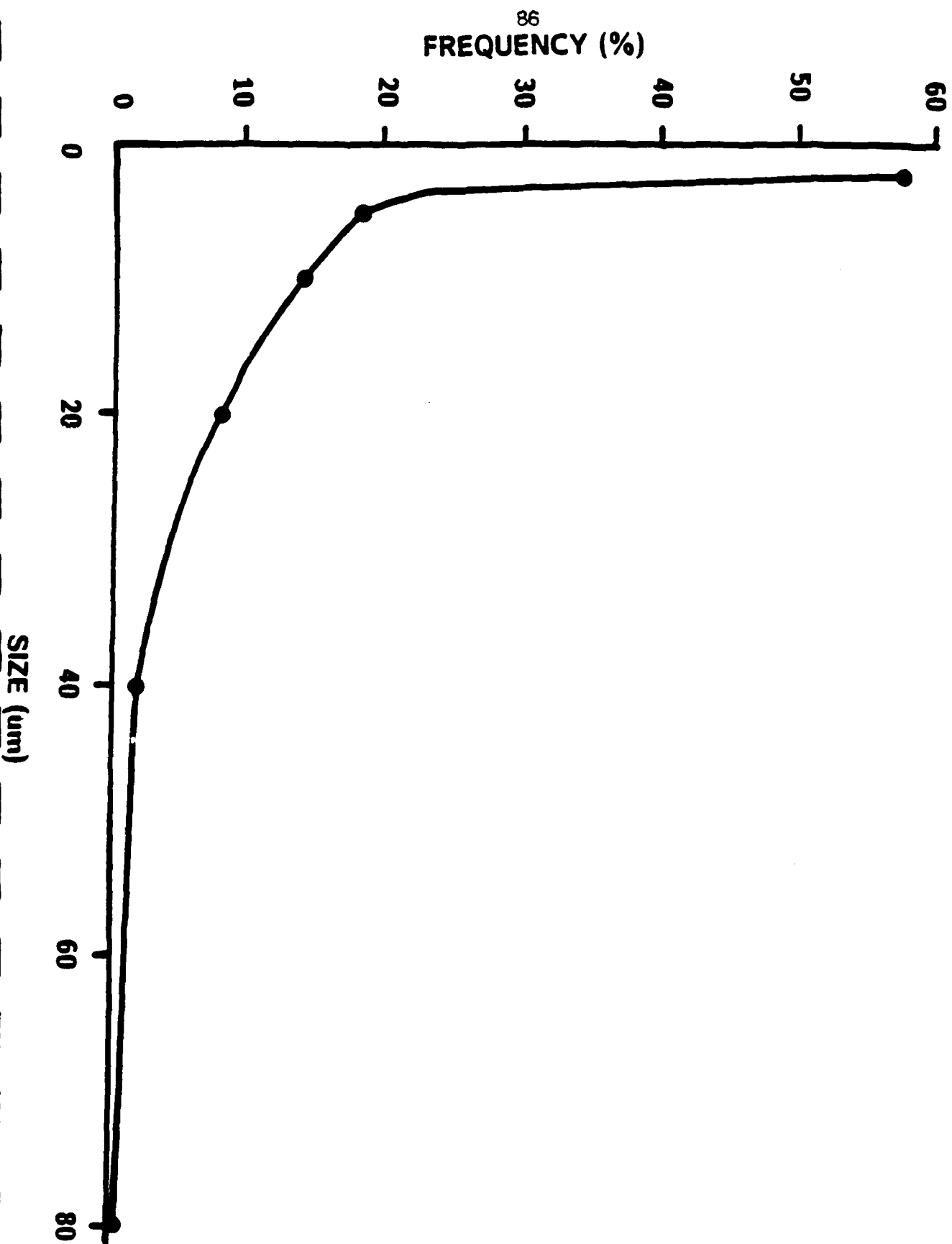
FIG 4



100 μm

FIG 5

SIZE DISTRIBUTION OF EJECTA FROM IMPACT CRUSHING OF
PETN



VI. Fracto-Emission Induced Electrical Breakdown in Vacuum

E. E. Donaldson, J. T. Dickinson, and Naiqiang Wu*
Department of Physics
Washington State University
Pullman, WA 99164-2814

ABSTRACT

In previous studies we have shown that when fracture takes place in the vicinity of a high voltage gap in air, it will induce electrical breakdown across the gap. In vacuum, we induced electrical breakdown directly across a crack involving the separation of an epoxy-metal interface. These breakdown events were explained in terms of fracto-emission (the emission of charged particles, neutral species and photons due to fracture) serving as a trigger which induced breakdown. Here, we explore further vacuum breakdown induced by fracture for a different electrode geometry. We examine the effect of creating a crack in a dielectric suspended between two electrodes, the dependence of the observed discharges on the magnitude of the applied voltage and on the nature of the fracto-emission, and the temporal relationship of the onset of breakdown to the fracture event. The materials studied are poly methyl methacrylate (PMMA) and a Kevlar-fiber reinforced composite)

*Permanent Address: Beijing Institute of Structure and Environmental Engineering.

INTRODUCTION

When an electrical voltage is applied across a pair of plane parallel electrodes in a low pressure gaseous medium, the probability of electrical breakdown vs gas pressure is predicted by the breakdown potential curves.¹ These curves are based on the assumption that cosmic rays or background radioactivity provides the few electrons necessary to initiate the discharge. If foreign charged particles are deliberately introduced into the gap, breakdown will be seen at potential differences much lower than the sparking potential. Thus, devices employing photoemission, field emission, and field ionization can be designed to trigger a discharge across a primary gap held at an otherwise stable potential. Subsequently this temporary source of charge carriers induces the discharge to initiate across the primary gap. This principle is used in practical

A source of charge not normally discussed in the breakdown literature involves the emission of electrons and ions created by fracture. These emissions are part of a group of effects known as *fracto-emission* [FE] which we have been studying in this laboratory as a probe of a number of aspects of fracture.³⁻⁵ Typically, the various FE components are produced at highest intensity during fracture and at lower intensity following fracture. Furthermore, the relative intensities of these emissions are strong functions of the types and failure modes of the

We have previously shown that when fracture takes place in the vicinity of a high voltage gap in air at one atmosphere the fracture event will cause electrical breakdown across the gap.⁶ Furthermore, in vacuum, we induced electrical breakdown *across* a crack involving a polymer-metal interface, a type of fracture known to produce copious electron and ion emission.⁷ In these experiments, aluminum, one component of the interface, served as one of the electrodes for the gap. These breakdown events were explained in terms of fracto-emission serving as a trigger to induce breakdown.

In this paper, we further explore vacuum breakdown induced by fracture. In particular, we examine the effect of creating a crack in a dielectric suspended between the electrodes, the dependence of the observed discharges on the magnitude of the applied voltage and on the nature

of the FE, and to examine the timing of the onset of breakdown with the fracture event. A relatively poor charged particle emitter was chosen as the major material studied, namely poly methyl methacrylate (PMMA), although we show that fracturing a very intense fracto-emitter (a Kevlar-fiber reinforced composite) greatly reduces the required voltage to obtain breakdown.

EXPERIMENTAL

The breakdown experiments were conducted in an oil-pumped vacuum system operating at a system pressure of 1×10^{-4} Pa as measured with a discharge gauge; auxiliary FE experiments were conducted in a turbomolecular pumped system operating at 2×10^{-6} Pa. Fig. 1 is a view of the physical arrangement of the breakdown experiment, including a schematic of the circuit used to detect the breakdown current. Samples of commercial grade PMMA and of a Kevlar-Epoxy composite were fractured by tensile elongation inside the high voltage gap and the electric current across the gap was measured during fracture. The dc high voltage was applied across a gap between 16 mm diameter brass electrode disks. The edges of the electrodes were rounded to prevent high local fields. The gap was adjusted so that the electrodes were close to but not touching the fracture specimen; gap separations ranged from 2-3.5 mm.

The PMMA samples were 75 mm x 22 mm and 3 mm thick. They were notched on both edges near the center with a saw blade leaving a center web 1 cm wide, thus assuring that fracture occurred in the center of the gap, generally starting at one of the notches and ending at the other.

The samples of Kevlar-Epoxy composite consisted of Dow DER 332 epoxy filled with 300 Kevlar-fibers(each 10 μ m in diameter, running the full length of the sample), forming what are called "strands" about 5 cm in length. A single strand was held in clamps and notched in the center with a scalpel approximately half way through the fiber bundle. Again, this assured fracture occurred in the center of the electrodes, although in the case of the composite samples, this was always accompanied by considerable splitting and delamination of the composite.

An acoustic transducer (AET Corp) with a characteristic frequency of 1 MHz was attached to the sample holder near the fixed end of the sample (See Fig. 1). The AE signal from this detector was used to produce a stop pulse for the digitizer (Lecroy Model 8210) to capture the current transient associated with breakdown. In the FE experiments the electron emission (EE) and photon emission (phE) were detected with a channel electron multiplier and a photomultiplier tube, respectively, both mounted in the vacuum system approximately 2 cm from

In the breakdown experiments, we wished to determine the actual time of fracture and the duration of crack propagation in the PMMA samples. To determine the duration of crack propagation we deposited two strips of gold on the surfaces of the sample at the two ends of the fracture region. A small voltage was placed across these gold resistors and the increase in resistance accompanying fracture produced a measurable change in voltage. A sketch of this arrangement and a typical output signal is shown in Fig. 2. The drops in voltage shown by arrows indicate the onset and completion of crack growth. For our samples, this duration of crack propagation was typically $\sim 20 \mu\text{s}$ which corresponds to an average crack velocity of 500 m/s, corresponding to unstable crack growth and is in agreement with similar measurements made on PMMA by other workers.⁸ Using similar thin film timing strips, we also determined that the acoustic signal arrived at our transducer $\sim 40 \mu\text{s}$ after the initiation of the crack. This time

During the breakdown experiments the positive high voltage was applied to one electrode and the other electrode passed to ground through a 50 ohm resistor. The resulting voltage change was amplified by an ORTEC 474 amplifier and subsequently digitized. The AE signal and a radio emission signal, picked up by a small coil (designated RE in Fig. 1) were recorded in other channels of the digitizer. The radio emission signal served only as a verification that a

RESULTS

We first summarize the general features of our observations:

1. When samples were fractured in the gap without the high voltage turned on, we saw no current across the vacuum gap.

2. For voltages ≤ 6 kV no discharge occurred in the absence of fracture.
3. When samples were fractured in the central region of the gap we generally detected a discharge current provided that the gap voltage was above the threshold value for each kind of sample material. The threshold voltage was higher for PMMA than for Kevlar-Epoxy.
4. When Kevlar-Epoxy samples fractured near the edge of the gap or a few mm from the edge of the gap, discharges still occurred, but the detected currents were smaller than in (3) above.
5. The total charge flow induced by fracture had a positive correlation with the magnitude of the high voltage.

Specific examples of this behavior will now be presented.

PMMA

When the PMMA samples were fractured in the gap, a discharge would occur for voltages ≥ 1.75 keV. The discharge currents were usually on the order of 10^{-4} - 10^{-3} A in magnitude and a duration of several microseconds. In Fig. 3 we show a current vs time record accompanying fracture of PMMA at a 3.7 kV gap voltage. Here we see a maximum current of 3 mA and a total charge flow of 64 nC. In all cases of PMMA fracture we observed that the onset of discharge current came within a few μ s after the fracture was complete and that the current continued to flow for 10 to 50 μ s. The current was always very noisy, suggesting multiple discharge events occurring once breakdown was initiated. Contrary to the study on aluminum-epoxy interfacial fracture, where breakdown was observed *during* fracture, with PMMA a short delay (1-2 μ s) was always evident. Note that the Al-epoxy geometry involved breakdown in a direction normal to the crack walls.

A series of experiments was carried out with PMMA samples for different gap voltages up to 5.54 kV. The plot shown in Fig. 4 indicate that when the voltage exceeded a breakdown threshold (1.75 kV), the total charge flowing during a discharge increased with increasing voltage. The current flowing across a gap should be an exponential function of the gap voltage.⁹

$$Q_{\text{total}} = a \exp(bV_{\text{applied}}) \quad 1)$$

where

$$\begin{aligned} Q_{\text{total}} &= \text{total charge flow} \\ V_{\text{applied}} &= \text{the applied voltage across the gap} \end{aligned}$$

a, b are adjustable parameters.

The best fit occurred for $a = 5.4 \text{ nC}$ and $b = 0.72 \text{ volts}^{-1}$. We note that above the threshold level we occasionally observed negligible current and we did not include these measurements in the fit. (At higher potentials, e.g., 5 kV, we always obtained breakdown upon fracture of PMMA).

The PMMA fracto-emission was extremely weak. Fig. 5 shows the FE as a function of time, summed over six specimens. The total detected emission was low averaging only ~12 counts of EE and of pH E per sample, typical of cohesive fracture of a number of polymers.⁵ The curves show however that the emissions reached their maximum rates immediately after fracture and decayed to background in ~100 μs . Because of the limited solid angle of the emission detectors we estimate that we detected about 10% of the photons and probably a similar percentage of the electrons. The quantum yield of the channeltron electron multiplier is ~90% so that the actual number of counts in the EE peak (which would correspond to during and immediately after fracture) is therefore on the order of 100 particles. Although the photon

Visual observation of the breakdown event accompanying fracture of PMMA suggested that the discharge indeed occurred between the electrodes and through the opening crack. Fig. 6a shows a sample prior to fracture indicating where the notched specimen is located. A time-exposure of this same view during fracture with 5.5 kV applied across the gap is shown in Fig. 6b. The high voltage electrode is at the top of the photograph and the camera axis is along the direction of crack propagation (away from the camera). The photograph shows that the discharge is more intense near the high voltage electrode than it is near the ground electrode and that the discharge extends across the gap. Evidence of localized higher intensity breakdown at the high voltage electrode (anode-spots) are seen here and more clearly on other photographs taken under similar conditions. These anode spots are caused by visible radiation resulting from

Kevlar-Epoxy

When Kevlar-Epoxy samples were fractured in the gap, we found that a discharge occurred when the gap voltage was ≥ 150 V. At these lower voltages, the discharge currents were smaller than measured from PMMA at higher potentials and they exhibited different time dependences. Typically, the discharges consisted of multiple (1-10), short (1-2 μ s) current pulses. Fig. 7 shows one of the current records during the fracture of Kevlar-Epoxy for an applied potential of 250 V. With fracture, we measure a maximum current of 0.2 mA with a total charge flow of 0.32 nC integrating over six short 1 μ s pulses observed. Digitization of the applied voltage showed no changes during this time, indicating that these fluctuations are indeed due to variations created in the gap. At much higher voltages in the kV range, the discharges took on more of the character of the sustained discharges cause by the fracture of PMMA. In general, the discharge current during Kevlar-Epoxy fracture is an increasing function of applied voltage, similar to the PMMA; however, due to considerable variation in the total fracture surface area created at failure in these composite samples (which strongly influences the intensity of the charged particle emission), i.e., we could not obtain a quantitative relation between Q_{total} vs V_{applied} .

Previously, we have published electron and positive ion emission curves for the same Kevlar-Epoxy strands used in these experiments.¹¹ It should be noted that this emission is $\sim 10^6$ more intense for these samples compared to the PMMA and that the fracture event is considerably longer in duration due to crack arrest and branching.

DISCUSSION

In this work we have produced electrical breakdown between electrodes in a vacuum environment by fracture of materials. This occurred in spite of the fact that sparking potential curves show that vacuum is an excellent insulator.¹² However the insulating properties of

vacuum can be degraded by many factors: electrode asperities,¹³ particulate contamination,¹⁴ or by the injection of energetic photons and charged particles into the gap.

In the present case our electrodes were sufficiently smooth and clean to resist discharge formation at voltages well above those we applied (6 kV). Breakdown was detected only when a sample was fractured in the gap. We propose that the fracto-emission breakdown mechanism in vacuum involves two components of these emissions: 1) the small quantity of charged particles already discussed above *and* 2) a supply of neutral molecules which are also released during and immediately following fracture. Evidence for neutral molecule emission accompanying fracture has been seen in a number of studies,^{15,16} including measurements made on PMMA¹⁷ The latter investigation showed that the dominant species emitted was the monomer (mass 100). Thus, the crack in PMMA contains many free molecules as it begins to open and this gas is released into the gap. From previous measurements on epoxy,¹⁶ we saw neutral emission intensities which lasted about 100 μ s after fracture. This combination of charged particle and neutral emission into the gap results in a discharge because the charged particles are accelerated by the high voltage and collide with the electrodes and/or with the emitted neutrals thereby producing secondary ions and

The few charged particles present in the FE correspond to a current of $\sim 100 \text{ e}^- / 20 \mu\text{s} = 10^{-12} \text{ A}$, whereas we observe $\sim 10^{-3} \text{ A}$. Thus, significant multiplication is necessary to produce the observed charge flow. Further evidence that multiplication is indeed occurring is the exponential dependence of Q_{total} on the applied gap voltage for PMMA; such a process requires multiplication to occur. The 1-2 μ s delay in breakdown following fracture appears to be due to achieving optimum conditions of free charge and gas pressure in the gap. We note that the glow of the discharge (e.g., Fig. 7) was always more intense near the positive electrode than near the negative electrode because electrons are most efficiently accelerated and most effective in producing secondary ionization.

We know that the Kevlar-Epoxy composite is an intense source of charge as in all cases studied to date of adhesive failure occurring during the fracture of composites. Adhesive failure also tends to produce much higher energy emissions.¹¹ Thus, the higher intensity/higher energy

emission in the case of the composite leads to breakdown at 150 V, compared to PMMA (which is a poor emitter) with a threshold for breakdown at 1.75 kV. Therefore, the injection of charged particles into the gap is effective in triggering breakdown and that more numerous and/or more energetic charged particles will trigger a discharge at a lower voltage. It should also be mentioned that neutral molecule emission accompanying the fracture of epoxy resin composites has been shown in our laboratory to be extremely intense, presumably due to trapped gas at the fiber-matrix interface. Gases such as H_2O and N_2 were the dominant products. This would further aid the breakdown process.

We noted that fracture of the Kevlar-Epoxy specimens in closer proximity to the center of the gap produced larger breakdown current; this would be expected to occur because more charged particles from fracture would be produced in the central region where the electrical field and where the probability of hitting an electrode are highest.

The time dependence of the discharge currents can be related to the nature of fracture in the two materials. PMMA fractures in a single, rapidly occurring event where the crack propagates across the sample in a few μs . In addition to our timing strip measurements, further evidence of rapid crack propagation is seen by examining the fracture surfaces, namely the presence of extensive hackle and crack branching. The discharge current is observed to arise immediately after fracture and is sustained in a single event for periods of time approaching 100 μs , as expected for a single burst of charged particle emission accompanying a single fracture event. In fact the discharges follow approximately the shape of the emission curves for this material, suggesting that the discharges may be sustained by the delayed emission. Because the voltages used in these experiments were relatively low, we did not produce self sustaining discharges.

The background pressure in the vacuum system was 1×10^{-4} Pa; however, it is certain that the local pressure was higher in the vicinity of the crack due to the release of gas from the sample (we estimate that in the crack, the pressure may be as high as 10^{-1} Pa). If one examines the sparking potential curves for various gases in a parallel electrode gap,¹ one sees for example that

the curve for air has a minimum at 330 V (in neon, the minimum is 244 V). Thus, it appears impossible to find untriggered sparking at 150 V at any pressure and in any gas and shows that the discharge current observed during the fracture of Kevlar-Epoxy could not be triggered by the neutral emission alone; the charged particle emission is clearly an essential component.

The fracture of PMMA presents a different case because the threshold voltage is at 1.75 kV. If we again look at the sparking potential curves we see that they yield double values and that when the product, (Pressure)(Gap Width), reaches a value of either 13 or 266 Pa-cm sparking can normally occur without triggering. With our gap fixed at 0.3 cm the sparking would require a local pressure of either 40 Pa or 9300 Pa. 9300 Pa is highly unlikely, whereas 40 Pa would require only 3×10^{11} molecules to be injected into the gap at a width of 1 μm . From other observations of the release of neutral gases during fracture of polymeric materials, this is well within the expected amount of gas released in such fracture. Consequently, "normal breakdown" could be occurring in the case of PMMA. However, the close correlation in time of the discharge and the fracture event (and therefore the charged particle emission), only a few μs , indicates that the charged particle emission is also triggering the discharges in the case of PMMA.

CONCLUSION

When a material fractures in an evacuated region containing high electrical fields, fracture-emission can trigger a discharge at potentials much lower than those necessary for untriggered breakdown. In the case of PMMA, the discharge originates just as the fracture is completed. We know that at just prior to and during this time, charged particles and gases are being released from the sample. The charged particles are accelerated and undergo multiplication at the electrode surfaces and in the neutral gases being released. The discharges are completed in a time of less than 100 μs as the charged particle emission decays and as the gases leave the rapidly opening crack.

The fracture of the Kevlar-Epoxy composite strands fracture in a sequence of fracture events that produce short-lived intense bursts of charge which undergo multiplication in the

fracture gases. These result in discharges of 1 μ s duration. Only at much higher gap voltages do we observe the sustained discharges which characterize the fracture of PMMA (which only occur at the higher potentials). In all cases when the gases are finally pumped out of the crack and the FE falls to a low level, the discharges are extinguished. Because the voltages used in these experiments were moderate we did not produce self sustaining discharges.

ACKNOWLEDGMENTS

This work was supported by the Office of Naval Research Contract No. N00014-87-K-0514, the Ceramics and Electronics Materials Division of the National Science Foundation DMR-8601281, and the Washington Technology Center.

REFERENCES

1. A. von Engel, *Ionized Gases* (Clarendon Press, Oxford 1965) Chapter 7.
2. E. Kuffel and M. Abdullah, *High-voltage Engineering*, (Pergamon Press, Oxford, 1970).
3. J. T. Dickinson, E. E. Donaldson, and M. K. Park, J. Mater. Sci. **16**, 2897 (1981).
4. J. T. Dickinson, M. K. Park, E. E. Donaldson, and L. C. Jensen, J. Vac. Sci. Technol. **20**, 436 (1982).
5. J. T. Dickinson, "Fracto-Emission from Adhesive Failure," to appear in *Fundamentals of Adhesion*, L. H. Lee, ed., (Plenum Press, New York, 1989).
6. M. L. Klakken, J. T. Dickinson, and L. C. Jensen, IEEE Trans. on Elec. Insul., **EI-19**, 578 (1984).
7. J. T. Dickinson, L. C. Jensen, and S. Bhattacharya, J. Vac. Sci. Technol. **A3**, 1398 (1985).
8. J. G. Williams, "Fracture Mechanics of Polymers and Adhesives," in *Fracture of Non-Metallic Materials*, K. P. Herrmann and L. H. Larsson, eds. (D. Reidel Publishing Co., Dordrecht, 1985), pp. 227-255.
9. M. J. Druyvesteyn and F. M. Penning, Rev. Mod. Phys. **12**, 87 (1940).
10. R. V. Latham, *High Voltage Vacuum Insulation: The Physical Basis*.(Academic Press, London, 1981), p. 188.
10. J. T. Dickinson, L. C. Jensen, and A. Jahan-Latibari, J. Vac. Sci. Technol. **A2**, 1112 (1984).
11. E. E. Donaldson , E.A.Braun and J. A. Muscari, IEEE Trans. Parts, Material and Packaging, **PMP-1** 32 (1965).
12. M. Rabinowitz, and E. E. Donaldson, J. Appl. Phys. **36** 1314 (1965)
13. E. E. Donaldson and M. Rabinowitz, J. Appl. Phys. **34**, 319 (1963).
14. M. A. Grayson and C. J. Wolf, J. Polym. Sci.: Polym. Phys. Ed. **23**, 1087 (1985).
15. J. T. Dickinson and A. S. Crasto, "Fracto-emission from Epoxy and Epoxy Composites," in *Cross-linked Polymers: Chemistry, Properties, and Applications* , R. A. Dickie, S. S. Labana, and R. S. Bauer, eds. ACS Symposium Series 367 (American Chemical Society, Washington, D.C., 1988) pp. 145-168.
16. V. R. Regel', T. M. Muinov, and O. F. Pozdnyakov, "A Mass Spectrometric Study of Volatile Products Evolving in Degradation of Solids," in *Proc. Conf. on the Physical Basis of Yield and Fracture*, Oxford University Press, London, 1976, pp. 194-199.

FIGURE CAPTIONS

- Fig. 1. Schematic diagram of the experimental arrangement and the electronic circuit used to measure breakdown current.
- Fig. 2. Schematic of sample used in crack timing experiments and typical signal accompanying fracture of PMMA..
- Fig. 3. Typical discharge current as a function of time for PMMA.
- Fig. 4. Voltage dependence of total charge flow (Q_{total}) during discharge induced by
- Fig. 5. Electron and photon emission curves from PMMA fracture.
- Fig. 6. a) Photograph of electrodes and sample (thickness = 3mm).
b) Time exposure of light from discharge with the same orientation and magnification as 6a.
- Fig. 7. Discharge current as a function of time following fracture of a Kevlar-Epoxy

Schematic Diagram of Experiment

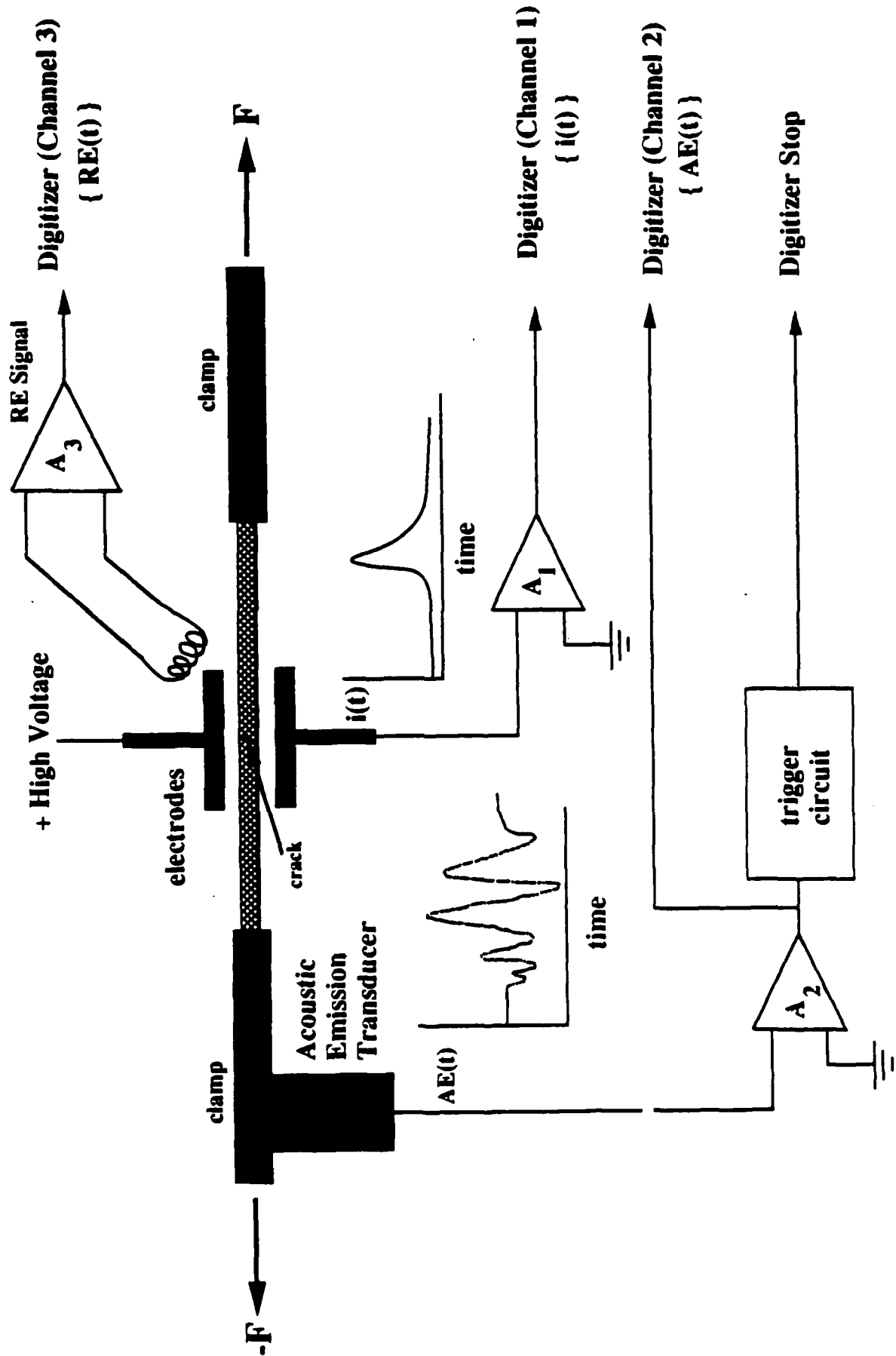


Fig. 1

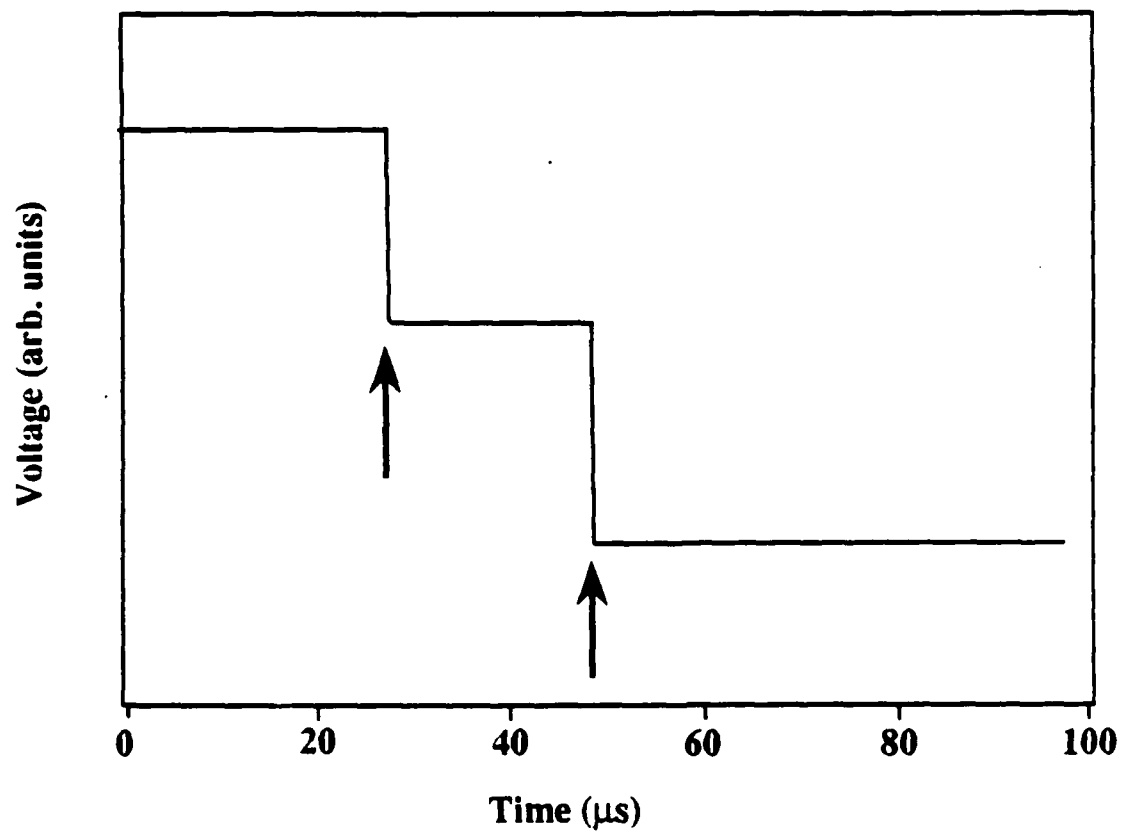
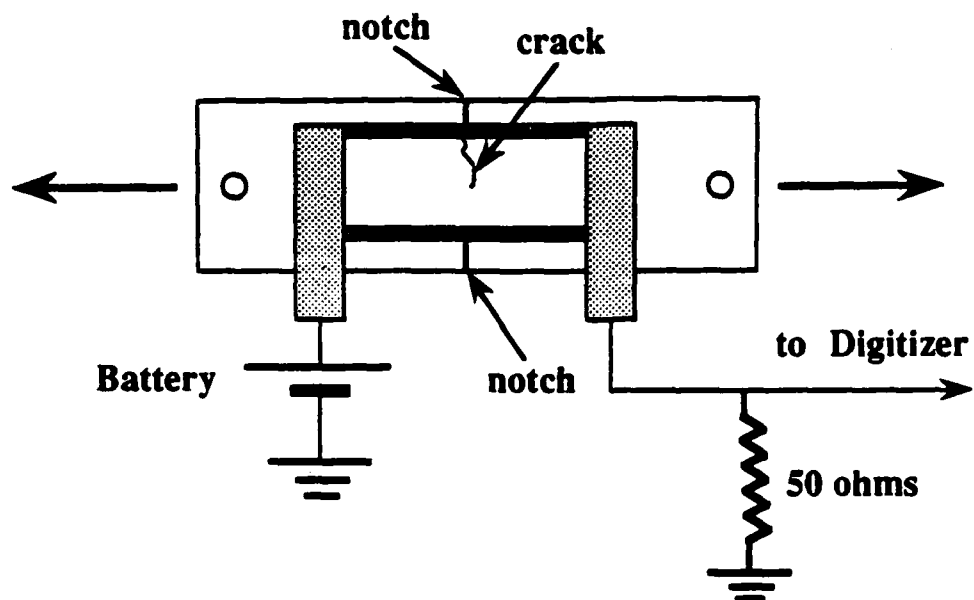


Fig. 2

Gap Current vs Time During/Following Failure of PMMA

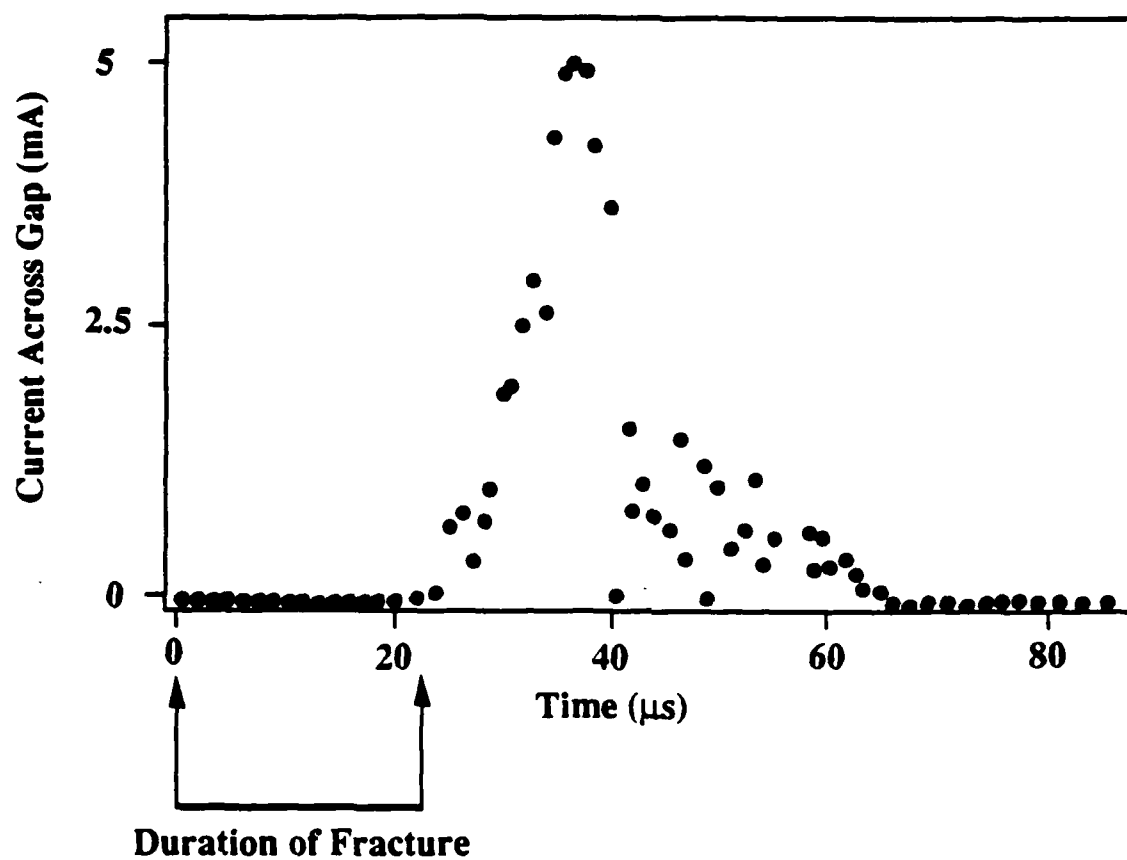


Fig. 3

Total Charge Flow vs Applied Voltage Accompanying Fracture

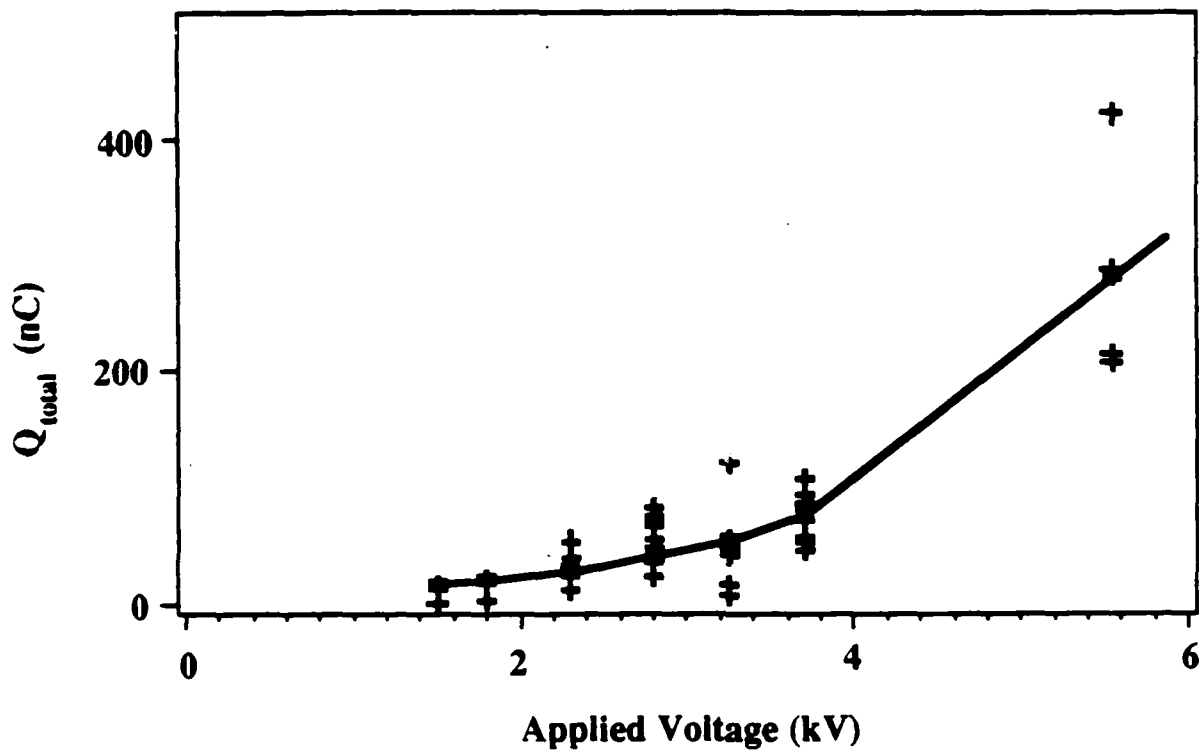


Fig. 4

EE and phE from Fracture of PMMA

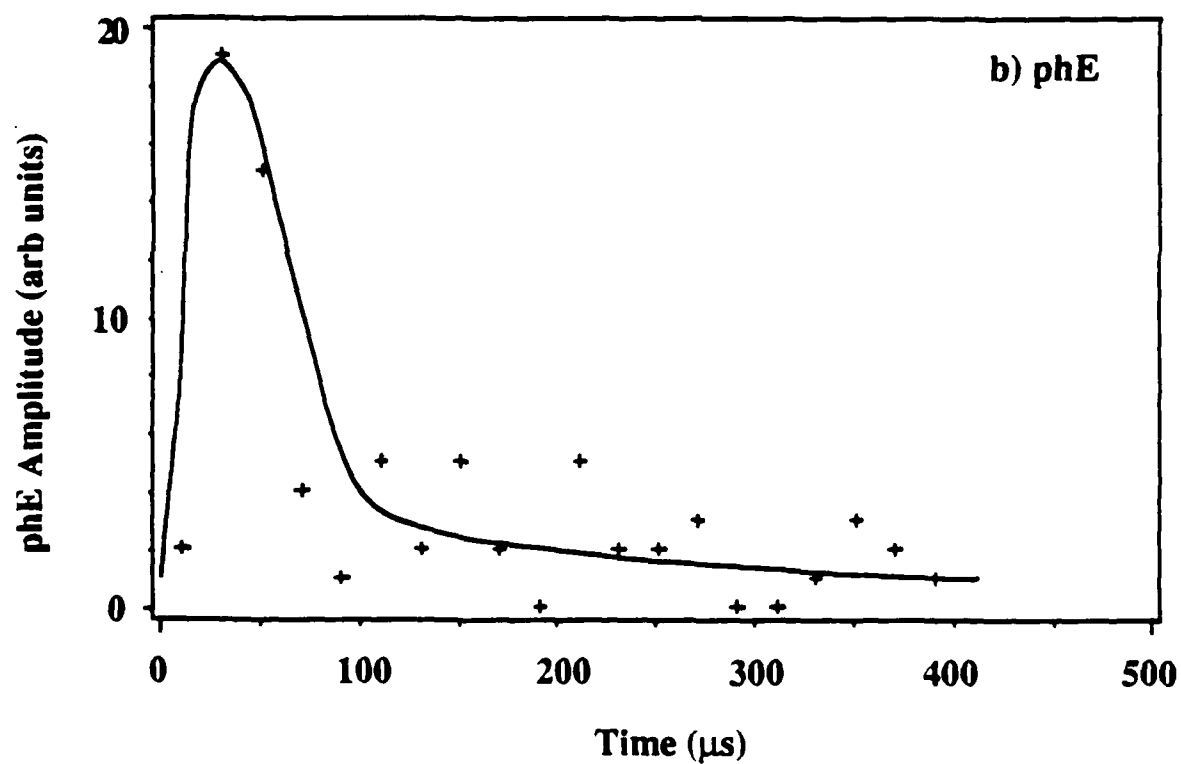
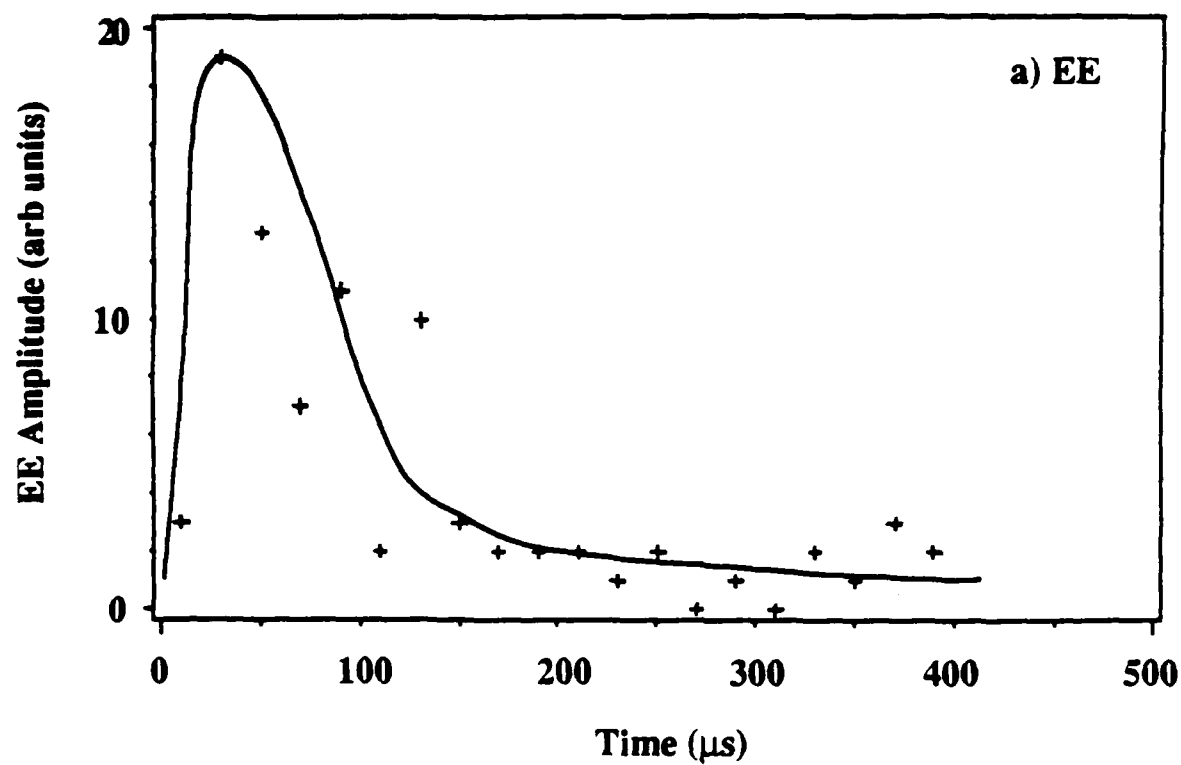
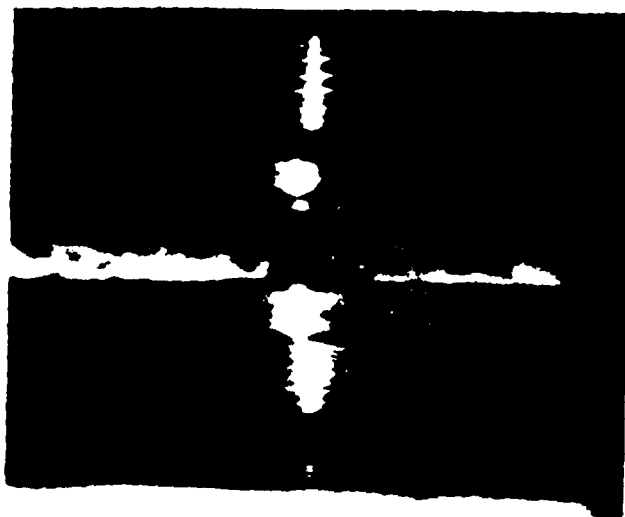


Fig. 5

a)



b)

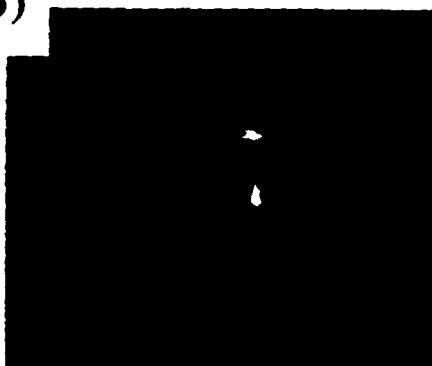


Fig. 6

Gap Current vs Time During Failure of Kevlar-Epoxy Strand

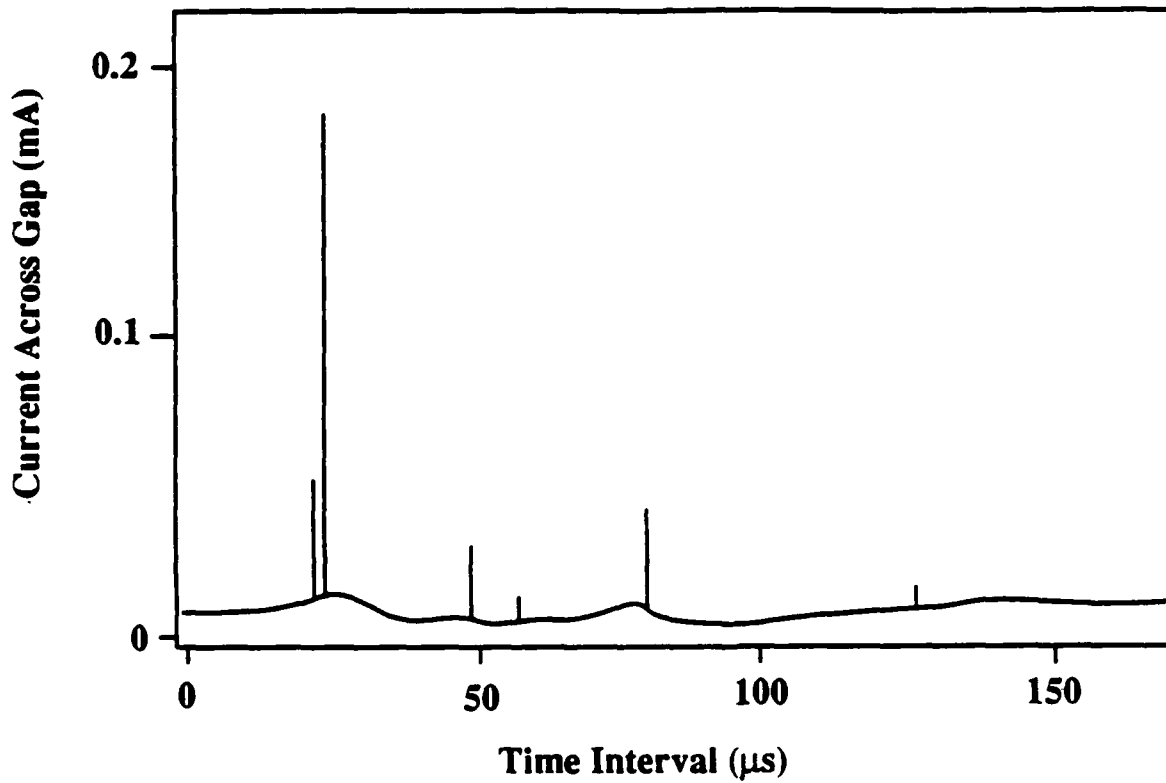


Fig. 7

VII. PRODUCTION OF FREE CHARGE CARRIERS DURING FRACTURE OF SINGLE CRYSTAL SILICON

S. C. Langford, D. L. Doering,^(a) and J. T. Dickinson
Department of Physics
Washington State University
Pullman, WA 99164-2814

Measurements of the time dependence and magnitude of fracture induced changes in electrical conductivity in single crystal Si are presented. A transient increase in conduction is observed during crack growth due to the production of free charge carriers. The presence and characteristics of this transient depend on the nature of the fracture.

During crack propagation, mechanical work of deformation is transformed into bond breaking in a relatively localized portion of the material. Energy release processes at or near the fracture surface can have irreversible components, as evidenced by various fracto-emission phenomena,¹ including the emission of visible light (triboluminescence), electrons, ions, neutral species, and long wavelength electromagnetic radiation. A number of these processes involve departures from equilibrium induced by fracture.

We have recently observed electron emission during the fracture of single crystal Si in vacuum.² It seemed plausible that fracture might also create free charge carriers in the Si near or at the fracture surface. We present for the first time evidence of the production of fracture induced charge carriers.

Commercial boron doped {111} Si wafers, with one face polished and having resistivities of 10 to 20 ohm-cm, were obtained from S.E.H. America, Inc. After an

HF acid etch, the wafers were coated with about 50 nm of gold on each side and cleaved into oriented tensile specimens of dimensions 6 mm x 25 mm x 0.52 mm. The gold coating process resulted in Schottky barrier contacts on the polished surfaces and ohmic contacts on the unpolished surfaces. The ohmic contacts were a consequence of the high density of recombination centers at the damaged surfaces. The specimens were epoxied to aluminum mounts and loaded in tension at an elongation rate of 0.01 mm/s. Contacts to the gold coated surfaces of the sample were made with silver print. On occasion, samples were loaded in cantilever beam or torsional modes. In all cases, edge flaws created during preparation were the dominant loci of failure. These flaws were left untreated, resulting in a wide range of strengths.

The basic experiment involved applying a small voltage across the Si sample and measuring the current passing through the specimen before, during, and following failure. Measurements were carried out in air or in vacuum (10^{-7} torr) at room temperature, or in streams of dry, cool N_2 , which reduced the specimen temperature to approximately 200 K. A schematic diagram of a typical experiment is shown in Fig. 1. R_i in Fig. 1 is the input resistor of a fast amplifier or transient recorder. Both AC and DC coupled amplifiers were used, with typical gains of 6X. Digitization rates were either 10 ns/channel or 320 ns/channel.

The current through the sample generally decreased during fracture. For the circuit of Fig. 1, this decrease was a consequence of cleavage along {111} planes, which resulted in fracture surfaces which were not perpendicular to the wafer surfaces. Therefore, a small region of the wafer became less effective in conduction as fracture progressed. This current drop correlated well with the duration of fracture, as determined by simultaneous measurements of gold foil conductivity. In many cases, crack bifurcation led to the removal of Si material from the circuit. Similarly, when only one end of the sample was connected into the circuit, fracture significantly reduced the amount of conducting Si. In these situations, a rapid, off-scale drop in

observed current resulted. Because the fracture surfaces were not normal to the loading direction, the crack experienced shear as well as normal stresses during loading.

Therefore, even under tensile loading, mixed mode fracture resulted.

A dramatic, transient increase in current through the sample was often observed during crack propagation. Fig. 2a shows the change in current for a sample tested in tension in dry, cooled N_2 at atmospheric pressure. The onset and completion of crack propagation are marked with vertical arrows. The total duration of crack propagation is 5 μ s, which corresponds to an average crack velocity of 1200 m/s. The downturn in current immediately preceding the transient indicates that the instantaneous crack velocity during the transient is significantly higher.

Similar transients were observed whether fracture occurred in air, dry nitrogen, or vacuum, and appeared to be independent of the ambient temperature (room temperature to 200 K). When integrated, the detected current transients per unit cross-sectional area of the sample corresponded to 10^9 to 10^{11} free carriers/cm². The larger transient currents were most evident in samples exhibiting high strength and fast crack growth and in those fractured in a torsional mode. The surfaces of samples yielding large transients often displayed areas of unusual roughness. Transients were rarely detected in low strength samples which often displayed very smooth fracture surfaces associated with slower crack growth. The change in current for such a specimen is presented in Fig. 2b, which shows little evidence of increased conductivity during fracture. Here, the total duration of crack propagation is 8 μ s, corresponding to an average crack velocity of 880 m/s. This observation lends further support to the hypothesis that free carrier generation is associated with high crack velocities.

Current transients were also associated with highly damaged fracture surfaces, which are commonly produced in torsional and cantilever beam modes of loading. Typical results for a specimen loaded in torsion are shown in Fig. 2c. The digitizer was

driven off scale during the most intense portion of the current transient, suggesting a very strong response. The duration of crack propagation was about 7 μ s.

These current measurements do not distinguish the sign of the participating charge carriers. However, under the conditions of bias used in this work, the depletion region near the Schottky interface served as a barrier to the transport of holes, but not to that of electrons. Further, the sample temperatures (200 K to room temperature) were sufficient to ensure that the acceptor impurities were fully ionized, ruling out the production of additional majority carriers (holes) by acceptor ionization. The minority carriers (electron) mean free path in this material is expected to be on the order of 100 μ m, a significant fraction of the sample thickness. Therefore, it seems likely that the observed current transients are due to minority carriers which have been promoted to the conduction band across the full width of the band gap. The excitation mechanism is not clear at this time, but may be electronic, thermal, or chemical in character.

Electronic excitations resulting in charge carrier production would most likely be associated with localized states of energy greater than or equal to that of the conduction band. Localization reduces the probability of recombination with valence band holes and thus increases the probability of transitions to the conduction band. The relatively low acceptor concentration in the material used also limits the recombination rate. The states involved in the excitation would probably be associated with surface defects or other localized phenomena.

As Si atoms are drawn away from each other in an advancing crack tip, the decreasing wavefunction overlap across the crack may result in localized states. Anderson localization is expected to result from variations in crack width and from mismatch across the crack due to shear displacements. Decreasing wavefunction overlap is generally associated with increasing electron energy. If the energies of these localized states approach that of the conduction band, transitions to the conduction band via tunneling would be possible, creating minority carriers. These transitions may

be further facilitated by shifts in the conduction band energy due to high stress fields near the crack tip.

Lemke and Haneman have identified localized states which they associate with wavefunction overlap across narrow indentation cracks in Si.³ Their electron spin resonance measurements indicate the presence of about 10^{14} spins/cm² of crack area. In contrast, well cleaved surfaces show very low spin densities. The high density of paramagnetic states suggests that "normal" surface relaxation is hindered while the crack width is less than about 0.5 nm. In crack propagation, particularly involving mixed fracture modes where crack opening displacements immediately behind the crack tip are small, a similar hindrance may increase the probability of high energy excitations.

Thermal generation of charge carriers during fracture could also explain the transients. Thermal generation of electron-hole pairs by excitation across the band gap would require temperatures in excess of 700 K to produce the observed current transients, assuming that 1 nm on each side of the crack tip were heated during fracture. This heating could be the result of irreversible processes in the region of the crack tip. Although the fracture of Si is generally not associated with macroscopic plastic deformation,⁴ surface relaxation behind the crack tip may yield significant energies. The energy of the relaxed surface is about 0.36 eV per surface atom lower than that of the ideal, truncated bulk.⁵ Some of this energy may be available for surface heating, as seems to be the case for various glasses. Rough measurements of the temperature rise during the fracture of glass and quartz have yielded values in excess of 2000 K.⁶ The intensity and duration of the thermal pulse is limited by conductive cooling. The high thermal diffusivity of Si relative to glass suggests that the temperature rise in Si is much less than in glasses. However, rapid crack growth would be associated with rapid heating and higher final temperatures, and thus higher carrier concentrations.

Other energetic processes occur on fracture surfaces, including the production of defects such as vacancies and adatoms.⁷ The density of such defects is expected to be a strong function of crack velocity and fracture mode. Recombination reactions involving these species could lead to the creation of charge carriers, similar to the creation of free electrons during chemisorption of reactive gases on some surfaces.⁸

We are currently exploring several unresolved issues concerning the production of charge carriers during fracture. For instance, the crack tip experienced significant shear stresses in each of the fracture modes employed in this work. Thus the influence of fracture mode is not clearly demonstrated, although it appears that shear stresses are important. The effects of crack velocity and microcracking remain to be quantified. Carrier generation is also expected to be affected by the electronic properties, e.g. band gap, of the fractured material.

We have demonstrated that a fundamental electronic excitation, the production of free carriers in a semiconductor, can accompany fracture under certain conditions. Free carrier generation, being a lower energy process than the previously mentioned electron emission, may serve as a probe of lower energy electronic processes induced by deformation and fracture. Such measurements may provide new insight into the process of dynamic crack growth in semiconducting materials.

The authors wish to thank Richard Hoagland, Washington State University, for helpful discussions and S. E. H. America, Inc. for providing the Si wafers. This work was supported by the Ceramics and Electronic Materials Division of the National Science Foundation under Grant DMR 8601281 and the Office of Naval Research, Contract No. N00014-87-K-0514.

(a)Permanent Address: Dept. of Physics, Wesleyan University, Middletown, CT 06457.

¹J. T. Dickinson and L. C. Jensen, in *Proceedings of SPIE-The International Society for Optical Engineering* 743, 68 (1987), and references therein.

²S. C. Langford and J. T. Dickinson, unpublished data.

³B. P. Lemke and D. Haneman, *Phys. Rev. B* 17, 1893 (1978).

⁴M. V. Swain, B. R. Lawn, and S. J. Burns, *J. Materials Sci.* 9, 175 (1974).

⁵K. C. Pandey, *Physica* 117B & 118B, 761 (1983).

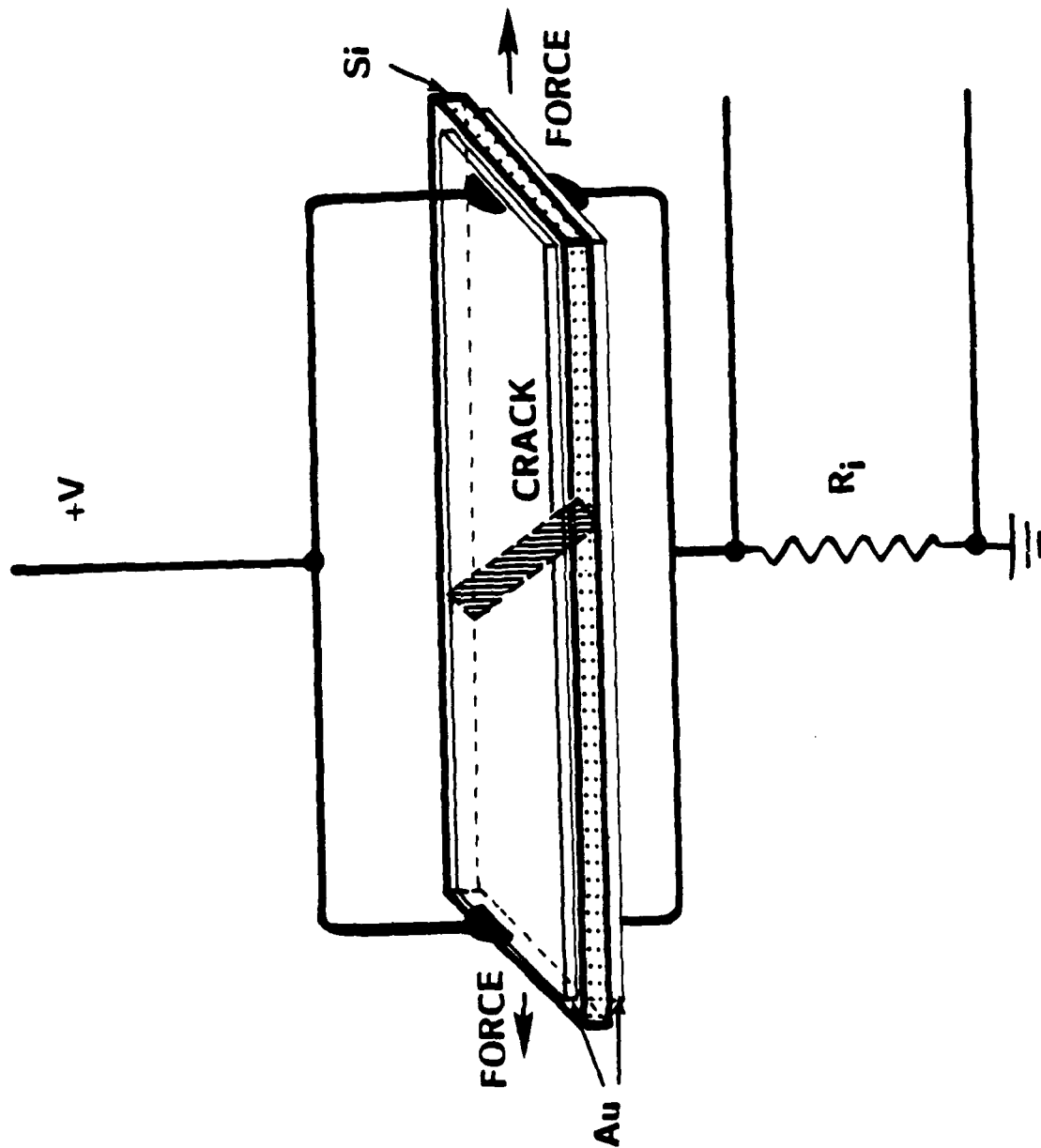
⁶R. Weichert and K. Schonert, *Mech. Phys. Solids* 26, 151 (1978).

⁷J. T. Dickinson, L. C. Jensen, M. R. McKay, and F. Freund, *J. Vac. Sci. Technol. A* 4, 1648 (1986).

⁸D. Anderson, B. Kasemo, and L. Wallden, *Chem. Phys. Letters* 111, 593 (1985).

FIGURE CAPTIONS

- Figure 1.** Diagram of tensile specimen, showing the circuit used to measure sample current. The crack shown represents a typical {111} cleavage plane. Samples broken in bending and torsional modes were supported at one end only.
- Figure 2.** Fracture induced current changes observed from a) a strong specimen loaded in tension, b) a weak specimen loaded in torsion, and c) a strong specimen loaded in torsion. The fracture of a) was performed in a cold, dry nitrogen atmosphere, while the fractures of b) and c) were performed in air at room temperature. Arrows mark times of crack initiation and completion.



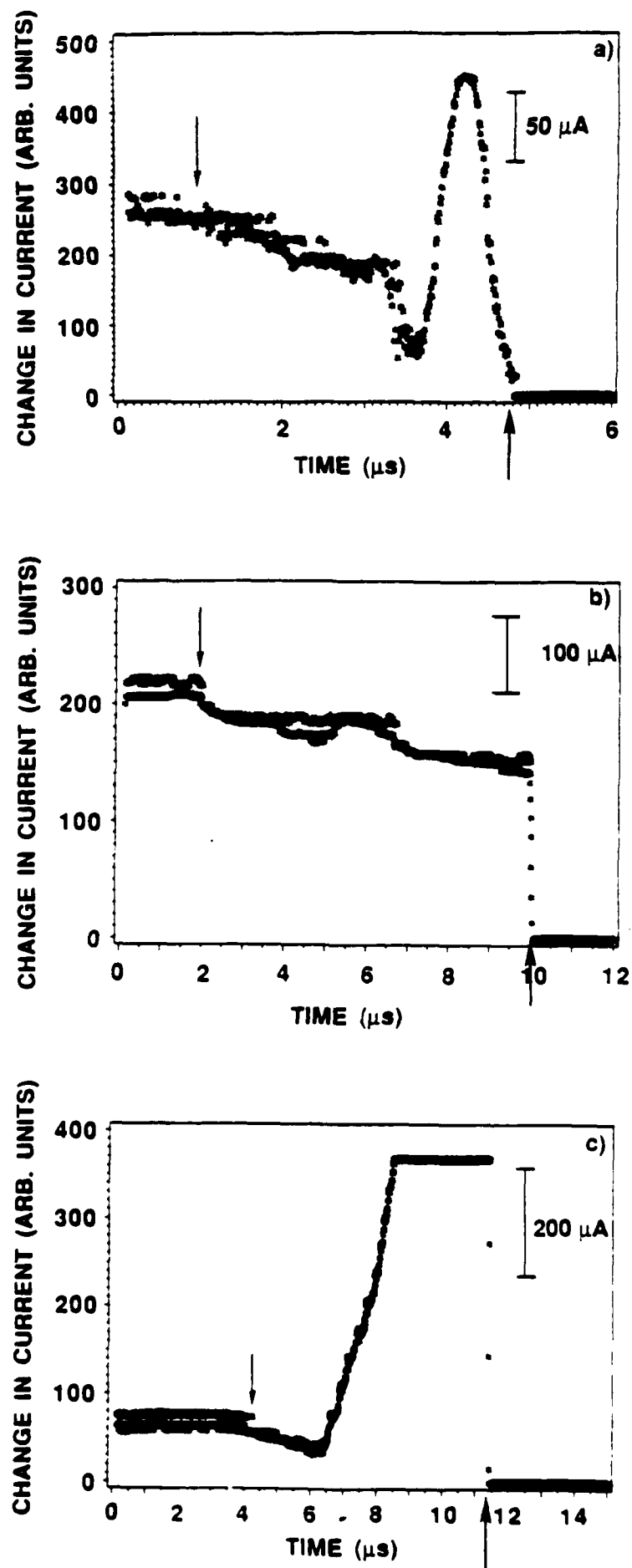


Fig. 2

VIII. Photon emission as a probe of chaotic processes accompanying fracture

S. C. Langford, Ma Zhenyi, and J. T. Dickinson

Physics Department, Washington State University, Pullman, WA 99164-2814

Photon emission accompanying the fracture of an epoxy and single crystal MgO is examined for evidence of deterministic chaos by means of the autocorrelation function, the Fourier transform, the correlation integral of Grassberger and Procaccia, and the fractal box dimension. A positive Lyapunov exponent is also obtained from the epoxy pH data. Each of these measures is consistent with a significant degree of deterministic chaos associated with attractors of relatively low dimension. A typical epoxy fracture surface was analyzed for fractal character by means of the slit island technique, yielding a fractal dimension of 1.32 ± 0.03 . The fractal dimensions of the fracture surface and the photon emission data (box dimension) of the epoxy are in good agreement. These observations suggest that fluctuations in photon emission intensity during fracture reflect the production of fractal surface features as they are being produced and thus provide important information on the process of dynamic crack growth.

1. Introduction

The fracture of many insulating materials is accompanied by the emission of photons, electrons, and other species during and following fracture.¹⁻⁵ These emissions are collectively known as *fracto-emission*, and can be especially intense during fracture. In earlier work, we have shown that photon emission (phE) during the fracture of an epoxy sample may display rapid fluctuations well in excess of detector and amplifier noise.⁴ The amplitude of these fluctuations correlates well with the roughness of the resulting fracture surfaces, suggesting that these fluctuations reflect mechanical processes during crack growth. Since photon emission intensity measurements are readily made at time intervals as short as a few ns, they may yield detailed information on the progress and energetics of crack growth during catastrophic failure.

In particular, phE fluctuations may shed light on the dynamics of possibly chaotic processes responsible for the fractal character of many fracture surfaces. Fractal dimension measurements have been made on the fracture surfaces of several metallic and ceramic materials.⁶⁻¹⁰ Since the underlying structure of many chaotic systems is fractal, this suggests that fracture is also to some degree chaotic, that is, deterministic, yet aperiodic and unpredictable. Recently, some simple models of the fracture process have been proposed which display chaos¹¹ or result in fractal surfaces.¹²⁻¹³ However, to date little evidence for chaotic processes has appeared except in the fractal nature of the resulting surfaces. Recent developments in the analysis of time series data, such as that formed by a series of phE measurements, raise the possibility that such measurements may yield information about chaotic processes accompanying fracture.

In this work, we describe a preliminary analysis of phE accompanying the fracture of two materials, an epoxy and single crystal MgO. The intense phE accompanying the fracture of both these materials has been previously studied.³⁻⁵ The epoxy is readily formed into rather large, strong samples. Although the epoxy fracture is macroscopically brittle, the fracture surfaces show features associated with severe, local plastic deformation in the near surface region. Single crystal MgO undergoes brittle fracture, often with very high crack velocities, and has been the object of

many studies of fracture and deformation. In this paper, we first describe autocorrelation and Fourier spectra computations which show that the faster fluctuations in pH_E are consistent with a non-stochastic, yet quasi-random origin. Then the fractal properties of the data are discussed. The fractal dimension of the pH_E data from the epoxy is also compared to fractal dimension measurements of the epoxy fracture surface. We then present correlation dimension calculations which show the pH_E data to be associated with a strange attractor of low dimension. Finally, a estimate of the largest Lyapunov exponent associated with the epoxy data is made. These results indicate that the processes underlying the pH_E accompanying fracture display deterministic chaos.

2. Experiment

The epoxy used in this work was formed from tetraglycidyl 4-4'diaminodiphenylmethane (TGGDM), known as MY720, cured with about 27% by weight diaminodiphenyl sulfone (DDS), known as Eporal or HT976. Both materials are manufactured by Ciba Geigy Corporation. Typical sample preparation procedures are outlined in Reference 4. The samples were cast in silicone rubber molds with a sample cross section of 3.5 by 8 mm². The samples were then notched and mounted in tension in a vacuum system maintained at pressures of about 2×10^{-4} Pa. pH_E measurements were carried out with an EMI Gencom 9924QB photomultiplier tube. This tube is sensitive to photons in the 200-600 nm range. The output of the photomultiplier tube was amplified and recorded at 10 ns intervals.

The MgO samples were prepared from nominally 99.99% pure single crystals obtained from W. & C. Spicer, Ltd. Samples were cut with a diamond saw to about 1.6 x 6 x 12 mm³ and polished. They were then mounted in a vacuum system maintained at less than 1×10^{-6} Pa. These samples were loaded in three-point bend across a 6 mm support span so that the tensile face of the sample was about 1 cm from the window of a photomultiplier tube identical to that used in the epoxy study. The output of the photomultiplier tube was amplified and digitized at 5 ns intervals. The high pH_E intensity associated with the fracture of MgO required that the photomultiplier tube

be operated at low gain in order to ensure linear output at peak intensity. At this gain, the 7-bit digitizer could not resolve individual photon detection events. Further experimental details are given in Reference 5.

Two pH_E measurements selected for analysis appear in Fig. 1. The pH_E from the epoxy is sustained for about 20 μ s, much longer than the 1.4 μ s of sustained pH_E from the MgO. The inset of Fig. 1a) shows the pH_E from the epoxy on an expanded scale. Rapid fluctuations with no apparent periodicity are observed. The analyses described below were performed on the quasistationary portions of the data during sustained emission. Due to the small sample sizes and rapid crack velocities in the MgO work, the resulting data set is smaller than desirable for the analysis of correlation dimension and Lyapunov exponents. This limitation is discussed further below. pH_E measurements made on samples with thin film timing strips attached for the measurement of crack location versus time confirm that by far the most intense emission occurs during crack growth, implying that the bulk of the emission is from the region of the advancing crack tip. A less intense, decaying emission following the completion of fracture is also observed.

3. Autocorrelation and Fourier Transform

Figure 2 shows the autocorrelation functions of the epoxy and MgO data. The epoxy curve shows an initial peak about 2 μ s in duration. The spike in the autocorrelation between 0 and 50 ns is due to the finite pulse width of the photomultiplier tube. Although the emission itself appears to be highly irregular, as shown in the inset of Fig. 1a), significant correlations persist for well over 1 μ s. This is inconsistent with purely stochastic fluctuations, for which autocorrelations would be limited to time scales on the order of the photomultiplier pulse width. The autocorrelation function of the MgO pH_E shows a main peak about 250 ns wide. This autocorrelation lacks the sharp peak in the 0-50 ns region because of the low photomultiplier tube gains used in the MgO observations. At these gains, the digitizer could not resolve individual photon peaks. Thus, the width of 250 ns indicates a true autocorrelation in pH_E rather than an artifact of the detector. The MgO

autocorrelation suggests the existence of some periodicity, although this may be an artifact of the small size of the data set. Again, the presence of correlated emissions suggests the operation of nonstochastic, although not necessarily chaotic, emission processes.

Conditional probability distributions were also computed for both sets of data to test for the presence of deterministic processes. In principle, the number of degrees of freedom in a deterministic system can be estimated by noting the number of conditions required to yield a narrow (noise limited) probability distribution.¹⁴ The required number of conditions corresponds to the dimensionality of the phase space required to describe the trajectory of the system. Stochastic processes are infinite dimensional in this sense. The conditional probabilities of purely stochastic data are identical to the first probability distribution (no condition). We observe a considerable narrowing of the probability distribution between the case of no conditions and that of one condition, but the number of data points is insufficient to carry the process to its conclusion. Nevertheless, this narrowing is further evidence for nonstochastic processes.

The power spectrum of the epoxy data displays an inverse power law behavior at high frequencies, as shown in Fig. 3a). The displayed spectrum consists of the sums of the squares of the two Fourier coefficients at each frequency. This spectrum displays a broad plateau in the region of 500 kHz to 20 Mhz, suggesting that stochastic processes dominate on time scales of 2 μ s to 50 ns. Assuming a typical crack speed of 300 m/s, this time scale corresponds to distances of 15-600 μ m on the fracture surface. At higher frequencies (20-50 MHz), corresponding to distances of 6-15 μ m on the fracture surface, the power spectrum shows $1/f^\beta$ -like behavior. The bandwidth of the detector/amplifier system is about 50 MHz, so that the effects of higher frequency power being "reflected" into this power spectrum should be small. Thus the Fourier spectrum below 50 MHz should be fairly free of artifacts due to the finite sampling interval.

$1/f^\beta$ -like behavior in has been associated with the fractal character of certain time series records (Brownian motion displacement vs time) and with profiles of various fracture surfaces.¹⁵⁻¹⁷ As the relevant dimensions of these systems are not strictly equivalent (e.g. displacement vs time), these systems are strictly not self-similar, but self-affine.¹⁷ Certain measures of fractal

character are not appropriate to self-affine structures, and the appropriate measures apply only in the high frequency limit. Typically, a structure associated with a $1/f^\beta$ -like power spectrum is described by a (Fourier) fractal dimension, D_f , of

$$D_f = 2.5 - \beta/2. \quad (1)$$

A least square fit of the power spectrum of the pH_E data in the region of 20-50 MHz yields $\beta = 2.1 \pm 0.1$. The rapid (20-50 MHz) fluctuations may thus be associated with a fractal dimension $D_f = 1.45 \pm 0.05$. Thus the power spectrum of the pH_E indicates that the high frequency pH_E fluctuations are fractal in character and hints that the fracture surface is fractal as well. The reported uncertainty in D_f is purely statistical, associated with the least squares fit to the line, so that the actual uncertainty is somewhat greater.

The power spectrum of the MgO data, shown in Fig. 3b), yields no clear evidence for such fractal behavior, although it is consistent with the presence of chaos. The Fourier coefficients below about 50 MHz approximate $1/f^\beta$ behavior with $\beta \sim 1$, much like the Fourier spectrum of $1/f$ noise. Again, the sharp cut-off beginning at about 50 MHz results from the 30 ns pulse width of the photomultiplier tube and represents the bandwidth of the detector/amplifier system. Although $1/f$ noise has been interpreted in terms of chaos, the Fourier spectrum of the MgO data is very poorly sampled below 50 MHz due to the small number of data points used in the analysis. Therefore we are hesitant to interpret the MgO power spectrum in this way.

The fractal dimensions of the time series data defined by the pH_E measurements can be more directly estimated with a box-counting algorithm.¹⁷ A rectangular grid is superimposed upon the curve defined by the pH_E data and the number of grid cells intersected by the curve, $N(r)$, is determined as a function of the cell size of the grid, r . The fractal box dimension, D_b , is given by the slope of the linear portion of the graph of $N(r)$ vs $(1/r)$ on a log-log plot. Fitting the linear portion of the epoxy plot of Fig. 4a) to a straight line yields $D_b = 1.35 \pm 0.03$. Again, the reported uncertainty is that resulting from the curve fitting calculation, so that the true uncertainty is

somewhat greater. With this in mind, D_b is in good agreement with D_f , the fractal dimension measured from the Fourier spectrum. A similar analysis of the MgO data yields $D_b = 1.16 \pm 0.1$. Because of the much smaller uncertainties associated with the fractal box dimension measurements, D_b is preferred over D_f as a measure of fractal character for both sets of data. On the basis of the non-integral D_b measurements from both the epoxy and the MgO, we are confident that both pH data sets are indeed fractal.

4. Fractal Dimension of Fracture Surface (Epoxy)

The fractal dimension of a typical epoxy sample was also measured by the slit island technique.⁶ The fracture surface was coated with about 90 nm of gold and potted in a clear epoxy. The potted sample was then polished by hand to yield a flat surface roughly parallel to the fracture surface. Polishing was continued until the fracture surface was intersected by the polished surface, yielding "islands" of brown epoxy surrounded by as yet unbroken gold. Photographs of the island structure were analyzed to determine the fractal dimension of the islands, D_i . Since the perimeter P and area A of these islands are related by the relation $A = k_i P^{2/D_i}$, D_i can be determined from the slope, β , of a log-log plot of the island area vs island perimeter, namely:

$$D_i = 2/\beta. \quad (2)$$

An island area vs perimeter plot taken from photographs of a roughly 1 mm² area of the epoxy sample at one point in the polishing process is shown in Fig. 5. The observed slope of 1.51 implies that $D_i = 1.32 \pm 0.03$. The reported uncertainty is again the statistical uncertainty in the slope determination. Slope measurements on different area vs perimeter plots suggest that the uncertainty is greater, on the order of 0.09. Within the accuracy of our measurements, the fractal dimension of the pH data from epoxy fracture has in fact the same fractal dimension as a one dimensional cross section of the island structures on the fractal surface ($D_b = 1.35 \pm 0.03$,

$D_i = 1.32 \pm 0.03$). Therefore, it is reasonable to conclude that pH_E fluctuations during a given time interval reflect variations in the local surface topography associated with the advance of the crack tip during the same interval.

The relationship between the fractal dimension of the fracture surface and the fractal box dimension of the pH_E data may be readily explained if the rapid fluctuations in pH_E are caused by fluctuations in the progress of crack growth. The roughness of many fracture surfaces, including those which may be described as fractal, is most easily understood as the result of crack branching and void growth. Both phenomena represent temporal and spatial fluctuations in the process of crack growth which appear to be reflected in the accompanying pH_E. Attempts to model the process of crack branching in brittle solids have met with limited success.^{18,19} Ravi-Chandar and Knauss have demonstrated that crack branching in Hormalite 100 involves the nucleation, interaction, and coalescence of microcracks or voids in the process zone of an advancing crack.¹⁹ This branching activity may be responsible for the fractal nature of many fracture surfaces, as well as for the relatively slow crack growth (relative to the Rayleigh wave speed) observed in many materials. They argue that similar processes can occur in other brittle materials as well.

Preliminary attempts to apply the slit island technique to the fracture surface of single crystal MgO failed due to the relatively small relief of the dominant surface features.

5. pH_E Correlation Dimension Estimate

A hallmark of chaotic behavior is the fractal nature of the associated strange attractor. This description assumes that a suitable phase space exists in which the evolution of the system may be traced as a trajectory. An attractor is a subset of this phase space to which all nearby trajectories are attracted, i.e. all trajectories asymptotically approach the attractor as time progresses. Chaotic systems are typically associated with "strange" attractors, which have non-integral, fractal dimensions. If one determines that the dimension of such an attractor is indeed non-integral, the underlying system can safely be said to be chaotic.²⁰ Unfortunately, the most straightforward

fractal measure, a generalization of the box dimension noted above, is computationally untractable for systems of dimension greater than about two. An alternative measure of fractal character described by Grassberger and Procaccia²¹ is much easier to compute and also reflects fractal character. Their correlation dimension, D_c , is strictly a lower bound on the box dimension, but in most cases of physical importance near or exact equality is obtained. Although the data sets analyzed here are smaller than those typically used to measure fractal dimensions of model systems, our experience with small data sets of known fractal character suggests that the correlation integral can still yield useful information. A similar conclusion was reached by Kurths and Herzog.²²

A suitable phase space and trajectory can generally be constructed from time series data, such as our pH measurements, using the method of delays^{21,24} proposed by Packard et al.¹⁴ and Takens.²⁵ The pH data consists of a series of N intensity measurements made at regular intervals, Δt . These measurements define a time series $\{I_i = I(t = i \cdot \Delta t): i = 1 \dots N\}$. Measurements made at sufficiently widely spaced intervals ($n \cdot \Delta t$) may be treated as independent variables, allowing one to construct m -dimensional vectors $X_i = \{I_i, I_{i+n}, I_{i+2 \cdot n}, \dots, I_{i+m \cdot n}\}$ for $i = 1 \dots (N-m)$. The quantity $\tau = n \cdot \Delta t$ is called the phase space delay time. A necessary requirement is that τ be chosen long enough to ensure significant variation among the components of X_i , but short enough to ensure that chaotic and stochastic fluctuations do not destroy the correlation between the components of X_i . A priori the appropriate dimension, m , is not known, but consistent results are obtained in the ideal case for any sufficiently large m . The trajectory defined by the vectors X_i in this phase space will differ in detail from the true trajectory in the true phase space, but the geometry of the trajectory, including its fractal dimension, is invariant in most systems of physical significance.

Grassberger and Procaccia define the correlation integral, $C(r)$, as

$$C(r) = \lim_{N \rightarrow \infty} \frac{1}{N^2} \times \{\text{the number of pairs of points } (i, j) \text{ whose separation } |X_i - X_j| \text{ is less than } r\}.$$

For finite sets of data, this function may be approximated by

$$C'(r) = \frac{1}{N(N-1)} \sum_{i,j=1}^{N-m} H(r - |X_i - X_j|) , \quad (3)$$

where $H(r)$ is the Heaviside function, defined as $H(r) = 1$ if $r > 0$; otherwise, $H(r) = 0$. Like $N(r)$ in the fractal box dimension, a plot of $C(r)$ versus r on a log-log plot typically yields a straight line in the limit of small r . The correlation dimension, D_c , is just the slope of this line. The appropriate phase space dimension, m , may be found by computing $C'(r)$ for phase spaces defined by $\{X_i\}$ of increasingly higher dimensions. For dimensions $m < D_c$, the slope of the $\log(C'(r))$ vs $\log(r)$ plot should be equal to m , the dimension of the phase space used in the computation. If the trajectory is associated with a strange attractor, the slope of the $\log(C'(r))$ vs $\log(r)$ plot will be nonintegral and equal to D_c for sufficiently large phase space m . In the analysis of numerical data, the choice of m involves a trade off. While increasing m generally reduces systematic errors, it also increases statistical errors.

Figure 6 displays log-log plots of $C'(r)$ for several values of m for both the epoxy and the MgO data. The indicated dimension measurements were made using the darken portions of the curves, which were chosen to avoid the region of poor counting statistics at low values of $C'(r)$ and the region of stochastic fluctuations at low r . Both sets of correlation integrals show a clear tendency toward saturation for $m \geq 5$, with $D_c \sim 3.3$. This saturation is not complete, as we observe a small increase in slope with m for $m \geq 5$, most likely the consequence of the small data sets used in the analysis. Most importantly, the observed saturation is strong evidence that the larger fluctuations in the pH_E are not stochastic. Further, the saturation at a nonintegral slope is strong evidence that these fluctuations are associated with a strange attractor, and thus are chaotic in nature.

The correlation integrals of the epoxy data show some curvature at intermediate values of r which may indeed be real, not the result of poor statistics. If so, this suggests that the attractor may be best described by a fractal dimension which effectively depends on r . Analogous observations have been made concerning the fractal dimension of fracture surfaces of certain steels. When very wide ranges of surface feature sizes are used in the analyses, the effective surface fractal dimension is found to vary somewhat with feature size.⁹ However, over \sim two decades of surface feature dimension, this dimension is nearly constant, as observed in the above slit island analysis of the epoxy surface. The possible connection between deviations from strictly fractal behavior in surface features and in pH data is a promising area for further study.

At very low r , many of the correlation integrals of the MgO pH data show a sharp increase in slope. This transition occurs at $r \sim 4$ for low m , where the pair counting statistics are still rather good. In this low r region, the slopes of the correlation integral are nearly equal to m , the phase space dimension. This is characteristic of purely stochastic data,²² and implies that pH fluctuations below the transition are dominated by stochastic processes, such as white noise. Thus the MgO data are characterized by a low intensity white noise of amplitude $r \sim 3$, while the larger fluctuations are largely deterministic and fractal. The epoxy data show a similar transition at yet smaller value of r , not shown in Fig. 6a).

As noted above, the saturation of the correlation integrals at a nonintegral slope is strong evidence that these fluctuations are associated with a strange attractor, and are thus chaotic in nature. The correlation dimension, D_c , can be used to provide convenient if approximate bounds on the dimensionality of mathematical models which hope to describe the chaos associated with the pH data. A strict lower bound on the dimensionality of such models is provided by the box dimension of the attractor, D_b . Since $D_b > D_c \sim 3.3$, we expect that at least four dimensions, or degrees of freedom, are needed. A theorem due to Whitney gives an upper bound on the necessary dimensionality equal to twice the local topological dimension of the attractor.^{26,27} If $D_c \sim D_b$, this local dimension is four, and thus an upper bound on the necessary dimensionality is eight. This estimate is made without regard to the physical interpretation of the relevant dimensions, so a

physical model could in principle require more dimensions. However, many if not most of the commonly used model chaotic systems are described by mathematical models with dimensionality close to the local topological dimension of the attractor, which is in this case about four. Thus there is reason to hope that relatively low dimensional models may be constructed which reasonably describe the chaotic dynamics of the fracture process.

6. Lyapunov Exponent Estimates

Lyapunov exponents are among the most useful quantities in characterizing chaotic systems. On sufficiently small time scales, nearby trajectories in phase space tend to converge or diverge exponentially. The Lyapunov exponents indicate the average exponential rate of convergence or divergence for a dynamical system. Wolf et al. have developed a method often capable of determining the largest Lyapunov exponent for systems described by finite data sets in the presence of noise.²⁸ We have employed this method to study these two data sets. A positive Lyapunov exponent is conclusive evidence for chaos, and reflects the time scale over which the evolution of a dynamical system becomes unpredictable.

We start with a reconstructed phase space based on the method of delays, as described above. As the data define only one trajectory, we cannot in practice follow the progress of two nearby trajectories. However, as the trajectories associated with attractors are typically somewhat cyclic, the convergence or divergence of nearby points on different "orbits" of the same trajectory can be used to estimate the exponents. Whatever trajectories are used in the computation, their characteristic divergence cannot be maintained beyond the "diameter" of a typical orbit, i.e. the magnitude of the largest fluctuations characteristic of the system. To ensure that the separation between the trajectories used in the analysis remains sufficiently small, one periodically replaces the nearby trajectory with another, closer trajectory. The choice of replacement time interval, T , involves a trade off between sources of error associated with long propagation times, and sources of error associated with the replacement process. The robustness of the exponent estimate with

respect to changes in phase space dimension, m , phase space delay time, τ , and replacement interval T , are generally good indicators that the problems associated with this choice are under control. The maximum Lyapunov exponent is then estimated as

$$\lambda_{\max} = \frac{1}{t_f - t_0} \sum_{i=1}^P \log_2 \left(\frac{L'(t_i)}{L'(t_{i-1})} \right), \quad (4)$$

where $L'(t)$ is the separation of the fiducial trajectory and the nearby trajectory at time t , $\{t_i\}$ are the times at which the nearby trajectories are replaced, and P is the number of trajectory replacements. t_f and t_0 are final and initial times associated with the time series, respectively. Measuring time in units of sampling intervals and using base 2 in the logarithm of Eq. 4 yields Lyapunov exponent estimates in units of bits per sampling interval.

Figure 7 shows a series of Lyapunov exponent estimates made from epoxy phE data as a function of propagation time, T . These estimates show a region of relatively stable values in the region of 6-16 sampling intervals. The corresponding Lyapunov exponent estimate is 0.017 ± 0.003 bits per sampling interval, or 1.7 bits/ μ s. This estimate shows fair stability with respect to changes in phase space and dimension, and thus is reasonably reliable. The positive sign of this estimate is further strong evidence for deterministic chaos in the phE process.

The small amount of stationary phE data from the MgO sample makes the estimate of Lyapunov exponents computationally unreliable. However, the behavior of the estimates as the computations proceed suggests that the largest exponent is indeed positive

7. Discussion and Conclusion

The irregular fluctuations of phE during the fracture of many materials indicate that deterministic chaos is a feature of the phE in many materials. In the case of the epoxy and single

crystal MgO, several measures of fractal and chaotic behavior strongly support this interpretation. The most precise measure of fractal behavior used in this study, the fractal box dimension, indicates that the pH_E fluctuations are indeed fractal, with fractal dimensions of 1.35 for the epoxy and 1.16 for the MgO. The fractal dimensions determined from the Fourier spectrum of the epoxy pH_E data is consistent with the corresponding box dimension, but displays limited precision. The correlation integrals of pH_E data from both materials indicate that the observed fluctuations can indeed be described in terms of an attractor of nonintegral dimension and therefore associated with chaos. The positive Lyapunov exponent estimate for the epoxy data is additional evidence for chaos in the pH_E/fracture process in this material. We therefore conclude that the pH_E accompanying the fracture of the epoxy displays significant, chaotic fluctuations. The evidence for chaotic fluctuations in the pH_E from single crystal MgO is also strong.

Slit island analysis of the epoxy surface indicates that the fracture surface of this polymer is fractal. Measurements of fracture surface fractal dimensions have hitherto largely been restricted to single crystal and polycrystalline metals and ceramics. The observation of fractal geometry in a brittle polymer suggests that the techniques of fractal analysis are applicable to this class of materials as well. Further, pH_E fluctuations during the fracture of the epoxy have the same fractal dimension as a one-dimensional cross section of the fracture surface. Within a given class of materials, the fracture surface fractal dimension often correlates well with fracture toughness.^{6,7} pH_E fluctuations during fracture appear to reflect the the creation of the same set of self-similar (or self-affine) structures that constitute the fracture surface and which contribute to material toughness. Thus pH_E measurements may prove useful in studies of dynamic crack growth and arrest in which variations of toughness are important. For instance, the ease of data collection and analysis of pH_E data relative to the analysis of fracture surfaces may make pH_E measurements valuable in the identification of promising samples in surveys of materials prepared under a variety of conditions.

Dynamic crack growth is a dissipative, nonlinear process. Many dissipative, nonlinear systems display chaos over certain ranges of their parameters. Chaos may also result from the

perturbation of a nonlinear system. A crack might experience such perturbations upon encountering defects, which can serve as nucleation sites for voids and microcracks in the process zone of the advancing crack. Crack deflection accounts for the effect of microstructure upon fracture toughness observed in many materials. The interaction of the crack tip with acoustic waves generated in microfracture events and their reflections could represent significant perturbations in the fracture of single crystal materials such as the MgO in this study. Since diffusion and aggregation often result in fractal structures,²⁹ it is possible that in some systems a fractal distribution of defects actually results in chaotic perturbations. The correlation between fracture surface fractal dimension and toughness in some materials systems^{6,7} suggests that an understanding of the chaos producing mechanisms accompanying fracture may increase our control of material toughness through microstructural modifications.

Methods currently being developed to describe chaos in dynamical systems may prove useful in describing dynamic crack growth, particularly as they relate to fluctuations in the processes of crack growth and branching. Models of these processes have hitherto met with limited success, and the presence of processes which are extremely sensitive to noise or initial conditions would definitely be a complicating factor. Recently developed methods of data analysis may allow quantitative comparison of chaotic data with mathematical models.²⁷ The low dimensionality of the attractors observed in this study indicate that models realistically describing the chaotic aspects of fracture can be constructed with relatively few degrees of freedom.

The results of this study suggest that pH_E measurements are useful probes of the production of fractal surface structures in real time. Thus, phase space trajectories reconstructed from pH_E data may prove useful in testing models of dynamic crack growth, especially when chaotic processes are involved.

Acknowledgements

This work was supported by the Ceramics and Electronic Materials Division of the National Science Foundation under Grant DMR 8601281, the Office of Naval Research, Contract No. N00014-87-K-0514, the McDonnell Douglas Independent Research and Development Program, and the Washington Technology Center. The authors wish to thank Dan Passoja and Jack Mecholsky, Pennsylvania State University, and Rick Williford, Battelle Pacific Northwest Laboratories for helpful discussions.

References

- 1) J. T. Dickinson and L. C. Jensen, to appear in ASTM Proceedings for the 13th International Symposium for Testing and Failure Analysis, Los Angeles, 9-13 Nov., 1987.
- 2) J. T. Dickinson, L. C. Jensen, and A. Jahan-Latibari, *J. Vac. Sci. Technol. A* **2**, 1112 (1984).
- 3) J. T. Dickinson and A. S. Crasto, in **Cross-linked Polymers: Chemistry, Properties, and Applications**, edited by R. A. Dickie, S. S. Labana, and R. S. Bauer, (American Chemical Society, 1988) pp. 145-168.
- 4) J. T. Dickinson, L. C. Jensen, and S. K. Bhattacharya, *Makromol. Chem., Macromol. Symp.* **7**, 129 (1987).
- 5) S. C. Langford, J. T. Dickinson, and L. C. Jensen, *J. Appl. Phys* **62**, 1437 (1987).
- 6) B. B. Mandelbrot, D. E. Passoja, and A. J. Paullay, *Nature* **308**, 721 (1984).
- 7) J. J. Mecholsky, D. E. Passoja, and K. S. Feinberg-Ringel, in **Fractography of Glasses and Ceramics**, edited by J. R. Varner and V. D. Frechette, (American Ceramic Society, Westerville, OH, USA, 1988), p. 127.
- 8) J. J. Mecholsky, T. J. Mackin, and D. E. Passoja, *J. Am. Ceramic Soc.* **72**, 60 (1989).

- 9) E. R. Underwood and Kingshuk Banerji, *Materials Sci. and Eng.* **80**, 1 (1986).
- 10) D. E. Passoja, in *Fractography of Glasses and Ceramics*, edited by J. R. Varner and V. D. Frechette, (American Ceramic Society, Westerville, OH, USA, 1988), p. 101.
- 11) A. J. Markworth and J. K. McCoy, *J. Mater. Res.* **3**, 675 (1988).
- 12) E. Louis and F. Guinea, *Europhys. Lett.* **3**, 871 (1987).
- 13) Hiroaki Hara and Seiji Okayama, *Phys. Rev. B* **37**, 9504 (1988).
- 14) N. H. Packard, J. P. Crutchfield, J. D. Farmer, and R. S. Shaw, *Phys. Rev. Lett.* **45**, 712 (1980).
- 15) B. B. Mandelbrot, *The Fractal Geometry of Nature*, (W. H. Freeman, New York, 1983).
- 16) B. B. Mandelbrot and R. F. Voss, in *Noise in Physical Systems and 1/f Noise*, edited by M. Savelli, G. Lecoy, and J-P. Nougier, (Elsevier Science Publishers, Amsterdam, 1983), p. 31.
- 17) B. B. Mandelbrot, *Physica Scripta* **32**, 257 (1985).
- 18) J. P. Dempsey and P. Burgers, *Int. J. Fracture* **27**, 203 (1985).
- 19) K. Ravi-Chandar and W. G. Knauss, *Int. J. Fracture* **26**, 141 (1984).

- 20) D. S. Broomhead and G. P. King, *Physics* **20D**, 217 (1986).
- 21) Peter Grassberger and Itamar Procaccia, *Physica* **9D**, 189 (1983).
- 22) J. Kurths and H. Herzel, *Physica* **25D**, 165 (1987).
- 23) Avraham Ben-Mizrachi and Itamar Procaccia, *Phys. Rev. A* **29**, 975 (1984).
- 24) Pierre Bergé, Yves Pomeau, and Christian Vidal, *Order within Chaos*, (John Wiley and Sons, New York, 1984).
- 25) F. Takens, in *Lecture Notes in Mathematics*, edited by D. A. Rand and L. S. Young, (Springer, Berlin, 1981), p. 366.
- 26) H. Whitney, *Annals of Math.* **45**, 220 (1944).
- 27) J. P. Crutchfield and B. S. McNamara, *Complex Systems* **1**, 417 (1987).
- 28) Alan Wolf, J. B. Swift, H. L. Swinney, and J. A. Vastano, *Physica* **16D**, 285 (1985).
- 29) Paul Meakin, in *Phase Transitions and Critical Phenomena*, Vol. 12, edited by C. Domb and J. L. Lebowitz, (Academic Press, London, 1988), pp. 335.

Figure Captions

FIG. 1. *phE* measurements made during fracture of a) the epoxy and b) single crystal MgO. The

FIG. 2. Autocorrelations of *phE* data from a) the epoxy and b) single crystal MgO.

FIG. 3 The Fourier power spectra of a) the epoxy and b) single crystal MgO. Logarithmic scales are used on both axes.

FIG. 4. Plots of $N(r)$ vs $(1/r)$ used in the determination of the fractal box dimension, D_b , of the *phE* data from a) the epoxy and b) single crystal MgO. Logarithmic scales are used on both axes.

FIG. 5. Graph of island area vs island perimeter as measured in the slit island analysis of an epoxy fracture surface. The indicated slope is based on 63 island measurements. Logarithmic scales are used on both axes.

FIG. 6. Correlation integral computations for *phE* data from a) the epoxy and b) single crystal MgO as a function of phase space dimension. The slopes result from linear least squares fits to the darkened portions of the curves. The phase space delay time in both sets of calculations is 10 ns. Logarithmic scales are used on both axes.

FIG. 7 Lyapunov exponent estimates made from the epoxy *phE* data as a function of evolution time, T . The phase space delay time and dimension used in the computations are 30 μ s and 5, respectively.

phE accompanying Fracture of Epoxy and MgO

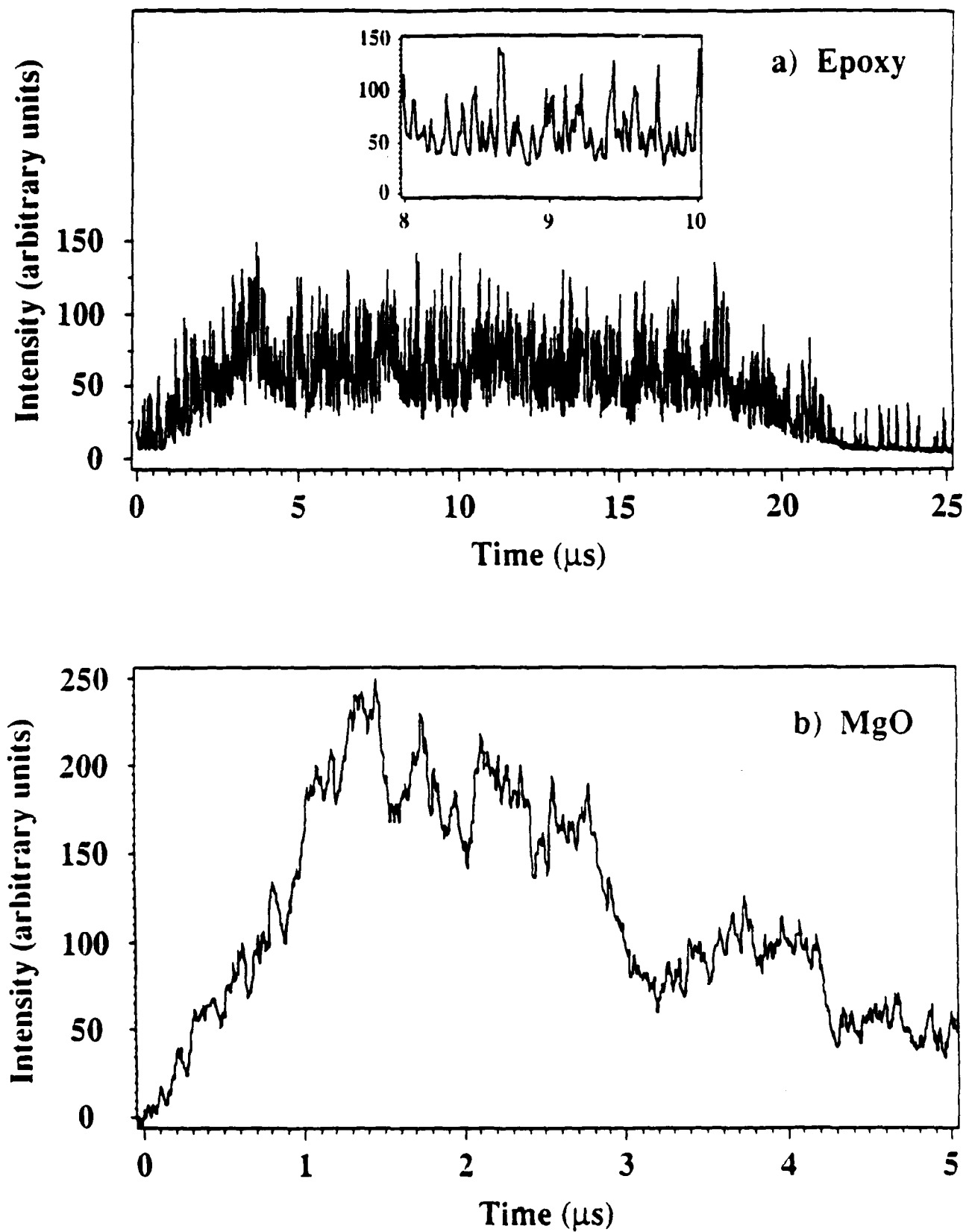


Fig. 1

Autocorrelations of phE from Epoxy and MgO

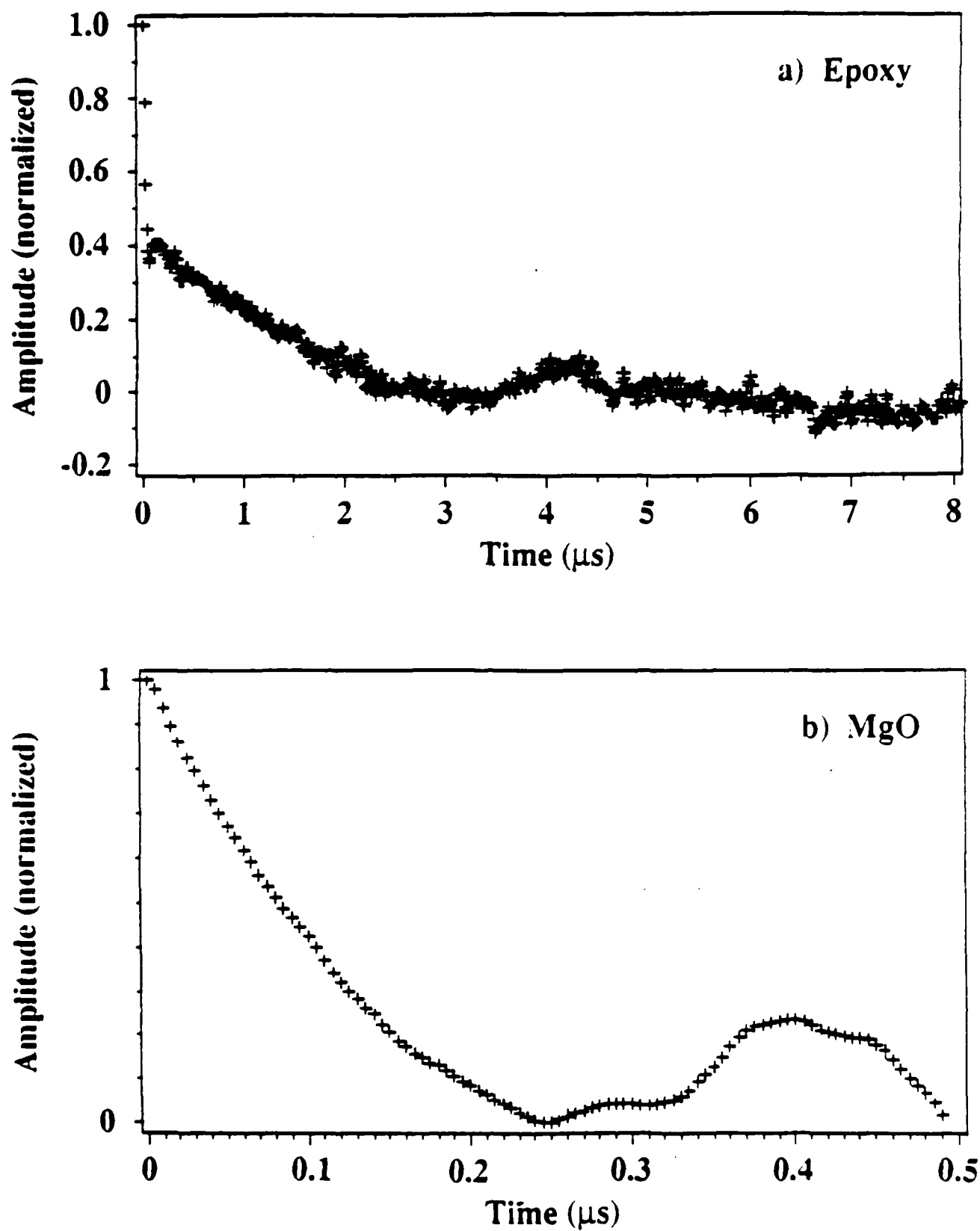


Fig. 2

Log/log Plot of Fourier Amplitudes

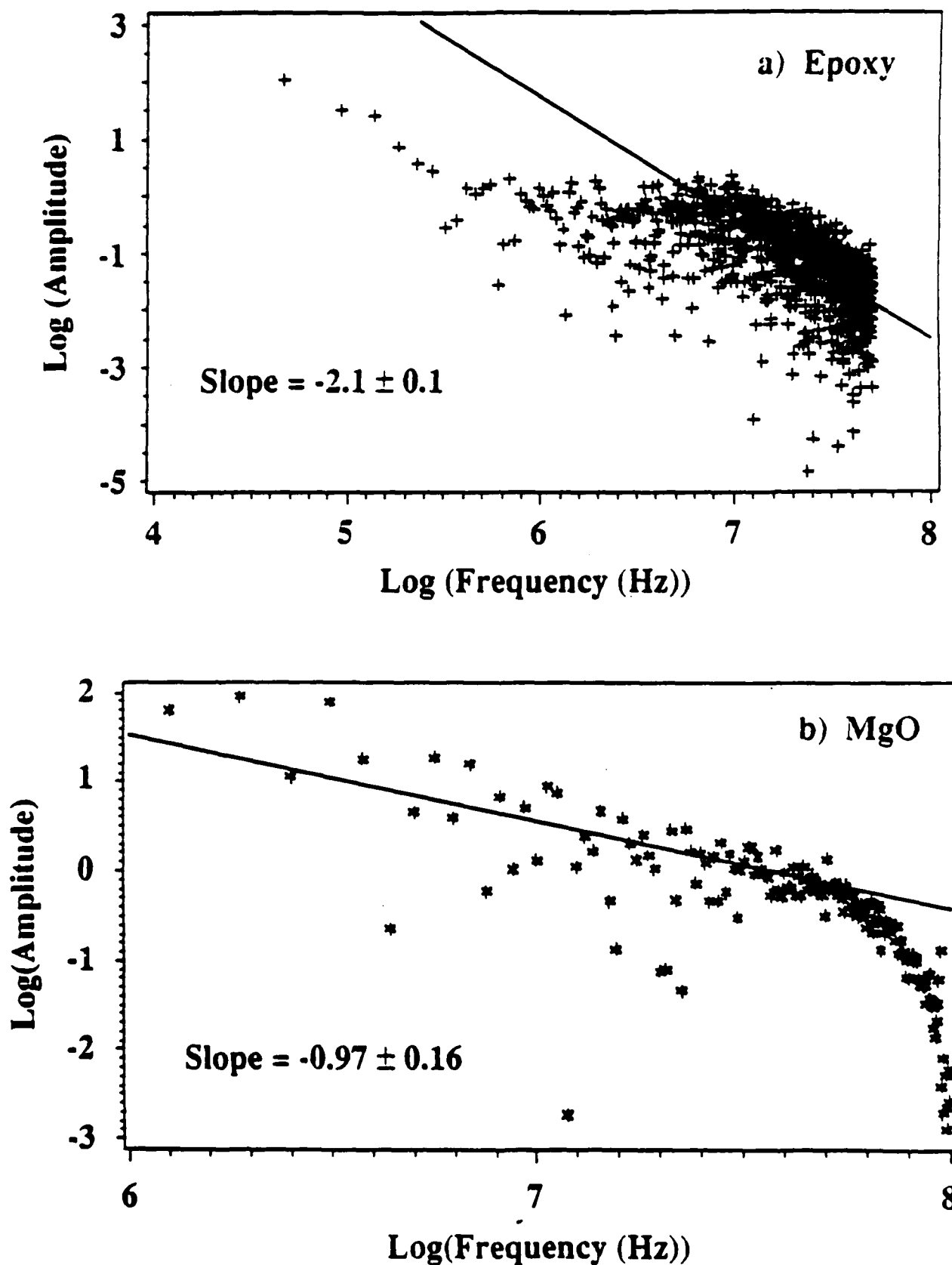


Fig. 3

Fractal Box Dimension Measurements of phE Data

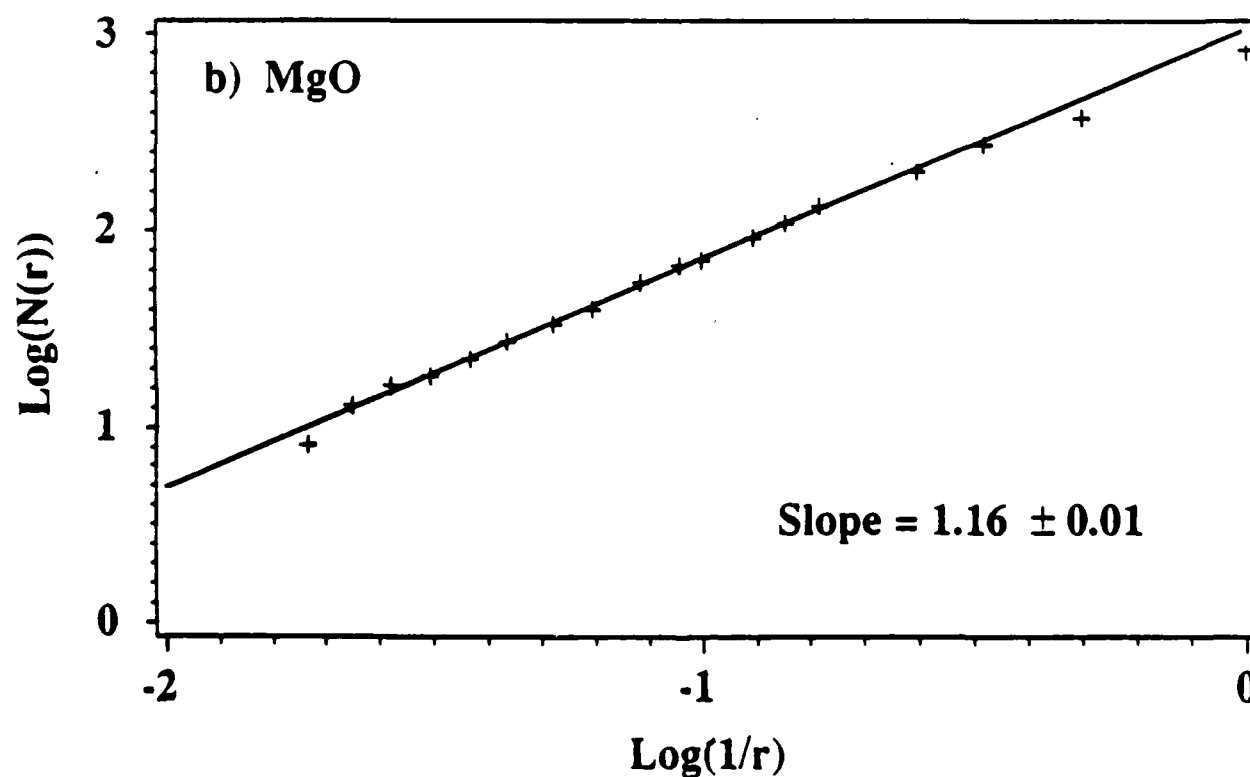
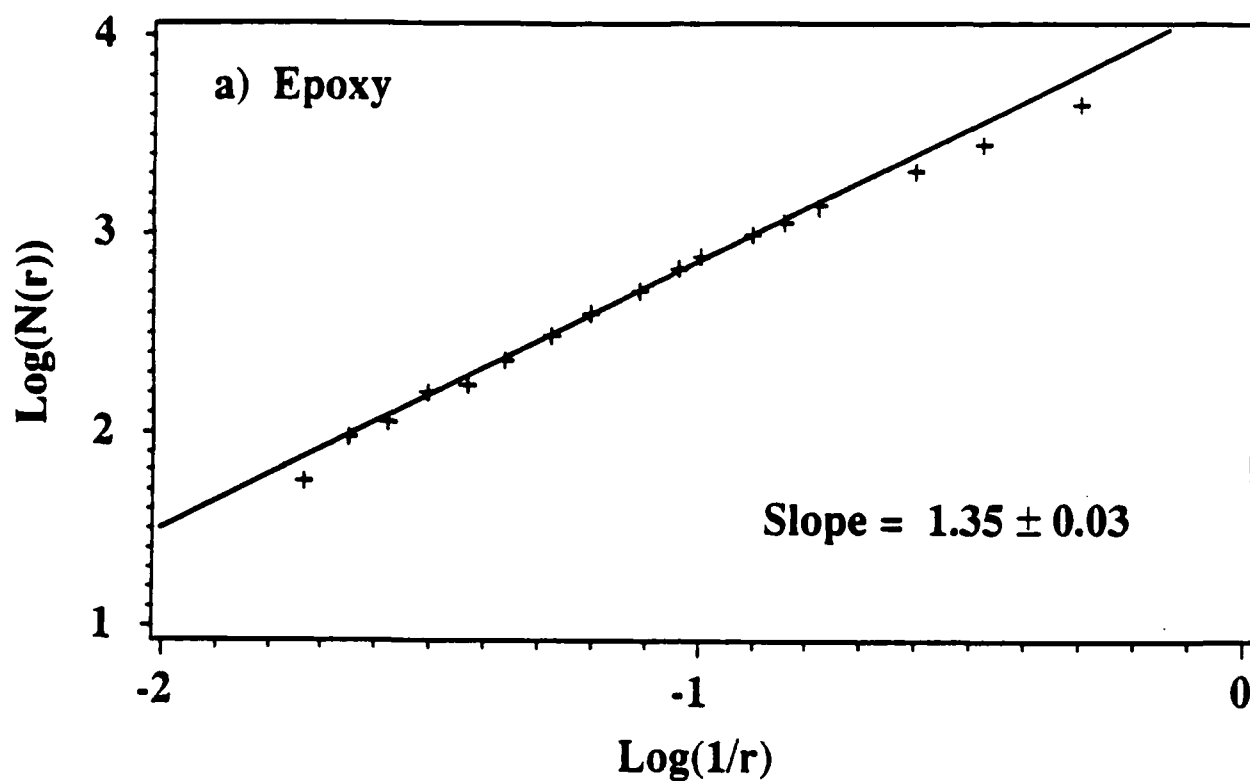


Fig. 4

Slit Island Analysis of Epoxy Fracture Surface

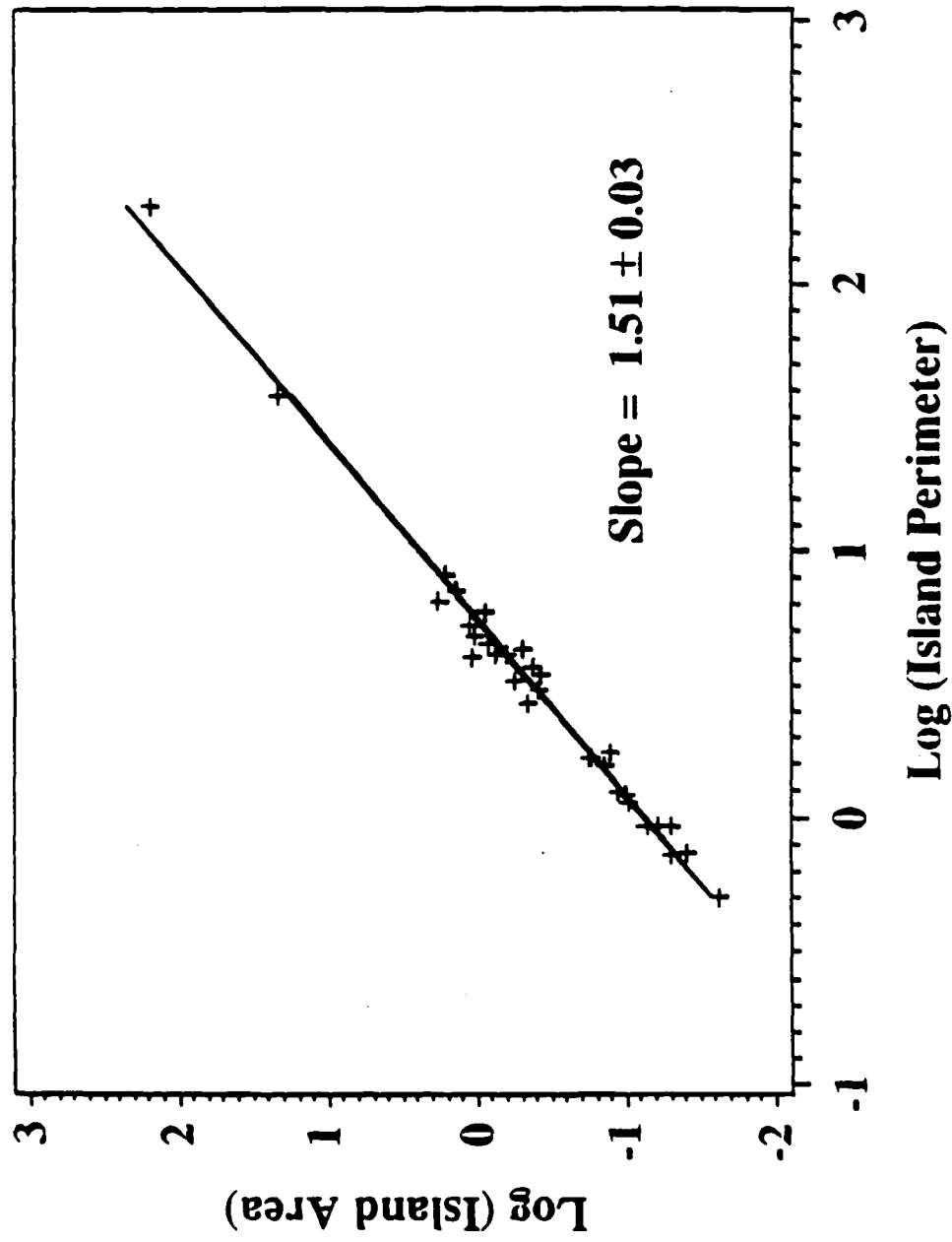


Fig. 5

Correlation Integrals of phE Data

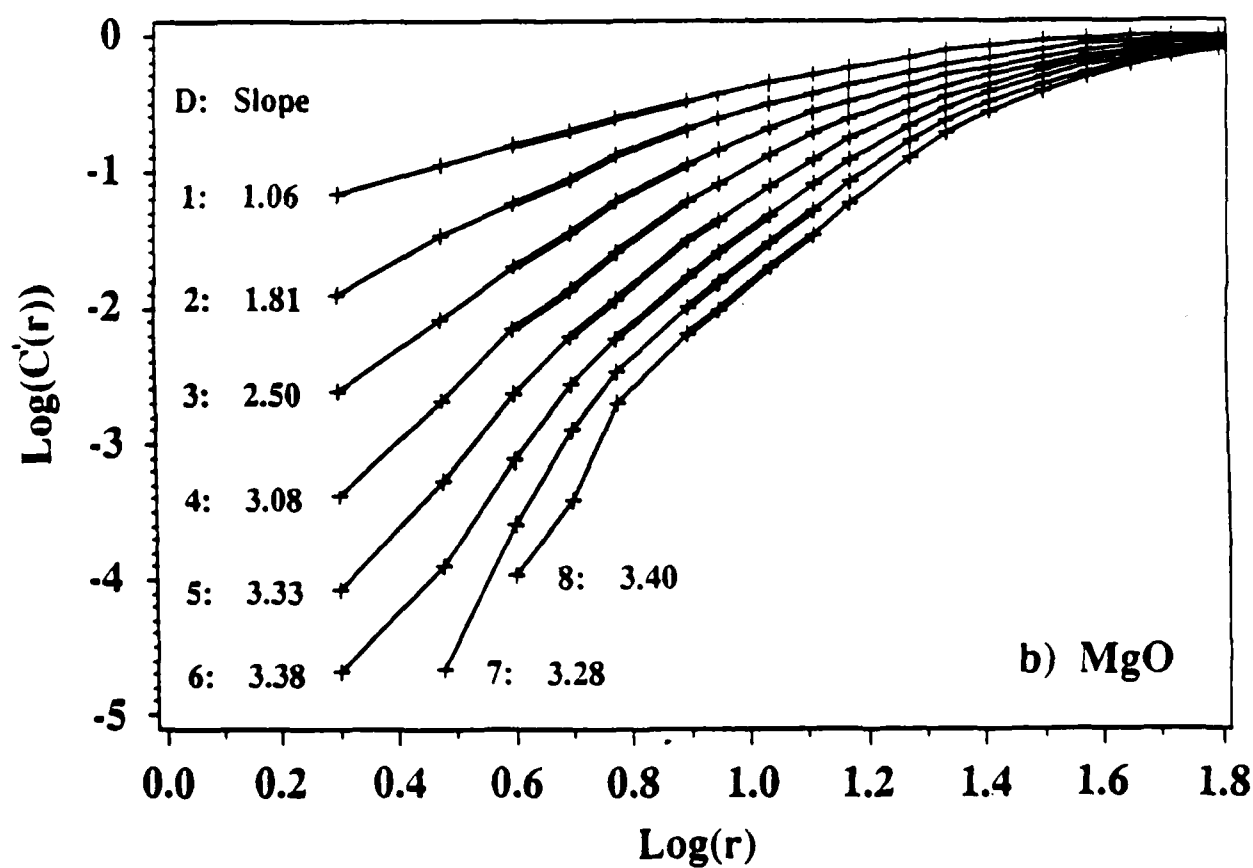
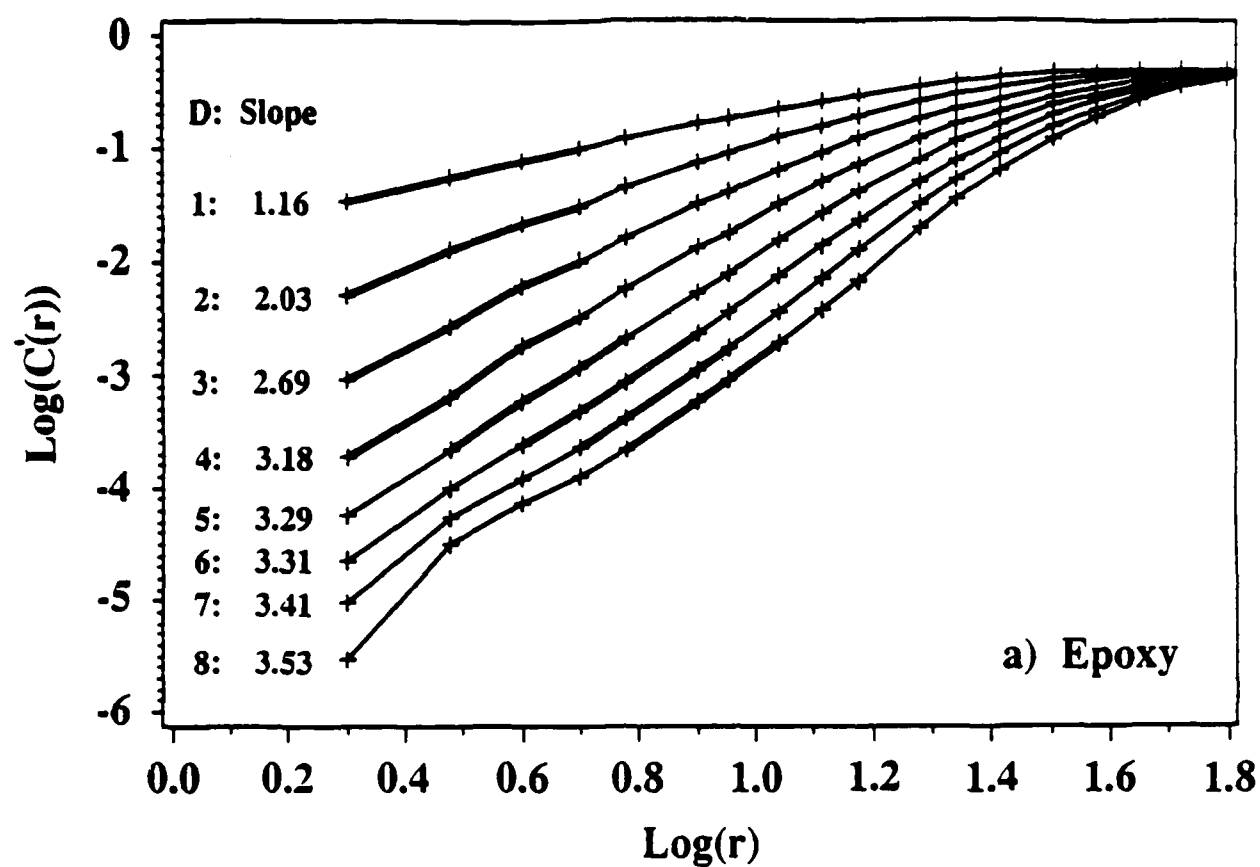


Fig. 6

Lyapunov Exponent Estimate vs Evolution Time

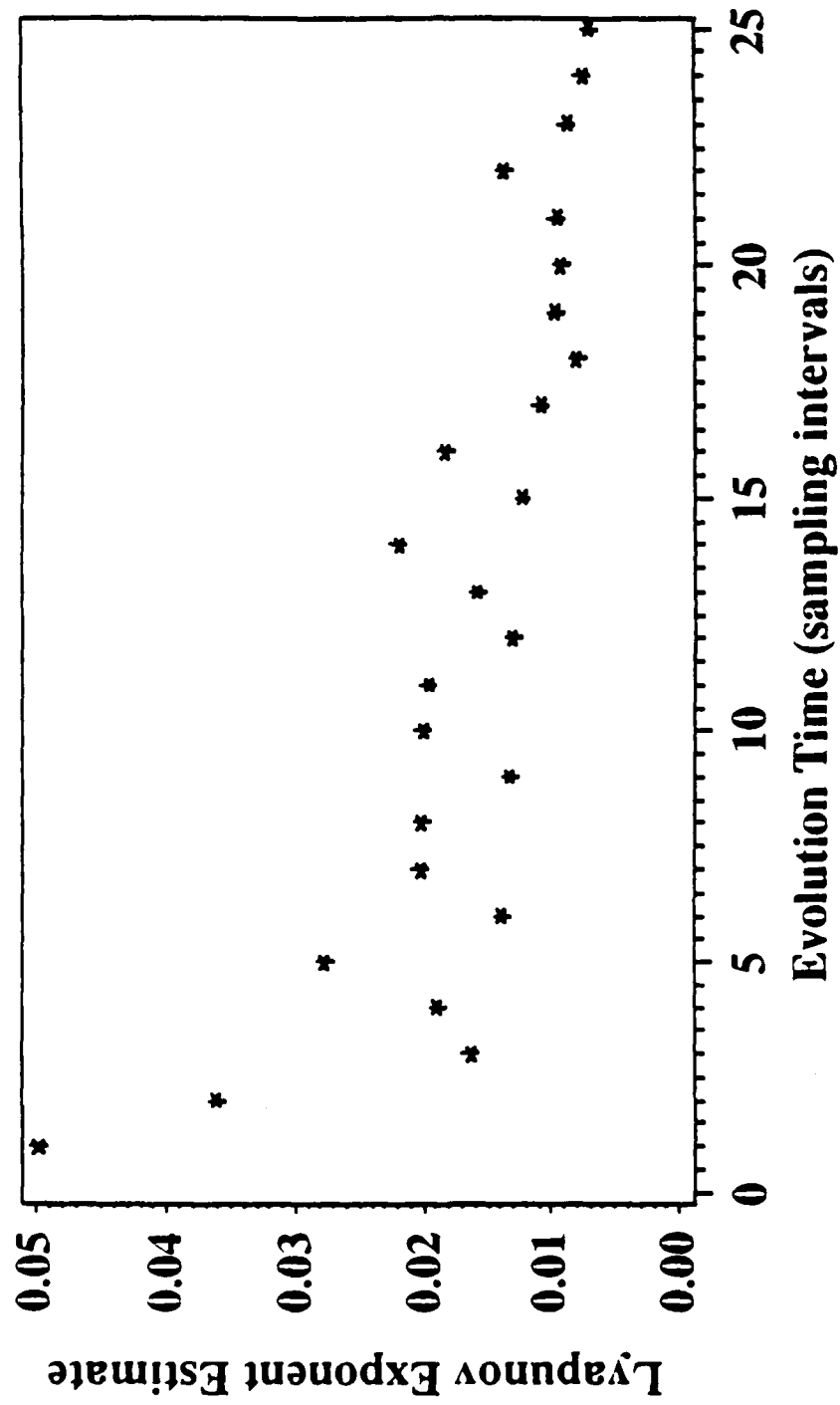


Fig. 7

IX. PROPERTIES OF THE PHOTON EMISSION ACCOMPANYING THE PEELING OF A PRESSURE SENSITIVE ADHESIVE

Ma Zhenyi, Fan Jiawen, and J. T. Dickinson
Department of Physics
Washington State University
Pullman, WA 99164-2814

ABSTRACT

During the peeling of pressure sensitive adhesives, it is well known that visible light is emitted from the region near the detachment zone. This photon emission due to adhesive failure is a unique form of *triboluminescence*. In this paper, we further investigate the properties of this light from the peeling of a filament tape with a natural rubber-resin adhesive from its backing at various peel speeds. We show conclusively that small electrostatic discharges are the major source of this radiation. Total intensity vs time measurements show that the light consists of very intense bursts with typical duration of 50 ns which frequently induce additional discharges for times as long as 50-100 μ s. Time resolved spectra of these emissions show them to be dominated by the line spectrum of molecular nitrogen for both the initial bursts and those that follow in the next 0.1-100 μ s. Thus, the "after-emission" is not due to phosphorescence of the polymer(s), but due to these additional electrostatic discharges.

KEYWORDS: adhesive, pressure sensitive, peeling, triboluminescence, photon emission, fracto-emission, charge separation, electrical breakdown, microdischarge, optical spectra, time resolved spectroscopy.

I. INTRODUCTION

A number of researchers¹⁻⁵ have investigated the well known *triboluminescence* observed during the peeling of adhesives from polymers and other substrates. This photon emission accompanying peeling of pressure sensitive adhesives and other forms of interfacial failure has been attributed to small gaseous discharges due to the intense charge separation which occurs during the separation between two dissimilar materials such as the adhesive and a substrate.¹⁻⁵ One test of these mechanisms which we performed involved peeling metal films from an inorganic insulator (glass) and found entirely similar behavior.⁶

In previous work we have presented details of the properties of the light as well as the charged particle emission from systems undergoing adhesive failure.⁴⁻¹¹ In particular, we have presented results showing that the detachment of a commercial brand of filament reinforced pressure sensitive tape from its own backing leads to strong bursts of photon and radiowave emission that were strongly correlated in time⁴ and that are highly localized spatially in the vicinity of the peel zone.⁵ Furthermore, we showed that the averaged intensity vs time behavior of these bursts consisted of a narrow, intense spike on the order of 50 ns in duration followed by a decay lasting typically for 50 to 100 μ s. We interpreted the spike (found to be in coincidence with the onset of radio wave emission) to be the light from the discharge. The after-emission (the tail) was attributed to phosphorescence from the discharge activated surface.

Earlier published data on considerably different polymer/substrate combinations (e.g., PVC from glass) taken at low spectral resolution (by use of filters) have been presented by Ohara et al.¹ and Klyuev et al.³ Ohara et al. observed the most intense emission in the region of the spectrum below 490 nm, consistent with gaseous discharges in air. At low pressures, features ascribable to luminescence of the glass substrate were also observed.

In this paper, we present higher resolution spectral measurements of the photon emission from the peeling of 3M Scotch Filament Tape No. 893 detached from its own backing. We present measurements of the time dependence of this emission, acquired at a faster time scale.

In addition, we have obtained time-resolved and time integrated spectra of this light. We examine the spectrum as a function of time relative to the larger bursts of light over a time range of 100 ns to several tens of microseconds. These results verify that indeed the initial bursts are due to the breakdown of air, and show that the after-emission is due to additional, smaller microdischarges *triggered* by the initial burst, rather than phosphorescence from the adhesive/backing polymers. In addition, we have also compared the light emitted from the surface several mm from the crack tip vs from the crack tip and see again discharge-like spectra. The origin of this light is shown to be due to "light piping" of emission from the crack tip, along the filaments.

II. EXPERIMENT

We selected 3M Scotch Brand Filament Tape as a test material. The adhesive is a natural rubber combined with a tackifying agent which is a hydrocarbon resin appearing to be terpene based. More tackifier is used on the face of the adhesive and less in the saturating layer binding the glass filaments to the backing. The polyester tape backing has been treated with a release coating with a critical surface tension for wetting of approximately 21 dynes/cm. The experimental geometry consisted of a roller arrangement such that pre-made sandwiches of adhesive and backing may be peeled apart continuously in total darkness and in the vicinity of a photomultiplier or spectrometer in a T-Peel fashion. All experiments were performed in air at room temperature. The relative humidity during these tests can have an influence on the intensity of the emission and fell in the range from 25-35%.

In Fig. 1 we show a schematic diagram of the system for acquiring spectra of the photon emission accompanying adhesive failure. The detachment zone of the T-Peel was placed approximately 1 cm from the entrance slit of the spectrometer. The crack orientation was at right angles to the slit to minimize stray light in the spectrometer. A 1200 lines/mm grating spectrograph (Thermo Jarrell Ash Monospec-18) was used with a EG&G Model 1421 gatable,

intensified position sensitive detector, responsive to light in the region between 200-830 nm. Both time-averaged and time-resolved data were acquired utilizing an EG&G OMA-III system.

A photomultiplier (PMT in Fig. 1) located near the peel zone was used to monitor total light intensity vs time. With suitable circuitry, bursts of light in the peel zone were transformed to 10 ns trigger pulses within a few ns of the onset of the bursts. With a discriminator, large bursts could be easily selected from a distribution of sizes. The spectrometer detector could be gated on at any time relative to this pulse between 70 ns - 13 ms and held open for time intervals from 100 ns - 10 ms. Time integrated spectra were acquired for time intervals of approximately 10 s which would correspond to ~5000 bursts. This light thus represented an average of the light emitted before, during and following isolated bursts.

For wavelength calibration we used a commercial mercury lamp whose spectrum contains several shorter wavelength lines in the region of interest.

Fig. 2 shows a block diagram of the experimental apparatus for acquiring total intensity vs time measurements. In this experiment the PMT output for a larger burst of photons was treated as a rapidly varying current pulse. After converting this current into a voltage, the resulting signal was amplified by a fast DC amplifier. This amplified signal was then digitized at time intervals of 5 ns/channel. The data were stored in a LeCroy-3500 Data Acquisition System.

III. RESULTS

Preliminary studies of time integrated spectra (over the interval from 200-600 nm) of the visible-near uv light produced during the peeling of 3M Filament Tape from its own backing showed that the emission was all concentrated in the wavelength interval from 300-440 nm. The time integrated spectrum in this region is shown in Fig. 3. Since the data was acquired continuously (therefore before, during, and following a large number of bursts), it contains photons produced both during the discharges and afterwards. First, we note that it is a

discrete spectrum. When compared with the characteristic gaseous discharge emission of N_2 , O_2 , CO_2 , and other gaseous molecules, we found that each of the lines in the peel-induced spectrum corresponded to N_2 spectral lines. The transitions observed are the strong features of the Triple Headed Band¹² involving the N_2 electronic states: $B\ ^3\Pi \rightarrow C\ ^3\Pi$. The individual lines correspond to various vibrational states within each of these electronic levels. The fall off in intensity towards shorter wavelengths seen in several of the spectral lines is due to rotational fine structure.

It should be noted that at our resolution the strong O_2 emission lines in this region of the spectrum overlap with some of the N_2 lines, e.g., at 336.7 nm. However, another strong O_2 emission line at 410 nm was undetectable. Consequently, we can ignore any O_2 contribution to the observed lines, including 336.7 nm.

We emphasize that in no part of the spectrum do we observe any evidence of broadband emission, characteristic of a surface or solid state luminescence process, which as previously mentioned, we had expected.

In an attempt to separate out possible luminescence spectra from the discharge spectra, we acquired time resolved spectra of the light produced *after* the bursts, using the system shown in Fig. 1. Four time intervals were investigated:

- a) 70 ns to 10 μ s,
- b) 1 μ s to 11 μ s,
- c) 10 μ s to 20 μ s, and
- d) 50 μ s to 60 μ s.

Here, the $t=0$ pulse is within a few ns of the rise of the photons in single bursts. Each spectrum (Fig. 4) represents acquisition of 10^4 bursts. Because the light intensity is falling rapidly with time, it was necessary to sacrifice spectral resolution increasing the slit width. Nevertheless, we see that the basic shape of the spectrum does not change. The after-emission

has the same basic character of light from a discharge in air as opposed to some form of phosphorescence from the material surfaces.

In order to explain how such discharge-like spectra could occur so long after an initial burst, we examined in more detail the decay of the total light intensity following the bursts. Fig. 5 shows a signal averaged intensity vs time distribution of the photon bursts as detected by the PMT during peeling. The data were acquired at 5 ns/channel and represent an average over several thousand bursts. Fig. 5a are the results showing every channel (i.e., every 5 ns) in the vicinity of the burst; Fig. 5b shows the results with data displayed every 0.1 μ s. These time averaged intensities show that the major peak has a feature which lasts less than 50 ns, perhaps limited by the amplifier electronics. This is followed by a second decay of with an equivalent time constant of 1 μ s. Finally a third component decays with an equivalent time constant of 20 μ s. These results are consistent with earlier pulse counting studies.⁴ During all of these regions of time the spectra show discharge character.

Although the decaying emission shown in Fig. 5 appears very smooth, careful analysis of single bursts show that it is in fact a superposition of many bursts that:

- 1) occur in a time correlated fashion with the initial, generally stronger burst, and
- 2) decay in frequency and intensity as time progresses following the initial burst.

In Fig. 6, we show examples of these isolated PhE bursts produced during peeling of the adhesive tape, where the arrows indicate the onset of the initial burst. Both Fig. 6a and 6b show two to three bursts occurring on the time scale of a microsecond from single initial bursts. Also, viewing a large number of such data, we see no evidence of any smaller precursors to the initial, larger bursts.

If we allow large numbers of these events to accumulate by integrating their intensities by means of signal averaging, they form the smooth curves shown in Fig. 5. Thus, the decay constants are really determined by the frequency and size of these "multiple strikes", rather than

a solid state relaxation process such as observed in thermally stimulated luminescence.¹³ Instead, it involves a relaxation of surface charge and the interaction of the initial discharge with the charged surfaces and gases nearby.

One other observation that was suggestive of long decay in the light intensity was made by eye. When peeling the adhesive tape in the dark, one could clearly see light coming from the freshly detached surfaces, particularly on the adhesive side, for as far as 1-2 cm away from the crack. Could we be missing a long lasting phosphorescence? By use of proper baffles we could allow this light to enter the spectrometer and exclude the light from the crack. The resulting spectrum is shown in Fig. 7. Again, a discharge-like spectrum was observed with slight changes in the relative intensities (e.g., Fig. 3). Examination of the light propagating properties of the tape showed us that indeed photons could be transmitted from the crack tip region, most likely down the strands of glass reinforcing fibers, and be scattered out to the observer, normal to the tape surface. The changes in relative spectral line intensities can be attributed to the "filtering", i.e., the selective absorption of the light, which might occur in passing through the fibers and adhesive, apparently favoring the more violet part of the spectrum. So again, there is no evidence of long delayed emission after fracture and the light observed away from the crack is an artifact due to the "light piping" ability of this particular adhesive tape via the filaments it contains.

As we have reported earlier, the total photon emission intensities depend on peel speed.⁸ In Fig. 8 we show on a log scale the dependence on the peel speed of the integrated emission intensity between the wavelengths 300 nm-440 nm (\diamond) and the intensity of a single N₂ discharge spectral line at 336.7 nm (\circ), where we have normalized the data at a single point [26 cm/s]. The behavior is essentially the same in both curves, namely a rapid increase in intensity (nearly exponential) followed by a "saturation at a peel speed of ~ 10 cm/s with evidence of a slight decrease at the highest speeds.

In examining the relative spectral intensities of two lines taken at different peel speeds, we find that the ratio of the peaks at 316 and 335 nm changes, namely the ratio I_{316}/I_{335}

decreases with peel speed. These lines correspond to transitions involving two vibrational states, namely $v=1$ and $v=0$, and to a first approximation, this ratio represents the relative populations of these two vibrational levels. Letting n_1 and n_0 represent the respective populations, we have:

$$I_{316}/I_{335} = n_1/n_0 = \exp\{-(E_1-E_0)/kT\}$$

where E_1 and E_0 are the known vibrational energies of N_2 for $v=1$ and $v=0$. From the measured line intensities we can therefore calculate an average temperature in the discharges during peeling. Taking two extreme values in peel speed we calculate the following temperatures for the "sparks" created during peeling:

slow (0.7 cm/s)	4200 K
fast (15 cm/s)	3300 K.

Thus, at these particular peeling speeds, the slower peel yields "hotter" discharge events. These different temperatures suggest that discharge conditions in terms of charge separation and gas composition in the crack tip are more favorable at the lower speed for the production of higher energy breakdown events. As a consequence the gases in the "arc" reach higher temperatures at the lower peel speed. Thus, the much lower overall intensity at the lower peel speed (Fig. 8) is due to a much smaller number of discharge events per unit length of peel.

If we hold the peel speed constant but vary the water content of the air by artificially introducing water vapor in the region of the peel, we note that the intensity of the emission drops considerably. This so-called "wet" condition corresponded to 80% relative humidity. If we compare spectra for this "wet" condition with the "dry" condition (slightly different conditions than above), the ratio I_{316}/I_{335} decreases when the water content of the air is higher. For a peel speed of 2.7 cm/s, the calculated spark temperatures were:

- | | | |
|----|-----|---------|
| a) | WET | 3900 K |
| b) | DRY | 5100 K, |

thus showing that the higher humidity reduces the effective strength of the discharges occurring in the peel zone.

IV. DISCUSSION

From the experiment phenomenon we observed, we conclude that the photon emission is produced by excited electronic transitions in gaseous N_2 . The discharge responsible for this excitation initiates because of intense electric fields created by the charge separation as the rubber adhesive detaches from the release coated polyester backing. The breakdown of the gas takes place when the strength of the electric field attains a critical value for the particular gases in the crack tip.

Immediately following the discharge event, secondary "strikes" can occur in the vicinity of the initial discharge. Electrons or ions created in the first discharge move in a diffusion manner under the influence of the electric field and create secondary charge via collisions with gas molecules and surfaces.

The drift velocity in air at atmospheric pressure can be estimated and therefore the distance the charge might travel before a second "strike" might occur. Experimentally derived curves are used¹⁴ which depend on the electric field strength, gas pressure, and temperature. Assuming an electric field strength is 20,000 V/cm (the breakdown potential of dry air), a temperature of 293 K, and a pressure of 760 torr, we determine the following drift velocities in air and distances the particles move in various times following the initial breakdown event:

Particle	Drift Velocity	Dis. in 100 ns	Dis. in 50 μ s
electrons	8×10^6 cm/s	8.0 mm	40 cm
N_2^+	3×10^4 cm/s	0.03 mm	1.5 cm
O^-	1×10^5 cm/s	0.1 mm	5.0 cm

At atmospheric pressure, the ionic states are extremely probable, so that the distances we expect the charges to move are on the order of a cm or less. The crack only moves about 0.003 mm in a 50 μ s time period, so that it is not likely that the induced arcs are in the direction of the peel zone. More likely are regions along the peel zone. Since the tape is 2 cm in width, this sets an upper limit of about 100 μ s for the time secondary "strikes" may occur. This is consistent with the duration of the tail observed following the initial bursts. On a much larger scale, lightning bolts in the atmosphere often occur in a correlated fashion, perhaps for similar reasons.

V. CONCLUSIONS

In this paper we have presented further details of the photon emission accompanying peeling of an adhesive from a polymeric substrate. A consistent interpretation of these and earlier observations requires that all of the light is due to electrostatic discharges alone. In this particular adhesive-substrate combination, no evidence of an "after-glow", i.e., phosphorescence, involving excitations of the adhesive/backing surfaces was detected. Instead, the decaying light observed following the large bursts consists of a set of correlated bursts, generally of smaller intensity and less frequent occurrence over a time period of 50-100 μ s. We have argued that the charge released by the initial discharge drifts to other regions of the crack and initiates the observed secondary "strikes". Since the micromechanics of detachment are very likely critical to

the charge separation occurring, varying the rheology either chemically or by temperature variations would be an important direction to pursue.

VI. ACKNOWLEDGMENTS

This work was supported by the National Science Foundation DMR 8601281, The Office of Naval Research N00014-80-C-0213, McDonnell Douglas Independent Research Fund, and the Washington Technology Center.

REFERENCES

1. K. Ohara and T. Hata, *J. Appl. Polym. Sci.* **14**, 2097(1970).
2. B. V. Deryagin, L. A. Tyurikova, N. A. Krotova, and Y. P. Toporov, *IEEE Trans. Indust. Appl. VI. IA-14*, 541 (1978).
3. V.A. Klyuev, E. S. Revina, V. I. Anisimova, Yu. A. Khrustalev, and Yu. P. Toporov, *Colloid Journal (Kolloidn Zh.)* **41**, 287 (1979).
4. E. E. Donaldson, J. T. Dickinson, and X.A. Shen, *J. Adhesion* **19**, 267 (1986).
5. J. T. Dickinson and E. E. Donaldson, to be published in *J. Adhesion*.
6. L. A. K'Singam, J. T. Dickinson, and L. C. Jensen, *J. Am. Cer. Soc.* **68**, 510 (1985).
7. J. T. Dickinson, M. K. Park, E. E. Donaldson, and L. C. Jensen, *J. Vac. Sci. Technol.* **20** 436 (1982).
8. J. T. Dickinson, in *Adhesive Chemistry*, L. H. Lee, ed. (Plenum Pub. Co., New York, 1984), pp. 193-243.
9. J. T. Dickinson and L. C. Jensen, *J. Poly. Sci.: Polymer Physics Edition* **23**, 873 (1985).
10. J. T. Dickinson, L. C. Jensen, *J. Vac. Sci. Technol A*, **3**, 1398 (1985).
11. A. S. Crasto, R. Corey, J. T. Dickinson, R. V. Subramanian, and Y. Eckstein, to be published in *Composite Science and Technology*.
12. R. W. B. Pearse, and A. G. Gaydon, *The Identification of Molecular Spectra*, (J. Wiley & Sons, New York, 1941), pp 137-142.
13. A. Scharmann, R. Grasser, and M. Bohm, in *Thermally Stimulated Processes in Solids: New Prospects*, J. P. Fillard and J. van Turnhout, Editors, (Elsevier Scientific Publishing Co., New York, 1977) pp. 1-14.
14. C. F. Barnett, in *Physics Vade Mecum*, H. L. Anderson, ed. (American Insitute of Physics, New York, 1981), pp. 84-94.

FIGURE CAPTIONS

- Fig. 1. Schematic diagram of system for determining spectra of photon emission accompanying adhesive failure.
- Fig. 2. Block diagram of experimental apparatus for time vs intensity measurements.
- Fig. 3. Typical spectrum in the region from 300 nm to 440 nm of the photon emission during the peeling of 3M Filament tape. These spectra are not time resolved, so represent an integration over time.
- Fig. 4. Time resolved spectra of the photon emission during different time periods following an initial photon burst.
- Fig. 5. The signal averaged intensity vs time distribution of the bursts of light during peeling acquired at 5 ns / channel.
- Fig. 6. Multiple photon bursts which occur during peeling of the tape.
- Fig. 7. Time averaged spectrum of photon emission emanating from the tape surface approximately 1 cm from the peel zone.
- Fig. 8. Dependence on peeling speed of the integrated intensity of the total photon emission (\diamond) and intensity of the 336.7 nm spectral line (\diamond). The two data sets have been normalized to show their similarity.

APPARATUS FOR TIME RESOLVED SPECTROSCOPY

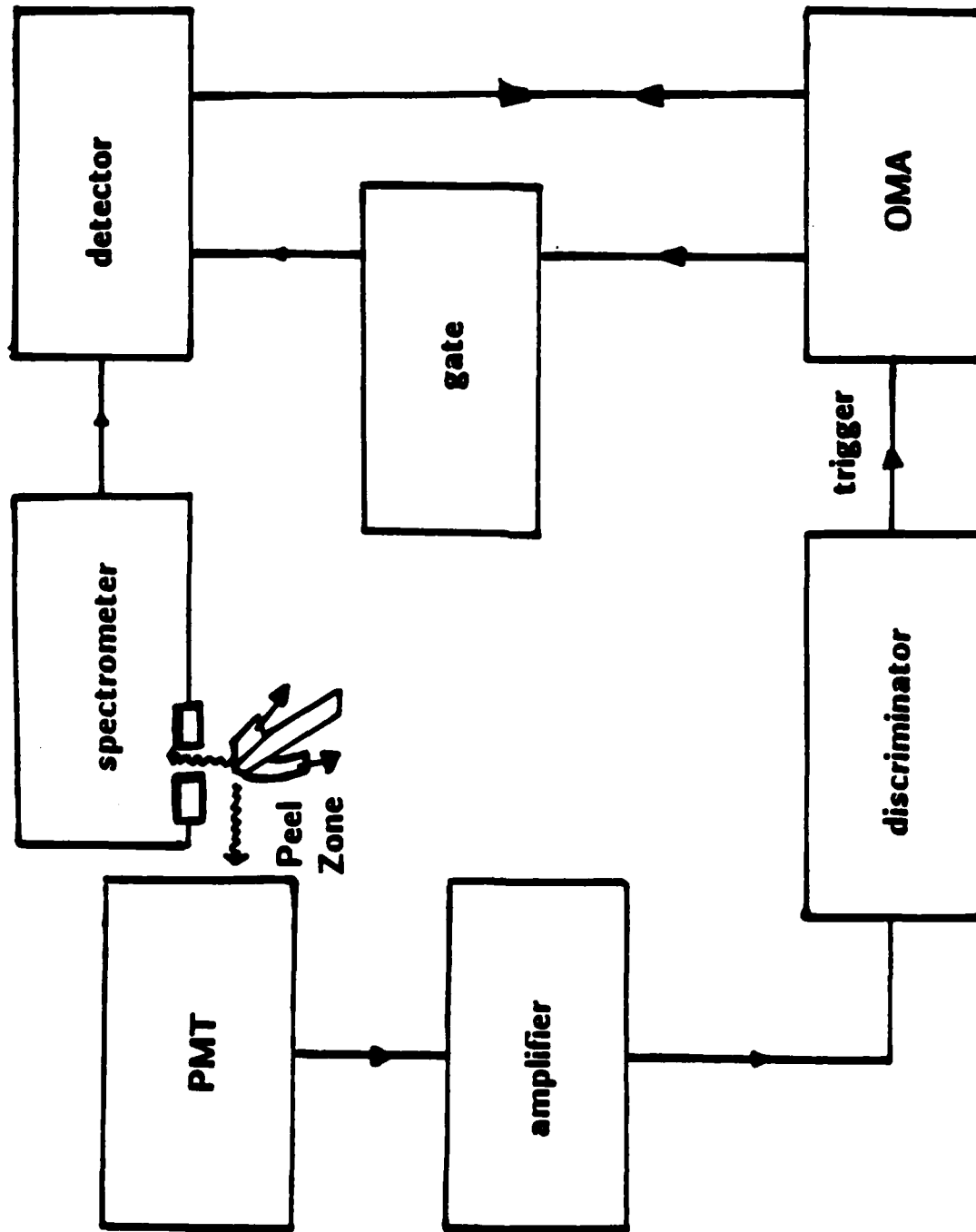


Fig. 1

APPARATUS FOR INTENSITY TIME MEASUREMENTS

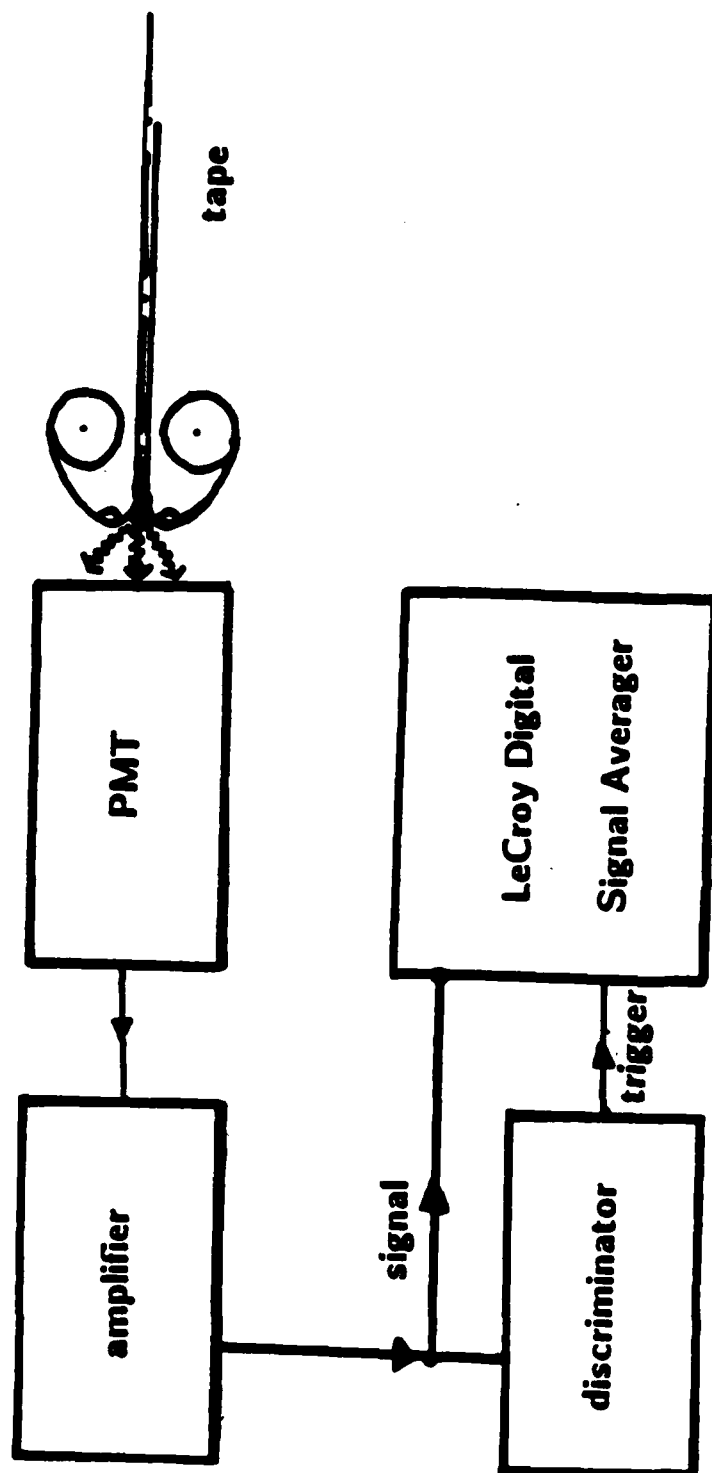


Fig. 2

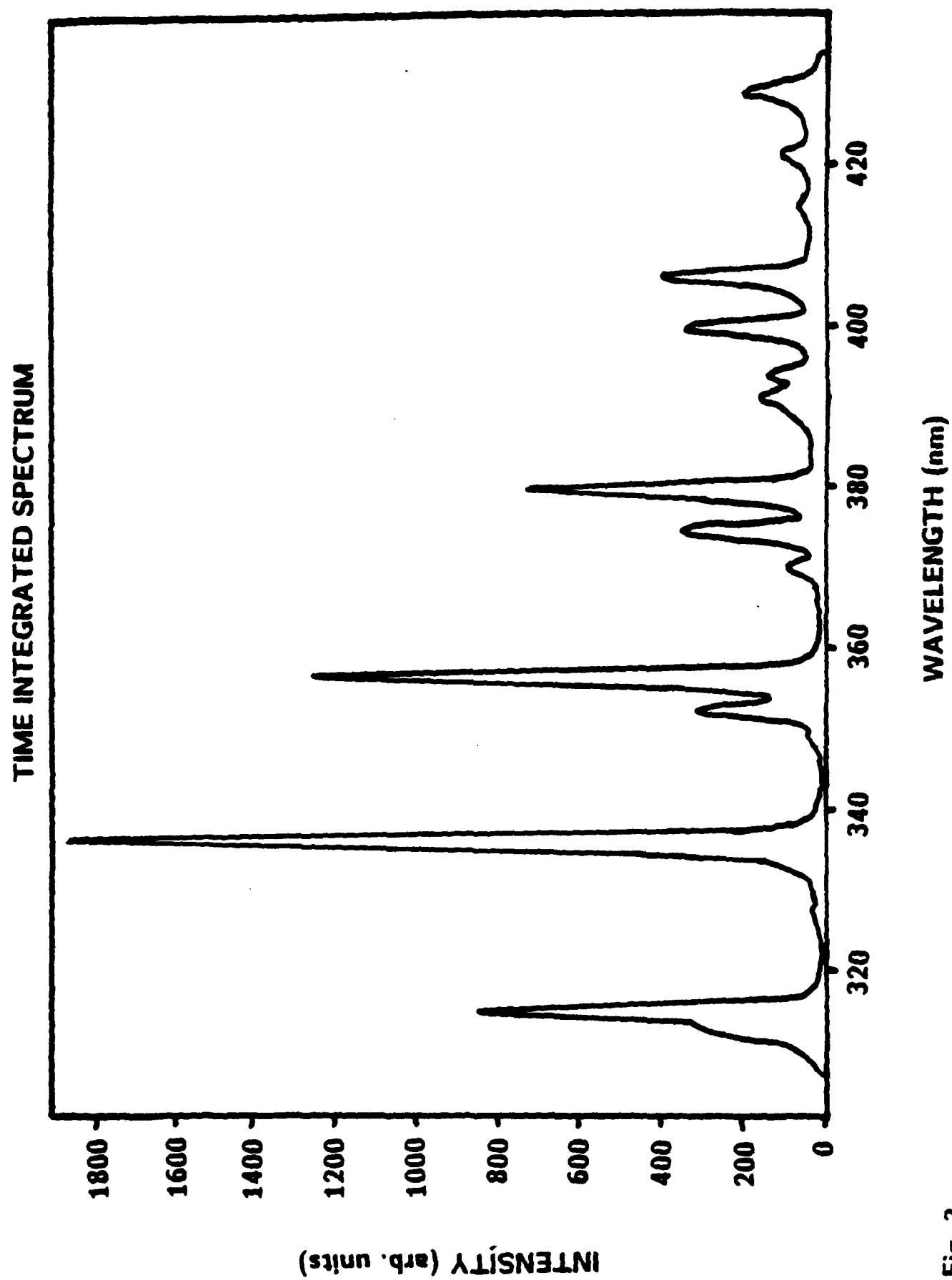


Fig. 3

160
TIME-RESOLVED SPECTRA

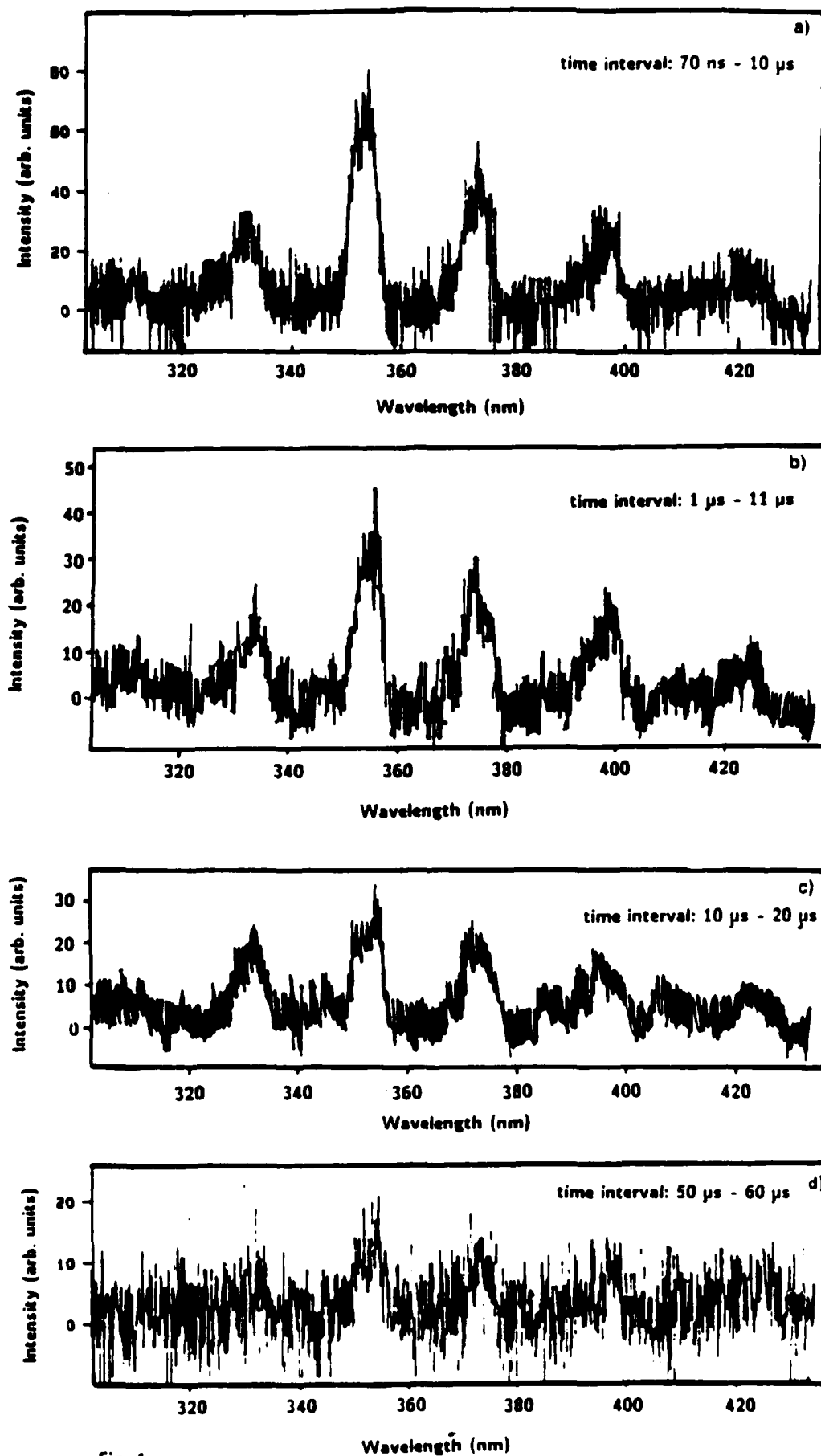


Fig. 4

SIGNAL AVERAGED PHOTON BURSTS

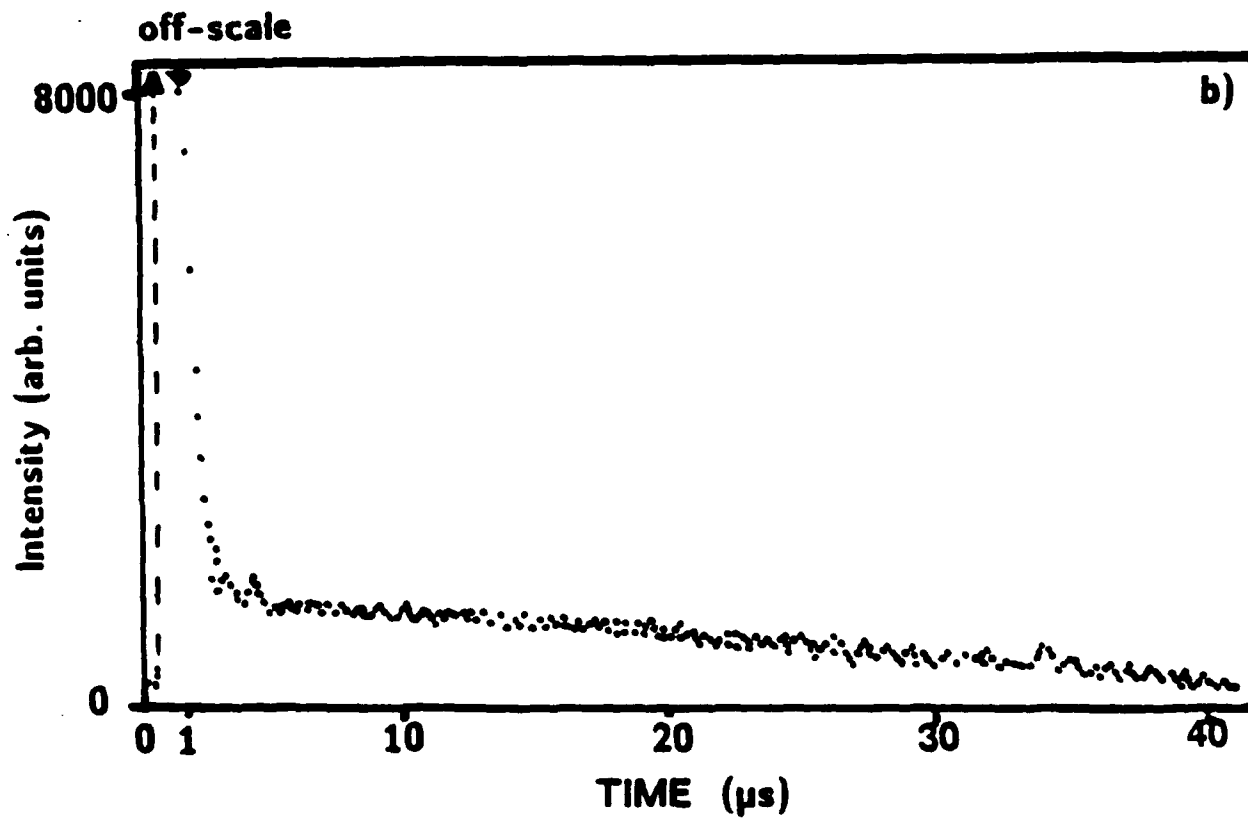
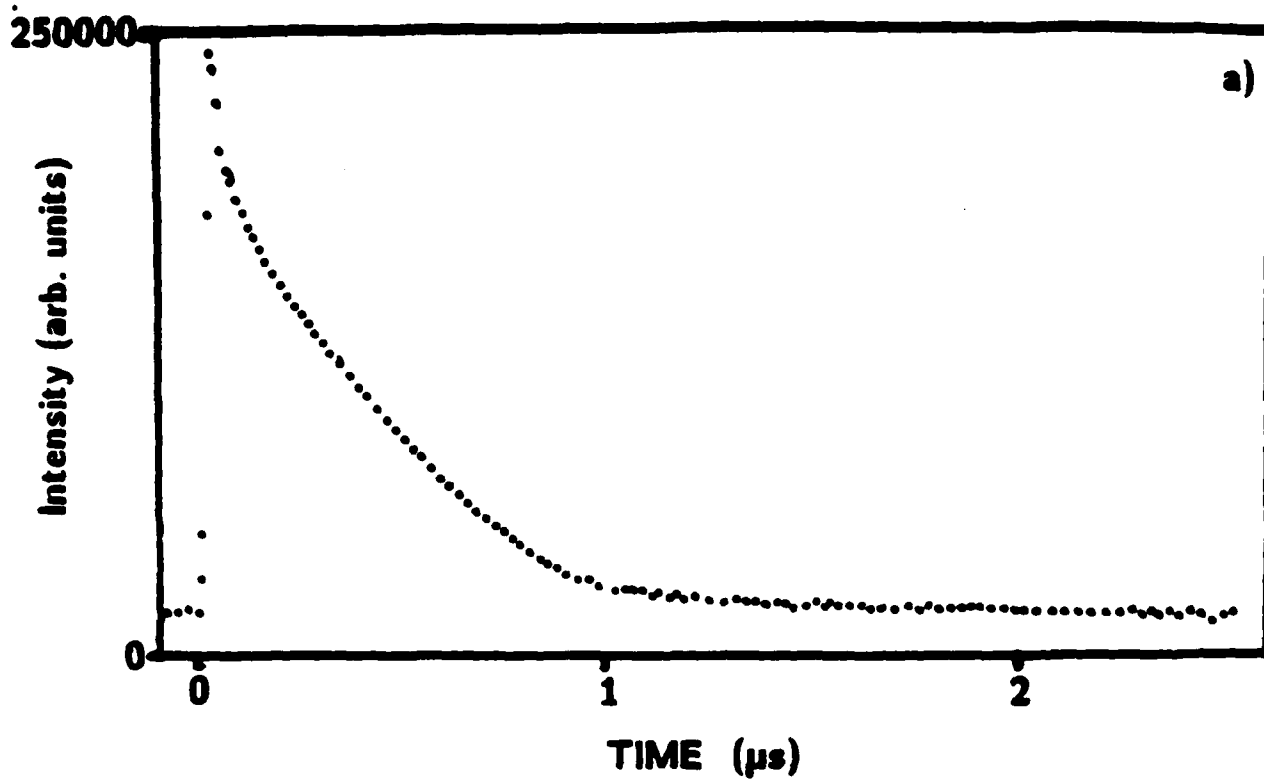


Fig. 5

MULTIPLE PHOTON BURSTS

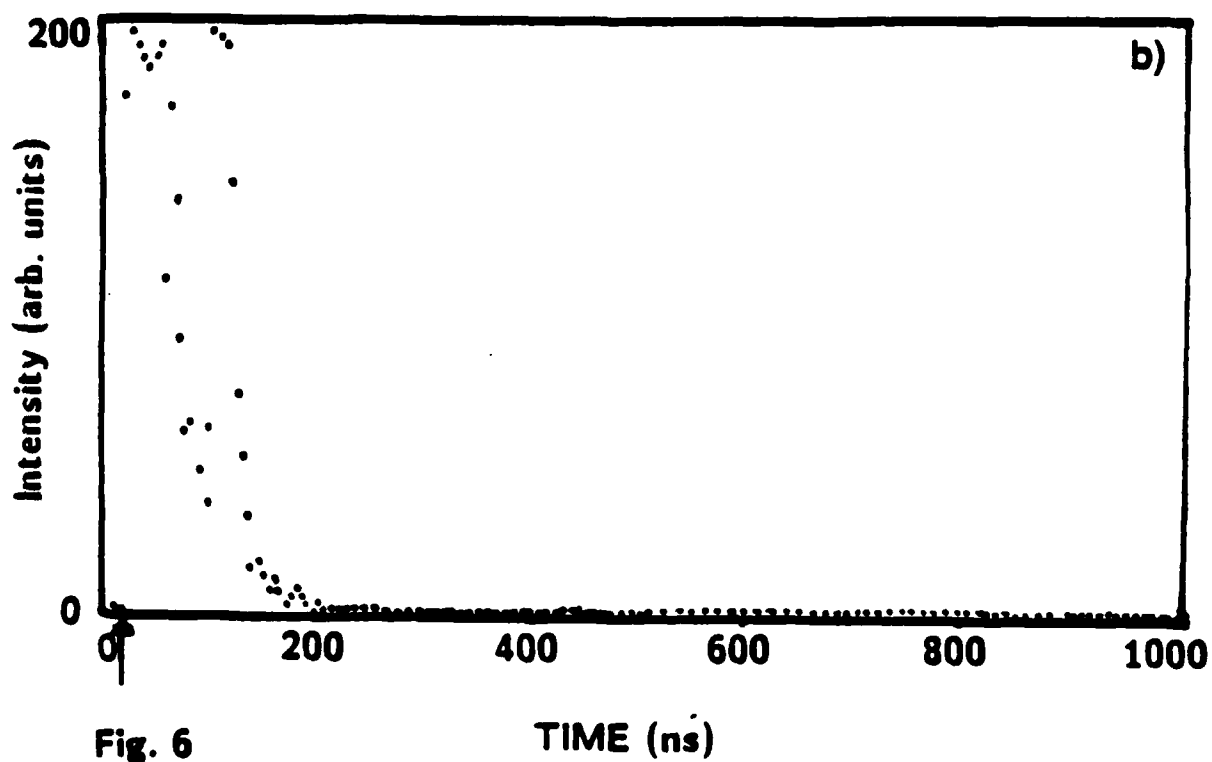
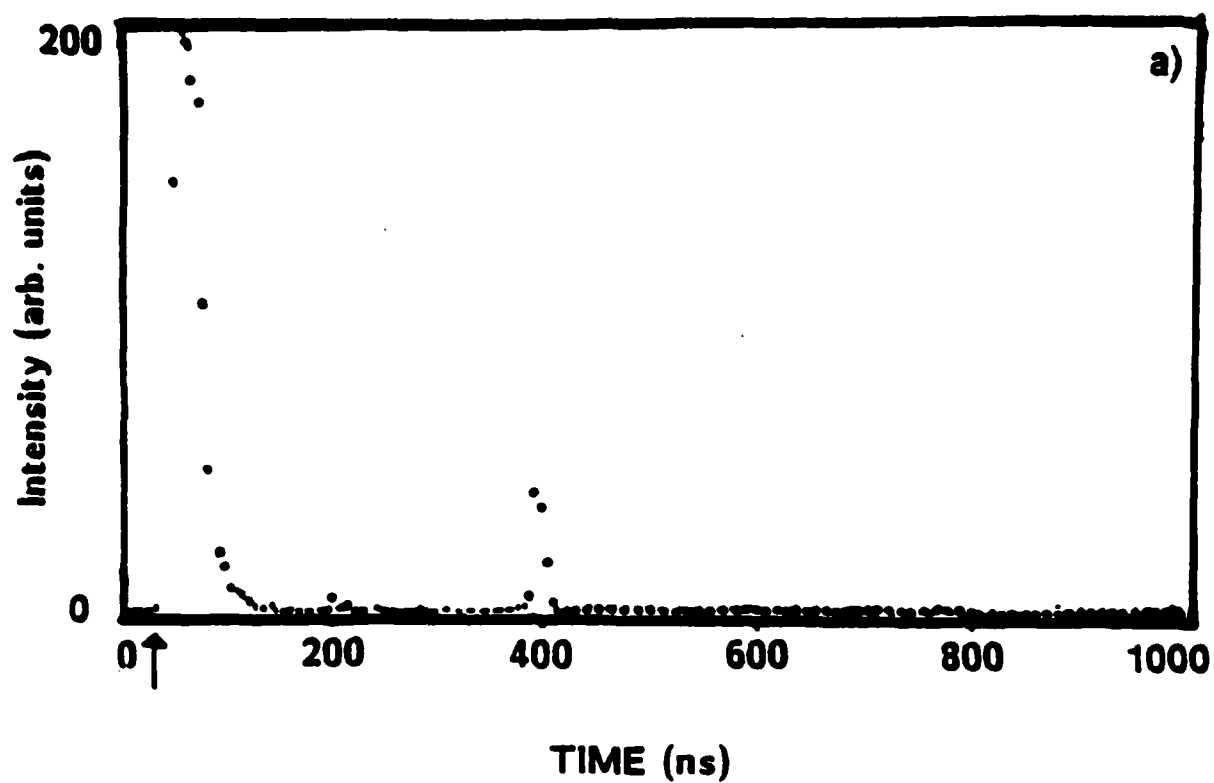


Fig. 6

TIME INTEGRATED SPECTRUM OF LIGHT EMITTED
BY SURFACE 1 CM FROM PEEL ZONE

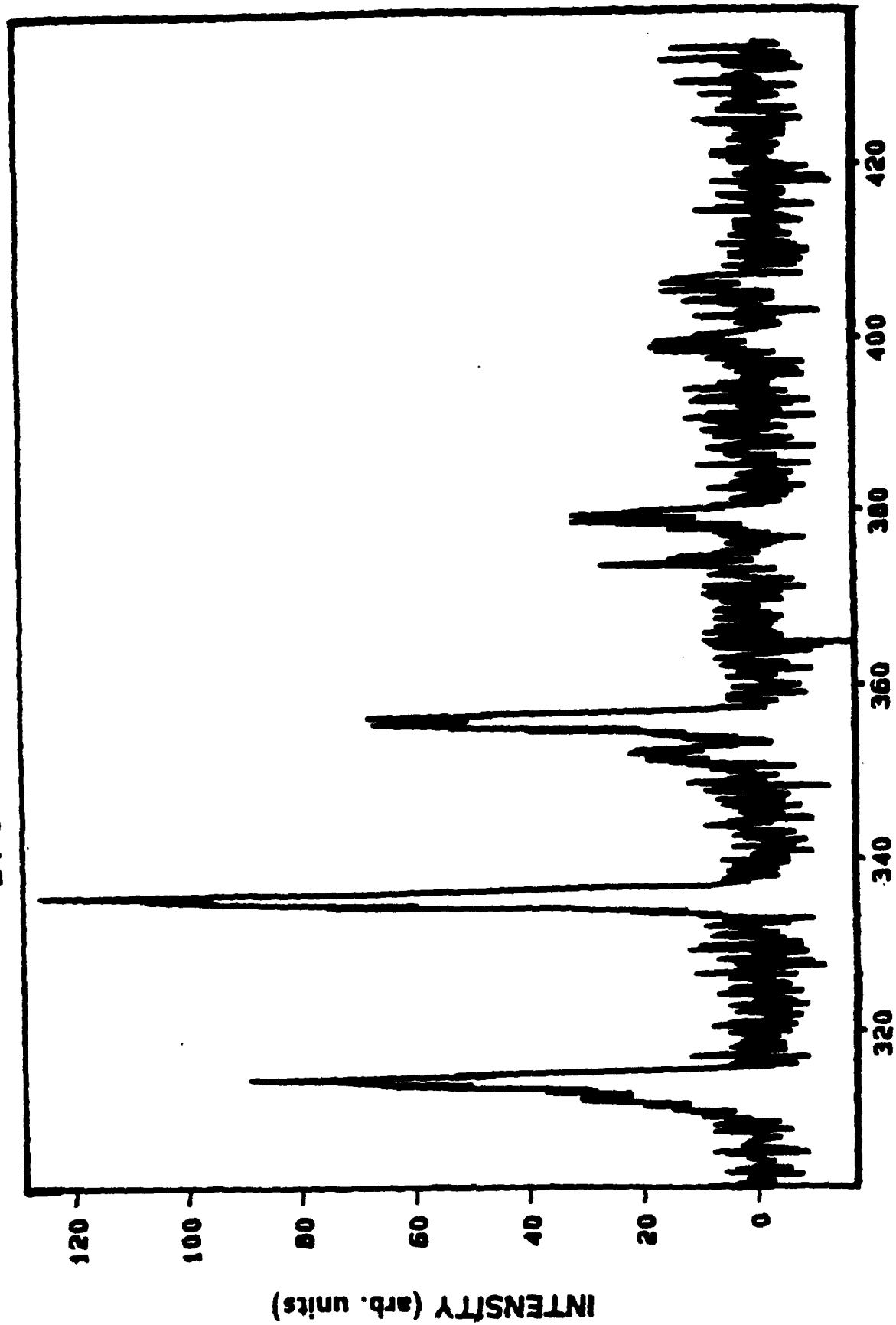


Fig. 7

WAVELENGTH (nm)

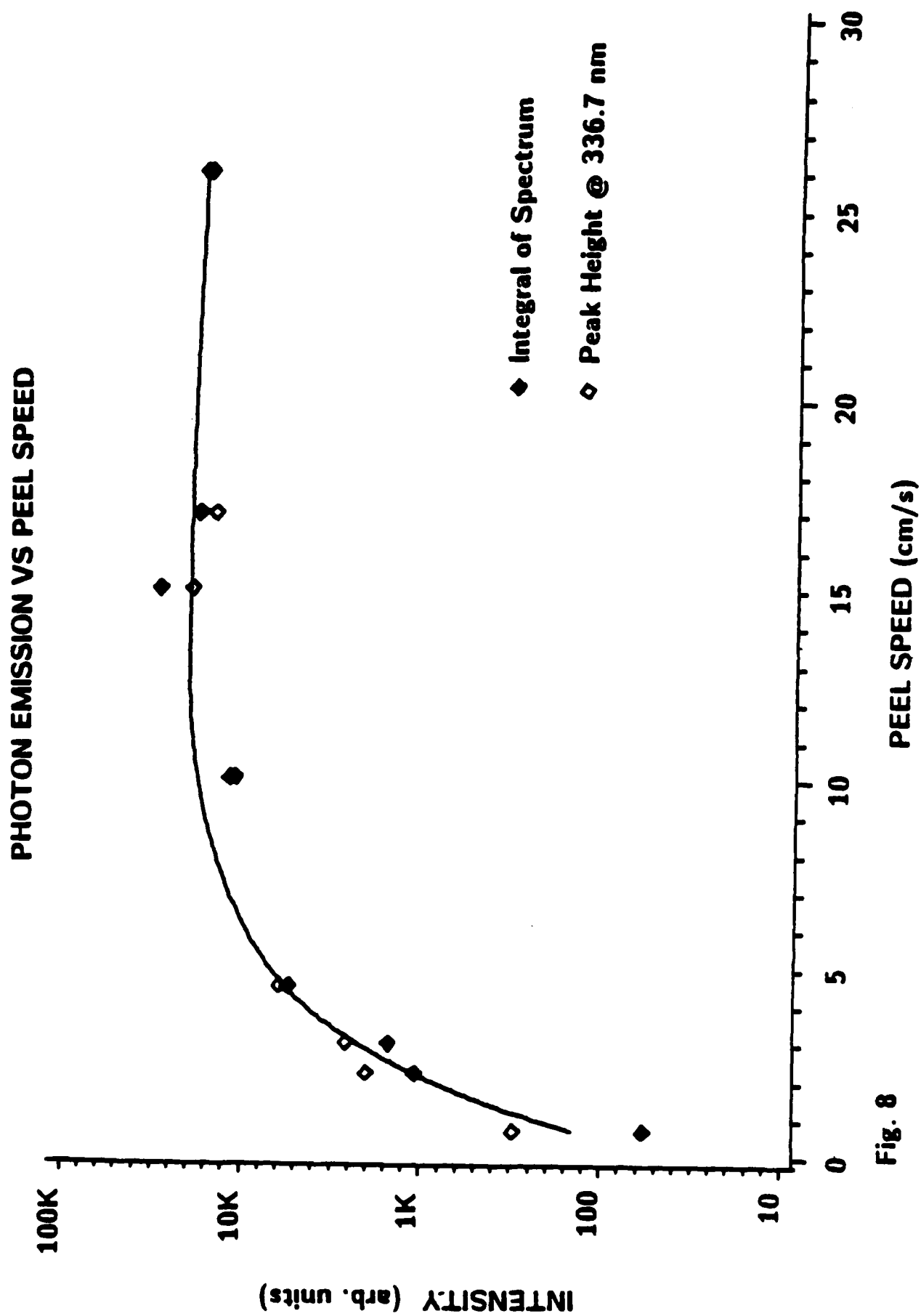


Fig. 8

X. Autographs from Peeling Fiber Reinforced Pressure Sensitive Adhesives: Correlation with Failure Mechanisms

E. E. DONALDSON and J. T. DICKINSON

Department of Physics, Washington State University, Pullman, WA 99164-2814, U.S.A.

In past studies, we have investigated the nature of the photon emission accompanying the peeling of pressure sensitive adhesive tapes. These studies included producing clear images of the emitted light created by direct attachment/detachment of the adhesive from photographic film (i.e., autographs). Here we present an extension of this work to very slow peeling rates (< 0.05 mm/s) in which we examine how the resulting autographs from fiber reinforced tape are influenced by the micro-mechanical behavior of this composite tape during high angle peeling.

KEY WORDS Pressure sensitive adhesives; fiber reinforced tape; peel test; triboluminescence; fracto-emission; photon imaging; autograph.

I INTRODUCTION

When two dissimilar materials are separated, the newly created surfaces are usually electrostatically charged. With the use of suitable probes and an electrometer, we have found that such surfaces carry net charges as well as alternating patches of both positive and negative electrostatic charge. During a fracture or peel process, oppositely charged surfaces form in close proximity, resulting in microdischarges between these surfaces. In some cases, we also find convincing evidence for discharges along the newly created surfaces. These small discharges cause the emission of photons (phE), and radiowaves (RE), as well as a variety of charged and neutral species. [These emissions are generally known as Fracto-Emission (FE)^{1-4,6,7}].

Our past investigations of the emission accompanying the peeling of pressure sensitive adhesive tapes from various substrates have included pulse counting experiments in which the phE, electron, and/or the RE bursts were detected and their size and time correlations determined,^{1,2} time resolved spectroscopic analysis of the phE³, and direct imaging of the phE by production of autographs on Polaroid films⁴.

These experiments verified that the phE arose predominantly from highly localized microdischarges and when peeling took place in air, consisted of discrete molecular nitrogen lines in the blue portion of the spectrum. This N_2 radiation was observed to originate both from the vicinity of the peel and also from the surface of the tape at several mm distances from the peel line,³ indicating that both discharges across separating surfaces in the peel zone and discharges along the surfaces resulted in gas phase excitation. In addition, it was shown that the emission

rate and spatial distributions depended strongly on the conditions of peeling: namely, the substrate, the peel geometry, the peeling rate, and the gas environment.

In this paper, we focus our attention on the peeling of 3M Filament Tape in a sharp angle peel using the autograph technique.⁴ This material exhibited a wide range of instantaneous peel rates (slow-fast peel behavior) due to the mechanical properties of this composite system in a high angle peel. Furthermore, we wish to illustrate that for this type of system, the autograph technique provides images at very low peel rates (~ 0.0016 mm/s), and that the observed images are intimately related to the micro-mechanical events accompanying slow, high angle peel.

II EXPERIMENTAL METHODS

We used 3M No. 893 Filament Tape in this study. This product has an adhesive of natural rubber combined with varying amounts of a tackifying agent which is a terpene based hydrocarbon resin. More tackifier is used on the face of the adhesive and less in the saturating layer binding the glass filaments to the backing. The back of the polyester tape carrier has been treated with a release coating having a critical surface tension for wetting of approximately 21 dynes/cm [mN/m]. The tape is 2 cm wide.

Peels from the photographic film were performed at either constant applied force or constant strain rate at a peel angle of 150° (dictated by constraints of the film holder). Constant force was supplied by hanging masses between 150-250 grams (a force of 1.5-2.5 N) on the tape's end, shown schematically in Fig. 1. For the extremely slow peel rates studied here, small fluctuations in the acceleration of the mass can be neglected. Constant strain rate loading down to 0.0016 mm/s was provided by a motor-driven mechanism. In all cases, only average peel rates were measured. A force transducer was used to measure the instantaneous peel force under condition of constant strain rate. [Note in Fig. 1 the definitions of "longitudinal and transverse directions."]

Autographs⁴ were recorded in the dark by peeling filament tape directly from Polaroid Type 107C film (ISO3000). The Polaroid film was developed and printed in a Polaroid camera back in the usual manner. Examination of the substrates and of the tape showed no evidence of cohesive failure.

To observe visually the slow-rate peeling process, we replaced the film with a PMMA substrate and used a stereoscopic microscope at magnifications in the range of 15 to 120X. With a transparent substrate the peeling could be viewed either through the substrate or from the edge of the tape (on an axis parallel to the peel line).

III RESULTS AND DISCUSSION

Peeling the tape from the surface of Polaroid Type 107C film at low rates produced autographs of the accompanying photon emission. Fig. 2 shows an autograph of the light emission as the tape is peeled in a slow then fast sequence where slow peel was at 0.04 mm/s and the fast peel was at ~ 5 mm/s. The patterns of light intensity show periodic variations in both longitudinal (along the length of the tape and fiber direction) and transverse (normal to the fiber direction and parallel to the peel line—across the width of the tape) directions. In the rapid peel region, we see patterns similar to those reported previously,⁴ namely bright spots due to localized, strong discharges with high correlation in position with the position of the fibers.

An enlargement of Fig. 2 is shown in Fig. 3 where the slow peel region is seen to exhibit many smaller localized discharges. The longitudinal variations in this pattern have an average "wavelength" of 3.8 mm and the transverse variations have spacings the same as distance between fiber bundles (0.54 mm). Following the very dark bands, the longitudinal bands arise showing a sharp increase in emission intensity at their leading edge (at A in Fig. 3) followed by a decay in both the intensity and in the average radii of the spots. Those features near the leading edge of the high emission band have a diffuse character, while those in the lower emission region (e.g., B in Fig. 3) are sharper and smaller in size. Subsequently (at C in Fig. 3) the phE nearly disappears from the autographs. Obviously, the mechanics of this particular sample and peel geometry are strongly influencing the spatial (and time) dependence of the phE.

The tape exhibits transverse creases after peeling at a peel angle of 150° - 180° from almost any surface, including the film. This pattern of creases resembles the transverse patterns of light in the autographs. Fig. 4 is a comparison of an autograph with the corresponding piece of tape after peeling at an average peel rate of 0.008 mm/s. The tape backing was illuminated with a beam of light at a low angle; both tape and autograph are shown

at the same magnification. As seen in Fig. 4, the creases display a pattern much like the transverse lines of strong emission and the longitudinal lines in the autograph correspond to the spacings of the fiberglass bundles.

To further investigate the mechanical behavior of this system, we peeled Filament Tape at constant strain rate from a rigid glass or PMMA substrates at a peel angle of nearly 180° simultaneously measuring the force and carefully observing the peel zone. The two kinds of experimental conditions namely peeling tape from flexible photographic film and peeling it from rigid, smooth glass or PMMA surfaces might be thought to be incomparable. However, we observed visually that the sequence of mechanical events observed during the peeling from the photographic film (observed in light) occurred in a similar fashion when tape was peeled from a rigid substrate.

A typical force vs time record is shown in Fig. 5a which shows major maxima of ~ 0.7 N, each followed by a rapid drop to minima of ~ 0.35 N. We observed in each case that the rapid build-up of force occurred during a period when the peel line appeared to have arrested, whereas the sudden drop in force accompanied the relatively sudden detachment of a creased region of tape. It is important to emphasize that these oscillating forces observed at these low peel rates are unrelated to the more customary stick-slip effects seen at much higher peel rates.

During this particular peel we marked the position of the peel zone on the edge of the tape each time that the peel force exhibited a sudden decrease. These marks allowed us to examine the correlation between the peel force variations and the resulting topography of the tape when photographed under low angle illumination (see Fig. 5b). Corresponding features A-K are identified in Fig. 5a and 5b. At position A the experiment was started where the force initially reached a plateau value corresponding to steady, slow peeling. After a slowly accelerating increase, the force reached a maximum then displayed a sharp decrease at B. The mark on the tape corresponding to this instant (B in Fig. 5b) aligned with the creased region of the tape which had detached from the substrate fairly quickly. As the peel continued, the force again increased, followed by a pair of sharp declines at C and D. In Fig. 5b, the corresponding creases were not formed transversely across the tape but in a diagonal manner; crease C had not completely detached before crease D began, thus causing the force to show a double maximum.

At point E the force again reached a maximum before a sharp drop which accompanied by fast peel and a crease at E in Fig. 5b. As the force rises toward G it goes through a small minimum at F. When we examine the tape in Fig. 5b we find a partial crease at F. The subsequent sharp force decreases, H-K, are typical of the majority

of other cycles we measured, namely they represent individual sudden reductions in the force, each accompanied by a single crease fairly well aligned in the transverse direction. All of these variations in the peeling sequence show up readily in the autographs (Fig. 2-4).

Kaelble has studied the peeling behavior of pressure sensitive adhesives and noted that the visco-elastic properties lead to the development of regions of compressive stress(+) as well as tensile stress (-) near the peel line.⁵ A sketch of the profile of filament reinforced tape during peeling from a rigid substrate is shown in Fig. 6, where the regions of compressive and tensile stress are identified. When the longitudinal edge of the tape is observed during peeling, one sees that the plasticized face adhesive is undergoing longitudinal flow and is squeezed from the region of compressive stress away from the peel line, into a region of tensile stress (-- in Fig. 6), about 1 mm ahead of the peel line. This causes curvature (concave downward in Fig. 6) to develop in both the tape backing and in some of the adjacent fibers as they are pushed away from the substrate. The formation of this bulge is assisted by the longitudinal compressive force on the backing due to the 150° loading. For a short distance (approximately 1 mm), as the peel line continues to advance, this bulge moves as a wave in concert with and ahead of the peel. This leads to the region of the autograph labeled B in Fig. 3, one of fairly uniform, low intensity

In a fairly abrupt fashion, this bulge becomes a permanent crease or fold in the tape backing. In addition, the glass filaments in the strands close to the peel zone are divided such that some of them remain attached to the polyester backing and some remain attached to the substrate. This configuration produces a stiff section in the tape which tends to be peeled as a unit and in essence has a large surface area associated with it. This results in an increased resistance to peeling, thus causing the the radius of curvature, (r in Fig. 6) to decrease. During this time, the crack front advances very slowly towards the creased region, yielding little evidence of photon emission (region C, Fig. 3).

When r reaches a critical minimum value, a number of the fibers fracture in a brittle fashion. On the average, we measure an r_{\min} of $\sim 30 \mu\text{m}$. Accompanying fiber fracture is a sudden change in the forces applied to the creased region of the tape causing it to pull from the substrate fairly quickly, usually propagating transversely from one fiber bundle to the next. This creates the brighter edge of the autograph pattern (region A in Fig. 3). After this stiff, folded section has peeled from the substrate, the cycle begins again and repeats every 3 to 6 mm along the length of the tape, where the largest spacing occurs at lowest peel rates.

After the peel is completed we can measure that the tape is slightly shortened (0.3%) due to the creasing process. Microscopic examination of the tape shows that approximately 20% of the fibers are broken at the leading edge of the crease, precisely where the bend became sharpest. As a further demonstration of this failure mechanism, using a roll of Filament Tape we deliberately delaminated the backing from a single bundle of fibers so that the fibers remained adhering to the release coated polyester. When this single bundle of fibers was peeled from the polyester in a 150° peel, we observed the same slow-fast peel previously described, with oscillations in the radius of curvature (which are even more extreme than seen in the tape). Similarly, when the single bundle is examined after peeling, extensive fiber breakage is observed at fairly uniform intervals of length (approx. 0.8 mm), roughly 1/3 the interval for the tape.

The origin of the highly localized features on the autographs in the region labeled B, Fig. 3 can be understood in terms of the normal behavior of a viscoelastic adhesive during peeling. Microscopic examination of the tape prior to attachment to the substrate shows that the adhesive face is not planar but follows the contour of the fiber bundles. When the tape is pressed onto any substrate the closest contact is made at these ridges whereas longitudinal bubbles lie in between the ridges and prevent good contact with the substrate. When the tape is subsequently peeled these "lines" of better contact and therefore form a locus of interfacial failure which in turn produces aligned spots on the autographs. In contrast, the valleys represent regions of very poor contact, thus

For moderately slow peeling the autographs, such as Fig. 3, allow us to identify approximately 2 to 4 discharges/mm² of tape area peeled in air. This is similar to the areal density of discharges which we counted previously arising from the T peel configuration for slow peeling² of this tape in a nitrogen atmosphere

It is interesting to compare the interval in which the peeling produces little or no light (e.g., region C, Fig. 3) for the cases of constant applied force vs constant strain rate. This region is noticeably wider and darker for constant force than for constant strain rate conditions, reflecting the differences in the mechanical response of the system to these different types of loading.

We should also note that at constant applied force we recorded emission at an average peel rate of 0.003 mm/s. At a peel rate of 0.0015 mm/s, the resulting autograph shown in Fig. 7 appears to be blank. On the original photo, one can see ~20 small discharges. This is consistent with other studies we have carried out

involving variations in fracto-emission intensities with crack speed^{3,6,7} which we have attributed to the charge separation process and leakage of charge occurring in the crack tip region.

Previously,² we learned that the number of photons (as well as the size of the accompanying RE bursts) associated with the microdischarges increases on exposure to N_2 . We suspected that this enhancement would make the autographs more intense and enhance the images at low peel rates. Conversely, we also had discovered that the number of photons created at a microdischarge were quenched in O_2 . The gas phase phenomena which explain these results are discussed in reference 2. In Figures 8a and 8b we compare the autographs of Filament Tape peeled from film at an average peel rate of 0.033 mm/s in air and when N_2 and O_2 were introduced at one atmosphere; we note the obvious enhancement of light by the N_2 and strong suppression of emission by O_2 . Obviously, if one desires to detect extremely slow peel, one could easily introduce N_2 to take advantage of the enhancement.

IV SUMMARY AND CONCLUSION

In summary, we have shown that:

1. pH_E caused by tape peeling of Filament Tape produced autographs which could be observed at average peel rates approaching 0.0016 mm/s.
2. The bright transverse bands of emission appearing in autographs are the result of periodic events involving viscous flow of adhesive, fiber fracture, and rapid detachment of adhesive from the substrate.
3. At peel rates averaging less than 0.001 mm/s. the intermittent nature of the peeling assures that there are periods when the interfacial failure is extremely slow and the corresponding light emission is nearly
4. Peeling in the presence of gases other than air has a striking effect on the autographs. Nitrogen supports electrical discharges and causes enhanced light emission. Oxygen quenches discharges and suppresses light emission. These dramatically effect the intensity of the light recorded in autographs, which could be useful for studying very slow failure.

This work illustrates that autographs provide details of the detachment process of a composite tape from a smooth substrate during high angle peeling. In this type of loading, the fiber reinforced tape undergoes a sequence of micro-mechanical steps which strongly influence the instantaneous rate of detachment, which in turn leaves a unique record on the exposed film. The occurrence of this type of failure at such slow peel rates appears to be quite distinct from the usual stick-slip failure seen at very high peel rates. We propose that these and other fracto-emission studies can aid our understanding of the various failure modes in a composite system including filament reinforced tape and therefore assist in improvements in tape design.

Acknowledgments

This work was supported by the Office of Naval Research, N00014-87-K-0514, McDonnell Douglas Independent Research Fund, and the Washington Technology Center.

REFERENCES

1. J. T. Dickinson, M. K. Park, E. E. Donaldson, L. C. Jensen, *J. Vac. Sci. Technol.* **20**, 436 (1982).
2. E. E. Donaldson, J. T. Dickinson, and X. A. Shen. *J. Adhesion* **19**, 267 (1986).
3. Ma Zhenyi, Fan Jiawen, and J. T. Dickinson, *J. Adhesion* **25**, 63 (1988).
4. J. T. Dickinson and E. E. Donaldson. *J. Adhesion* **24**, 199 (1987).
5. 90° peel: D. H. Kaelble, *Trans. Soc. Rheol.* **9**, 2 (1965).
180° peel: D. H. Kaelble and R. S. Reylek, *J. Adhesion* **1**, 124 (1969).
6. J. T. Dickinson and L. C. Jensen, *J. Polymer Sci., Polymer Phys. Ed.* **20**, 1925 (1982).
7. J. T. Dickinson, "Fracto-Emission Accompanying Adhesive Failure," in *Adhesive Chemistry--Developments and Trends*, ed. by L. H. Lee (Plenum Publishers, New York), 1984, pp. 193-243.
8. D. Satas, "Peel", in *Handbook of Pressure-Sensitive Adhesive Technology*, ed. by D. Satas (Van Nostrand Reinhold Co., New York), 1982, pp. 50-77.

FIGURE CAPTIONS

- Fig. 1 Schematic diagram of the experimental arrangement for peeling tape from a substrate under constant applied force conditions.
- Fig. 2 Autograph of slow then fast peel of filament tape from Polaroid Type 107C film. Tape is 2 cm wide. Slow peel at 0.05 mm/s.
- Fig. 3 Enlargement of Fig. 2.

- Fig. 4 Autograph of a slow peel experiment and photograph of creases in the backing of the corresponding piece of tape. Slow peel at 0.008 mm/s
- Fig. 5 a) Force vs time during intermediate rate peeling of filament tape from PMMA (2 cm tape width).
b) Photograph of creases in backing of corresponding piece of tape.
- Fig. 6 Drawing of filament tape profile during peeling from a rigid substrate.
- Fig. 7 Autograph of slow then fast peel of filament tape from Polaroid Type 107C film. Slow peel was at 0.0015 mm/s.
- Fig. 8 Autographs of slow peel (0.033 mm/s.) in air then a) in N₂ or b) in O₂ at one atmosphere, followed by fast peel in air.

Schematic of Experimental Arrangement

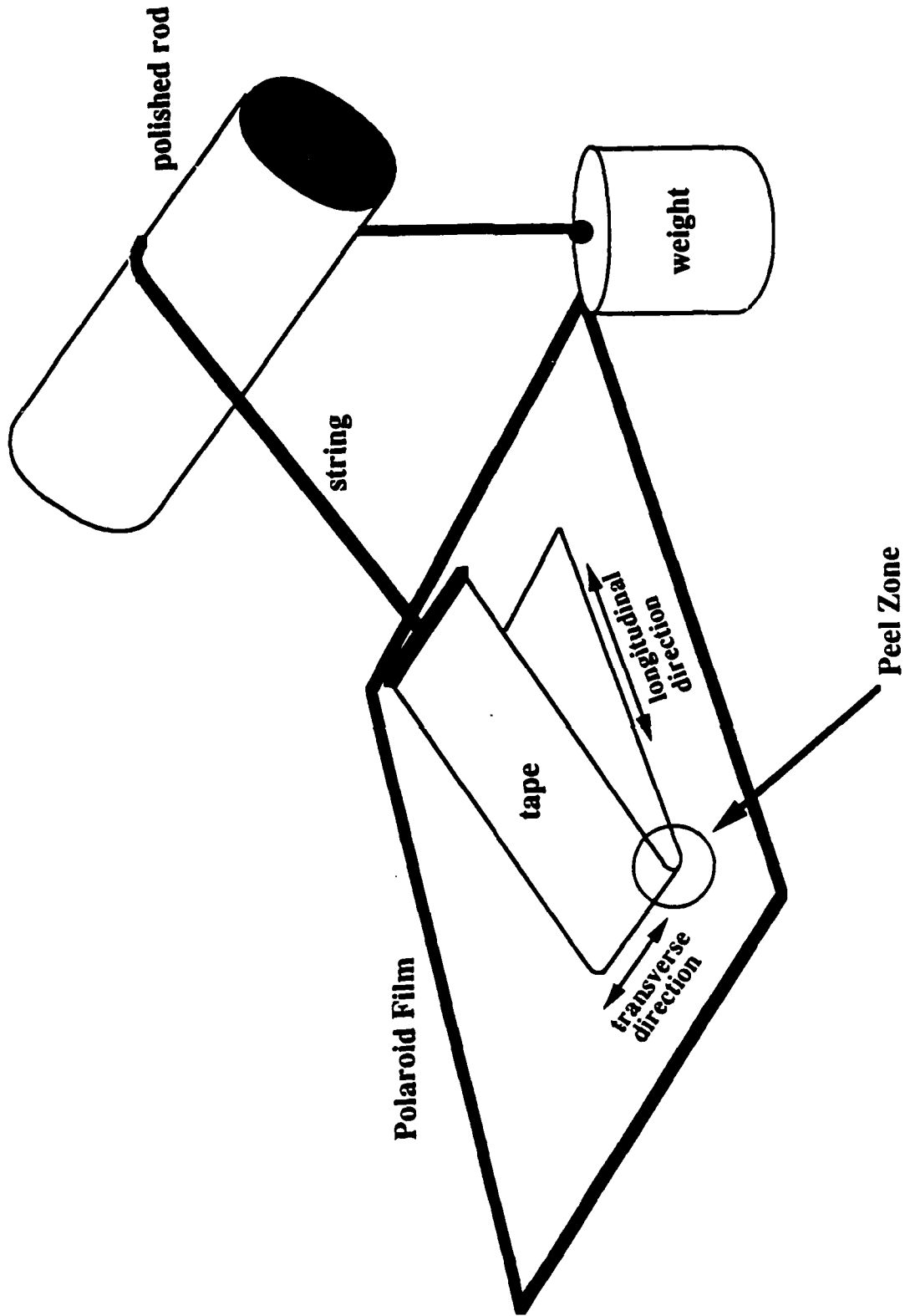
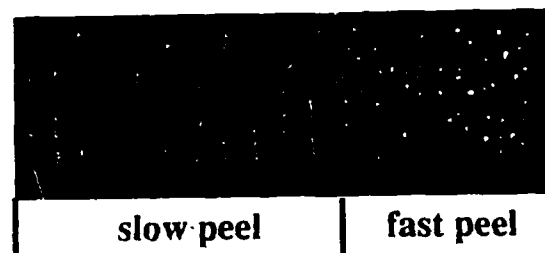


Fig. 1

Autograph



Direction of Peel

Fig. 2

176

Peel Direction



A B C

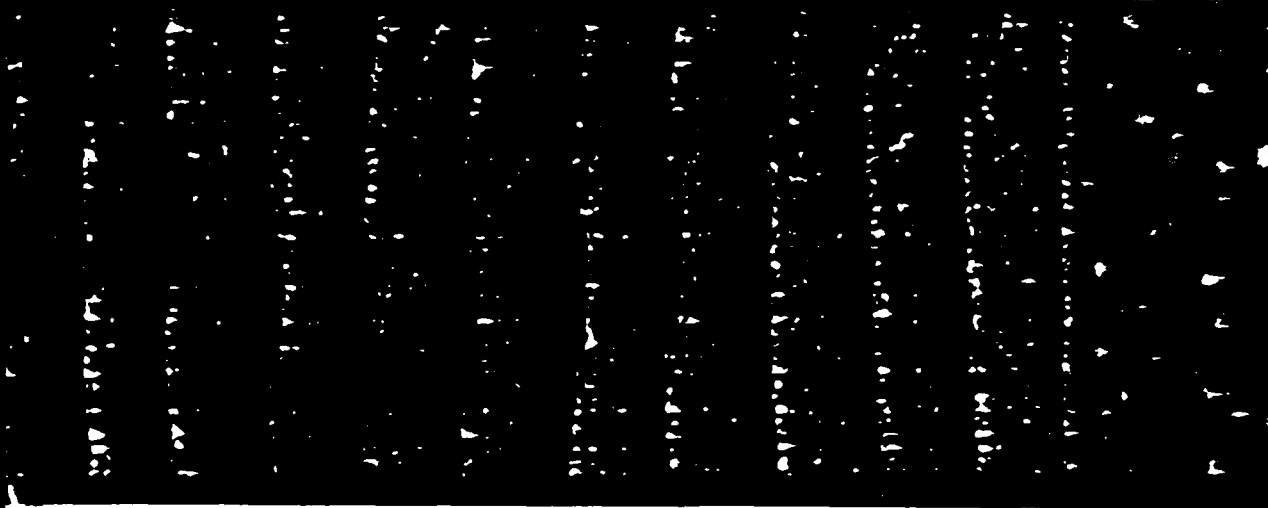
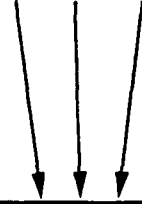


Fig. 3

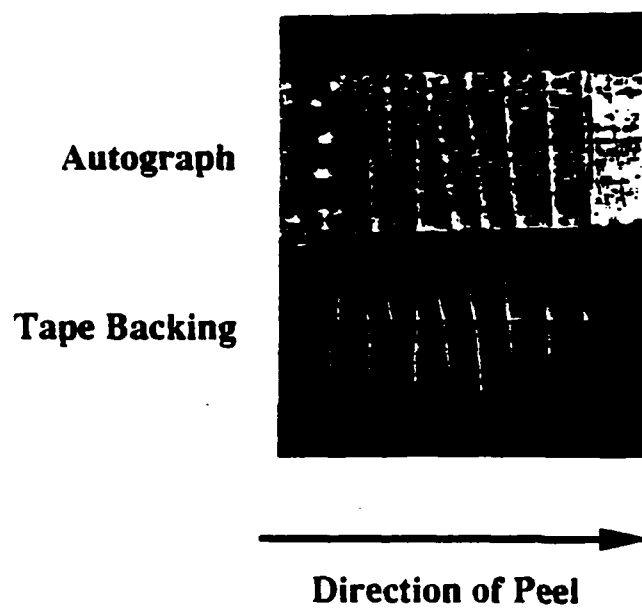


Fig. 4

**Force vs Time During 180° Peel of 3M Filament Tape
Average Peel Rate: 0.07 mm/s**

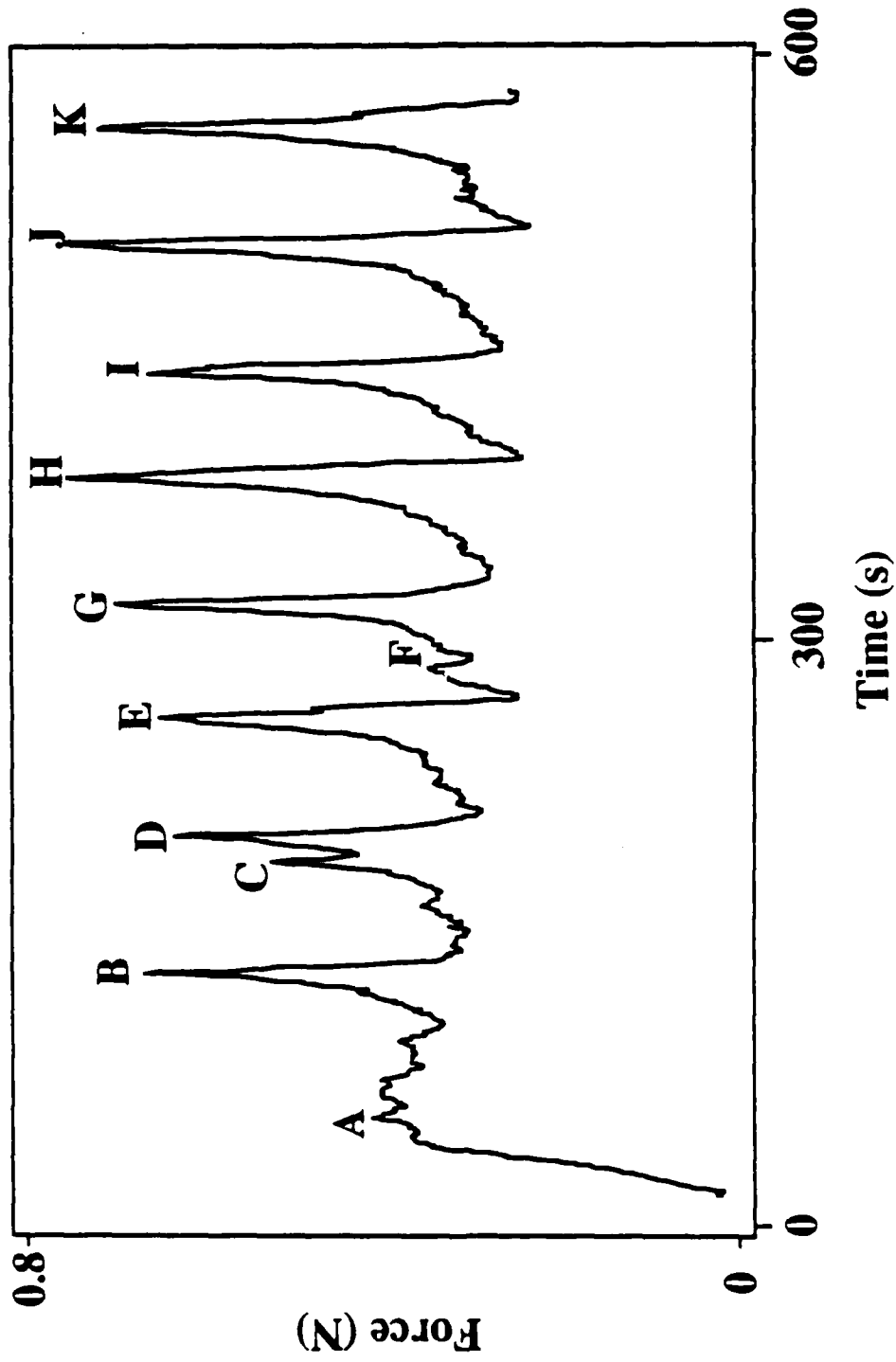


Fig. 5a

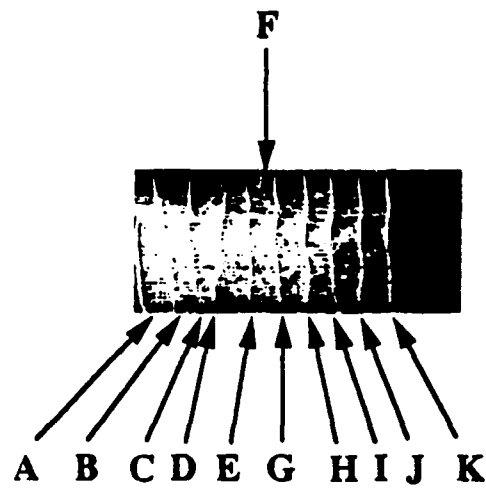


Fig. 5b

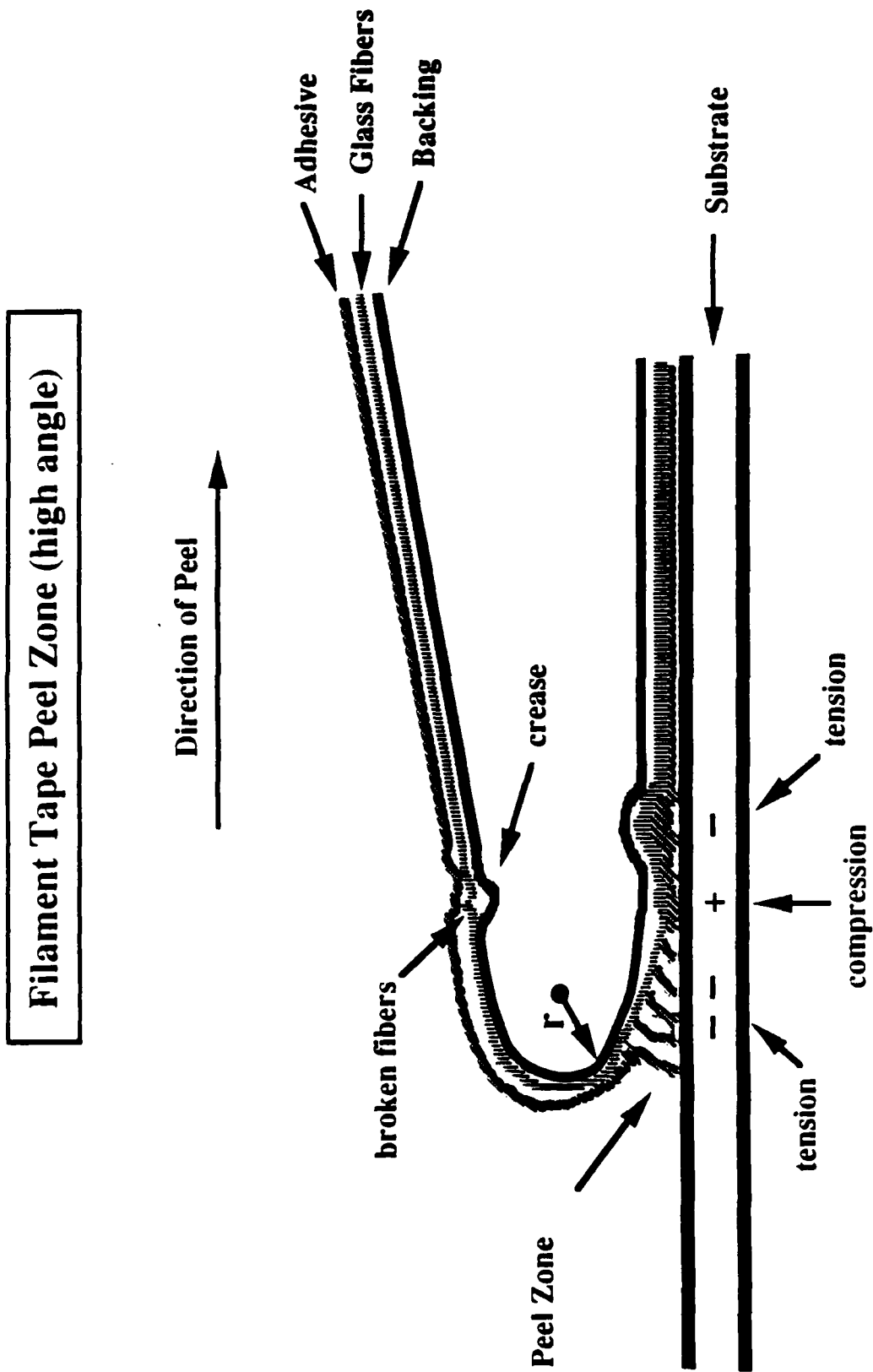


Fig. 6

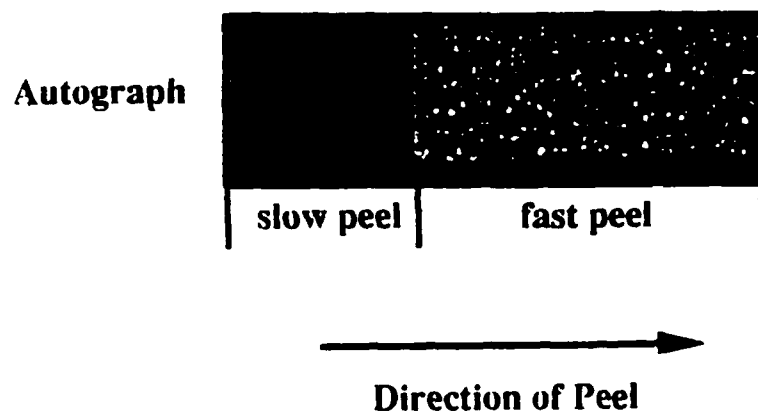


Fig. 7

Autograph

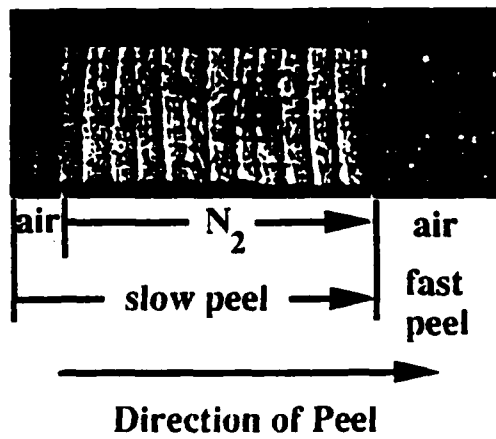


Fig. 8a

Autograph

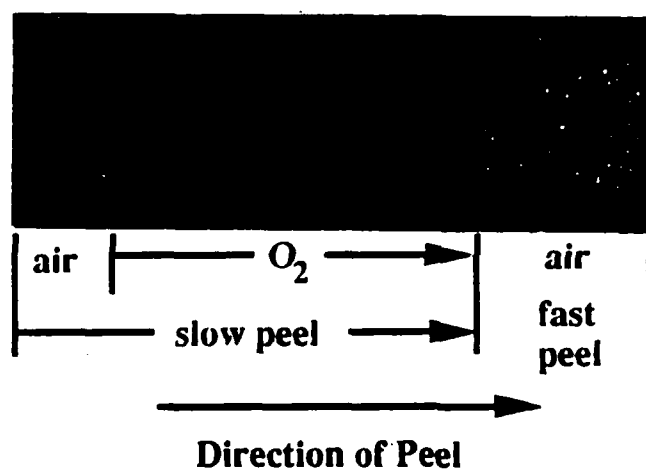


Fig. 8b

XI. The role of damage in post-emission of electrons from cleavage surfaces of single crystal LiF

J. P. Mathison, S. C. Langford, and J. T. Dickinson

Department of Physics, Washington State University, Pullman, WA 99164-2814

ABSTRACT

It has been previously reported that the cleavage of single crystal LiF produces intense, long lasting electron emission persisting several minutes after fracture (called post-emission). We find that this contrasts dramatically with the weak, rapidly decaying emission accompanying LiF fracture in 3-point bend or tension. We examine the dependence of intensity and duration of the electron emission produced by LiF cleavage on the interaction of the cleavage blade with the LiF crystal. We show that the damaged region where the cleavage blade and crystal come into contact is by far the major source of the post emission. Macroscopic particles ("ejecta") from the damaged region which frequently cling to the fracture surface are also shown to be highly emissive. In contrast, the "untouched" cleavage surface emits little, if any, post-emission (on the time scale of several seconds). We propose that the high intensity emission originates from defects created during the production of higher index plane fracture surfaces.

I INTRODUCTION

The emission of particles and electromagnetic radiation accompanying deformation and fracture is of long standing interest to those who study the atomistics of material failure.¹⁻⁶ Collectively we refer to these emissions as *fracto-emission*. Of particular historical and scientific interest have been studies of *fracto-emission* from alkali halides, which have a simple crystalline structure and are available in high purities. Of these, LiF is most amenable to study, due to its chemical stability with respect to water and its relative brittleness even in high purity forms. Several authors have reported intense, prolonged emission of electrons accompanying the cleavage of LiF, persisting as long as 10 minutes after fracture, and have offered various explanations of the effect.²⁻⁴

Wollbrandt and coworkers studied this post-emission as a function of sample temperature.^{2,3} They attributed the prolonged emission to field assisted EE from defect centers at or near the crystal surface. The decay kinetics were observed to be second order over a wide range of temperatures (80-300 K), suggesting that the decay kinetics are controlled by a recombination process involving tunneling. More recently, Lipson et al. have studied the prolonged electron emission (EE) and positive ion emission (PIE) accompanying the cleavage of LiF, concluding that charge carried to the surface by moving dislocations was responsible for the EE.⁴ The rate controlling process was believed to be the unpinning of dislocations as charged defects (vacancies) initially associated with the dislocations diffuse to the surface. Our interest in this phenomenon was stimulated by our observation that this prolonged emission after fracture of LiF in tension and 3-point bend was absent.

II EXPERIMENT

Nominally pure, single crystal LiF obtained from Optovac was cut into samples with a diamond saw, polished with 3 μm diamond paste, and ultrasonically cleaned in acetone. Samples to be cleaved or fractured in 3-point bend measured $2 \times 6.5 \times 13 \text{ mm}^3$, while samples to be fractured in tension measured $2 \times 3 \times 18 \text{ mm}^3$. These samples were not annealed prior to fracture, in contrast to those studied by Lipson and coworkers.⁴ The samples were mounted and fractured at room temperature in a vacuum system maintained at pressures of $\sim 10^{-5}$ Pa.

Experimental details are similar to those describe elsewhere.⁶ EE (and PIE) from LiF fractured in 3-point bend were detected with a Galileo Electro-Optics Model 4039 Channeltron electron multiplier (CEM) positioned

approximately 2 cm from the freshly formed surface. Unnotched tensile specimens were made by epoxying Al clamps to the ends of LiF crystals. Tensile loads resulted in linear stress/strain curves and led to cleavage-like fracture initiating at edge flaws. Cleavage experiments were also carried out on unnotched samples. In order to determine the effect of the cleavage blade/sample interaction on the resulting EE, we varied the blade wedge angle and impact velocity. The maximum penetration of the blade into the sample was determined by an adjustable stop positioned on the rod used to advance the blade. Measurements were also made of EE from LiF surfaces abraded with a variety of metal and diamond points to investigate the possible role of abrasion. The output of the CEM was pulse counted with a multichannel analyzer. The counting interval was either 1 or 100 ms/channel.

As certain surface features appeared to be correlated with prolonged EE, a device was built to scan the cleaved surfaces with a CEM. The sample to be cleaved was mounted on a platform which could be moved past the CEM, a Galileo Electro-Optics Model 4020. A grounded metal shield with a 0.5 mm diameter aperture was fixed in front of the entrance to the CEM so that the sample surface passed 1 mm from the shield on the side opposite the CEM. Thus the CEM detected EE from a limited area of the sample surface. After cleavage, the platform was used to move the sample back and forth past the shield aperture at rates of 50-150 $\mu\text{m/s}$ with a variable speed motor. The location of the sample at any given time was determined from the starting position and scan rate. The scanning experiment thus involved cleaving the sample, positioning the cleavage surface in front of the shield aperture, and then translating it back and forth past the aperture. We estimate the resolution of the scanning system to be $\sim \pm 1$ mm.

III RESULTS

Figure 1(a) shows typical EE data accompanying the fracture of LiF in tension acquired at a rate of 1 ms/channel. A burst of emission essentially one channel in width was observed, followed by a second, smaller peak about 8 ms wide. No measurable emission was observed at later times. Figure 1(b) shows EE on a much slower time scale from fracture of LiF loaded in 3-point bend. The EE decay was essentially complete within one counting interval, 100 ms. Data taken on faster time scales indicated that EE decayed to background levels in 10-20 ms. Photographs of the fracture surfaces showed generally smooth (100) planes marked by occasional river lines.

This contrasts with previous observations of MgO fractured in 3-point bend, in which substantial portions of the fracture surface were not (100) in orientation, but inclined about 16° to the $\langle 100 \rangle$ direction.⁶ phE and EE from MgO fractured in 3-point bend persisted some seconds after fracture, while EE from cleavage had the same dependence on surface damage as that from LiF.

In contrast, cleavage of LiF often resulted in prolonged post-emission, as shown in Fig. 2(a). The duration of this emission was typically about ten minutes, i.e. consistent with that reported by Lipson et al.⁴ and Wollbrandt et al.² The peak intensity and total integrated emission due to cleavage was generally much greater than that due to fracture in tension and 3-point bend. However, as shown in Fig. 2(b), cleavage did not always produce such intense, long lasting post-emission. Since the interaction of the cleavage blade with the sample is unique to the cleavage mode of loading, we examined some of the obvious parameters and determined the following:

- Intense post-emission was associated with low blade velocities (which by necessity, required significant blade penetration).
- Blunt blades were also associated with large post emissions.
- Conversely, weak post-emission was consistently observed from samples cleaved with high blade velocities *and* minimal sample penetration.
- Intense post-emission was always associated with significant blade penetration into the sample.

Examination of the resulting cleavage surfaces showed that particular types of damage in the region where the cleavage blade struck the crystal correlated well with intense post-emission. SEM photos of two fracture surfaces exhibiting intense, prolonged EE are shown in Fig. 3. The surface of Fig. 3(a) shows a damaged region 100-200 μm deep resulting from contact with the cleavage blade. A magnified view of this end of the crystal shows a high density of small, dust-like particles on the surface adjacent to the damaged zone. These particles, known as ejecta,⁷ appear white under the SEM due to high secondary electron escape probabilities for small particles. This surface yielded unusually intense post-emission. Another surface yielding intense post-emission is shown in Fig. 3(b). The cleavage blade shattered a modest portion of the crystal extending about 2.5 mm from the point of impact. Some ejecta is also evident in the magnified view of the damaged region. Both crystals display broad (100) cleavage planes in the region beyond the damaged zone. Occasionally, the end of the crystal opposite the point of impact was significantly damaged by the reaction forces exerted by the sample holder. This damage is

evident in both surfaces shown in Fig. 3. Samples exhibiting intense post-emission always displayed significant damage at the point of impact. This surface damage is the most striking difference between surfaces created in cleavage and those created in the other deformation modes.

By scanning the sample past a CEM with a small effective aperture, we were able to show that the intense, prolonged EE associated with cleavage was much more intense in the region of the sample which had been damaged by the blade. Figure 4 shows the EE observed during scans of the cleaved surfaces shown in Fig. 3. The initial detector position during cleavage is such that in spite of reduced solid angle, healthy, long lasting emission curves are evident. A few seconds are required for positioning the manipulator for scanning. Comparison with the SEM photos of Fig. 3 shows that the extent of the damaged region roughly correlates with the extent of peak emission. (Note that the EE intensity is displayed on a log scale.) The scan of Fig. 4(a) shows fairly narrow peaks superimposed on a continuous decay, consistent with the narrow damaged region shown in Fig. 3(a). The EE observed during the scan of relatively undamaged portions of the surface is largely due to the limited spatial resolution and to small damaged regions along a portion of the surface edges. The EE displayed in Fig. 4(b) drops to background levels between the peaks. This is consistent with the more perfect cleavage surface displayed in the undamaged portion of Fig. 3(b). In spite of limited spatial resolution of our scanning system, we see that the peak EE from the damaged regions of both samples is one to two orders of magnitude greater than that from the (predominantly) smoother portions.

Some of the damaged regions yielding long EE decays had features very similar to those found in wear studies of MgO ,⁸ which, like LiF , has the NaCl structure. We therefore abraded LiF surfaces with a diamond up to compare the resulting EE with that associated with cleavage. As shown in Fig. 5, this form of stimulation resulted in intense post-emission quite similar to the intense cleavage-induced post emission. LiF surfaces abraded with metal tips yielded similar results. As in the case of cleavage, we found a strong correlation between the intensity of the post-emission and the degree of surface damage created by abrasion.

The ejecta frequently observed on cleaved surfaces yielding intense post-emission were also evident on abraded surfaces. To investigate the EE associated with ejecta, we abraded a clean LiF crystal in vacuum with a metal file. The ejecta was allowed to fall 10 cm through a grounded metal tube onto a platform positioned approximately 3 cm from the entrance cone of a CEM. Care was required to prevent the accumulation of ejecta on

the front cone of the CEM. The detector was shielded from the LiF crystal so that only electrons from the ejecta were detected. As shown in Fig. 6, EE from ejecta was extremely intense, even after 10 minutes, and showed decay kinetics similar to that of EE from abraded and cleaved LiF crystals.

We attempted to remove the ejecta from the damaged region corresponding to an intensely emitting cleavage surface to determine if the underlying damage zone of the crystal contributed significantly to the observed emission. Unfortunately, the adhesion of the ejecta to the crystal was so extreme (very likely due to electrostatic attraction of charged surfaces) that our attempts failed. However, the damaged regions of a number of cleaved crystals yielding intense EE differed considerably in the quantity of adhered ejecta. Therefore, it is unlikely that the ejecta is the sole source of the intense emission. We suspect that the underlying damaged surface also contributes significantly to the prolonged EE.

IV DISCUSSION

The weak, short-lived EE from LiF fractured in tension and 3-point bend relative to the intense post-emission often observed following cleavage suggests that post-emission is not intrinsic to the fracture process. Cleaved LiF displaying post-emission consistently showed a damaged region at the point of blade impact. CEM scans of cleaved surfaces yielding post-emission showed that the bulk of the emission originated from the damaged end of the crystal. Therefore we conclude that the smooth (100) fracture surface is not responsible for the intense, prolonged EE observed following cleavage.

Discussions of post-emission mechanisms must therefore focus on the highly damaged regions at or adjacent to the surfaces that have interacted with the cleavage blade. Previously proposed emission mechanisms may well be appropriate, e.g., those involving the production of point defects (e.g., Wollbrandt³) or dislocations (e.g., Lipson⁴). Cathodoluminescence studies of indented and abraded LiF have shown high densities of point defects at or near the surface of the damaged regions.⁹ The region of the crystal struck by the cleaving blade is also likely to undergo severe plastic deformation, which requires dislocation growth and multiplication. Thus, we expect the damaged region of the cleaved surface to have both kinds of defects in abundance. The same is true of the abraded surfaces and the ejecta, which also displayed intense post-emission.

As noted above,⁶ previous fracto-emission studies of MgO loaded in 3-point bend showed that surfaces which coincide with the (100) cleavage plane are less effective in pHE and EE than surfaces which do not. We call surfaces inclined to the favored cleavage plane(s) "off-axis" surfaces. With the exception of cleavage steps, the off-axis surfaces created during the fracture of MgO in 3-point bend appear quite smooth even when observed at high magnifications under an SEM. We believe that the submicroscopic steps required to accommodate the observed 16° inclination to the cleavage plane contribute significantly to the pHE and EE observed during fracture, and most likely participate in post-emission as well. These surfaces would have a higher density of defects than the (100) cleavage plane and a lower defect density than the damaged regions produced by cleavage blade impact. Significantly, the persistence of the post-emission is intermediate as well. To facilitate comparisons with MgO fractured in 3-point bend, we cleaved a few MgO single crystals. We found that "well-cleaved" MgO (minimal surface damage by the cleaving blade) showed little, if any, post emission, while samples damaged by the cleavage blade yielded post-emission lasting several minutes. Neither MgO nor LiF displayed post-emission following cleavage except when significant damage resulted from the impact of the cleavage blade. Yet another correlation between post-emission and the degree of off-axis fracture is evident in the EE decay from MgO relative to LiF, both fractured in 3-point bend. EE from MgO fractured in 3-point bend lasts some tens of seconds, in contrast to the tens of milliseconds required for EE decay from LiF fractured in the same mode. The fracture of LiF in 3-point bend does not result in off-axis surfaces, whereas the fracture of MgO in 3-point bend does. We therefore conclude that the post-emissions from both materials are strongly correlated with the occurrence of off-axis fracture surfaces.

Off-axis fracture and high defect densities and may also be associated with high crack velocities. High crack velocities often lead to instabilities in crack propagation and crack bifurcation, and thus higher degrees of off-axis fracture. Experimentally, high crack velocities may be realized in tensile loading and 3-point bend by reducing the maximum size of surface defects. This results in stronger specimens and thus higher elastic strain energy densities at failure. Providing that the crack velocities are well below the Rayleigh wave limiting velocity, higher strain energy densities result in higher crack speeds. In the case of MgO loaded in 3-point bend, we have shown that that peak photon emission intensities increase with sample strength.⁶ This is readily explained if surface defect densities increase with crack velocity and sample strength.

We have also found that EE intensity can be a strong function of crystal orientation when orientation affects the degree of off-axis fracture. In work on oriented MgF_2 fractured in 3-point bend we have found that orientations favoring clean cleavage typically yields a quarter or less of the EE intensity characteristic of orientations favoring off-axis fracture.¹⁰

With regard to the identities of the defects associated with the post-emission process, we note that thermally stimulated electron emission and photon emission (TSEE, TSL) work suggest that the common V-type centers (H , V_K , V_I , and V_F) decay by the emission of a hole well below room temperature.¹¹ Thus V-type centers probably do not participate in post-emission. However, a number of workers have observed intense TSEE and TSL between 300 and 400 K.^{3,11,12} These emissions have been attributed to the release of electrons from traps formed by surface lattice defects.¹³ The modest stability of these traps at room temperature make them good candidates for sources of mobile electrons following room temperature fracture. We have little information about the participating recombination centers, although as noted above, they are probably not simple V-type centers. Fracture surfaces, especially damaged or off-axis surfaces, may well display a wide variety of more complex electron and hole centers associated with vacancy aggregates or surface steps and corners.

Wollbrandt et al. suggest that the surface F^- -center (an anion vacancy associated with two trapped electrons) is the participating electron trap and that the surface F^+ -center (an anion vacancy associated with no trapped electrons) is the recombination center.³ The electron density of the F^- -center extends well beyond the vacancy itself, facilitating tunneling to nearby F-centers (anion vacancies associated with one trapped electron) and F^+ -centers. Electron tunneling from F^- -centers to nearby F-centers is equivalent to the motion of the F^- -centers among the surface anion vacancies. This defect motion, being the result of tunneling, is relatively insensitive to temperature.⁵ This would explain the relative insensitivity of the decay kinetics to temperature observed by Wollbrandt. Auger recombination at F^+ -centers would yield EE. A parallel process producing photons with identical kinetics should be detectable, similar to that seen in MgO .⁶

Further evidence concerning the nature of the recombination process is provided by the decay kinetics. Wollbrandt observed second order kinetics in the post-emission decay. In our data, the emission decay was not described by kinetics of a single order. Figure 7 represents the EE decay of Fig. 2(a) on a log/log plot. Although the EE decay kinetics over the entire time interval are not described by a simple $1/t^n$ relationship, $1/t^{1.6}$ provides a

fair description over a decade in time. The gradual increase in the exponent of the EE decay ($n = -\text{slope}$) to a roughly constant value of 1.6 in Fig. 7, is characteristic of tunneling recombination involving randomly distributed electron and hole centers. Thomas et al. modeled this decay assuming that the recombination probability is an exponential function of the separation between the electron and hole centers.¹⁴ Williams et al. extended this model to include the case of thermally activated hopping and used the result to describe the temperature dependence of the 4.9 eV luminescence decay following electron bombardment of MgO.¹⁵ In these models, equal initial electron and hole center concentrations yield second order decay kinetics in the long time limit. The time required to establish second order decay is sensitive to initial defect densities and can be much less than our sampling times. Variable decay kinetics, displaying a gradual increase in decay exponent, n , apply in the short time limit and in the case of electron or hole center density excess. Thus these models have the potential to describe the decay kinetics of both our results and those of Wollbrandt et al. Decay data taken at a variety of temperatures and initial defect concentrations would help resolve the details of the processes involved. We also note that the decay of Fig. 7 shows a distinctly slower decay at times longer than about 1500 s and a distinctly faster decay at times less than about 5 s (the first two data points shown), suggesting that other emission processes are important at these times.

Lipson et al. concluded that charge carried to the surface by moving dislocations accounted for the long decay of the post-emission.⁴ They propose that these dislocations are initially pinned by charged defects, which after fracture are free to diffuse under the influence of the electric fields produced by nearby surface charges. As these defects diffuse away, the dislocations are free to move toward the surface under the influence of image forces. Along the way, they can sweep charge from nearby F-centers. This charge may participate in emission processes upon its arrival at the surface. Since diffusion is a first order process, one would expect the resulting EE decay to be first order. Although this was not observed in the present work, a non-linear dislocation mechanism might still be possible. Indeed, it may be that the emission peak about 4 ms after fracture in Fig. 1(a) is associated with dislocations popping out of the newly formed fracture surface. A similar delayed peak was observed in EE from single crystal Si fractured in 3-point bend on a slightly faster time scale.¹⁶ Finally, we note that dislocation related mechanisms are extremely important in EE and phE occurring *during* plastic deformation.^{6,17}

V CONCLUSIONS

The present work suggests that the intense, prolonged EE from cleaved LiF is a relatively localized phenomena associated with highly damaged regions of the sample surface. These damaged regions are associated with significant plastic deformation as well as high densities of surface defects. Measurements of EE from smooth (100) cleavage planes produced in cleavage indicate that they are associated with little, if any, post-emission. The duration of post-emission from MgO and LiF in various modes also correlates well with the degree of 'off-axis' fracture which is associated with high defect densities. A mechanism involving tunneling recombination of charge carriers trapped at surface defects would explain the variable decay kinetics observed, although contributions from moving dislocations cannot be ruled out. In a general sense, we are able to conclude that the EE post-emission intensities are highly sensitive to the details of localized energy deposition during the loading and fracture events, namely regions containing higher densities of surface (or near surface) damage yield dramatically increased emission.

VI. ACKNOWLEDGMENTS

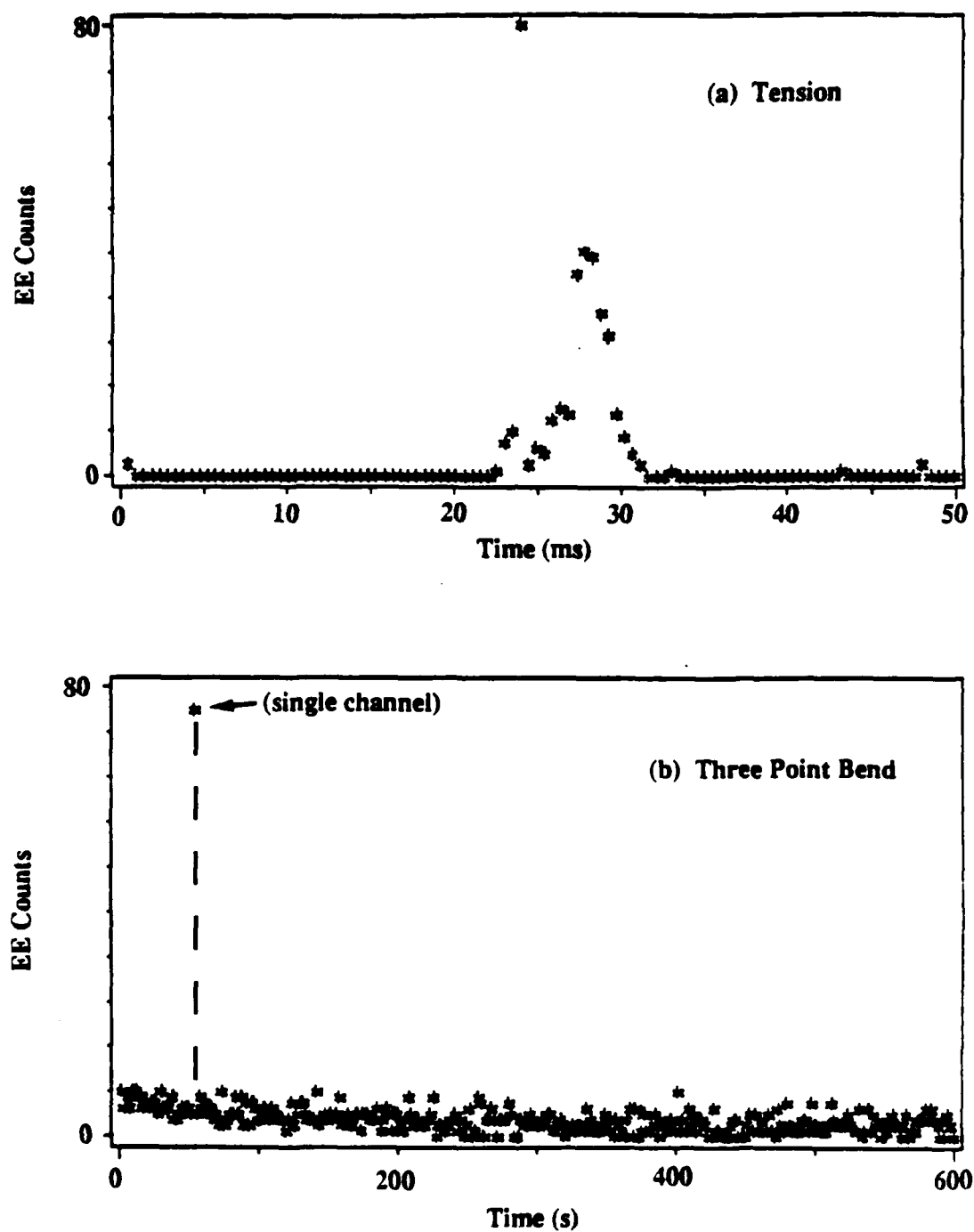
The authors wish to thank Les Jensen and Steve Behler for their assistance in carrying out the experimental aspects of this research. This work was supported by the National Science Foundation Grant DMR-8601281, the Office of Naval Research, Project N00014--87-K-0514, and the Washington Technology Center.

References

1. B. V. Deryagin, N. A. Krotova, and V. P. Smilga, *Adgeziya Tverdykh Tel*, (Nauk, Moscow, 1973) [*Adhesion of Solids*, (Consultants Bureau, New York, 1978), Robert K. Johnston, translator].
2. J. Wollbrandt, U. Bruckner, and E. Linke, in *Proc. 6th International Symp. on Exoelectron Emission and Applications*, H. Glaefke and W. Wild, editors, (Wilhelm-Pieck-Universitat, Rostock, GDR, 1979), pp. 137-138.
3. J. Wollbrandt, U. Bruckner, and E. Linke, *Phys. Status Solidi (a)* **78**, 163-168 (1983).
4. A. G. Lipson, V. A. Kuznetsov, V. A. Klyuev, Yu. P. Toporov, and B. V. Deryagin, *Dok. Akad. Nauk SSSR* **294**(5), 1161-1164 (1987) [*Dok. Phys. Chem.* **294**(5) 575-579 (1987)].
5. M. I. Molotskii, *Fiz. Tverd. Tela (Leningrad)* **29**, 3168-3170 (1987) [*Sov. Phys. Solid State* **29**(10), 1821-1822 (1987)].
6. S. C. Langford, J. T. Dickinson, and L. C. Jensen, *J. Appl. Phys.* **62**(4), 1437 (1987).
7. E. E. Donaldson, J. T. Dickinson, S. K. Bhattacharya, "Production and properties of ejecta released by fracture of materials," *J. Adhesion* **25**, 281-302 (1988).
8. Yuji Enomoto, *Wear* **89**(1), 19-28 (1983).
9. M. M. Chaudhri, J. T. Hagan, and J. K. Wells, *J. Materials Sci.* **15**(5), 1189-1193 (1980).
10. K. C. Yoo, R. G. Rosemeier, J. T. Dickinson, and S. C. Langford, "Anisotropy effects of fracture emission from MgF₂ single crystals," to be published.
11. Akihiro Tomita, Hatsuo Nakamura, Masao Kamada, and Kenjiro Tsutsumi, *Jpn. J. Appl. Phys.* **15**(10), 1899-1908 (1976).
12. V. A. Kuznetsov, D. M. Sakov, A. G. Lipson, V. A. Klyuev, Yu. P. Toporov, S. N. Tolstaya, and B. V. Deryagin, *Dok. Akad. Nauk SSSR* **289**(6), 1416-1420 (1986) [*Dok. Phys. Chem.* **289**(6), 755-759 (1987)].
13. Akihiro Tomita, Hatsuo Nakamura, Masao Kamada, and Kenjiro Tsutsumi, *Jpn. J. Appl. Phys.* **18**(2), 389-390 (1979).
14. D. G. Thomas, J. J. Hopfield, and W. M. Augustyniak, *Phys. Rev.* **140**(1A), 202-220 (1965).
15. R. T. Williams, J. W. Williams, Thomas J. Turner, and K. H. Lee, *Phys. Rev. B* **20**(4), 1687-1699 (1979).
16. J. T. Dickinson, D. L. Doering, and S. C. Langford, in *Atomic and Molecular Processing of Electronic and Ceramic Materials*, edited by I. H. Aksay, et al., (Materials Research Society, Pittsburgh, 1988), pp 39-46.
17. A. V. Poletaev and S. Z. Shmurak, *Fiz. Tverd. Tela (Leningrad)* **26**, 3567-3575 (1984) [*Sov. Phys. Solid State* **26**(12), 2147-2152 (1984)].

Figure Captions

- FIG. 1. EE from LiF fractured in (a) tension and (b) 3-point bend. Note the different time scales in (a) and (b).
- FIG. 2. EE from cleaved LiF samples showing (a) intense post-emission and (b) weak post-emission.
- FIG. 3. SEM photographs of two cleaved LiF surfaces exhibiting intense post-emission, with magnified views of the damaged regions on the right. The point of cleavage blade impact is at the top of each photograph.
- FIG. 4. EE observed by scanning a CEM repeatedly across (a) the surface shown in Fig. 3(a), and (b) the surface shown in Fig. 3(b). Note that the vertical scale is logarithmic.
- FIG. 5. EE from a LiF surface abraded with a diamond point.
- FIG. 6. EE from macroscopic particles (ejecta) produced by filing a LiF crystal in vacuum.
- FIG. 7. A log/log plot of the EE shown in Fig. 2 (a). The line represents a fit of the data in the nearly linear region centered at ~ 400 s.

EE from LiF: Tension and Three Point Bend**Fig. 1**

EE from LiF: Cleavage

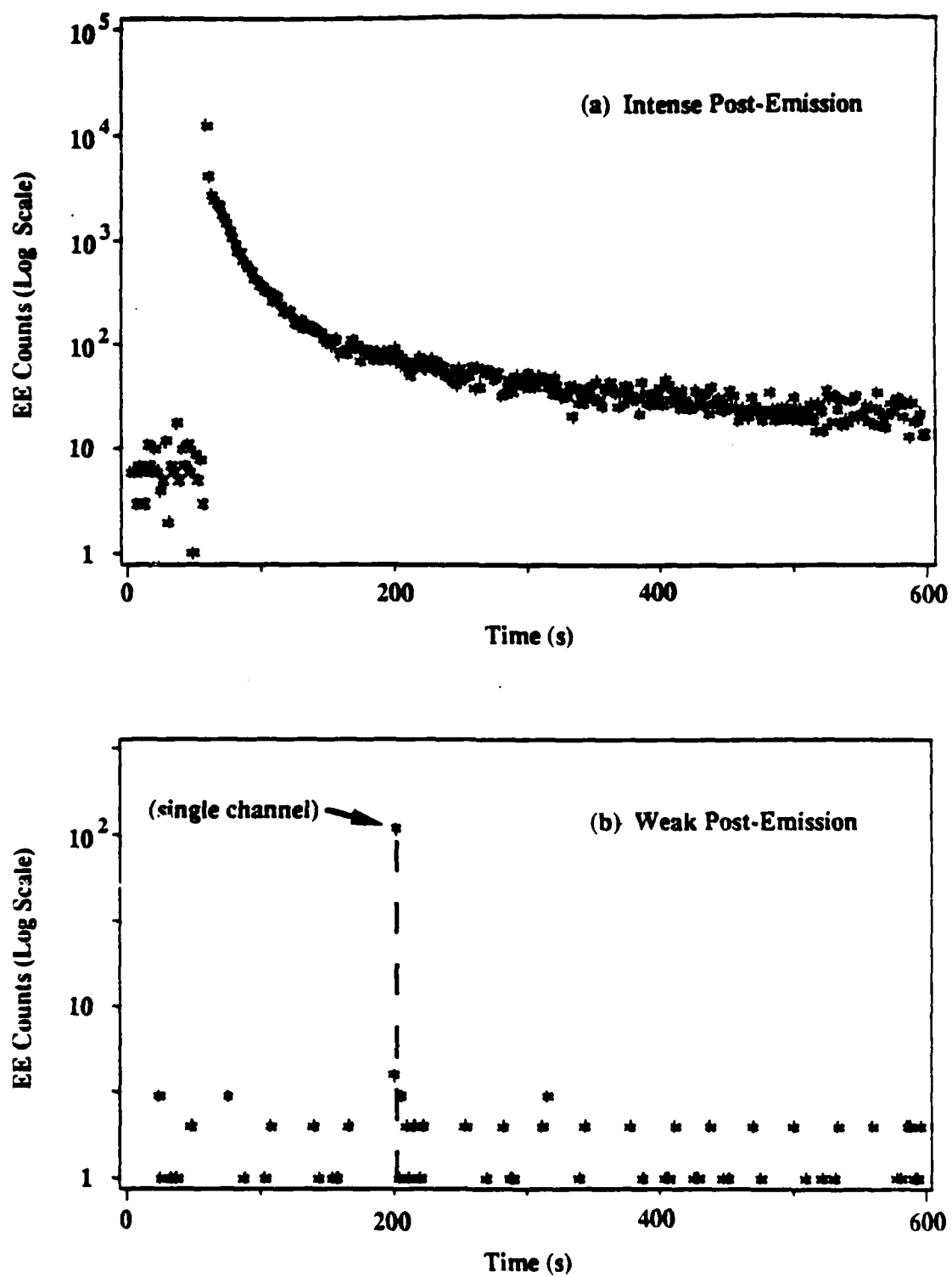


Fig. 2

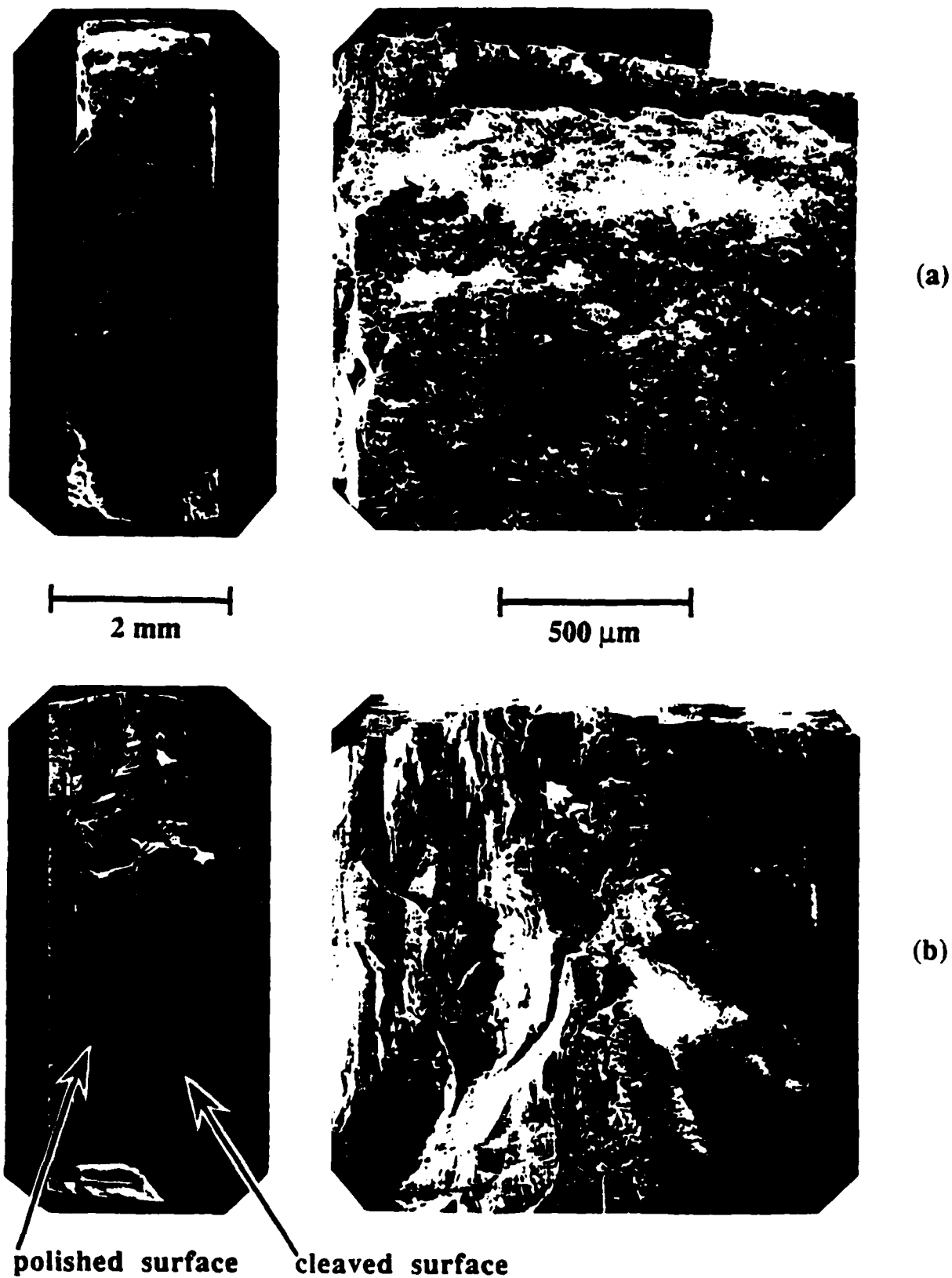


Fig. 3

Scan of Cleavage Surface with EE Detector

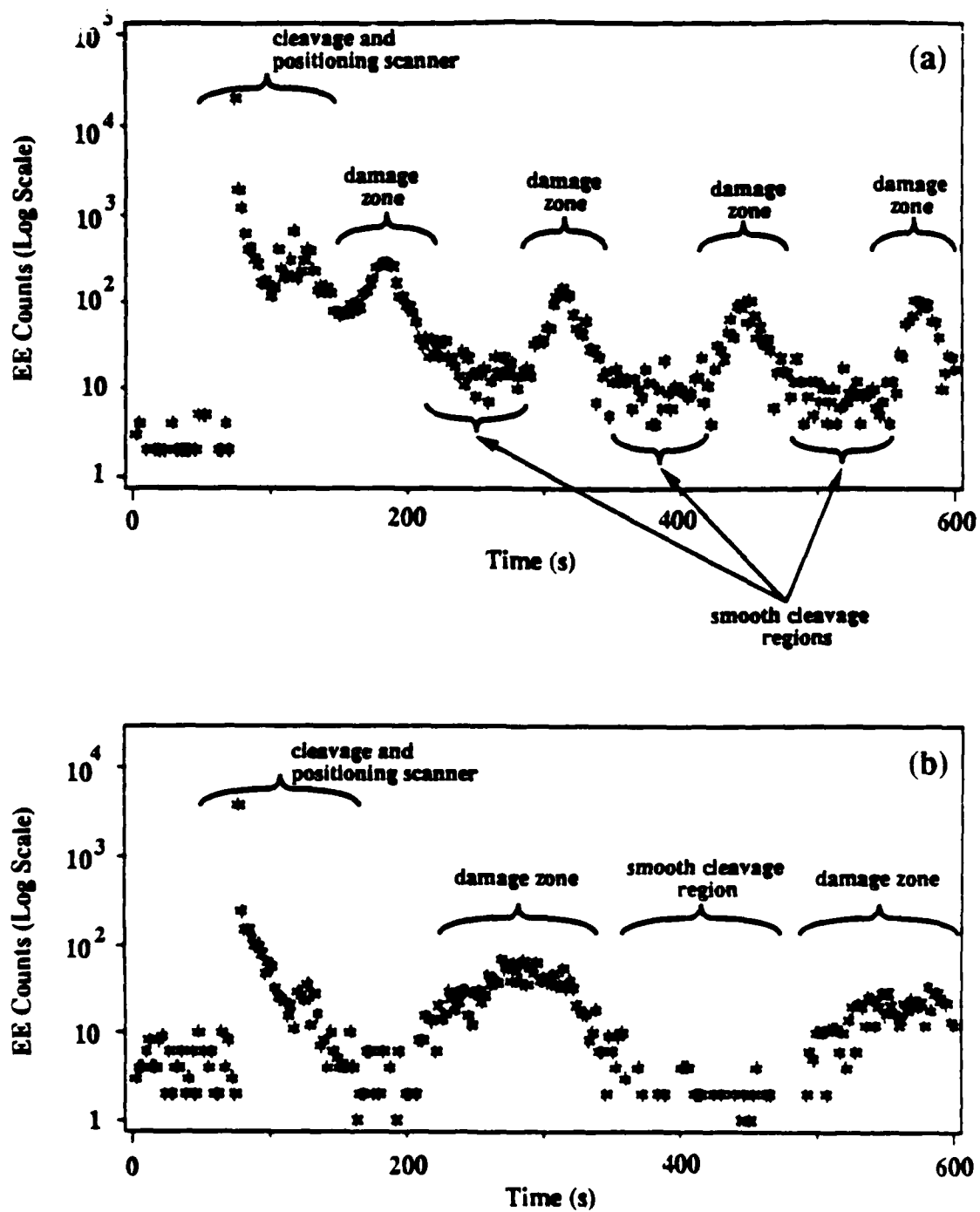


Fig. 4

EE from LiF: Abrasion with Diamond

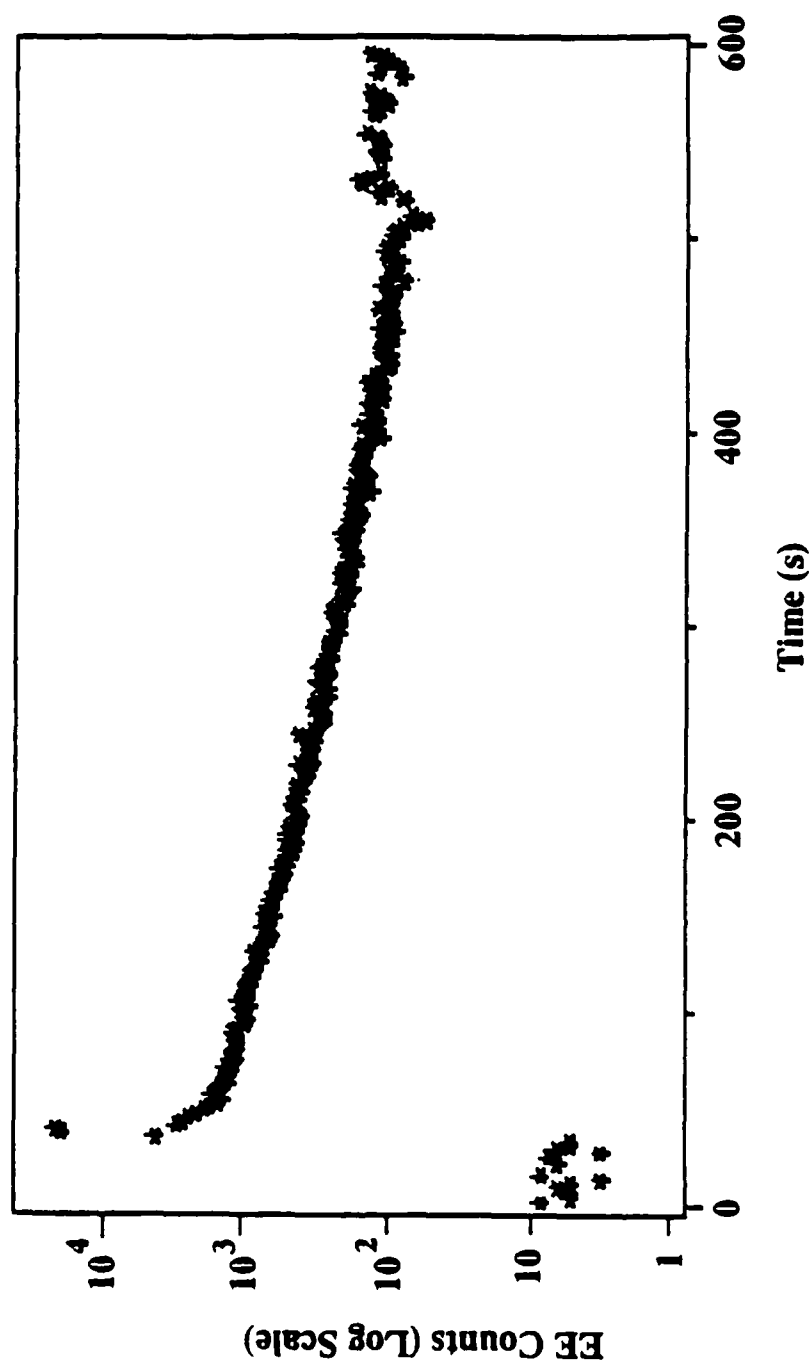


Fig. 5

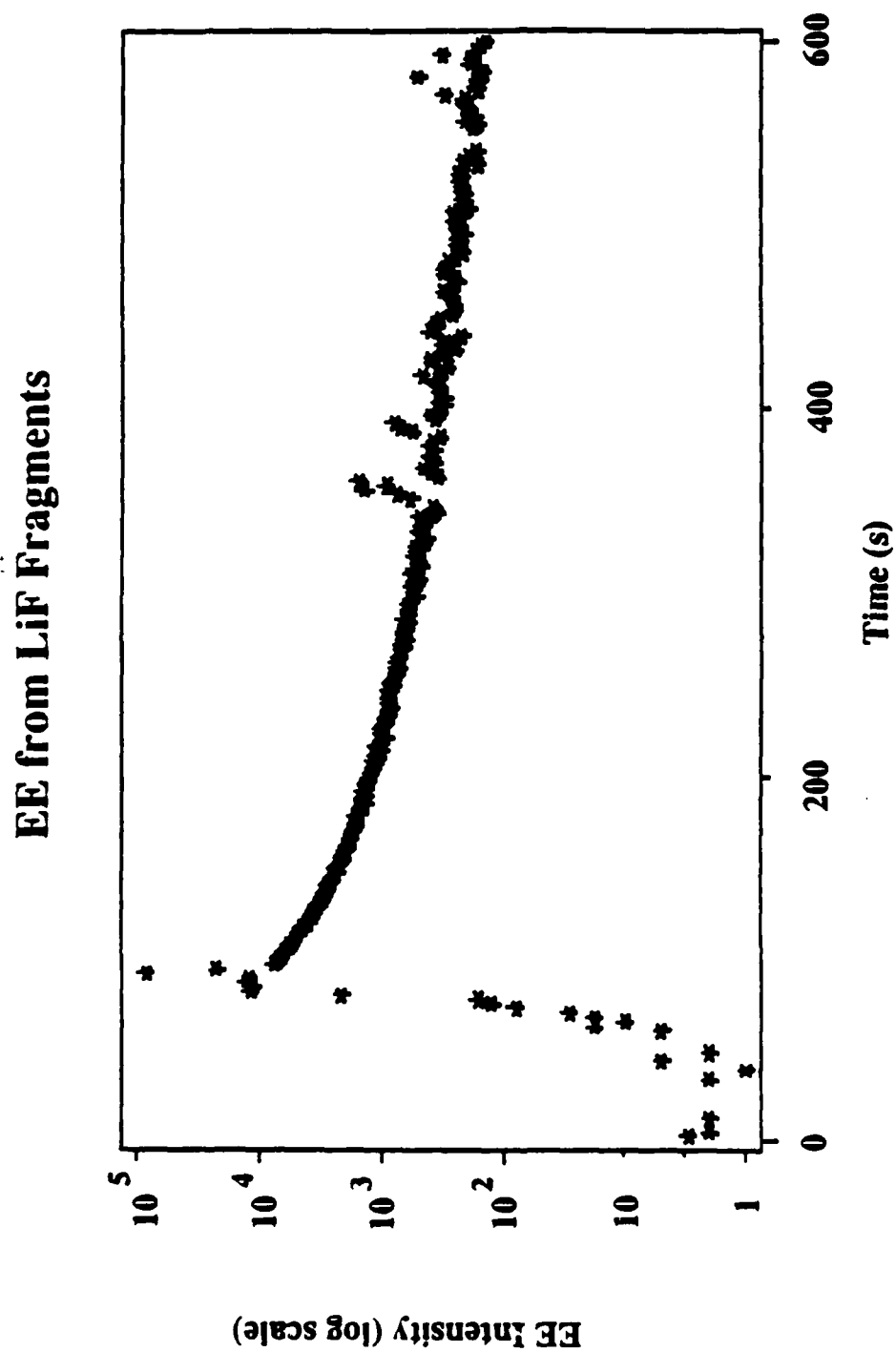


Fig. 6

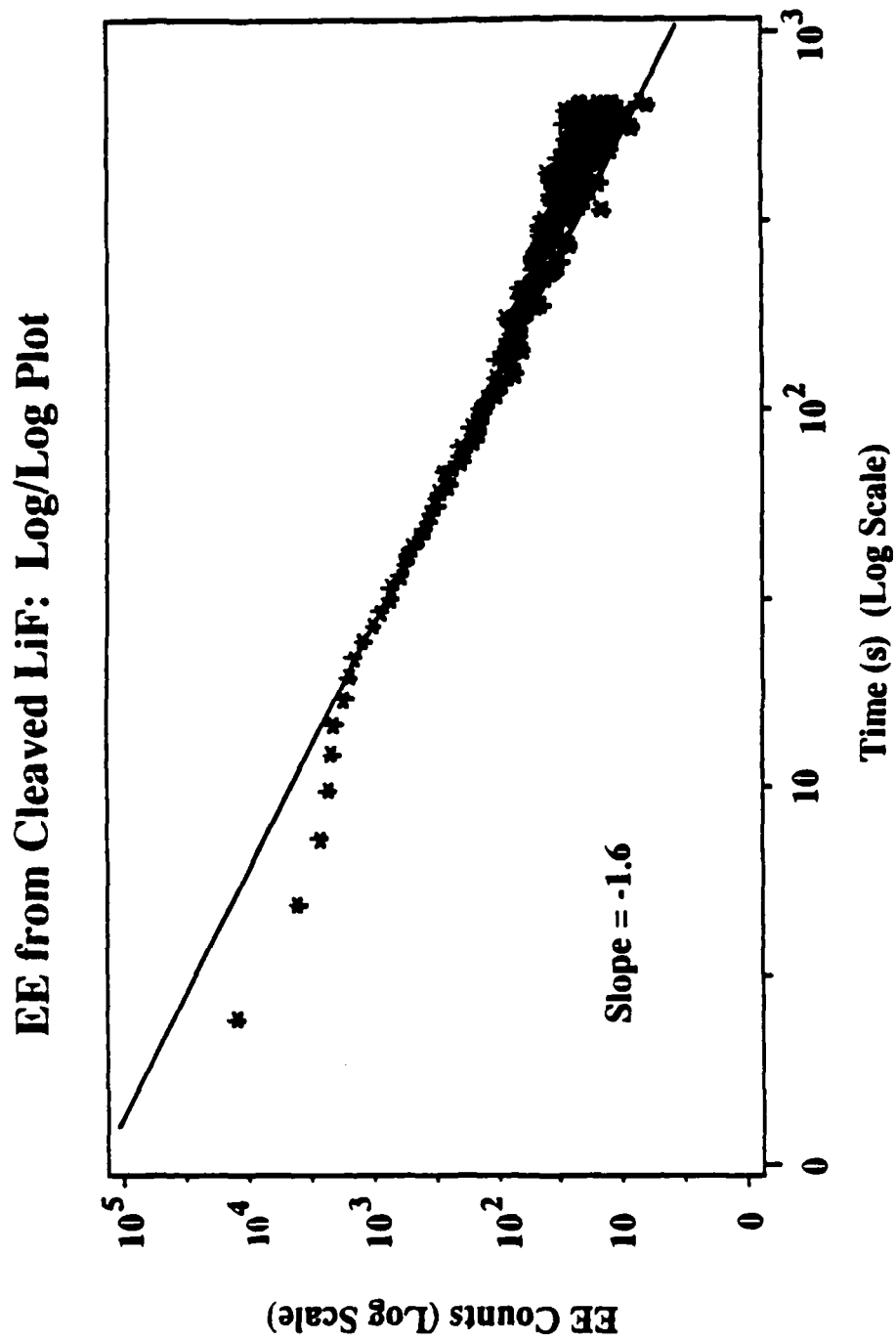


Fig. 7

XII. Anisotropy effects on fracto-emission from MgF_2 single crystals

K. C. Yoo^{a)} and R. G. Rosemeier^{b)}

Department of Mechanical Engineering, University of Maryland, College Park, MD 20742

J. T. Dickinson and S. C. Langford

Department of Physics, Washington State University, Pullman, WA 99164-2814

An important component of fracto-emission is the emission of electrons (EE) accompanying the fracture of materials. In this paper, we present measurements of EE accompanying the fracture of MgF_2 single crystals loaded in three-point bend. In particular, we examine the effect of changing the crystal orientation relative to the loading direction on emission intensity. We find that fracture surfaces with different crystal orientations yield significantly different EE. We propose that this is due to differences in the density of defects produced by such fracture.

^{a)} Present Address: Westinghouse Research and Development, Pittsburgh, PA 15235

^{b)} Present Address: Brimrose Corporation of America, Baltimore, MD 21236

Earlier experimental and theoretical studies on various fracto-emission phenomena have been reported involving brittle materials including alkali halides, metal oxides, silica glasses, and molecular crystals [1-18]. A number of features of the observed emissions can be described in terms of bond breaking induced excitations and defect production during crack growth. The density and stability of excitations and defects created during fracture are a function of the crystallographic environment of the surface. Defect densities may also be strongly dictated by the dynamic behavior of dislocations in the near-surface region. Indentation studies of MgO single crystals have shown that internal strain energy is often released by dislocations escaping through the fracture surface [19]. The crystallographic orientation of the fracture surface could dictate the kinetics of dislocation motion and greatly influence energetic processes at the surface [20], including the energetics and stability of point defects.

In earlier studies of fracto-emission from cyclotrimethylene trinitramine (RDX) [7] and pentaerythritol tetranitrate (PETN) [11] explosive single crystals, we showed that the mode of fracture relative to the crystallographic orientation again influenced the emission characteristics. In two recent studies, we have shown that fracto-emission intensities depend strongly on the amount of non-(100) plane fracture in MgO and LiF single crystals [14, 18], where extensive "off-axis" fracture yielded substantial increases in emission. In the present investigation, we examine the effect of crystal orientation on the electron emission (EE) for two different orientations of MgF_2 single crystals. The orientations were chosen so that the resulting fracture surfaces would have different atomic bonding structures with the potential to influence the microscopic processes accompanying fracture.

To ensure that any differences in emission intensities were due to orientation effects and not to differences in defect density, crystal history, or sample size, all samples were cut to the same size from material from a single monocrystal. MgF_2 single crystal plates were prepared in (110) and (101) orientations from random crystals from the same macrocrystal based on the Laue x-ray back-reflection measurements. All crystals experienced the same history in terms of environment and therefore were assumed to have similar defect densities. $10 \times 5 \times 1 \text{ mm}^3$ specimens were cut from these plates and loaded in three-point bend so that (101) surfaces of the (110) plates were centered in the support span and (110) surfaces of the (101) plates were centered

the support span. Thus fracture of the (110) plates was favored along {101} planes and fracture of the (101) plates was favored along {110} planes. In these orientations, two {101} planes in the (110) plates are equally favored fracture planes, while a uniquely favored {110} fracture plane exists in the (101) plates.

Experimental details are similar to those described elsewhere [6]. EE was detected with a Galileo Electro-Optics Model 4039 Channeltron electron multiplier (CEM) positioned approximately 1 cm from the freshly formed surface. This CEM produces fast (10 ns) pulses with approximately 90 % absolute detection efficiency for electrons. The output of the CEM was pulse counted with a multichannel analyzer. Experiments were carried out in a vacuum of 10^{-5} Pa. The fracture surface orientations were determined by Laue back-reflection measurements and confirmed by geometric configuration relative to the orientation of the specimen surfaces. The topography of the fracture surfaces was carefully examined by scanning electron microscopy (SEM), confirming the surface orientations.

Figures 1(a) and (b) are SEM micrographs of the fracture surfaces obtained from the two types of specimens. The direction of loading in each case lies along the surface normal of the plate used to prepare the sample. The fracture surface of the (110) plate in Fig. 1(a) shows two different {101} facets, while the fracture surface of the (101) plate in Fig. 1(b) shows a single, flat {110} plane. Thus, the fracture surfaces are predominantly crystallographic, following the fracture mechanisms of MgF_2 single crystals shown in a previous study [21].

Typical EE curves for the two orientations are shown in Fig. 2. On this slow time scale, one finds that fracture (marked with an arrow) is accompanied by a burst of electrons followed by sustained emission after the fracture event. The peak intensities for the {101} fracture surfaces are higher and the duration of the post-emission is longer, thus yielding more total emission. Mechanisms for both the emission at fracture and the post-emission have been discussed elsewhere [6,18]. Direct excitation and very rapid decay processes dominate *during* fracture and charge recombination at defects dominates *after* fracture. The different decay kinetics seen for these two surfaces are both consistent with a mobile charge carrier/recombination mechanism.

The total number of EE counts acquired over a time of ~300 seconds from eight different samples which yielded four fracture surfaces of the two orientations labeled in Table I by their dominant orientations. The results for these eight samples show that the EE intensity from the {110} fracture surfaces are greater than

those from $\{101\}$ fracture surfaces by a substantial margin, typically a factor of 5-10. The fracture of one sample (marked with a) resulted in a small piece of ejecta [22] landing on the front cone of the CEM, which might account for the anomalously high intensity. Measurements of EE from LiF ejecta have shown that these fragments are highly emissive [18]. Ejecta particles are expected to have extreme variations in the distribution of crystallographic planes on their fracture surfaces and are consequently strong sources of EE. Even ignoring this anomaly, the data in Table I strongly suggest that the creation of these two types of fracture surfaces yield different EE intensities.

In the present investigation, the fracture surfaces appear to coincide with the $\{110\}$ and $\{101\}$ planes, which are the cleavage planes of MgF_2 . In general, fracture surface energy scales with Young's modulus. Based on the elastic constant anisotropy of MgF_2 , the formation of a $\{110\}$ cleavage surface would be expected to require about 35% more energy per unit area than the formation of a $\{101\}$ surface. In practice, much of the strain energy expended in fracture goes to irreversible processes, including fracto-emission. We have observed a strong correlation between peak photon emission intensity and load at fracture in single crystal MgO , which we attribute to the greater strain energies in the stronger samples, a portion of which is channeled into mechanical and electronic processes in the region of the crack tip. During crack growth, such processes lead to the excitations and defects required for emission. The observation of substantially increased EE from the $\{110\}$ fracture surfaces is therefore expected on these grounds.

The different arrangements of magnesium and fluorine ions on the $\{110\}$ and $\{101\}$ fracture surfaces may also affect the observed EE. Magnesium fluoride has a tetragonal structure where magnesium atoms sit at the corners and center of the unit cell. Six fluorines coordinate octahedrally about each magnesium and each fluorine is bonded to three magnesium atoms as shown in Fig. 3. Thus the structural arrangement or atomic packing is different on the $\{110\}$ and $\{101\}$ planes. The $\{110\}$ planes consist of both fluorines and magnesiums, however the $\{101\}$ planes consist of magnesiums or fluorines only as shown in Fig. 4. In both cases, fracture tends to take place *between* the densely populated planes shown in Fig. 4. Fluorines between these densely packed planes must also associate with the new fracture surfaces, and in doing so must relax substantially from their equilibrium positions in the bulk. Even in more stable surfaces, the detection of neutral species accompanying fracture has shown that the fracture surface is out of chemical equilibrium for several

seconds. For example, we have shown the fracture of single crystal MgO is always accompanied by magnesium atom emission *following* fracture [13]. This suggests that the atomic structure of a freshly created fracture surface departs considerably from perfection. Thus, we propose that when two surfaces with different structures are created in fracture, differences in local geometry and instantaneous rates of energy release would display considerable differences in the density and types of excitations and surface defects, which in turn would result in different emission behaviors.

To date, we have not identified the possible excitations and defects involved in both the emission during fracture and the post-emission in MgF_2 , nor have we examined the role of dislocations. Nevertheless, we have shown here that the EE intensities are sensitive to the locus of crack growth in an anisotropic, crystalline material. Studies of the accompanying photon, positive ion, and neutral particle (atoms/molecules) emissions from MgF_2 are currently underway.

The authors wish to thank Les Jensen for his assistance in carrying out the experimental aspects of this research. This work was supported by the Office of Naval Research N00014-82-K-0263, N00014-83-20129, N0014-80-C-0213, and N00014--87-K-0514 (Dr. R. S. Miller, Program Manager), National Science Foundation Grant DMR-8601281, and the Washington Technology Center.

References

1. B. V. Deryagin, N. A. Krotova, and V. P. Smilga, *Adgeziya Tverdykh Tel*, (Nauk, Moscow, 1973) [*Adhesion of Solids*, (Consultants Bureau, New York, 1978), Robert K. Johnston, translator].
2. J. Wollbrandt, U. Bruckner, and E. Linke, in *Proc. 6th International Symp. on Exoelectron Emission and Applications*, H. Glaefke and W. Wild, editors, (Wilhelm-Pieck-Universitat, Rostock, East Germany, 1979), pp. 137-139.
3. J. T. Dickinson, E. E. Donaldson, and M. K. Park, *J. Mater. Sci* **16**, 2897 (1981).
4. M. H. Miles and J. T. Dickinson, *Appl. Phys. Lett.* **41**, 924 (1982).
5. J. Wollbrandt, U. Bruckner, and E. Linke, *Phys. Status Solidi (a)* **78**, 163-168 (1983).
6. J. T. Dickinson, L. B. Brix, and L. C. Jensen, *J. Phys. Chem.* **88**, 1698 (1984).
7. J. T. Dickinson, M. H. Miles, W. L. Elban, and R. G. Rosemeier, *J. Appl. Phys.* **55**, 3994 (1984).
8. A. G. Lipson, V. A. Kuznetsov, V. A. Klyuev, Yu. P. Toporov, and B. V. Deryagin, *Dok. Akad. Nauk SSSR* **294**, 1161 (1987) [*Dok. Phys. Chem.* **294** 575 (1987)].
9. M. I. Molotskii, *Fiz. Tverd. Tela (Leningrad)* **29**, 3168 (1987) [*Sov. Phys. Solid State* **29**, 1821 (1987)].

10. J. T. Dickinson, W. D. Williams, and L. C. Jensen, *J. Am. Ceramic Soc.* **68**, 235 (1985).
11. M. H. Miles, J. T. Dickinson, and L. C. Jensen, *J. Appl. Phys.* **57**, 5048 (1985).
12. L. A. K'Singam, J. T. Dickinson, and L. C. Jensen, *J. Am. Ceramic Soc.* **68**, 510 (1985).
13. J. T. Dickinson, L. C. Jensen, and M. R. McKay, *J. Vac. Sci. Technol. A* **4**, 1648 (1986).
14. S. C. Langford, J. T. Dickinson, and L. C. Jensen, *J. Appl. Phys.* **62**, 1437 (1987).
15. J. T. Dickinson, L. C. Jensen, and M. R. McKay, *J. Vac. Sci. Technol. A* **5**, 1162 (1987).
16. J. T. Dickinson, D. L. Doering, and S. C. Langford, in *Atomic and Molecular Processing of Electronic and Ceramic Materials*, edited by I. H. Aksay, G. L. McVay, T. G. Stoebe, and J. F. Wagner, ed., (Materials Research Society, Pittsburgh, 1988), pp 39-46.
17. J. T. Dickinson, S. C. Langford, L. C. Jensen, G. L. McVay, J. F. Kelso, and C. G. Pantano, *J. Vac. Sci. Technol. A* **6**, 1084 (1988).
18. J. P. Mathison, S. C. Langford, and J. T. Dickinson, *J. Appl. Phys.* **65**, 1923 (1989).
19. K. C. Yoo, R. G. Rosemeier, W. L. Elban and R. W. Armstrong, *J. Mater. Sci. Lett.* **3**, 560, (1984).
20. R. W. Armstrong, C. S. Coffey and W. L. Elban, *Acta Metallurgica*, **30**, 2111 (1982).

21. W.L. Elban, J. C. Hoffsommer, C. S. Coffey, K. C. Yoo and R. G. Rosemeier, Navy Surface Weapons Center Document MP 84-200, May 1984.
22. E. E. Donaldson, J. T. Dickinson, S. K. Bhattacharya, J. Adhesion 25, 281 (1988).

TABLE I. Total Electron Emission Counts for Eight Different Samples of Single Crystal MgF_2 Yielding Two Different Fracture Surface Orientations.

FRACTURE SURFACE ORIENTATION	Total EE Counts			
{101}	5,500	6,700 ^{b)}	5,000	10,000
{110}	433,000 ^{a)}	22,500 ^{b)}	22,500	34,700

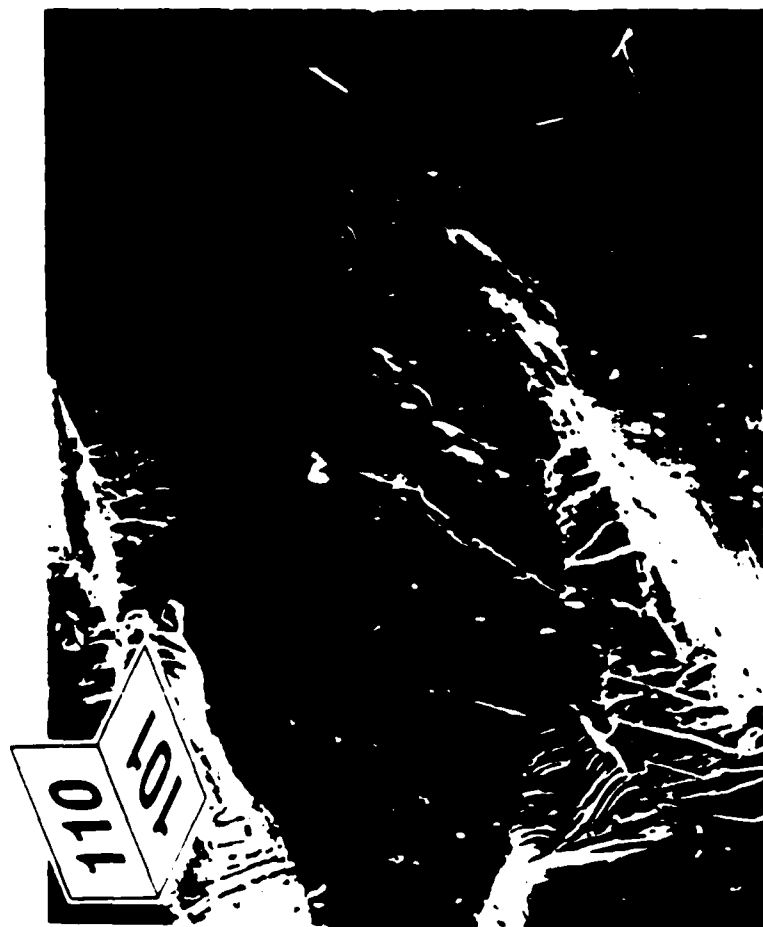
^{a)}A small piece of ejecta from the fractured sample was on the detector after fracture.

^{b)}Data corresponds to EE shown in Fig. 2.

Figure Captions

- Fig. 1. Scanning electron micrographs of (a) the $\{101\}$ fracture surfaces, and (b) the predominantly $\{110\}$ fracture surface. In each micrograph, the vertical label indicates the orientation of the tensile surface of the sample, while the horizontal label indicates the orientation of the corresponding fracture surface.
- Fig. 2. Typical electron emission curves from (a) $\{101\}$ and (b) $\{110\}$ fracture surfaces .
- Fig. 3. Crystal structure of MgF_2 .
- Fig. 4. The atomic structure of the unrelaxed, most densely packed $\{101\}$ and $\{110\}$ planes of MgF_2 .

SEM Micrographs of MgF_2 Fracture Surfaces



1 mm

a)

b)

213

Fig. 1

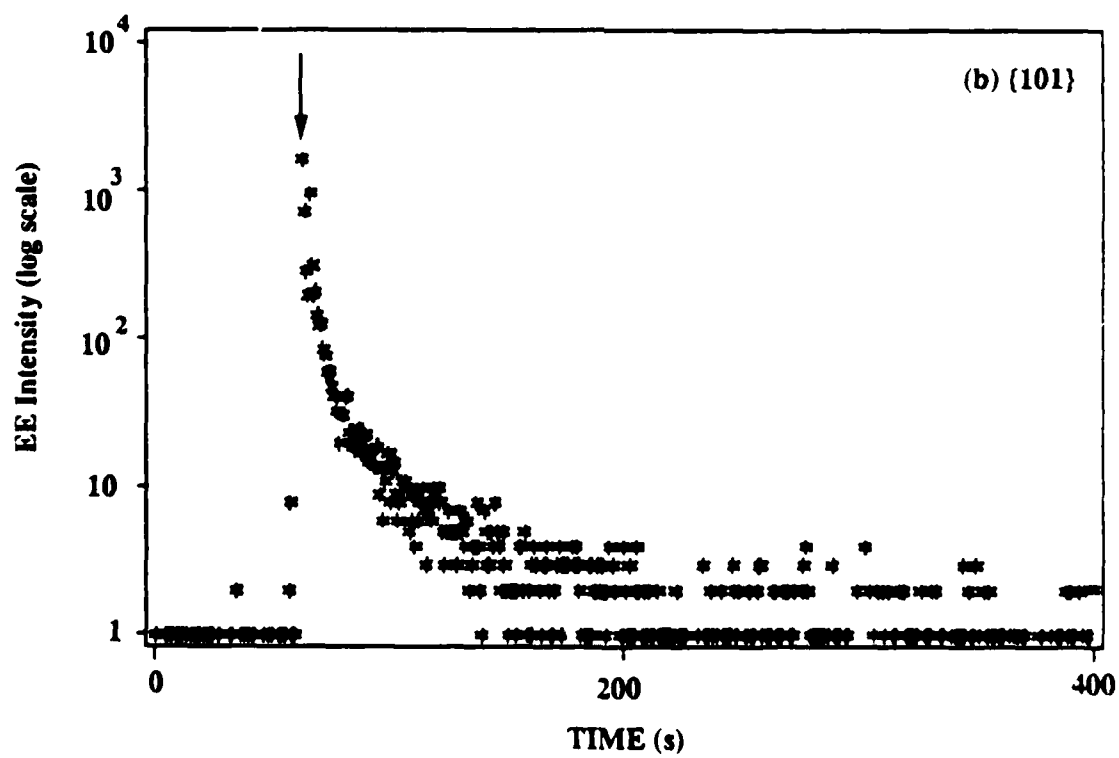
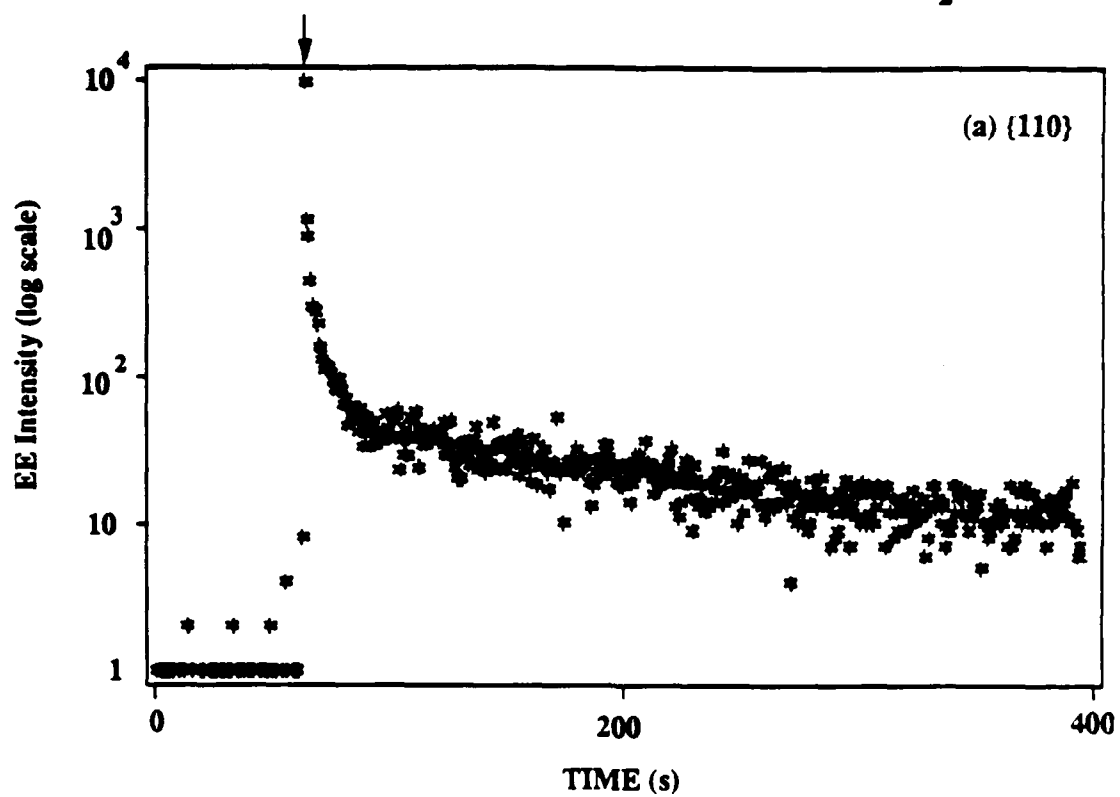
Electron Emission from Fracture of MgF_2 

Fig. 2

Structure of MgF_2

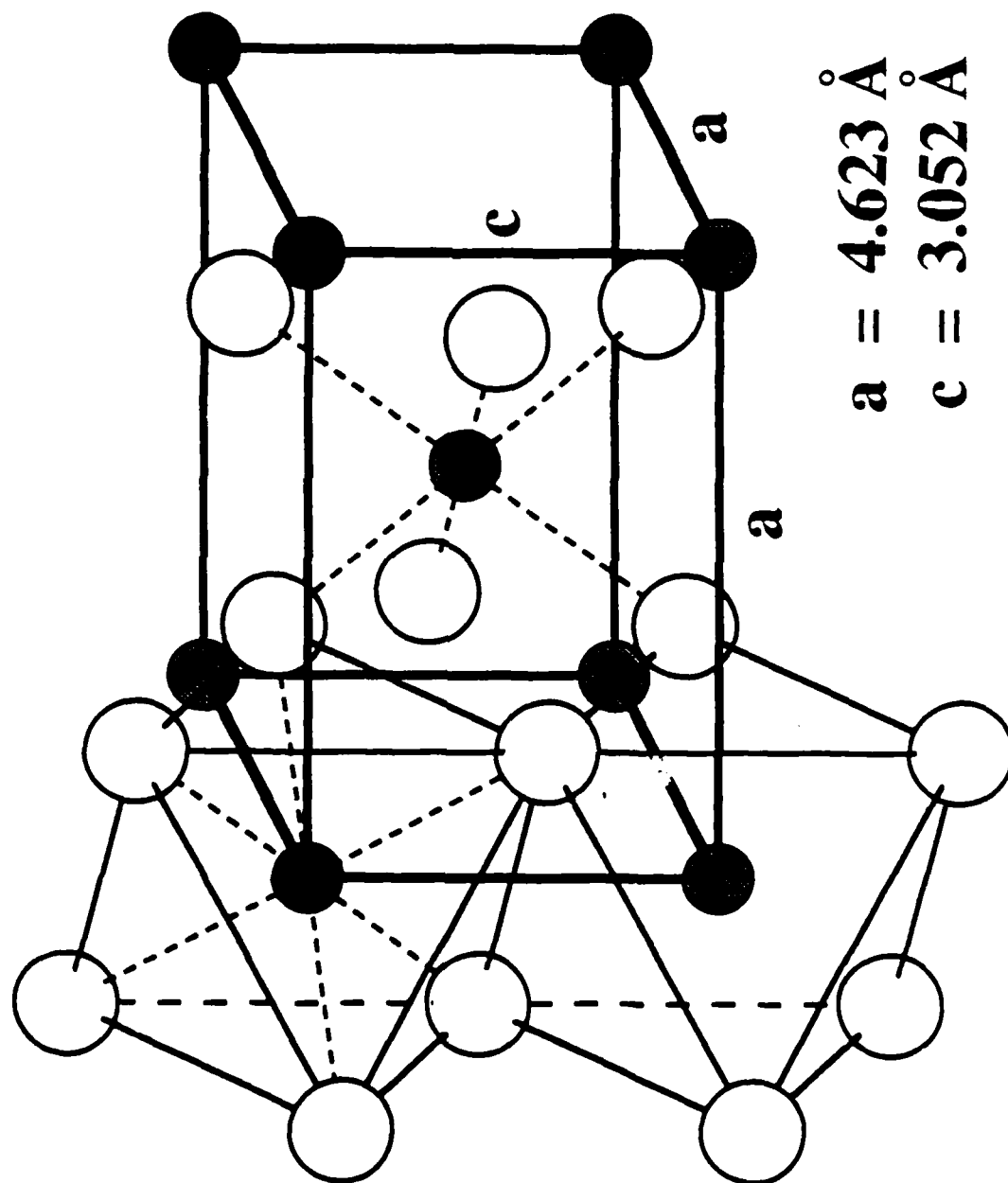


Fig. 3

Structure of Densely Packed $\{110\}$ and $\{011\}$ Planes

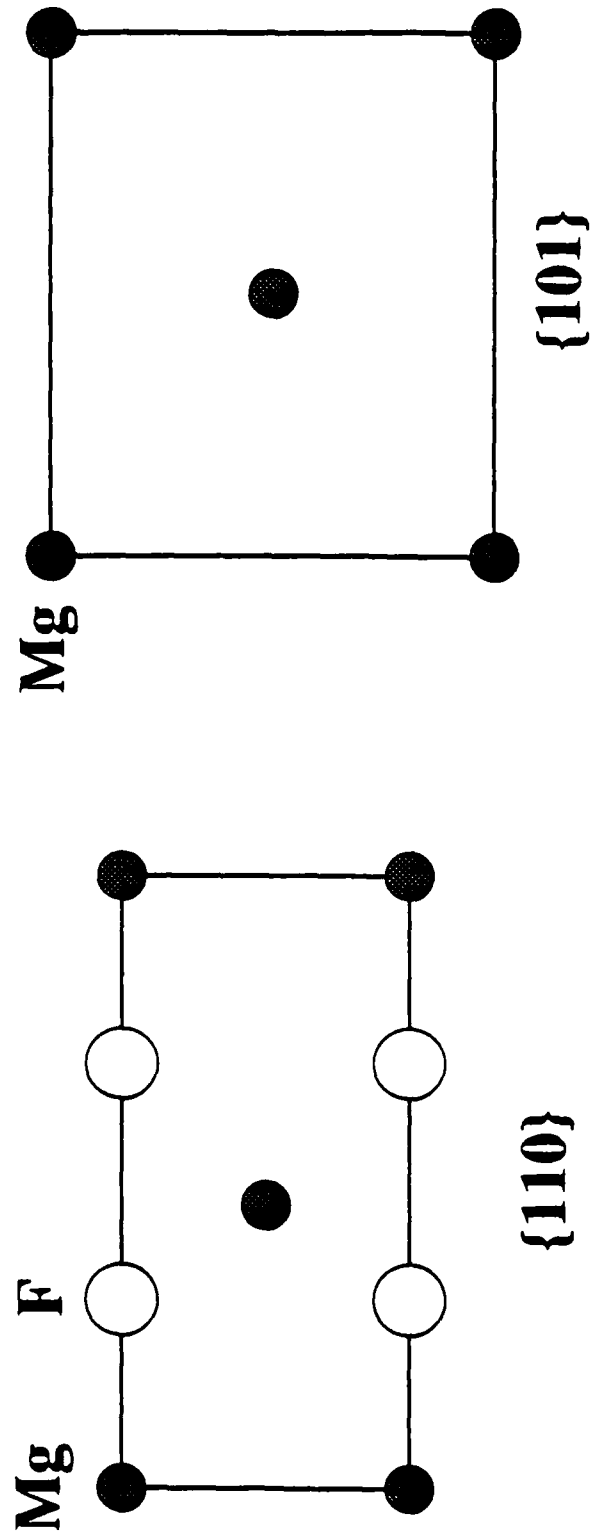


Fig. 4

XIII. Fracto-emission from fused silica and sodium silicate glasses

J.T. Dickinson, S.C. Langford, L.C. Jensen,
Physics Department, Washington State University, Pullman, WA 99164-2814

G.L. McVay
Battelle Pacific Northwest Laboratories, Richland, WA 99352

J.F. Kelso
Alcoa Technical Center, Alcoa Center, PA 15069

and

C.G. Pantano
Department of Materials Science, Pennsylvania State University, University Park, PA 16802

ABSTRACT

Fracto-emission is the emission of photons and particles due to the fracture of materials. In this paper we present characteristic intensity vs time measurements of photon emission (phE), electron emission (EE), positive ion emission (PIE), and neutral emission (NE) due to the fracture of fused silica and sodium trisilicate glass. We show, for example, that the trisilicate is a copious emitter of atomic Na and both atomic and molecular oxygen. The phE, EE, and PIE from the two glasses share a number of properties.

I. INTRODUCTION

The emission of particles and light due to fracture has been demonstrated for a wide variety of materials, including fused silica and a few silicate glasses.¹⁻³ Collectively, we refer to these emissions as fracto-emission (FE). In general, our interests focus on characterizing FE, understanding the emission mechanisms, and applying FE as a probe of failure processes. A number of the FE processes are related to the chemical reactivity of fracture surfaces, which is of fundamental interest in tribology and material/environment interactions. Fracture related surface chemistry can often dictate the useful life of a material.⁴ In geological situations, the fracture and wear of minerals (including those in glass phases) form chemical interfaces with gases and water involving extremely large surface areas and material exchanges. As discussed by

Freund⁵, these interactions can involve significant quantities of the components of planetary atmospheres.

In this paper we present recent measurements of photon emission (phE), electron emission (EE), positive ion emission (PIE), and neutral emission (NE) due to the fracture of fused silica and sodium trisilicate glass. Regarding NE, we focus on the emission seen at masses 23 and 32 involving sodium and oxygen, which play important roles in the surface chemistry of these materials.

II. EXPERIMENT

UV grade fused silica rod was obtained from Heraus-Amersil, Inc. (Suprasil II). Sodium trisilicate rod was prepared by melting sodium carbonate and quartz (Min-U-Sil) in a platinum crucible. Both sets of rod were nominally 4 mm in diameter. The samples were cut into 12 mm lengths and mounted in three point bend across a support span of 6.4 mm. The sample holder carried 20-24 samples in a carousel arrangement which could be mounted in a vacuum system and manipulated from outside. Experiments were carried out at a background pressure of 10^{-7} Pa.

The neutral emission from the sample was monitored with a UTI 100C quadrupole mass spectrometer (QMS) and a modified Bayard-Alpert ion gauge positioned 1.2 and 20 cm from the sample, respectively. Emission currents for the two detectors were 2 ma and 4.7 ma, respectively. The ion gauge was out of sight of the specimen; thus, only volatile gases contributed to the observed pressure changes. The electrometer outputs of these devices were digitized and recorded with a LeCroy Data Acquisition System. The response time of the QMS electrometer was typically 200 μ s; the ion gauge electronics response time was 40 ms. The applied force was monitored with a Sensotec Model 31 force transducer.

phE, EE, and PIE measurements were carried out in a separate vacuum system under similar conditions. phE was detected with an EMI Gencom 9924QB photomultiplier tube with a bialkali phosphor and a quartz window. EE and PIE were detected with a Galileo Electro-optics 4039 Channeltron electron multiplier (CEM). Both the photomultiplier tube and the CEM were mounted at a distance of 1-2 cm from the samples. The applied force was monitored with a Kistler 9202 quartz force transducer mounted behind the loading device. The photomultiplier tube and CEM outputs were pulse counted and summed in a multichannel scaler at 100 μ s intervals. The output of the force transducer was digitized and recorded at identical intervals. In all of our experiments, care was taken to minimize artifacts created by vibrations from the fracture event itself.

III. RESULTS

The neutral emissions which we have observed to date from fused silica and sodium trisilicate glass are summarized in Table I. By continuously scanning various mass ranges, we were able to estimate the relative magnitudes of the observed peaks and correlate them in time. On the basis of cracking fractions, we have made the indicated identifications. As noted in the table, some of these emissions are most intense immediately following fracture (P = prompt), while others are delayed to some extent (D = delayed). Several of the NE measurements were repeated with a shield between the sample and the ionizer of the mass spectrometer to ensure that the observed signals were not due to ejecta. Although the shield significantly reduced NE intensities, it did not affect their existence or time behaviors.

Both the silica and the trisilicate show mass 32 emission accompanying fracture. In Fig. 1, we show the mass 32 emissions from these materials for the first few ms following fracture. The times of fracture were determined from load measurements and are indicated with arrows. During this interval, the emissions are remarkably similar in

intensity and time behavior. The emission from silica is essentially complete after 10-20 ms. These peaks rise roughly in times given by the response time of our electronics, but fall slower than predicted. The initial mass 32 emissions from both glasses appear to be rising *with fracture* and showing a fairly rapid decaying emission after fracture. For the silica glass, this is the only mass 32 emission observed. Although the number of higher mass peaks examined is limited, all evidence suggests that this fast mass 32 peak is due to molecular oxygen emission.

In stark contrast, mass 32 emission from the trisilicate continues to "erupt" hundreds of milliseconds later, as shown in Fig. 2a. A portion of this emission is displayed on an expanded time scale in the inset, showing that the intense emission of Fig. 2a consists of a series of well defined peaks. These peaks are not periodic. The later stages of decay in mass 32 emission parallels the decay of the total pressure following fracture, shown in Fig. 2b. Fast mass scan data acquired during and following fracture of the trisilicate glass show that mass 32 is again due to O_2 emission. O_2 partial pressures calculated from the detected mass current are in agreement with the total pressure measured by the Bayard-Alpert ion gauge. Thus, the bulk of the pressure change during this sustained emission appears to be due to O_2 . Some contribution from mass 16 is probable.

The initial O_2 emission peaks from both fused silica and the trisilicate appear to have a common origin strongly associated with fracture. This is supported by the observed similarity in the dependence of O_2 emission intensity vs strength. In Fig. 3 we show a plot of the measured mass 32 intensities vs load at fracture for the two glasses. Data from the two types of glass fall on the same straight line. We have observed similar behavior in a number of fracto-emission studies, including the neutral emission from the fracture of glassy polymers.^{6,7}

The initial emission of mass 16 from these glasses is typically an order of magnitude more intense than the emission of mass 32 at fracture. Mass scans after the

fracture of sodium trisilicate show mass 16 signals about 30 times more intense than those predicted from cracking fractions of CH_4 (estimated from mass 15 peak), O_2 , and other oxygen containing gases. Emission curves with the QMS tuned to mass 16 are similar to the O_2 emission curves, with the exception of the much more intense initial emission peak. We therefore conclude that atomic oxygen is also a very important product emitted from the fracture surface.

Significant quantities of neutral sodium emission are observed from the fracture of the sodium trisilicate; most of it is emitted long after fracture. The time behavior of the mass 23 emission from sodium trisilicate is similar to the O_2 emission from the same material, as may be seen by comparing Figures 2a and 4. However, the mass 23 emission is less regular than the mass 32 emission, showing a greater tendency to spike. Frequently, the mass 23 emission lacked the initial peak at fracture displayed consistently in mass 32. Further, the mass 23 emission from the stronger samples tended to be significantly less intense. Mass scans (one scan every 80 ms) during this sustained emission show only small peaks at other sodium containing compounds so that the majority of the mass 23 signal can be assigned to atomic sodium desorbing from the fracture surface. The delayed emission of sodium is quite similar to the emission of atomic Mg from the fracture of single crystal MgO reported earlier⁸.

The sodium content of the fused silica is quite low (0.04 ppm by weight). Fractures of the silica performed with the mass spectrometer set at mass 23 generally showed no response. On occasion, small peaks four orders of magnitude smaller than from the sodium trisilicate were seen; we attribute these small responses to artifacts which appear to be due to vibrations in the system created by the fracture.

phE, PIE, and EE from these glasses persist long after fracture. Measurements on nanosecond time scales indicate that these emissions probably peak during the fracture event itself, which typically lasts a few microseconds. With the exception of spikes, these emissions then decay monotonically. PIE and EE emission curves from

different samples of sodium trisilicate glass are compared in Fig. 5. In both signals, the emission rose to a maximum in a single channel (i.e., $< 10^{-4}$ s). These measurements were made with a shield positioned between the samples and the detector. With the shield in place, the signal measured with a negative bias on the entrance to the CEM detector may be confidently attributed to positive ions, as opposed to high energy electrons or excited neutrals. Similarly, with a positive bias on the CEM entrance, only negatively charged particles are detected, which we tentatively attribute to electrons only.

Although the shield blocked much of the emission, the CEM was saturated during the early portion of these decays. PIE and EE measurements on smaller samples (lower emission intensities) suggest that the intensities during this saturation drop about three orders of magnitude. Note that the PIE and EE decays from the trisilicate glass follow similar kinetics. Although generally more intense, the kinetics of the PIE and EE decay from fused silica are similar to those from sodium trisilicate.

Simultaneous measurements of pH_E and PIE from fused silica are shown in Fig. 6. The PIE from both materials display spikes, as noted above. Some of these spikes are reflected in the pH_E, although they appear to be obscured by the high pH_E "background." The smoothed decays show distinctly nonexponential kinetics, similar to phosphorescence decay. pH_E intensity, like the initial O₂ emission, appears to increase with sample strength, although this is obscured somewhat by detector saturation. In contrast, PIE emission tended to decrease with sample strength. Generally, the emissions from fused silica samples were more intense than those from sodium trisilicate samples of comparable strength. During the early stages of pH_E decay, this difference was especially pronounced, at least a factor of 50. Table II summarizes these findings.

IV. DISCUSSION

A number of phenomena may contribute to the observed FE. As fracture proceeds, the material behind the crack tip is left in a highly excited state. Vibrational excitations with effective surface temperatures in excess of 1000 K may be possible.⁹⁻¹¹ Immediately behind the crack tip, energetic broken bonds render the surface chemically active.^{12,13} Intense electron bombardment may further excite the surface.¹⁴ The recombination of charge carriers trapped during these initial excitations can continue long after fracture.⁸ In some glasses, residual stresses¹⁵ and high pressure phases^{16,17} near the surface may leave the surface mechanically stressed as well.

High surface temperatures during fracture can be expected to lead to thermal desorption of neutrals and thermal excitation of charge carriers in defect states. The thermal pulse should decay quickly, within picoseconds after heating stops. This is orders of magnitude shorter than the crack propagation time, which is a few microseconds in the case of a fast crack. In static heating experiments, Kelso and Pantano observed significant evaporation of Na metal from sodium trisilicate glass at 750 C.¹⁹ Thermal desorption may play an important role in releasing species from the fracture surfaces during fracture. However, the decays of even the prompt, initial neutral emissions are far longer than expected from such a thermal spike. Other mechanisms must apply to NE occurring significantly after the fracture event.

Thermal excitations at fracture probably play an important role in phE, EE, and PIE as well. The phE spectra observed by Chapman and Walton while cutting various silicate glasses resembled black body radiation.¹¹ The cutting process is believed to take place by repeated fracture. During fracture, intense thermal radiation may be the dominant source of phE. Thermal excitation of charge carriers from surface defect sites is also likely. Charge carriers trapped in high lying states during this initial excitation would be available to participate in a number of delayed emission processes.

As fracture proceeds, the newly broken bonds quickly react to minimize the surface energy. The molecular dynamics simulations of Levine and Garofalini indicate that this initial reorganization is essentially complete in 1-2 ps for fused silica and sodium trisilicate glass.^{12,13} Slower reactions are expected on times scales greater than 10-20 ps. They predict a surface excess of oxygen on fused silica fracture surfaces, and a surface excess of sodium on sodium trisilicate fracture surfaces. A subsurface excess of oxygen is expected in the trisilicate. Ion scattering spectroscopy on fresh fracture surfaces (which requires several minutes to perform) has confirmed the existence of a surface excess of oxygen on fused silica,¹⁹ and a sodium excess on sodium trisilicate glass. An excess of oxygen and sodium at the fracture surfaces of these glasses would facilitate the emission of O, Na, and O₂.

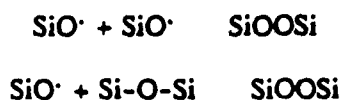
Fracture in the silicate glasses may induce local charge separation and even microdischarges in the crack tip, although we have not yet attempted to verify this experimentally. However, we have observed long wavelength electromagnetic signals associated with the fracture of single crystal quartz which we attribute to microdischarges near the crack tip. Several workers have observed surface charges of both signs on fresh fracture surfaces of alkali halides.^{20,21} Charge separation in the silicate glasses may be possible over small patches of new surface due to the piezoelectric character of the quartz structure,²² which is reproduced locally in the structure of these glasses. Once EE begins, further stimulation of the surface could result as the emitted electrons are accelerated back toward surface regions of positive charge.¹⁴ This self-bombardment of the surface [a form of "self-flagellation"] is certainly a potential source of PIE and NE by electron stimulated desorption (ESD) which we have previously proposed.

ESD is known to result in the emission of H⁺, Na⁺, and O⁺ from soda silica glasses.^{23,24} Si⁺ is also observed after the formation of a Si-rich surface layer. The changes in the stoichiometry of fused silica surfaces under electron bombardment are

believed to be the result of oxygen emission.²⁵ The similarity of EE and PIE would be explained by ESD induced PIE since the latter would depend directly on the EE emission rate.²⁶

After fracture, phE takes place due to the recombination of electrons trapped at surface E' centers (dangling Si sp^3 orbitals) and holes trapped at nonbridging oxygen (NBO) p orbitals. Zink, Beese, and Schindler have observed 430 nm phE characteristic of this recombination associated with the fracture of silica core optical fibers.²⁷ Surface E' centers have been identified as participants in thermally stimulated electron emission processes in fused silica.²⁸ This EE is attributed to thermal excitation of E' centers with energies near the top of the band gap, or to Auger emission involving doubly occupied E' centers. We have found that a simple one trap, one recombination center model, assuming recombination via thermal activation of a mobile charge carrier, describes the decay of phE and EE from MgO quite well.⁸ The similarity in the shape of the decay curves for the phE from the silicate glasses suggests that such a model will also explain these emissions.

The emission of O_2 from these fracture surfaces suggests that defect reactions are taking place milliseconds after fracture is complete. Levine and Garofalini's molecular dynamics work predict significant concentrations of NBO's and strained siloxane bonds (Si-O-Si structures), both chemically active defects.¹² The NBO's are themselves likely precursors for NE and PIE involving O. The peroxy radical would seem to be a likely precursor for O_2 emission. Butyagin suggests that excited NBO's are mobile on the fracture surface, and thus are able to participate in chemical reactions with other NBO's and strained siloxane bonds.²⁹ Reactions of the form



may lead to the production of peroxy radicals on the surface, and eventual formation of molecular oxygen. Butyagin also observes that the reactivity of fractured quartz with

respect to hydrogen gas decreases with time after fracture. He attributes this to a surface relaxation that takes 1-10 ms at room temperature. This relaxation time is consistent with the duration of initial mass 32 emission in this work. Hydrogen is believed to react with NBO's and strained siloxane bonds, both of which would be consumed in reactions which result in mass 32 emission.

The energy released in these defect reactions may be sufficient to lead to desorption, perhaps assisted by electron-hole recombination. If carrier recombination at a NBO site were to result in a transition to a nonbonding state, the affected oxygen could be desorbed.

The similarity of the prompt, initial O₂ emissions from silica and sodium trisilicate suggests that the chemistry of their fracture surfaces is similar as well. The atomic percentage of oxygen in the bulk of the two materials is similar, 67% in the fused silica and 58% in the trisilicate, so significant differences in emission are not expected on this ground. The formation of molecular oxygen would seem to require mobile NBO's. It is likely that sodium ions are only weakly bound to NBO's associated with trapped holes, and thus may often be shed in the excitation process. If the mobile NBO's are excited, as Butyagin suggests, then they may be relatively free from the influence of sodium. Then, even in the trisilicate glass, the reaction of NBO's to form peroxy groups could proceed relatively unimpeded.

The reduced intensity of phE, EE, and PIE in the soda glass may reflect lower concentrations of charge carrier traps. Fracture surfaces of sodium glasses are expected to have a surface excess of sodium,¹³ which may occupy defect sites preferentially. The lower glass transition temperature of the soda glass may also be associated with more complete reconstruction under fracture induced heating. The tendency of sodium and oxygen ions to occupy defects sites may also explain the reduced mass 23 and PIE emissions in the strong samples of both materials. The intense phE decays from the stronger samples imply that the fracture of strong samples, which would tend to be at

higher crack velocities, create higher densities of surface defects. Some of these defects may trap relatively mobile, loosely bound sodium and oxygen ions that would otherwise participate in NE or PIE.

Although the identities of the ions participating in the PIE have not been established, the most likely candidate is the O^+ ion in both glasses. At fracture, the mass 16 peak at fracture is the only relatively intense NE component whose time behavior is at all similar to that of the PIE. However, Na^+ may contribute to PIE from the trisilicate glass, especially in the later stages of decay. O^+ would be readily trapped by the E' centers, which are essentially oxygen vacancies, which would be consistent with the trap mechanism for reduced PIE intensities in the stronger samples. Time-of-flight measurements, feasible on glass fibers,² may clarify this point by establishing the PIE mass(s).

The delayed emission of O_2 and Na in the sodium glass may well have its basis in surface chemistry. However, a mechanical mechanism also suggests itself. Silica, an "anomalous" glass, generally fails catastrophically at the onset of crack growth. Fractured material tends to have low residual stresses.¹⁵ Conversely, sodium trisilicate is a "normal" glass. Normal glasses often display slow, subcritical crack growth, even in vacuum. Deformed material is characterized by relatively high residual stresses.¹⁵ In this study, extensive crack branching was observed in both glasses. In the trisilicate glass, arrested crack branches may have had the opportunity to undergo slow growth after fracture under the influence of residual stresses. Slow crack growth is often associated with low pHE intensities and thus low densities of surface defect formation. This may explain the relatively intense O_2 and Na emission from sodium trisilicate glass long after fracture.

Mechanical energy may also be released during phase changes accompanying fracture. Castano, Takamori, and Shafer observed small crystalline regions of alpha-cristobalite, typically 70-80 nm in length, in crushed fused silica similar to that used in

this study.¹⁶ These crystallites were attributed to metastable beta cristobalite retained in the glass during manufacture. They believe that the observed alpha phase resulted from a phase change induced by the relief of pressure during crushing. Crystallites in the region of the fracture surface may undergo a similar phase change. This transformation is associated with a volume increase, which may result in further microcracking. Interestingly, Phillips has suggested that these crystallite boundaries are associated with peroxy structures.¹⁷ Other investigators have identified the peroxy structure as an intrinsic defect in fused silica.³¹ We hope to investigate soon the dependence of O and O₂ emission intensities on peroxy group concentration.

V. CONCLUSION

We have observed the emission several neutral and charged particles emitted during and after the fracture of fused silica and sodium trisilicate glass. phE, EE, and PIE rise to their maximum intensities within microseconds of the fracture event and thereafter decay. We attribute emission during the decay to recombination of charge carriers trapped at surface defect sites. In contrast, NE exhibits more complex kinetics, including a relatively slow rise. The emission mechanism is not clear, but may be ESD or chemically induced desorption.

Molecular and atomic oxygen is observed from newly fractured samples of both materials, rising to a peak soon after fracture. The trisilicate glass also displays an intense, lasting mass 32 peak beginning somewhat later. Sodium emission, mass 23, is also observed from trisilicate glass. Its time behavior is less reproducible than that of the oxygen peaks, but is generally quite intense and often delayed from fracture. The delayed emissions from the trisilicate glass may be due to delayed crack growth or to rate limited chemical reactions on the fracture surface. Both oxygen and sodium related

emissions are probably facilitated by local concentrations of these ions at the fracture surface.

The correlation between initial mass 32 emission with load at fracture suggests that the local chemical and electrical environment of a fracture surface is strongly affected by the macroscopic stress and strain in the region of the propagating crack. This observation complements previously reported relationships between the chemical state of a silicate glass surface and its fracture behavior.⁴ The presence of free oxygen at the fracture surface may have important implications concerning wear and corrosion at metal-glass rolling or rubbing contacts.

The emission of neutral molecules and charged particles provides information on the chemical and electronic processes accompanying fracture. The time scales involved in this study ranged from fractions of milliseconds to seconds, far in excess of the time scales typical of molecular dynamics calculations, and far less than the time required to perform a typical surface analysis. These emissions thus provide information about surface processes occurring after fracture and before the application of surface analytical tools.

IV. ACKNOWLEDGMENTS

This work was supported by the Ceramics and Electronics Materials Division of the National Science Foundation, Grant No. DMR 8601281, and the Washington Technology Center. We wish to thank Larry Pederson and Don Baer of Pacific Northwest Laboratories and Friedemann Freund, NASA-Ames Research Center for useful discussions.

REFERENCES

1. J. T. Dickinson, E. E. Donaldson, and M. K. Park, *J. Materials, Sci.* 16, 2897 (1981).
2. J. T. Dickinson, L. C. Jensen, and M. K. Park, *J. Mat. Sci.* 17, 3173 (1982).
3. A. J. Walton, *Adv. in Physics* 26 887 (1977).
4. C. G. Pantano, in *Strength of Inorganic Glass*, C. L. Kurkjian, ed., (Plenum Press, New York, 1985), pp. 37-66.
5. F. Freund, personal communication.
6. J. T. Dickinson, L. C. Jensen, and S. K. Bhattacharya, *Makromol. Chem., Macromol. Symp.* 7, 129 (1987).
7. L. C. Jensen, J. T. Dickinson, unpublished data.
8. S. C. Langford, J. T. Dickinson, and L. C. Jensen, *J. Appl. Phys.* 62, 1437 (1987).
9. R. Weichert and K. Schonert, *Mech. Phys. Solids* 26, 151 (1978).
10. P. J. Miller, C. S. Coffey, and V. F. DeVost, *J. Appl. Phys.* 59, 913 (1986).
11. G. N. Chapman and A. J. Walton, *J. Appl. Phys.* 54, 5961 (1983).
12. S. M. Levine and S. H. Garofalini, *Materials Res. Soc. Symp. Proc.* 61, 29 (1986).
13. S. H. Garofalini and S. M. Levine, *J. Am. Ceramic Soc.* 68, 376 (1985).
14. J. T. Dickinson, L. C. Jensen, and A. Jahan-Latibari, *J. Vac. Sci. Technol. A* 2, 1112 (1983).
15. S. M. Wiederhorn, H. Johnson, A. M. Diness, and A. H. Heuer, *J. Am. Ceramic Soc.* 57, 336 (1974).
16. V. M. Castano, Takeshi Takamori, and M. W. Shafer, *J. Am. Ceramic Soc.* 70, C-77 (1987).
17. J. C. Phillips, *Phys. Rev. B* 35, 6409 (1987).
18. J. F. Kelso and C. G. Pantano, *J. Vac. Sci. Technol. A* 3, 1343 (1985).
19. J. F. Kelso, C. G. Pantano, and S. H. Garofalini, *Surface Sci.* 134, L543 (1983).
20. M. I. Kornfeld, *J. Phys. D* 11, 1295 (1978).
21. J. Wollbrandt, U. Bruckner, and E. Linke, *Phys. Status Solidi A* 77, 545 (1983).
22. B. P. Chandra, *Nucl. Tracks* 10, 225 (1985).
23. Y. X. Wang, F. Ohuchi, and P. H. Holloway, *J. Vac. Sci. Technol. A* 2, 732 (1984).

24. F. Ohuchi and P. H. Holloway, *J. Vac. Sci. Technol.* 20, 863 (1982).
25. Simon Thomas, *J. Appl. Phys.* 45, 161 (1974).
26. J. T. Dickinson, L. C. Jensen, and M. K. Park, *Appl. Phys. Lett.* 41, 443 (1982).
27. J. I. Zink, William Beese, and J. W. Schindler, *Appl. Phys. Lett.* 40, 110 (1982).
28. V. S. Kortov, *Jap. J. Appl. Phys. Suppl.* 24-4, 65 (1985).
29. P. Yu. Butyagin, *Reactivity of Solids* 1, 345 (1986).
30. A. Arora, D. B. Marshall, and B. R. Lawn, *J. Non-Crystalline Solids* 31, 415 (1979).
31. E. J. Friebele, D. L. Griscom, and M. Stapelbroek, *Phys. Rev. Lett.* 42, 1346 (1979).

FIGURE CAPTIONS

- Fig. 1. Mass 32 emission (a) and total pressure change (b) due to fracture of sodium trisilicate glass. The inset of (a) shows a portion of the emission on an expanded time scale. The extent of the expanded portion is indicated by the bar above the time axis of (a). The arrows mark the time of fracture.
- Fig. 2. Mass 32 emission from the fracture of fused silica and sodium trisilicate glass. Only the first 12 ms of emission are shown. The arrows mark the time of fracture.
- Fig. 3. Peak mass 32 emission as a function of load at fracture for both glasses. In the case of the trisilicate glass, the value plotted is that of the initial mass 32 peak.
- Fig. 4. Mass 23 emission from sodium trisilicate glass. The arrow marks the time of fracture.
- Fig. 5. EE and PIE from sodium trisilicate glass. Fracture occurred at time $t = 0$.
- Fig. 6. pH_E and PIE from fused silica. Fracture occurred at time $t = 0$.

TABLE I. Masses and identities of neutral emission observed following fracture of fused silica and sodium trisilicate glass. Emissions peaking promptly at fracture are indicated with a P, while emissions peaking somewhat later are indicated with a D. Very weak or occasionally observed emissions are indicated with an *. Peaks not as yet measured are marked nm.

MASS	SiO ₂	Na ₂ O-3SiO ₂	PROBABLE IDENTITY
2	P	P	H ₂
16	P	P	O, some O ₂
18	P	P	H ₂ O
23	D*	P,D	Na
28	P	P	Si, some CO
32	P	P,D	O ₂
39	nm	D*	NaO
44	nm	P	SiO, some CO ₂
60	nm	D*	SiO ₂

Table II. A summary of the major fracto-emission components from silica and sodium trisilicate glasses.

EMISSION	RELATIVE CHARACTERISTICS	
	Fused Silica	Sodium Trisilicate
Initial O ₂	very similar for both glasses; prompt; typ. duration: 10 ms; intensity increases linearly with sample strength (see Fig. 2).	
Delayed O ₂	does not occur	strong; long lasting; erratic fluctuations typ. duration: 400 ms.
Atomic O	very strong; similar to O ₂ emission.	very strong; similar to O ₂ emission.
Atomic Na	zero to extremely small; probably artifact.	strong; typ. duration: 600 ms; erratic fluctuations; intensity <u>decreased</u> with sample strength.
phE	very intense; typ. duration: 1s; evidence of spikes after fracture; intensity increased with strength.	intense, but smaller. typ. duration: 500 ms. evidence of spikes after fracture; intensity increased with strength.
EE	very intense; typical duration: 1 s; spikes after fracture;	intense; typical duration: 500 ms; spikes after fracture;
PIE	typical duration: 1 s; spikes after fracture; intensity <u>decreased</u> with strength	typical duration 500 ms; spikes after fracture; intensity <u>decreased</u> with strength.

NEUTRAL EMISSION FROM SODIUM TRISILICATE

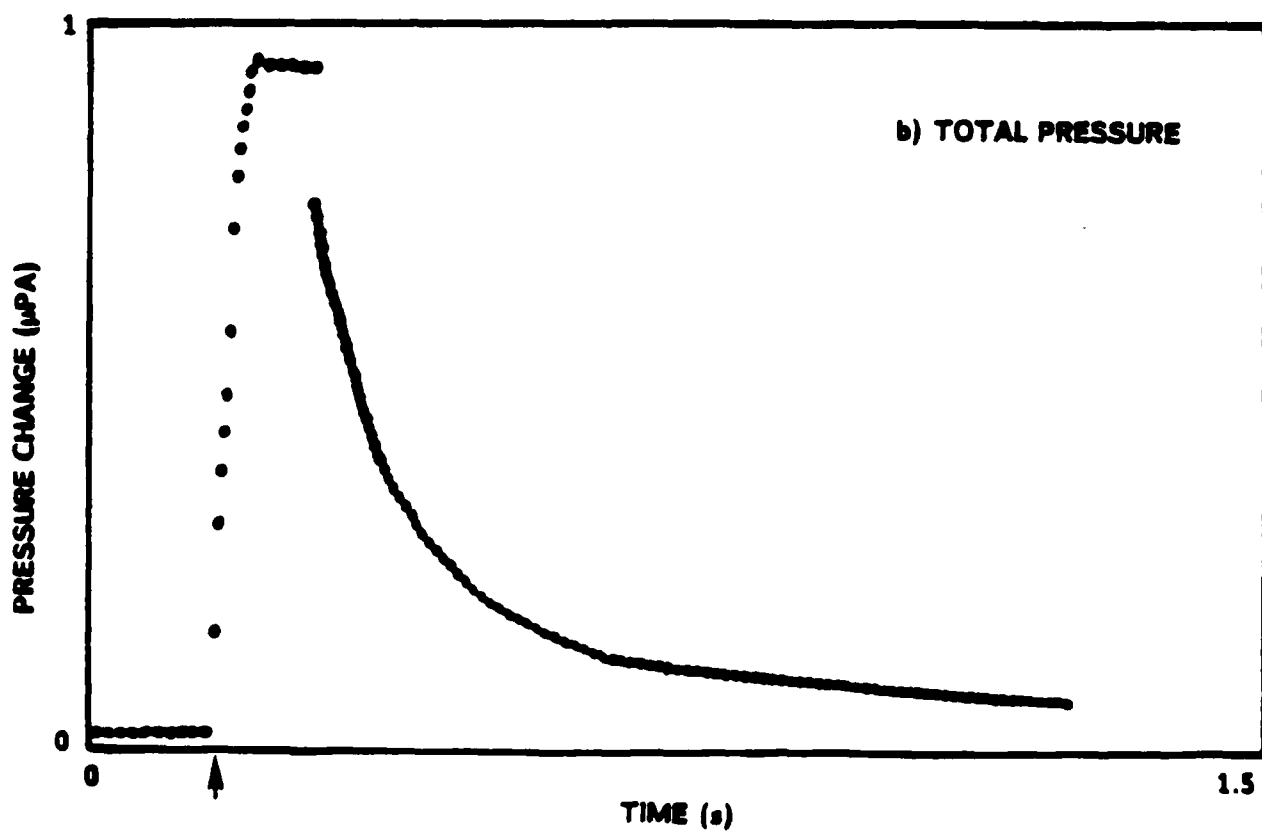
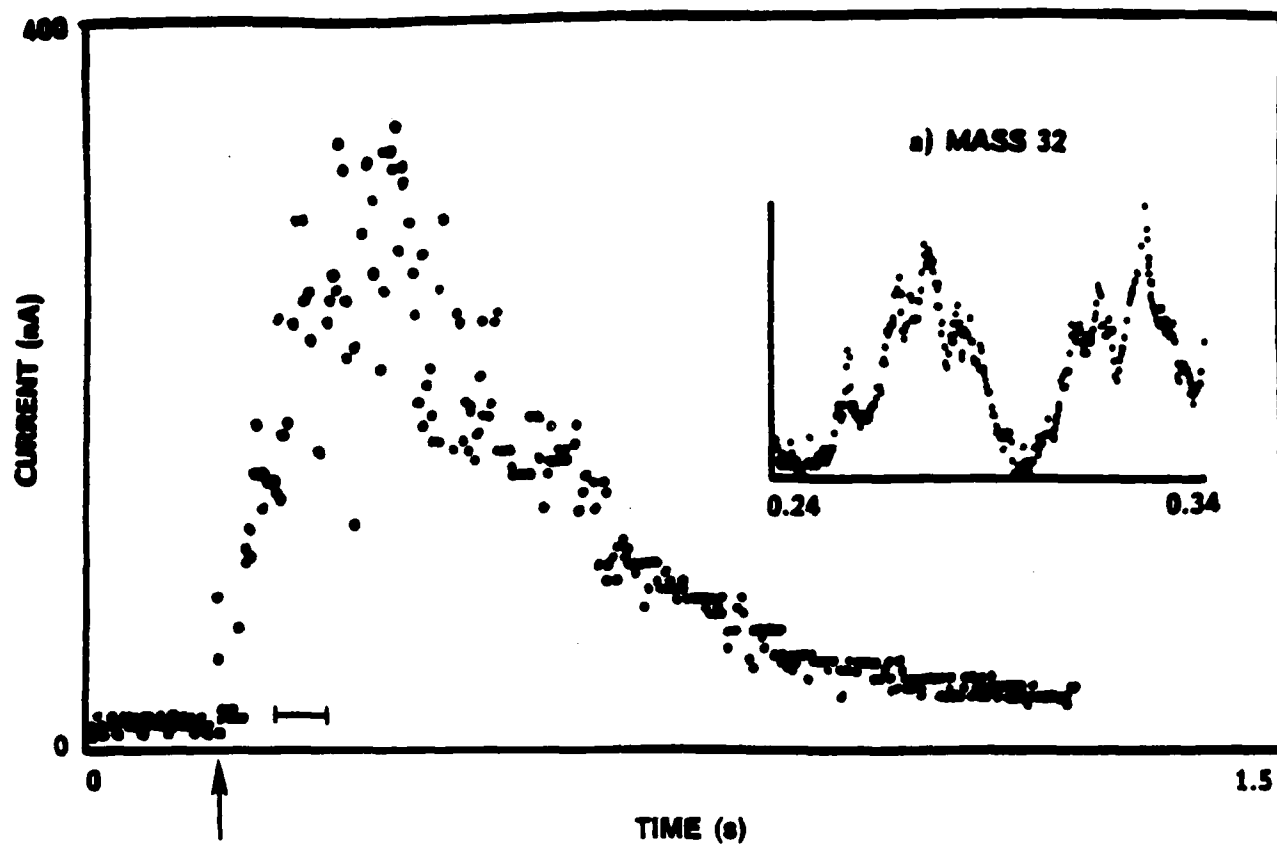


Fig. 1

INITIAL M32 EMISSION

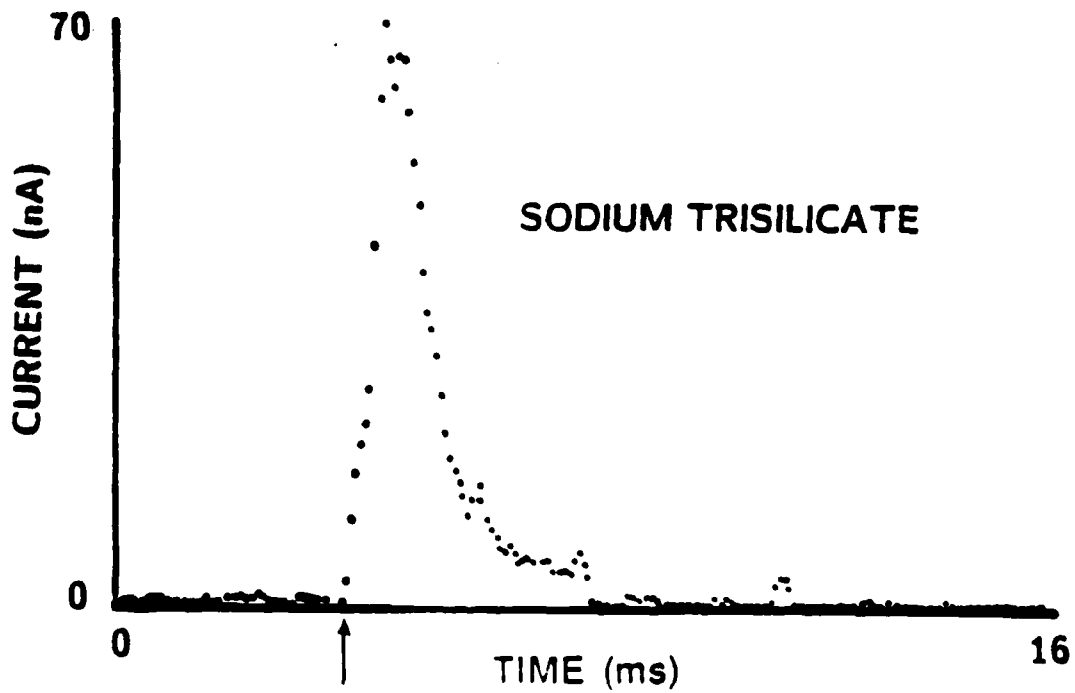
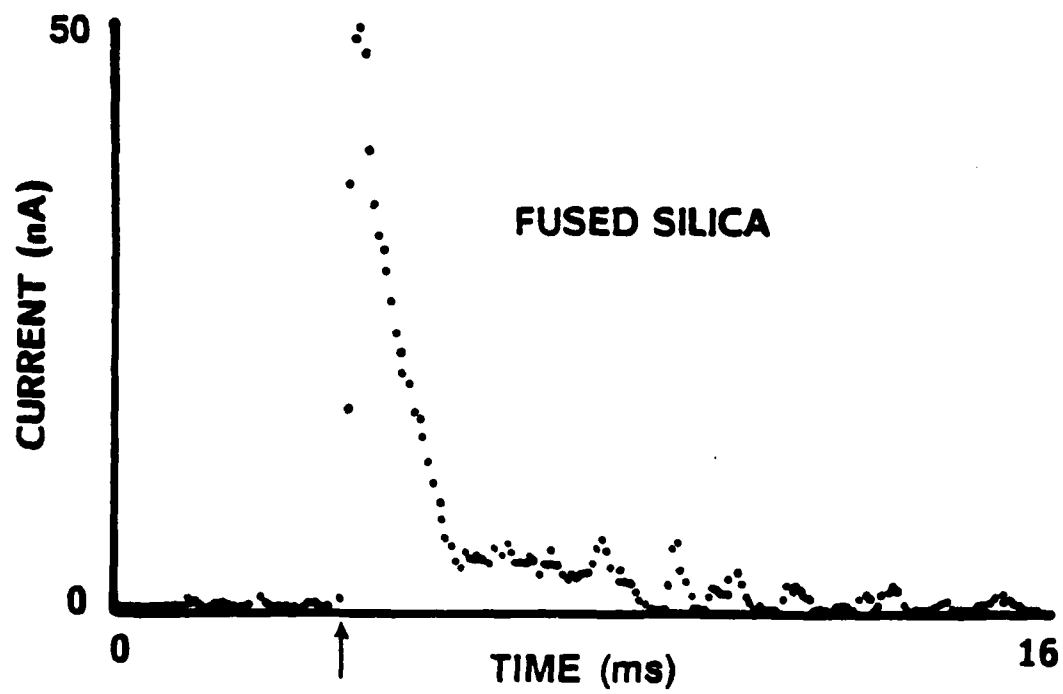


Fig. 2

INITIAL M32 PEAK CURRENT VERSUS LOAD AT FRACTURE

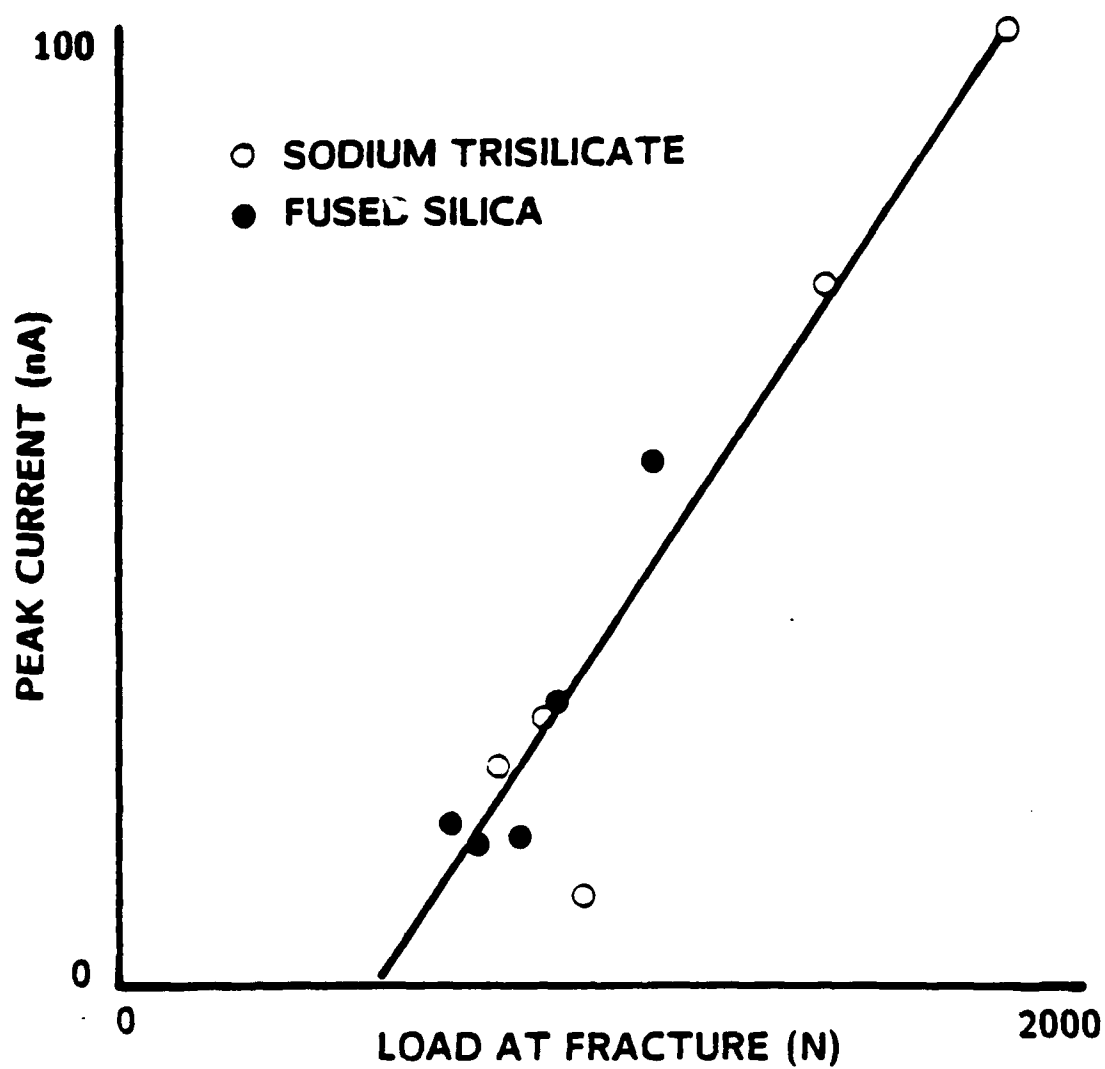


Fig. 3

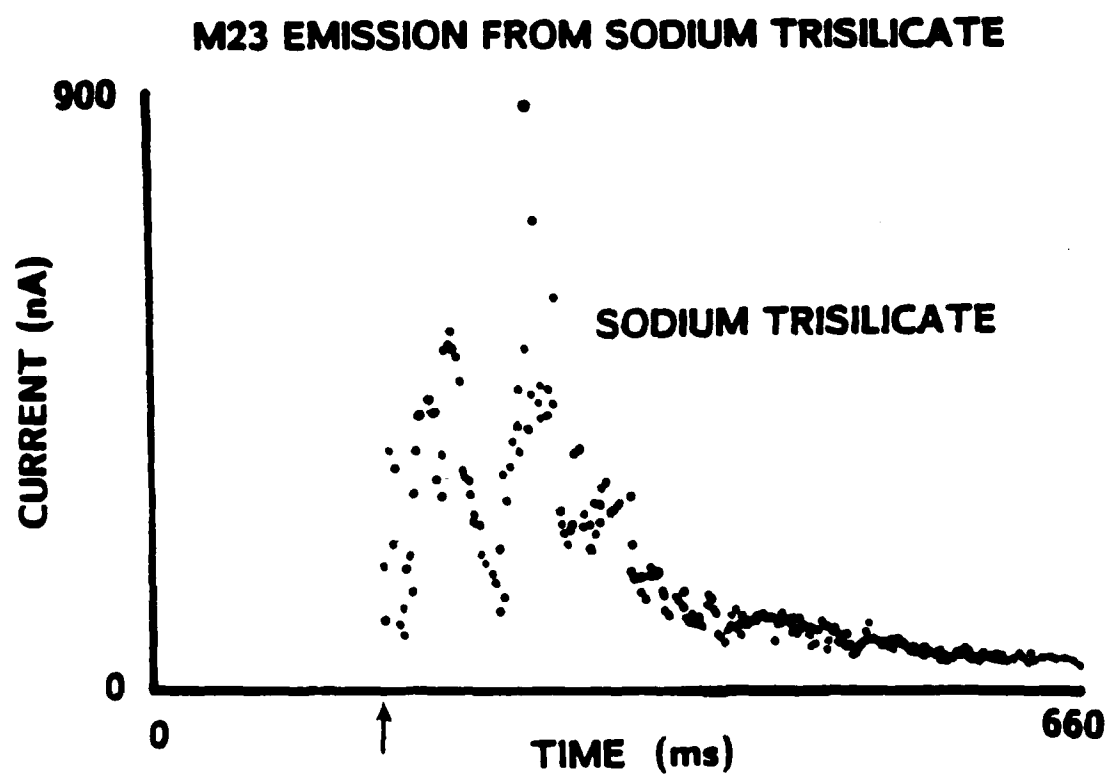


Fig. 4

EE AND PIE FROM SODIUM TRISILICATE GLASS

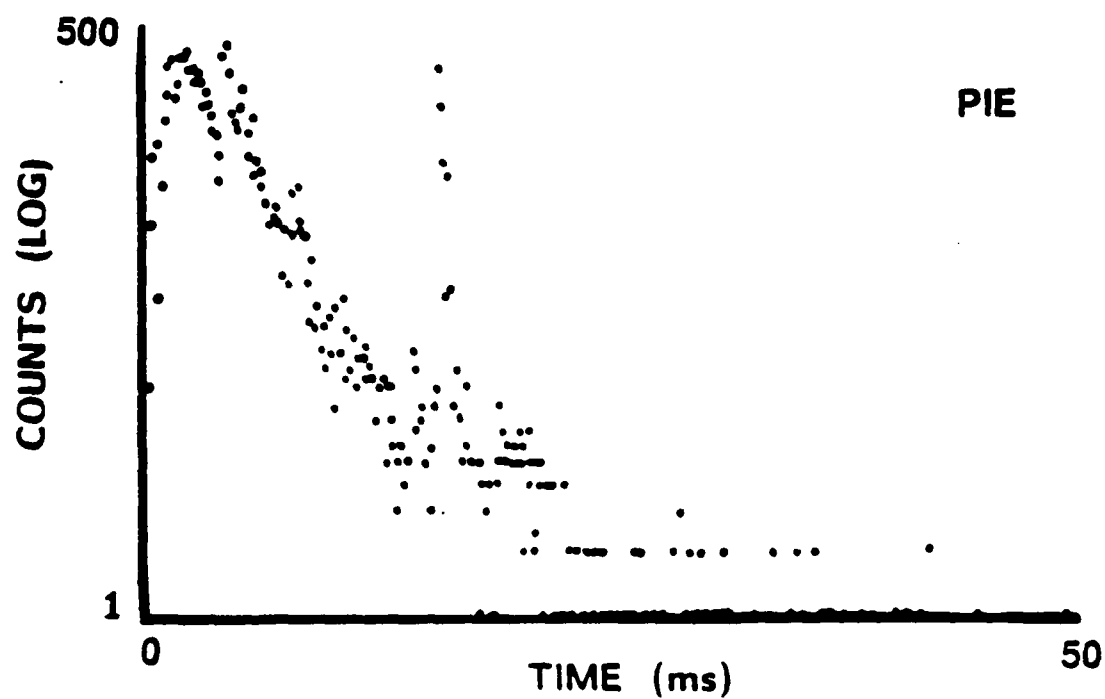
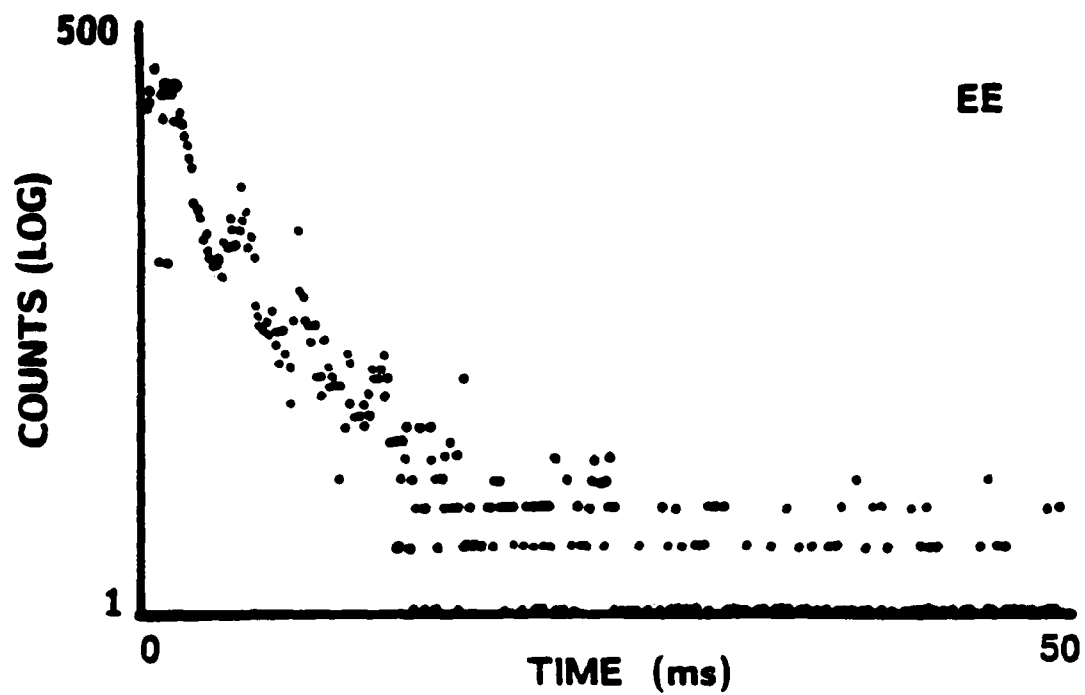


Fig. 5

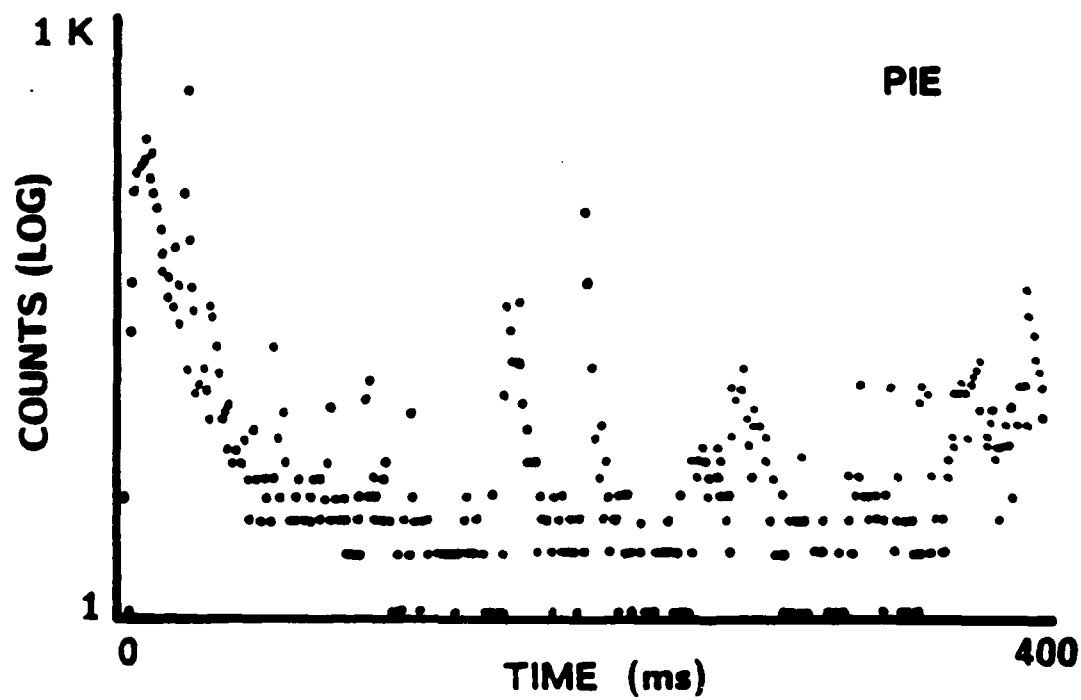
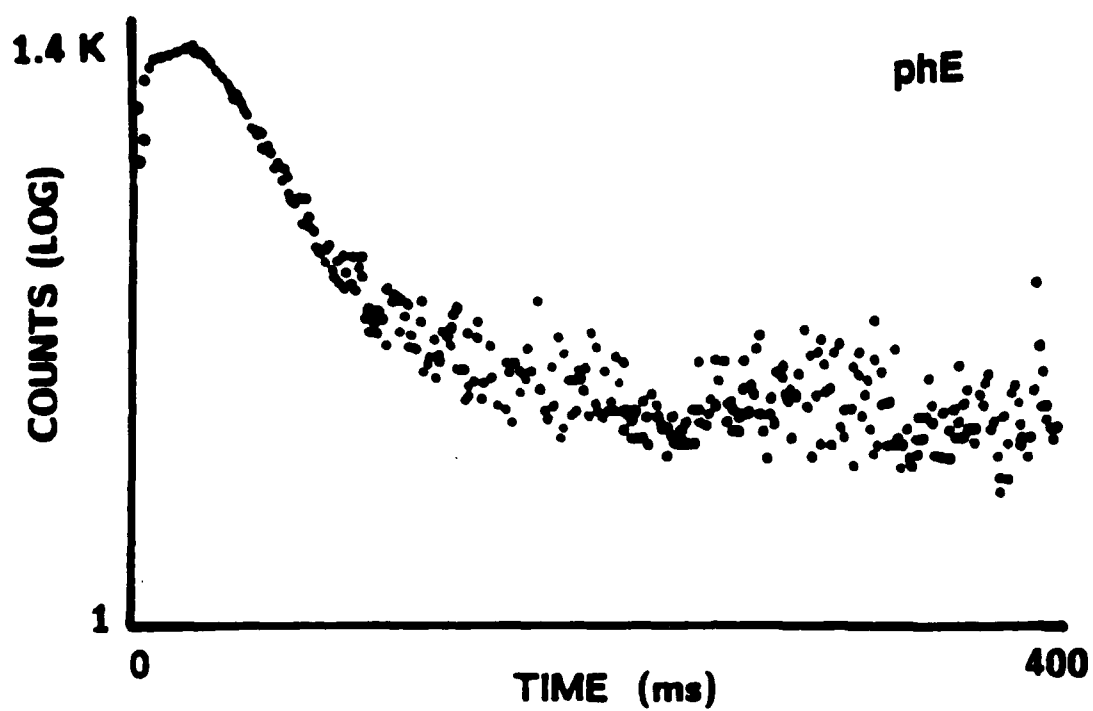
pHE AND PIE FROM FUSED SILICA

Fig. 6

XIV. Positive ion emission from the fracture of fused silica

S. C. Langford, J. T. Dickinson, L. C. Jensen

Physics Department, Washington State University, Pullman, WA 99164-2814

L. R. Pederson

Pacific Northwest Laboratories, Richland, WA 99352

Positive ion emission was observed during and after the fracture of fused silica using time-of-flight techniques and quadrupole mass spectroscopy. Emissions attributed to Si^+ , SiO^+ , and Si_2O^+ were observed during the fracture event itself. An emission mechanism for the silicon containing ions was proposed involving the mechanical scission of at least three of the bonds joining a silica tetrahedron to the rest of the silica network. The production of silicon-containing ions suggests the activity of nonequilibrium processes which may contribute significantly to the fracture energy of fused silica. A long lived emission was attributed to the ESD of O^+ .

I. INTRODUCTION

The emission of photons, electrons, neutral molecules, and ions during and after fracture provides information on atomic processes occurring at the crack tip and on the newly formed fracture surface. We refer to deformation and fracture related emissions collectively as *fracto-emission*. Particularly in the silicate glasses, recent progress in the understanding of fracture has required consideration of bond breaking processes on the atomic scale.¹⁻³ Due to the difficulty of fast time scale measurements of atomic properties, much of the experimental work has been restricted to slow crack growth. Fracto-emission, which is readily amenable to study on very short time scales, may offer opportunities for measurements of nanosecond phenomena accompanying crack propagation.

In previous work we have observed photon emission (phE), electron emission (EE), and positive ion emission (PIE), as well as the emission of long wavelength electromagnetic radiation and neutral molecules from the fracture of fused silica.⁴ phE and EE persist many seconds after fracture and are especially intense during crack growth. The identity and intensity of the emitted atomic and molecular species are expected to reflect the nature of the bond breaking processes associated with fracture.

In this work we focus on PIE, which is efficiently detected as no intermediate ionization step is required for charged particles. PIE measurements are readily made on times scales small relative to the duration of fracture. Further, as we shall show, time-of-flight techniques and quadrupole mass spectroscopy can be used to identify the emitted ions. We have observed relatively intense PIE during fracture which we attribute to Si^+ , SiO^+ , and Si_2O^+ . We propose that mechanical bond scissions are responsible for their creation. The ability of fused silica to deform by the rotation and elongation of its tetrahedral units may facilitate these scissions. A relatively weak PIE signal attributed to O^+ persists long after fracture. We attribute this post-emission to electron stimulated desorption.

II. EXPERIMENT

Flame fused, synthetic silica ingot and rod (Suprasil II) were obtained from Heraeus-Amersil. Rectangular samples, 1.6 x 6 x 12 mm, were cut from the ingot and mechanically polished. The rod, nominally 3 mm in diameter, was broken into 12 mm lengths. The samples were mounted in a carousel apparatus which allowed them to be rotated into place between a loading mechanism and the detectors. The carousel was mounted in a vacuum system maintained at pressures of about 10^{-6} Pa. The samples were loaded in three point bend at a rate of 70 $\mu\text{m/s}$. The rod samples were significantly stronger than the plate samples due to their surface finish, and generally yielded much more intense PIE.

Total PIE measurements were made with a Galileo Electro-Optics 4039 Channeltron electron multiplier (CEM) mounted about 10 mm in front of the tensile surface of the sample. The voltage on the front cone of the CEM ranged from -500 V to -3000 V, with a constant potential difference maintained between the front and back. A large increase in the observed signal with increasing bias voltage indicated that the signal was almost entirely due to positive ions, rather than high energy electrons or excited neutral molecules. Intense PIE was also observed in previous experiments with a physical barrier between the sample and the CEM⁴ which proved conclusively that positive ions were indeed emitted.

A time-of-flight (TOF) tube and a quadrupole mass spectrometer (QMS) were used to identify the masses of the emitted ions. The TOF studies utilized a 25.4 cm flight tube mounted 7 mm in front of the samples' tensile surface. A CEM mounted behind the tube detected the ions. The voltage on the flight tube was varied from -100 V to -5000 V. The front cone of the CEM was maintained at a potential at least 1000 V below that of the flight tube. At flight tube voltages less negative than -1000 V, plate samples did not yield sufficient intensities for mass determination. Rod samples yielded sufficient PIE intensities for mass determination at flight tube voltages up to -100 V. The duration of fracture resulted in large timing uncertainties ($\sim 1 \mu\text{s}$), so that the longer flight times associated with less negative potentials were desirable.

In order to confirm the mass identifications and to examine the time distributions of the individual mass peaks, PIE measurements were made with the QMS. The entrance to the QMS was about 25 mm from the tensile face of the sample. To provide for efficient ion collection, the ionizer was removed and replaced by a short flight tube

maintained at -2300 V and mounted between the sample and the spectrometer. In the presence of the resulting electric field, the electrostatic potential energy of ions emitted from the sample was below system ground. Detection of these ions required that the flight path through the quadrupole be maintained at a negative potential. Therefore, the QMS focus plate and rods were floated at a DC potential of -280 V. The QMS backplate, which was normally grounded to the vacuum system, had to be removed. To further increase the detection efficiency, a focus plate with a large, 12 mm diameter aperture was used at the entrance to the mass filter. The resolution of the QMS was tested using a W filament containing alkali metal (heating it produces K^+ ions by surface ionization) mounted in front of the flight tube. The width of the mass 39 (K^+) peak was about ± 2 AMU.

Simultaneous pH_E and mechanical load measurements were made during each of the above experiments. An EMI Gencom 9924QB photomultiplier tube mounted about 30 mm to one side of the sample was used to monitor pH_E. Despite the fairly poor detection geometry, the photomultiplier tube had to be operated at low gains to avoid saturation. The pH_E measurements provided an accurate time reference relative to the initiation and completion of fracture. Load measurements were made with a Kistler 9202 quartz transducer mounted inside the vacuum system behind the loading device.

The CEM and photomultiplier tube outputs were amplified, then digitized at 10 ns intervals using a LeCroy data acquisition system. The force measurements were digitized at 1 μ s intervals. The data were acquired continuously during loading, the new data being stored in place of the old at regular intervals. The load signal was differentiated and the resulting rapid load drop at fracture was used to stop the digitizers.

III. RESULTS

The total PIE and pH_E from a strong plate sample is shown in Fig. 1. In this and subsequent figures, the time scale indicates the time relative to the onset of pH_E. The onset of pH_E is an excellent indication of the onset of catastrophic crack growth. At these PIE intensities, the CEM gain is decidedly nonlinear. However, the CEM output still reflects changes in PIE intensity as evidenced by occasional peaks in the decay, often associated with pH_E peaks. Accounting for the TOF, the PIE intensity generally rises until the pH_E curve reaches its shoulder. Experience suggests that in plate samples, the pH_E shoulder is associated with major changes in crack propagation,

such as the arrival of the main crack at the end of the sample. pHIE immediately following the shoulder is often due to branch cracks which continue to propagate briefly after the main crack completes its course. The decaying PIE in this region of the pHIE curve suggests that the ion escape geometry for the crack branches is generally poor. Post-fracture examination of the samples shows that branch cracks often do not extend through the entire thickness of the sample. Peak ion emission generally occurs as the main crack branch completes its path through the sample. A decaying, intense emission persists for several μs . We have observed similar behavior in PIE from the fracture of a brittle epoxy.⁵ Fracture of some silica samples showed intense oscillations in PIE intensity during the initial rise, which we attribute to rapid variations in crack velocity.

Figure 2 shows a TOF record taken with -5000 V on the flight tube. The indicated mass identifications were made on the basis of a number of TOF measurements made at various flight tube voltages. The high collection efficiencies at -5000 V result in more reproducible results than measurements at less negative voltages. This curve shows some early spikes which we associate with mass 16. Comparing the measured TOF's with those predicted for species native to fused silica, we identified the major emissions with the following masses:

Mass 16	O^+
Mass 28	Si^+
Mass 44	SiO^+
Mass 72	Si_2O^+

The intensities of the lower mass peaks, especially that of mass 16, were greatly enhanced at the more negative flight tube potentials. This is presumably due to better detection efficiencies at the more negative potentials.

The width of the peaks in the TOF record is on the order of 400 ns, much less than the duration of the fracture event. PIE measurements with various ion optics suggest that the angular distribution of ion velocities from plate samples is a strong function of time during fracture. Using the calculated TOF's and the mass assignments shown in Fig. 2, the time of ion emission is found to coincide with the shoulder in the pHIE curve. This was observed in the majority of experiments at high flight tube voltages, and suggests that the detected ions were emitted at the completion of fracture along the tensile side.

The absolute uncertainty of these mass determinations is rather high, ~ 6 AMU in the mass region of interest. This is largely due to the large uncertainty in the time of ion emission, about 1 μs . The uncertainty in the

arrival times of the mass peaks, however, is much less, about 0.2 μ s. Once a consistent set of mass assignments was made, comparison of spectra taken at different tube voltages allowed reduction of the uncertainty in the relative masses to 1-2 AMU. In order to resolve the ambiguity in our TOF mass determinations, we performed QMS measurements.

PIE measurements made with the QMS confirmed the existence of emission at masses 16, 28, 44, and 72 AMU. Figure 3 shows pH_E and PIE signals observed at masses 44 and 72. These signals are among the most intense we observed. At their peaks, the CEM is again saturated. The duration of PIE at these masses is similar to the duration of the major portion of the pH_E peak. Although the complex ion optics of the system make TOF calculations difficult, the more intense signals show a consistent trend in TOF, as shown in Fig. 3.

The bulk of the emission at mass 16 consisted of single counts. In contrast to PIE at other masses, counts were often observed 10's and sometimes 100's of μ s after fracture. The mass resolution of the quadrupole appeared to be significantly lower in the region of mass 16. As the resolution of the quadrupole is a function of ion energy, this could be explained if the kinetic energy of the mass 16 emission were significantly greater than that of the more massive ions. The mass 16 TOF through the QMS is also consistent with higher kinetic energies relative to the other masses.

Measurements at masses 32 and 60 were not convincing. Some emission was occasionally observed at mass 60, but the observed TOF's suggest that these signals were due to intense PIE of mass 44 and 72. By far the most intense emission observed was that of mass 44, corresponding to the emission of SiO^+ .

IV. DISCUSSION

The observed PIE at masses 16, 28, 44, and 72 AMU are readily identified with O^+ , Si^+ , SiO^+ , and Si_2O^+ , respectively. In earlier work, we observed electron stimulated desorption (ESD) of O^+ from SiO_2 at incident electron energies of 1 keV.⁶ This emission is also expected on theoretical grounds.⁷ Each of the Si-containing ions has been observed in Secondary Ion Mass Spectroscopy (SIMS) studies of thin SiO_2 films.⁸ Significantly, signals corresponding to O_2^+ , SiO_2^+ , and SiO_3^+ were not observed, either in the SIMS work or in ours.

The bulk of O^+ emission is most likely the result of ESD. Previous work has shown that intense, long lived phE and electron emission (EE) accompany the fracture of fused silica. These emissions can persist for 10's of seconds.⁴ Data taken on shorter time scales indicate that PIE persists at least 100's of ms after fracture, with a decay similar in form to that of EE. It is reasonable to expect that the fresh fracture surfaces experience intense electron bombardment, particularly if the fracture surfaces are locally charged. Although the intensity of O^+ emission is apparently rather low during fracture, it is the only species repeatedly observed well after fracture. We believe that the long lived PIE emission observed in previous work on SiO_2 is due to ESD of O^+ . However, we cannot rule out that during fracture, O^+ production may involve another mechanism.

The production of locally charged surfaces during the fracture of an amorphous material is not necessarily expected, and deserves further investigation. Locally charged surfaces would not only provide for intense electron bombardment, but would also result in the acceleration of desorbed positive ions. This acceleration would result in O^+ ions with kinetic energies larger than expected on the basis of the applied electric field. This is consistent with our observations of an unusually low QMS TOF at mass 16.

The emission of silicon containing ions requires multiple bond breaking. The large free volume of fused silica is associated with some unusual degrees of freedom which favor mechanical bond breaking. The silica structure may be viewed as a network of interconnected silica tetrahedra, each with a Si atom in the center and O atoms at the four corners. Each tetrahedron is thus normally joined to four others at the corners. These tetrahedra form a network of five to seven member rings. A considerable variation in Si-O bond angle is noted in silica even in the absence of applied stress. Silica deforms by the rotation and stretching of the tetrahedra making up the rings. These deformation modes are associated with the unusual behavior of silica and other 'anomalous' glasses under high pressures as well as fracture.^{9,10} As the structure is not periodic, the distribution of stresses among the bonds near a crack tip may vary considerably.

One possible sequence of deformation and bond breaking is schematically presented in Fig. 4. Consider a silica tetrahedron near the crack tip, oriented such that two adjacent tetrahedra are on one side of the crack tip and two on the other. As the stress increases, the tetrahedron at the tip will rotate to minimize the stress on the most highly strained pair of bonds, as shown in Fig. 4(a). For the sake of clarity, these motions have been grossly exaggerated. Eventually, one of these bonds will break, and the tetrahedron will reorient so as to minimize the stress on the next

most highly strained pair of bonds, as shown in Figs. 4(b) and (c). In most cases, fracture will be complete with the next broken bond, as two tetrahedra on one side of the crack will be pulling against the one remaining bond on the other side. However, the geometry of the lattice may occasionally favor the breaking of a bond on the strong side, as shown in Fig. 4(d). Another rotation will precede the scission of one of the remaining bonds, shown in Fig. 4(e). Thus in some cases, fracture can produce silica tetrahedra with three broken bonds. Ion emission and subsequent escape requires one more broken bond, as indicated in Fig. 4(f). Depending upon where the corner oxygen atoms go, the resulting species would be Si^+ or a polyatomic ion.

Several factors may enhance the probability of multiple bond breaking at the crack tip. Spatial nonuniformities in stress have already been noted. Phonon interactions can result in temporal variations, although it may be conceptually easier to view these as simple collisions or thermal effects. The scission of nearby bonds are expected to result in vibrationally and rotationally excited states. The breaking of the last bond may involve a mechanical, whiplash-like effect. Due to the high probability of reaction with nearby dangling bonds, the last bond must be broken quickly, say within a few periods of molecular vibration.

Haneman and Lagally¹¹ have recently proposed that the cleavage of crystalline Si along (111) planes involves the scission of three bonds per surface atom. They suggest that Si bonds are more likely to break in a shear mode than in a longitudinal mode; that is, silicon bonds oriented parallel to the applied stress can accommodate higher stresses than bonds oriented along other directions. This tendency reflects the highly directional character of the covalent bonds. In crystalline Si, the broken bonds reform with nearby atoms on the fracture surface, i.e., the surface reconstructs. We propose that Si-O-Si bonds in silica respond similarly to applied stresses and that the disorder of the silica lattice hinders the immediate reforming of multiple broken bonds, thus allowing emission of Si-containing species.

Such processes could account for the production of free Si^+ , SiO^+ , SiO_2^+ , SiO_3^+ , and perhaps SiO_4^+ during fracture. The apparent lack of SiO_n^+ for $n > 1$ may be due to the lack of appropriate bond breaking sequences to form these fragments. However, their absence in fracto-emission may be for the same reason they are absent in the SIMS observations,⁸ which we assume is due to electronic instabilities in these particular ions. In preliminary work, we have shown that negative ions are also emitted during fracture. Since a number of negatively charged, larger mass

fragments are seen in SIMS spectra, we are encouraged to investigate the identity of these negative ions in the near future.

Mass 72 emission, due to Si_2O^+ , could conceivably take place by a more convoluted process similar to that shown in Fig. 4. Simple computer simulations of fracture in two dimensional triangular lattices with randomly placed defects can yield short chains of atoms.¹² Although these models are suspect once bond breaking begins, the sequence of bond breaking, deformation, and subsequent bond breaking is similar to that proposed here. A multiple bond breaking process such as that proposed by Haneman and Lagally for the fracture of Si may enhance the probability of Si_2O^+ emission markedly. Si_2O^+ is observed in SIMS studies of glass surfaces,⁸ suggesting that detection is not hindered by electronic instability.

Although the energy required for PIE during fracture is a very small fraction of the fracture energy, the emission itself is indicative of highly dissipative processes. The mechanical relaxation following bond breaking in this mode should be quite dissipative. This mechanism for energy dissipation is much more localized than the shear deformations displayed by the 'normal' glasses and many crystalline materials. This would help explain the intense pH_E and EE accompanying the fracture of fused silica, relative to that of sodium trisilicate glass.⁴ The rotational and stretching modes of deformation in fused silica may accommodate large local strains prior to the final bond scission, which may contribute to the experimentally observed fracture energy of silica. The fracture energy of fused silica is much higher than the estimated energy of free surface formation.¹³

V. CONCLUSIONS

We have observed the emission of O^+ , Si^+ , SiO^+ , and Si_2O^+ accompanying the fracture of fused silica. SiO^+ is the dominant positive ion species. 10 μs after fracture, only O^+ was observed, suggesting that the long lasting PIE reported in earlier work is due to O^+ . ESD can account for the persistent emission of O^+ . The other species are emitted during the fracture event itself. We propose that the emission of the silicon containing species involves a series of mechanical bond scissions. The unusual deformation modes exhibited by fused silica and other anomalous glasses may facilitate this bond scission.

Photon and particle emission during fracture reflect various aspects of the fracture process and the resulting surfaces. In this study photon emission was used to mark the overall progress of fracture. The bond breaking activity required for the production of silicon containing species suggests an unusually high degree of molecular motion at the crack tip, which may contribute to the fracture energy. The proposed ESD of O^+ would require the production of charged surfaces during fracture. Our measurements indicate that there are a number of interesting phenomena occurring at or near the crack tip and on the newly formed fracture surfaces over a variety of distance scales and over interesting time ranges (ns to ms). An understanding of these processes will potentially lead to new insights into the fracture process.

ACKNOWLEDGMENTS

This work was supported by the Ceramics and Electronic Materials Division of the National Science Foundation under Grant DMR 8601281, the Office of Naval Research, Contract No. N00014-87-K-0514, the McDonnell Douglas Independent Research and Development Program, and the Washington Technology Center.

REFERENCES

1. B. R. Lawn, *J. Materials Sci.* **10**(3), 469 (1975).
2. B. R. Lawn, K. Jakus, and A. C. Gonzalez, *J. Am. Ceramic Soc.* **68**(1), 25 (1985).
3. T. Michalske and B. C. Bunker, *Sci. Am.* **257**(6), 122 (1987).
4. J. T. Dickinson, S. C. Langford, L. C. Jensen, G. L. McVay, J. F. Kelso, and C. G. Pantano, *J. Vac. Sci. Technol. A* **6**(3), 1084 (1988).
5. J. T. Dickinson, L. C. Jensen, and S. K. Bhattacharya, *Makromol. Chem., Macromol. Symp.* **7**, 129-152 (1987).
6. J. T. Dickinson, M. A. Loudiana, and A. Schmid, to appear in *Proceedings of the International Symposium on Adhesion, Sealants, and Coatings for Space and Harsh Environments*, Plenum Press.
7. M. L. Knotek and Peter J. Feibelman, *Surf. Sci.* **90**(1), 78 (1979).
8. K. Nakamura, H. Hirose, A. Shibata, and H. Tamura, *Jpn. J. Appl. Phys.* **16**(8), 1307 (1977).
9. S. M. Wiederhorn, H. Johnson, A. M. Diness, and A. H. Heuer, *J. Am. Ceramic Soc.* **57**(8), 336 (1974).
10. F. M. Ernsberger, in *Elasticity and Strength in Glasses*, D. R. Uhlmann and N. J. Kreidl, eds., (Academic Press, New York, 1980) pp. 1-19.
11. D. Haneman and M. G. Lagally, *J. Vac. Sci. Technol. B* **6**(4), 1451 (1988).
12. D. J. Srolovitz and P. D. Beale, *J. Am. Ceramic Soc.* **71**(5), 362 (1988).
13. S. M. Wiederhorn, *J. Am. Ceramic Soc.* **52**(2), 99 (1969).

FIGURE CAPTIONS

- FIG. 1. a) Total PIE and b) accompanying phE during the fracture of fused silica. Time $t = 0$ has been chosen to coincide with the initial rise in phE.
- FIG. 2. a) PIE TOF data and b) accompanying phE. The arrows in the PIE diagram indicate the calculated TOF's for the indicated masses, assuming an emission time marked by the arrow in the phE diagram.
- FIG. 3. phE (bold lines) and mass selected PIE (fine lines) accompanying fracture for masses 44 and 72.
- FIG. 4. Proposed mechanical mechanism for the production of a silicon ion during fracture. No attempt has been made to accurately represent the bonding of the silicate tetrahedra to the rest of the silica structure.

Total PIE and phE from Fracture of Fused Silica

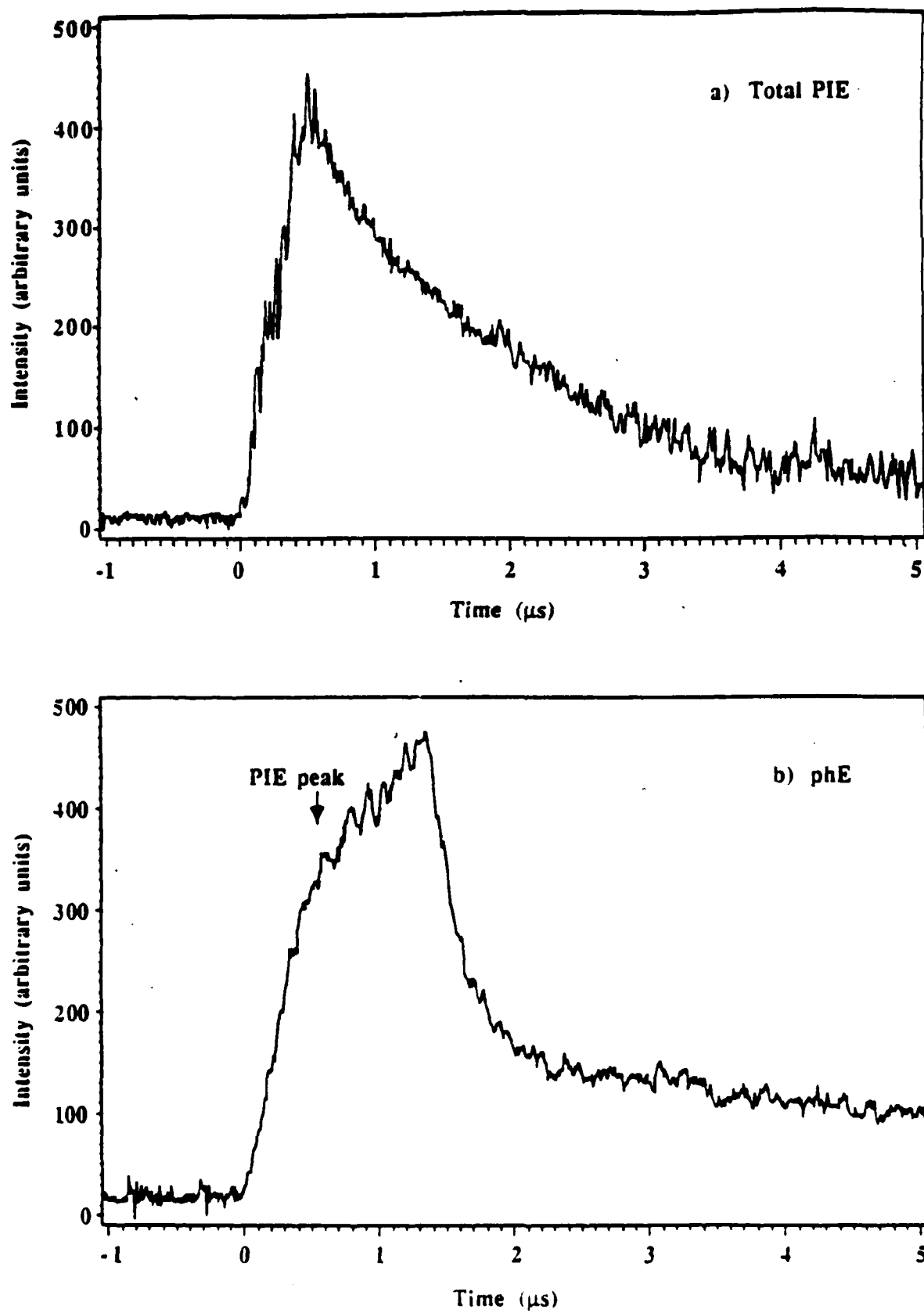


Fig. 1

PIE Time-of-Flight and phE from Fracture of Fused Silica

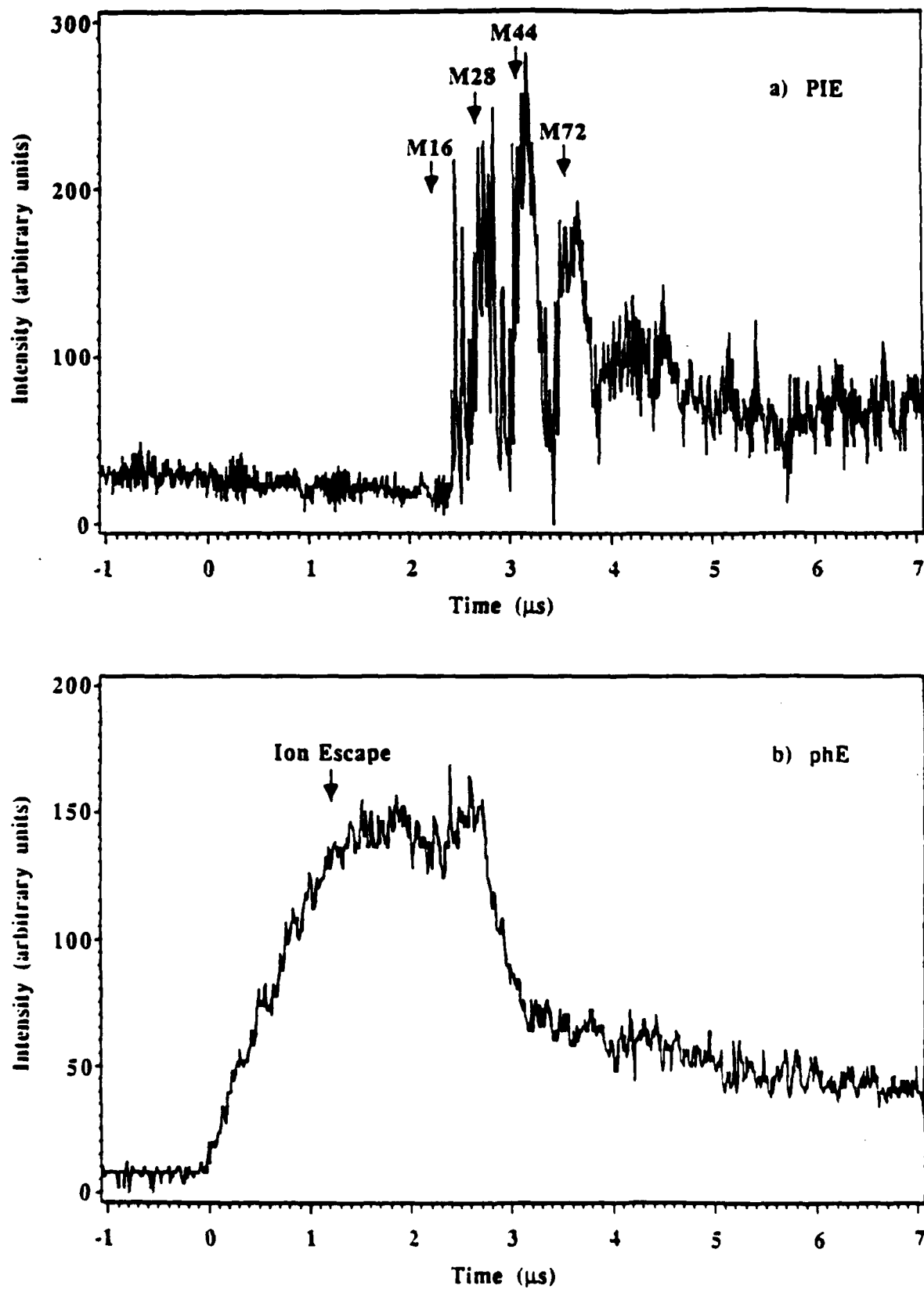


Fig. 2

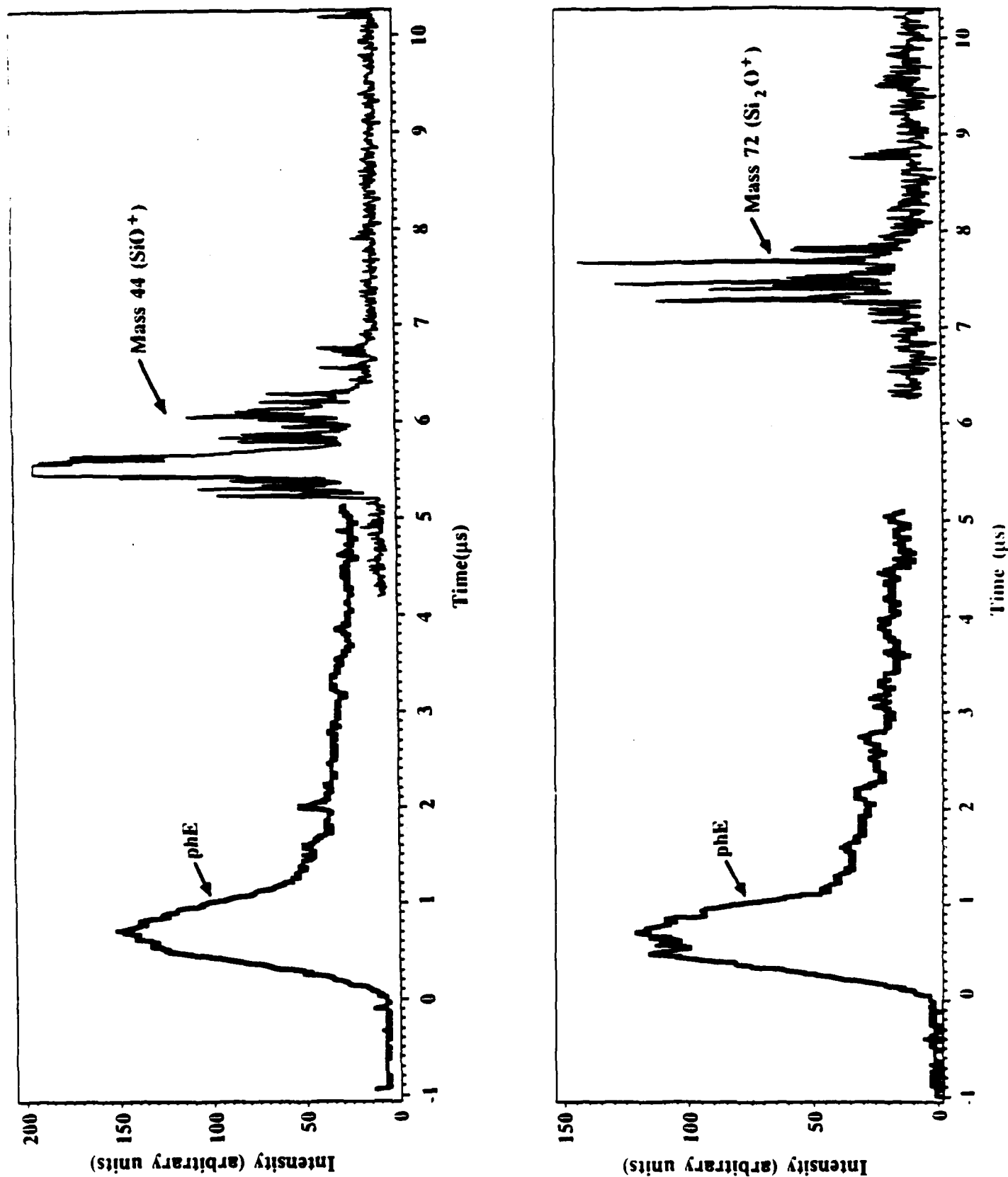


Fig. 3

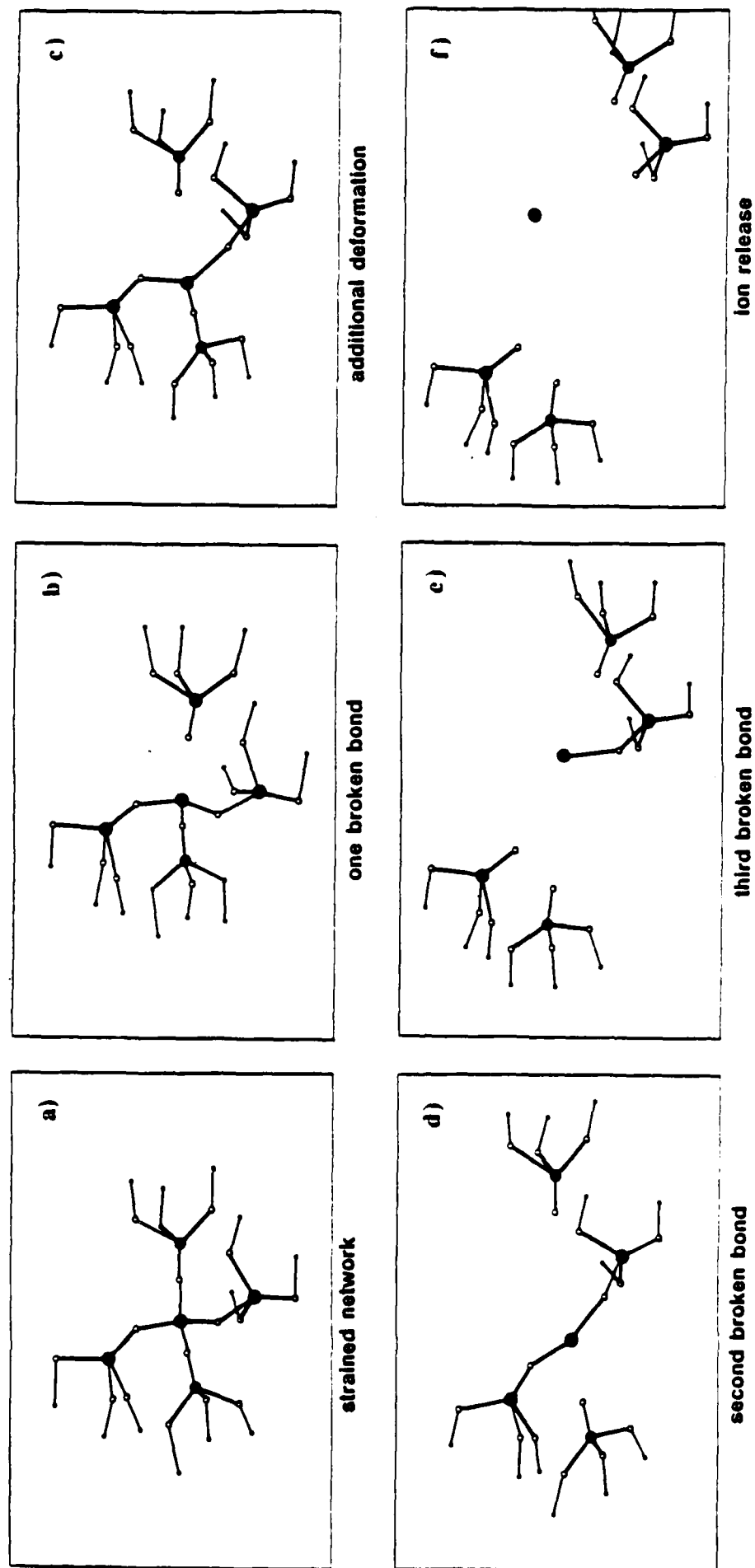
Si^+ FROM SiO_2 

Fig. 4

XV. Fracto-Emission from High Density Polyethylene: Consequences of Abrasion

J. T. Dickinson and S. C. Behler
Department of Physics
Washington State University
Pullman, WA USA 99164-2814

J. Fuhrmann and L. Nick
Institut für Physikalische Chemie
der Technischen Universität Clausthal
Arnold-Sommerfeld Str. 4
D-3392 Clausthal-Zellerfeld
Federal Republic of Germany

ABSTRACT

We examine the emission of electrons (EE) and positive ions (PIE) from high density polyethylene from tensile deformation at strain rates on the order of 30%/s. In particular, we focus on the role of small amounts of frictional effects on the polymer at the edges of the clamps due to slippage during elongation. When such slipping is eliminated, the deformation-induced particle emission vanishes. Thus, the pre-failure EE and PIE appear not to be due to bond scissions occurring due to tensile deformation of the polymer but to abrasion which occurs during this slipping. We discuss the role of bond breaking during a) macroscopic fracture (which produces a very short burst of emission) and b) during tribological loading (which produces intense, longer lasting emission signals after stimulation).

I INTRODUCTION

Fracto-Emission (FE) is the emission of particles (e.g., electrons, ions, neutral species, and photons) due to the deformation and failure of a material. A number of researchers have reported the observation of charged particle emission from tensile deformation of polymers. Polyakov and Krotova¹ first observed electron emission (EE) during the extension of Gutta Percha. Zakrevskii and Pakhotin^{2,3} observed pre-failure EE from elongation of polyethylene, polyethylene terephthalate, polyurethane rubber, and polycaprolactam. Kurov et al.⁴ observed pre-failure EE from tensile deformation of notched, unfilled EPD epoxy. Fuhrmann et al.^{5,6} observed pre-failure EE and positive ion emission (PIE) from high density polyethylene. Most of these measurements were at relatively high strain rates (5-10 mm/s for initial sample lengths of ~ 20 mm). This pre-failure emission is sometimes referred to as mechano-emission.

An extremely important aspect of these results is the possible use of these emissions to measure the rate of bond breaking during the deformation process prior to failure. Measurements of unpaired spin densities as a function of deformation show indirectly that bond scissions are indeed occurring as the polymer is strained.⁷ However, one must be very careful in determining the origin of the fracto-emissions observed. We have re-examined the EE and PIE from the tensile deformation and fracture of high density polyethylene and found that the observed emissions are very sensitive to the type of clamps used to transfer the load to the sample. In this paper, we shall show that for this particular material the origin of the pre-emission is due to frictional loading of the polymer due to minute amounts of slipping in the clamps and accompanying abrasion of the polymer. When slipping is eliminated, a characteristic, reproducible burst of emission is observed coincident with fracture, followed by a fairly rapid decay on the order of a few seconds in duration. We attribute these emissions to fracture induced bond scissions, similar to those previously reported. In addition, we discuss some of the properties of the abrasion-induced emission, in particular in terms of surface damage.

II EXPERIMENTAL

The high density polyethylene (HDPE) used in this study was a blown film of BASF Lupolen 6041. The film had a crystallinity of 86%, a density of 9.6041 g/cm^3 , and a thickness of 80-90 μm . The samples were washed with methanol before use and straining was performed in the machine direction of the manufacturing process.

The samples were cut to a width of 10 mm and placed in clamps with a length of 20 mm between the clamps. Unnotched samples of HDPE were strained at a constant rate until fracture at relatively high elongation rates of 6 mm/s or 30%/s.

Electron emission (EE) and positive ion emission (PIE) measurements were carried out during the deformation and fracture of the polymer samples. The charged particles were detected with two channeltron electron multipliers (CEMs) with the front cone biased at +300 V for collection of electrons and -2600 V for positive ions, respectively. The CEMs produced fast (10ns) pulses with approximately 90% absolute detection efficiency for electrons and nearly 100% efficiency for positive ions. Standard data acquisition techniques were used to count and store the pulses as a function of time. The background for the EE and PIE was typically 1 count/s.

Two different clamping systems were used for elongating the polymer samples. One system (A), shown in Fig. 1a, used uncoated metal clamps which compressed the sample ends. As we were to discover, this system resulted in minute amounts of slipping, particularly at strain rates above a few percent/s. The other system (B), shown in Fig. 1b, employed rectangles of #600 sandpaper (very fine) inserted between the HDPE and the metal clamps with the grit pointing towards the HDPE. This arrangement resulted in firm gripping of the HDPE during the fast straining.

Because differences in the emission behavior occurred between A and B type clamping which we suspected was due to an tribological action, we also measured EE and PIE during abrasion of HDPE, where the chosen abrading surfaces were a stainless steel razor blade and a sharp glass blade. This arrangement is shown in Fig. 1c.

The onset of deformation and the instant of fracture were determined by measuring the force applied to the sample. The force was measured with a load cell mounted in the load train inside the vacuum. The load cell output voltage was amplified and then recorded as a function of time with a digitizer. The timing of the start and end of abrasion for the blade abrasion experiments was determined by timing markers generated manually with a pulse generator. The uncertainty of determining the onset and completion of abrasion was approximately 0.2 s.

III RESULTS

Figures 2a and 2b show typical EE and PIE curves (intensities are on log scales) from type A (metal) clamps, showing emission measured both during and following elongation. In both the EE and PIE, we observe considerable pre-failure emission as well as extensive after-emission. This after-emission has been shown to require substantial excitation of the polymer surface, frequently in the form of high energy electron bombardment or electrostatic discharges.⁸ It involves a relaxation of high lying trapped charge carriers which are mobile at room temperature and recombine at low lying recombination centers, similar to a number of thermally stimulated luminescence and electron emission phenomena.⁹

Figures 3a and 3b are the same data as Fig. 2 on an expanded time scale to show in more detail the EE and PIE during deformation. Fig. 3c shows the corresponding force vs time curve plotted on the same time scale. Note that there is no evidence of any drop in force that correlates with the onset of the pre-failure emission. Nevertheless, visual inspection shows that a small amount of slipping is occurring and exposing slightly abraded HDPE at the edge of the clamp. When the HDPE under the clamps is marked with a felt-tip pen prior to clamping, then elongated, repeatedly, the color from the pen is seen to extend for 1-5 mm away from the clamp edge.

When steps are taken to prevent such slipping, the emissions are dramatically altered. This can be seen in Figures 4 and 5. In Figures 4a and 4b we show typical EE and PIE for type B (+ sandpaper) clamps. First, compared with type A clamps, the total emission intensity is reduced considerably. Furthermore, the pre-failure emission is essentially gone; the major feature is the burst of emission at failure and a dramatic reduction in the after-emission. Fig. 5 shows a) the EE, b) PIE, and c) force vs time curves for the same test shown on an expanded time scale. The pre-emission is seen to be only a few counts above background (typically 1 count/s). Also, Type B clamps yielded at most sub-millimeter pullout when tested with the felt-tip pen as described in the paragraph above.

Table I summarizes the emission results for nine samples for each of the two clamping systems. In Table I, the peak count is the number of charged particles in the 0.01 s time interval at fracture, the pre-fracture count is the number of charged particles counted between the onset of straining and failure, and the post-fracture count is the number of charged particles counted in the first 10 seconds *after* fracture. One notices the significant decrease in the number of pre-fracture

and post-fracture counts when type B (+sandpaper) clamps are used instead of type A clamps. Although the scatter for each category is high, the differences between Type A and Type B clamping are dramatic and statistically significant. In the case of Type A clamps, the degree of damage due to slipping varied from sample to sample, which would produce widely varying changes in the emission intensities both during slipping and following fracture. Nevertheless, in comparing these clamping arrangements, we observe differences of over a factor of 100 in the pre-failure EE counts and almost a factor of 20 in the pre-failure PIE. Equally dramatic decreases in the EE and PIE after-emission are also observed when slipping is eliminated.

Equally effective in suppressing the pre-emission from Type A clamps was the use of aluminum foil wrapped around the ends of the sample to cover the region of the sample that would slip out of the clamps. In contrast, enhanced pre-failure emission could be obtained by placing the detectors near one of the clamps and/or tightening the clamps just the right amount so that the sample slips and becomes visibly damaged as it slips and twists through them.

Thus, we can conclude that the prefailure emission does not originate from the elongation and drawing out of the HDPE, nor does fracture of the polymer alone create significant surface excitation to produce long lasting after-emission. When "clean" fracture or catastrophic failure of the sample does occur, we do see reproducible bursts of EE and PIE. We propose that these signals are in fact due to rapid bond breaking accompanying failure of the polymer. Although these signals are relatively small, correlations with parameters which vary the number of bonds broken during failure should be pursued and would yield very useful information. Tribological loading of the HDPE surface appears to be very effective in producing relatively intense EE and PIE both during and following relative motion of the surfaces.

To test further the concept that abrasion was responsible for these observed differences in emission from HDPE, several abrasion experiments were done. Fig. 1c shows the arrangement of the surfaces. The HDPE was strung across a sharp blade similar to a bow of a violin and translated at a speed of approximately 1 cm/s. Figs. 6a and 6b show the EE caused from abrading HDPE with a stainless steel razor blade, and Figs. 7a and 7b show the EE caused from abrading HDPE with a sharp glass blade, itself produced by fracture. It is seen that when HDPE was abraded with either sharp edge, a steady EE occurs both during abrasion and for minutes afterwards. The damage done by such abrasion was quite visible with the naked eye and could be classified as extensive. Thus, although more intense because of the more severe damage, the emission during and following abrasion of the HDPE is seen to be very similar to the EE and PIE caused from straining a HDPE gripped with metal (Type A) clamps.

The probable origin of the fracto-emission induced by the tribological loading during the slipping of material out from under the Type A clamps is the degree of damage (broken bonds) created by the microscopic abrasion process. The fact that both metal and glass blades produced essentially identical results suggests that the degree of damage to the surface of the polymer is the critical factor rather than the type of material doing the abrading. Also the amount of damage appears to be important since a visual inspection of samples which slipped in the clamps showed that the samples with the most intense EE's also had the most visible damage in the regions that slid from under the clamps.

IV CONCLUSION

When HDPE samples are held firmly and strained, pre-failure EE and PIE are negligible, a burst of emission occurs at the split second of fracture, and the after emission lasts for only a few seconds. However when HDPE samples are not held firmly (particularly at high strain rates), for example samples held only with metal clamps, easily detected EE and PIE can occur during straining. This pre-failure emission is caused by small amounts of slipping of the samples from beneath the clamps causing fairly localized abrasion and accompanying excitation of the polymer. Abrasion experiments with two different materials (metal and glass) damaging the HDPE support the concept that abrasion is the stimulus for these intense signals. The emission accompanying failure is still a possible tool for studying the extent of bond breaking occurring during failure of samples firmly gripped. Furthermore, the prospects of using fracto-emission to study tribological phenomena in polymers where damage to the surface is of considerable interest are considerable and worthy of further study. In the near future we hope to measure the neutral products created during abrasion of HDPE while simultaneously detecting the charged particle emission. Particular neutral species may be indicative of direct bond breaking (for an example, see ref. 10) and thus correlate in intensity with the charged particle FE, and provide support for bond scissions created by abrasion being responsible for the charged particle FE.

ACKNOWLEDMENTS

This work was supported by the Office of Naval Research, N00014-87-K-0514, McDonnell Douglas Independent Research Fund, and the Washington Technology Center.

References

1. A. M. Polyakov and N. A. Krotova, *Dokl. Akad. Nauk. SSSR* **151**, 130 (1963).
2. V. A. Zakrevskii and V. A. Pakhotin, *Vysokomol. soyed.* **A17**, 568 (1975).
3. V. A. Zakrevskii and V. A. Pakhotin, *Sov. Phys. Solid State* **20**, 214 (1978).
4. I. E. Kurov, A. V. Movshovich, and V. P. Novozhilov, *Mekhanika Kompositnykh Materialov* **4**, 579 (1983).
5. J. Fuhrmann, G. H. Scherer, and R. Hofmann, *Polym. Commun.* **27**, 164 (1986).
6. J. Fuhrmann, G. H. Scherer, and L. Nick, *Makromol. Chem.* **188**, 2241 (1987).
7. H. H. Kausch, *Polymer Fracture*, 2nd Edition, Springer-Verlag, Berlin (1987) pp. 141-197.
8. J. T. Dickinson and L. C. Jensen, *J. Poly. Sci.: Poly. Phys. Ed.*, **23**, 873 (1985).
9. R. Chen and Y. Kirsh, *Analysis of Thermally Stimulated Processes*, Pergamon, Oxford, 1981, pp. 16-23.
10. e.g., M. A. Grayson and C. J. Wolf, *J. Polym. Sci.: Polym. Phys. Ed.* 1985, **23**, 1087.

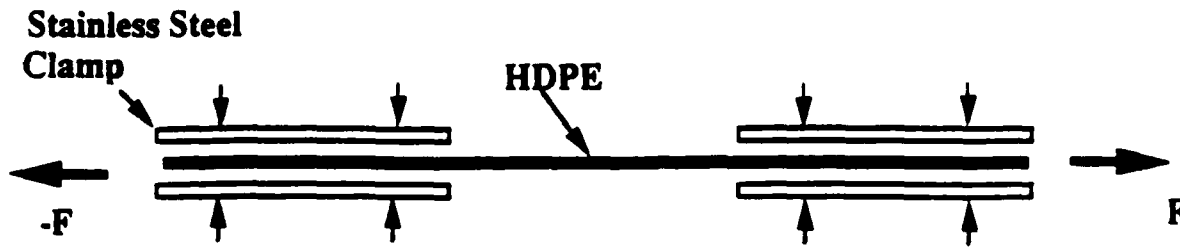
Figure Captions

- Figure 1.** Schematic representation of sample arrangements showing a) HDPE clamped between metal only (Type A) and b) HDPE clamped between small pieces of fine grit sand paper and metal. The arrangement for abrading the HDPE by sharp blades of stainless steel or glass is shown in c).
- Figure 2.** a) EE and b) PIE produced from the tensile deformation and fracture of HDPE using Type A clamps (metal only).
- Figure 3.** The same emission as Fig. 2 displayed on a faster time scale. a) EE, b) PIE, and c) the applied force vs time.
- Figure 4.** a) EE and b) PIE produced from the tensile deformation and fracture of HDPE using Type B clamps (metal + sandpaper).
- Figure 5.** The same emission as Fig. 4 displayed on a faster time scale. a) EE, b) PIE, and c) the applied force vs time. Note the lack of pre-failure emission.
- Figure 6.** a) EE accompanying and following the abrasion of HDPE with a stainless steel blade, and b) the same data showing electron emission during the abrasion on an expanded time scale.
- Figure 7.** a) EE accompanying and following the abrasion of HDPE with a sharp glass blade, and b) the same data showing electron emission during the abrasion on an expanded time scale.

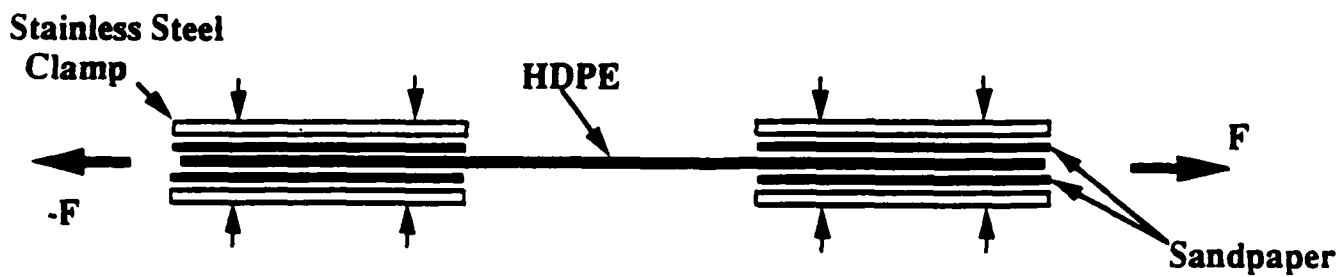
Table I

HDPE EE and PIE Counts from Two Different Sample Clamping Systems

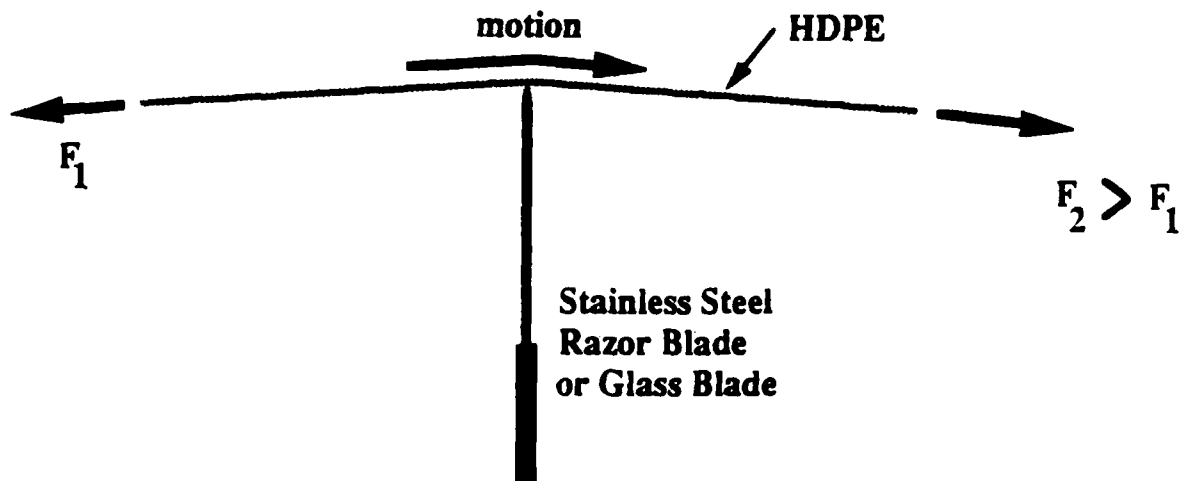
	EE Counts			PIE Counts		
	peak	pre- frac	post- frac	peak	pre- frac	post- frac
Type A						
Clamps	370 ±130	6640 ±2400	54000 ±25000	160 ±90	720 ±400	5500 ±4500
Type B						
Clamps (+Sand- paper)	640 ±210	65 ±20	250 ±90	290 ±70	40 ±10	40 ±16



a) Type A Sample Clamp



b) Type B Sample Clamp



c) Direct Abrasion of HDPE

Fig. 1

Electron and Positive Ion Emissions from HDPE

Type A Clamps

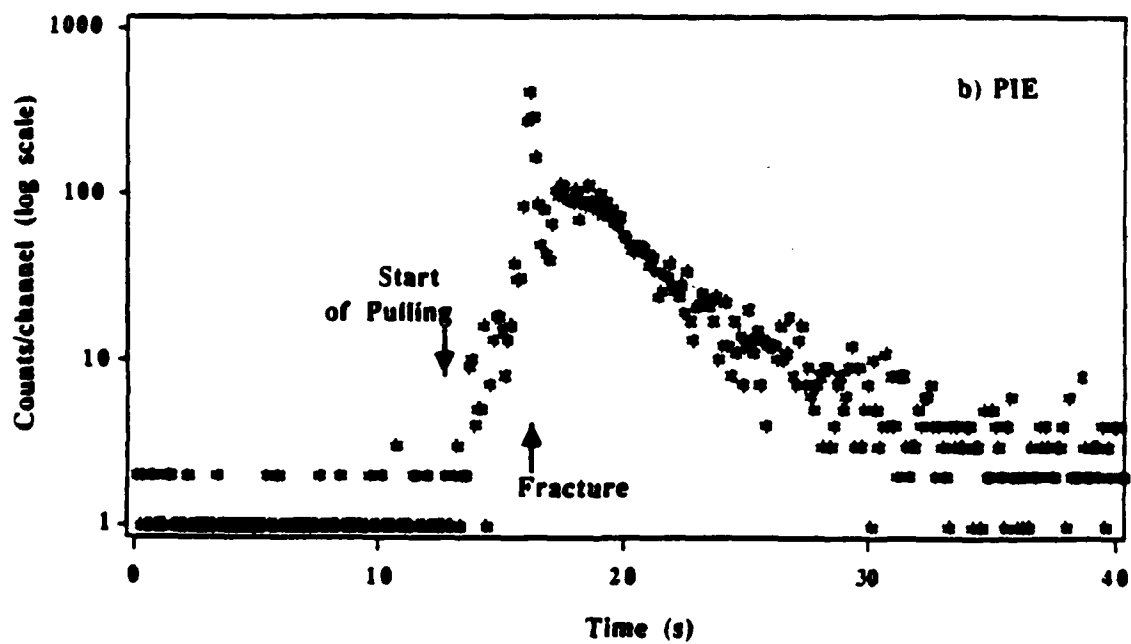
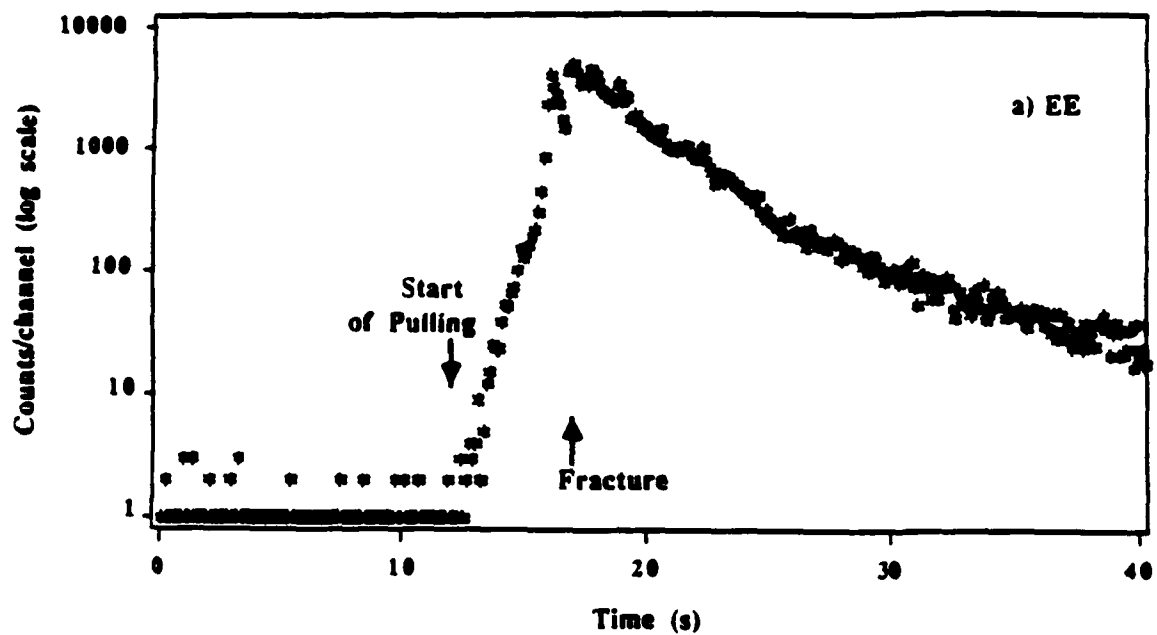


Fig. 2

Type A Clamps

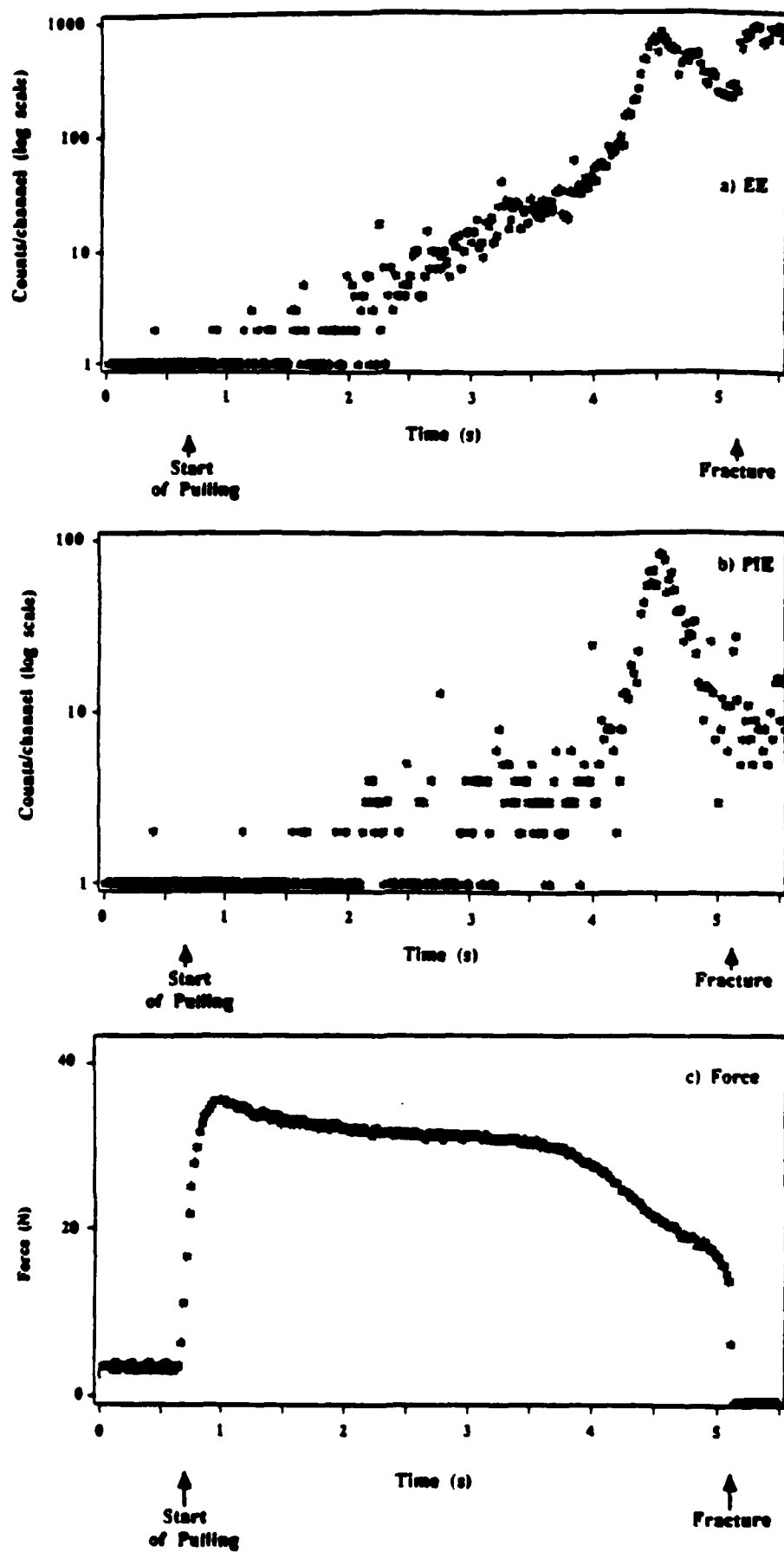


Fig. 3

Electron and Positive Ion Emissions from HDPE

Type B Clamps

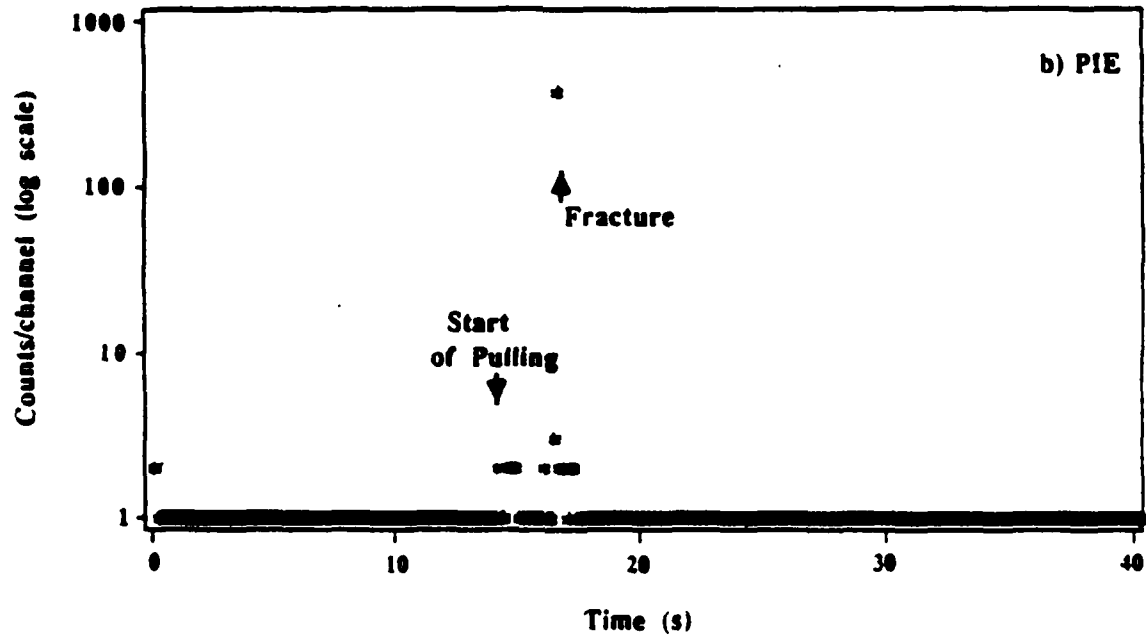
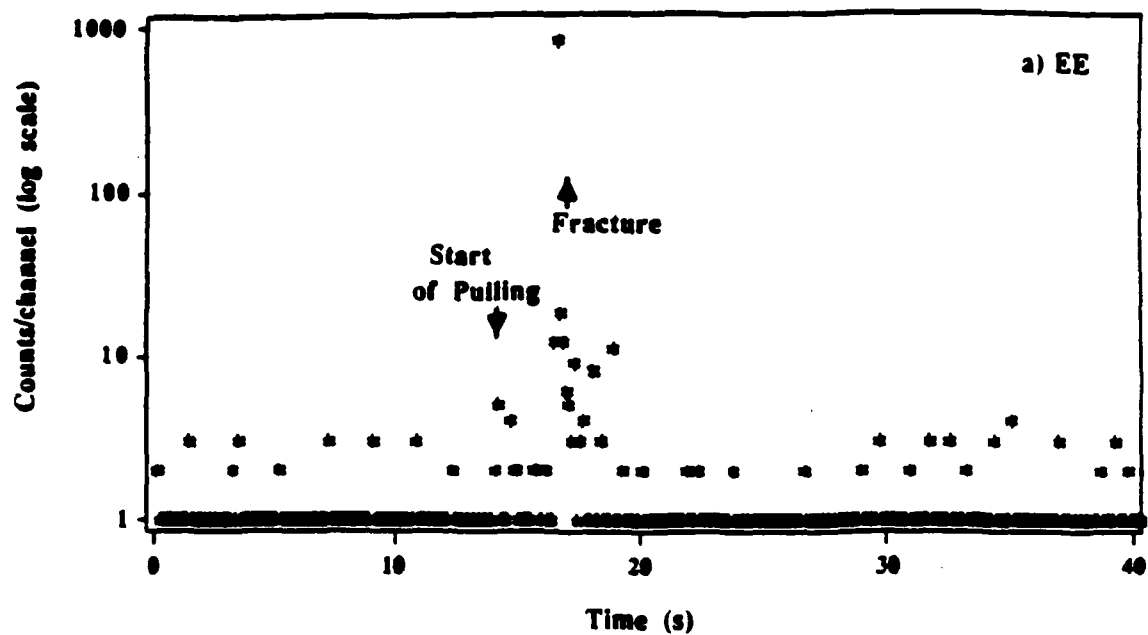


Fig. 4

EE, PIE, and Applied Force vs Time During Elongation

Type B Clamps

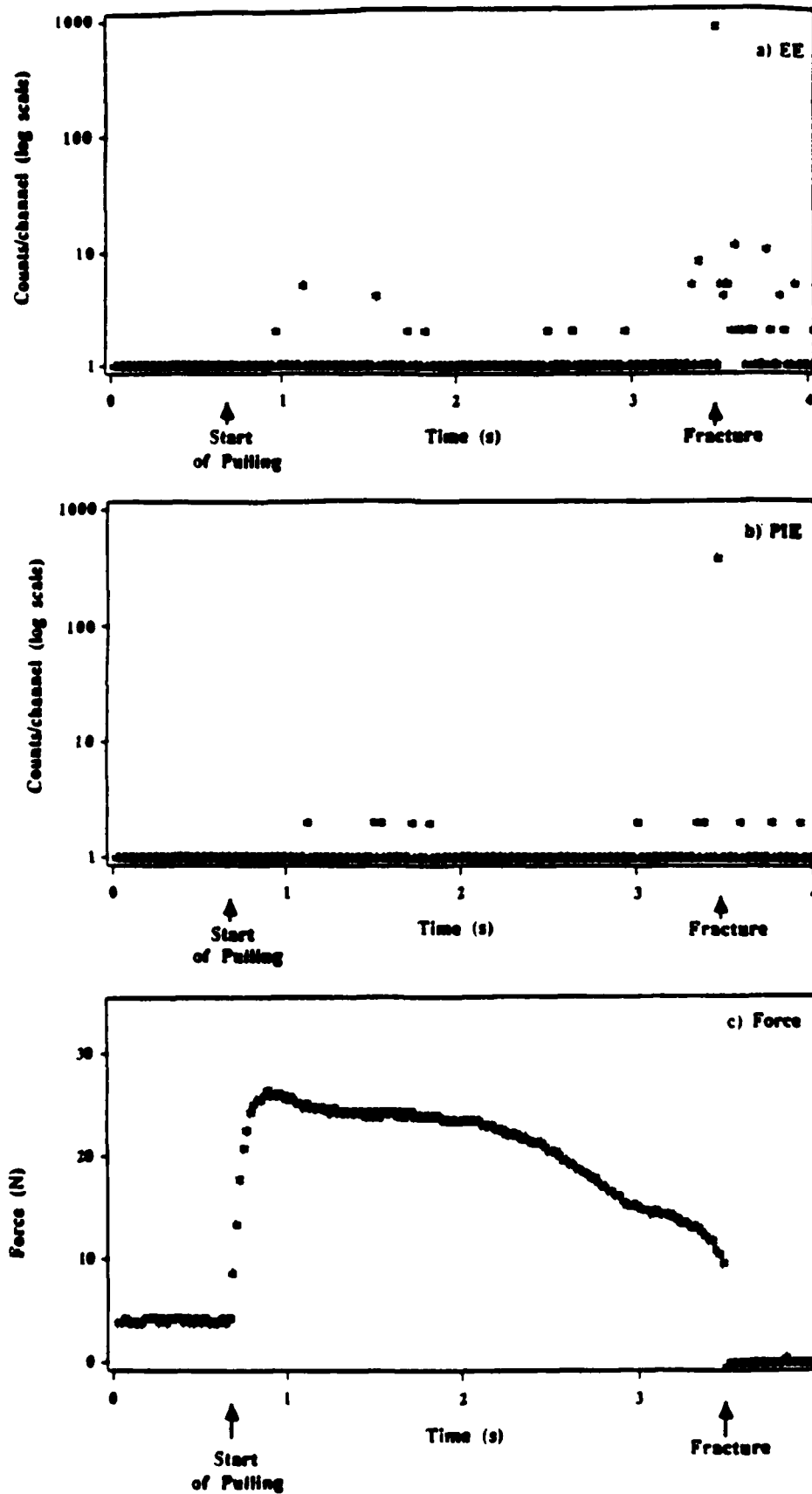
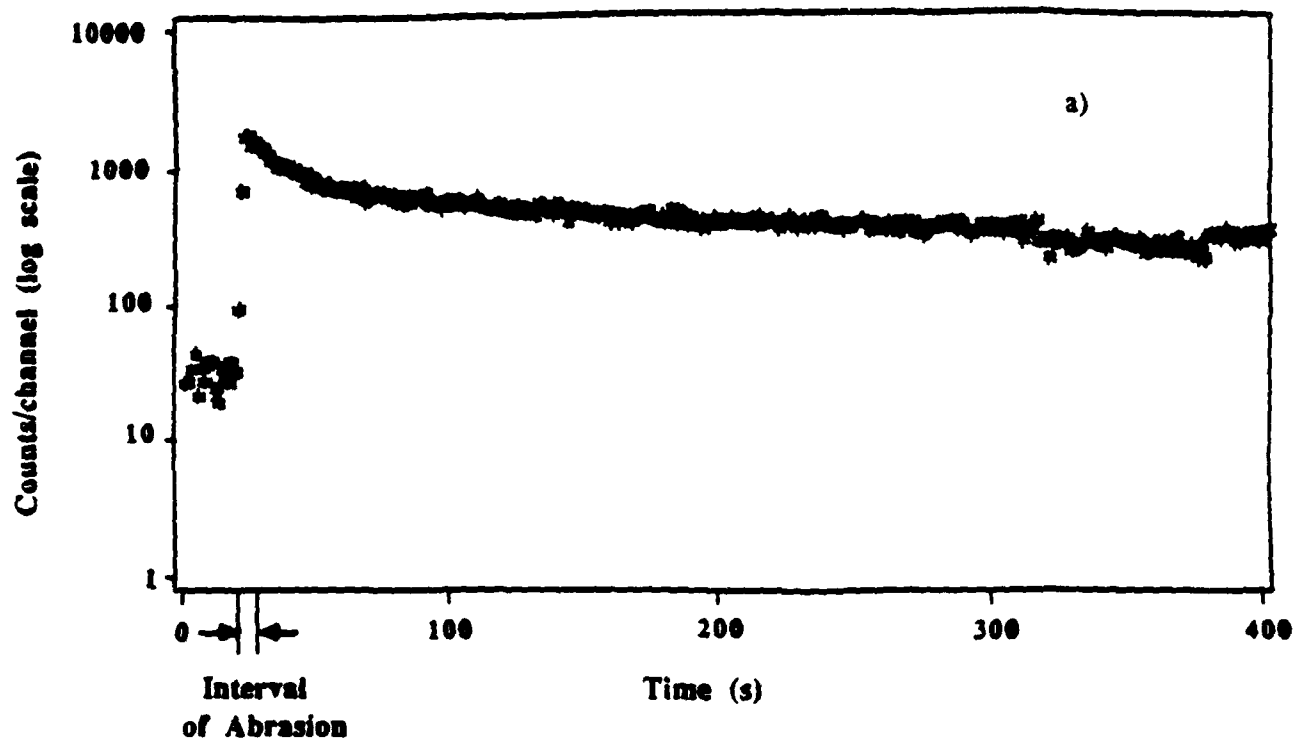


Fig. 5

**Electron Emission During and Following Abrasion of HDPE
With a Stainless Steel Razor Blade**



**Electron Emission During Abrasion of High Density Polyethylene
With a Stainless Steel Razor Blade**

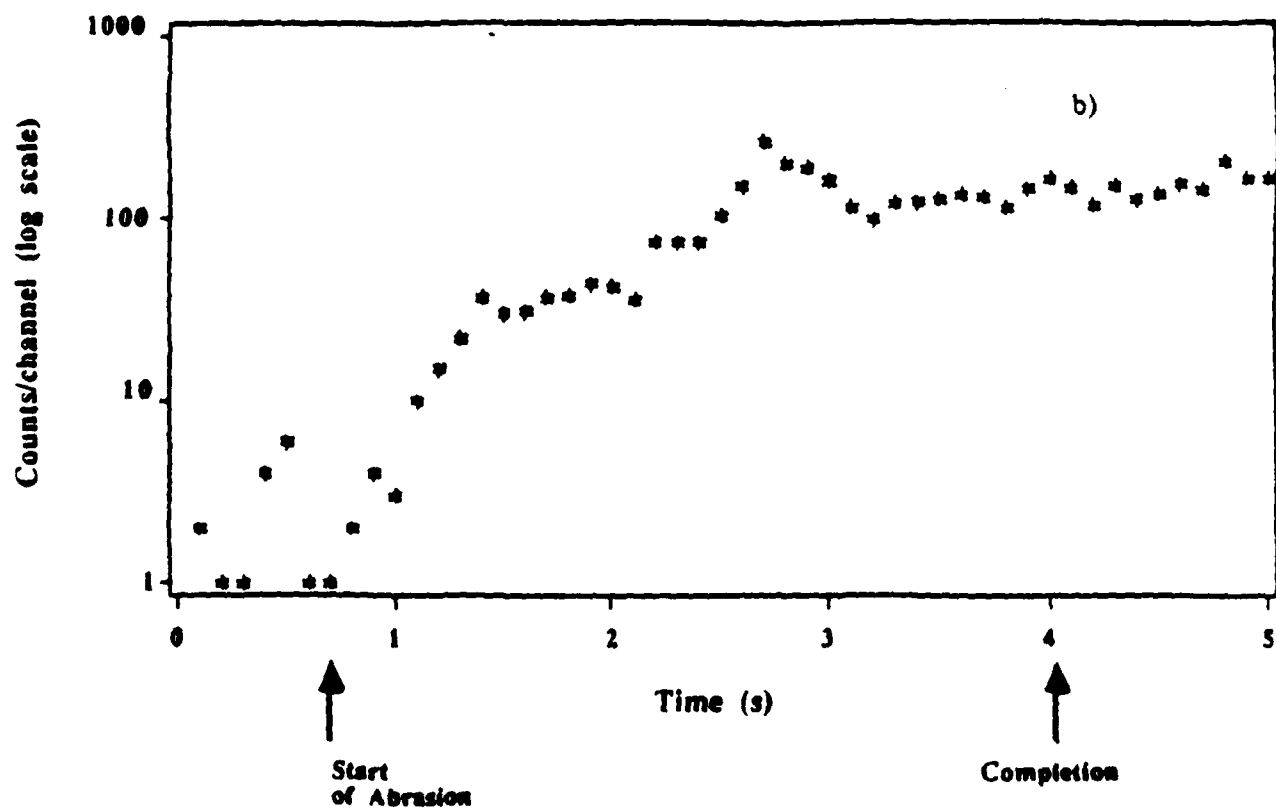
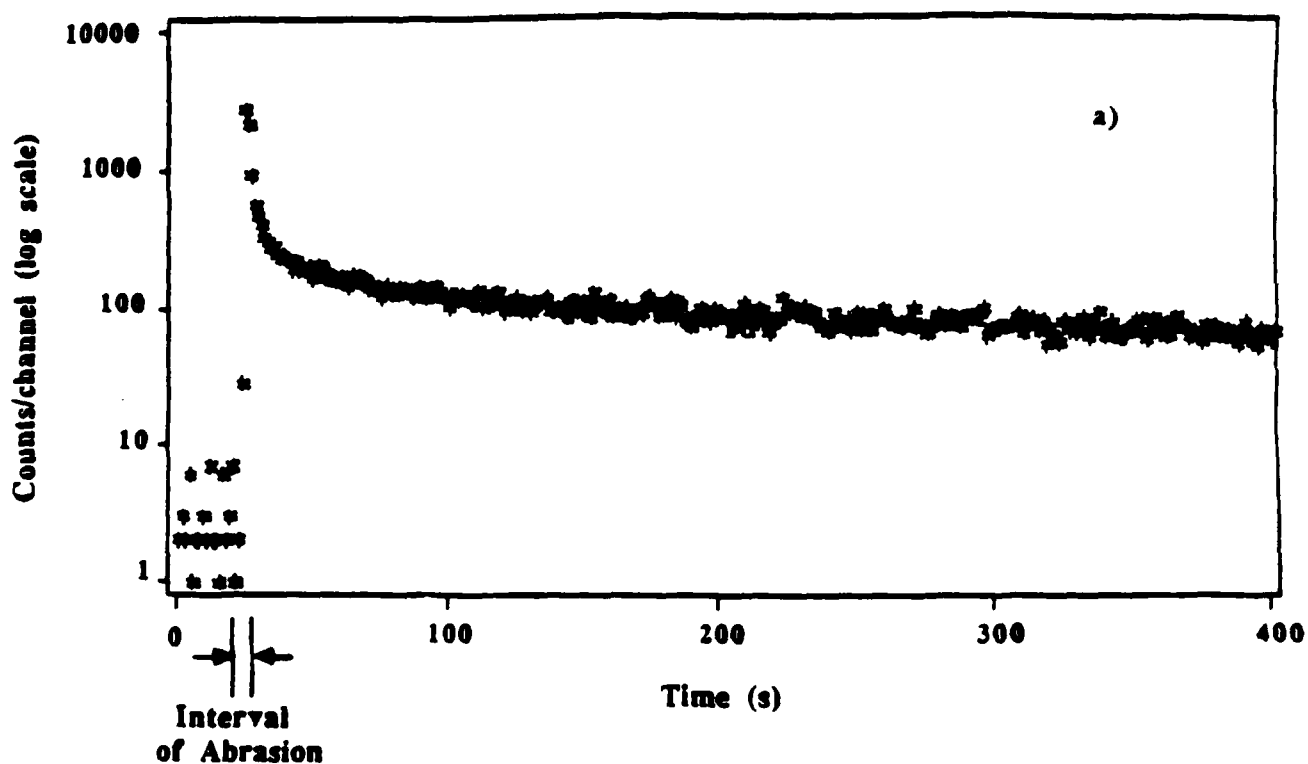


Fig. 6

Electron Emission During and Following Abrasion of HDPE With a Sharp Glass Blade



Electron Emission During Abrasion of High Density Polyethylene With a Sharp Glass Blade

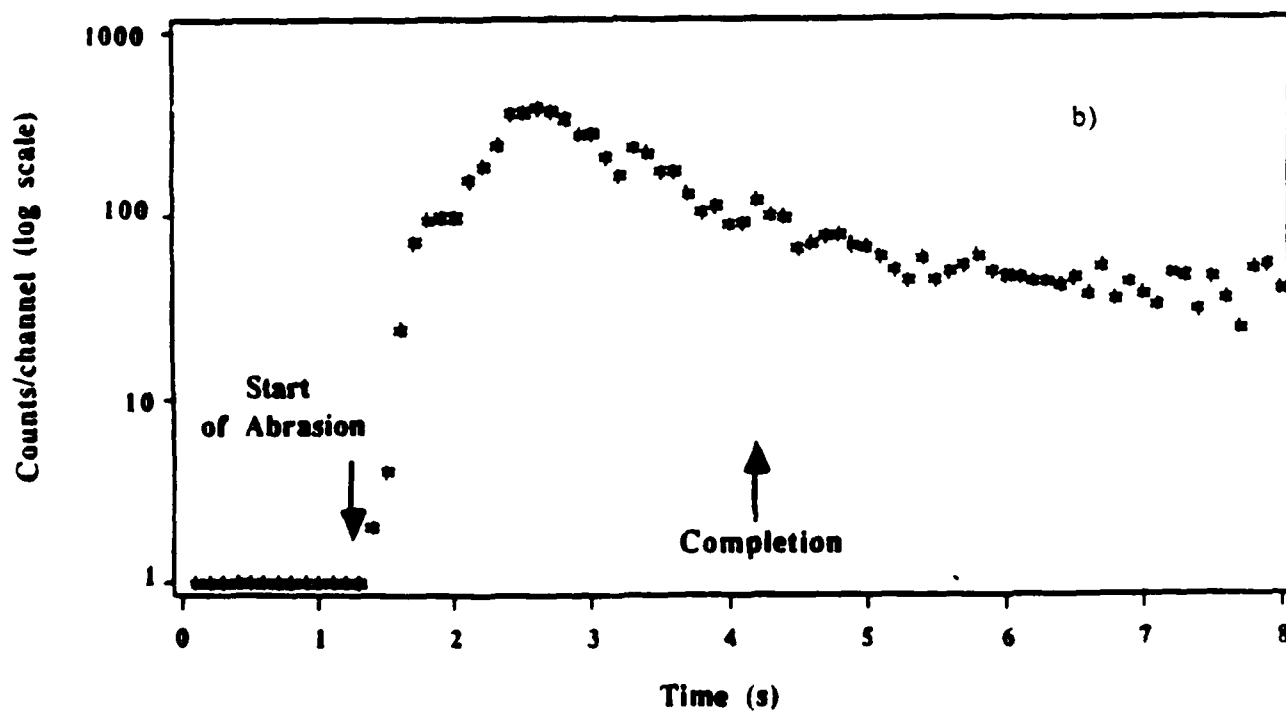


Fig. 7

XVI. The interaction of excimer laser ultraviolet radiation with KAPTON-H in vacuum and under mechanical stress

K. Tonyali, L. C. Jensen, and J. T. Dickinson, Department of Physics, Washington State University, Pullman, WA 99164-2814

We examine the response of highly stressed polyimide films to excimer laser radiation (20 ns pulses @ 248 nm wavelength) in vacuum. We present changes in surface topography due to surface/near surface damage, crack initiation, and eventually crack growth over a wide range of applied stress. We show that the morphology of the stressed material has a significant influence on the resulting damage and suggest that the regions of highest damage are those experiencing the highest local stress. Finally, we present initial results on the effect of mechanical stress on yields of the photo-ablation products ejected from the polymer surface.

I. INTRODUCTION

The interaction of polymers and their composites with energetic particles and photons has been an area of interest for many years. In environments involving energetic electrons, ions, and ultraviolet (UV) radiation, a number of damage processes can occur which may modify the properties of polymers and result in surface damage and the deterioration of mechanical properties.¹⁻⁸ These harmful environments include space, various plasmas, and solid rocket propellents during burning. Beneficial applications of radiation/polymer interactions include applications regarding *controlled* direct rupture of bonds, e.g. controlled cutting and shaping of materials, as well as roughening and chemical modification of surfaces in preparation for applying coatings, adhesive bonding, etc. Finally, the use of polymers as sensitive resist materials in the microelectronics industry and the use of excimer lasers for surgical removal of tissue has encouraged additional studies of intense photon interactions with organic materials.

We have previously reported on the consequences of simultaneously subjecting polymers to tensile stress and particle bombardment, principally electrons.²⁻⁷ In such studies and the present work we are examining the resultant damage mechanisms as well as a unique probe of fracture. We have shown, for example, that crack initiation and

crack growth in stressed polymers were greatly enhanced by electron beam irradiation. We have proposed that damage formation and microcracking via enhanced, irreversible bond breaking are the main contributors to the failure of polymers under these combined stimuli. Furthermore, we have suggested that there is a localization of excitation produced by electron collisions with stressed molecular bonds which promotes this irreversible bond breaking.

Very recently, we have reported on the surface damage and crack initiation process which occurs when another radiation source, namely short pulses of UV laser light were applied to stressed Kapton-H (a polyimide produced by E. I. Dupont de Nemours & Co.) in air at 1 atmosphere.⁸ Short pulses of UV light are known to cause photochemical bond scissions as well as thermal excitation in polymers.⁹⁻¹⁷ This type of radiation has been shown to cleanly etch a number of polymers such as polyimide and poly(methyl methacrylate) at excimer wavelengths (e.g., 193 nm and 248 nm). Under the action of UV laser radiation, bond scissions occur breaking molecular chains, and atomic and molecular fragments are ejected from the surface at supersonic velocities. This process has been termed ablative photodecomposition by Sirinivasan and coworkers.⁹⁻¹⁶

In this paper, we study the mechanical response of Kapton-H films subjected to mechanical stress and 248 nm pulsed UV excimer laser radiation simultaneously in vacuum. Scanning electron microscopic investigation of radiation exposed surfaces of stressed/unstressed samples are presented, and crack initiation and growth mechanisms are discussed. In addition, initial results on the effect of mechanical deformation on the yields of the photoablation products ejected from the polymer surface are presented.

II. EXPERIMENTAL

A Lambda Physik model EMG-203 MSC Excimer Laser producing 20 ns pulses at 248 nm wavelength (KrF) was used as a radiation source. The laser power was measured using a Gentec ED-500 Joulemeter. The laser pulse repetition rate was maintained at 1 Hz during most of the experiments. The laser beam was incident to the sample at 34 degrees (relative to the surface normal). The laser beam was focused by a 1 meter focal length lens to produce a 0.7 mm x 3.5 mm rectangular beam with a maximum fluence of 3.5 J/cm^2 at the sample. Neutral density filters were used to reduce the fluence by calibrated amounts. The beam profile was examined by burning patterns into unexposed, developed Polaroid film. The beam was generally uniform in the central portion but showed some irregularities on the edges due to slight misalignment of the optical components.

Typical sample dimensions were $75 \mu\text{m} \times 8 \text{ mm} \times 30 \text{ mm}$ produced by cutting specimens from commercial films of Kapton-H (Dupont). Occasionally dogbone samples were cut to produce localization of the strain to the central portion of the specimen. No surface treatment was performed prior to mounting the specimens in the vacuum chamber. The samples were loaded in a tensile stress-strain apparatus to a constant strain. The applied load, measured with a Sensotec Model 11 load cell, was digitized vs time using a LeCroy Data Acquisition System and stored on disk for later analysis. Strain was measured in an engineering sense, namely through measurements of the separation of the grips. All tests were carried out at a pressure of 10^{-5} Pa at ambient temperature. The penetration depth of Kapton-H at 248 nm wavelength is 0.06 μm (95% absorption).¹⁷

Fractured and exposed specimens were coated with a 300 – gold film prior to examination in a scanning electron microscope (SEM). A 20 keV electron beam voltage was used for the SEM analysis.

Three very simple, but slightly different particle detector arrangements were used in the ablation product experiments:

1. **Total Neutral Emission Detector.** This detector consisted of a commercial mass spectrometer ionizer [EAI Model 150A quadrupole mass spectrometer] mounted in front of a channel electron multiplier (CEM), Galileo Electro-Optics Model 4039. Appropriate potentials focused the positive ions onto the front cone of the CEM which was located out of sight of the irradiated surface. The distance from the surface to the center of the ionizer was 5 cm. The electron emission current in the ionizer was typically 10 μ A to prevent saturation of the high gain CEM. Ionizer and CEM potentials inhibit detection of externally created charged particles.
2. **Excited Neutral Emission Detector.** This detector consisted of a bare CEM mounted inside of a metal box where the cone of the CEM was 9 cm from the irradiated portion of the sample. Charged particles were deflected with plates mounted near the sample. The observed signals, due to the de-excitation of excited neutral species (e.g., involving long lived metastable or Rydberg states), were usually pulse counted.
3. **Charged Particle Emission Detector.** This detector consisted of a CEM mounted in the rear of a metal box such that the cone of the CEM was out of sight of the irradiated portion of the sample. Neutral particles could pass directly through grid-covered entrance and exit holes in line with the surface normal. An attractive potential would attract charged particles of the opposite sign to the cone of the CEM yielding pulses which could be counted or digitized. Electrons, which arrived in times less than 1 μ s, were digitized at 5 ns intervals.

In addition, several mass selected time-of-flight (TOF) measurements were made using a quadrupole mass spectrometer; most of these results will be reported elsewhere.

For each of the above detector arrangements we could use either pulse counting (with 1 μ s minimum time resolution) or signal averaging (with 5 ns minimum time resolution). The output of a photodiode sensing part of the laser light was used as a trigger pulse. Time delays, when important, were measured to 5 ns precision. Ablation products were typically averaged or summed over 25-50 laser pulses.

III. RESULTS AND DISCUSSION

As expected, the stress-strain curves for Kapton-H show inelastic behavior at high strains. The initial part of the stress-strain curve was linear with a yield point at approximately 10% strain, which is not well defined. After 25% strain the rate of increase in the applied stress was approximately constant. The deformation was reasonably uniform without evidence of neck formation until failure at approximately 80% strain and 150 MPa stress.

KrF excimer laser bombardment of Kapton-H under stress introduced damage at the specimen surface which caused premature failure. Figure 1 compares SEM photos of the morphology of the stressed samples irradiated in air and vacuum under the same conditions. Both specimens were strained to 50%, and both samples were bombarded with KrF excimer laser pulses at a fluence of 2.3 J/cm^2 at the sample surface. The resulting morphology of the irradiated surfaces under stress displays "hollowed-out" regions. Not shown are micrographs of the surfaces of the unstressed, irradiated samples⁸ and the stressed, unirradiated samples, which were both featureless.

The structures produced on the stressed vacuum samples tended to be more distinct and clean (Fig. 1a) than the structures produced in air (Fig. 1b). It is also interesting to note that the air samples exhibited small grain-like particles on the exposed surface. We have suggested elsewhere⁸ that these particles are due to the redeposition of etch products on the surface due to the presence of 1 atm of air. Under the conditions of our experiment, the work of Lazare et.al.⁹ suggests that UV oxidation of the polyimide surface does not occur due to the continual ablation of fragments and therefore would not be causing these protuberances.

The opening of the hollowed-out structures, which are always oriented perpendicular to the stress direction, occurs along the edge of the fracture surface possibly due to high stress intensity in front of the growing crack. These damaged regions stimulate localized crack growth, eventually link, and cause final failure of the specimen.

We have attributed the morphology which develops in the stressed, exposed samples to inhomogeneous ablation caused by the applied stress.⁸ In the unstressed material, UV radiation

can lead to direct bond breaking due to electronic excitations.¹³⁻¹⁵ We have suggested that enhanced, irreversible bond breaking occurs at bonds under high stress compared to molecular units under lower stress. In addition, there is evidence that the probability of bond A breaking will increase if a nearby bond B ruptures, thereby producing an increase in the strain field at A. Thus, the presence of both mechanically deformed bonds and radiation results in a "synergistic effect" which does not occur if one of the stimuli is absent. This highly localized damage that results in the formation of microcracks in a dense array on the surface of the polymer. It is this array of damage which leads to the premature failure of Kapton-H films under the combined stimuli of tensile deformation and UV radiation.

Using the various particle detector configurations described above, we have made a preliminary study of the ejected species for both the stressed and unstressed Kapton-H specimens. The types of particles that have been observed include the following: electrons, positive ions, negative ions, excited neutrals, and ground state neutrals. These particles have been partially characterized by use of simple electrostatic deflection experiments and measured flight times of the particles. For example, any negative particle ejected from the surface with velocities higher than 5×10^6 cm/s is clearly an electron. Although the individual masses contributing to the spectra will be discussed in a future paper, Mass 28, which we identify as principally CO, is the primary etch product.

A comparison of the TOF spectra of the stress dependent products shown in Fig. 2, where the laser fluence was 0.7 J/cm^2 . A careful investigation on the production of ground state neutrals and the positive ions did not show any measurable dependence on the applied stress.

In contrast, the excited neutrals, negative ions, and electrons showed easily detectable increases when the Kapton-H was elongated. For example, Fig. 2a compares the TOF spectra of the excited neutrals from the stressed and unstressed samples, using the excited neutral emission detector. At high stress, the excited neutral emission yield was a factor of two larger than the emission from the unstressed Kapton-H. The excited neutrals, which will be discussed further in a later paper, are most probably excited states of mass 28, which at this fluence would correspond to

an average kinetic energy of 0.3 eV. A likely candidate is CO molecules in either the metastable $a^3\pi$ state or high n Rydberg states. Chemisorbed CO has been shown to result in the release of metastable neutral CO in Electron Stimulated Desorption from a metal surface.¹⁸ Related measurements in our laboratory show that CO is the major constituent both of the positive ion emission and ground state neutral emission from laser induced ablation of Kapton-H.¹⁹ Brannon et. al.²⁰ have also identified CO in the IR absorption spectra of laser etched polyimide both in air and in vacuum.

The excited neutral emission remains intense as ablation proceeds through the material. Although the CO partial pressure in the system was approximately 10^{-7} Pa, which could potentially result in the chemisorption of CO on the bombarded region of the polymer, the excited neutral emission yield was found to be independent of laser repetition rate (1-250 Hz). We therefore conclude that this signal is in fact due to the ablation process. It should be pointed out that per particle the internal energy carried away from the surface by these excited neutrals is several eV, which is significant.

Low resolution TOF spectra for the negative ions created during ablation are shown for stressed and unstressed samples in Fig. 2b. The yield of negative ions increases by a factor of 10 when the applied load was 75 N (the force at failure for this sample size averaged 84 N).

The negative ion spectrum has a peak at 10 μ s and a slower component at approximately 32 μ s. With higher resolution (longer flight path) TOF measurements, we have determined that the major negative ion products peak at 40 (15) amu. The large uncertainty is due to the tendency of the irradiated Kapton-H surface to charge in the presence of external electric fields (necessary to accelerate the ions to the potential of the TOF flight tube). In Fig. 2b, the spectra of the unstressed specimens in Fig. 2b appear flat because of the scale chosen to show the stressed sample emission. When expanded, the unstressed TOF spectrum has similar form to the stressed TOF spectrum.

Copious photoelectrons are produced from 248 nm bombardment of Kapton. Typically, two electron emission peaks were observed in the TOF spectra as illustrated in Fig. 2c. The data were digitized using signal averaging of pulses at 5 ns time intervals for 50 laser pulses. The effect

of applied stress on the electron emission is shown in Fig. 2c where three peaks are observed in the spectra. The peak at 560 ns is stationary in time but the peak height increases as the stress is raised. The peak, which is initially observed at 165 ns, diminishes with increasing exposure time and applied stress. With stress, a third peak appears at 140 ns. The 140 ns peak increases with both stress and the number of pulses. In the unstressed specimens the peak at 140 ns appears as a small shoulder on the 165 ns peak.

These three peaks appear to be distinct, unique states. If we assume no surface charging, we can calculate rough binding energies for the electron contributing to these peaks: 4.9-5.0 eV (560 ns), 4.5-4.6 eV (165 ns), and 4.6-4.7 eV (140 ns), respectively. UPS studies by Hahn et al.²¹ of polyimide films show valence band structure which range from 4 to 8 eV. A calculated density of states by Bredas and Clark²² sets the Fermi level of polyimide at 4 eV. Thus, the 560 ns peak appears to be due to photoelectrons from states near the Fermi level. We attribute the peak at 165 ns, which decays with repeated laser pulses, to filled defect states created during processing. The 140 ns peak is a unique state created only under the combination of stress and radiation. We propose that this state is created by photodissociation of strained bonds. The dramatic increase in the 140 ns peak and in the negative ion emission with stress may well be due to a corresponding negative ion precursor on and near the polymer surface.

A graph of the yield of the excited neutrals, negative ions, and electrons vs stress is presented in Fig. 3. Note that the total negative ion emission and the electron emission at 560 ns are highly stress dependent and follow similar trends. The electron peak at 140 ns is inseparable from the 165 ns peak at low stress but we estimate that it also increases by a factor of eight in increasing the stress to maximum load. The excited neutral emission was less sensitive to the applied stress, but still showed a reproducible, constant increase.

The excited neutral yield does not follow the stress dependence of the positive or negative ions and thus does not appear to be created by reneutralization of ions leaving the surface. Instead, it may be created during a recombination reaction either at the surface or in the plume.

The various emission components show their strongest increases when the specimen is loaded *beyond* its yield point. Kapton-H displays high plastic deformation when stressed above its yield point. At this stress level, polymer chains tend to align in the stress direction in an extended conformation. Such chains are slightly distorted regarding bond angles and interatomic separations which may encourage channeling photofragments into intermediates which then yield the increased negative ions, photoelectrons, and high lying excited neutral products. Also to be considered is the possibility that the stressed bonds also might permit higher survival probabilities of these products (i.e., inhibiting reneutralization and deexcitation).

The lack of increase of the ground state neutral emission and positive ion emission suggests that these species are predominantly coming from dissociative processes that are not sensitive to the presence of stress. This would be consistent with a photothermal process. Furthermore, when we look at the time-of-flight distributions of particular masses (using a quadrupole mass spectrometer) we find that the distributions are thermal in nature and independent of the presence of stress. Possible linkage of positive ion production to the ground state neutrals is at this time not obvious.

IV. CONCLUSION

In conclusion, we have presented preliminary results on the consequences of simultaneous application of mechanical stress and excimer laser radiation @ 248 nm to Kapton-H. We are seeing clear evidence that such conditions create a unique, textured morphology on the radiation exposed surface. In air, we have shown that there are additional nodules on the irradiated, stressed specimens which we believe are due to a redeposition mechanism. In general, higher stress levels and/or repeated laser pulses lead to microcrack formation, a linkage of this damage, and eventually crack initiation and crack growth which causes failure of the sample. Finally, the negative ion, photoelectron, and metastable/Rydberg neutral emissions are strongly enhanced in samples stressed above the yield point. The presence of mechanical stress encourages irreversible bond breaking, probably in regions of high stress, leading to localized damage. The increased emission

of negative ions, photoelectrons, and excited neutrals with stress appears to be due to a shift in the concentrations of the intermediate species created by this bond breaking which occurs under this unique combination of strained bonds and UV excitation.

V. ACKNOWLEDGMENTS

We thank D. Stulik, Washington State University, and Clarence Wolf, McDonnell Douglas Research Laboratories, for helpful discussions. This work was supported by the Office of Naval Research, Contract N00014-87-K-0514, McDonnell Douglas Independent Research and Development Program, and the Washington Technology Center.

VI. REFERENCES

1. A. Garton, W. T. K. Stevenson, and P. D. McLean, *Materials and Design* **7**, 319 (1986).
2. J. T. Dickinson, M. L. Klakken, M. H. Miles, and L. C. Jensen, *J. Polym. Sci. Polym. Phys. Ed.* **23**, 2273 (1985).
3. J. T. Dickinson, L. C. Jensen, and M. L. Klakken, *J. Vac. Sci. Technol. A* **4**, 1501 (1986).
4. R. Michael, S. Frank, D. Stulik, and J. T. Dickinson, in *Proceedings of 13th International Symposium on Effects of Radiation on Materials*, ASTM E-10, Seattle, WA, 1986.
5. J. T. Dickinson, M. L. Klakken, and L. C. Jensen, in *Proceedings of the 18th SAMPE International Technical Conference* (SAMPE, Corvina, CA, 1986), p. 983.
6. J. T. Dickinson, K. Tonyali, M. L. Klakken, and L. C. Jensen, *J. Vac. Sci. Technol. A* **5**, 1076 (1987).
7. J. T. Dickinson, *Proceedings of the ACS Division of Polymeric Materials: Science and Engineering* **56**, 282 (1987).
8. K. Tonyali, L. C. Jensen, and J. T. Dickinson, submitted to *Proceedings of the Materials Research Society, Boston Meeting*, 1987.
9. S. Lazare, P.D. Hoe, J.M. Baker, and R. Sirinivasan, *J. Am. Chem. Soc.* **106**, 4288 (1984).
10. R. Sirinivasan, *J. Vac. Sci. Technol. B* **1**, 923 (1983).
11. R. Sirinivasan and B. Braren, *J. Polym. Sci. Polym. Chem. Ed.* **22**, 2601 (1984).

12. R. Sirinivasan, B. Braren, R. W. Dreyfus, L. Fadel, and D. E. Seeger, *J. Opt. Soc. B* **3**, 785 (1986).
13. B. J. Garrison and R. Sirinivasan, *Appl. Phys. Lett.* **44**, 9 (1984).
14. E. Sutcliffe and R. Sirinivasan, *J. Appl. Phys.* **60**, 3315 (1986).
15. R. Sirinivasan, *Science* **234**, 560 (1986).
16. R. Sirinivasan, B. Braren, and R. W. Dreyfus, *J. Appl. Phys.* **61**, 372 (1987).
17. J.T.C. Yeh, *J. Vac. Sci. Technol. A* **4**, 653 (1986).
18. I.G. Newsham, J.V. Hogue, and D.R. Sandstrom, *J. Vac. Sci. Tech.*, **9**, 596, 1971.
19. K. Tonyali, L. C. Jensen, J. T. Dickinson, unpublished work.
20. J.H. Brannon, J.R. Lankard, A.I. Baise, F. Burns, and J. Kaufman, *J. Appl. Phys.* **58**, 2036, 1985.
21. P.O. Hahn, G.W. Rubloff, and P.S. Ho, *J. Vac. Sci. Technol. A* **2**, 756 (1984).
22. J.L. Bredas and T.C. Clark, *J. Chem. Phys.* **86**, 253 (1987).

Figure Captions

- Fig. 1. SEM micrographs of Kapton-H samples fractured under pulsed excimer laser radiation. The samples were strained to 50% (125 MPa) and then exposed to 30 pulses of 2.3 J/cm^2 radiation. (a) in vacuum, and (b) in air. Notice that the hollowed-out structures open up more near the edge of the fracture surface. Small nodules appear to have grown on the irradiated surface in air apparently due to a redeposition process.
- Fig. 2. (a) Excited neutral, (b) negative ion, and (c) electron emission TOF spectra of stressed and unstressed Kapton-H samples. The positive ion and ground state emissions showed no change with stress and are therefore not shown. The specimens were elongated to 70% strain and then subjected to 0.7 J/cm^2 pulsed laser radiation.
- Fig. 3. The effect of the applied force on the negative ion, electron and excited neutral emission yield. The laser fluence to the sample was 0.7 J/cm^2 .



Fig. 1

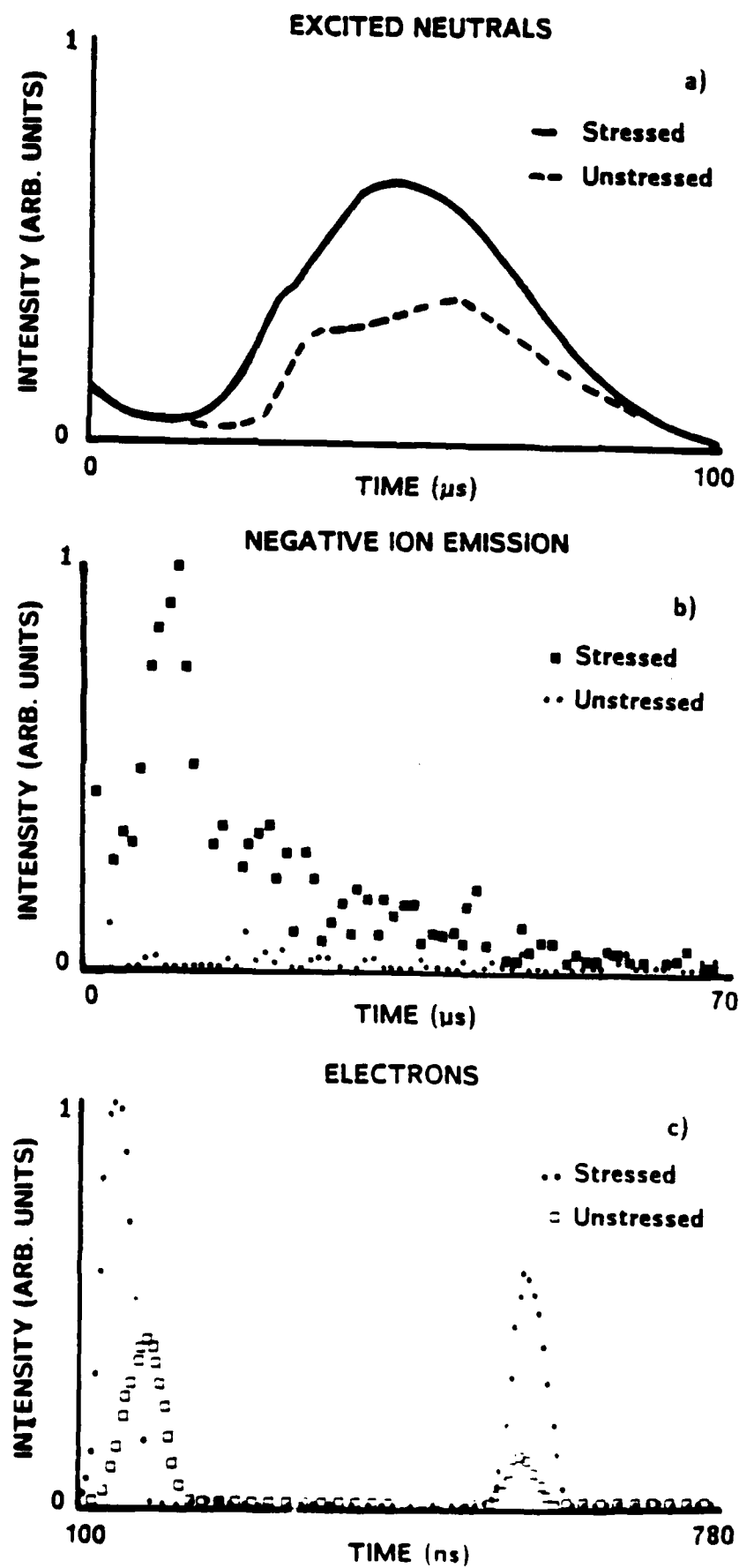


Fig. 2

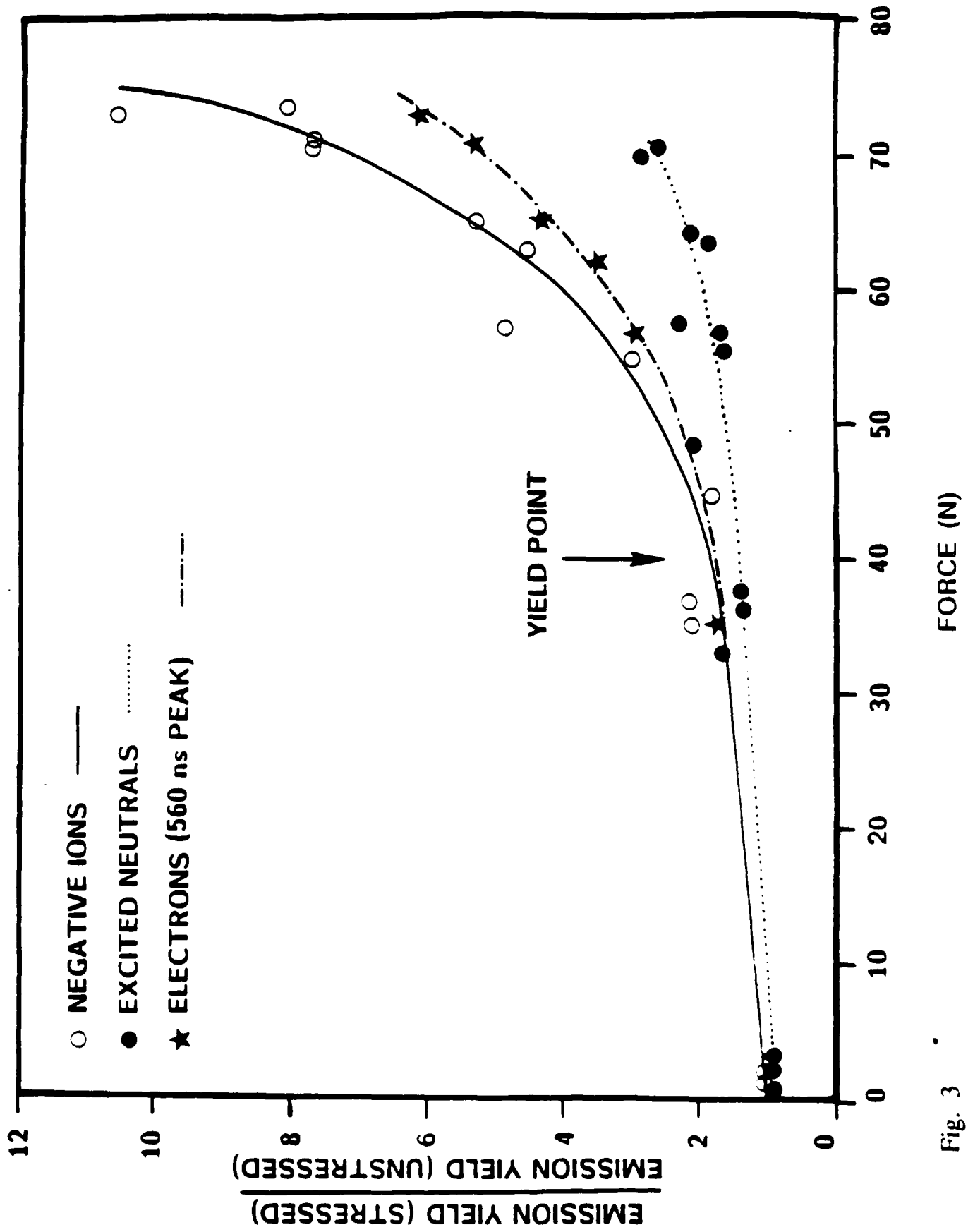


Fig. 3

XVII. The interaction of UV excimer laser light with sodium trisilicate

P. A. Eschbach, J. T. Dickinson, S. C. Langford
Washington State University, Pullman, WA 99164-2814

L. R. Pederson
Battelle Pacific Northwest Laboratories, Richland, WA 99352

We describe the results of irradiating sodium trisilicate glass ($\text{Na}_2\text{O} \cdot 3\text{SiO}_2$) with 248 nm excimer laser light at fluences from 1 to 5 J/cm². A threshold for the onset of etching occurs at 3 J/cm². We investigate the changes in surface topography as a function of laser fluence. We also identify the ionic and neutral species contained in the emission plume. A clear correlation is observed between the etching threshold and a) onset of emission of fast excited neutrals, as well as b) the appearance of atomic Na D resonance radiation. The high velocities (10-15 km/s) of the excited neutrals and ions (H^+ , Na^+ , and Si^+) are attributed to laser/plume interactions. The character and origin of lower velocity neutral species (atomic O, Si, and molecular NaO) are presented. The possible role of surface fracture in the onset of etching is also discussed.

I. INTRODUCTION

Controlled ablation by laser irradiation has considerable potential in microelectronic and micromechanical machining processes as well as in the production of high quality thin films of electronic and optical materials.¹⁻³ However, ablation mechanisms are complex, often involving both thermal and photochemical processes.²⁻⁸ A better understanding of these mechanisms is needed to provide a scientific foundation for future applications. In view of the wide range of materials and structures under consideration, predictive capabilities as well as descriptive capabilities are desired. In particular, the interaction of excimer laser radiation with silicate glasses is important in potential electronic applications. Laser damage mechanisms in these materials also affect their use as optical windows, where performance is often limited by radiation induced damage.

In applications in which the emphasis is on the removal of material by ablation, an understanding of the emission mechanism is important. However, the production of thin film formation by laser ablation also requires a detailed understanding of the chemical state and energy of the products incident on the substrate. The existence of energetic ions and highly

excited neutrals in the ablation plume may facilitate certain otherwise improbable or slow chemical reactions with the substrate material and on the growing film. Variations in the kinetic energy of these products with laser fluence indicate that some degree of control over these energy distributions, and thus the surface chemistry, is possible.

In this paper, we present initial observations of surface morphology and particle emission accompanying the exposure of sodium trisilicate glass to 20 ns pulses of 248 nm light from an excimer laser. This material, transparent in the visible, absorbs rather weakly at this wavelength. Correlations between surface damage and the time required for the onset of ablation suggest that surface defects play an important role in the ablation process. Mass spectrometry was used to identify the major neutral and ionic components of the plume, and time-of-flight measurements were used to determine energies. The results point to strong laser/plume interactions in the near surface region.

II. EXPERIMENT

Sodium trisilicate glass was prepared by melting stoichiometric quantities of Na_2CO_3 and SiO_2 powders.⁹ The resulting material was transparent and bubble-free. Samples were cut with a diamond saw, mechanically polished, and washed in ethanol. The samples were mounted on a translatable stage in a vacuum chamber maintained at a pressure of 10^{-4} Pa or less. The laser beam was directed through a quartz window at an angle of about 20° to the sample surface normal.

The radiation source was a Lambda Physik Model EMG 203 excimer laser, which produced 20 ns pulses of 248 nm radiation (KrF). The laser energy/pulse was measured with a Gentec ED 500 joule meter. The laser beam was focused by a lens of 1 m focal length to produce a $0.2 \times 1 \text{ mm}^2$ rectangular spot on the sample surface with a maximum fluence of 5 J/cm^2 . Neutral density filters were used to reduce the fluence by calibrated amounts. SEM images of the ablated surfaces demonstrated that the beam was generally

uniform in the central portion, but showed some irregularities on the edges due to slight misalignment of the optical components.

Time-of-flight (TOF) measurements of ions and excited neutral particles were made with a Channeltron electron multiplier (CEM), Galileo Electro-Optics Model 4039. Excited neutrals can be detected when their internal energy is sufficient to cause Auger de-excitation (e.g. metastable atoms and molecules) or autoionization upon collision with the CEM (e.g. high lying Rydberg states). Ions and excited neutrals were distinguished by comparing intensity measurements made with positive and negative biases on the CEM front cone. The CEM front cone was typically masked so that only a small portion was in line-of-sight with the sample to prevent detector saturation.

Mass resolution of ions and neutral particles was obtained with UTI Model 100C and EAI Model 160 quadrupole mass spectrometers (QMS's) using CEM's as particle detectors. With the ionizer "on" and the axis of the QMS aligned to provide a line-of-sight path from the target through the QMS to the CEM, both ions and neutral particles were detected. Mass resolution of neutrals was readily obtained in this geometry. However, the broad range of energies exhibited by the ions (0-70 eV) extended well beyond the ion energies for which these QMS's were designed, severely degrading the performance of the quadrupole mass filter. By replacing the QMS ionizer with a Bessel box energy filter operated at 20 eV, 1 amu mass resolution was obtained. The design and calibration of the Bessel box are described by Craig and Hock.¹⁰

Measurements of light emission from excited species in the ablation plume were made with a Gencom Thorn EMI Model 9924QB photomultiplier tube (PMT) positioned at the end of a fiber optic cable mounted on a vacuum system flange. The target end of the fiber optic cable was equipped with a slit aperture and collimating lenses to ensure that only light directed along the axis of the cable (perpendicular to the target surface normal) was detected. This allowed the observation of temporal variations in light intensity as light emitting atoms/molecules passed in front of the slit. For spectral analysis of this

spatially selected light, the output of the fiber optic cable was attached to a Thermo Jarrell Ash Monospec-18 spectrometer employing a 150 lines/mm grating. An EG&G Model 1421 gated, intensified, position-sensitive detector responsive to light in the region between 200-830 nm was used with an EG&G Model 1460 optical multichannel analyzer to acquire both time-averaged and time-resolved spectra.

III. RESULTS

A. Surface topography

When sodium trisilicate glass is exposed to 248 nm excimer laser light at fluences above 3 J/cm^2 , we observe etching of the glass in the central portion of the laser beam. Outside of this central portion there tends to be a gentle modification or clean-up of the defects (e.g., scratches) on the surface. Figures 1 and 2 are SEM photos of the etched region showing very rough features in the etch pit, indicating considerable texturing in addition to melting. These "coral-like" features are similar to those seen by Braren and Srinivasan in laser ablated borosilicate glasses.¹ Further evidence of surface melting is shown in Fig. 3. The top portion of Fig. 3 is a magnified view of a region close to the edge of the ablated area showing many spherical particles with diameters ranging from 0.5 to $3 \mu\text{m}$. These particles are apparently due to the ejection of molten glass from the etched region.

Even at fluences well above the threshold, we find that polished surfaces require a "pre-exposure" of several laser pulses before etching is observed. If the surface is highly damaged (e.g., an unpolished surface with diamond saw cutting marks), no pre-exposure is required to induce etching. The changes in surface morphology as radiation progresses can be seen in Fig. 4, which shows four different etch pits formed by exposure to an increasing number of laser pulses at a fluence of 3.6 J/cm^2 . After 10 and/or 20 pulses, substantial surface fracture is seen along the center and borders of the exposed region. (The border region experiences especially high thermal gradients.) A small amount of highly localized

etching (pitting) can be seen at an exposure of 10 pulses, especially in the bottoms of the fracture craters. A higher pit density is found after 20 pulses. With continued irradiation, the pitted region grows, eventually joining and smoothing the fractured areas and developing the coral-like structure noted above. This smoothing always left an etched region with rolling topography. The average spacing between major features of the fine coral structure converges to approximately 1 μm .

Etch rates were estimated from the apparent depth of the etched region in SEM photos. In Fig. 1, a depth of about 100 μm was attained in the central portion of the etch pit after 400 laser pulses. The average etch rate is thus about 250 nm per pulse, corresponding to the removal of several hundred monolayers per pulse.

B. Particle emission

Overview. Because of the short duration of the emission process, the detected species are highly correlated in time with the laser pulse. Figure 5(a) shows the dominant TOF signal with the QMS ionizer turned "on" and the rods of the mass filter grounded to provide a nearly field-free drift region for the particles. The front cone of the CEM in the rear of the QMS was biased at -2700 V to favor detection of positive ions and reject negative particles. With the ionizer "off," as in Fig. 5(b), the faster components of the detected signal are still observed. Peaks 1 and 2 of Fig. 5 are strongly effected by electric fields consistent with positive ions. Peak 3 is a robust peak, often saturating the detector. The peak position is not affected by strong electric fields, suggesting that it is associated with neutral particles; note that this peak is also observed with the ionizer "off." Such behavior is associated with neutral particles with sufficient internal energy to yield a secondary electron at the detector surface. Peaks 4 and 5 of Fig. 5(a) disappear when the ionizer is turned off, as shown in Fig 5(b), and are thus attributed to ground state neutral species.

Positive Ions. The positive ion emission (PIE) was examined using a QMS equipped with a Bessel box energy filter set at 20 eV. With the Bessel box, we were able to mass resolve the PIE at masses 1 (H^+), 23 (Na^+), and 28 (Si^+). Figure 6 shows mass selected PIE TOF data summed over 50 laser pulses at these three masses. By far the largest ion intensity occurs at mass 23 (Na^+). The relatively high intensity of Na^+ is presumably related to the ease of removing Na from the glass and the low ionization energy of Na. The H^+ peak persists after many shots and does not depend on the laser pulse repetition rate; therefore this H^+ emission is not due to the dissociation of adsorbed H_2O from the background. The delayed shoulder in the mass 1 emission of Fig. 6 is an artifact due to the "ion blast" which is poorly discriminated from emission at mass 1. These TOF curves indicate significant ion intensities at an energy of 20 eV, four times the energy of the laser photons. Below we present experimental energy distributions for Na^+ which extend out to ~60 eV. It is highly unlikely that these high energies are due to multiphoton processes; as we shall argue, these high energies are most likely due to laser/plume interactions.

Excited Neutrals. Characterization of TOF measurements of the excited neutral species were made with a bare CEM mounted 8.5 cm from the target surface at an angle of 30° relative to the surface normal. Figure 7 curve (i) shows the TOF spectrum acquired with a negatively biased CEM front cone. Again, the initial peak is due to prompt, unresolved positive ions. When the CEM cone is biased at various positive and negative voltages, the arrival time and general shape of the broad peak commencing at 3 μs is *unchanged*, indicating that this peak is due to excited neutral particles with sufficient internal energy to release electrons at the front surface of the detector. Because the observed flight times are much longer than 10 ns (associated with typical dipole transitions) we conclude that this peak is due to a long-lived excited species detected upon collision with the CEM cone. We present below strong evidence that this species is excited atomic Na (Na^*). With this mass identification, the translational energy corresponding to

the peak in the TOF curve of Fig. 7 curve (i) is about 30 eV. Again, this is well in excess of the laser photon energy, and reflects strong laser/plume interactions.

Ground State Neutrals. The slower, ground state neutral peak 4 of Fig. 5(a) consists of a distribution of masses which can be resolved with a QMS. Figure 8 shows three peaks recorded with the QMS tuned to masses 16 (O), 28 (Si), and 39-40 (NaO or NaOH, hereafter referred to as NaOH_x ; we had insufficient resolution at masses 39-40 to distinguish between $x = 0$ and $x=1$). These curves have been normalized to a common peak height to facilitate comparisons of their position and shape. The ratio of the area under each of the curves is approximately $\text{O:Si:NaOH}_x = 1000:6:1$. The solid lines appearing in Fig. 8 are least squares fits of the data to "drifting Maxwellians" (Maxwellian velocity distributions with a center of mass velocity) and will be discussed below. The translational kinetic energies of these emissions are typically ~ 0.1 to ~ 0.6 eV, orders of magnitude less than the energies of the ions and excited neutrals. Peak 5 of Fig. 5(a) indicates the presence of an even slower neutral species. A corresponding late peak was observed at mass 28, but this peak was observed only during the early stages of etching, decaying rapidly as etching proceeded.

Neutral emission is observed at mass 23 (Na°), but is somewhat obscured by the large excited neutral peak at this mass. With the QMS tuned to mass 23 and the ionizer "off" the Na^* peak is detected. When the ionizer is turned "on," this peak grows in size and develops a shoulder on the trailing, low energy side. As the ionization cross section of Na^* is relatively large, some of this increased intensity must be due to the ionization of Na^* . However, we suspect that a good fraction of the increase, including the component responsible for the shoulder at 50-100 μs , is due to Na° . The evidence for a Na° peak in this region suggests that the velocity distribution of Na° is more like that of Na^* (and Na^+) than the velocity distributions of the other neutrals, O, Si and NaOH_x .

Negative Particles. Electron emission can also be observed using a bare, CEM biased for detection of negative particles. As expected, the electron TOF is considerably

shorter than that of the more massive positive ions and neutrals and is quite intense. Surprisingly, no negative ion emission was observed.

C. Photon emission.

At fluences sufficient to yield etching, a plume is easily observed with the naked eye. The plume exhibits a bright, spherical central region tangent to the surface, surrounded by a less bright, yellow cloud decaying with distance from the surface. A time exposure of this visible light (f8 on Kodak Tri-X 35 mm film) for ~20 successive laser pulses is shown in Fig. 9(a). The rectangular structure in Fig. 9(a) is the sample, which is clearly delineated by the fluorescence of the glass. Although the film response is non-linear, a real transition in intensity appears ~1 cm from the glass surface. Figure 9(b) is a photo of the plume exposed over several more laser pulses. It shows that the outer, less intense region is also spherical and approximately tangent to the surface at the irradiated region. These spherical structures are consistent with a $\cos\theta$ angular distribution. In both of these photos (more clearly in Fig. 9(b)) a smaller plume is observed on the back surface of the target. Reflection of the laser beam at the back surface can enhance the local electric field¹¹ by a factor of 1.5 or more. Despite the attenuation of the beam in the sample, a plume is generated at the back surface at high beam fluences.

Figure 10 shows the spectrum of the visible plume as it passed a point about 2 cm from and along the normal to the glass surface. The spectrum is a line spectrum dominated by the atomic Na D resonance line. Five other known Na lines are also resolved and identified in Fig. 10. These lines reveal the presence of highly excited neutral Na atoms in the plume. The lifetime of the $3P_{1/2,3/2}$ states is only about 15 ns, so that the Na D line observed from particles this far away from the surface (corresponding to TOF's of several μ s) cannot be due to $3P_{1/2,3/2}$ states created during irradiation. The spectrum of Fig. 10 indicates that the $3P_{1/2,3/2}$ states are fed by higher lying excited states. We propose that

all the observed Na lines are due to the decay of long lived, highly excited Rydberg states created in the escape process.

The time dependence of the Na D line intensity at a given position can be compared with the time dependence of the excited neutral intensity detected by impact with a CEM. A PMT with a Na D line interference filter and a lense/aperture arrangement was used to provide spatial and wavelength discrimination of the light from the plume. The optics were arranged to monitor intensity of the Na D radiation emanating from a narrow cone 8.7 cm from the glass surface. In Fig. 7, curve (i) is the excited neutral flux detected by the CEM, while curve (ii) is the corresponding Na D line TOF. The time dependence of the photon intensity is nearly identical with that of the excited neutral intensity measured at the same distance from the sample. Furthermore, the Na light appears only at laser fluences above J/cm^2 , in close coincidence with the appearance of the excited neutral peak and the onset of etching. These correlations between the CEM excited neutral emission and the Na D line intensity strongly suggest that both are due to the same particle, and that this particle is indeed excited neutral Na. Thus, both lifetime considerations and spectral measurements indicate that the visible plume is due to the radiative decay of short-lived excited states produced by the decay of long-lived Na Rydberg states.

As the Na D line intensity reflects the excited neutral density as a function of time in the region of detection, the position of the TOF intensity peak can be used to infer a characteristic kinetic energy. This characteristic energy increases with laser fluence above the threshold for plume formation, as shown in Fig. 11. The magnitude of this energy is typically in excess of 10 eV, well above the photon energy of the laser and also well in excess of any thermal energy which can be associated with the irradiated surface (e.g., 10 eV \approx 100,000 K). The influence of laser fluence on particle energy is further evidence of strong laser/plume interactions.

IV. DISCUSSION

In the early stages of irradiation, flaws near the surface can lead to localized fracture due to stress induced by differential heating. This is the source of the fracture craters observed early in irradiation, starting with the first few laser pulses. The prebombardment of the surface required to produce etching in sodium trisilicate glass was not observed in borosilicate glasses,¹ which are strong UV absorbers at 248 nm. In contrast, the absorption edge of pure sodium trisilicate is well below 240 nm.¹² Absorption in the near surface region can be enhanced by defects. For instance, Nielsen et al.¹³ have proposed that surface defect states play a critical role in the multiphoton desorption of ionic species from crystalline dielectrics. These defects can be produced by interaction of the laser light with the irradiated material. Devine et. al.¹⁴ report that excimer laser irradiation of amorphous silica at 248 nm can produce both E'_1 centers and a non-bridging oxygen defect, each capable of absorbing 248 nm radiation. The delay in the onset of etching observed in this work may be the time required for the production of a critical density of absorption centers.

Mechanical processes may contribute to the density of absorption centers near the surface. Our observation that damaged surfaces require no pre-exposure for the onset of etching indicates that mechanically created defects play an important role in near-surface absorption. One effect of mechanical surface defects is the enhancement of local electric fields,¹⁵ which in the limit of sharp cracks should be about a factor of two in this material. However, absorbance in the near surface region can also be enhanced by mechanically produced electronic defects. Interestingly, E-centers have been observed by Tomozawa in crushed silica using ESR techniques.¹⁶ Dreyfus et al.¹⁷ have found that chemically etched sapphire surfaces display significantly lower UV absorption at 193 and 248 nm in the near surface region relative to "as received" commercially prepared samples. They attribute this reduction to the removal of absorption centers in the "as received" samples (with presumably mechanically polished surfaces). The delay in the onset of etching in mechanically polished glass surfaces relative to "as cut" surfaces observed in our

work is likely due to the reduction in defect densities (and therefore a reduction in absorption) at the surface of the polished samples. In a similar manner, thermally induced fracture may play an important role in the onset of etching by providing a relatively high density of absorption centers in the near surface region.

The coral-like features observed after the onset of etching are associated with hydrodynamic sputtering similar to reported by Kelly and Rothenberg due to excimer ablation of several metals.⁴ If the depth of material melted under irradiation is fairly uniform, any asperities on the surface tend to grow due to the volume expansion associated with repeated melting and heating. Under certain conditions, molten droplets may be expelled from the surface. This would explain the spherical structures in Fig. 3. The diameters of the observed droplets, 0.5-3 μm , correspond well with the range of droplet diameters reported by Kelly and Rothenberg.

Electron emission begins early in the irradiation process in conjunction with the production of absorbing defects. Filled E' states produced and populated during early pulses are likely initial states for photoelectron production. Mackey et al. have studied these states in sodium silicate glasses.¹⁸ They form a broad band lying about 1 eV below the Na ion levels which form the conduction band of this material. Photoelectron production involving these states is a two step process: a) the population of an E' state by the adsorption of a 5 eV photon followed by b) the adsorption of a subsequent photon to yield photoelectrons. Presumably, once sufficient absorption at 248 nm is attained, etching commences simultaneously with the onset of intense neutral and ion emission.

The interaction of the laser pulse with the cloud of electrons, ions, and neutrals formed early in the pulse results in the formation of a plasma in which electron impact can produce additional ionization. The high velocities observed for the ions and the excited Na species cannot be explained by photothermal or photochemical processes at the surface. Interparticle collisions in the near surface region (Knudsen layer) can raise the apparent temperature of ablated particles,^{19,20} but this effect is again far too small to account for

these velocities. Figure 12 shows experimental energy distributions for excited neutral and ion data. The excited neutral energy distribution was obtained by transforming the Na D line intensity data of Fig. 7 curve (ii), which reflects the excited neutral density. The ion energy distribution data was obtained by successive ion flux measurements made with the Bessel box energy filter tuned to increasing energies. Each energy distributions is accompanied by the appropriate Maxwellian energy distribution fit to one point (the distribution peak). Both the excited neutral and ion energy distributions are decidedly non-Maxwellian. The production of the high energy charged particles and excited neutrals most likely involves the acceleration of electrons in the field of the laser beam by inverse bremsstrahlung.^{21,22}

Inverse bremsstrahlung involves the absorption or scattering of a photon by an electron in the presence of a third body. Multiple absorption/scattering events can result in electrons with energies several times the photon energy. As the electrons are accelerated, ions can be accelerated along with them by means of electrostatic attraction. Interferometer measurements by Walkup et al.²² indicate the presence of high electron densities ($>10^{16}$ electrons/cm³) in plasmas formed by excimer ablation of Al₂O₃. At these densities, Coulomb forces maintain approximate charge neutrality over distances larger than a Debye length (~20 nm). Despite the limited spatial extent of the electric fields in such a plasma, their strength is sufficient to yield considerable ion acceleration. For instance, Bykovskii et al. have estimated that singly charged ions can be accelerated to 40-60 eV by a laser with a power density of 10^9 W/cm² in a plasma with an electron temperature of 1 eV.²³ Once the laser pulse decays, the electric fields disappear and local charge neutrality is re-established in the plume. Electron/ion recombination (requiring a third body) can then result in the production of excited neutral, Rydberg atoms. The expanding plume thus carries electrons, positive ions, and Na Rydberg atoms. The latter eventually decay into lower lying states which yield the observed visible radiation via dipole allowed transitions.

It is the finite lifetime of the Rydberg atoms which allow the resonance radiation to be observed at large distances from the surface over times of several tens of μs .

Electrostatic acceleration of the ions by the faster electrons accounts for the high energy of ionic and excited neutral species. Simultaneous measurements of Na^+ and Na^* energy distributions are compared in Fig 12(b). At a fluence of 3 J/cm^2 , the Na^+ energy distribution peaks at around 20 eV, while the excited neutral energy distribution peaks around 6 eV. This difference in energy is consistent with the electrostatic acceleration of Na^+ accompanied by the electron/ion recombination to form Na^* ; early recombination prevents further acceleration, resulting in a lower energy distribution. The ions that survive have presumably experienced greater acceleration, and thus are more energetic than the excited neutrals.

The ground state neutral particles show considerable variation in their TOF curves. As shown in Fig. 8, the TOF peak at mass 16 (atomic O) is fast and broad, while the TOF peaks at masses 28 and 40 are slower and much narrower. Kelly suggests that the energy distribution of a photochemically emitted species is initially nearly monoenergetic (e.g., due to a Frank-Condon-like transition), but that this distribution could be broadened by subsequent collisions.²⁴ The degree of broadening is a function of the collisional history of the particles, and thus may yield a variety of energy distributions.

In order to characterize these distributions, we have modeled the TOF data with a particle velocity distribution formed by summing a Maxwellian velocity distribution, characterized by temperature T , and a center of mass component, v_{cm} . T and v_{cm} are model parameters, chosen to fit the data. The intensity of the QMS signal corresponding to this distribution was calculated by integrating the estimated particle density over the length of the ionizer, according to the formula:

$$I(t) = \frac{N \cdot A}{t^3} \left(\frac{m}{2\pi k T} \right)^{3/2} \int_D^{D+L} e^{-\frac{m \left(\frac{x}{t} - v_{cm} \right)^2}{2kT}} dx$$

where $I(t)$ is the QMS signal intensity as a function of time, N is proportional to the total number of emitted particles, A is the cross-sectional area of the ionizer, m is the particle mass, k is the Boltzmann constant, and the integral is performed over the length of the ionizer, which extends along the x -axis from distance D to $D+L$. The factor of t^{-3} arises from the transformation of the Maxwell-Boltzmann velocity distribution to a spatial distribution ($dv_x = dx/t$, $dv_y = dy/t$, $dv_z = dz/t$), which yields the particle density as a function of time and position. Least squares fits of this model to the TOF data of Fig. 7 yield the following values of v_{cm} and T :

mass (amu)	assigned species	T (K)	v_{cm} (m/s)
16	O	2420	410
28	Si	200	1420
39-40	NaOH_x ($x = 0,1$)	110	1380

The unrealistically low temperatures and large center of mass velocities necessary to fit the mass 28 and 40 data are consistent with photochemical emission followed by collisions in the near surface region, as suggested by Kelly. The narrowness of these TOF peaks is inconsistent with thermal emission. Thermal TOF distributions can be narrowed by collisions in the near surface region with or without adiabatic expansion, but not to the degree observed at these masses.

The narrowing of these TOF distributions appears to be a function of mass, with the more massive particle (NaOH_x) possessing a more narrow distribution than the less massive particle (Si). In collisions between particles of different masses and nearly equal velocities, the more massive particles experience the smaller energy changes, so that more collisions are required for their thermalization than that of the less massive particles. Further, the more massive particles of a given energy have lower velocities, so that they eventually fall behind the lighter particles and cease to interact with them. If, as in this

case, the density of the massive particles is quite low, their collision probability drops markedly as they fall behind the others, further limiting the degree of thermalization. These effects would explain the relative widths of the Si and NaOH_x TOF distributions.

In contrast, the mass 16 emission is associated with a relatively large effective temperature and low center of mass velocity. The low v_{cm} suggests that the velocity distribution is consistent with a Maxwellian velocity distribution. A least squares fit of the mass 16 data to a pure Maxwellian ($v_{\text{cm}} = 0$) yields a very good fit with an effective temperature of 3040 K. The observation of an equilibrium thermal distribution indicates that the O is sampling a region whose temperature is on the order of 3000 K. The most simple explanation of the energy distribution is the thermal emission of O from a surface at roughly 3000 K. However, in a study of particles emitted from heated sodium trisilicate glass surfaces, Kelso and Pantano²⁵ observed significant emission of Na and O_x at temperatures greater than 850 C; at this temperature, the ratio of Na:O was estimated to be greater than 40:1. If our atomic O were simply thermally emitted from the surface, we would expect to see a strong Na^+ peak in this region. Because we do not observe such a peak, we conclude that the neutral O is produced by a photochemical process, and that its nearly Maxwellian velocity distribution is due to nearly complete thermalization by repeated collisions. This thermalization would be facilitated by the relatively small mass of atomic O, as noted above.

V. CONCLUSION

We have examined the surface topographical changes and accompanying particle emissions from sodium trisilicate glass due to exposure to 248 nm excimer laser pulses. At fluences above 3 J/cm^2 , the surface initially experiences thermally induced fracture which, after some ten's of pulses, is followed by simultaneous etching and plasma formation. The initial heating of the substrate due to photon absorption is strongly dependent on absorption centers which are induced by repeated laser pulses. Small surface

cracks created early in irradiation may significantly enhance the density of these centers or the rate at which they are formed.

Electrons, positive ions (H^+ , Na^+ , Si^+), and neutral species (O , Na , Si , and NaO_x) are emitted during the ablation process. The ions and the excited neutrals are quite energetic due to the acceleration of ions resulting from laser/plume interactions. Excited (and some ground state) Na neutrals are formed as accelerated Na ions and electrons recombine in the near surface region. The other ground state neutrals are much less energetic, with energy distributions consistent with a photochemical emission mechanism for neutral Si and $NaOH_x$. The neutral O emission appears to have a similar photochemical emission mechanism, followed by nearly complete thermalization of the energy distribution.

In the future, we expect to perform measurements on the very weak emissions at subthreshold fluences. Energy distribution measurements of neutral emission at low fluences would help confirm the photochemical mechanism proposed above, perhaps yielding insight into the nature of the bond breaking processes involved. These measurements may also provide further understanding of the the processes which modify the energy distributions as the fluence is raised.

ACKNOWLEDGMENTS

We wish to thank Roger Kelly, IBM T. J. Watson Research Center, for helpful discussions. This work was supported by the Ceramics and Electronic Materials Division of the National Science Foundation under Grant DMR 8601281, the Office of Naval Research under Contract No. N00014-87-K-0514, and the Washington Technology Center.

REFERENCES

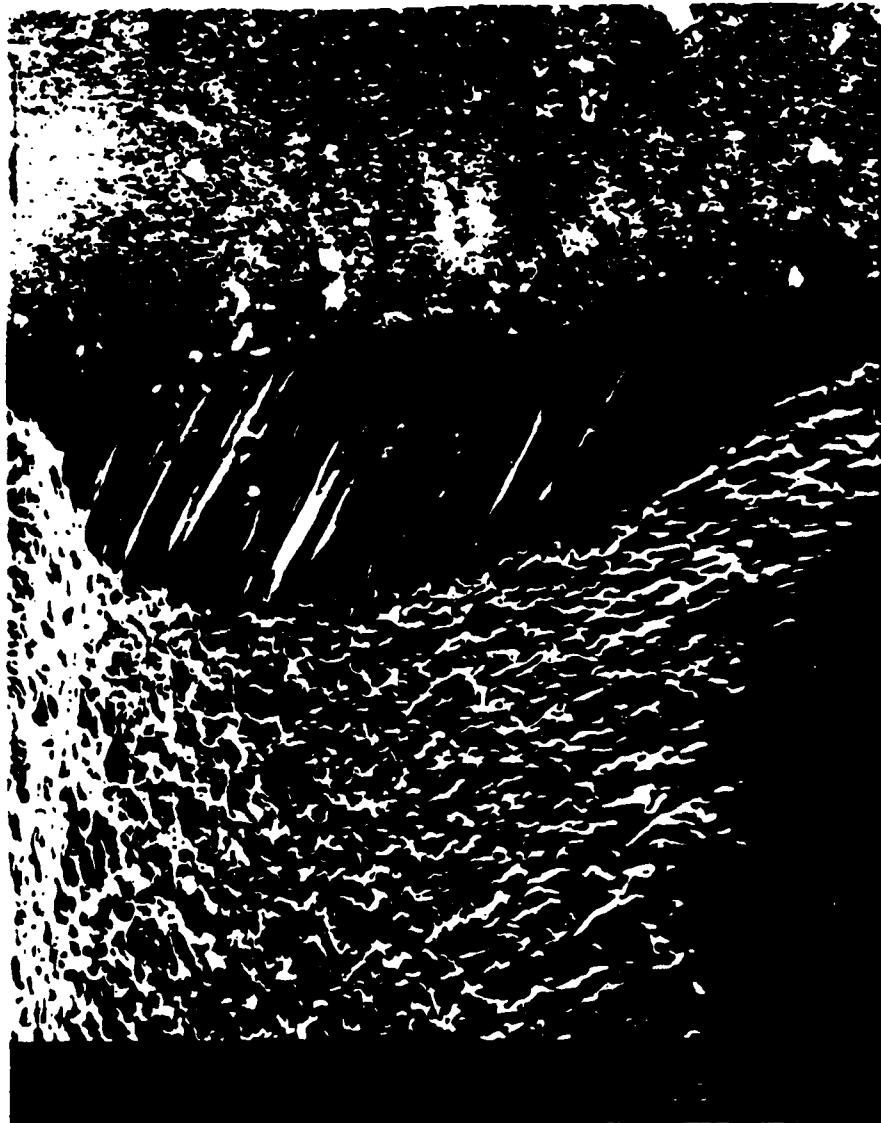
1. B. Braren and R. Srinivasan, *J. Vac. Sci. Technol. B* 6, 537 (1988).
2. G. B. Shinn, F. Steigerwald, H. Stiegler, R. Sauerbrey, F. K. Tittel, and W. L. Wilson, Jr., *J. Vac. Sci. Technol. B* 4, 1273 (1986).
3. M. Hanabusa, M. Suzuki, and S. Nishigaki, *Appl. Phys. Lett.* 38, 385 (1981).
4. R. Kelly and J. E. Rothenberg, *Nucl. Instrum. and Meth. in Phys. Res. B* 7/8, 755 (1985).
5. H. Kang and J. L. Beauchamp, *J. Phys. Chem.* 89, 3364 (1985).
6. J. E. Rothenberg and G. Koren, *Appl. Phys. Lett.* 44, 664 (1984).
7. J. E. Rothenberg, G. Koren, and J. J. Ritsko, *J. Appl. Phys.* 57, 5072 (1985).
8. R. W. Dreyfus, Roger Kelly, and R. E. Walkup, *Appl. Phys. Lett.* 49, 1478 (1986).
9. D. R. Baer, L. R. Pederson, and G. L. McVay, *J. Vac. Sci. Technol. A* 2, 738 (1984).
10. J. H. Craig and J. L. Hock, *J. Vac. Sci. Technol.* 17, 1362 (1980).
11. N. L. Boling, M. D. Crisp, and G. Dube, *Appl. Optics* 12, 650 (1973).
12. H. L. Smith and A. J. Cohen, *Phys. Chem. Glasses* 4, 173 (1963).
13. H. B. Nielsen, J. Reif, E. Matthias, E. Westin, and A. Rosen, in *Desorption Induced by Electronic Transitions III*, edited by R. H. Stulen and M. L. Knotek, (Springer-Verlag, Berlin, 1988) pp. 266-273.
14. R.A.B. Devine, C. Fiori, and J. Robertson, *Mat. Res. Soc. Symp. Proc.* 61, 177 (1986).
15. N. Bloembergen, *Appl. Optics* 12, 661 (1973).
16. M. Tomozawa, to appear in *J. Non-Crystalline Solids*.
17. R. W. Dreyfus, F. A. McDonald, and R. J. von Gutfeld, *J. Vac. Sci. Technol. B* 5, 1521 (1987).

18. J. H. Mackey, H. L. Smith, and A. Halperin, *J. Phys. Chem. Solids* 27, 1759 (1966).
19. R. Kelly and R. W. Dreyfus, *Surface Science* 198, 263 (1988).
20. R. Kelly and R. W. Dreyfus, *Nucl. Instrum. and Methods in Phys. Res.* B32, 341 (1988).
21. J. M. Green, W. T. Silfvast, and O. R. Wood II, *J. Appl. Phys.* 48, 2753 (1977).
22. R. E. Walkup, J. M. Jasinski, and R. W. Dreyfus, *Appl. Phys. Lett.* 48, 1690 (1986).
23. Y. Bykovskii et. al., *Sov. Phys. Tech. Phys.*, Vol. 18, No. 12, June 1974.
24. R. Kelly, Private communication.
25. J. F. Kelly and C. G. Pantano, *J. Vac. Sci. Technol. A* 3, 1343 (1985).

Figure Captions

- FIG. 1. The edge of a typical etched region on sodium trisilicate glass (400 shots, 5 J/cm²).
- FIG. 2. "Coral-like" structure at the bottom of a typical etch pit (400 shots, 5 J/cm²).
- FIG. 3. Edge of a typical etch pit (bottom) and a close-up of the glass surface near the etch pit (top), showing spherical droplets deposited on the glass surface outside of the etch pit (400 shots, 3.5 J/cm²).
- FIG. 4. Four exposed regions formed by increasing numbers of laser pulses: a) 10, b) 20, c) 40, and d) 80 shots, each at a fluence of 3.5 J/cm².
- FIG. 5. TOF spectra from sodium trisilicate glass taken a) with ionizer "on" and b) with ionizer "off." Time $t=0$ corresponds to the arrival time of the laser pulse
- FIG. 6. Mass selected positive ion signals detected masses 1, 23, and 28 with a Bessel Box/QMS detector. The axis of the QMS was somewhat inclined to the surface normal.
- FIG. 7. Excited neutral TOF measurements made by (i) a CEM detector positioned 8.5 cm from the sample surface and (ii) a photomultiplier tube with a Na D line filter and collimator viewing a region 8.7 cm from the sample surface.
- FIG. 8. Mass selected neutral signals detected at masses 16, 28, and 40, normalized to a common peak height. The solid lines represent best fit "drifting Maxwellians." The early portion of the mass 16 curve has been removed to eliminate interference from the excited neutral peak.

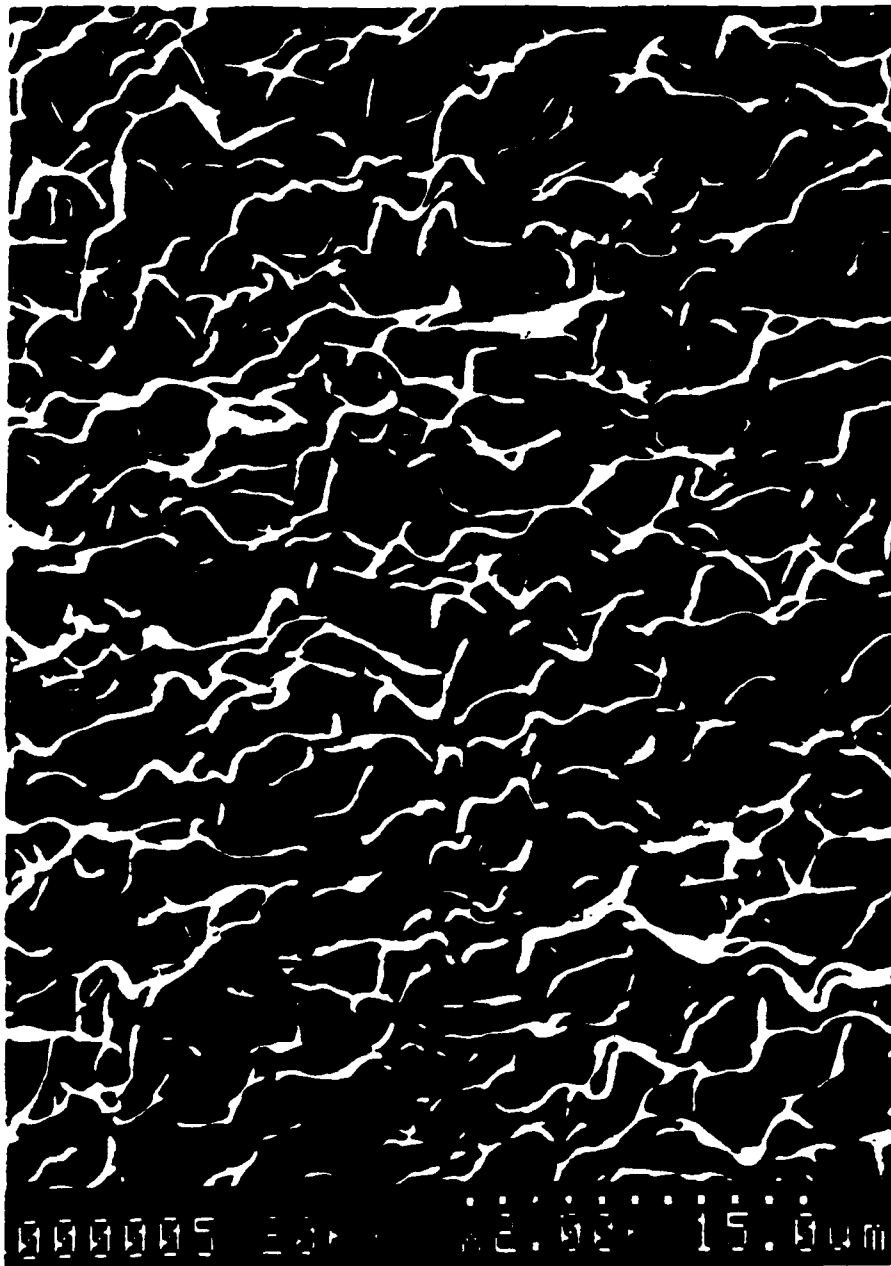
- FIG. 9.** Time exposures of the ablation plume recorded taken over several laser pulses. b) is overexposed relative to a) to bring out the geometry of the less intense portion of the plume. Note the near-spherical symmetry of both regions.
- FIG. 10.** Visible spectrum of the light emission from the ablation plume at a distance of 2 cm from the surface. Almost all of the lines can be assigned to atomic Na.
- FIG. 11** Kinetic energy corresponding to the arrival time of the peak Na D line intensity as a function of laser fluence.
- FIG. 12.** Energy distributions of a) the excited neutral Na density, as inferred from the Na D line TOF curves, and b) the Na ionic flux as measured with a Bessel box energy filter. Both measurements were made at a fluence of 3.0 J/cm^2 . The solid lines correspond to the appropriate simple Maxwellian distribution fit to the data at one point (the peak). In b), the excited neutral density is also shown to facilitate comparison with the ion energy distribution.



Masked

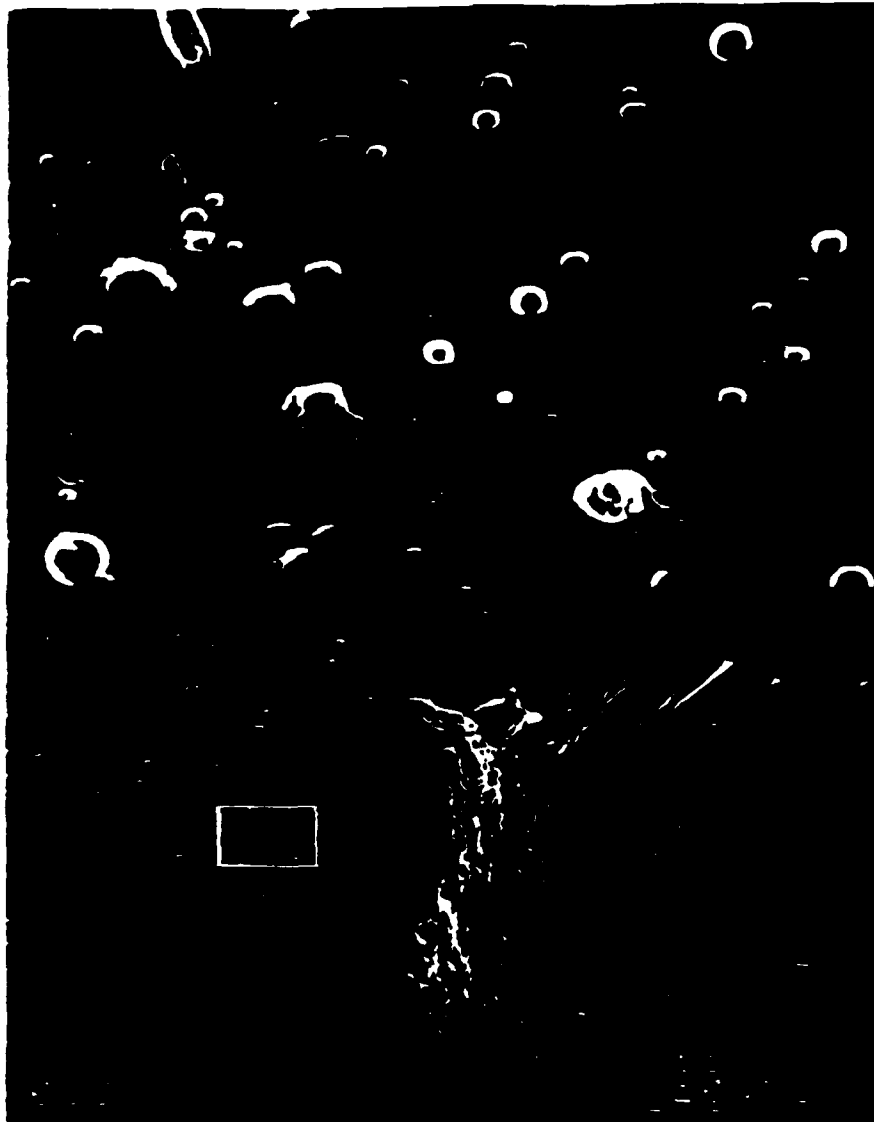
350X

Unmasked



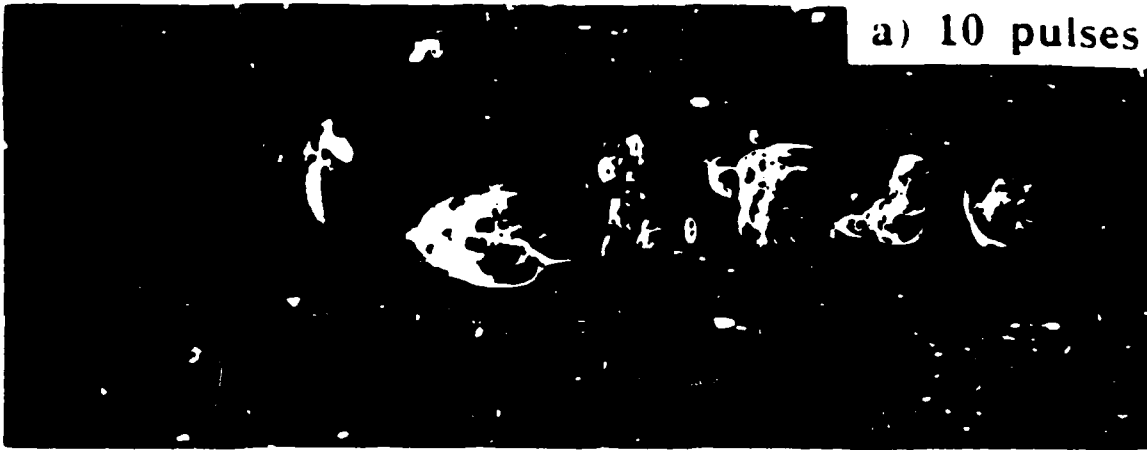
2000X

Fig. 2



2500X

250X



b) 20 pulses



c) 40 pulses



d) 80 pulses



200 μm

Fig. 4

TOF Spectra from Sodium Trisilicate

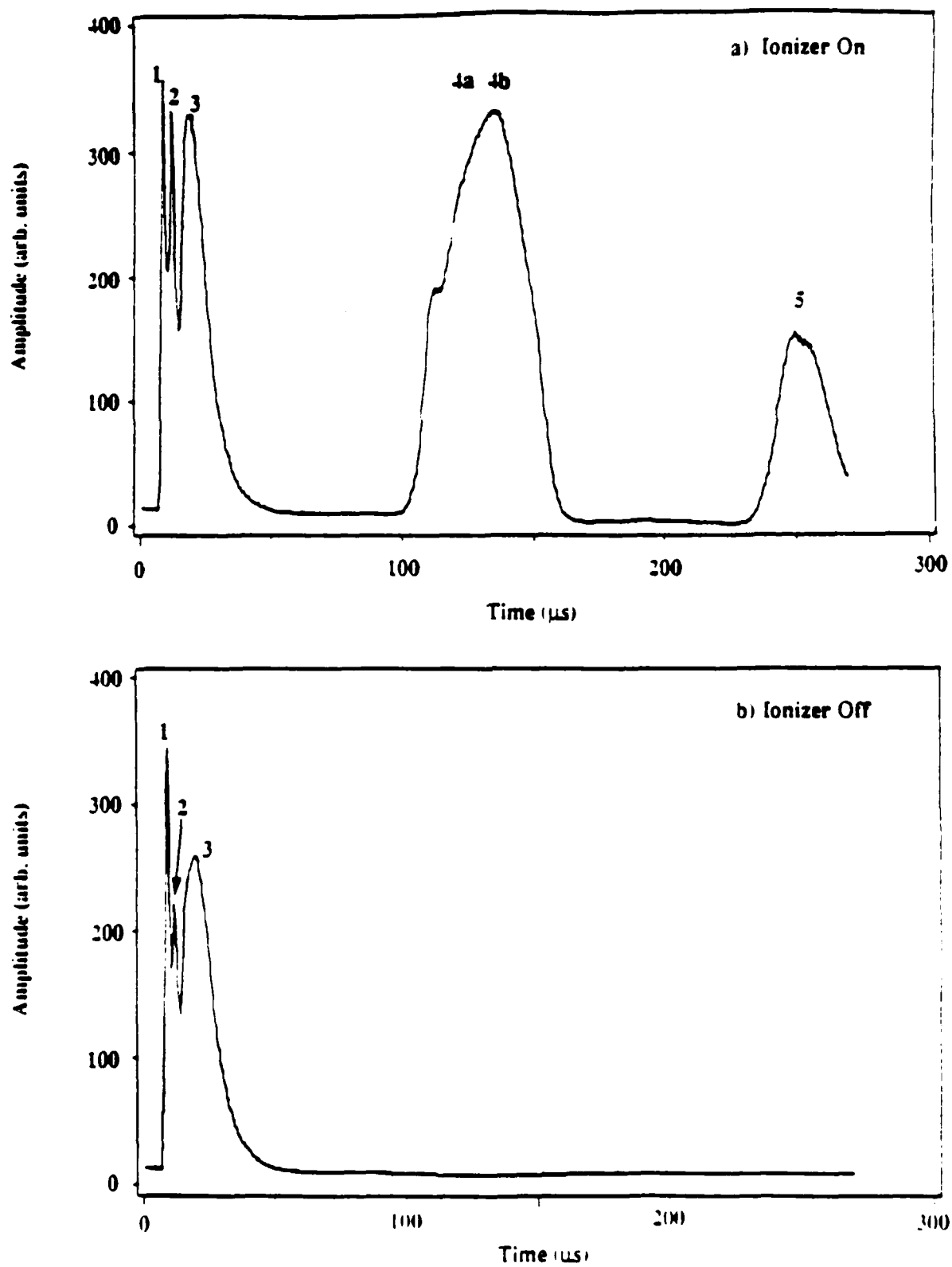


Fig. 5

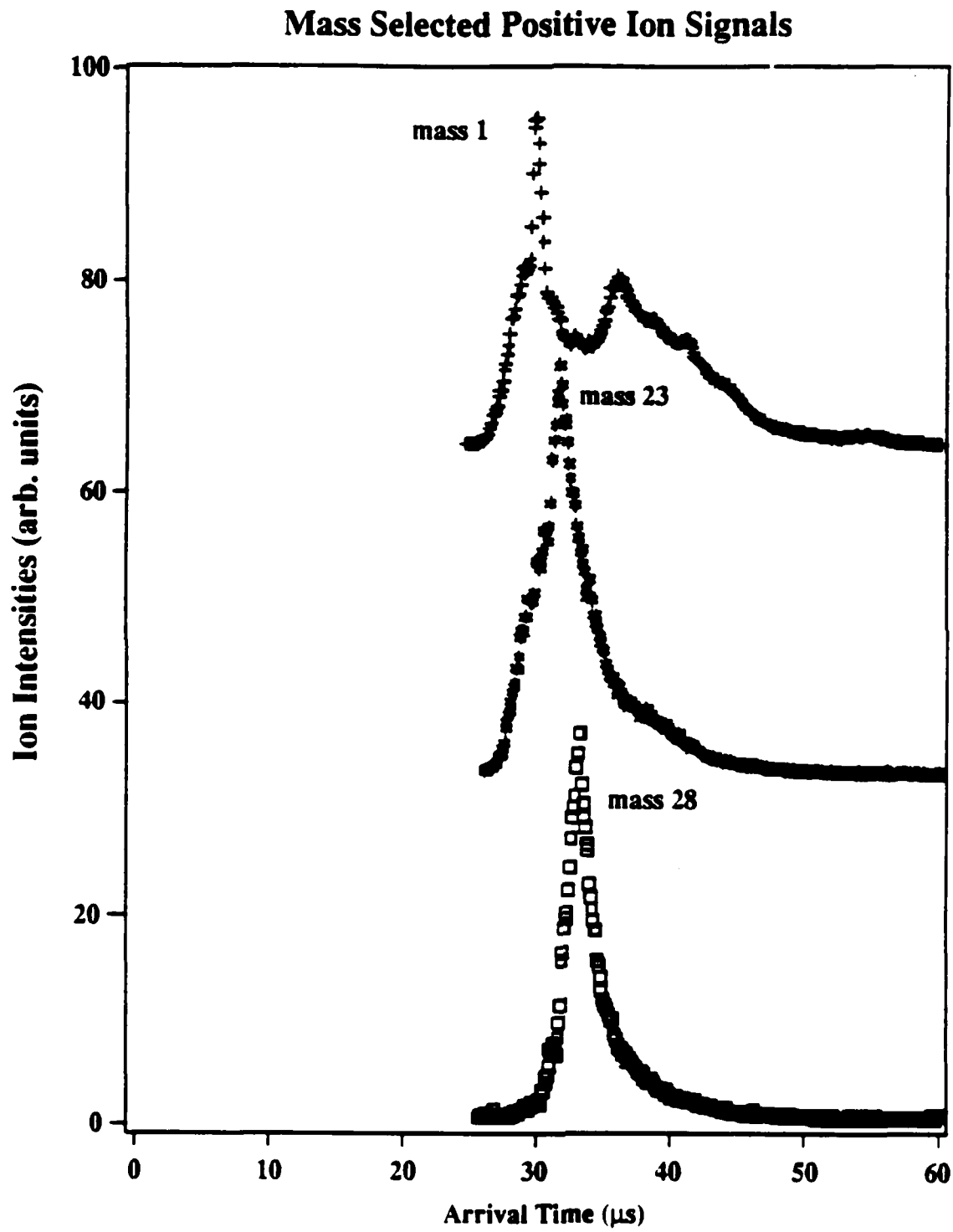


Fig. 6

Time Distributions of Detected Particles and Photons

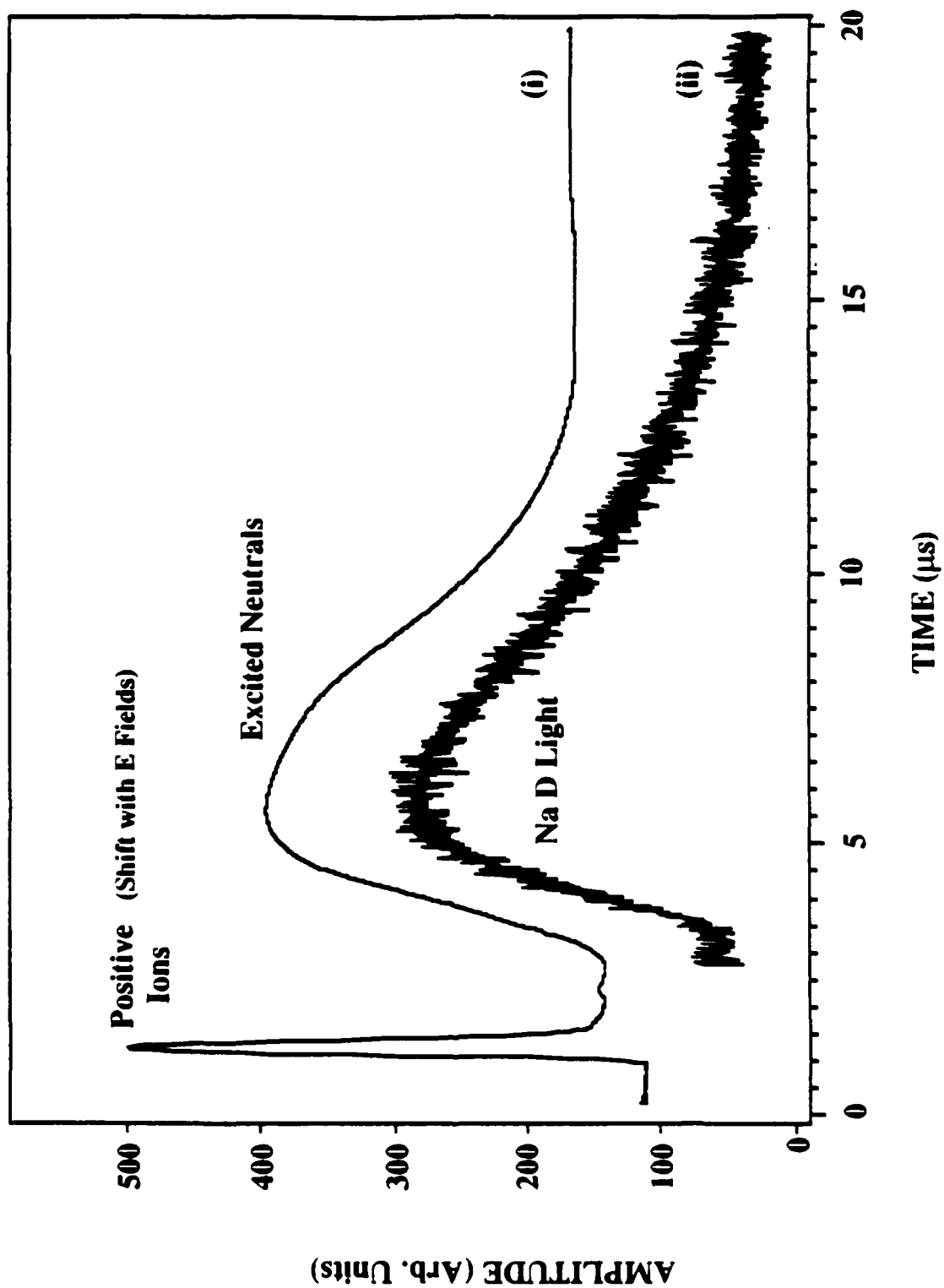


Fig. 7

Slow Neutral Emission

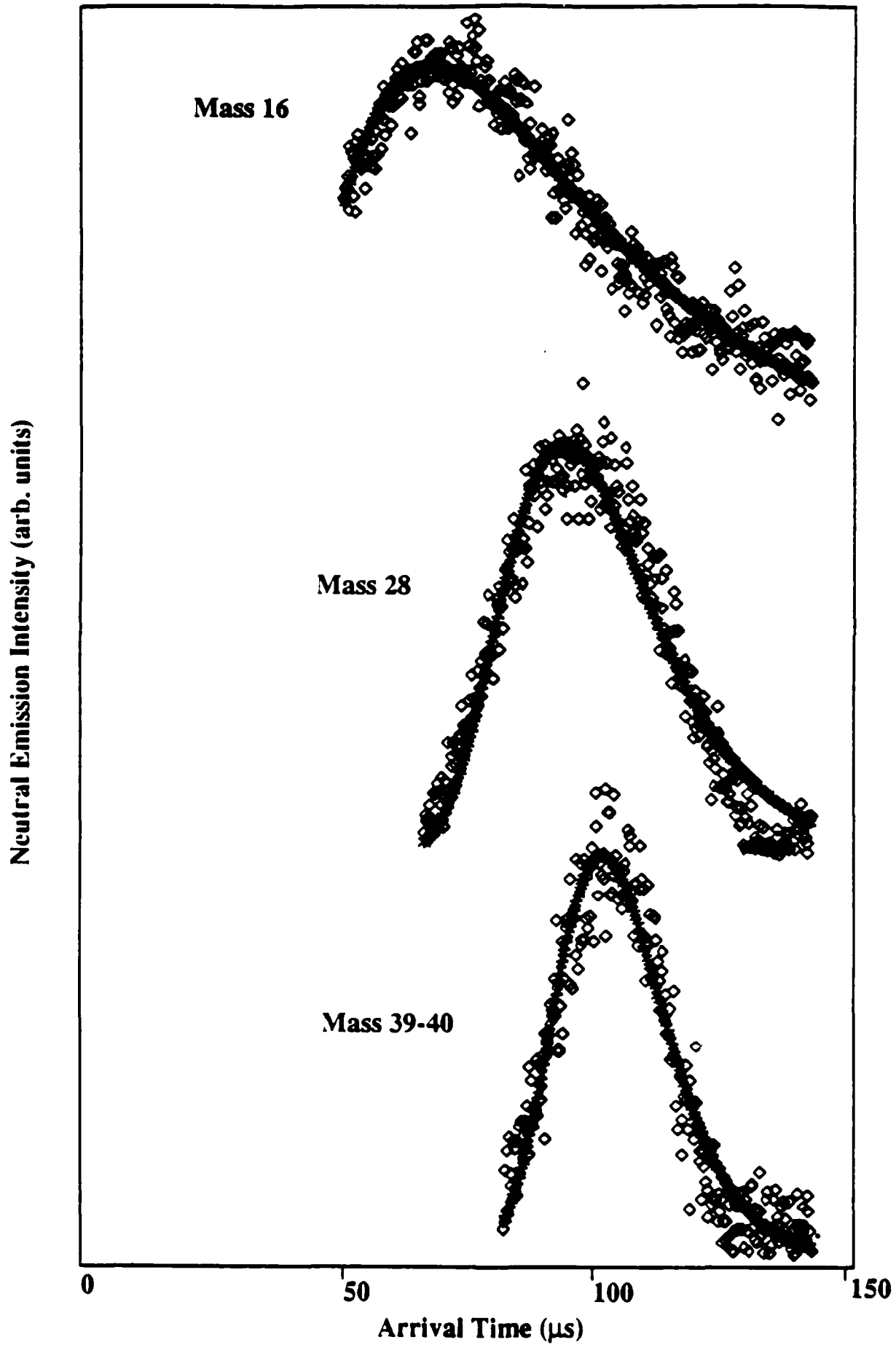
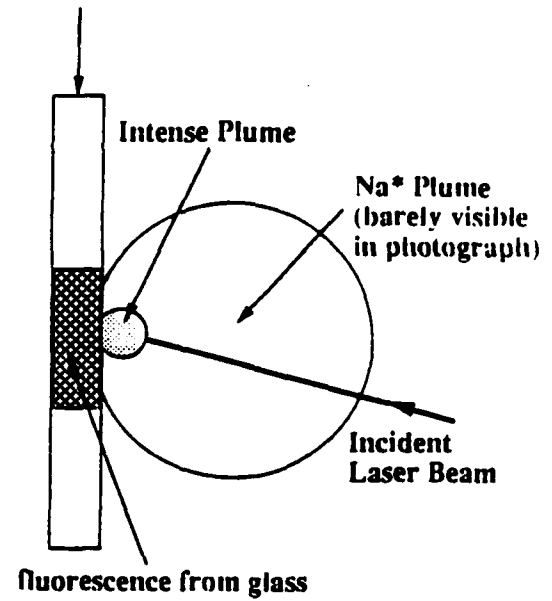


Fig. 8

Sodium Trisilicate Glass Sample



Sodium Trisilicate Glass Sample

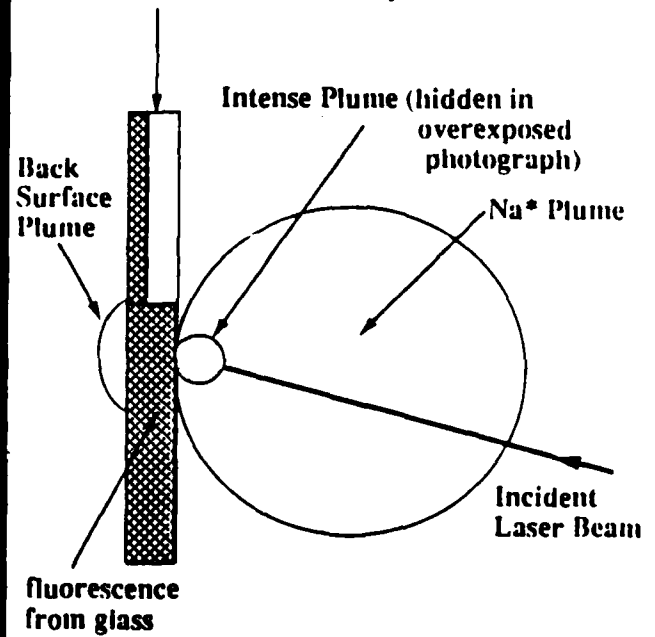


Fig. 9

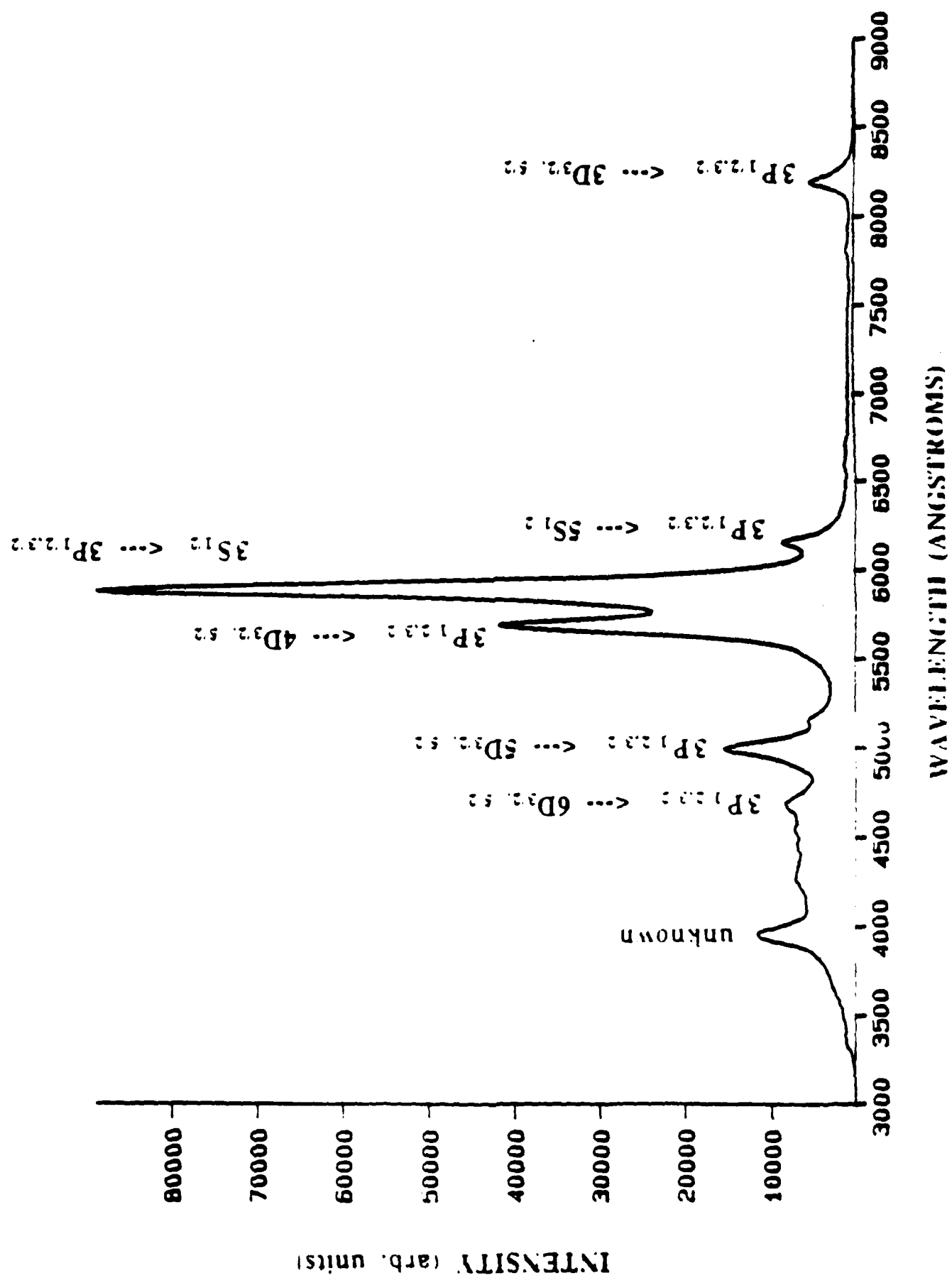


Fig. 10

Kinetic Energy Corresponding to Peak of TOF of Excited Na Atoms vs Laser Fluence

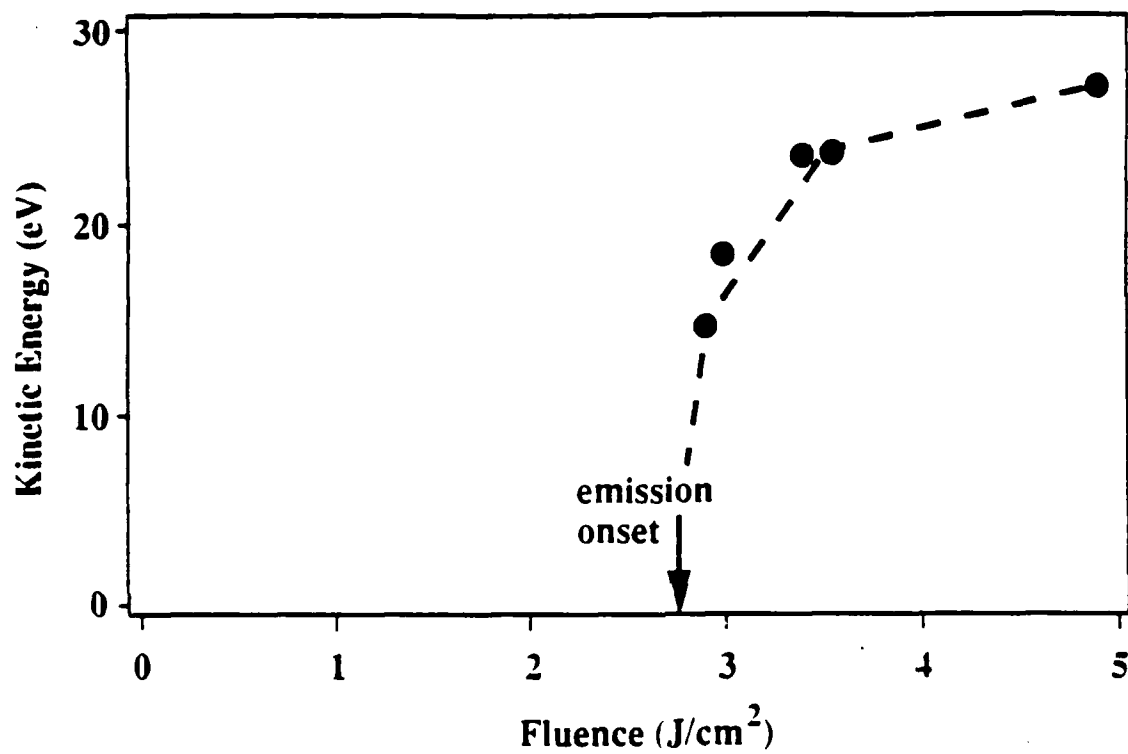


Fig. 11

Sodium Excited Neutral and Ion Energy Distributions

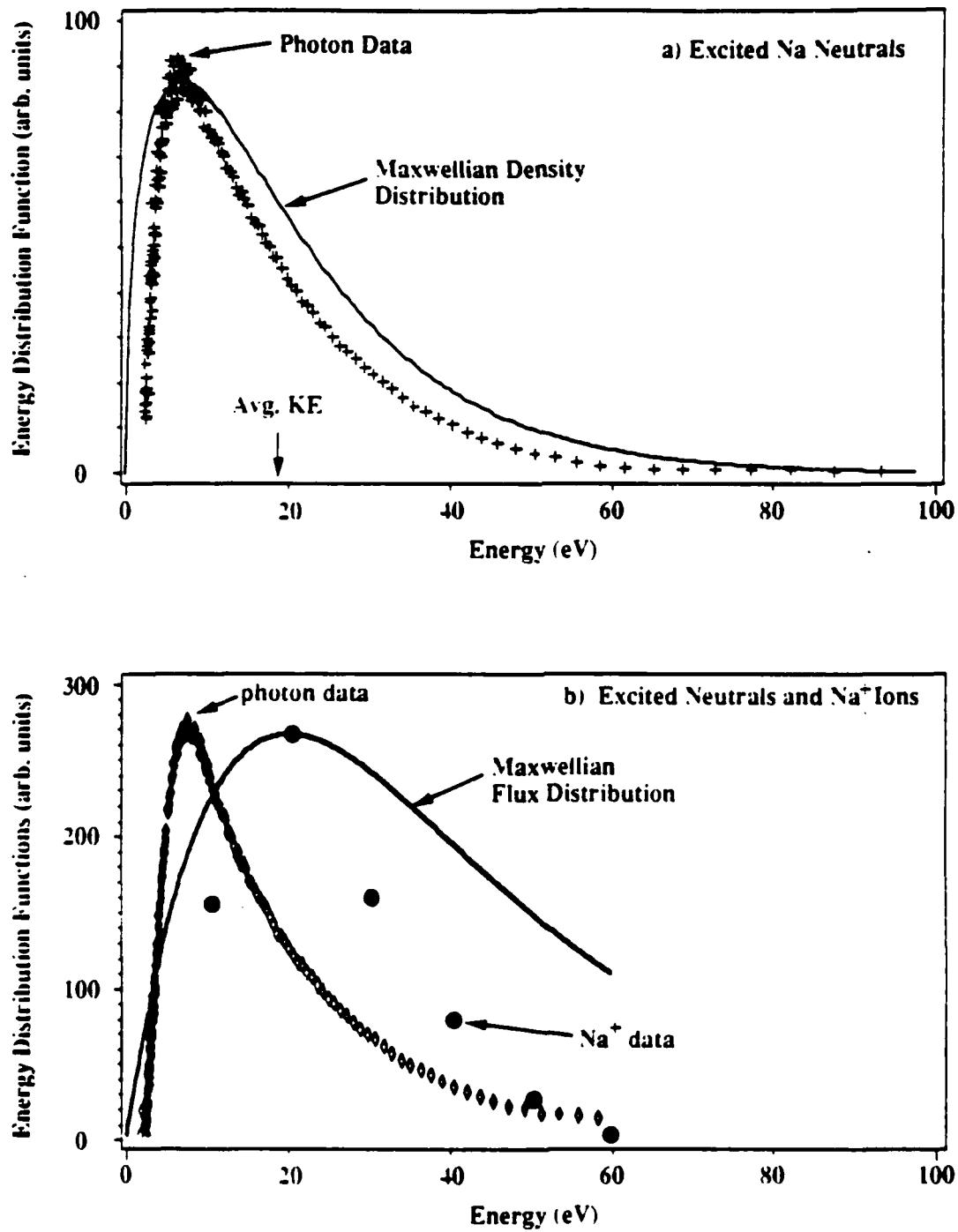


Fig. 12

XIII. Additional Work

Neutral Particle Emission from TGDDM/DDS epoxy: We have measured a number of properties of the neutral molecule emission accompanying fracture of TGDDM/DDS epoxy. This includes the time evolution of the emission of masses 18 (H_2O), 28 (N_2) and 64 (SO_2). The H_2O and N_2 are believed to be occluded gases, but the SO_2 appears to be generated by bond scissions. In Fig. 1, we show the time dependence of mass 18 (H_2O) for two different distances of the mass spectrometer ionizer from the sample where $t=0$ represents the fracture event (typically 10 μs in duration). Note that the onset of detected signal and the peak position of these curves shifts over as the distance from the sample is increased. From these measurements (taken at two flight distances from the sample) we have obtained an average temperature of the gases and the time dependence of the emission (on a microsecond time scale) relative to fracture. For this particular epoxy, gas temperatures of ~ 425 K are obtained. The rate of gas release is shown to be a maximum *after* the fracture event. This suggests that the major source of the gases arises in the plastic zone surrounding the moving crack tip as opposed to the free surface created by fracture. In the case of SO_2 emission, the evolution intensities could be probing bond breaking processes in the plastic zone during fracture. In principle, neutral emissions from any brittle material can be studied using this new method. We are constructing a system that employs two mass spectrometers which will greatly facilitate the acquisition of this type of data.

Scanning Tunneling Microscopy of Cracks and Fracture Surfaces.

We have installed and have running a scanning tunneling microscope which exhibits atomic resolution on standard surfaces such as the cleavage plane of graphite. Also visible are steps of 2-3 atom heights. We are attempting to image the region around a single crack in single crystal Si. With limited resolution, Bonnell and Clark (IBM T. J. Watson, personal communication) have imaged a single crack in single crystal Si with the STM. Although we have not yet found the tip of the crack, we expect that improvements in our ability to position the tip precisely will remedy this difficulty. The shape and features of the surface of any material in the region of a crack have never been imaged with atomic resolution and would provide new information about the fracture process.

In addition, we have succeeded in tunneling to very thin Au coated surfaces of highly insulating surfaces such as NaCl and MgO. We have observed good stability and conductivity in films ~ 20 -100 \AA in thickness, with no evidence of Au clusters. The best resolution to date is ~ 3 \AA laterally (in the plane of the surface) and 5-10 \AA vertically (normal to the surface). It is important to emphasize that we are using STM techniques on insulating surfaces and striving for maximum resolution. The major advantage of the STM relative to the atomic force microscope (AFM), which has potentially higher resolution, is the *reliability* of the STM. We have successfully obtained topographical information on 100% of the gold coated surfaces produced to date.

Three STM scan of a gold-coated MgO fracture surface (single crystal broken in three point bend) are shown in Fig. 2. The scans shown in Figs. 2a and 2b were taken on the tensile side of the fracture surface, while that of Fig. 2c was taken on the compressive side of the fracture surface. As shown in Fig. 2d, the surface near the tensile side of samples broken in this geometry is inclined at $\sim 16^\circ$ to the compressive surfaces. The compressive surfaces are macroscopically (100) in orientation, while the tensile surfaces are approximately (720). Fig. 2a shows a typical flat region of the tensile side. It is $\sim (720)$ in orientation on the scale of hundreds of nm, with deviations from the dominate plane of less than 36 \AA . A number of similar planes were found over the entire tensile side and were typically of micron dimensions. Interspersed between the smooth regions were patches of rough topography, one of which is shown in Fig. 2b. Again, the larger facets are of $\sim (720)$ orientation. At our present resolution (5-10 \AA), these facets do not appear to be composed of (100) (cleavage plane) steps. The sloping regions connecting the larger facets might still be crystallographic.

On the compressive side (2c) a variety of crystal orientations are observed; each facet tends to be considerably smaller than on the tensile side, typically a few hundred \AA in size. The dominant orientation was (100) with significant numbers of (720) planes. In addition, we observed small patches of (210), (920), (811), (731), (321), (381), and (140) surfaces. It should be emphasized that these surfaces could be atomically stepped which would not be detected. No microscopic (110) or (111) surfaces were observed, even though (110) is a known secondary fracture plane and is frequently macroscopically observed in MgO.

Fracture through the compressive side of a crystal loaded in three-point bend is probably complicated by plastic deformation prior to fracture. In the region of the loading nose, stresses can be quite high and for strong samples (small surface flaws on the tensile side), significant plastic deformation is possible. As the

crack propagates through regions that have experienced slip and/or dislocation pile up, it can be strongly deflected. In addition, the crack front at the boundary of the tensile and compressive sides can be quite complicated, actually occupying a variety of different crystal planes. Figure 3 shows another region on the compressive side where, in addition to facets of several hundred Å dimensions, there appears a set of parallel steps 20-50 Å high running parallel to the direction of propagation. Some of these steps appear to merge or emerge at points. Similar step creation has been observed on MgO fracture surfaces where the crack is intersected by screw dislocations. Interactions between cracks propagating on nearby planes may also be responsible for the merging of some steps. We have yet to determine the crystallographic directions of these features, but we suspect that (100) orientations will dominate in the central portion. Note that each corner of this plot is tipped at a sharp angle to the central plateau.

As additional evidence of the strong dependence of topography on previous plastic deformation, Fig. 4 shows two scans of a distinct feature which appears on the compressive side of MgO fractured in three point bend. Several similar features were found in a $3\text{ }\mu\text{m} \times 3\text{ }\mu\text{m}$ neighborhood (the current limit of our large area scan). Each of these triangular depressions were associated with long troughs lying along the (100) direction and comprising substantial amounts of crack deflection. Active slip planes on the compressive side of the crystal are known to intersect the fracture surface along the same direction. We suggest that these unusual features result from the crack interacting with these slip bands. It should be noted that the density of dissipated energy on a local scale of a few tens of Angstroms could be quite high and could be considered a type of hot spot. A question of interest that relates to our previous studies (see Sections 11 and 12) would be the influence of these localized, high energy events on the emission of light and particles.

Construction of Atomic Force Microscope.

We have made substantial progress on the design and construction of an Atomic Force Microscope utilizing electron tunneling for sensing the motion of a cantilever beam. This motion is in response to the atomic and electrostatic forces between a tip and a fracture surface of an insulating material, and can include energetic materials. The advantage of such an instrument for insulators is that no conducting coating is necessary. One major difficulty is the interpretation of the resulting scans. One is in fact using a macroscopic tip as a stylus, but sensing the response on an Å size scale.

As expected, vibrations have been a major problem and we are focusing on various vibration isolation schemes to minimize their influence. The very small size of the atomic force cantilever system requires that all fabrication be performed under a microscope. The design we are currently using was first suggested by Bryant (P.J. Bryant, U. Missouri-Kansas City, private communication). The first step in the fabrication process is to cut platinum foil for the AFM lever, where the platinum foil is prepared by hammering a $25\text{ }\mu\text{m}$ wire into a thin $4\text{ }\mu\text{m}$ foil. This foil is sliced into levers approximately $170\text{ }\mu\text{m} \times 15\text{ }\mu\text{m}$. A cantilever support consisting of a $400\text{ }\mu\text{m}$ tungsten wire bevelled to 15 degrees at one end, is attached via insulating epoxy to an etched STM tip. A wire lead is attached to the cantilever support by conducting epoxy. The final step in the fabrication process is to attach the lever to the cantilever support. This is accomplished using a micromanipulator with a microscopic capillary tube with applied suction acting as a microforcep. The lever is fastened to the support with a small amount of conducting epoxy. After curing the atomic force cantilever system is ready to be used in our "conventional" STM apparatus with the wire lead to the cantilever support supplying the "sample" bias. The current mode of operation is a compression, i.e., the tip is pushed against the surface, in analogy to a stylus profilometer, with forces on the order of 10^{-8} N .

In Fig. 5 we show a 64 line scan of a relatively smooth region of the compressive side of a MgO three-point bend fracture surface. A possible artifact is a "jitter" corresponding to a few Å deflection of the tip. In Fig. 5 this jitter corresponds to the fine structure observed most clearly in the smooth regions of the surface. This jitter could be due to stick-slip of the force lever producing relative lateral motion between the tunneling tip and the force lever. This shows up in a periodic increase/decrease in tunneling current, which activates the Z piezo. Some features, usually of much lower frequency, may represent deflections at the mechanical resonance frequency of the lever. Nevertheless, we are starting to get topographical information on fracture surfaces of insulators. It should be realized that this probe is extremely fragile and eventually a crash on the surface results in irreversible damage, requiring replacement of the force probe.

Figure 6 and 7 show AFM images of two considerably more rough regions of the compressive side of the same MgO crystal. Figure 6 has features less than 6Å in the Z direction that are resolved and reproducible under repeated scans. To date, no evidence of damage to the surface at the forces we are applying has been observed. There does appear to be a problem with oscillations in the force lever when passing over stepped features on the order of 100 Å in height. The edges of these features are surprisingly sharp, matching in many ways the results from the STM on Au coated MgO. Fig. 7 illustrates the scan over a very rough portion of

the surface with excursions in Z equivalent to ~ 1000 Å. On such a large scale, the oscillations in the lever arm are not really very significant.

Future work will concentrate on improvements in resolution and noise reduction to provide more routine scans of fracture surfaces. In addition, we have built the electronics for an attractive force AFM which utilizes the deflection of a laser beam sensed by a position sensitive detector. We then will be able to probe surfaces without contact between the force lever tip and the surface. This is particularly important in our efforts to characterize charge distributions on fracture surfaces of insulators.

Figure Captions

- Fig. 1. The time dependence of the emission of water from the fracture of epoxy. The two curves represent signals obtained for two different distances of the mass spectrometer from the sample. Note the arrival time of the fastest molecules shifts to later times for the longer distance. Similarly, the peak position shifts and the entire curve broadens due to the velocity distribution of the water molecules emitted from the epoxy.
- Fig. 2. Scanning Tunneling Microscope scans of gold coated MgO fracture surfaces. The crystal was broken in three point bend. a) and b) were scans over portions of the surface towards the tensile side of the sample; c) is a region on the compressive side. d) shows the basic orientation of these two portions of the fracture surface.
- Fig. 3. An STM image of a portion of the compressive side of an MgO fracture surface which shows a series of steps 20- 50 Å in height across a square facet (probably (100) in orientation).
- Fig. 4. STM images of a feature which appears in regions of high plastic deformation created during loading. Severe crack deflection and possibly branching have occurred in this region.
- Fig. 5. An Atomic Force Microscope scan (64 lines) on the compressive side of an uncoated MgO fracture surface.
- Fig. 6. An AFM scan on the compressive side of MgO showing both flat and rougher regions.
- Fig. 7. AFM scan on the compressive side of MgO in an extremely rough region.

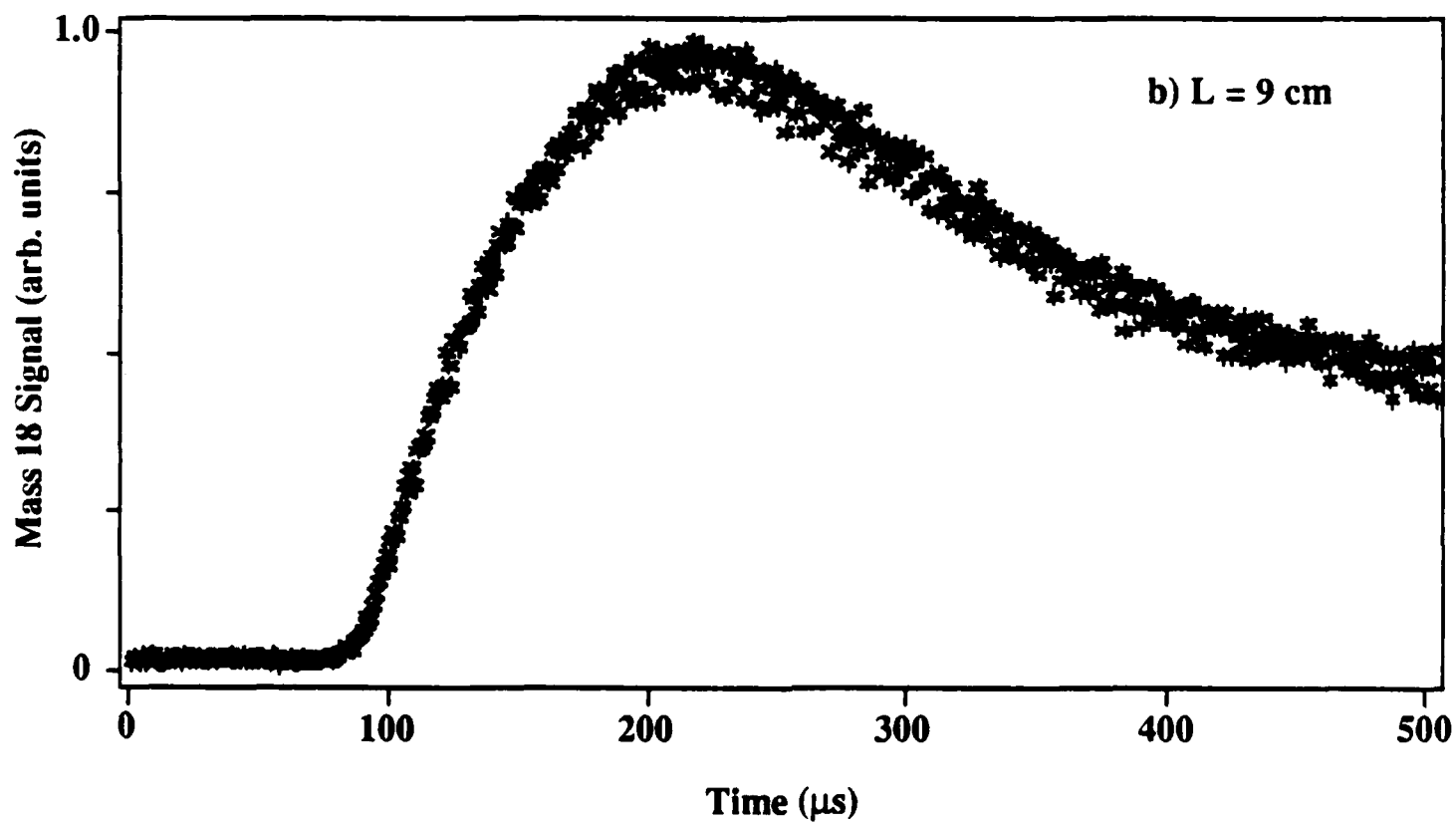
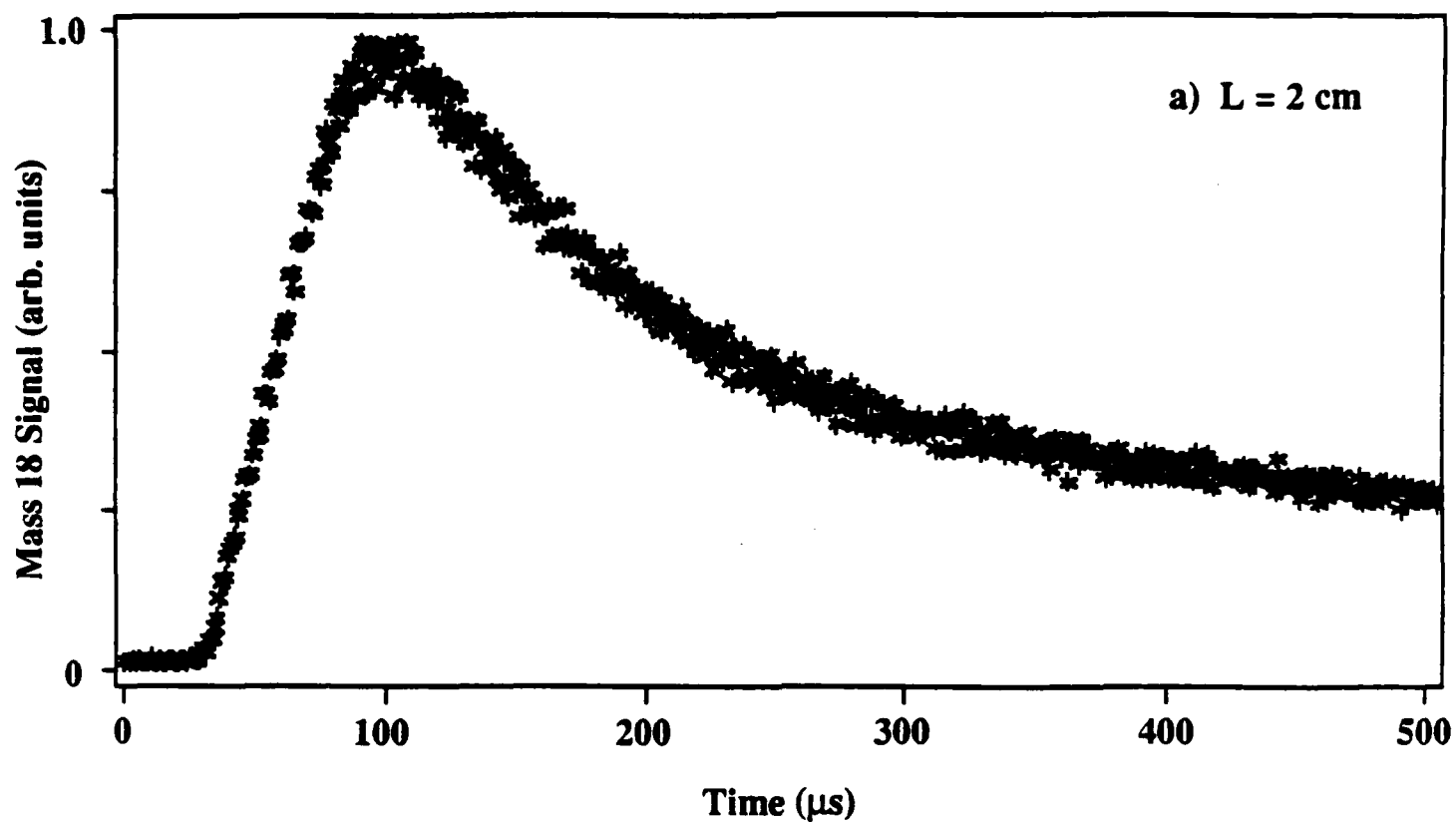
Mass 18 (H_2O)

Fig. 1

STM Scans of an MgO Fracture Surface

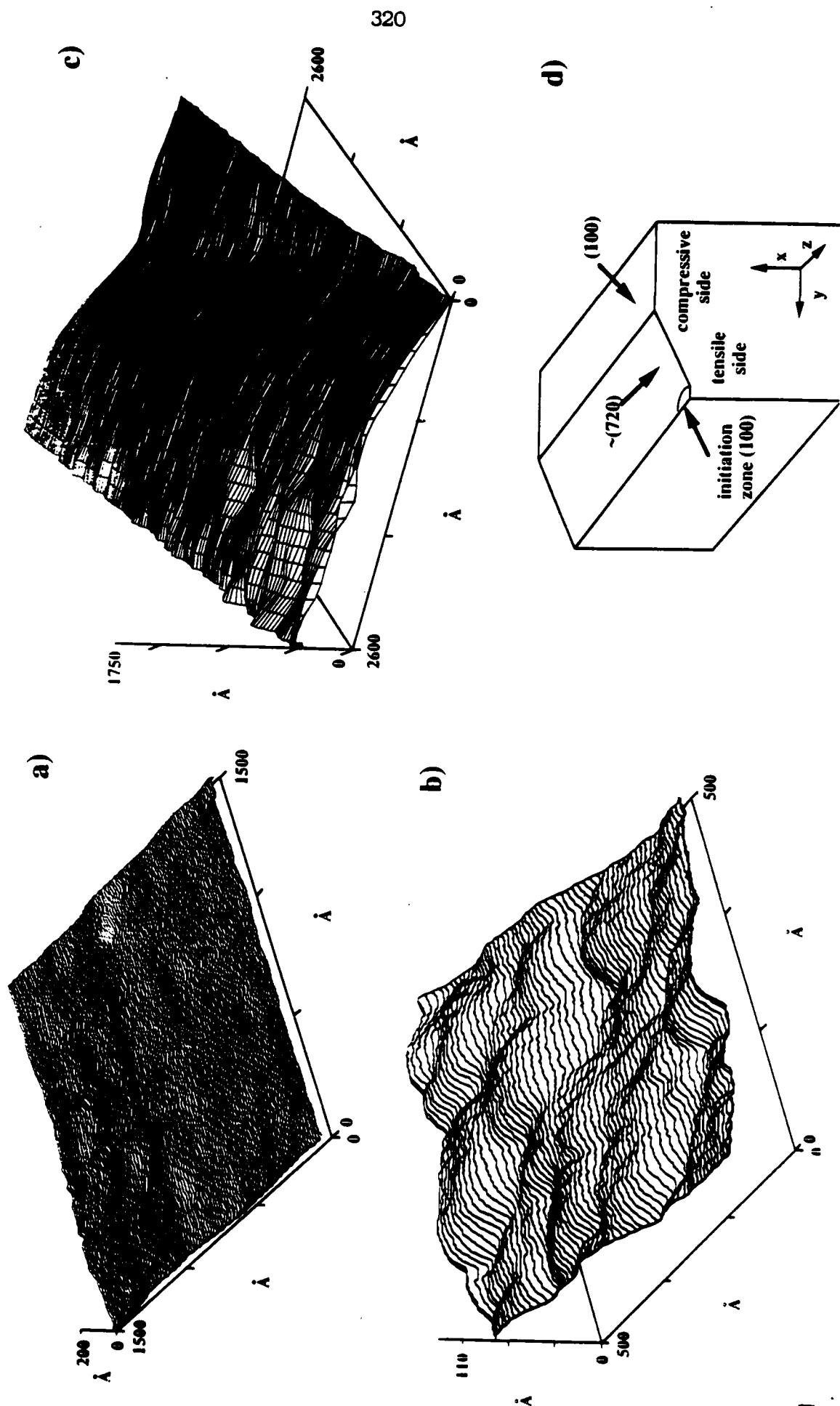


Fig 2

**STM Image of the MgO Fracture Surface
(Compressive Side in 3 Pt-Bend)**

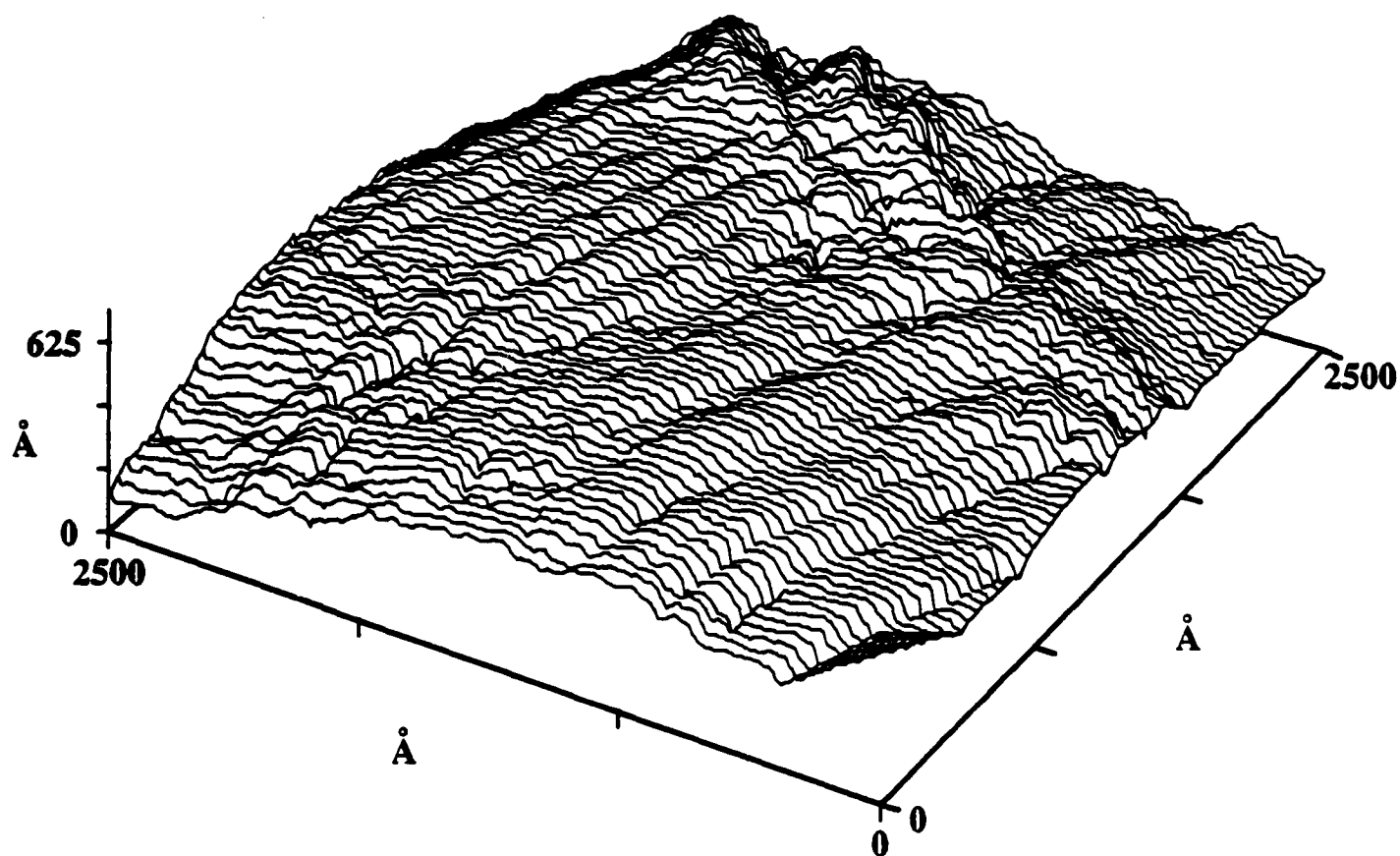
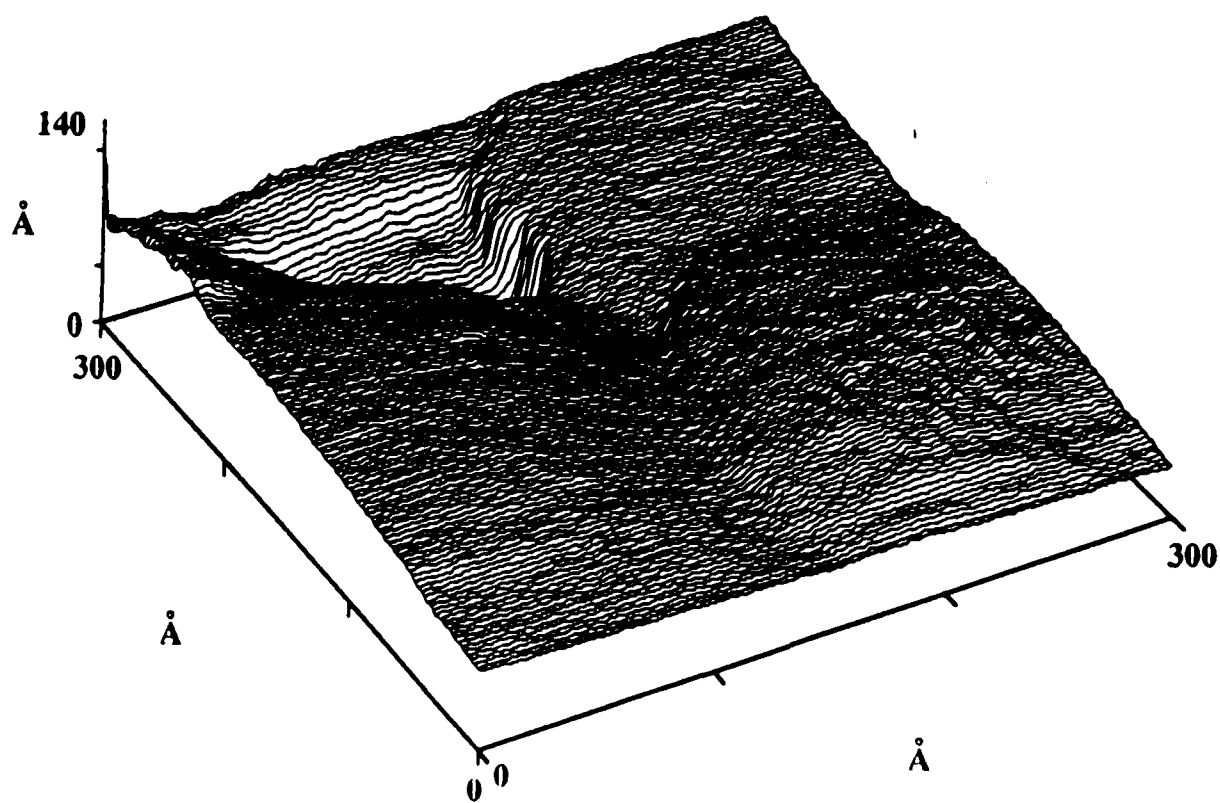
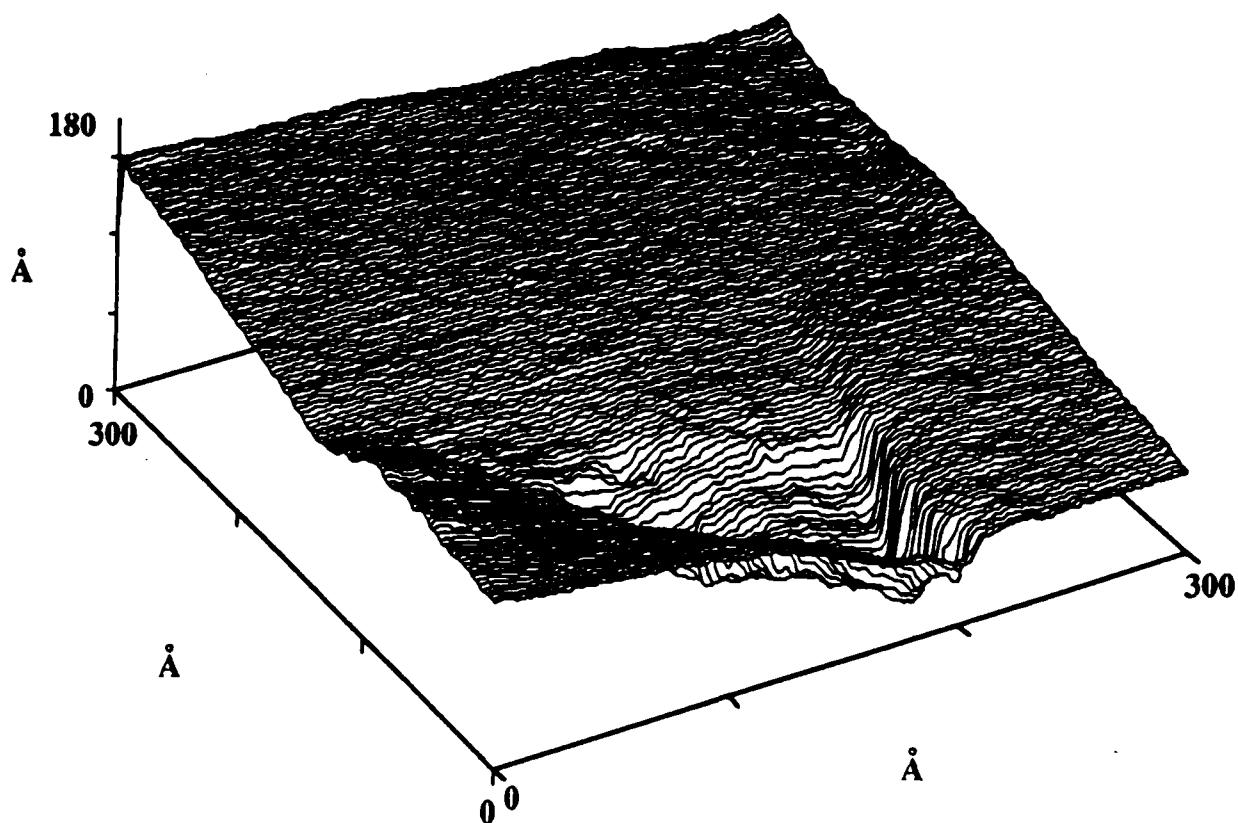


Fig 3

MgO Fracture Surface Compressive Side



AFM Image of MgO Fracture Surface
Compressive side in 3 Pt-Bend

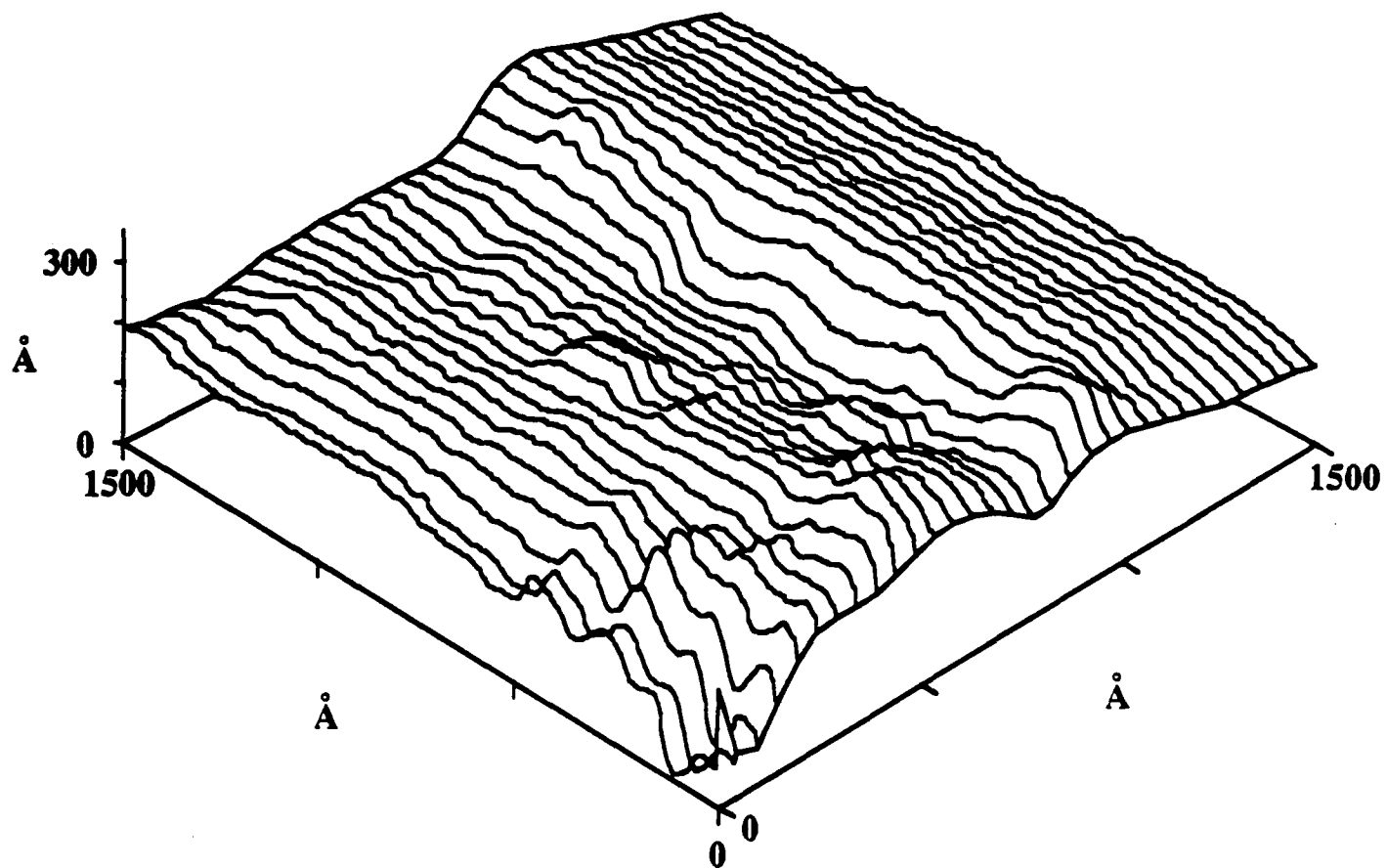


Fig 5

**AFM Image of a MgO Fracture Surface
(Compressive side in 3 Pt-Bend)**

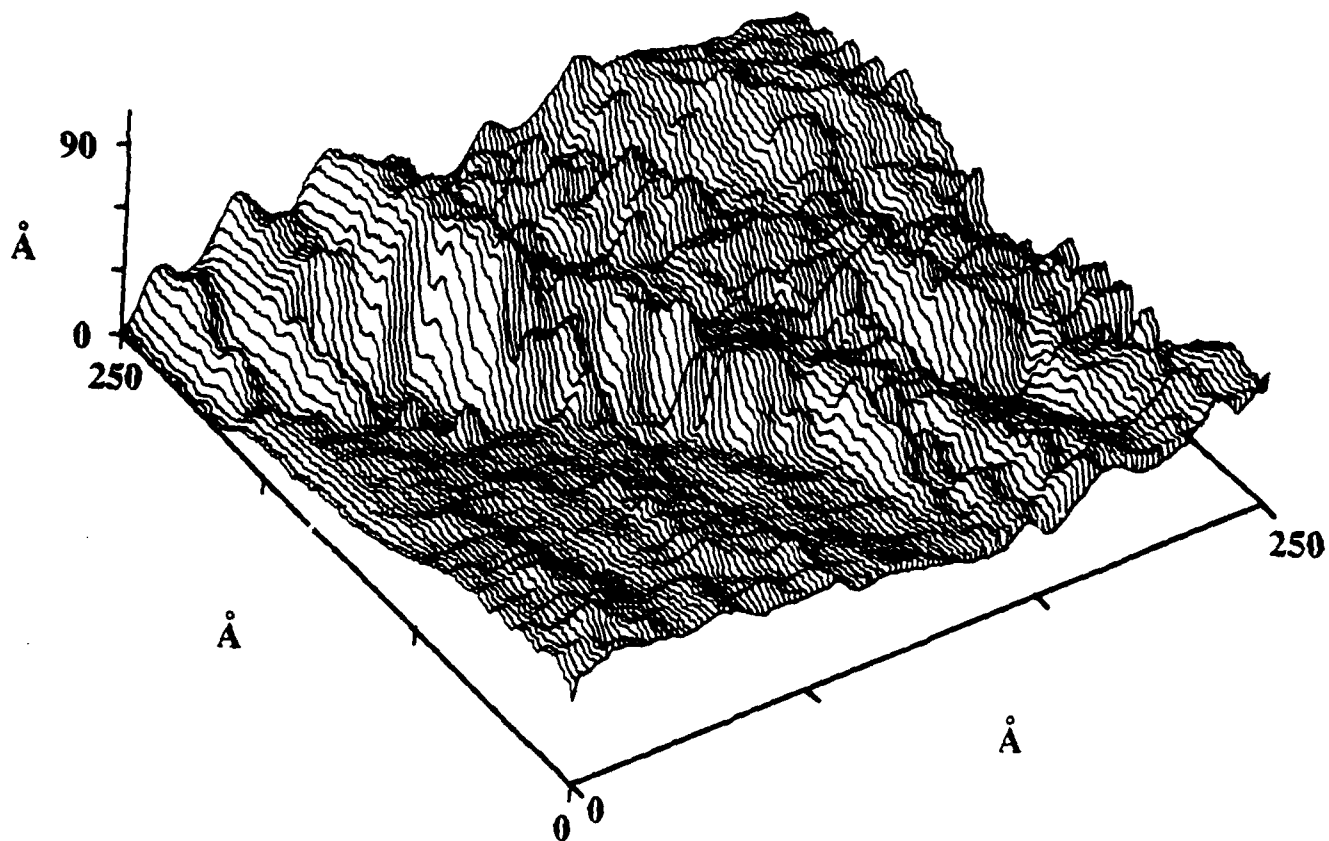


Fig. 6

AFM Image of the MgO Compressive Side Fracture Surface

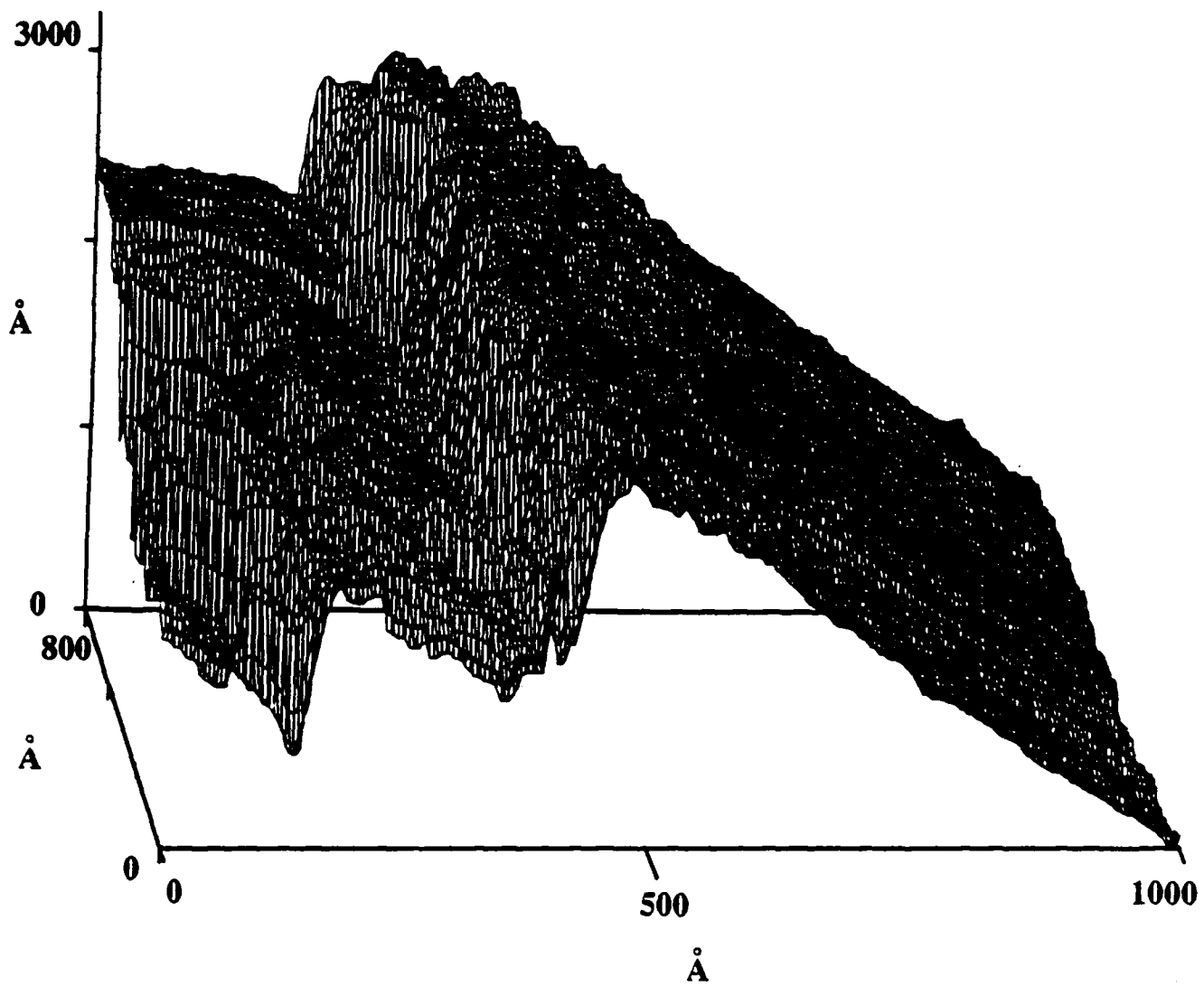


Fig. 7

APPENDIX I

FRACTO-EMISSION FROM INTERFACIAL FAILURE

J. T. DICKINSON

Department of Physics

Washington State University

Pullman, WA 99164-2814

ABSTRACT

Fracto-Emission is the emission of particles and photons during and after fracture of materials. The observed emission includes electrons, negative and positive ions, neutral species in both ground states and in excited states, and visible photons. This emission can often serve as a sensitive probe of crack growth and may prove to be a useful tool for investigating molecular and microscopic events accompanying crack growth and for studying the details of failure modes in a variety of materials. Interfacial failure provides unique fracto-emission signals due to the extensive charge separation accompanying separation of dissimilar materials. Here we present the results of several recent studies of interfacial failure involving a variety of materials and relate them to electronic and mechanical processes accompanying failure.

INTRODUCTION

During and after fracture of materials one can measure the emission of photons (phE) (often called triboluminescence^{1,2}) and particles including: electrons (EE), negative and positive ions (NIE and PIE), and neutral species in both ground states (NE) and in excited states (NE*). This emission can often serve as a sensitive probe of crack growth and may prove to be a useful tool for investigating molecular and microscopic events accompanying crack growth and for studying the details of failure modes in a variety of materials. These effects are also of interest in terms of their relations to electrostatic consequences of bond breaking (e.g., noise generated in sensitive circuits under stress, grinding of materials in confined spaces, mechanical and interfacial effects associated with explosives and solid propellents), the detection of fracture inside the earth's crust, and the transport of atoms and gases in geological systems. For a lengthy list of fracto-emission (FE) references, see ref. 3.

Past studies of FE³ have included work on the fracture of oxide coatings on metals, inorganic crystals and glasses, adhesive failure (including composites), organic crystals, neat polymers, and studies of electrical phenomena/breakdown accompanying fracture. A number of investigations have focused on the emission of charged particles and photons from the fracture of materials in vacuum. The origin of electron and photon emission from cohesive fracture is best explained in terms of bond breaking phenomena where non-adiabatic processes involving fundamental excitations (e.g., excitons), or creation and recombination of point-like defects and charge carriers (electrons, holes) occur. These energy releasing processes are thus initiated by bond breaking through the creation of localized departures from equilibrium. For polymeric systems, the likely analogous participants are free radicals, ionic states, and electrons all generated by bond scissions during crack growth. Again, recombination provides the release of energy necessary for particle or photon emission.

We have proposed a simpler model for systems involving *charge separation* during fracture. These systems include piezoelectric materials and a wide variety of composite materials in which fracture involves interfacial failure (filled materials, fiber/matrix composites, etc.). The basic features of this model as they relate to the fracture of materials in vacuum are the following:

- (a) During crack propagation, charge separation occurs on the freshly created fracture surfaces.
- (b) During crack propagation, neutral species are emitted into the crack tip region, producing a region of elevated pressure.

- (c) A microdischarge thus occurs during fracture yielding charged particles (generally electrons and positive ions) as well as photons and long wavelength electromagnetic radiation (RE for radiowave emission).
- (d) The fracture surfaces are bombarded by the discharge products during fracture. It is this bombardment which provides the stimulation of the fracture surfaces and yields the after-emission from the fracture surfaces.
- (e) The static charge on the fracture surfaces leads to acceleration of the emitted electrons, modifying their energy distributions. A large portion of the EE is pulled back to the surface resulting in a self-bombardment process. This results in the emission of positive and negative ions and excited neutrals via electron stimulated desorption (ESD).⁴

Different types of phE have been observed. phE can occur *prior* to fracture in a number of systems. In some cases, this light is due to microfracture events that precede failure. In single crystal inorganics there is evidence that moving dislocations can generate defects which recombine to yield light. Following fracture, some materials "glow" with characteristic decaying signals, much like phosphorescence. In addition, where charge separation is intense, light from microdischarges is quite evident. Typically, these events yield sharp spectral lines characteristic of the gases present in the crack tip.

Neutral emission accompanying fracture has two origins: a) basically "degassing" from a freshly exposed surface of gases that are trapped in the material (within voids, grain boundaries, inclusions, etc.) and b) species resulting from bond scissions (sometimes referred to as mechanochemically derived). As pointed out by Grayson and Wolf,⁵ one must be very careful in distinguishing these two sources of gas. Type b) emission is fundamentally more interesting and intimately related to the energetics of fracture, although type a) emission can in fact be useful for characterizing the failure of materials.

In this paper, we examine the fracto-emission from some recent studies involving several materials and geometries and examine some of the relationships between these emissions and failure mechanisms.

EXPERIMENT

Details of our experimental arrangements have been described elsewhere.³ The majority of the experiments shown here were performed in vacuums ranging from 10^{-7} to 10^{-9} torr. During straining of the samples, either in tension, 3-point bend, or in a peeling geometry, one to three types of emission can be monitored (e.g., electrons, positive ions, photons, neutrals, and/or low-frequency electromagnetic radiation). Charged particles were detected with Galileo Electro-optics Corporation Channeltron Electron Multipliers (CEM), which produce fast (10 ns) pulses with high detection efficiency for both electrons and positive ions. Background noise counts typically ranged from 1 to 10 counts/s. The detectors were positioned within a centimeter of the sample, with proper bias voltage on the front cone to attract the charged particles of interest. It should be noted that in studies on organic polymers we have shown that the principle particles detected for plus and minus bias on the CEM front cone are electrons and positive ions, respectively.

Photon detectors (e.g., Thorn-EMI 9924QB) were mounted inside the vacuum system or, when used in air, were mounted in a cooled housing which greatly reduces the background noise level (to ~5 counts/s).

Low-frequency electromagnetic waves (RE--for radiowave emission) were detected with coil antennas placed a few mm from the sample. Such an antenna couples to a changing B field. It should be emphasized that this arrangement detects the *near-field* electromagnetic "emission" because of the close proximity of the coils to the source. A simultaneous burst of visible photons coincident with the observed RE burst reinforces the interpretation that these signals are caused by microdischarges.

Neutral particles were detected with a quadrupole mass spectrometer, generally tuned to a single mass peak. The spectrometer is equipped with an ionizer, in which neutrals are ionized by electron impact at an energy of 70 eV. The resulting charged particles are mass selected as they pass through a region of alternating electric fields and are then detected by a CEM. Excited

neutrals may also be detected by Auger de-excitation at a CEM front cone surface (creating a detectable electron) or sometimes by the light these species emit (fluorescence) provided the relevant lifetimes are sufficiently short.

RESULTS AND DISCUSSION

Filled vs Unfilled Epoxy

Figure 1 shows the striking difference (*several orders of magnitude*) in intensity and duration of the EE accompanying the fracture of an epoxy [bisphenol-A/epichlorohydrin resin - Epon 828; Z-Hardener] with and without a filler material consisting of small ($7\ \mu\text{m}$) alumina particles. (Note that most of the data presented here are plotted on logarithmic intensity scales.) For the unfilled material, the bulk of this emission is attributed to bond breaking occurring during fracture which produces free radicals on and near the fracture surface (similar to the mechanical production of free radicals studied by DeVries⁶ in other polymers). Subsequent recombination reactions (e.g., radicals + electrons) provide discrete transitions which yield photons (radiative transitions) and electrons (Auger-like transitions). In contrast, the fracture of the filled material yields intense charge separation and thus much more intense emission.

Supporting the idea that the slow decay following fracture seen in the electron emission from the filled epoxy is a thermally activated process, we show in Fig. 2 the consequences of heating the surface approximately $50\ \text{C}$ in a few seconds immediately following fracture (at the arrow) with a heating strip attached to the sample. The response to this increase in temperature is essentially a "glow curve," similar to those obtained from materials following exposure to radiation.

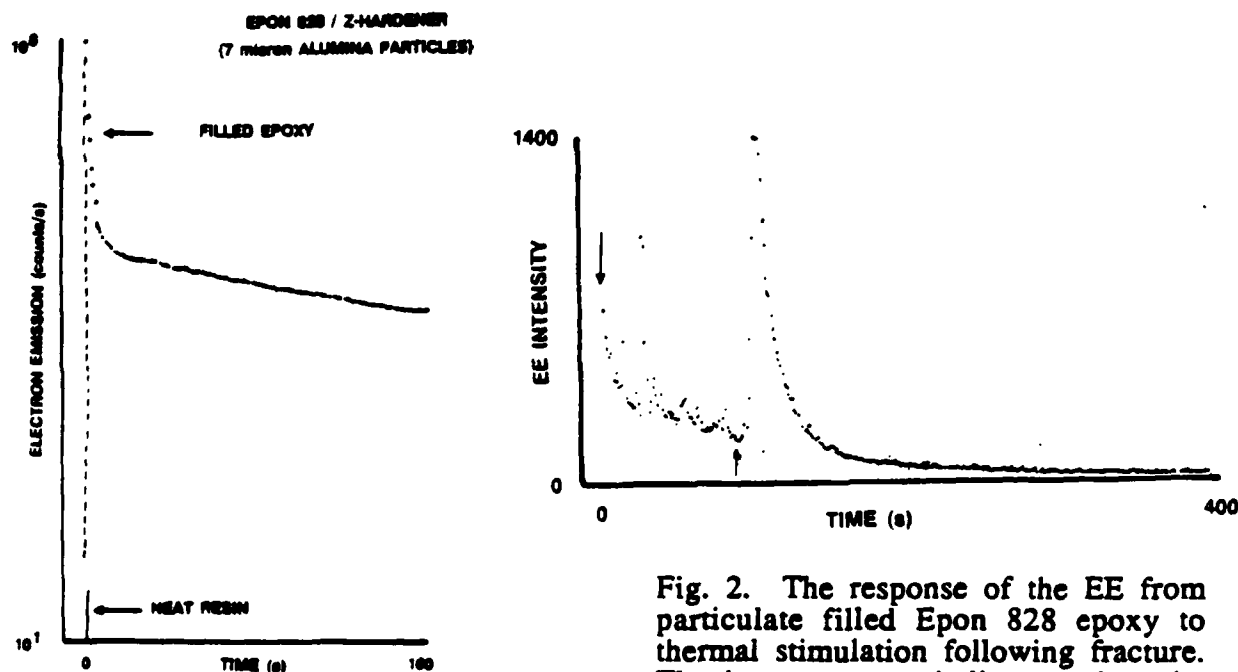


Fig. 1. EE plotted for both unfilled and filled ($7\ \mu\text{m}$ alumina particles) Epon 828 epoxy. Several orders of magnitude difference in intensities are observed; the larger and longer lasting emissions occur when interfaces fail.

Fig. 2. The response of the EE from particulate filled Epon 828 epoxy to thermal stimulation following fracture. The bottom arrow indicates when the temperature increase began. This supports the concept of a thermally stimulated process.

Chaotic Fluctuations in Photon Emission from Neat Epoxy

Although the unfilled material results in intensities several orders of magnitude smaller, we have found that *during* fracture, we obtain very easily measured and interesting curves. We have examined a number of unfilled epoxies using fine gold wire strips to measure the advancing

crack. On sub-microsecond time scales, we have shown⁷ that the onset of EE, PIE, and pH_E agree well with the beginning of crack motion and that the greatest pH_E intensities are observed during crack motion. The tail observed in the pH_E *after fracture* is actually of longer duration than indicated here. In order to prevent saturation of the photomultiplier during fracture it was necessary to reduce the gain considerably, thereby losing sensitivity. During relatively constant average crack velocity (approximately 400 m/s), the photon emission is *rapidly fluctuating*. Fig. 3 shows a typical pH_E amplitude (I) vs time (t) acquired during fracture of an epoxy, tetraglycidyl-4-4'-diaminodiphenylmethane (TGDDM) cured with diaminodiphenyl sulphone (DDS). We have analyzed the statistics of these I(t) signals in light of (no pun intended) the expected fluctuations from a photomultiplier and found that all of the larger fluctuations were well outside the predicted noise. Furthermore, several analyses of the data show⁸ that these fluctuations are non-stochastic, i.e., *chaotic* in their behavior. One such test is to treat the I vs t data as a basically geometric object (analogous to the coastline of Spain) and to measure the fractal dimension of the curve. This measurement yields a so-called Fractal Box Dimension,⁹ D_b , of 1.35 ± 0.03 which can be shown to agree fairly well with fractal dimensions of these data determined from Fourier transform methods. The non-integral value of D_b strongly supports the notion of chaotic behavior.

pH_E Accompanying Fracture of Epoxy

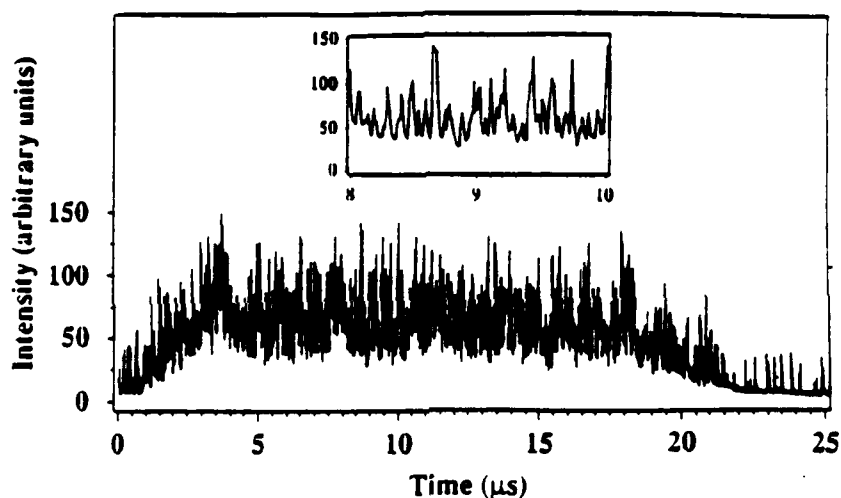


Fig. 3. pH_E measurement made during fracture of neat epoxy. The inset shows a portion of the pH_E data on an expanded time scale.

We also determined the fractal dimension of a typical epoxy sample by using the slit island method described by Mandelbrot, *et al.*¹⁰ Photographs of the island structure created by coating and polishing the fracture surfaces were analyzed to determine the fractal dimension of the surface, D_s . The results of this study yielded $D_s = 2.32 \pm 0.09$. We can conclude, therefore, that the epoxy fracture surface is indeed fractal. We note that the fractional part of D_b (measuring the photon fluctuations) and D_s (measuring the surface roughness) are very close in magnitude.

The roughness of many fracture surfaces, including those which may be described as fractal, is most easily understood as the result of crack branching. These branches represent fluctuations in the process of crack growth which appear to be reflected in the pH_E accompanying fracture. Attempts to model the process of crack branching in brittle solids has met with limited success.^{11,12} Ravi-Chandar and Knauss have demonstrated that crack branching in Hormalite 100 involves the nucleation, interaction, and coalescence of microcracks or voids in the process zone of an advancing crack.¹¹ This branching activity may be responsible for the fractal nature of many fracture surfaces, as well as for the relatively slow crack growth (relative to the Rayleigh wave speed) observed in many materials. It is very likely that similar processes occur in other brittle materials as well.

If crack branching is responsible for the rapid fluctuations in pH_E, one might expect the fractal dimension of the pH_E data to be simply related to the fractal dimension of the fracture surface. This would be most plausible in cases of "constant" crack velocity, as observed in much of the work of Ravi-Chandar and Knauss. Since the pH_E data is one-dimensional and the fracture surface is two-dimensional, the proper comparison appears to be that of the *fractional* parts of the appropriate fractal dimension, that is, the fractal dimension increments. These fractal dimension increments observed in this work are 0.32 ± 0.09 for the fracture surface and 0.35 ± 0.03 (average from all the methods) for the pH_E data, suggesting that in fact there exists a correlation. Further evidence for such a connection comes from current studies on the fracture of single crystal MgO where both the pH_E and fractography are showing very low fractal dimension increments due to the cleavage nature of the fracture (e.g., large smooth areas).

The rapid fluctuations of pH_E during the fracture of many materials suggest that deterministic chaos is a feature of the pH_E process. The autocorrelation function and conditional probability distributions are consistent with this initial impression. Fourier transform and fractal box dimension analyses show the pH_E to be fractal in nature, implying chaos. The strongest evidence for chaos results from an analysis of the correlation dimension of the attractor associated with the epoxy data. A clearly non-integral dimension of about 3.2 is found.

If the fluctuations in pH_E during fracture are due to the fluctuations in crack growth, pH_E data may prove useful in testing models of dynamic crack growth and branching. The low dimensionality of the underlying process suggests that rather simple models of crack branching may yet be constructed. Of particular interest is the nature of the processes occurring in the process zone of the advancing crack tip and how they are influenced by pre-existing defect distributions and other perturbations during crack growth. Evidence to date suggests that this process is not merely stochastic, but at least in materials like the epoxy, chaotic. This chaos may be associated with significant nonlinear, dissipative processes perhaps due to a fractal distribution of defects acting as nucleation sites for voids and microcracks in the process zone. Fractal structures commonly result from diffusion and aggregation. The fractal dimension of the fracture surfaces of some steels is a function of annealing temperature,^{10,13} consistent with a diffusion or aggregation mechanism. Of considerable importance, however, is that the fracture energy of these steels and several brittle ceramics have been shown to be related to the fractal dimension of the resulting surfaces.^{14,15} This suggests that our pH_E measurements reflect rapid variations in the bond breaking rate as the crack advances, perhaps due to fibril fracture and/or crack branching, and thus provide energy dissipation information on a nearly instantaneous time scale. We are currently making measurements and analyses of pH_E and EE produced during fracture of an alumina filled epoxy, where the emission mechanisms are quite different. We predict that the fractal dimension of the pH_E fluctuations will change, perhaps losing their fractal character altogether (i.e. the fluctuations may be merely stochastic).

Electron Emission from Interply Failure in a Composite

A study underway on the role of fiber treatment on interply failure modes in graphite-epoxy composites utilizes samples loaded in a double cantilever beam configuration as shown in Fig. 4a. Unidirectional composites were made from Hercules AU (untreated) and AS4 (surface treated) graphite fibers. Fiber tows were impregnated with Epon 828 cured with m-phenylene diamine. The prepreg was cut into plies and compression molded with 16 plies to a composite. Thin teflon strips were inserted between plies 8 and 9 prior to molding. This allowed us to initiate an interlaminar crack when the bar was loaded as shown.

EE measurements show at least 2-3 orders of magnitude difference in intensity between the two fiber surfaces. Typical emission curves during testing are shown in Figs. 4b and 4c, where the untreated (and therefore poorly bonded) fibers yield the intense emission. Here, fluctuations in intensity are correlated with jumps in the crack as seen by both drops in the applied force and in the accompanying acoustic emission. SEM micrographs of the fracture surfaces reveal interfacial failure with an abundance of resin-free fibers in the AU samples, in contrast to extensive cohesive matrix failure associated with good fiber-matrix adhesion in the AS4 specimens. Thus, the EE intensities correlate strongly with the extent of interfacial failure occurring in this type of test.

Fracture of Graphite/Epoxy Uniaxial Specimens

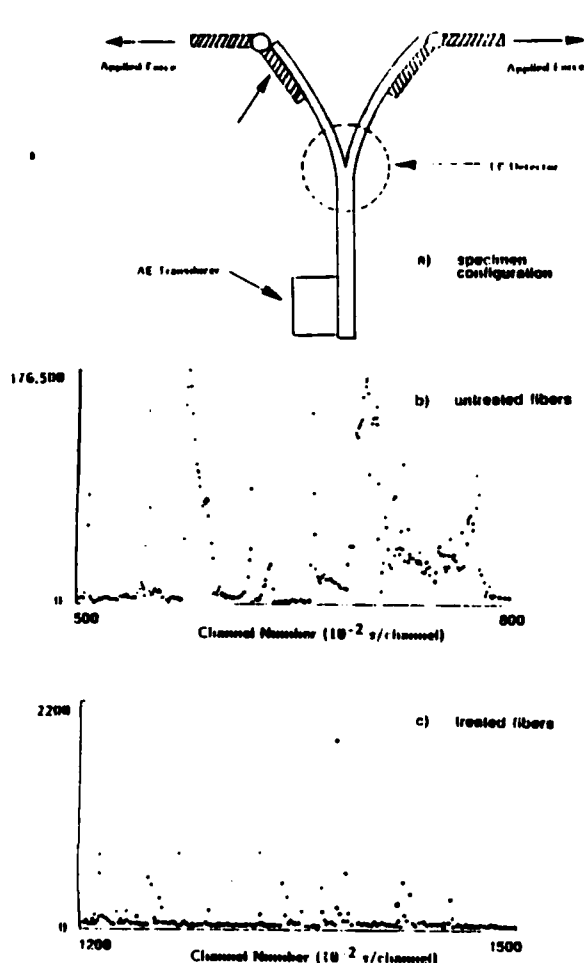


Fig. 4. a) Schematic of cantilever beam sample used to study interply failure in uniaxial carbon fiber/epoxy composites. Typical EE curves for b) untreated (poorly bonded) and c) treated (well bonded) specimens.

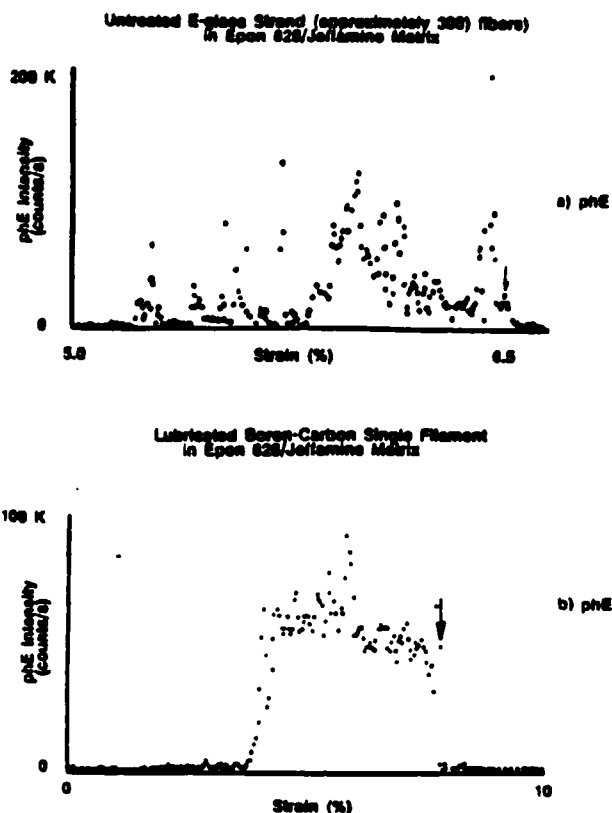


Fig. 5. a) pH E from an E-glass fiber/epoxy composite in which the fibers debonded inside the epoxy matrix, and b) pH E from a composite sample formed with a single boron-carbon filament treated with a release agent and embedded in an epoxy matrix. The arrows indicate the times of macroscopic matrix failure.

pH E from Embedded Interfaces

When reinforcing particles or fibers are placed in a matrix such as an epoxy, deformation frequently leads to debonding along the interface between the two dissimilar materials. When this occurs internally, it is often difficult to determine when and where this occurs. For semi-transparent matrices, we have recently been able to obtain measurements of photons which originate at these interfaces and escape through the matrix to the detector.¹⁶ Because photomultipliers function in air as well as vacuum, we are able to perform the pH E experiments in both environments. By simultaneously measuring EE (electrons--thus requiring vacuum), we can identify any failure event which exposes a surface to the outside world, i.e., a crack reaching the outer surface.

Poorly Bonded Fibers Embedded in Epoxy. In the case of fiber reinforced epoxy, a poor bond between the fibers and the matrix can lead to pre-failure emission.¹⁶ Approximately 100

E-glass fibers (10 μm in diameter) were embedded in Epon 828/Jessamine Hardener (which produces a clear, flexible epoxy) and strained in tension. Figure 5a is the phE resulting from internal failure of fibers and subsequent debonding. The arrow indicates the time of ultimate failure of the specimen (i.e., when the entire specimen breaks). Because the epoxy is semi-transparent many of the photons created during debonding can escape and be detected. These experiments were performed in air since there is no need to protect the photomultiplier from a gaseous environment. When epoxy compatible sizing coats the fibers, greatly enhancing the fiber/matrix adhesion, very little phE is observed before failure, even though fiber fracture has occurred. To further test this observation, we embedded a single boron-carbon filament (100 μm in diameter) into the same matrix. When a release agent (silicone oil) was applied to the fiber before embedding it in the resin, debonding was easily observed under a microscope. On an identical sample, we saw the photon emission shown in Fig. 5b, where again, the arrow indicates when the epoxy sample fractured. Without the release agent, the boron-carbon filament adhered very well to the epoxy, and no pre-emission was observed. In terms of probing the failure mechanisms of composites, this type of study may be of considerable value.

Metal Rod Pull Out from Epoxy. Another geometry which results in internal interfacial failure is a fiber or cylindrical rod partially embedded into a material and pulled out. Depending on the ratio of the fiber or rod diameter to the embedded depth, the matrix will either usually fail cohesively or the rod will pull out, the latter occurring in the case of shallow depths. Atkinson, *et al.*¹⁷ have discussed the fracture mechanics of this problem and have shown that debonding typically starts by detachment of the *end* or *tip* of the rod. This is generally followed by debonding from the sides of the rod, most frequently starting from the upper surface and moving down towards the tip.

The insert in Fig. 6 shows a diagram of the experiment for testing the pullout of a metal (steel) cylinder out of "5-Minute" Epoxy, the latter being semi-transparent. The resulting phE (a), EE (b), and applied force (c) also are shown. Note that the phE was sustained for approximately 2 s before the drop in force and the accompanying rise in EE. These last two events correspond to the pullout of the rod. Pullout produces exposed surfaces capable of releasing electrons from the sample. Again, the pre-failure emission of light is coming from *inside* the epoxy. Tests stopped prior to pullout show that the end or tip of the rod has indeed detached (observed optically by means of interference fringes viewed from the right-hand side of the diagram). One important question is the presence or absence of debonding along the sides of the rod *before* pullout. We believe this can be determined by optical methods to collect photons from the sides only vs the tip region only. Also, to provide more detailed information on the sequence of failure events, we point out that we can acquire these signals at considerably faster rates (at 5 ns intervals if necessary). Finally, it should be noted that in these experiments the rod was removed from the region of the detectors soon after pullout, within some milliseconds. Thus, the "tail" observed in both the phE and EE is coming from the epoxy. The hole left behind is glowing and shooting out electrons like a "Roman Candle".

phE from Peeling Pressure Sensitive Adhesives

Several workers have shown that during the peeling of pressure sensitive adhesives, one observes phE and long-wavelength electromagnetic radiation (RE). We have shown that this emission is in the form of bursts, and have measured the time distribution of the phE bursts, the time and intensity correlations of the phE and RE bursts,¹⁸ the optical spectra of the phE,¹⁹ and the spatial distributions (i.e., images) of the phE for particular adhesive/substrate systems.²⁰⁻²²

The production of radiation during the failure of an adhesive joint was previously observed by Deryagin and co-workers,²³ who reported that such failure produces light and radio-frequency radiation in the form of bursts. Ohara *et al.*²⁴ and Klyuev *et al.*²⁵ have published low resolution spectra (acquired by use of filters) on considerably different polymer/substrate combinations (e.g., PVC on glass), observing that the most intense emission is in the region of the spectrum below 490 nm. This is consistent with gaseous discharges in air.

Fig. 6. a) phE, b) EE, and c) load force accompanying the loading of a metal rod embedded in epoxy. The phE before pullout is due to interfacial failure inside the epoxy.

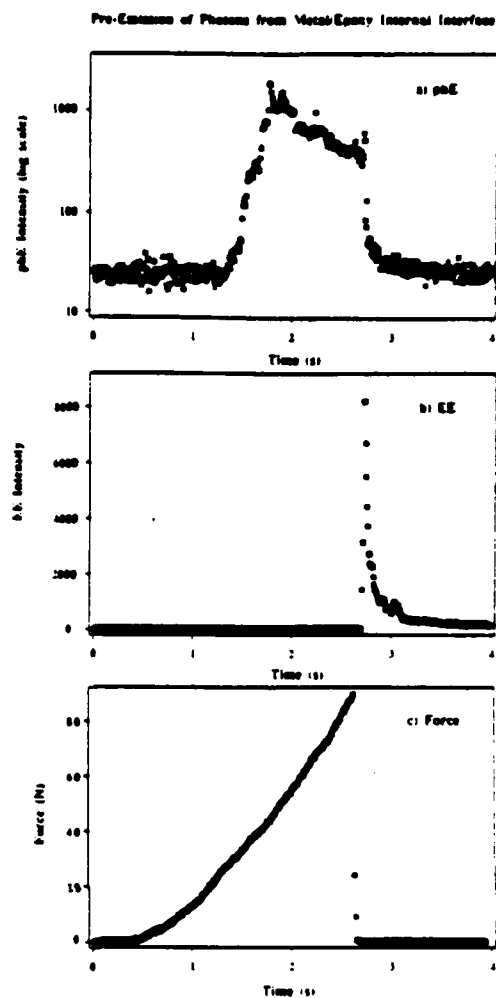
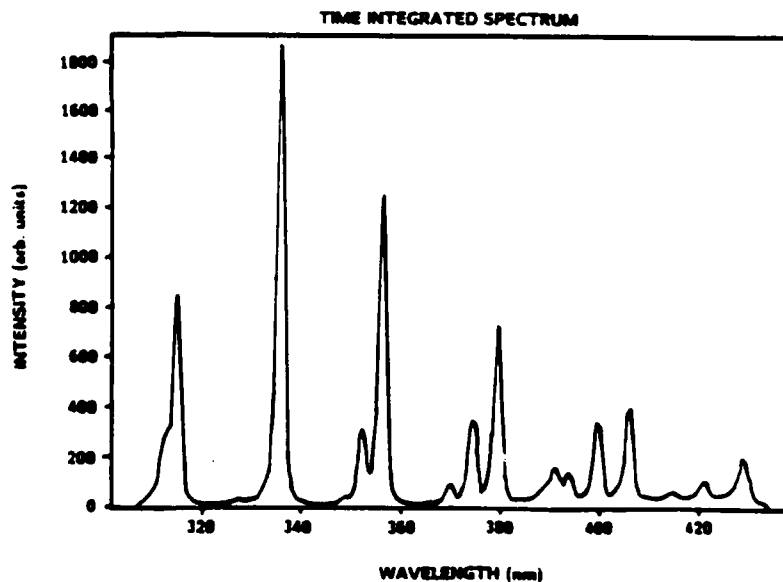


Fig. 7. Typical spectrum of the light emitted when 3M Filament Tape is peeled from its own backing. This spectrum is not time resolved; therefore it represents an integration over time.



Spectral Characteristics of the Light. We have obtained time averaged spectra of the phE during peeling of 3M Filament Tape from its own backing, one of which is shown in Fig. 7 over the wavelength interval where discernible features can be distinguished from the noise. This spectrum, which contains photons produced both during the discharges and afterward, falls in the interval 300-440 nm and consists of discrete lines. When compared with the characteristic gaseous discharge emissions of N_2 , O_2 , CO_2 , and other atmospheric gases, we found that each of the lines in the peel-induced spectrum corresponds to a N_2 spectral line. The transitions observed are the strong features of the triple-headed band²⁶ involving the N_2 electronic transition: $B^3\pi \rightarrow C^3\pi$. The individual lines correspond to various vibrational states within each of these electronic levels. The fall-off in intensity towards the shorter wavelengths seen in several of the spectral lines is due to rotational fine structure. No evidence of broadband emission characteristic of fluorescence from polymers is observed.

We have developed methods^{20,21} to produce autographs of the peel event by placing the tape directly on Polaroid film or by using fiber optics to bring the light to the film. Once the peel has occurred, the film can be developed in the usual fashion to obtain spatial distributions of the bursts of light. Fig. 8 displays autographs of this light taken on Polaroid film for both 3M Filament Tape and 3M Magic tape. The images show considerable spatial fine structure due to very localized, intense events and effects such as the stick-slip phenomenon. There is also evidence that accompanying bursts are occurring along the peel zone. In addition, we have shown that the micromechanics of the peel strongly influence the position, frequency, and size of the phE bursts seen on the film.^{20,21}

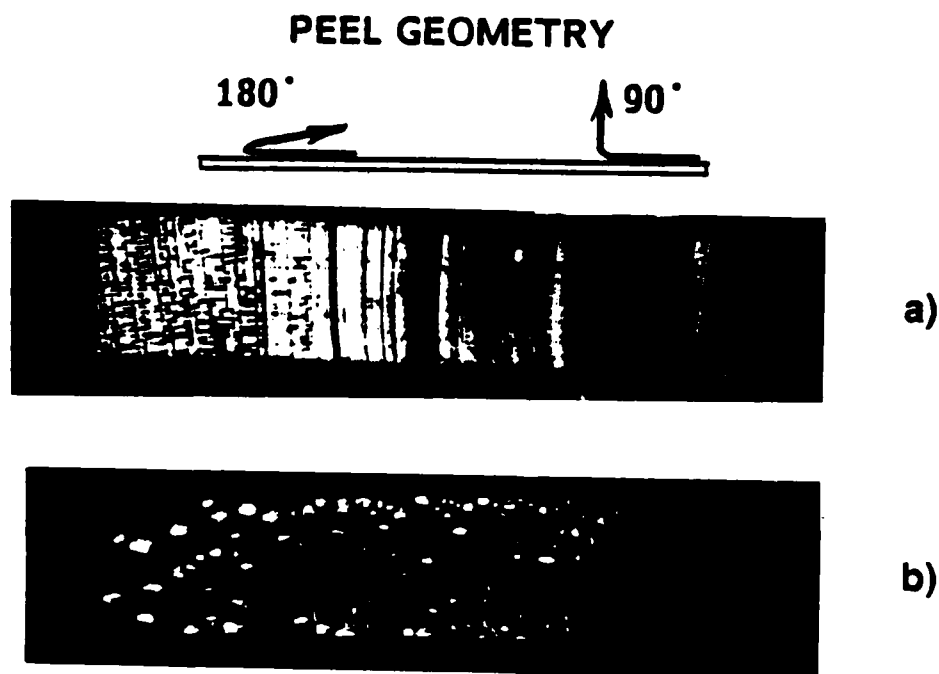


Fig. 8. Autographs of the phE produced by peeling pressure sensitive tapes directly from the emulsion of Polaroid film (see refs. 20, 22). Relatively fast peels of a) 3M Magic Tape and b) 3M Filament Tape.

We therefore have further evidence of intense charge separation produced on fracture surfaces during adhesive failure leading to microdischarges in the region of the crack tip. This charge separation is due to the rapid separation of two dissimilar polymers at the crack tip during the peel. The resulting micro-discharges are responsible for the production of electromagnetic bursts (RE) and the accompanying, initial "spikes" of pH_E which are extremely rapid and have decay times of less than 50 ns. In terms of count rate, the peak pH_E can exceed 10^{10} photons/s. The onset of pH_E and RE are in coincidence to within 100 ns (this number appears to be limited by the time constant of the antenna circuit) and are correlated in size. Following this initial burst, time-correlated bursts can occur in the next few microseconds with decaying frequency and amplitude. These secondary "strikes" are most likely occurring along the peel zone and are triggered by the release of secondary charges from the initial discharge. Imaging of these photons show considerable detail, including large bursts and many smaller features. We also see a spatial dependence on factors such as peel speed, peel angle, and pretreatment of the interface.^{20,21}

A number of RE and pH_E characteristics should be similar to the characteristics of EE and PIE which are necessarily observed in vacuum. We are currently measuring the pH_E and RE for the same peeling system in vacuum and are observing interesting changes due to lower pressures at the crack tip, including a factor of 10 increase in intensity. Our major goals are to further characterize these emissions, determining the emission mechanisms in more detail, and relating the characteristics of fracto-emission to the details of failure (see, for example, reference 21). As detectors and spectrometers become more sensitive, pH_E offers considerable promise as a tool for determining failure mechanisms involving interfaces.

Interfacial Failure Involving the Au-SiO₂-Si Interface

The metal-oxide-semiconductor (MOS) thin film system is of great importance in modern electronics and other areas of high technology. An understanding of interfacial properties under a wide range of conditions is critical. In a number of circumstances, the mechanical properties of the interface are of key importance. Interfacial failure can occur as a consequence of several factors including mechanical and thermal stress. We are interested in the role of the oxide on the adhesive strength of a gold film and on the fracto-emission properties during adhesive failure.

We know that in general, insulators have long excited state lifetimes and produce the most intense FE, whereas clean metals produce no FE. Silicon has recently been shown to also produce some electron emission during fracture, although the dominant excitation is the production of free charge carriers. Here, we report observations of EE and pH_E resulting from the peeling of a gold thin film from an oxidized silicon surface. The thickness of the oxide plays a critical role in the emission, suggesting that the lifetime of the surface excitations (on the oxide) associated with FE are influenced by the Si substrate. Also, the resistivity of the oxide may prevent the discharging of the surface on short time scales.

The samples used in this study were cut from commercial boron doped (111) Si wafers obtained from S.E.H. America, Inc. One surface was polished and the resistivity of the bulk material was between 10 and 20 Ω -cm. After an HF acid etch, the wafers were divided into two groups. One was heated to 1000 C in atmosphere to form a thermally grown oxide layer. Typical oxide thicknesses ranged from 500 to 1200 Å as roughly determined from the color of the wafer in white light. The other group was not deliberately oxidized after the HF etch. However, these surfaces have a native oxide with a thickness of about 20 Å. All of the samples were coated on the polished side with a vapor deposited gold layer about 50 nm thick. The deposition was done in an ion pumped vacuum system at a pressure of 10^{-8} torr.

The basic experiment consisted of pulling (peeling) the Au film from the clean and oxide covered Si surfaces in vacuum while monitoring both the EE and pH_E simultaneously. The samples were held by an aluminum holder epoxied to the unpolished and uncoated side of the samples, and a small region of Au film (0.25 to 0.5 cm²) was loaded in tension by pulling on a metal pin embedded in an epoxy drop on the Au coated surface. The pulling pin was loaded in tension using a polymer monofilament line to avoid torsional stresses. This arrangement also ensured that the peeled Au film was quickly removed from the detection region after fracture, so that all the subsequent emission was from the surface of the oxidized Si only. A load cell attached to the sample mount measured the applied force versus time and the critical stress at failure. A Channeltron electron multiplier and a photomultiplier tube were placed on opposite sides for

simultaneous EE and pH E detection. The data were recorded at 2 ms intervals for about 8 s. About 50 samples of each type (thick and thin oxide) were tested.

When the experiments were performed, the EE, pH E and the maximum force (force at failure), F_m , were found to vary over a wide range for each type of sample. This is undoubtedly due to the sensitivity of this type of test to the fracture mechanics. Thus, although the adhesive forces may be quite uniform, the value of F_m depends critically on the flaws and stress concentrations at the edges of the epoxy pad. Nevertheless, the significant trends were found.

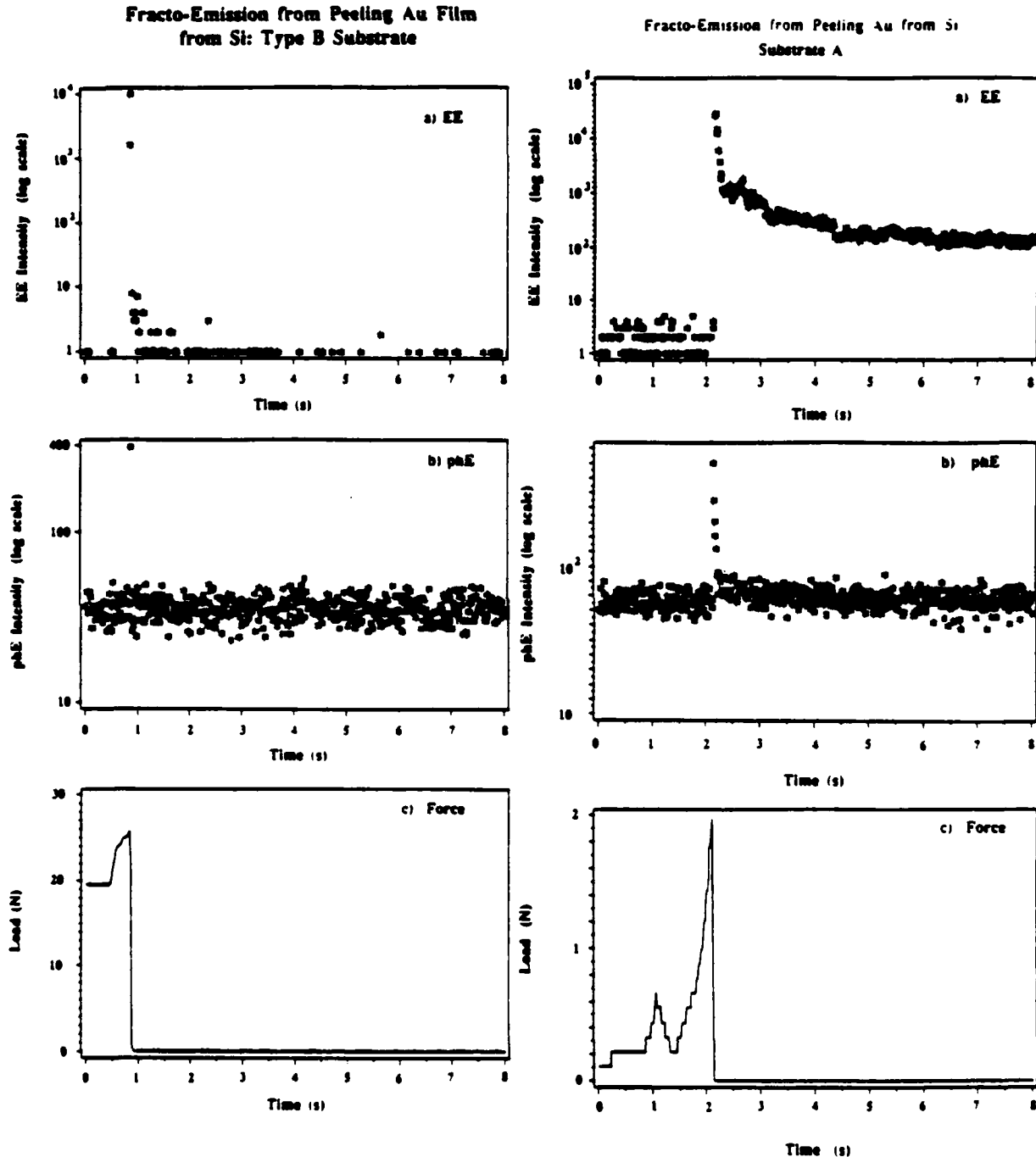


Fig. 9. a) pH E, b) EE, and c) load force during the peel of an Au film from an Au-SiO₂-Si structure with only a thin, native oxide layer.

Fig. 10. a) pH E, b) EE, and c) load force during the peel of an Au film from an Au-SiO₂-Si structure with a thermally grown oxide layer about 1000 Å thick.

Au peel from thin oxide on Si. Figure 9 shows the electron and photon emission from a sample of Au on Si with only the native oxide. The time and force at fracture are indicated by the load curve, Fig. 9c. The force required to peel the Au film was about 26 N in this case which was typical of these samples although some samples were found to exceed the strength of the monofilament line. Both the EE and pH E signals show a peak of emission immediately upon fracture. The peak electron intensity of about 10^4 counts per channel is about 25 times higher than the peak pH E due to the relative collection efficiency of these detectors. The width of the main peak is only one or two channels (2 to 4 milliseconds) consistent with emission limited to the duration of fracture. A weak tail in the EE remains above the background level for a few seconds after fracture. The corresponding tail in the pH E, if it exists, is obscured by the relatively high background level of the photomultiplier tube.

Au peel from Oxidized Si. The EE, pH E and force data for a sample with an oxide thickness of about 1000 Å are shown in Figure 10. Again, emission begins immediately at fracture with a rise time of only one channel. However, the load at fracture was much smaller for these thick oxides, typically 2 N. Both EE and pH E decay exponentially over the next 10 to 12 ms. Since the force is nearly 10 times smaller than for the thin oxide samples, the rate of Au peeling will be correspondingly slower. Thus, the initial burst of emission again is associated with emission during fracture. After the initial burst, there is an intense, slowly decaying EE tail persisting for several seconds. This signal continued well beyond the data collection time for the sample shown. EE from the thickest oxides continued for over a minute. The pH E of Fig. 10 also continues for at least a few seconds, and the subsequent integrated emission intensity also remains higher than prefracture levels for some time. We believe that the close agreement of these two curves suggests a similar mechanism for both EE and pH E. The better signal to noise ratio for the EE provides much more information about the emission tail.

The thickness of the oxide layer plays a critical role in the emission behavior both during and following failure. As in the systems discussed above, charge separation on the newly created surfaces can lead to electrical breakdown. The charge separation occurring in this MOS system is directly related to the electronic states induced by contact. A simplified charge density vs position diagram of the MOS structure is shown in Fig. 11. We assume that the locus of fracture is between the Au film and the oxide layer, resulting in a negative charge on the metal and a positive charge on the oxide surface. Electrometer measurements made during fracture confirm the existence of these particular charges. The Au and the Si act as oppositely charged capacitive plates which support less charge as they are separated. This may produce the observed microdischarges and consequently the EE and pH E. Such discharges would depend exponentially on the separation of the two plates as the observed emission decay suggests.

Charge Density vs Position

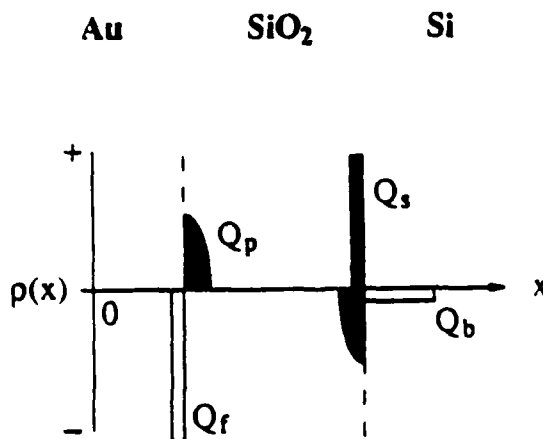


Fig. 11. A schematic plot of the charge density across an Au-SiO₂-Si structure.

Likewise, the increased separation of the Au and Si surfaces due to the presence of a thick oxide layer reduces the capacitance of this system and may be partly responsible for the reduction of the critical force at failure with oxide thickness. Otherwise, one might expect the adhesive strength of the Au on the native oxide and the thick oxide to be roughly the same. However, this was not observed.

The EE and pH_E after-emission occurs well after the Au film is out of the interaction region. This rules out small arcs or microdischarges between surfaces as a source of this emission. However, excited states and surface defects will remain on the oxide. On a thin oxide, the nearby conductive Si substrate will allow the surface excitations to dissipate rapidly. On thicker films, the excited states will have longer lifetimes due to the decreased interaction with the substrate. In addition, the thicker oxides will support a greater number of defects. The relaxation or annealing of these defects can then provide energy for promoting an electron into the vacuum or for photon emission. The combination of increased defect densities and longer excitation lifetimes could produce the dramatic increases in emission noted for the thick oxide layers.

If the emission during fracture were to result from bond breaking or localized heating, the FE intensity should strongly depend on the force of fracture. However, the observed emission increases with oxide thickness but inversely with the strength of the film. This suggests that processes such as charge separation or increased excited state lifetimes are critical to the increased emission. For thin or no oxide surfaces the excitations are dissipated too rapidly to result in significant emission.

CONCLUSIONS

The use of FE signals accompanying the deformation and fracture of filled and unfilled polymers, adhesive and composite systems often allow details of failure mechanisms and fracture phenomena to be obtained. Information provided by FE may potentially assist in the interpretation data provided by other probes such as acoustic emission, as well as providing an independent probe of micro-events occurring prior to failure. For instance, we have shown that FE is sensitive to the locus of failure in several composite materials. For a given material and mode of fracture, FE during fracture often reflects the instantaneous rate of energy dissipation. Our goal is to continue to study FE mechanisms and to apply FE methods to the study of the early stages of fracture and failure modes in a variety of materials.

ACKNOWLEDGMENTS

This work was supported by the Ceramics and Electronics Materials Division of the National Sciences Foundation DMR-8601281, the Office of Naval Research Contract No. N00014-87-K-0514, the McDonnell Douglas Independent Research Program, and the Washington Technology Center. I wish to thank my Washington State University colleagues S. C. Langford, L. C. Jensen, Ma Zhenyi, and Brian Mielke for their assistance in this work and E. E. Donaldson and R. V. Subramanian for helpful discussions. I also wish to thank D. L. Doering, Wesleyan University, for his contribution to the Au-SiO₂-Si study.

REFERENCES

1. J. I. Zink, "Squeezing Light out of Crystals: Triboluminescence," *Naturwissenschaften*, 6688, 507-512 (1981).
2. A. J. Walton, "Triboluminescence," *Adv. Phys.*, 2266, 887-948 (1977).
3. J. T. Dickinson, "Fracto-Emission from Adhesive Failure", to appear in *Advances in Adhesion*, edited by L. H. Lee, (Plenum Press, New York).
4. M. L. Knotek, "Electron- and Photon Stimulated Desorption," *AIP Conference Proc. No. 94*, 772-786 (1982).
5. M. Grayson and C. Wolf, "Mechanochemical reactions in an epoxy resin system," *J. Polym. Sci., Polym. Phys. Ed.*, 23, 1087-1097 (1985).
6. K. L. DeVries, "Free Radical Processes in Mechano-Chemical Degradation of Plastics and Rubbers," *J. Appl. Polym. Sci.: Appl. Polym. Symp.*, edited by B. Ranby and J. F. Rabek, (John Wiley & Sons, New York, 1979), p. 3355.
7. J. T. Dickinson, L. C. Jensen, and S. Bhattacharya, "Fracto-emission from Neat Epoxy Resin," in *Die Makromole. Chemi. Macromole. Symp.*, 7, 129 (1987).

8. S. C. Langford, Ma Zhenyi, and J. T. Dickinson, submitted to *J. Mater. Res.*
9. B. B. Mandelbrot, "Self-affine fractals and fractal dimension," *Physica Scripta* **32**, 257-260 (1985).
10. B. B. Mandelbrot, D. E. Passoja, and A. J. Paullay, "Fractal character of fracture surfaces of metals," *Nature* **308**, 721-722 (1984).
11. K. Ravi-Chandar and W. G. Knauss, "An experimental investigation into dynamic fracture: III. On steady-state crack propagation and crack branching," *Int. J. Fracture* **26**, 141-154 (1984).
12. J. P. Dempsey and P. Burgers, "Dynamic crack branching in brittle solids," *Int. J. Fracture* **27**, 203-213 (1985).
14. J. J. Mecholsky, T. J. Mackin, and D. E. Passoja, "Self-similar crack propagation in brittle materials," in *Fractography of Glasses and Ceramics*, edited by J. R. Varner and V. D. Frechette, (American Ceramic Society, Westerville, OH, USA, 1988), pp. 127-134.
15. D. E. Passoja, "Fundamental relationships between energy and geometry in fracture," in *Fractography of Glasses and Ceramics*, edited by J. R. Varner and V. D. Frechette, (American Ceramic Society, Westerville, OH, USA, 1988), pp. 101-126.
16. A. S. Crasto, R. Corey, J. T. Dickinson, R. V. Subramanian, and Y. Eckstein, "Correlation of Photon and Acoustic Emission with Failure Events in Model Composites," *Composites Sci. & Technol.* **30**, 35 (1987).
17. C. Atkinson, J. Avila, F. Betz, and R. E. Smelser, "The Rod Pull-out Problem. Theory and Experiment," *J. Mech. Phys. Solids* **30**, 97 (1982).
18. E. E. Donaldson, J. T. Dickinson, and X. A. Shen, "Time and Size Correlations of Photon and Radiowave Bursts from Peeling Pressure Sensitive Adhesives in Air," *J. Adhes.* **19**, 267 (1986).
19. Ma Zhenyi, Fan Jiawen, and J. T. Dickinson, "Properties of the Photon Emission Accompanying the Peeling of a Pressure Sensitive Adhesive," *J. Adhes.* **25**, 63 (1988).
20. J. T. Dickinson and E. E. Donaldson, "Autographs from Peeling Pressure Sensitive Adhesives: Direct Recording of Fracture Induced Photon Emission," *J. Adhes.* **24**, 199 (1987).
21. E. E. Donaldson and J. T. Dickinson, "Autographs from Peeling Fiber Reinforced Pressure Sensitive Adhesives: Correlation with Failure Mechanisms," to appear in *J. Adhesion*.
22. J. Walker, "How to capture on film the faint glow emitted when sticky tape is peeled off a surface," *Sci. Am.* **257**(6), 138-141 (December, 1987).
23. B. V. Deryagin, L. A. Tyurikova, N. A. Krotova, and Y. P. Toporov, "Electromagnetic Radiation of a Gas Discharge Arising when Separating Two Dielectrics," *IEEE Trans. Indust. Appl.* **VI**, IA-14, 541 (1978).
24. K. Ohara and T. Hata, "Light Emission due to Peeling of Polymer Films from Various Substrates," *J. Appl. Polym. Sci.* **14**, 2097 (1970).
25. V. A. Klyuev, E. S. Revina, V. I. Anisimova, Yu. A. Khrustalev, and Y. P. Toporov, "Light Emission in Breaking of Adhesive Bonds under High Vacuum," *Colloid J. (Kolloidn Zh.)* **41**, 287 (1979).

APPENDIX II. PARTICIPANTS, COLLABORATORS, RECENT PRESENTATIONS AND PUBLICATIONS

Participants in this Work

J. Thomas Dickinson	Principal Investigator
Les Jensen	Physicist, Full time
Steve Langford	Physics Ph.D. Student
Peter Eschbach	Physics Ph.D. Student
Ma Zhenyi	Physics M.S. Student; Ph.D Student
Brian Mielke	Physics M.S. Student
Steven Anderson	Physics M.S. Student
Jon Mathison	Physics Undergraduate Student
Koksai Tonyali	Materials Sci. Post Doc
Alan Crasto	Materials Sci. Post Doc
Howard Miles	WSU Physics Faculty
Miles Dresser	WSU Physics Faculty
Ed Donaldson	WSU Physics Faculty (Emeritus)

Collaborators/Visiting Researchers

Dale Doering	Wesleyan University
Heidi Stacer	Air Force Astronautics Lab
Gary McVay	Battelle Pacific Northwest Labs
Larry Pederson	Battelle Pacific Northwest Labs
Carlo Pantano	Pennsylvania State University
Jack Mecholsky	Pennsylvania State University
John Kelso	Alcoa Technical Center

INVITED PRESENTATIONS:

"Radiation Induced Damage of Optical Coatings", Symposium on Adhesives, Sealants, and Coatings for Space and Harsh Environments, National ACS Meeting, Denver, April, 1987.

"Fracto-Emission Accompanying the Deformation and Failure of Crosslinked Polymers and Interfaces", Symposium on Chemistry, Properties, and Applications of Crosslinking Systems, National ACS Meeting, Denver, April, 1987.

"Bombardment Induced Crack Initiation and Crack Growth in Polymers and Polymer Surfaces", Symposium on Adhesives, Sealants, and Coatings for Space and Harsh Environments, National ACS Meeting, Denver, April, 1987.

"Fracto-Emission from Minerals", U.S. Bureau of Mines, Denver, April, 1987.

"Fracto-Emission from Crystals, Polymers, and Interfaces", Univ. Washington Materials Science Dept., April, 1987.

"Particle Emission Accompanying Fracture", Michigan Technological University, Physics Department, April, 1987.

"Energetic Processes Accompanying Fracture", ONR Workshop on Fracture and Deformation, Great Oak Harbor, MD, May, 1987.

"Surface Phenomena Related to Contamination Problems in Space," NASA Workshop on Space Station Contamination Problems, Hilton Head, SC, November, 1987.

"Fracto-Emission from Polymers and Composites," International Symposium on Testing and Failure Analysis, AMS, Anaheim, November, 1987.

"Fracto-Emission from Crystals and Interfaces," International Society for Optical Engineering, OE-LASE '88, Los Angeles, January, 1988.

"Fracto-Emission: A New Way of Studying Failure," IBM-Almaden Research Center, San Jose, June, 1988.

"Fracto-Emission from Elastomers," Elastomer Gordon Conference, New London, July, 1988.

"Fracto-Emission from Inorganic Materials," Glass Science Gordon Conference, Tilton, August, 1988.

"Fracto-Emission from Interfaces," Science of Adhesion Gordon Conference, New Hampton, August, 1988.

"Fracto-Emission as a Tool for Failure Analysis", ASM, Seattle, September, 1988.

"The Emission of Particles and Photons from the Fracture of Minerals and Inorganic Materials," American Chemical Society, Los Angeles, September, 1988.

"Fracto-Emission from Polymers and Interfaces," 20th Europhysics Conference on Macromolecular Physics: Physical Mechanisms in Polymer Failure, Lausanne, Switzerland, September, 1988.

"The Interaction of Radiation with Mechanically Deformed Materials," 9th International Symposium on Exoelectron Emission and Applications," Wroclaw, Poland, September, 1988.

"Fracto-Emission from Materials," 9th International Symposium on Exoelectron Emission and Applications," Wroclaw, Poland, September, 1988.

"Crack Initiation and Growth in Polymers Due to Radiation," Materials Science And Engineering Society, Prague, Czechoslovakia, October, 1988.

"Fracto-Emission as a Probe of Failure Mechanisms", Macromolecular Chemistry Institute, Prague, Czechoslovakia, October, 1988.

"Fracto-Emission from Polymers and Interfaces," 3M Adhesion Technical Forum, November, 1988.

"The Emission of Particles from Deformation and Fracture of Composites," McDonnell Douglas Corporation, November, 1988.

"Fracto-Emission from Interfaces and Composites," DOW Chemical Co., January, 1989.

"Fracto-Emission from Polymers and Interfaces", Boeing Co, January, 1989.

"Fracto-Emission from Cohesive and Adhesive Failure of Materials", Materials Science Dept. U. of Michigan, March, 1989.

"Fracto-Emission from Interfacial Failure", Symposium on Adhesion, Materials Research Society, San Diego, April, 1989.

"Fracto-Emission from Elastomers", Frontiers in Elastomer Science Symposium, ACS, Mexico City, May, 1989.

"Fracto-Emission Accompanying Adhesive Failure", Symposium on Adhesion, ACS, Seattle, June, 1989.

"Fracto-Emission from Insulators and Interfaces", International Conference on Fracture, Irsee, Germany, June, 1989.

CONTRIBUTED PRESENTATIONS

"Emission of Atoms and Molecules from Fracture of Inorganic Single Crystals," American Ceramics Society, Pittsburgh, April, 1987.

"Neutral Atom and Molecule Emission from the Fracture of Alkali Silicate Glasses, American Ceramics Society, Pittsburgh, April, 1987.

"The Production of Free Charge Carriers During the Fracture of Single Crystal Silicon," Conference on Atomic & Molecular Processing of Electronic and Ceramic Materials, U. Washington, August, 1987.

"Excimer Laser Induced Damage in Stressed Polyimide Films," MRS Symposium on Fundamentals of Beam-Solid Interactions and Transient Processing, Boston, November, 1987.

"Fracto-Emission From Polymers and Interfaces," MRS Symposium on Polymer Surfaces, Interfaces, and Adhesion, Boston, November, 1987.

"The Interaction of Excimer Laser Ultraviolet Radiation with Kapton-H Under Mechanical Stress," American Vacuum Society, Anaheim, November, 1987.

"Fracto-Emission from Fused Silica and Sodium Silicate Glasses," American Vacuum Society, Anaheim, November, 1987.

"The Production of Free Charge Carriers During the Fracture of Single Crystal Silicon," American Physical Society, New Orleans, March, 1988.

"The Interaction of Excimer Laser UV Radiation with Polymers Under Mechanical Stress," American Physical Society, New Orleans, March, 1988.

"The Emission of Molecular Species from the Fracture of Epoxy, American Physical Society, New Orleans, March, 1988.

"Emission of Gases and Vapors Upon Fracture of Obsidian," (with F. Freund and S. Chang, NASA-Ames) 19th Lunar and Planetary Science Conference, Houston, March, 1988.

"The Production of Free Charge Carriers During the Fracture of Single Crystal Silicon," American Ceramics Society, Cincinnati, May, 1988.

"The Emission of Neutral Atoms and Molecules from the Fracture of Fused Silica and Alkali Silicates," American Ceramics Society, Cincinnati, May, 1988.

"The Interaction of UV Excimer Laser Light with Sodium Trisilicate Glass," American Vacuum Society, Atlanta, October, 1988.

"The Emission of Charged Particles and Photons from the Fracture of Insulators," American Vacuum Society, Atlanta, October, 1988.

"The Interaction of UV Excimer Laser Radiation with Sodium Trisilicate Glass," Materials Research Society Symposium on Laser and Particle Beam Chemical Processes on Surfaces, Boston, November, 1988.

"The Time Dependence of Photon Emission During Fracture: Evidence for Chaos," American Physical Society March Meeting (Materials Physics Topical Conference on Breakdown in Materials), St. Louis, March, 1989.

"The Emission of Particles Accompanying the Adhesive Failure of Metals from Inorganic Substrates," American Physical Society March Meeting, St. Louis, March, 1989.

"The Emission of Particles Accompanying the Failure of Embedded Interfaces," American Physical Society March Meeting, St. Louis, March, 1989.

"UV Excimer Laser Radiation Interactions with Sodium Trisilicate Glass," American Ceramics Society, Indianapolis, April, 1989.

"Positive Ion Emission from Fused Silica," American Ceramics Society, Indianapolis, April, 1989.

PUBLICATIONS:

J. T. Dickinson, L. C. Jensen, and M. R. McKay, "Neutral Molecule Emission from the Fracture of Crystalline MgO," *J. Vac. Sci. Technol. A* **5**, 1162 (1987).

J. T. Dickinson, K. Tonyali, M. L. Klakken, and L. C. Jensen, "Crack Initiation and Crack Growth in Polymers Induced by Electron Bombardment," *J. Vac. Sci. Technol. A* **5**, 1076 (1987).

A. S. Crasto, R. Corey, J. T. Dickinson, R. V. Subramanian, and Y. Eckstein, "Correlation of Photon and Acoustic Emission with Failure Events in Model Composites," *Composites Sci. & Technol.* **30**, 35 (1987).

R. Michael, S. Frank, D. Stulik, and J. T. Dickinson, "Changes in Surface Morphology and Microcrack Initiation in Polymers under Simultaneous Exposure to Stress and Fast Atom Bombardment," in *Influence of Radiation on Material Properties Part II*, ASTM Special Technical Publication STP 956, edited by F. A. Garner, C. H. Henager, and N. Igata, (American Society for Testing and Materials, Philadelphia, 1987), pp. 682-687.

J. T. Dickinson, L. C. Jensen, and S. Bhattacharya, "Fracto-emission from Neat Epoxy Resin" (invited review article), in *Die Makromolekulare Chemie: Macromolecular Symposia* **7**, 129 (1987).

M. A. Loudiana, J. T. Dickinson, A. Schmid, and E. J. Ashley, "Electron Enhanced Sorption of Fluorine by Silver Surfaces," *Appl. Surf. Sci.* **28**, 311 (1987).

S. C. Langford, J. T. Dickinson, and L. C. Jensen, "Simultaneous Measurements of the Electron and Photon Emission Accompanying Fracture of Single Crystal MgO," *J. Appl. Phys.* **62**, 1437 (1987).

J. T. Dickinson and L. C. Jensen, "Fracto-Emission from Polymers, Crystals, and Interfaces," *Proceedings of The International Society for Optical Engineering (SPIE): Fluorescence Detection I* **743**, 68 (1987).

M. Guardalben, A. Schmid, M. Loudiana, and J. T. Dickinson, "Photothermal Analysis if Synergistic Radiation Effects in ThF₄ Optical Thin Films," *Phys. Rev. B* **35**, 4026 (1987).

J. T. Dickinson and E. E. Donaldson, "Autographs from Peeling Pressure Sensitive Adhesives: Direct Recording of Fracture Induced Photon Emission," *J. Adhesion* **24**, 199 (1987).

J. T. Dickinson and M. A. Loudiana, "Radiation Induced Damage of Optical Coatings", *Proceedings of the ACS Division of Polymeric Materials: Science and Engineering* **56**, 680 (1987).

J. T. Dickinson, "Fracto-Emission Accompanying the Deformation and Failure of Crosslinked Polymers and Interfaces", *Proceedings of the ACS Division of Polymeric Materials: Science and Engineering* **56**, 264 (1987).

J. T. Dickinson, "Bombardment Induced Crack Initiation and Crack Growth in Polymers and Polymer Surfaces," *Proceedings of the ACS Division of Polymeric Materials: Science and Engineering* **56**, 282 (1987).

J. T. Dickinson, L. C. Jensen, M. H. Miles, and R. Yee, "Fracto-Emission Accompanying Adhesive Failure Between Rocket Propellant Constituents," *J. Appl. Phys.* **62**, 2965 (1987).

- J. T. Dickinson, "Surface Interactions Relevant to Space Station Contamination Problems," in *A Study of Space Station Contamination Effects*, M. R. Torr, et al. editors, NASA Conference Publication 3002, (National Aeronautics and Space Agency, 1988), pp. 109-121.
- Ma Zhenyi, Fan Jiawen, and J. T. Dickinson, "Properties of the Photon Emission Accompanying the Peeling of a Pressure Sensitive Adhesive," *J. Adhesion* 25, 63 (1988).
- E. E. Donaldson, J. T. Dickinson, and S. K. Bhattacharya, "Production and Properties of Ejecta Produced by Fracture of Materials," *J. Adhesion* 25 281 (1988).
- S. C. Langford, D. L. Doering, and J. T. Dickinson, "The Production of Free Charge Carriers by Fracture of Single Crystal Silicon," *Phys. Rev. Lett.* 59, 2795 (1987).
- K. Tonyali, L. C. Jensen, and J. T. Dickinson, "The Interaction of Excimer Laser Ultraviolet Radiation with Kapton-H Under Mechanical Stress," *J. Vac. Sci. Technol. A* 6, 941 (1988).
- J. T. Dickinson, S. C. Langford, L. C. Jensen, J. Kelso, C. Pantano, and G. McVay, "Fracto-Emission from Fused Silica and Sodium Silicate Glasses," *J. Vac. Sci. and Technol. A* 6, 1084 (1988).
- J. P. Mathison, S. C. Langford, and J. T. Dickinson, "The Role of Damage in the Post Emission of Electrons from Cleavage Surfaces of Single Crystal LiF," *J. Appl. Phys.* 65(5), 1923-1928 (1989).
- S. C. Langford, J. T. Dickinson, and L. C. Jensen and L. R. Pederson, "Positive Ion Emission from the Fracture of Fused Silica," to appear in *J. Vac. Sci. Technol. A*.
- E. E. Donaldson, M. H. Miles, and J. T. Dickinson, "Electrical Charge Measurements on Ejecta from Impact Loading of Explosive Crystals," to appear in *J. Mater. Sci.*
- J. T. Dickinson and A. S. Crasto, "Fracto-Emission Accompanying the Deformation and Failure of Crosslinked Polymers and Interfaces", in *Cross-linked Polymers: Chemistry, Properties and Applications*, edited by R. A. Dickie, S. S. Labana, and R. S. Bauer, ACS Symposium Series 367 (American Chemical Society, Washington, D.C., 1988), pp. 145-168.
- J. T. Dickinson, M. A. Loudiana, and A. Schmid, "Consequences of Exposure of Optical Coatings to Reactive Gases and Energetic Particles," (Invited Review Article) in *Adhesion, Sealants and Coatings for Space and Health Environments*, edited by L. H. Lee, (Plenum Press, New York, 1988), pp. 467-475.
- J. T. Dickinson and L. C. Jensen, "Fracto-Emission from Polymers, Interfaces, and Single Crystals," to appear in *ASM Proceedings for 13th International Symposium for Testing and Failure Analysis*, Los Angeles, November, 1987).
- J. T. Dickinson, D. L. Doering, and S. C. Langford, "Electron Emission and Free Charge Carrier Production Due to Fracture of Single Crystal Silicon," in *Atomic and Molecular Processing of Electronic and Ceramic Materials: Preparation, Characterization, and Properties*, edited by I. H. Aksay et. al., (Materials Research Society, Pittsburgh, 1988), pp. 39-46.
- K. Tonyali, L. C. Jensen, and J. T. Dickinson, "Excimer Laser Induced Damage in Stressed Polyimide Films," *MRS Symposium Proceedings*, Vol. 100: *Fundamentals of Beam-Solid Interactions and Transient Thermal Processings*, edited by M. J. Aziz et. al., (Materials Research Society, Pittsburgh, 1988), pp. 665-670.

J. T. Dickinson, "Bombardment Induced Crack Initiation and Crack Growth in Polymers and Polymer Surfaces," (Invited Review Article) in *Adhesion, Sealants and Coatings for Space and Health Environments*, edited by L. H. Lee, (Plenum Press, New York, 1988), pp. 97-109.

R. Y. Yee, J. T. Dickinson, L. C. Jensen, and M. H. Miles, "Charge Emissions Accompanying Solid-Binder Interfacial Separation," *Proceedings of the JANNAF Workshop on Rocket Propellant Ignition*, 1988.

J. T. Dickinson, "Photon Emission from Peeling Pressure Sensitive Adhesives," review article, R. Menzel, ed., *SPIE Symposium Proceedings on Fluorescence Detection II*, 1988.

J. T. Dickinson and L. C. Jensen, "Radiation Induced Crack Initiation and Crack Growth in Polymers," to appear in *Proceedings of the 9th International Symposium on Exoelectron Emission and Applications*, Wroclaw, Poland, 1988.

S. C. Langford and J. T. Dickinson, "The Emission of Particles and Photons from the Fracture of Minerals and Inorganic Materials," Invited Review Article, *Structures and Active Sites of Minerals*, S. McKeever, editor, ACS Symposium Series Publication.

P. A. Eschbach, J. T. Dickinson, and L. R. Pederson, "Excimer Laser Ablation of Sodium Trisilicate Glass," to appear in *Materials Research Society Symposium B Proceedings*, 1989.

J. T. Dickinson, "Fracto-Emission from Adhesive Failure", Invited Review Article, to appear in *Advances in Adhesion*, edited by L. H. Lee, (Plenum Press, New York).

E. E. Donaldson and J. T. Dickinson, "Autographs from Peeling Fiber Reinforced Pressure Sensitive Adhesives: Correlation with Failure Mechanisms," to appear in *J. Adhesion*.

S. C. Langford, Ma Zhenyi, and J. T. Dickinson, "Photon emission as a probe of chaotic processes accompanying fracture", to appear in *J. Materials Research*.

K. C. Yoo, R. G. Rosemier, J. T. Dickinson, and S. C. Langford, "Anisotropy Effects in Fracto-Emission from MgF₂ Single Crystals," to appear in *Appl. Phys. Lett.*

J. T. Dickinson, "Fracto-Emission from Interfacial Failure", Invited Review Article, to appear in *MRS Proceedings of Symposium J*, 1989.

J. T. Dickinson, L. C. Jensen, H. Stacer, "Electron and Photon Emission from Fracture of Metal-Elastomer Interfaces," Invited Paper, submitted to *Journal of Rubber Chemistry and Technology*.

P. A. Eschbach, J. T. Dickinson, S. C. Langford, and L. R. Pederson, "The Interaction of UV Excimer Laser Light with Sodium Trisilicate," to appear in *J. Vac. Sci. Technol. A*. (1989).

E. E. Donaldson, J. T. Dickinson, and N. Wu, "Fracto-Emission Induced Electrical Breakdown in Vacuum," submitted to *IEEE Transactions Elec. Insulation*.

(DYN)

DISTRIBUTION LIST

Dr. R.S. Miller
Office of Naval Research
Code 432P
Arlington, VA 22217
(10 copies)

Dr. J. Pastine
Naval Sea Systems Command
Code 06R
Washington, DC 20362

Dr. Kenneth D. Hartman
Hercules Aerospace Division
Hercules Incorporated
Allegheny Ballistic Lab
P.O. Box 210
Washington, DC 21502

Mr. Otto K. Heinay
AFATL-DLJG
Elgin AFB, FL 32542

Dr. Merrill K. King
Atlantic Research Corp.
5390 Cherokee Avenue
Alexandria, VA 22312

Dr. R.L. Lou
Aerojet Strategic Propulsion Co.
Bldg. 05025 - Dept 5400 - MS 167
P.O. Box 15699C
Sacramento, CA 95813

Dr. R. Olsen
Aerojet Strategic Propulsion Co.
Bldg. 05025 - Dept 5400 - MS 167
P.O. Box 15699C
Sacramento, CA 95813

Dr. Randy Peters
Aerojet Strategic Propulsion Co.
Bldg. 05025 - Dept 5400 - MS 167
P.O. Box 15699C
Sacramento, CA 95813

Dr. D. Mann
U.S. Army Research Office
Engineering Division
Box 12211
Research Triangle Park, NC 27709-2211

Dr. L.V. Schmidt
Office of Naval Technology
Code 07CT
Arlington, VA 22217

JHU Applied Physics Laboratory
ATTN: CPIA (Mr. T.W. Christian)
Johns Hopkins Rd.
Laurel, MD 20707

Dr. R. McGuire
Lawrence Livermore Laboratory
University of California
Code L-324
Livermore, CA 94550

P.A. Miller
736 Leavenworth Street, #6
San Francisco, CA 94109

Dr. W. Moniz
Naval Research Lab.
Code 6120
Washington, DC 20375

Dr. K.F. Mueller
Naval Surface Weapons Center
Code R11
White Oak
Silver Spring, MD 20910

Prof. M. Nicol
Dept. of Chemistry & Biochemistry
University of California
Los Angeles, CA 90024

Mr. L. Roslund
Naval Surface Weapons Center
Code R10C
White Oak, Silver Spring, MD 20910

Dr. David C. Sayles
Ballistic Missile Defense
Advanced Technology Center
P.O. Box 1500
Huntsville, AL 35807

(DYN)

DISTRIBUTION LIST

Mr. R. Geisler
ATTN: DY/MS-24
AFRPL
Edwards AFB, CA 93523

Naval Air Systems Command
ATTN: Mr. Bertram P. Sobers
NAVAIR-320G
Jefferson Plaza 1, RM 472
Washington, DC 20361

R.B. Steele
Aerojet Strategic Propulsion Co.
P.O. Box 15699C
Sacramento, CA 95813

Mr. M. Stosz
Naval Surface Weapons Center
Code R10B
White Oak
Silver Spring, MD 20910

Mr. E.S. Sutton
Thiokol Corporation
Elkton Division
P.O. Box 241
Elkton, MD 21921

Dr. Grant Thompson
Morton Thiokol, Inc.
Wasatch Division
MS 240 P.O. Box 524
Brigham City, UT 84302

Dr. R.S. Valentini
United Technologies Chemical Systems
P.O. Box 50015
San Jose, CA 95150-0015

Dr. R.F. Walker
Chief, Energetic Materials Division
DRSMC-LCE (D), B-3022
USA ARDC
Dover, NJ 07801

Dr. Janet Wall
Code 012
Director, Research Administration
Naval Postgraduate School
Monterey, CA 93943

Director
US Army Ballistic Research Lab.
ATTN: DRXBR-IBD
Aberdeen Proving Ground, MD 21005

Commander
US Army Missile Command
ATTN: DRSMI-RKL
Walter W. Wharton
Redstone Arsenal, AL 35898

Dr. Ingo W. May
Army Ballistic Research Lab.
ARRADCOM
Code DRXBR - 1BD
Aberdeen Proving Ground, MD 21005

Dr. E. Zimet
Office of Naval Technology
Code 071
Arlington, VA 22217

Dr. Ronald L. Derr
Naval Weapons Center
Code 389
China Lake, CA 93555

T. Boggs
Naval Weapons Center
Code 389
China Lake, CA 93555

Lee C. Estabrook, P.E.
Morton Thiokol, Inc.
P.O. Box 30058
Shreveport, Louisiana 71130

Dr. J.R. West
Morton Thiokol, Inc.
P.O. Box 30058
Shreveport, Louisiana 71130

Dr. D.D. Dillehay
Morton Thiokol, Inc.
Longhorn Division
Marshall, TX 75670

G.T. Bowman
Atlantic Research Corp.
7511 Wellington Road
Gainesville, VA 22065

(DYN)

DISTRIBUTION LIST

R.E. Shenton
Atlantic Research Corp.
7511 Wellington Road
Gainesville, VA 22065

Mike Barnes
Atlantic Research Corp.
7511 Wellington Road
Gainesville, VA 22065

Dr. Lionel Dickinson
Naval Explosive Ordnance
Disposal Tech. Center
Code D
Indian Head, MD 20340

Prof. J.T. Dickinson
Washington State University
Dept. of Physics 4
Pullman, WA 99164-2814

M.H. Miles
Dept. of Physics
Washington State University
Pullman, WA 99164-2814

Dr. T.F. Davidson
Vice President, Technical
Morton Thiokol, Inc.
Aerospace Group
110 North Wacker Drive
Chicago, Illinois 60606

Mr. J. Consaga
Naval Surface Weapons Center
Code R-16
Indian Head, MD 20640

Naval Sea Systems Command
ATTN: Mr. Charles M. Christensen
NAVSEA-62R2
Crystal Plaza, Bldg. 6, Rm 806
Washington, DC 20362

Mr. R. Beauregard
Naval Sea Systems Command
SEA 64E
Washington, DC 20362

Brian Wheatley
Atlantic Research Corp.
7511 Wellington Road
Gainesville, VA 22065

Mr. G. Edwards
Naval Sea Systems Command
Code 62R32
Washington, DC 20362

C. Dickinson
Naval Surface Weapons Center
White Oak, Code R-13
Silver Spring, MD 20910

Prof. John Deutch
MIT
Department of Chemistry
Cambridge, MA 02139

Dr. E.H. deButts
Hercules Aerospace Co.
P.O. Box 27408
Salt Lake City, UT 84127

David A. Flanigan
Director, Advanced Technology
Morton Thiokol, Inc.
Aerospace Group
110 North Wacker Drive
Chicago, Illinois 60606

Dr. L.H. Caveny
Air Force Office of Scientific
Research
Directorate of Aerospace Sciences
Bolling Air Force Base
Washington, DC 20332

W.G. Roger
Code 5253
Naval Ordnance Station
Indian Head, MD 20640

Dr. Donald L. Ball
Air Force Office of Scientific
Research
Directorate of Chemical &
Atmospheric Sciences
Bolling Air Force Base
Washington, DC 20332

(DYN)

DISTRIBUTION LIST

Dr. Anthony J. Matuszko
Air Force Office of Scientific Research
Directorate of Chemical & Atmospheric
Sciences
Bolling Air Force Base
Washington, DC 20332

Dr. Michael Chaykovsky
Naval Surface Weapons Center
Code R11
White Oak
Silver Spring, MD 20910

J.J. Rocchio
USA Ballistic Research Lab.
Aberdeen Proving Ground, MD 21005-5066

G.A. Zimmerman
Aerojet Tactical Systems
P.O. Box 13400
Sacramento, CA 95813

B. Swanson
INC-4 MS C-346
Los Alamos National Laboratory
Los Alamos, New Mexico 87545

Dr. James T. Bryant
Naval Weapons Center
Code 3205B
China Lake, CA 93555

Dr. L. Rothstein
Assistant Director
Naval Explosives Dev. Engineering Dept.
Naval Weapons Station
Yorktown, VA 23691

Dr. M.J. Kamlet
Naval Surface Weapons Center
Code R11
White Oak, Silver Spring, MD 20910

Dr. Henry Webster, III
Manager, Chemical Sciences Branch
ATTN: Code 5063
Crane, IN 47522

Dr. A.L. Slafkosky
Scientific Advisor
Commandant of the Marine Corps
Code RD-1
Washington, DC 20380

Dr. H.G. Adolph
Naval Surface Weapons Center
Code R11
White Oak
Silver Spring, MD 20910

U.S. Army Research Office
Chemical & Biological Sciences
Division
P.O. Box 12211
Research Triangle Park, NC 27709

G. Butcher
Hercules, Inc.
MS X2H
P.O. Box 98
Magna, Utah 84044

W. Waesche
Atlantic Research Corp.
7511 Wellington Road
Gainesville, VA 22065

Dr. John S. Wilkes, Jr.
FJSRL/NC
USAF Academy, CO 80840

Dr. H. Rosenwasser
AIR-320R
Naval Air Systems Command
Washington, DC 20361

Dr. Joyce J. Kaufman
The Johns Hopkins University
Department of Chemistry
Baltimore, MD 21218

Dr. A. Nielsen
Naval Weapons Center
Code 385
China Lake, CA 93555

(DYN)

DISTRIBUTION LIST

K.D. Pae
High Pressure Materials Research Lab.
Rutgers University
P.O. Box 909
Piscataway, NJ 08854

Dr. John K. Dienes
T-3, B216
Los Alamos National Lab.
P.O. Box 1663
Los Alamos, NM 87544

A.N. Gent
Institute Polymer Science
University of Akron
Akron, OH 44325

Dr. D.A. Shockey
SRI International
333 Ravenswood Ave.
Menlo Park, CA 94025

Dr. R.B. Kruse
Morton Thiokol, Inc.
Huntsville Division
Huntsville, AL 35807-7501

G. Butcher
Hercules, Inc.
P.O. Box 98
Magna, UT 84044

W. Waesche
Atlantic Research Corp.
7511 Wellington Road
Gainesville, VA 22065

Dr. R. Bernecker
Naval Surface Weapons Center
Code R13
White Oak
Silver Spring, MD 20910

Prof. Edward Price
Georgia Institute of Tech.
School of Aerospace Engineering
Atlanta, GA 30332

J.A. Birkett
Naval Ordnance Station
Code 5253K
Indian Head, MD 20640

Prof. R.W. Armstrong
University of Maryland
Dept. of Mechanical Engineering
College Park, MD 20742

Herb Richter
Code 385
Naval Weapons Center
China Lake, CA 93555

J.T. Rosenberg
SRI International
333 Ravenswood Ave.
Menlo Park, CA 94025

G.A. Zimmerman
Aerojet Tactical Systems
P.O. Box 13400
Sacramento, CA 95813

Prof. Kenneth Kuo
Pennsylvania State University
Dept. of Mechanical Engineering
University Park, PA 16802

T.L. Boggs
Naval Weapons Center
Code 3891
China Lake, CA 93555

(DYN)

DISTRIBUTION LIST

Dr. C.S. Coffey
Naval Surface Weapons Center
Code R13
White Oak
Silver Spring, MD 20910

D. Curran
SRI International
333 Ravenswood Avenue
Menlo Park, CA 94025

E.L. Throckmorton
Code SP-2731
Strategic Systems Program Office
Crystal Mall #3, RM 1048
Washington, DC 23076

Dr. R. Martinson
Lockheed Missiles and Space Co.
Research and Development
3251 Hanover Street
Palo Alto, CA 94304

C. Gotzmer
Naval Surface Weapons Center
Code R-11
White Oak
Silver Spring, MD 20910

G.A. Lo
3251 Hanover Street
B204 Lockheed Palo Alto Research Lab
Palo Alto, CA 94304

R.A. Schapery
Civil Engineering Department
Texas A&M University
College Station, TX 77843

J.M. Culver
Strategic Systems Projects Office
SSPO/SP-2731
Crystal Mall #3, RM 1048
Washington, DC 20376

Prof. G.D. Duvall
Washington State University
Department of Physics
Pullman, WA 99163

Dr. E. Martin
Naval Weapons Center
Code 3858
China Lake, CA 93555

Dr. M. Farber
135 W. Maple Avenue
Monrovia, CA 91016

W.L. Elban
Naval Surface Weapons Center
White Oak, Bldg. 343
Silver Spring, MD 20910

G.E. Manser
Morton Thiokol
Wasatch Division
P.O. Box 524
Brigham City, UT 84302

R.G. Rosemeier
Brimrose Corporation
7720 Belair Road
Baltimore, MD 20742

Administrative Contracting
Officer (see contract for
address)
(1 copy)

Director
Naval Research Laboratory
Attn: Code 2627
Washington, DC 20375
(6 copies)

Defense Technical Information Center
Bldg. 5, Cameron Station
Alexandria, VA 22314
(12 copies)

Dr. Robert Polvani
National Bureau of Standards
Metallurgy Division
Washington, D.C. 20234

Dr. Y. Gupta
Washington State University
Department of Physics
Pullman, WA 99163